

*Research Project Number SPR-P1(13)
NDOR Sponsoring Agency Code RHE-08*

CONCEPTUAL DEVELOPMENT OF AN IMPACT-ATTENUATION SYSTEM FOR INTERSECTING ROADWAYS

Submitted by

Joseph G. Putjenter, M.S.M.E., E.I.T.
Former Graduate Research Assistant

Robert W. Bielenberg, M.S.M.E., E.I.T.
Research Associate Engineer

Ronald K. Faller, Ph.D., P.E.
Research Associate Professor
MwRSF Director

John D. Reid, Ph.D.
Professor

MIDWEST ROADSIDE SAFETY FACILITY

Nebraska Transportation Center
University of Nebraska-Lincoln
130 Whittier Research Center
2200 Vine Street
Lincoln, Nebraska 68583-0853
(402) 472-0965

Submitted to

NEBRASKA DEPARTMENT OF ROADS

1500 Nebraska Highway 2
Lincoln, Nebraska 68502

MwRSF Research Report No. TRP-03-312-15

September 30, 2015

TECHNICAL REPORT DOCUMENTATION PAGE

1. Report No. TRP-03-312-15	2.	3. Recipient's Accession No.	
4. Title and Subtitle Conceptual Development of an Impact-Attenuation System for Intersecting Roadways		5. Report Date September 30, 2015	
		6.	
7. Author(s) Putjenter, J.G., Bielenberg, R.W., Faller, R.K., and Reid, J.D.		8. Performing Organization Report No. TRP-03-312-15	
9. Performing Organization Name and Address Midwest Roadside Safety Facility (MwRSF) Nebraska Transportation Center University of Nebraska-Lincoln 130 Whittier Research Center 2200 Vine Street Lincoln, Nebraska 68583-0853		10. Project/Task/Work Unit No.	
		11. Contract © or Grant (G) No. SPR-P1(13)	
12. Sponsoring Organization Name and Address Nebraska Department of Roads 1500 Nebraska Highway 2 Lincoln, Nebraska 68502		13. Type of Report and Period Covered Final Report: 2012 – 2015	
		14. Sponsoring Agency Code RHE-08	
15. Supplementary Notes Prepared in cooperation with U.S. Department of Transportation, Federal Highway Administration.			
16. Abstract (Limit: 200 words) <p>Longitudinal barriers are commonly used to shield hazards, including stiff bridge rail ends and slopes. In some locations, a secondary roadway intersects the primary roadway within the guardrail's length-of-need (LON). Some intersections may have as little as 15 ft (4.6 m) between the intersection and beginning of the bridge railing, which require short-radius guardrail systems. One short-radius guardrail system has passed several crash tests under AASHTO <i>Manual for Assessing Safety Hardware</i> (MASH) standards.</p> <p>Site conditions provided by the Nebraska Department of Roads were used to determine the constraints for a new safety treatment for intersecting roadways and include intersection radii, bridge railing offset distances, and clear zone distances. An examination of the site conditions determined that the bridge railing end should be treated as a hazard, as defined in the AASHTO <i>Roadside Design Guide</i>. The hazard would begin at the bridge railing end with a width extending to the clear zone. Several design concepts were developed to treat these situations with a preference on using existing technologies that could be adapted for this hazard scenario.</p> <p>Fifteen concepts were brainstormed, with three considered for further analysis and evaluation. These concepts included net attenuation/end terminal, inertial barrel array/end terminal, and a bullnose with a secondary energy absorber inside of it. All three systems were capable of stopping a vehicle in the space available, but only the net attenuation/end terminal concept was considered likely to accommodate the site conditions using a moderate slope behind the system. Four dynamic bogie tests and two static tests were performed on potential net attenuators to evaluate their use as energy absorbers in the preferred design concept. Recommendations for further development of the net attenuation system were provided.</p>			
17. Document Analysis/Descriptors Highway Safety, Crash Test, Roadside Appurtenances, Inertial Barrel, Compliance Test, MASH, Component Test, Crash Cushion, Guardrail End Terminal, Short-Radius, Net Attenuation, and Energy Absorber		18. Availability Statement No restrictions. Document available from: National Technical Information Services, Springfield, Virginia 22161	
19. Security Class (this report) Unclassified	20. Security Class (this page) Unclassified	21. No. of Pages 534	22. Price

DISCLAIMER STATEMENT

This report was completed with funding from the Federal Highway Administration, U.S. Department of Transportation as well as the Nebraska Department of Roads. The contents of this report reflect the views and opinions of the authors who are responsible for the facts and the accuracy of the data presented herein. The contents do not necessarily reflect the official views or policies of the Nebraska Department of Roads or the Federal Highway Administration, U.S. Department of Transportation. This report does not constitute a standard, specification, regulation, product endorsement, or an endorsement of manufacturers.

UNCERTAINTY OF MEASUREMENT STATEMENT

The Midwest Roadside Safety Facility (MwRSF) has determined the uncertainty of measurements for several parameters involved in standard full-scale crash testing and non-standard testing of roadside safety features. Information regarding the uncertainty of measurements for critical parameters is available upon request by the sponsor and the Federal Highway Administration. Test nos. IRAS-1 – IRAS-2 and IRA-1 – IRA-4 were non-certified component tests conducted for research and development purposes only.

INDEPENDENT APPROVING AUTHORITY

The Independent Approving Authority (IAA) for the data contained herein was Ms. Karla Lechtenberg, Research Associate Engineer.

ACKNOWLEDGEMENTS

The authors wish to acknowledge several sources that made a contribution to this project: (1) the Nebraska Department of Roads for sponsoring this project; (2) MwRSF personnel for constructing the systems and conducting the crash tests; and (3) Impact Absorption Inc. for providing net attenuation materials.

Acknowledgement is also given to the following individuals who made a contribution to the completion of this research project.

Midwest Roadside Safety Facility

J.C. Holloway, M.S.C.E., E.I.T., Test Site Manager
K.A. Lechtenberg, M.S.M.E., E.I.T., Research Associate Engineer
S.K. Rosenbaugh, M.S.C.E., E.I.T., Research Associate Engineer
J.D. Schmidt, Ph.D., P.E., Research Assistant Professor
C.S. Stolle, Ph.D., Research Assistant Professor
A.T. Russell, B.S.B.A., Shop Manager
K.L. Krenk, B.S.M.A., Maintenance Mechanic
S.M. Tighe, Laboratory Mechanic
D.S. Charroin, Laboratory Mechanic
Undergraduate and Graduate Research Assistants

Nebraska Department of Roads

Jodi Gibson, Research Coordinator
Jim Knott, P.E., Roadway Design Engineer/Division Manager
Matt Neemann, Traffic Control Engineer
Mark Osborn, P.E., Secondary Roads Engineer
Amy Starr, P.E., Research Engineer
Phil TenHulzen, P.E., Design Standards Engineer
Dan Waddle, Traffic Engineer/Division Manager

Federal Highway Administration

John J. Perry, P.E., Safety/IPS Engineer

Impact Absorption

Michael Kempen, President

TABLE OF CONTENTS

TECHNICAL REPORT DOCUMENTATION PAGE	i
DISCLAIMER STATEMENT	ii
UNCERTAINTY OF MEASUREMENT STATEMENT	ii
INDEPENDENT APPROVING AUTHORITY.....	ii
ACKNOWLEDGEMENTS	iii
TABLE OF CONTENTS.....	iv
LIST OF FIGURES	ix
LIST OF TABLES	xviii
1 INTRODUCTION	1
1.1 Background and Project Statement.....	1
1.2 Research Objective	2
1.3 Scope.....	2
2 SHORT-RADIUS AND BULLNOSE.....	4
2.1 Introduction.....	4
2.2 Historical W-Beam Short-Radius Guardrail Systems.....	5
2.2.1 Systems Tested to NCHRP Report No. 230	5
2.2.2 System Tested to AASHTO <i>Guidance Specifications for Bridge Railings</i> . 15	
2.3 Short-Radius Systems Tested to NCHRP Report No. 350 and MASH.....	16
2.3.1 TTI Thrie-Beam Short-Radius	17
2.3.2 MwRSF Short-Radius Guardrail System – R&D Project.....	19
2.4 Bullnose Systems Tested Prior to NCHRP Report No. 230	23
2.5 Bullnose Systems Tested to NCHRP Report No. 350	24
2.6 Current Best Practices – Short-Radius Guardrail Systems	26
2.6.1 FHWA Technical Memorandum T5040.32.....	26
2.6.2 Roadside Design Guide 4 th Ed.	26
2.6.3 TTI Modified Yuma County System at TL-2 Acceptance	27
2.6.4 Best Practices for Barrier Protection of Bridge Ends (2014).....	27
3 END TERMINALS	32
4 CRASH CUSHIONS	36
5 TRUCK- AND TRAILER-MOUNTED ATTENUATORS.....	41
6 NET AND CABLE ATTENUATION SYSTEMS.....	44
7 DESIGN CRITERIA	48
7.1 Design Space Requirements	48

7.2 Impact Conditions Determined By Length of Need	49
7.3 Line of Sight Considerations	52
7.4 Preference for Existing Technologies	54
7.5 Other Considerations	54
8 DESIGN CONCEPTS	55
8.1 Concept A – Net Attenuator/End Terminal or Crash Cushion	56
8.2 Concept B – Dual Bullnose.....	58
8.3 Concept C – Bullnose with Sand Barrels.....	59
8.4 Concept D - Bullnose.....	62
8.5 Concept E – Two End Terminals with Secondary Energy-Absorbing Guardrail.....	63
8.6 Concept F – Two Disconnected Guardrails	64
8.7 Concept G – Cable or Net Attached Behind Two End Terminals	66
8.8 Concept H – Energy Absorbers Between Impact Panel and Portable Concrete Barriers	67
8.9 Concept I – Energy Absorbers, Rails, and Posts	69
8.10 Concept J – Rubber Cylinders Between Impact Panel and Restoring Barrier.....	70
8.11 Concept K – Sand Barrels with End Terminal or Crash Cushion.....	71
8.12 Concept L – TMA(s) Between Two End Terminals.....	72
8.13 Concept M - TMA(s) or Crash Cushion(s) with End Terminal.....	74
8.14 Concept N – TMA between End Terminal and Bullnose	75
8.15 Concept O – Bullnose with Net Attenuator	76
9 RANKING AND SELECTION OF DESIGN CONCEPTS	79
10 QUASI-STATIC TAPE COMPONENT TEST SETUP AND CONDITIONS	81
10.1 Purpose.....	81
10.2 Scope.....	81
10.3 Equipment and Instrumentation.....	81
10.3.1 Test Jig.....	82
10.3.2 Digital Photography	84
10.3.3 Load Cells	84
10.4 Data Processing.....	84
11 QUASI-STATIC TAPE COMPONENT TESTING RESULTS AND CONCLUSIONS	85
11.1 Results.....	85
11.1.1 Test No. IRAS-1	85
11.1.2 Test No. IRAS-2	88
11.2 Discussion	90
12 NET ATTENUATOR COMPONENT TESTING SETUP AND CONDITIONS	91
12.1 Purpose.....	91
12.2 Scope.....	91
12.3 Equipment and Instrumentation.....	92
12.3.1 Vehicle Tow and Guidance System.....	92
12.3.2 Bogie	92
12.3.3 Accelerometers	93
12.3.4 Rate Transducers.....	95

12.3.5 Speed Trap	96
12.3.6 Digital Photography	96
12.4 Data Processing.....	97
13 DESIGN DETAILS - TEST NOS. IRA-1 AND IRA-2	102
14 NET ATTENUATOR COMPONENT TEST NO. IRA-1	126
14.1 Test No. IRA-1.....	126
14.2 Weather Conditions	126
14.3 Test Description	126
14.4 System Damage	127
14.5 Vehicle Damage.....	128
14.6 Occupant Risk.....	128
14.7 Discussion	129
15 NET ATTENUATOR COMPONENT TEST NO. IRA-2	144
15.1 Test No. IRA-2.....	144
15.2 Weather Conditions	144
15.3 Test Description	144
15.4 System Damage	145
15.5 Vehicle Damage.....	146
15.6 Occupant Risk.....	146
15.7 Discussion	147
16 DESIGN DETAILS - TEST NOS. IRA-3 AND IRA-4	159
17 NET ATTENUATOR COMPONENT TEST NO. IRA-3	183
17.1 Test No. IRA-3.....	183
17.2 Weather Conditions	183
17.3 Test Description	184
17.4 System Damage	184
17.5 Vehicle Damage.....	185
17.6 Occupant Risk.....	185
17.7 Discussion	186
18 NET ATTENUATOR COMPONENT TEST NO. IRA-4	197
18.1 Test No. IRA-4.....	197
18.2 Weather Conditions	197
18.3 Test Description	197
18.4 System Damage	198
18.5 Vehicle Damage.....	199
18.6 Occupant Risk.....	199
18.7 Discussion	200
19 EVALUATION OF NET ATTENUATOR PERFORMANCE	213
20 DEVELOPMENT OF NET ATTENUATOR MODEL	217
20.1 Methodology	217

20.2 Bogie Model.....	217
20.3 Modified Dragnet Vehicle Arresting Barrier Model	218
20.3.1 Energy Absorbers.....	218
20.3.2 Cable Net	220
20.3.3 Cable Spreaders	220
20.3.4 Net End Conditions.....	221
21 SIMULATION OF TEST NOS. IRA-3 AND IRA-4.....	224
21.1 Correlation Between Baseline Model and Full-Scale Crash Test No. IRA-4.....	224
21.1.1 Graphical Comparison	225
21.1.2 Velocity Profiles	228
21.1.3 Occupant Risk	228
21.1.4 Discussion of Test No. IRA-4.....	229
21.2 Correlation Between Baseline Model and Full-Scale Crash Test No. IRA-3.....	230
21.2.1 Graphical Comparison	231
21.2.2 Velocity Profiles	234
21.2.3 Occupant Risk.....	234
21.2.4 Discussion of Test No. IRA-3.....	235
21.3 Discussion.....	236
22 NET ATTENUATOR ANALYSIS	238
22.1 Methodology.....	238
22.2 Comparison of Original and New Analytical Technique	244
22.3 Analysis of Test Nos. IRA-3 and IRA-4.....	246
22.3.1 Analysis of Test No. IRA-3	247
22.3.2 Analysis of Test No. IRA-4	250
22.4 Discussion.....	252
23 IMPACT ANALYSIS FOR INERTIA BARRIERS	254
23.1 Inertia Barrier Analysis for Head-On Impacts.....	254
23.2 Analyzing Inertia Barrier Impacts - General Form.....	257
23.2.1 Mass Distribution.....	260
23.2.1.1 Ideal Mass Distribution.....	263
23.2.1.2 Mass Distribution by Linear Approximation.....	265
23.2.1.3 Mass Distribution by Partial Areas Approximation	268
23.2.2 Comparison of Mass Distribution Methods.....	270
23.2.3 Spreadsheet Procedure.....	271
23.2.4 Large Sand Barrel Array Example Calculations.....	273
24 COMBINED END TERMINAL AND SAND BARREL IMPACTS.....	277
24.1 Analysis.....	277
24.2 Limitations of Procedure.....	283
25 WIDE BULLNOSE CONCEPT – ANALYTICAL MODEL.....	284
25.1 Bullnose with Secondary Energy Absorption.....	284
25.2 Determine Average Resistive Force of Bullnose.....	286
25.3 Combined Bullnose and Sand Barrel System	288
25.4 Bullnose and Net Attenuator System	288

25.5	Limitations of procedure.....	289
26	POTENTIAL LAYOUTS	290
26.1	Introduction.....	290
26.2	Concept A – Net Attenuator/End Terminal or Crash Cushion	290
26.2.1	Estimating Net Widths.....	290
26.2.2	Predicting Deflections with MASH Vehicles	291
26.2.3	Potential Layout for Net Attenuator Concept	293
26.2.4	Net Attenuator Concept Discussion.....	294
26.3	Concept K – Sand Barrels with End Terminal or Crash Cushion.....	295
26.3.1	Potential Layouts for Sand Barrel Concept	295
26.3.1.1	Barrel Layout with Standard Spacing	296
26.3.1.2	Barrel Layout with Mixed Spacing.....	298
26.3.2	Grading Requirements	299
26.3.3	Sand Barrel Concept Discussion.....	300
26.4	Concept C and O – Bullnose with Secondary Energy Absorption	301
26.4.1	Concept O – Bullnose with Net Arrestor Potential Layout	301
26.4.2	Concept C – Bullnose with Sand Barrels Potential Layout	302
26.4.3	Grading Requirements	303
26.4.4	Combined Bullnose Concept Discussion.....	304
26.5	Concept Recommendations Summary	305
27	SUMMARY, CONCLUSIONS, AND RECOMMENDATIONS	307
27.1	Net Attenuator with End Terminal or Crash Cushion	307
27.2	Sand Barrels with End Terminal or Crash Cushion.....	312
27.3	Bullnose with Secondary Energy Absorption.....	312
27.4	Recommendations for Future Research	314
28	REFERENCES	316
29	APPENDICES	321
Appendix A.	Material Specifications	322
Appendix B.	Accelerometer and Rate Transducer Data Plots, Test No. IRA-1	325
Appendix C.	Accelerometer and Rate Transducer Data Plots, Test No. IRA-2	362
Appendix D.	Accelerometer and Rate Transducer Data Plots, Test No. IRA-3	395
Appendix E.	Accelerometer and Rate Transducer Data Plots, Test No. IRA-4	428
Appendix F.	Accelerometer Data Plots, Baseline Simulation	465
Appendix G.	Potential Layout Analysis.....	478

LIST OF FIGURES

Figure 1. Washington W-Beam Short-Radius Guardrail System [9]	13
Figure 2. TTI W-Beam Short-Radius Guardrail System [10].....	14
Figure 3. Yuma County Short-Radius Guardrail System – Final Details [6, 28]	16
Figure 4. Final TTI Thrie-Beam Short-Radius Guardrail System [11]	18
Figure 5. Preliminary MwRSF Thrie-Beam Short-Radius Guardrail System [12-13]	21
Figure 6. Final MwRSF Thrie-Beam Short-Radius Guardrail System [15]	22
Figure 7. Required Bullnose Crash Tests According to NCHRP Report No. 350	25
Figure 8. Acceptable Short-Radius Guardrail System, FHWA Technical Memorandum [8]	29
Figure 9. Recommended Short-Radius Guardrail System, TTI NCHRP Report No. 350 TL-2 System [26]	30
Figure 10. Acceptable Short-Radius Guardrail Designs, TTI NCHRP Report No. 350 TL-2 System [26]	31
Figure 11. Example Intersection [44]	48
Figure 12. Site Constraints for New Impact Attenuation System.....	49
Figure 13. (a) Approach Guardrail with Variables [1], (b) Intersection Near Bridge with Variables	51
Figure 14. Clear Sight Distance Triangles for 4-Leg Stop-Controlled Intersections [45].....	53
Figure 15. Concept A - Net Attenuator/End Terminal or Crash Cushion	57
Figure 16. Concept B – Dual Bullnose	59
Figure 17. Concept C – Bullnose with Sand Barrels	61
Figure 18. Concept D - Bullnose	63
Figure 19. Concept E – Two End Terminals with Secondary Energy-Absorbing Guardrail	64
Figure 20. Concept F – Two Disconnected Guardrails.....	66
Figure 21. Concept G – Cable or Net Attached Behind Two End Terminals	67
Figure 22. Concept H – Energy Absorbers Between Impact Panel and Temporary Concrete Barriers.....	68
Figure 23. Concept I – Energy Absorbers, Rails, and Posts	70
Figure 24. Concept J – Rubber Cylinders Between Impact Panel and Restoring Barrier	71
Figure 25. Concept K – Sand Barrels with End Terminal	72
Figure 26. Concept L – Barrels, Crash Cushion, or TMA(s) Between Two End Terminals.....	73
Figure 27. Concept M - TMA(s) or Crash Cushion(s) with End Terminal	74
Figure 28. Concept N – TMA between End Terminal and Bullnose.....	76
Figure 30. Dagnet Energy Absorber.....	82
Figure 31. Component Testing Setup, Test Nos. IRAS-1 and IRAS-2	83
Figure 32. Tension Force vs. Time, Test No. IRAS-1	86
Figure 33. Energy Absorber Component Testing, Test No. IRAS-1	87
Figure 34. Tension Force vs. Time, Test No. IRAS-2.....	88
Figure 35. Energy Absorber Component Testing, Test No. IRAS-2.....	89
Figure 36. Pulling Force vs. Time Comparisons, Test Nos. IRAS-1 and IRAS-2	90
Figure 37. Rigid-Frame Bogie on Guidance Track	93
Figure 38. Camera Locations, Speeds, and Lens Settings, Test No. IRA-1	98
Figure 39. Camera Locations, Speeds, and Lens Settings, Test No. IRA-2	99
Figure 40. Camera Locations, Speeds, and Lens Settings, Test No. IRA-3	100
Figure 41. Camera Locations, Speeds, and Lens Settings, Test No. IRA-4	101
Figure 42. Bogie Test Installation, Test Nos. IRA-1 and IRA-2	103

Figure 43. 0 Deg. Central Impact, Test No. IRA-1.....	104
Figure 44. 0 Deg. Offset Impact, Test No. IRA-2	105
Figure 45. Anchor Bracket Layout, Test Nos. IRA-1 and IRA-2.....	106
Figure 46. Cable Net Assembly, Test Nos. IRA-1 and IRA-2	107
Figure 47. BCT Cable Detail, Test Nos. IRA-1 and IRA-2.....	108
Figure 48. End Attachment Components, Test Nos. IRA-1 and IRA-2	109
Figure 49. Energy Absorbers and Anchors, Test Nos. IRA-1 and IRA-2	110
Figure 50. Energy Absorber and Connection Components, Test Nos. IRA-1 and IRA-2.....	111
Figure 51. Energy Absorber Connection Components, Test Nos. IRA-1 and IRA-2	112
Figure 52. Eye Nuts and Shackles, Test Nos. IRA-1 and IRA-2.....	113
Figure 53. Anchor Plate Assembly, Test Nos. IRA-1 and IRA-2.....	114
Figure 54. Anchor Plate and Hoop, Test Nos. IRA-1 and IRA-2.....	115
Figure 55. Bogie Head Assembly, Test Nos. IRA-1 and IRA-2.....	116
Figure 56. Bogie Head Components, Test Nos. IRA-1 and IRA-2	117
Figure 57. Bogie Head Cover Plate, Flat Pattern, Test Nos. IRA-1 and IRA-2	118
Figure 58. Wood Supporting Post and Base, Test Nos. IRA-1 and IRA-2.....	119
Figure 59. Fasteners, Test Nos. IRA-1 and IRA-2	120
Figure 60. Bill of Materials, Test Nos. IRA-1 and IRA-2	121
Figure 61. Test Installation, Test No. IRA-1	122
Figure 62. Test Installation, Test No. IRA-1	123
Figure 63. Test Installation, Test No. IRA-2	124
Figure 64. Test Installation, Test No. IRA-2	125
Figure 65. Sequential Photographs, Test No. IRA-1	131
Figure 66. Additional Sequential Photographs, Test No. IRA-1	132
Figure 67. Additional Sequential Photographs, Test No. IRA-1	133
Figure 68. Additional Sequential Photographs, Test No. IRA-1	134
Figure 69. Additional Sequential Photographs, Test No. IRA-1	135
Figure 70. Additional Sequential Photographs, Test No. IRA-1	136
Figure 71. Documentary Photographs, Test No. IRA-1	137
Figure 72. Documentary Photographs, Test No. IRA-1	138
Figure 73. Impact Location, Test No. IRA-1	139
Figure 74. Vehicle Final Position and Trajectory Marks, Test No. IRA-1.....	140
Figure 75. System Damage, Test No. IRA-1	141
Figure 76. System Damage – Fractured Energy Absorber Tape, Test No. IRA-1	142
Figure 77. System Damage, Test No. IRA-1	143
Figure 78. Sequential Photographs, Test No. IRA-2	149
Figure 79. Additional Sequential Photographs, Test No. IRA-2	150
Figure 80. Additional Sequential Photographs, Test No. IRA-2	151
Figure 81. Additional Sequential Photographs, Test No. IRA-2	152
Figure 82. Additional Sequential Photographs, Test No. IRA-2	153
Figure 83. Impact Location, Test No. IRA-2.....	154
Figure 84. Vehicle Final Position and Trajectory Marks, Test No. IRA-2.....	155
Figure 85. System Damage, Test No. IRA-2	156
Figure 86. System Damage – Fractured Energy Absorber Tape, Test No. IRA-2	157
Figure 87. System and Vehicle Damage, Test No. IRA-2.....	158
Figure 88. Bogie Test Installation, Test Nos. IRA-3 and IRA-4	160
Figure 89. Offset Impact, 30 Deg. From Perpendicular, Test No. IRA-3	161

Figure 90. Center Impact, 0 Deg. From Perpendicular, Test No. IRA-4.....	162
Figure 91. Anchor Bracket Layout, Test Nos. IRA-3 and IRA-4.....	163
Figure 92. Cable Net Assembly, Test Nos. IRA-3 and IRA-4	164
Figure 93. BCT Cable Detail, Test Nos. IRA-3 and IRA-4.....	165
Figure 94. End Attachment Components, Test Nos. IRA-3 and IRA-4	166
Figure 95. Energy Absorbers and Anchors, Test Nos. IRA-3 and IRA-4	167
Figure 96. Energy Absorber and Connection Components, Test Nos. IRA-3 and IRA-4.....	168
Figure 97. Energy Absorber Connection Components, Test Nos. IRA-3 and IRA-4	169
Figure 98. Eye Nuts and Shackles, Test Nos. IRA-3 and IRA-4.....	170
Figure 99. Anchor Plate Assembly, Test Nos. IRA-3 and IRA-4.....	171
Figure 100. Anchor Plate and Hoop, Test Nos. IRA-3 and IRA-4.....	172
Figure 101. Bogie Head Assembly, Test Nos. IRA-3 and IRA-4.....	173
Figure 102. Bogie Head Components, Test Nos. IRA-3 and IRA-4	174
Figure 103. Bogie Head Cover Plate, Flat Pattern, Test Nos. IRA-3 and IRA-4	175
Figure 104. Wood Supporting Post and Base, Test Nos. IRA-3 and IRA-4.....	176
Figure 105. Fasteners, Test Nos. IRA-3 and IRA-4	177
Figure 106. Bill of Materials, Test Nos. IRA-3 and IRA-4	178
Figure 107. Test Installation, Test No. IRA-3	179
Figure 108. Test Installation, Test No. IRA-3	180
Figure 109. Test Installation, Test No. IRA-4	181
Figure 110. Test Installation, Test No. IRA-4	182
Figure 111. Sequential Photographs, Test No. IRA-3	188
Figure 112. Additional Sequential Photographs, Test No. IRA-3	189
Figure 113. Additional Sequential Photographs, Test No. IRA-3	190
Figure 114. Additional Sequential Photographs, Test No. IRA-3	191
Figure 115. Documentary Photographs, Test No. IRA-3	192
Figure 116. Impact Location, Test No. IRA-3.....	193
Figure 117. Vehicle Final Position and Trajectory Marks, Test No. IRA-3.....	194
Figure 118. System Damage, Test No. IRA-3	195
Figure 119. System and Vehicle Damage – Fractured Support Post, Test No. IRA-3.....	196
Figure 120. Sequential Photographs, Test No. IRA-4	202
Figure 121. Additional Sequential Photographs, Test No. IRA-4	203
Figure 122. Additional Sequential Photographs, Test No. IRA-4	204
Figure 123. Additional Sequential Photographs, Test No. IRA-4	205
Figure 124. Documentary Photographs, Test No. IRA-4	206
Figure 125. Impact Location, Test No. IRA-4.....	207
Figure 126. Vehicle Final Position and Trajectory Marks, Test No. IRA-4.....	208
Figure 127. System Damage, Test No. IRA-4	209
Figure 128. System Damage, Test No. IRA-4.....	210
Figure 129. System Damage, Test No. IRA-4.....	211
Figure 130. System Damage, Test No. IRA-4.....	212
Figure 131. Modified Dragnet Vehicle Arresting Barrier, Test No. IRA-4	217
Figure 132. Bogie Finite Element Model	218
Figure 133. Force vs. Deflection of Energy Absorbers	219
Figure 134. Connection of Cable Spreaders: (a) Actual and (b) Simulation	221
Figure 135. Energy Absorber and Net Connection: (a) Actual and (b) Simulation	222
Figure 136. Final Model Setup	223

Figure 137. Simulation of Test No. IRA-4	224
Figure 138. Test No. IRA-4 and LS-DYNA Simulation Sequentials.....	226
Figure 139. Test No. IRA-4 and LS-DYNA Simulation Sequentials.....	227
Figure 140. Velocity Profiles – Baseline Simulation and Test No. IRA-4.....	228
Figure 141. Simulation of Test No. IRA-3	230
Figure 142. Test No. IRA-3 and LS-DYNA Simulation Sequentials.....	232
Figure 143. Test No. IRA-3 and LS-DYNA Simulation Sequentials.....	233
Figure 144. Velocity Profiles – Baseline Simulation and Test No. IRA-3.....	234
Figure 145. Net Attenuator Analytical Method and FBD setup	239
Figure 146. Free-Body-Diagram of the Vehicle	241
Figure 147. Effective Length of Versions 1 and 2.....	247
Figure 148. Analytical Solution for Test No. IRA-3	248
Figure 149. Analytical Model, Angled Simulation, and Test No. IRA-3 Accelerations.....	249
Figure 150. Analytical Solution for Test No. IRA-4	251
Figure 151. Analytical Model, Baseline Simulation, and Test No. IRA-4 Accelerations.....	252
Figure 152. Typical Sand Barrel System [1]	254
Figure 153. Large Sand Barrel Array	258
Figure 154. Effective Masses of Each Impacted Barrel	258
Figure 155. Impact Order and Deceleration Distance	259
Figure 156. Length of Contact Description	259
Figure 157. Mass Distribution Between Impact Events	260
Figure 158. Details of Partially Impacted Sand Barrel	261
Figure 159. Mass Distribution Between Impact Events	263
Figure 160. Ideal Mass Distribution	265
Figure 161. Linear Mass Distribution Approximation	267
Figure 162. Partial Areas Mass Distribution Approximation.....	269
Figure 163. Simple Vehicle Model and Sand Barrel	271
Figure 164. Inertia Barrier Example Summary.....	274
Figure 165. Inertia Barrier Example Displacement, Velocity, and Average Acceleration.....	276
Figure 166. Combined Crash Cushion and Sand Barrel Array.....	277
Figure 167. Combined Sand Barrel and End Terminal Impact Scenario	280
Figure 168. Bullnose with Secondary Energy Absorber System.....	284
Figure 169. USPN-4 Bullnose Dimensions [25].....	285
Figure 170. Force vs Displacement – Test No. USPN-4	287
Figure 171. Potential Layout for Net Attenuator	291
Figure 172. Potential Layout for Net Attenuator System	294
Figure 173. Standard-Spacing Sand Barrel Array	297
Figure 174. 1100C and 2270P Impact Scenarios for Standard-Spacing Sand Barrel Array	297
Figure 175. Mixed-Spacing Sand Barrel Array	298
Figure 176. 1100 C and 2270P Impact Scenarios for Mixed-Spacing Sand Barrel Array	299
Figure 177. Sand Barrel Grading Suggestions for Standard-Spacing Systems	300
Figure 178. Sand Barrel Grading Suggestions for Mixed-Spacing Systems	300
Figure 179. Bullnose and Net Attenuator Concept.....	302
Figure 180. Bullnose and Sand Barrel Array Concept	303
Figure 181. Grading Suggestions for Thrie-Beam Bullnose Concepts.....	303
Figure A-1. Material Certifications, Test Nos. IRA-1 through IRA-4	323
Figure A-2. Material Certifications, Test Nos. IRA-1 through IRA-4	324

Figure B-1. Test No. IRA-1 Results (DTS) [English Units]326
Figure B-2. Test No. IRA-1 Results (DTS) [Metric Units]327
Figure B-3. Test No. IRA-1 Results (DTS-SLICE) [English Units]328
Figure B-4. Test No. IRA-1 Results (DTS-SLICE) [Metric Units].....329
Figure B-5. 10-ms Average Longitudinal Deceleration (DTS), Test No. IRA-1330
Figure B-6. Longitudinal Occupant Impact Velocity (DTS), Test No. IRA-1331
Figure B-7. Longitudinal Occupant Displacement (DTS), Test No. IRA-1332
Figure B-8. 10-ms Average Lateral Deceleration (DTS), Test No. IRA-1.....333
Figure B-9. Lateral Occupant Impact Velocity (DTS), Test No. IRA-1334
Figure B-10. Lateral Occupant Displacement (DTS), Test No. IRA-1335
Figure B-11. Vehicle Angular Displacements (DTS), Test No. IRA-1336
Figure B-12. Acceleration Severity Index (DTS), Test No. IRA-1337
Figure B-13. 10-ms Average Longitudinal Deceleration (DTS-SLICE), Test No. IRA-1338
Figure B-14. Longitudinal Occupant Impact Velocity (DTS-SLICE), Test No. IRA-1.....339
Figure B-15. Longitudinal Occupant Displacement (DTS-SLICE), Test No. IRA-1340
Figure B-16. 10-ms Average Lateral Deceleration (DTS-SLICE), Test No. IRA-1341
Figure B-17. Lateral Occupant Impact Velocity (DTS-SLICE), Test No. IRA-1342
Figure B-18. Lateral Occupant Displacement (DTS-SLICE), Test No. IRA-1343
Figure B-19. Vehicle Angular Displacements (DTS-SLICE), Test No. IRA-1344
Figure B-20. Acceleration Severity Index (DTS-SLICE), Test No. IRA-1.....345
Figure B-21. 10-ms Average Longitudinal Deceleration (EDR-3), Test No. IRA-1346
Figure B-22. Longitudinal Occupant Impact Velocity (EDR-3), Test No. IRA-1347
Figure B-23. Longitudinal Occupant Displacement (EDR-3), Test No. IRA-1348
Figure B-24. 10-ms Average Lateral Deceleration (EDR-3), Test No. IRA-1.....349
Figure B-25. Lateral Occupant Impact Velocity (EDR-3), Test No. IRA-1.....350
Figure B-26. Lateral Occupant Displacement (EDR-3), Test No. IRA-1351
Figure B-27. Acceleration Severity Index (EDR-3), Test No. IRA-1352
Figure B-28. 1100C ORD-OIV Estimation, Test No. IRA-1353
Figure B-29. 1500A ORD-OIV Estimation, Test No. IRA-1354
Figure B-30. Local Accelerations, Test No. IRA-1355
Figure B-31. Global Accelerations, Test No. IRA-1356
Figure B-32. Global Velocities, Test No. IRA-1357
Figure B-33. Global Displacements, Test No. IRA-1.....358
Figure B-34. Euler Yaw Angle, Test No. IRA-1359
Figure B-35. Actual Yaw Angle, Test No. IRA-1360
Figure B-36. Planar Trajectory, Test No. IRA-1361
Figure C-1. 10-ms Average Longitudinal Deceleration (DTS), Test No. IRA-2363
Figure C-2. Longitudinal Occupant Impact Velocity (DTS), Test No. IRA-2.....364
Figure C-3. Longitudinal Occupant Displacement (DTS), Test No. IRA-2.....365
Figure C-4. 10-ms Average Lateral Deceleration (DTS), Test No. IRA-2.....366
Figure C-5. Lateral Occupant Impact Velocity (DTS), Test No. IRA-2367
Figure C-6. Lateral Occupant Displacement (DTS), Test No. IRA-2368
Figure C-7. Vehicle Angular Displacements (DTS), Test No. IRA-2.....369
Figure C-8. Acceleration Severity Index (DTS), Test No. IRA-2370
Figure C-9. 10-ms Average Longitudinal Deceleration (DTS-SLICE), Test No. IRA-2.....371
Figure C-10. Longitudinal Occupant Impact Velocity (DTS-SLICE), Test No. IRA-2.....372
Figure C-11. Longitudinal Occupant Displacement (DTS-SLICE), Test No. IRA-2373

Figure C-12. 10-ms Average Lateral Deceleration (DTS-SLICE), Test No. IRA-2374
Figure C-13. Lateral Occupant Impact Velocity (DTS-SLICE), Test No. IRA-2.....375
Figure C-14. Lateral Occupant Displacement (DTS-SLICE), Test No. IRA-2.....376
Figure C-15. Vehicle Angular Displacements (DTS-SLICE), Test No. IRA-2377
Figure C-16. Acceleration Severity Index (DTS-SLICE), Test No. IRA-2.....378
Figure C-17. 10-ms Average Longitudinal Deceleration (EDR-3), Test No. IRA-2379
Figure C-18. Longitudinal Occupant Impact Velocity (EDR-3), Test No. IRA-2380
Figure C-19. Longitudinal Occupant Displacement (EDR-3), Test No. IRA-2381
Figure C-20. 10-ms Average Lateral Deceleration (EDR-3), Test No. IRA-2.....382
Figure C-21. Lateral Occupant Impact Velocity (EDR-3), Test No. IRA-2.....383
Figure C-22. Lateral Occupant Displacement (EDR-3), Test No. IRA-2384
Figure C-23. Acceleration Severity Index (EDR-3), Test No. IRA-2385
Figure C-24. 1100C ORD-OIV Estimation, Test No. IRA-2386
Figure C-25. 1500A ORD-OIV Estimation, Test No. IRA-2.....387
Figure C-26. Local Accelerations, Test No. IRA-2388
Figure C-27. Global Accelerations, Test No. IRA-2389
Figure C-28. Global Velocities, Test No. IRA-2390
Figure C-29. Global Displacements, Test No. IRA-2.....391
Figure C-30. Euler Yaw Angle, Test No. IRA-2392
Figure C-31. Actual Yaw Angle, Test No. IRA-2393
Figure C-32. Planar Trajectory, Test No. IRA-2394
Figure D-1. 10-ms Average Longitudinal Deceleration (DTS-SLICE-1), Test No. IRA-3396
Figure D-2. Longitudinal Occupant Impact Velocity (DTS-SLICE-1), Test No. IRA-3397
Figure D-3. Longitudinal Occupant Displacement (DTS-SLICE-1), Test No. IRA-3398
Figure D-4. 10-ms Average Lateral Deceleration (DTS-SLICE-1), Test No. IRA-3.....399
Figure D-5. Lateral Occupant Impact Velocity (DTS-SLICE-1), Test No. IRA-3400
Figure D-6. Lateral Occupant Displacement (DTS-SLICE-1), Test No. IRA-3401
Figure D-7. Vehicle Angular Displacements (DTS-SLICE-1), Test No. IRA-3.....402
Figure D-8. Acceleration Severity Index (DTS-SLICE-1), Test No. IRA-3403
Figure D-9. 10-ms Average Longitudinal Deceleration (DTS-SLICE-2), Test No. IRA-3404
Figure D-10. Longitudinal Occupant Impact Velocity (DTS-SLICE-2), Test No. IRA-3405
Figure D-11. Longitudinal Occupant Displacement (DTS-SLICE-2), Test No. IRA-3406
Figure D-12. 10-ms Average Lateral Deceleration (DTS-SLICE-2), Test No. IRA-3.....407
Figure D-13. Lateral Occupant Impact Velocity (DTS-SLICE-2), Test No. IRA-3408
Figure D-14. Lateral Occupant Displacement (DTS-SLICE-2), Test No. IRA-3409
Figure D-15. Vehicle Angular Displacements (DTS-SLICE-2), Test No. IRA-3.....410
Figure D-16. Acceleration Severity Index (DTS-SLICE-2), Test No. IRA-3411
Figure D-17. 1100C ORD-OIV Estimation, Test No. IRA-3412
Figure D-18. 1500A ORD-OIV Estimation, Test No. IRA-3.....413
Figure D-19. Local Accelerations (DTS-SLICE-1), Test No. IRA-3.....414
Figure D-20. Global Accelerations (DTS-SLICE-1), Test No. IRA-3415
Figure D-21. Global Velocities (DTS-SLICE-1), Test No. IRA-3.....416
Figure D-22. Global Displacements (DTS-SLICE-1), Test No. IRA-3417
Figure D-23. Euler Yaw Angle (DTS-SLICE-1), Test No. IRA-3.....418
Figure D-24. Actual Yaw Angle (DTS-SLICE-1), Test No. IRA-3.....419
Figure D-25. Planar Trajectory (DTS-SLICE-1), Test No. IRA-3.....420
Figure D-26. Local Accelerations (DTS-SLICE-2), Test No. IRA-3.....421

Figure D-27. Global Accelerations (DTS-SLICE-2), Test No. IRA-3	422
Figure D-28. Global Velocities (DTS-SLICE-2), Test No. IRA-3	423
Figure D-29. Global Displacements (DTS-SLICE-2), Test No. IRA-3	424
Figure D-30. Euler Yaw Angle (DTS-SLICE-2), Test No. IRA-3	425
Figure D-31. Actual Yaw Angle (DTS-SLICE-2), Test No. IRA-3	426
Figure D-32. Planar Trajectory (DTS-SLICE-2), Test No. IRA-3	427
Figure E-1. Test No. IRA-4 Results (DTS-SLICE-1) [English Units]	429
Figure E-2. Test No. IRA-4 Results (DTS-SLICE-1) [Metric Units]	430
Figure E-3. Test No. IRA-4 Results (DTS-SLICE-2) [English Units]	431
Figure E-4. Test No. IRA-4 Results (DTS-SLICE-2) [Metric Units]	432
Figure E-5. 10-ms Average Longitudinal Deceleration (DTS-SLICE-1), Test No. IRA-4	433
Figure E-6. Longitudinal Occupant Impact Velocity (DTS-SLICE-1), Test No. IRA-4	434
Figure E-7. Longitudinal Occupant Displacement (DTS-SLICE-1), Test No. IRA-4	435
Figure E-8. 10-ms Average Lateral Deceleration (DTS-SLICE-1), Test No. IRA-4	436
Figure E-9. Lateral Occupant Impact Velocity (DTS-SLICE-1), Test No. IRA-4	437
Figure E-10. Lateral Occupant Displacement (DTS-SLICE-1), Test No. IRA-4	438
Figure E-11. Vehicle Angular Displacements (DTS-SLICE-1), Test No. IRA-4	439
Figure E-12. Acceleration Severity Index (DTS-SLICE-1), Test No. IRA-4	440
Figure E-13. 10-ms Average Longitudinal Deceleration (DTS-SLICE-2), Test No. IRA-4	441
Figure E-14. Longitudinal Occupant Impact Velocity (DTS-SLICE-2), Test No. IRA-4	442
Figure E-15. Longitudinal Occupant Displacement (DTS-SLICE-2), Test No. IRA-4	443
Figure E-16. 10-ms Average Lateral Deceleration (DTS-SLICE-2), Test No. IRA-4	444
Figure E-17. Lateral Occupant Impact Velocity (DTS-SLICE-2), Test No. IRA-4	445
Figure E-18. Lateral Occupant Displacement (DTS-SLICE-2), Test No. IRA-4	446
Figure E-19. Vehicle Angular Displacements (DTS-SLICE-2), Test No. IRA-4	447
Figure E-20. Acceleration Severity Index (DTS-SLICE-2), Test No. IRA-4	448
Figure E-21. 1100C ORD-OIV Estimation, Test No. IRA-4	449
Figure E-22. 1500A ORD-OIV Estimation, Test No. IRA-4	450
Figure E-23. Local Accelerations (DTS-SLICE-1), Test No. IRA-4	451
Figure E-24. Global Accelerations (DTS-SLICE-1), Test No. IRA-4	452
Figure E-25. Global Velocities (DTS-SLICE-1), Test No. IRA-4	453
Figure E-26. Global Displacements (DTS-SLICE-1), Test No. IRA-4	454
Figure E-27. Euler Yaw Angle (DTS-SLICE-1), Test No. IRA-4	455
Figure E-28. Actual Yaw Angle (DTS-SLICE-1), Test No. IRA-4	456
Figure E-29. Planar Trajectory (DTS-SLICE-1), Test No. IRA-4	457
Figure E-30. Local Accelerations (DTS-SLICE-2), Test No. IRA-4	458
Figure E-31. Global Accelerations (DTS-SLICE-2), Test No. IRA-4	459
Figure E-32. Global Velocities (DTS-SLICE-2), Test No. IRA-4	460
Figure E-33. Global Displacements (DTS-SLICE-2), Test No. IRA-4	461
Figure E-34. Euler Yaw Angle (DTS-SLICE-2), Test No. IRA-4	462
Figure E-35. Actual Yaw Angle (DTS-SLICE-2), Test No. IRA-4	463
Figure E-36. Planar Trajectory (DTS-SLICE-2), Test No. IRA-4	464
Figure F-1. 10-ms Average Longitudinal Deceleration, Baseline Simulation	466
Figure F-2. Longitudinal Occupant Impact Velocity, Baseline Simulation	467
Figure F-3. Longitudinal Occupant Displacement, Baseline Simulation	468
Figure F-4. 10-ms Average Lateral Deceleration, Baseline Simulation	469
Figure F-5. Lateral Occupant Impact Velocity, Baseline Simulation	470

Figure F-6. Lateral Occupant Displacement, Baseline Simulation.....471
Figure F-7. 10-ms Average Longitudinal Deceleration, Angled Simulation.....472
Figure F-8. Longitudinal Occupant Impact Velocity, Angled Simulation473
Figure F-9. Longitudinal Occupant Displacement, Angled Simulation474
Figure F-10. 10-ms Average Lateral Deceleration, Angled Simulation.....475
Figure F-11. Lateral Occupant Impact Velocity, Angled Simulation.....476
Figure F-12. Lateral Occupant Displacement, Angled Simulation.....477
Figure G-1. Sand Barrel and End Terminal Impact, 1100C Small Car, Full Bullnose Crush
Force479
Figure G-2. Sand Barrel and End Terminal Impact, 2270P Truck, Full Bullnose Crush Force..479
Figure G-3. Standard-Spacing Sand Barrel Array, 1100C, Case 1 Summary480
Figure G-4. Standard-Spacing Sand Barrel Array, 1100C, Case 1 Acceleration481
Figure G-5. Standard-Spacing Sand Barrel Array, 1100C, Case 1 Displacement and Velocity .482
Figure G-6. Standard-Spacing Sand Barrel Array, 1100C, Case 2 Summary483
Figure G-7. Standard-Spacing Sand Barrel Array, 1100C, Case 2 Acceleration484
Figure G-8. Standard-Spacing Sand Barrel Array, 1100C, Case 2 Displacement and Velocity .485
Figure G-9. Standard-Spacing Sand Barrel Array, 1100C, Case 3 Summary486
Figure G-10. Standard-Spacing Sand Barrel Array, 1100C, Case 3 Acceleration487
Figure G-11. Standard-Spacing Sand Barrel Array, 1100C, Case 3 Displacement and
Velocity.....488
Figure G-12. Standard-Spacing Sand Barrel Array, 1100C, Case 4 Summary489
Figure G-13. Standard-Spacing Sand Barrel Array, 1100C, Case 4 Acceleration490
Figure G-14. Standard-Spacing Sand Barrel Array, 1100C, Case 4 Displacement and
Velocity.....491
Figure G-15. Standard-Spacing Sand Barrel Array, 2270P, Case 1 Summary.....492
Figure G-16. Standard-Spacing Sand Barrel Array, 2270P, Case 1 Acceleration.....493
Figure G-17. Standard-Spacing Sand Barrel Array, 2270P, Case 1 Displacement and
Velocity.....494
Figure G-18. Standard-Spacing Sand Barrel Array, 2270P, Case 2 Summary.....495
Figure G-19. Standard-Spacing Sand Barrel Array, 2270P, Case 2 Acceleration.....496
Figure G-20. Standard-Spacing Sand Barrel Array, 2270P, Case 2 Displacement and
Velocity.....497
Figure G-21. Standard-Spacing Sand Barrel Array, 2270P, Case 3 Summary.....498
Figure G-22. Standard-Spacing Sand Barrel Array, 2270P, Case 3 Acceleration.....499
Figure G-23. Standard-Spacing Sand Barrel Array, 2270P, Case 3 Displacement and
Velocity.....500
Figure G-24. Standard-Spacing Sand Barrel Array, 2270P, Case 4 Summary.....501
Figure G-25. Standard-Spacing Sand Barrel Array, 2270P, Case 4 Acceleration.....502
Figure G-26. Standard-Spacing Sand Barrel Array, 2270P, Case 4 Displacement and
Velocity.....503
Figure G-27. Mixed-Spacing Sand Barrel Array, 1100C, Case 1 Summary504
Figure G-28. Mixed-Spacing Sand Barrel Array, 1100C, Case 1 Acceleration505
Figure G-29. Mixed-Spacing Sand Barrel Array, 1100C, Case 1 Displacement and Velocity ...506
Figure G-30. Mixed-Spacing Sand Barrel Array, 1100C, Case 2 Summary507
Figure G-31. Mixed-Spacing Sand Barrel Array, 1100C, Case 2 Acceleration508
Figure G-32. Mixed-Spacing Sand Barrel Array, 1100C, Case 2 Displacement and Velocity ...509
Figure G-33. Mixed-Spacing Sand Barrel Array, 1100C, Case 3 Summary510

Figure G-34. Mixed-Spacing Sand Barrel Array, 1100C, Case 3 Acceleration511
Figure G-35. Mixed-Spacing Sand Barrel Array, 1100C, Case 3 Displacement and Velocity ...512
Figure G-36. Mixed-Spacing Sand Barrel Array, 1100C, Case 4 Summary513
Figure G-37. Mixed-Spacing Sand Barrel Array, 1100C, Case 4 Acceleration514
Figure G-38. Mixed-Spacing Sand Barrel Array, 1100C, Case 4 Displacement and Velocity ...515
Figure G-39. Mixed-Spacing Sand Barrel Array, 2270P, Case 1 Summary516
Figure G-40. Mixed-Spacing Sand Barrel Array, 2270P, Case 1 Acceleration517
Figure G-41. Mixed-Spacing Sand Barrel Array, 2270P, Case 1 Displacement and Velocity ...518
Figure G-42. Mixed-Spacing Sand Barrel Array, 2270P, Case 2 Summary519
Figure G-43. Mixed-Spacing Sand Barrel Array, 2270P, Case 2 Acceleration520
Figure G-44. Mixed-Spacing Sand Barrel Array, 2270P, Case 2 Displacement and Velocity ...521
Figure G-45. Mixed-Spacing Sand Barrel Array, 2270P, Case 3 Summary522
Figure G-46. Mixed-Spacing Sand Barrel Array, 2270P, Case 3 Acceleration523
Figure G-47. Mixed-Spacing Sand Barrel Array, 2270P, Case 3 Displacement and Velocity ...524
Figure G-48. Mixed-Spacing Sand Barrel Array, 2270P, Case 4 Summary525
Figure G-49. Mixed-Spacing Sand Barrel Array, 2270P, Case 4 Acceleration526
Figure G-50. Mixed-Spacing Sand Barrel Array, 2270P, Case 4 Displacement and Velocity ...527
Figure G-51. Combined Net Arrestor and Bullnose Impact, 2270 Truck, Full Bullnose Crush
Force528
Figure G-52. Combined Net Arrestor and Bullnose Impact, 2270 Truck, 75 Percent Bullnose
Crush Force529
Figure G-53. Combined Net Arrestor and Bullnose Impact, 1100C Small Car, Full Bullnose
Crush Force530
Figure G-54. Combined Net Arrestor and Bullnose Impact, 1100C Small Car, 75 Percent
Bullnose Crush Force.....531
Figure G-55. Combined Sand Barrel and Bullnose Impact, 2270 Truck, Full Bullnose Crush
Force532
Figure G-56. Combined Sand Barrel and Bullnose Impact, 2270 Truck, 75 Percent Bullnose
Crush Force532
Figure G-57. Combined Sand Barrel and Bullnose Impact, 1100C Small Car, Full Bullnose
Crush Force533
Figure G-58. Combined Sand Barrel and Bullnose Impact, 1100C Small Car, 75 Percent
Bullnose Crush Force.....533

LIST OF TABLES

Table 1. Summary of Short-Radius Guardrail Systems and Full-Scale Crash Testing7
Table 2. Summary of Short-Radius Guardrail Systems and Full-Scale Crash Testing8
Table 3. Summary of Short-Radius Guardrail Systems and Full-Scale Crash Testing9
Table 4. Summary of Bullnose Guardrail Systems and Full-Scale Crash Testing10
Table 5. Summary of Bullnose Guardrail Systems and Full-Scale Crash Testing11
Table 6. Summary of Bullnose Guardrail Systems and Full-Scale Crash Testing12
Table 7. NCHRP Report No. 350 Test Matrix Conditions [2]33
Table 8. MASH Test Matrix and Conditions [3]34
Table 9. Summary of Energy-Absorbing, Guardrail End Terminals with Dynamic Deflections35
Table 10. Non-Redirecting Crash Cushions and Dynamic Deflections38
Table 11. Redirecting, Non-Gating Crash Cushions and Dynamic Deflections.....39
Table 12. Redirecting, Gating Crash Cushions, and Dynamic Deflections40
Table 13. Truck- and Trailer-Mounted Attenuator Systems and Dynamic Deflections43
Table 14. SD-STD-02.01 Impact Condition Designations for 15,000-lb (6,800-kg) Vehicle [32].....45
Table 15. ASTM F 2656-07 Impact Condition Designations [33]45
Table 16. ASTM F 2656-07 Penetration Rating System [33]46
Table 17. Net and Cable Systems and Dynamic Deflections47
Table 18. Suggested Runout Length (L_R) for Barrier Design Given Traffic Volume (ADT) [1].....52
Table 19. Sight Distance at Intersections [45]54
Table 20. Ranking of Design Concepts80
Table 21. Bogie Test Matrix92
Table 22. Weather Conditions, Test No. IRA-1126
Table 23. Energy-Absorber Tape Pullout, Test No. IRA-1128
Table 24. Summary of OIV, ORA, THIV, PHD, and ASI Values, Test No. IRA-1129
Table 25. 1100C and 1500A Displacement, OIV, and ORA Estimations, Test No. IRA-1130
Table 26. Weather Conditions, Test No. IRA-2144
Table 27. Energy-Absorber Tape Pullout, Test No. IRA-2146
Table 28. Summary of OIV, ORA, THIV, PHD, and ASI Values, Test No. IRA-2147
Table 29. 1100C and 1500A Displacement, OIV, and ORA Estimations, Test No. IRA-2148
Table 30. Weather Conditions, Test No. IRA-3183
Table 31. Energy-Absorber Tape Pullout, Test No. IRA-3184
Table 32. Summary of OIV, ORA, THIV, PHD, and ASI Values, Test No. IRA-3186
Table 33. 1100C and 1500A Displacement, OIV, and ORA Estimations, Test No. IRA-3187
Table 34. Weather Conditions, Test No. IRA-4197
Table 35. Energy-Absorber Tape Pullout, Test No. IRA-4198
Table 36. Summary of OIV, ORA, THIV, PHD, and ASI Values, Test No. IRA-4200
Table 37. 1100C and 1500A Displacement, OIV, and ORA Estimations, Test No. IRA-4201
Table 38. Occupant Risk Summary, Test Nos. IRA-1 through IRA-4214
Table 39. Estimated Occupant Risk for 1100C and 1500A Vehicles, Test Nos. IRA-1 through IRA-4214
Table 40. Comparison of OIV and ORA Values, Baseline Simulation and Test No. IRA-4229
Table 41. Comparison of OIV and ORA Values, Baseline Simulation and Test No. IRA-4235

Table 42. Comparison of Dragnet System with Analytical Calculations245
Table 43. Input Parameters for Analytical Solution of IRA-3248
Table 44. Input Parameters for Analytical Solution of IRA-4250
Table 45. Mass Distribution Method Comparison270
Table 46. Inertia Barrier Example Calculations275
Table 47. Average End Terminal Forces [54]279
Table 48. Calculation Procedure for Impacts Into Combined Bullnose and Sand Barrel
System289
Table 49. Predicted Distance and Peak Deceleration for 1100C and 2270P Vehicles292
Table 50. Design, Operational, and Constructability Challenges for Potential Layouts306

1 INTRODUCTION

1.1 Background and Project Statement

Bridge rails are commonly used to shield errant vehicles from falling into a hazard that is spanned by the bridge. A common occurrence in many rural and some urban locations is the presence of a secondary road intersecting near a bridge located on a higher classification roadway. This intersection often provides very little distance for installing an effective approach guardrail and stiffness transition to shield the bridge rail end. Crashworthy guardrail systems with transitions and end terminals are frequently utilized to shield the ends of the bridge railings and to provide guardrail runout length upstream from the bridge hazard. The minimum length of guardrail required to shield a hazard is determined using length-of-need (LON) formulas found in the American Association of State Highway and Transportation Officials' (AASHTO's) *Roadside Design Guide* [1]. In some instances, the location of a bridge end is very close to an intersection, such as the secondary or intersecting roadway located within the guardrail LON.

Historically, short-radius guardrail systems were designed to address this situation and prevent errant vehicles from interacting with the bridge hazard as well as to provide a stiffness transition to the bridge rail end. To date, no systems have been approved according to the Test Level 3 (TL-3) impact safety standards identified in either the National Cooperative Highway Research Program (NCHRP) Report No. 350 [2] or the AASHTO *Manual for Assessing Safety Hardware* (MASH) [3]. Recently, the Texas A&M Transportation Institute (TTI) has developed and tested a system that has passed several crash tests using the TL-3 MASH guidelines [4]. Early short-radius guardrail systems were tested in accordance with NCHRP Report No. 230 [5]. The Yuma County short-radius guardrail system [6] was first tested in accordance with the

AASHTO *Guide Specifications for Bridge Railings* [7] and was later approved for use according to NCHRP Report No. 350 TL-2 impact conditions [2].

Short-radius guardrails have been recommended in Federal Highway Administration (FHWA) Technical Advisory T5040.32 [8]. Further, other testing has led to acceptance of short-radius systems under NCHRP Report No. 350 TL-2 impact conditions. Thus, there still exists the need to develop a new TL-3 attenuation system that can accommodate practical site constraints. The new design should address the issues inherent in current short-radius systems, including improved impact performance and decreased system length.

1.2 Research Objective

The objective of this study was to pursue the long-term development of a MASH-compliant attenuation system for intersecting roadways while minimizing its footprint. This initial phase would consist of brainstorming new concepts, analysis/design of those concepts, preliminary component testing, and recommendations as to their feasibility. Preference was given to designs that incorporated existing technologies, such as end terminals, cable elements, arrestor systems, and/or other energy-absorbing devices.

1.3 Scope

The proposed research began with a review of previous short-radius designs as well as potential terminal, crash cushion, and arrestor systems that could be used in the design concepts. Standards provided by the Nebraska Department of Roads (NDOR) for intersecting roadways were used to identify general site constraints. Next, new concepts were also brainstormed. Engineering analysis and LS-DYNA computer simulations were then used to evaluate and refine the three most promising concepts. These concepts included a net attenuation/end terminal, inertial barrel/end terminal, and a bullnose with secondary energy absorption.

Critical components of the most promising concepts were subjected to dynamic testing in order to investigate failure mechanisms and quantify failure loads. In some cases, promising concepts were subjected to high-speed bogie tests to examine the dynamic performance and structural adequacy for impact conditions believed to produce the greatest risk of failure. A net attenuation/end terminal concept was considered most likely to accommodate the site conditions as well as a moderate slope behind the system. Four dynamic bogie tests and two static tests were performed on potential net attenuators to evaluate their use as energy absorbers in the design concept. Finally, recommendations were provided for further system development.

2 SHORT-RADIUS AND BULLNOSE

2.1 Introduction

Prior to the development of new concepts for safety treatments at intersecting roadways, a literature search was conducted to investigate various short-radius and bullnose guardrail systems that have been tested and/or are currently in use. The site constraints and testing methods used to develop, test, and evaluate those systems would then be considered for this study.

Several short-radius guardrail systems were successfully tested according to criteria presented in NCHRP Report No. 230 [5]. The tested systems typically consisted of W-beam guardrail with radii between 8 and 10 ft (2.4 and 3.0 m) mounted on rectangular or circular Controlled Release Terminal (CRT) posts with 42-in. (1,067-mm) embedment depths and anchorages [9-11]. Safety criteria presented in NCHRP Report No. 230 required a minimum of four crash tests to be conducted at 60 mph (97 km/h):

- 1) 4,500-lb (2,041-kg) sedan at 0 degrees, centerline aligned with stiff bridge rail;
- 2) 4,500-lb (2,041-kg) sedan at 25 degrees, at the critical impact point (CIP) near the transition;
- 3) 4,500-lb (2,041-kg) sedan at 25 degrees, centerline aligned with midpoint of radius;
- and
- 4) 1,900-lb (862-kg) small car at 20 degrees, centerline aligned with midpoint of radius.

The Yuma County short-radius guardrail system was tested in accordance with the Performance Level 1 (PL-1) impact conditions found in the AASHTO *Guide Specifications for Bridge Railings* [6]. A total of six tests conducted at 45 mph (72 km/h) were required:

- 1) 1,984-lb (900-kg) small car at 20 degrees, at the CIP near the transition;

- 2) 5,401-lb (2,450-kg) pickup truck at 20 degrees, at the CIP near the transition;
- 3) 1,984-lb (900-kg) small car at 20 degrees, centerline aligned with midpoint of radius;
- 4) 5,401-lb (2,450-kg) pickup truck at 20 degrees, centerline aligned with midpoint of radius;
- 5) 1,984-lb (900-kg) small car at 0 degrees, centerline aligned with stiff bridge rail; and
- 6) 5,401-lb (2,450-kg) pickup truck at 0 degrees, centerline aligned with stiff bridge rail.

No short-radius guardrail systems have been approved under NCHRP Report No. 350 [2] or MASH [3] for TL-3 impact conditions. The Texas Transportation Institute (TTI) has tested a system that has passed several crash tests according to the TL-3 impact criteria under MASH [4]. Seven tests were required according to NCHRP Report No. 350 crash test conditions and are discussed in literature [11-12].

A summary of previously-tested short-radius guardrail systems are shown in Tables 1 through 3. Bullnose systems, which share many similar features with short-radius systems, are summarized in Tables 4 through 6.

2.2 Historical W-Beam Short-Radius Guardrail Systems

2.2.1 Systems Tested to NCHRP Report No. 230

Two W-beam short-radius systems were successfully tested according to NCHRP Report No. 230 criteria and included the Washington [9] and Texas A&M Transportation Institute (TTI) [10] designs. Each design consisted of curved W-beam guardrail mounted on wooden breakaway posts, which was connected to a downstream anchorage and a rigid or semi-rigid bridge railing.

The final Washington short-radius guardrail system is shown in Figure 1. The system consisted of a curved W-beam end termination and 25 ft (7.6 m) of W-beam, including a Breakaway Cable Terminal (BCT) end anchorage system with two cable anchors, one attached to each BCT post. The cables were spliced together near the groundline. The guardrail radius was 8

ft - 6 in. (2.6 m), and 25 ft (7.6 m) of W-beam guardrail was used to transition to a rigid bridge rail. The system was configured such that the barrier adjacent to the secondary roadway was installed parallel with the road, whereas the primary side of the system had a 10:1 flare upstream from the bridge rail. Posts installed at the transition were 6-in. x 8-in. x 72-in. (152-mm x 203-mm x 1,829-mm) rectangular timber posts, and posts installed on the radius and secondary side of the system were 6-in. x 8-in. x 72-in. (152-mm x 203-mm x 1,829-mm) rectangular CRT posts. One CRT post on the primary roadway side and all six transition posts utilized 6-in. x 8-in. x 14¼-in. (152-mm x 203-mm x 362-mm) timber blockouts. The final design was determined to pass all crash tests according to the NCHRP Report No. 230 criteria.

The TTI W-beam short-radius system utilized round CRT timber posts instead of rectangular posts, and anchored the W-beam on the secondary roadway with a W-beam turndown anchor [10]. The TTI system is shown in Figure 2. The W-beam guardrail was nested throughout the radius section. The transition utilized tubular, nested rail with an additional rail mounted backwards against the post. A cable anchor was attached to the rail downstream from the radius to develop tension in the transition region.

The TTI W-beam system was tested and evaluated according to NCHRP Report No. 230 evaluation criteria. The system performed acceptably during each crash test, with one exception. After the 4,500-lb (2,041-kg) sedan impacted the curved rail at 15 degrees, and 90 percent of the vehicle's energy was dissipated, the rail disengaged away from the bumper and rose up the vehicle's front end, crushing the windshield. Although this performance was determined to be unacceptable, researchers postulated that this impact type was both infrequent and relatively severe. Thus, the system would perform acceptably in the majority of impacts and was recommended for use in locations with intersecting roadways.

Table 1. Summary of Short-Radius Guardrail Systems and Full-Scale Crash Testing

Test No.	Reference No.	Vehicle	Impact Conditions	Impact Location	Rail Height (in.)	Result
WA-1	9	1978 Plymouth sedan 4,520 lb	60.0 mph and 0 deg	Centerline of vehicle with center point of radius	27	Failed - vehicle vaulted system
WA-1M		1978 Honda small car 1,903 lb	60.8 mph and 23.7 deg	Angled hit into guardrail	27	Conditionally Failed - longitudinal ΔV exceeded limits
WA-2M		1977 Dodge sedan 4,789 lb	60.6 mph and 13.4 deg	Angled hit into guardrail	27	Failed - all posts on secondary side fractured
WA-3M		1978 Dodge sedan 4,640 lb	58.9 mph and 16.6 deg	Angled hit into guardrail	27	Failed - W-beam fractured during impact
WA-4M		1978 Dodge sedan 4,650 lb	58.8 mph and 14.6 deg	Angled hit into guardrail	27	Passed (despite yaw, back tires overriding system)
WA-5M		4,640 lb 1978 Plymouth sedan	59.0 mph and 1.1 deg	Centerline of vehicle aligned with center point of radius	27	Passed
1263-1	10	1987 Yugo GV small car 1,970 lb	58.4 mph and 20.5 deg	Center point of radius	~27.1	Failed - High occupant accelerations, overrode system
1263-2		1987 Yugo GV small car 1,970 lb	59.0 mph and 20.4 deg	Center point of radius	~27.1	Failed - splice rupture, car penetrated system
1263-3		1987 Yugo GV small car 1,970 lb	60.2 mph and 20.7 deg	Center point of radius	~27.1	Passed
1263-4		1982 Cadillac sedan 4,500 lb	57.1 mph and 24.7 deg	75 in. from end of concrete barrier	~27.1	Passed
1263-5		1985 Cadillac coupe sedan 4,500 lb	58.5 mph and 26.8 deg	Centerline of vehicle with center point of radius	~27.1	Failed - underride and roof crush
1263-6		1983 Cadillac coupe 4,500 lb	58.3 mph and 2.0 deg	Centerline of vehicle aligned with bridge rail	~27.1	Passed

Table 2. Summary of Short-Radius Guardrail Systems and Full-Scale Crash Testing

Test No.	Reference No.	Vehicle	Impact Conditions	Impact Location	Rail Height (in.)	Result
YC-1	6	1982 Chevrolet pickup 5,376 lb	45 mph and 1.4 deg	Centerline of vehicle with tangent line to bridge rail	27	Passed
YC-2		Volkswagen Rabbit 1,978 lb	50.3 mph and 0.7 deg	Centerline of vehicle with tangent line to bridge rail	27	Passed
YC-3		Chevrolet pickup 5,380 lb	44.8 mph and 19.7 deg	Centerline of vehicle aligned with radius	27	Failed - rail released from BCT post
YC-4		Chevrolet pickup 5,381 lb	44.9 mph and 20.1 deg	Centerline of vehicle aligned with radius	27	Passed
YC-5		Volkswagen Rabbit 1,980 lb	44.2 mph and 20 deg	Centerline of vehicle with center of 2nd freestanding CRT	27	Passed
YC-6		Volkswagen Rabbit 1,980 lb	51.1 mph and 19.4 deg	13 ft upstream of bridge end	27	Passed
YC-7		1982 Chevrolet pickup 5,424 lb	45.2 mph and 20.7 deg	12 ft upstream of bridge end	27	Passed
1442-1	11	1986 Chevrolet 2500 4,409 lb	60.9 mph and 26.0 deg	3.5 posts upstream from concrete barrier	31.625 (thrie beam)	Passed
1442-2		1985 Chevrolet pickup 4,409 lb	63.0 mph and 25.6 deg	Centerline of vehicle with center post of radius	31.625 (thrie beam)	Overrode system - rail formed ramp
1442-3		1988 Ford F250 4,409 lb	63.0 mph and 24.6 deg	Centerline of vehicle with center post of radius	31.625 (thrie beam)	Overrode system - rail formed ramp
1442-4		1988 Chevrolet Sprint 1,978 lb	60.1 mph and 19.1 deg	Centerline of vehicle with center post of radius	31.625 (thrie beam)	Marginal pass - rail crushed windshield
1442-5		1984 Lincoln Town Car 4,500 lb	60.4 mph and 24.5 deg	Centerline of vehicle with center post of radius	31.625 (thrie beam)	Limited pass - rail released from terminal

Table 3. Summary of Short-Radius Guardrail Systems and Full-Scale Crash Testing

Test No.	Reference No.	Vehicle	Impact Conditions	Impact Location	Rail Height (in.)	Result
SR-1	12,13	1995 Ford F-250 pickup 4,473 lb	61.5 mph and 19.0 deg	Centerline of pickup with centerpoint of radius	31.625 (thrie beam)	Failed - rollover on top of system
SR-2		1994 Chevrolet C2500 pickup 4,440 lb	64.7 mph and 16.1 deg	Centerline of pickup with centerpoint of radius	31.625 (thrie beam)	Failed - rollover on top of system
SR-3		Ford F250 pickup 4,489 lb	63.9 mph and 0.9 deg	Centerline of pickup with centerline of primary-side post no. 1	31.625 (thrie beam)	Failed - rollover on top of system
SR-4		1999 Chevrolet C2500 pickup 4,420 lb	66.0 mph and 1.8 deg	Centerline of pickup with centerline of primary-side post no. 1	31.625 (thrie beam)	Failed - tear in floorboard
SR-5	14	1997 Ford F250 pickup 4,411 lb	63.3 mph and 0.9 deg	Centerline of pickup with centerline of primary-side post no. 1	31 (thrie beam)	Passed
SR-6		1996 Geo Metro small car 1,969 lb	61.8 mph and 0.8 deg	Right front quarter point of vehicle with centerline of nose	31 (thrie beam)	Failed - windshield crushed by rail and hood
SR-7	15	2002 Dodge Ram pickup 4,989 lb	62.3 mph and 18.1 deg	Centerline of pickup with centerpoint of radius	31 (thrie beam)	Failed - rollover at end of event
SR-8		2002 Dodge Ram pickup 5,000 lb	62.8 mph and 17.9 deg	Centerline of pickup with centerpoint of radius	31 (thrie beam)	Failed - vehicle overrode rail at end of impact sequence

Table 4. Summary of Bullnose Guardrail Systems and Full-Scale Crash Testing

Test No.	Reference No.	Vehicle	Impact Conditions	Impact Location	Rail Height (in.)	Result
B1	16	1971 Chevrolet Vega small car 2,290 lb	61.5 mph and 0 deg	Centerline of vehicle with furthest extent of system	27	Passed
B2		1969 Chrysler sedan 4,500 lb	62.3 mph and 0 deg	Centerline of vehicle with furthest extent of system		Passed
271	17	1968 Dodge Polara sedan 4,780 lb	41 mph and 0 deg	Centerline of vehicle aligned with centerline of system	27	Failure - rail rupture permitted vehicle penetration
275		1970 Mercury Monterey sedan 4,960 lb	63 mph and 0 deg	Centerline of vehicle aligned with centerline of system	27	Failure - vehicle struck feature behind rail
277		1970 Mercury Monterey sedan 4,960 lb	59 mph and 0 deg	Centerline of vehicle aligned with centerline of system	27	Passed
278		1970 Mercury Monterey sedan 4,960 lb	64 mph and 10 deg	Centerline of vehicle aligned with center of posts on traffic-side flare	27	Failure - rail formed ramp and vehicle vaulted rail
1	18	Small car 2,400 lb	29.1 mph and 0 deg	Centerline of vehicle aligned with centerline of system	27	Passed
2		Sedan 4,520 lb	62.7 mph and 0 deg	Centerline of vehicle aligned with centerline of system	27	Deflection was greater than desired, but passed
2A		Sedan 4,540 lb	62.7 mph and 0 deg	Centerline of vehicle aligned with centerline of system	27	Passed
4		1976 Gran Fury sedan 4,500 lb	57.4 mph and 24 deg	At cable anchor rail connection attached to post no. 2	27	Marginal - excessive deflection

Table 5. Summary of Bullnose Guardrail Systems and Full-Scale Crash Testing

Test No.	Reference No.	Vehicle	Impact Conditions	Impact Location	Rail Height (in.)	Result
BN-1	19	Sedan 4,635 lb	60 mph and 0 deg	Centerline of vehicle aligned with centerline of system (NCHRP Report 230 test 41/50)	30 (post 2) 34 (post 6)	Failed - vehicle underrode barrier
BN-2		Sedan 4,333 lb	59.1 mph and 4.7 deg	Centerline of vehicle aligned with centerline of system (NCHRP Report 230 test 41/50)	27 (post 2) 34 (post 6)	Passed
BN-3		Small car 1,940 lb	56.9 mph and 0 deg	Centerline of vehicle aligned with centerline of system (NCHRP Report 230 test 52/45)	27 (post 2) 34 (post 6)	Failed - excessive decelerations
BN-4		Small car 1,990 lb	61.0 mph and -4.0 deg	Centerline of vehicle aligned with centerline of system (NCHRP Report 230 test 52/45)	27 (post 2) 34 (post 6)	Marginal - excessive decelerations
BN-5		Sedan 4,675 lb	58.47 mph and -0.5 deg	Centerline of vehicle aligned with centerline of system (NCHRP Report 230 test 41/50)	27 (post 2) 34 (post 6)	Passed
BN-6		Sedan 4,870 lb	59.5 mph and 18.7 deg	Critical impact point (NCHRP Report 230 test 54)	27 (post 2) 34 (post 6)	Marginal - vehicle came to rest on top of system
BN-7		Sedan 4,665 lb	59.9 mph and 0.5 deg	Centerline of vehicle aligned with centerline of system (NCHRP Report 230 test 41/50)	29 (post 2) 34 (post 6)	Passed
BN-8		Sedan 4,695 lb	61.4 mph and 19.0 deg	Critical impact point (NCHRP Report 230 test 54)	29 (post 2) 34 (post 6)	Passed
BN-9		Sedan 4,680 lb	59.9 mph and 15.5 deg	Critical impact point (NCHRP Report 230 test 54)	29 (post 2) 34 (post 6)	Failed - rail ruptured
BN-10		Sedan 4,640 lb	59.9 mph and 15.0 deg	Critical impact point (NCHRP Report 230 test 54)	29 (post 2) 34 (post 6)	Passed
BN-11	18	Sedan 4,305 lb	59.9 mph and 16.2 deg	Critical impact point (NCHRP Report 230 test 54)	29 (post 2) 34 (post 6)	Vehicle came to rest on top of rail - passed
BN-12		Pickup truck 5,400 lb	55 mph and 0.1 deg	Centerline of vehicle aligned with centerline of system (NCHRP Report 230 test 41/50)	29 (post 2) 34 (post 6)	Passed
BN-13		Small car 1,820 lb	59.4 mph and	Centerline of vehicle aligned with centerline of system (NCHRP Report 230 test 52/45)	29 (post 2) 34 (post 6)	Failed - excessive decelerations
BN-14		Small car 1,800 lb	58.7 mph and 2.7 deg	Centerline of vehicle aligned with centerline of system (NCHRP Report 230 test 52/45)	29 (post 2) 34 (post 6)	Failed - underride caused rail to crush windshield (due to vehicle bouncing in approach ditch)
BN-15		Small car 1,935 lb	58.7 mph and	Centerline of vehicle aligned with centerline of system (NCHRP Report 230 test 52/45)	29 (post 2) 34 (post 6)	Failed - underride caused rail to crush windshield
BN-16		Small car 1,935 lb	60.2 mph and	Centerline of vehicle aligned with centerline of system (NCHRP Report 230 test 52/45)	29 (post 2) 34 (post 6)	Despite windshield crush, passed

Table 6. Summary of Bullnose Guardrail Systems and Full-Scale Crash Testing

Test No.	Reference No.	Vehicle	Impact Conditions	Impact Location	Rail Height (in.)	Result
MBN-1	19	1989 Ford F250 pickup 4,404 lb	63.0 mph and 0.1 deg	Centerline of vehicle aligned with centerline of system	31.625 (thrie-beam)	Failure - rail rupture permitted vehicle penetration
MBN-2		1988 Ford Festiva small car 1,953 lb	64.2 mph and -3.4 deg	1/4-point offset of vehicle with centerline of system	31.625 (thrie-beam)	Passed
MBN-3	20	1990 Chevrolet C2500 pickup 4,384 lb	62.2 mph and -1.1 deg	Centerline of vehicle aligned with centerline of system	31.625 (thrie-beam)	Failure - rail rupture permitted vehicle penetration
MBN-4		1991 Chevrolet C2500 pickup 4,431 lb	64.3 mph and 0.58 deg	Centerline of vehicle aligned with centerline of system	31.625 (thrie-beam)	Passed
MBN-5	21	1993 Chevrolet C2500 pickup 4,493 lb	64.0 mph and 13.4 deg	Centerline of vehicle aligned with center point of nose	31.625 (thrie-beam)	Passed
MBN-6		1991 Chevrolet C2500 pickup 4,477 lb	63.1 mph and 20.4 deg	CIP along length of thrie beam	31.625 (thrie-beam)	Failure - rail formed ramp, vehicle vaulted
MBN-7		1992 Chevrolet C2500 pickup 4,488 lb	62.1 mph and 24.9 deg	CIP along length of thrie beam	31.625 (thrie-beam)	Failure - rail formed ramp, vehicle vaulted
MBN-8		1992 GMC 2500 pickup 4,482 lb	62.0 mph and 21.5 deg	CIP along length of thrie beam	31.625 (thrie-beam)	Passed
MBN-9		1990 Ford Festiva small car 1,993 lb	65.2 mph and 15.7 deg	Centerline of vehicle aligned with center point of nose	31.625 (thrie-beam)	Passed
USPBN-1	22,23	2000 GMC 2500 pickup 4,474 lb	63.2 mph and 22.6 deg	Centerline of truck aligned with center of post no. 3	31.625 (thrie-beam)	Failure - rail formed ramp, vehicle vaulted
USPBN-2	24	GMC 2500 pickup 4,564 lb	62.9 mph and 21.7 deg	Centerline of truck aligned with center of post no. 3	31.625 (thrie-beam)	Passed

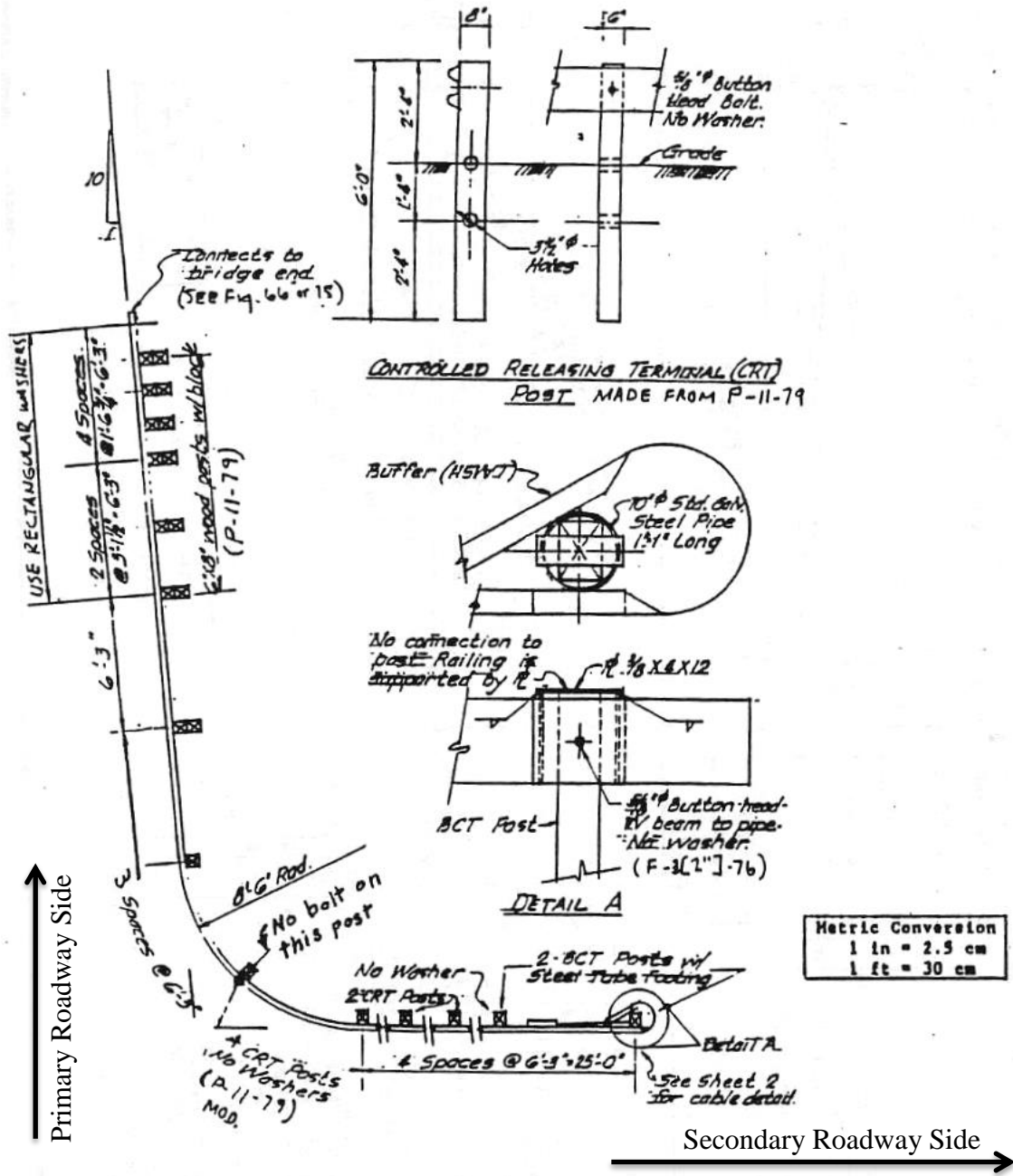


Figure 1. Washington W-Beam Short-Radius Guardrail System [9]

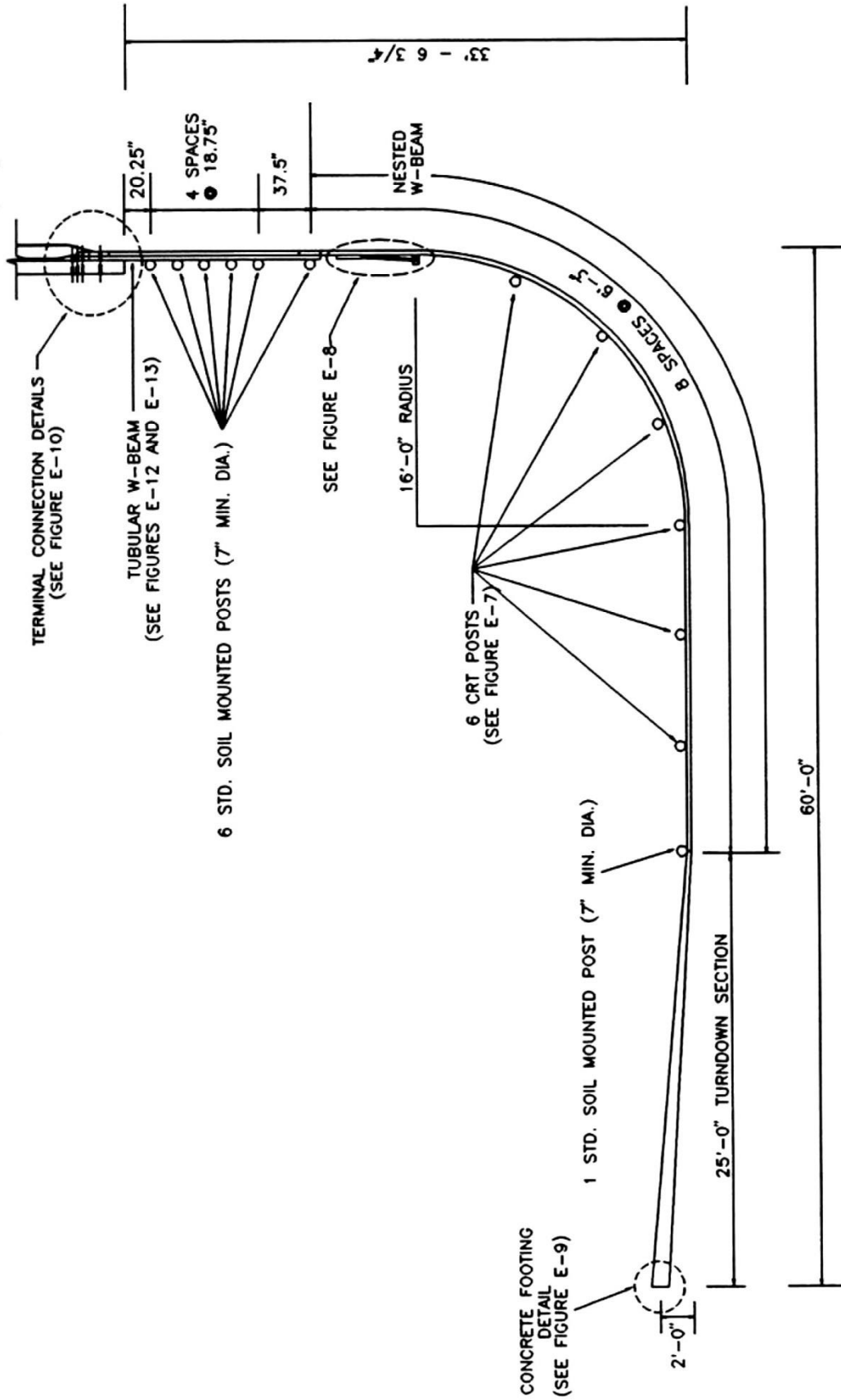


Figure 2. TTI W-Beam Short-Radius Guardrail System [10]

2.2.2 System Tested to AASHTO *Guidance Specifications for Bridge Railings*

The Yuma County system [6] was designed specifically for one oblique intersection, which used a 5.5-degree system flare. The final details for the successfully tested system are shown in Figure 3. Researchers identified five different critical impact locations with associated impact angles to assess system performance. Light-truck impacts were used to assess structural adequacy and pocketing near the transition when impacted tangentially to the bridge rail, as well as for an angled impact on the nose. Small-car impacts were used to evaluate the tendency to underride the system when impacting tangentially to the bridge rail and at an angle to the nose.

The preliminary design of the Yuma County system performed acceptably according to AASHTO PL-1 criteria, with one exception. For one test, both of the secondary-side anchorage BCT posts fractured, and the spliced two-cable BCT anchor released, thus allowing the vehicle to encroach behind the barrier system. Researchers lengthened the secondary side of the system to increase anchoring capacity, and the system was determined to be successful.

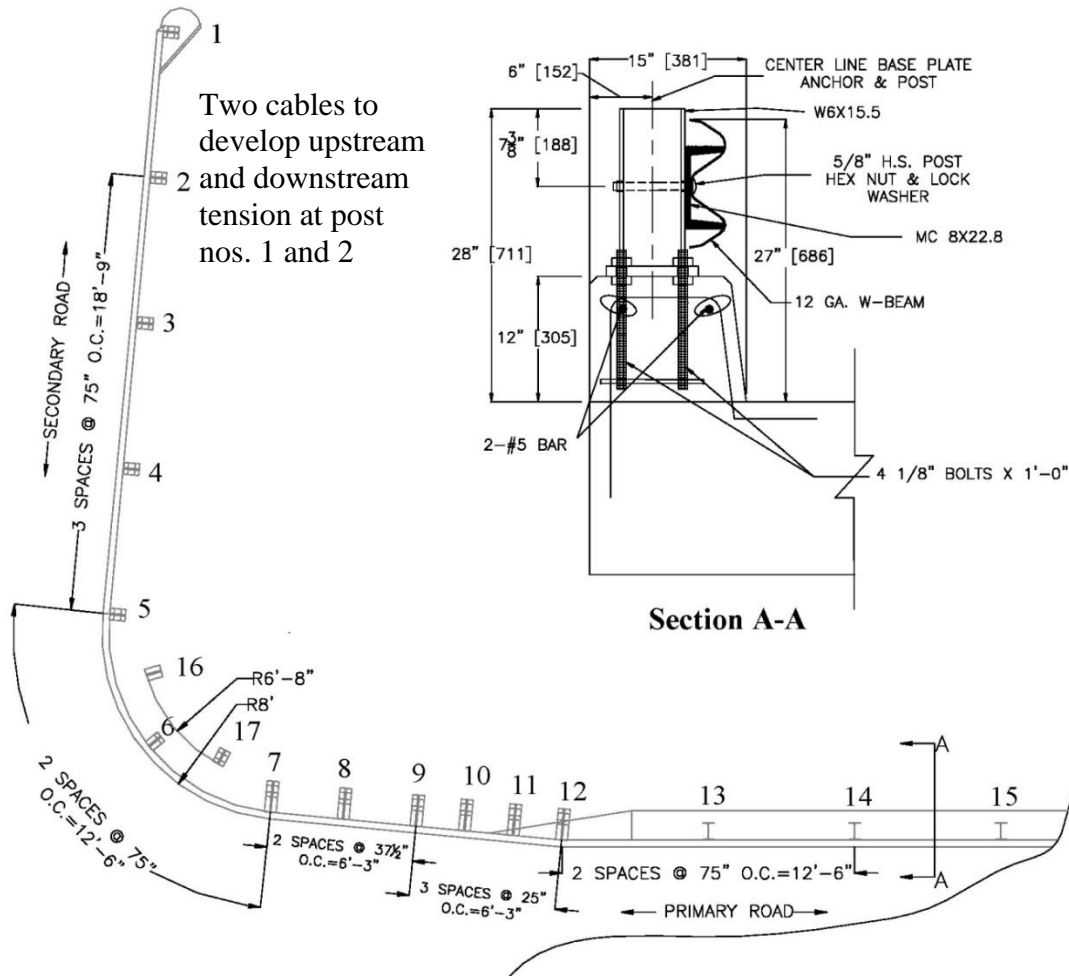


Figure 3. Yuma County Short-Radius Guardrail System – Final Details [6, 28]

2.3 Short-Radius Systems Tested to NCHRP Report No. 350 and MASH

TTI researchers have created a short-radius guardrail system that has passed several crash tests under MASH [4]. No short-radius systems have yet been approved according to the TL-3 crash test conditions required in NCHRP Report No. 350 or MASH. TTI researchers have tested a system that has passed several crash tests according to the TL-3 impact safety criteria found in MASH. The majority of NCHRP Report No. 350 and MASH-compliant tests on short-radius systems were conducted at either TTI or the Midwest Roadside Safety Facility (MwRSF).

2.3.1 TTI Thrie-Beam Short-Radius

TTI researchers designed a thrie-beam alternative to the TTI W-beam short-radius system successfully tested according to NCHRP Report No. 230 [11]. Final design details are shown in Figure 4. Researchers observed that the bending section of a nested 12-gauge (2.7-mm) W-beam section was approximately equivalent to the bending strength of a 10-gauge (3.4-mm) thrie-beam section. Due to the broader capture area of the thrie-beam, the higher top mounting height and lower bottom corrugation height, and ease of construction relative to the nested W-beam guardrails, particularly at splice locations, researchers postulated that the thrie-beam should perform approximately as well as the W-beam system.

Initially, the design was tested according to the TL-3 impact condition criteria presented in NCHRP Report No. 350. The first crash test, consisting of a 2000P vehicle impacting the system at 60.9 mph (98.0 km/h) and 26 degrees near the transition, was determined to be successful. The remaining two tests conducted with a 2000P vehicle into the curved nose of the system were both determined to be failures, due to override and vaulting. Researchers concluded that the system would require extensive modification to be considered crashworthy according to NCHRP Report No. 350.

Testing continued with the 1,800-lb (816-kg) small car and 4,500-lb (2,041-kg) sedan with angled hits into the center of the curved radius in compliance with NCHRP Report No. 230. The two tests passed with marginal performance due to the release of the rail from the upstream turned-down anchor in the sedan test and underide of the small car. The marginal performance of the system was unexpected, because the increased top mounting height of 31 in. (787 mm) also resulted in a lower bottom mounting height of 13 in. (330 mm), so underide was not expected.

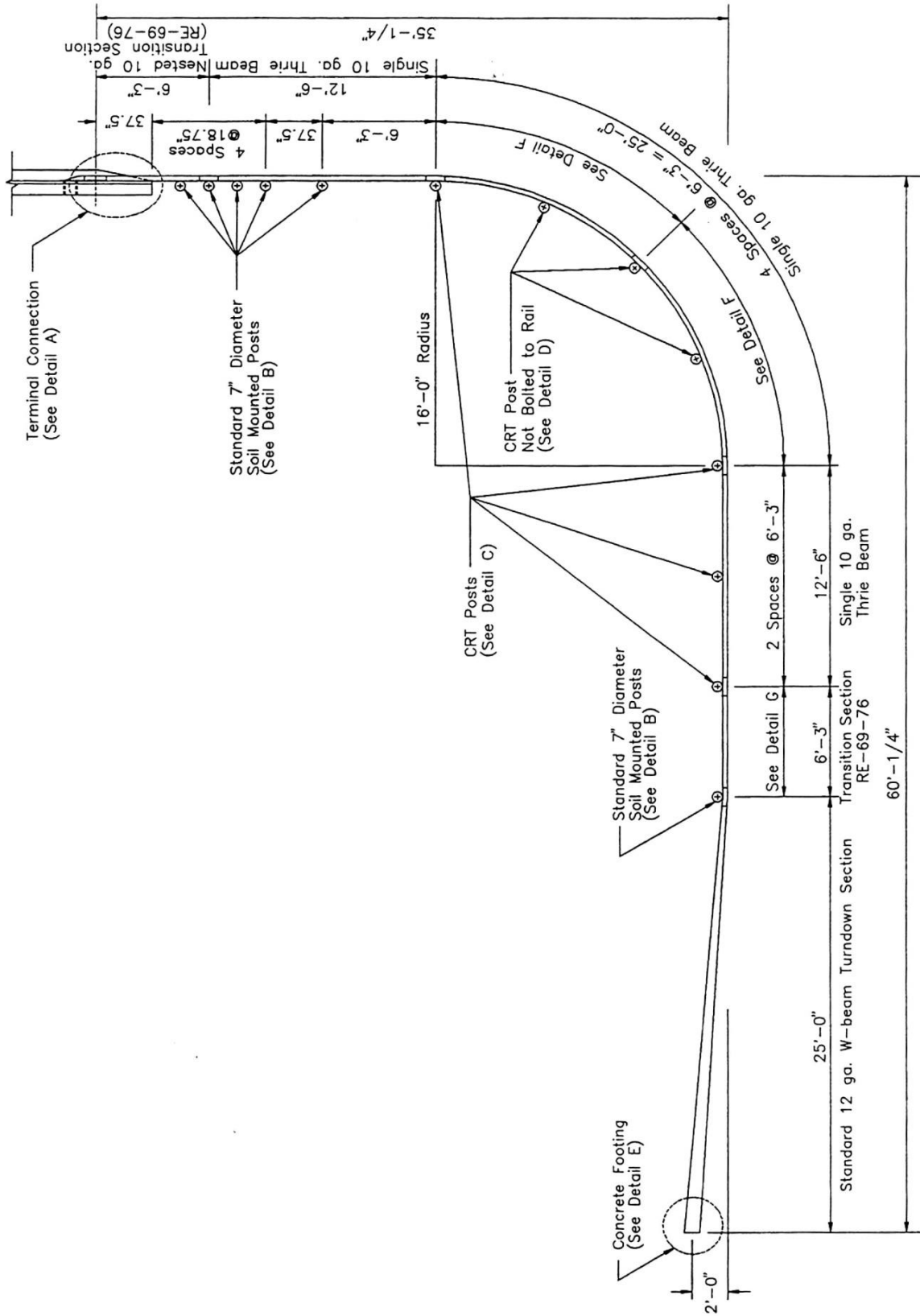


Figure 4. Final TTI Thrie-Beam Short-Radius Guardrail System [11]

2.3.2 MwRSF Short-Radius Guardrail System – R&D Project

MwRSF researchers also attempted to develop a crashworthy system according to the TL-3 test criteria presented in NCHRP Report No. 350 [12-14], as shown in Figure 5, and subsequently began to test the system using the criteria presented in MASH [15]. The final system that was tested under MASH is shown in Figure 6. The short-radius guardrail system was based on the NCHRP Report No. 350-tested, three-beam bullnose system and was constructed using curved three-beam elements. Rectangular CRT posts were used to support the rail along both the primary and secondary roads.

The curved nose piece initially had a 7-ft 9³/₄-in. (2,381-mm) radius, which was later changed to 8 ft – 11³/₈ in. (2,727 mm) when a parabolic flare was added to the system. Early tests utilized sloped terrain behind the system to replicate real-world conditions with roadside slopes, but the slopes were removed due to the increased risk of vaulting and artificial increase in instability due to interaction with the back side of the sloped cutout.

A total of six tests were conducted in compliance with NCHRP Report No. 350 TL-3 test criteria [12-14], and two tests were conducted in compliance with MASH TL-3 test criteria [15]. Impact conditions for each test are described in Table 3. Only one test was determined to be successful, which consisted of a 2000P pickup truck impacting the system with the centerline of the truck aligned with a tangent line to the bridge rail. The remaining tests, primarily consisting of angled impacts with 2000P, 820C, and 2270P vehicles into the center of the nose, failed due to vaulting, rollover, or underride.

Researchers concluded that the system performed reasonably well despite the failure to comply with the evaluation criteria. Thus, it was believed that it would likely be acceptable according to TL-2 safety criteria. However, the system was excessively large on the primary and

secondary sides, and it was generally undesirable to test under a lower performance level. Thus, no further testing was conducted.

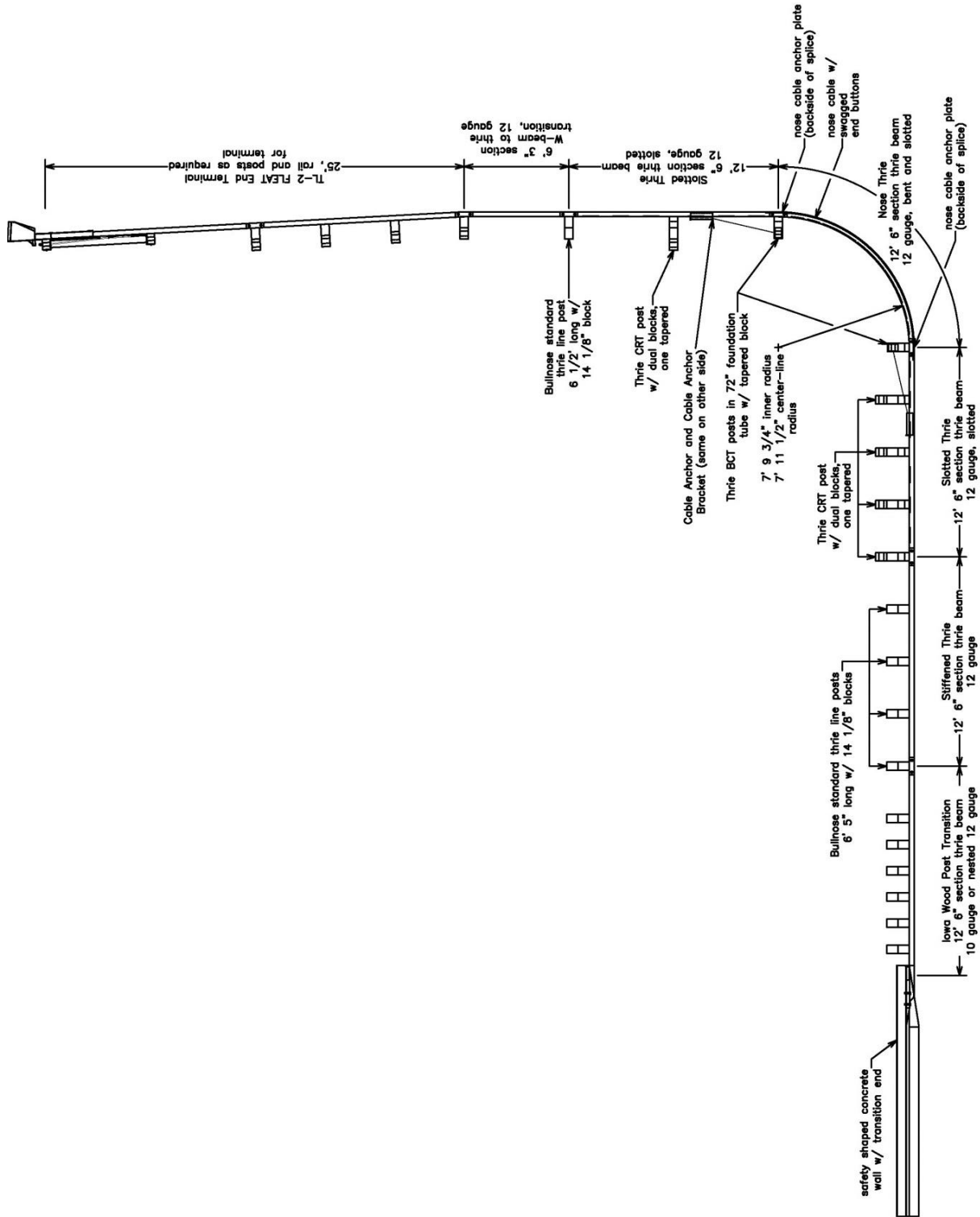


Figure 5. Preliminary MwRSF Thrie-Beam Short-Radius Guardrail System [12-13]

2.4 Bullnose Systems Tested Prior to NCHRP Report No. 230

Bullnose systems vary widely, but all systems utilized W-beam or thrie-beam as the primary rail element. One of the oldest crash-tested bullnose systems was the asymmetrical Minnesota W-beam bullnose [16]. The system resembled a parabolically-flared W-beam guardrail system located upstream from a median hazard that was connected to an identical, parabolically-flared system shielding the hazard from opposite direction crashes. Flares were transitioned over approximately $2\frac{1}{3}$ sections of 12-ft 6-in. (3,810-mm) W-beam. A single curved, W-beam rail section connected the flared rail on one side of the system to the straight rail on the other side. The system was tested in the early 1970s before NCHRP Report No. 230 was published. Tests consisted of a 4,500-lb (2,041-kg) sedan and a 2,290-lb (1,039-kg) small car impacting at approximately 60 mph (97 km/h) and 0 degrees relative to the nose of the system and with the centerline of the vehicle aligned with the center point of the radius. Both tests were determined to be satisfactory.

All of the remaining bullnose systems that were tested under the NCHRP Report No. 230 test criteria were symmetrical. One system design utilized a W-beam guardrail with a 4-ft 6-in. (1,372-mm) radius and a 10-degree flare from the nose. It was successfully tested by the California Department of Transportation (Caltrans) after extensive revisions to the initial design [17].

A novel crumpling bullnose system with a very sharp front-end profile was evaluated by TTI for the Colorado Department of Transportation [18]. The crumpling bullnose system consisted of W-beam rail flattened at the first four post locations, with staggered post locations to control W-beam buckling. A flattened, curved buffer nose piece was attached at the front of the system to act as the impact head, eliminating the need for any curved W-beam rail segments.

Four successful end-on crash tests were conducted into variations of the flattened-rail system, although one crash result was marginal due to occupant compartment deformation.

A third W-beam bullnose system was tested and modified by the Southwest Research Institute (SwRI), incorporating a curved frontal W-beam nose section, a curved W-beam transition section, and straight sections of W-beam downstream from the nose [19]. Cable anchors, ground struts, foundation tubes, post sizes, spacings and orientations, and rail slots were extensively modified during the development of the W-beam bullnose system. The system was successfully tested according to NCHRP Report No. 230 with 4,500-lb (2,041-kg) sedans and 1,800-lb (816-kg) small cars. A total of 16 tests were conducted on design modifications before the system was determined to be crashworthy according to NCHRP Report No. 230 performance criteria.

2.5 Bullnose Systems Tested to NCHRP Report No. 350

MwRSF conducted a series of tests on a bullnose system according to NCHRP Report No. 350 between 1997 and 2010 [20-25]. The crash test matrix for the bullnose system was similar to the required tests on the short-radius guardrail crash tests, as shown in Figure 7. The initial concept for the bullnose system was similar to the design that was tested and evaluated by SwRI according to NCHRP Report No. 230 test criteria. The system was composed of a 12-ft 6-in. (3,810-mm) curved and slotted thrie-beam section which formed the nose, a 12-ft 6-in. (3,810-mm) curved and slotted transition thrie-beam section, and two 12-ft 6-in. (3,810-mm) straight thrie-beam sections parallel to the roadways on the respective sides.

Initially, the 2000P pickup truck vaulted the system when struck at a 0-degree angle, and the slot tabs were shortened. In subsequent tests, the 2000P vehicle ruptured the rail and penetrated the system. The design was modified to include cables in the nose section of the thrie-beam to facilitate capture after the rail tore through the slot tabs.

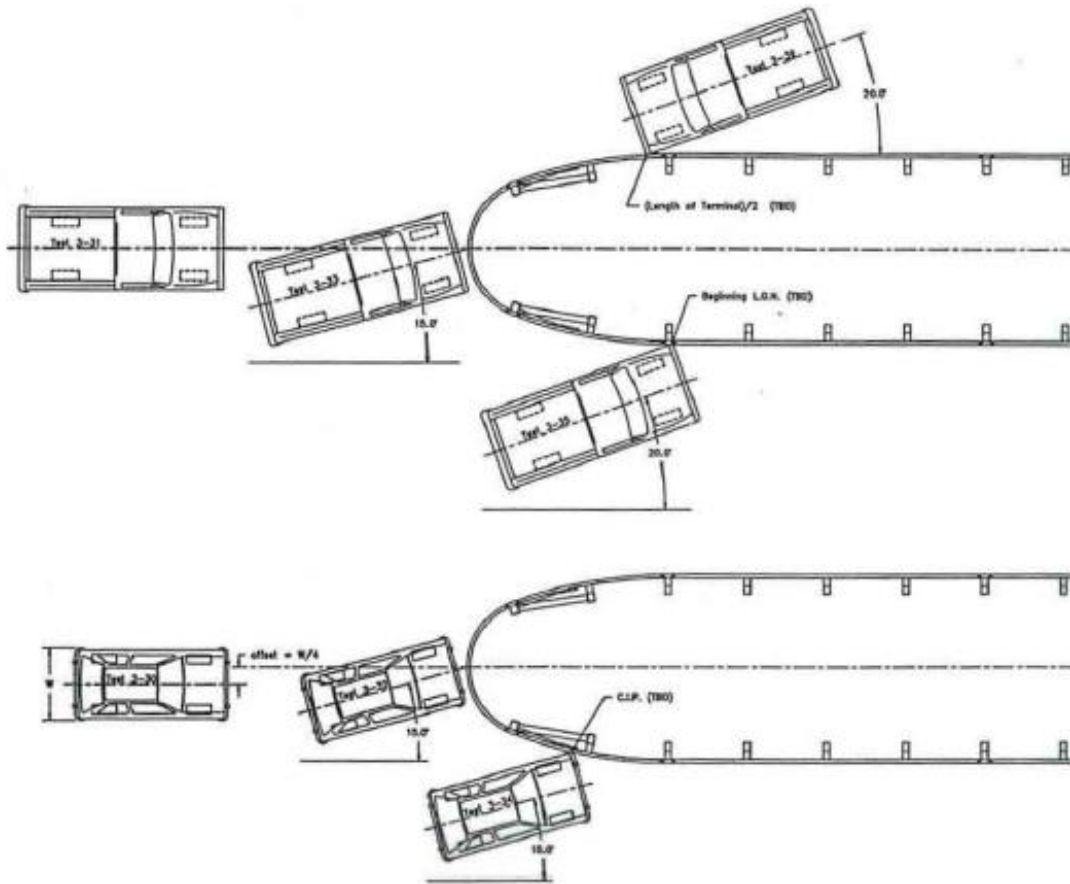


Figure 7. Required Bullnose Crash Tests According to NCHRP Report No. 350

Further tests with the 2000P vehicle into the critical impact point (NCHRP Report No. 350 test no. 3-35) resulted in vehicular launching. Researchers determined that the groundline strut connecting the first and second posts along each side of the system facilitated vehicle launching by lifting the vehicle and allowing the rail to pass beneath the vehicle's tire on the impacting corner. After further modifying the system, including eliminating the groundline strut, modifying several soil tubes, and reducing post spacing, the system successfully passed to the NCHRP Report No. 350 test designation no. 3-35, consisting of a 2000P vehicle impacting at 20 degrees and 62.1 mph (100.0 km/h) at the critical impact point (CIP) of the system. Additionally, the system was successfully tested in accordance with NCHRP Report No. 350 test designation

nos. 3-30 and 3-32, consisting of an 820C small car impacting the center of the nose of the system with a ¼-point offset at 62.1 mph (100 km/h) and 0 degrees, respectively.

2.6 Current Best Practices – Short-Radius Guardrail Systems

2.6.1 FHWA Technical Memorandum T5040.32

In 1992, the Federal Highway Administration published a technical advisory with regards to curved W-beam guardrail installations at intersecting roadways [8]. This advisory suggested using a curved guardrail system similar to the Yuma County system, with radii ranging between 8 ft - 6 in. and 35 ft (2,591 mm and 10,668 mm), as shown in Figure 8.

Recommendations were also included for the installation of short-radius guardrail systems, including: design drawings, capture area criteria based on radius size, slopes, and other important installation guidelines. The FHWA advised that existing curved guardrail installations may be replaced or upgraded as the opportunity becomes available [8].

2.6.2 Roadside Design Guide 4th Ed.

The AASHTO *Roadside Design Guide* (RDG) provided guidance on how to treat a minor road or driveway that intersects a main road close to a bridge end, a location that is difficult to adequately shield [1]. The RDG-preferred solution is to close or relocate the intersecting road and install a standard transition section with approach railing and crashworthy end terminal. When this option is not feasible, other alternatives should be considered even though the crashworthiness of the barrier may be reduced in some instances. The guide also notes that the use of appropriate crash cushions or other commercially available appurtenances may provide cost-effective solutions for shielding the bridge rail end. However, these systems may not provide adequate length-of-need (LON) for treating all hazards.

One possible solution outlined by the RDG is to use a curved guardrail system that was successfully crash-tested according to the requirements found in NCHRP Report No. 230. Based

on research conducted by TTI, it was acknowledged and determined appropriate that the NCHRP Report No. 230 system continue to be used for this installation on all high-speed routes, including the National Highway System (NHS), until an acceptable system was developed. When the 4th edition of the RDG was published, no NCHRP Report No. 350 or MASH-approved system had been developed. The guide also recommended following FHWA Technical Advisory T5040.32 for guardrail installations at intersecting side roads.

2.6.3 TTI Modified Yuma County System at TL-2 Acceptance

In 2010, TTI investigated the performance of previously-tested short-radius guardrail systems to determine if any of these systems would meet TL-2 of NCHRP Report No. 350 [26]. The system that was tested for Yuma County, Arizona formed the basis for developing a short-radius guardrail system that satisfied the TL-2 evaluation criteria of NCHRP Report No. 350. The nose section of this short-radius guardrail system consisted of a 12-ft 6-in. (3.8-m) curved W-beam segment, which had an 8-ft (2.4-m) radius. The curved section was mounted on breakaway CRT posts. Using dynamic bogie testing, the researchers determined that two CRT posts could be removed without significant change in system performance. Based on a review of previous short-radius guardrail systems, a short-radius guardrail system was developed to satisfy TL-2 of NCHRP Report No. 350, as shown in Figures 9 and 10.

2.6.4 Best Practices for Barrier Protection of Bridge Ends (2014)

In 2014, TTI completed a study to identify best practices for treating situations where the length-of-need requirements for bridge approach rails cannot be met [27]. Surveys were sent to state departments of transportation (DOTs) to acquire data concerning: practices or standards for bridge barriers when LON cannot be met, variation in practices according to design speed, use of different types of crash cushions, and installation of a short-radius guardrail in front of a slope.

From the information collected, short-radius guardrails were generally the preferred option by state DOTs for bridge locations where LON could not be met. Although a few state DOTs indicated the use of crash cushions at bridge locations where LON cannot be met, other states noted a very limited use due to higher installation and maintenance costs. In addition, crash cushion use may be impractical and undesirable on rural road sections with multiple driveway and side roads when considering their footprint. Some state DOTs preferred to relocate obstacles and driveway access to a point beyond the LON. When unfeasible to relocate obstacles and driveway access, state DOTs used different treatments to shield obstacles and included the use of short-radius guardrail systems, crash cushions, or even an adjustment to the LON equation.

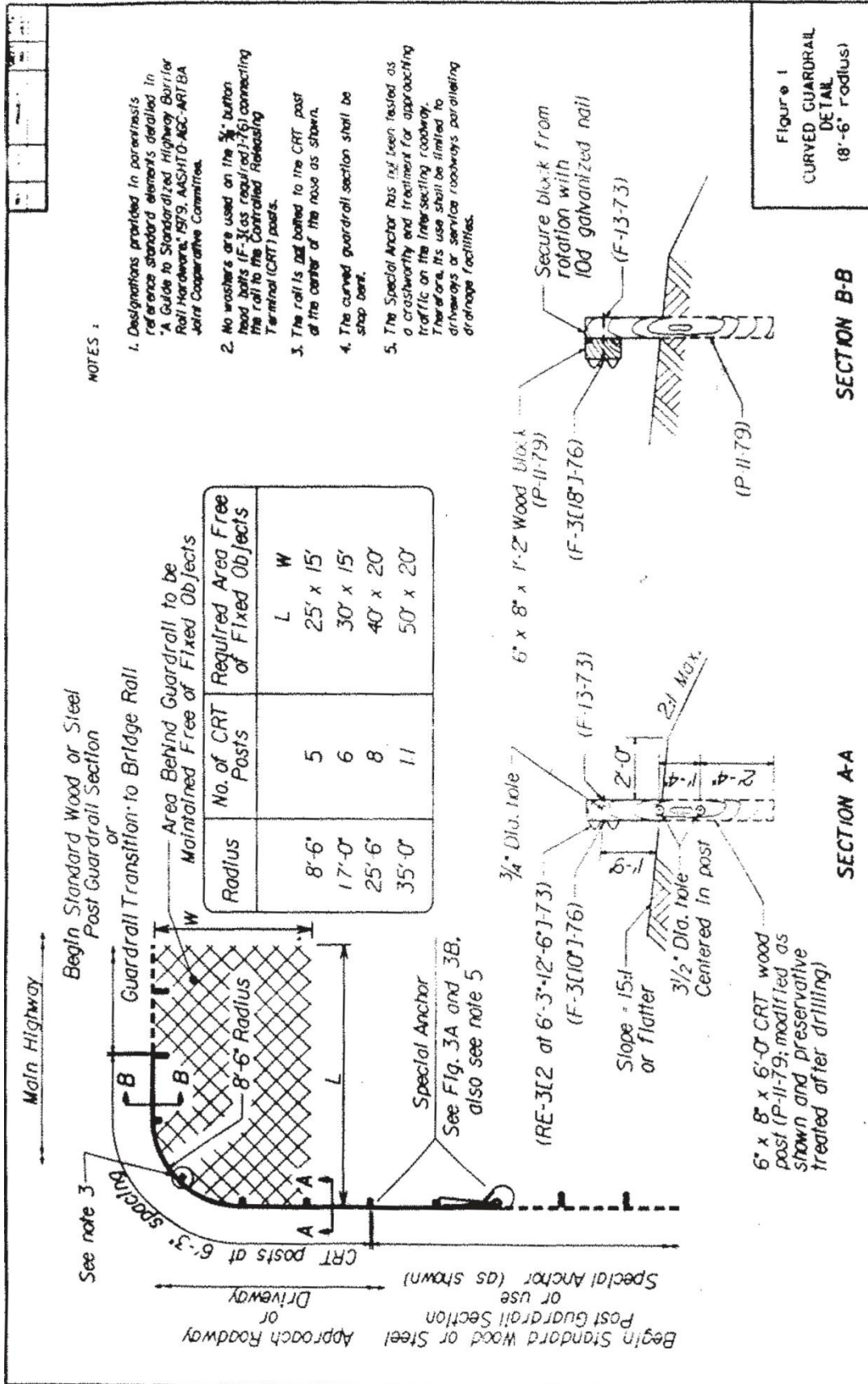


Figure 8. Acceptable Short-Radius Guardrail System, FHWA Technical Memorandum [8]

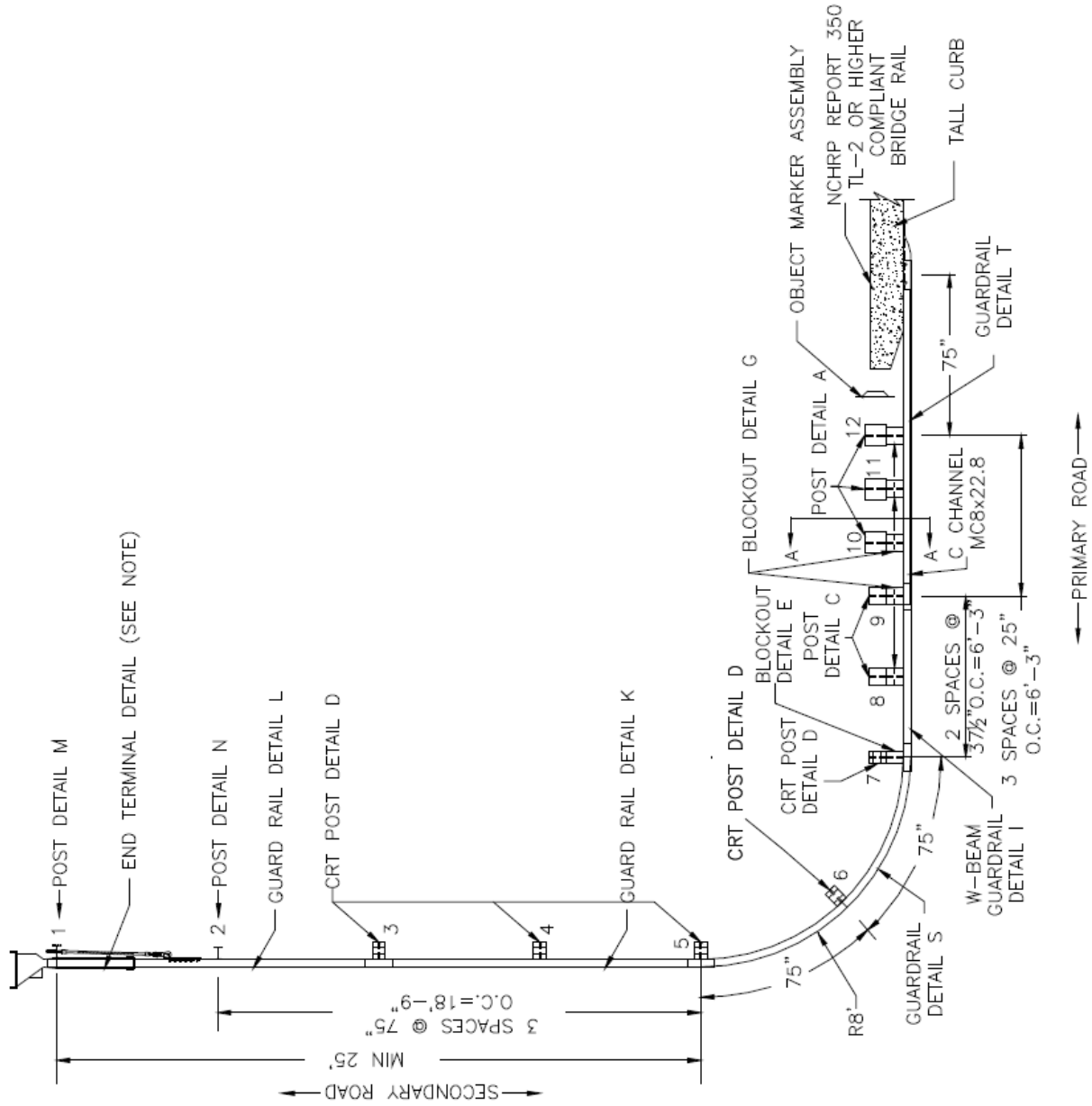


Figure 9. Recommended Short-Radius Guardrail System, TTI NCHRP Report No. 350 TL-2 System [26]

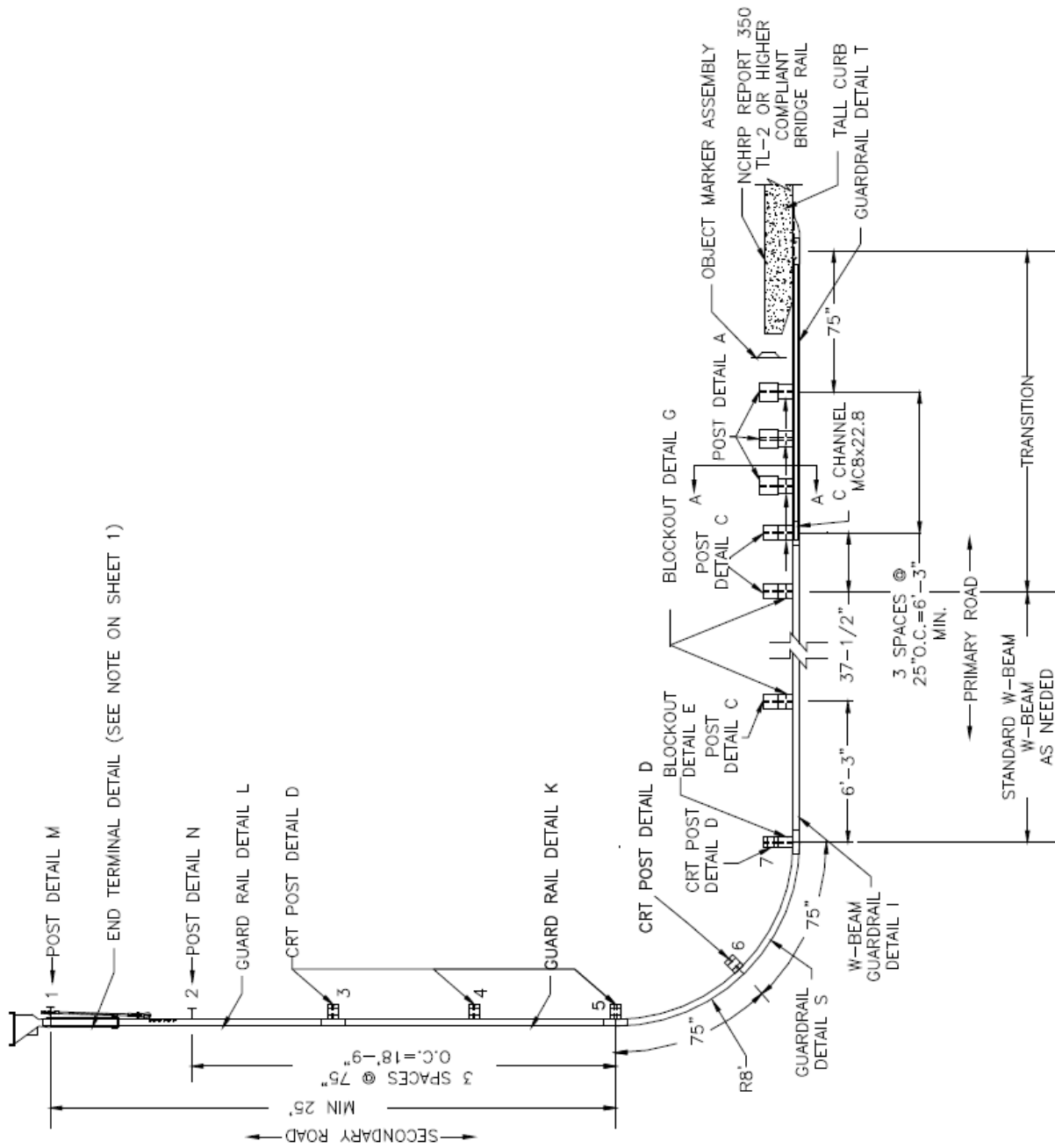


Figure 10. Acceptable Short-Radius Guardrail Designs, TTI NCHRP Report No. 350 TL-2 System [26]

3 END TERMINALS

A literature search was performed on existing guardrail end terminal systems to investigate their potential use in new concepts for safely treating intersecting roadways. These situations often occur where there is limited space adjacent to a bridge end. Therefore, the overall dimensions and dynamic deflections were collected for existing guardrail end terminals to determine their suitability for this application.

End terminals are used to prevent a vehicle from stopping abruptly when impacting the end of a roadside barrier. These devices are essentially crashworthy anchorages and are used to anchor a flexible or semi-rigid barrier on its upstream and downstream ends, likely when located within the clear zone. For this research study, only energy-absorbing guardrail end terminal systems meeting Test Level 3 conditions of NCHRP Report No. 350 or MASH were investigated. These crash test conditions are summarized in Tables 7 and 8.

FHWA resource charts for roadside and median end terminals served to aid field and design personnel in identifying and selecting barrier hardware [28-29]. These charts served as the basis for the list of systems shown in Table 9. The list contains all available TL-3 energy-absorbing, guardrail end terminal systems. Except for the Trinity SOFT-STOP Terminal, all systems were tested under NCHRP Report No. 350 TL-3 conditions. The overall dimensions and dynamic deflections for these systems were found using the approval letters for End Treatments and Crash Cushions on FHWA's website [30]. The data were gathered from the listed approval letters or one of their derivatives. The length value in the table refers to the distance from the end of the terminal to the beginning of standard guardrail. With typical end terminal lengths of at least 37 ft - 6 in. (11.4 m), most systems were potentially too long for the shortest intersection geometries. This finding was more concerning when these systems would also require a guardrail-to-bridge rail transition system in addition to the listed system. Many end terminal

systems allow oblique impacts to gate through the system from posts one through three. Tension-based, energy-absorbing end terminals that do not allow the vehicle to gate in this region may offer advantages due to a LON closer to the upstream end of the system.

Table 7. NCHRP Report No. 350 Test Matrix Conditions [2]

Test Level	Feature	Feature Type	Test Designation	Impact Conditions		
				Vehicle	Nominal Speed mph (km/h)	Nominal Angle Θ (deg)
3	Terminals and Redirective Crash Cushions	G/NG	3-30	820C	62.1 (100)	0
		G/NG	S3-30	700C	62.1 (100)	0
		G/NG	3-31	2000P	62.1 (100)	0
		G/NG	3-32	820C	62.1 (100)	15
		G/NG	S3-32	700C	62.1 (100)	15
		G/NG	3-33	2000P	62.1 (100)	15
		G	3-34	820C	62.1 (100)	15
		G	S3-34	700C	62.1 (100)	15
		G	3-35	2000P	62.1 (100)	20
		NG	3-36	820C	62.1 (100)	15
		NG	S3-36	700C	62.1 (100)	15
		NG	3-37	2000P	62.1 (100)	20
		NG	3-38	2000P	62.1 (100)	20
		NG	3-39	2000P	62.1 (100)	20
	Nonredirective Crash Cushions	G	3-40	820C	62.1 (100)	0
		G	S3-40	700C	62.1 (100)	0
		G	3-41	2000P	62.1 (100)	0
		G	3-42	820C	62.1 (100)	15
		G	S3-42	700C	62.1 (100)	15
		G	3-43	2000P	62.1 (100)	15
		G	3-44	2000P	62.1 (100)	20

Table 8. MASH Test Matrix and Conditions [3]

Test Level	Feature	Feature Type	Test Designation	Impact Conditions		
				Vehicle	Nominal Speed mph (km/h)	Nominal Angle Θ (deg)
3	Terminals and Redirective Crash Cushions	G/NG	3-30	1100C	62 (100.0)	0
		G/NG	3-31	2270P	62 (100.0)	0
		G/NG	3-32	1100C	62 (100.0)	5/15
		G/NG	3-33	2270P	62 (100.0)	5/15
		G/NG	3-34	1100C	62 (100.0)	15
		G/NG	3-35	2270P	62 (100.0)	25
		G/NG	3-36	2270P	62 (100.0)	25
		G/NG	3-37	2270P	62 (100.0)	25
		G/NG	3-38	1500A	62 (100.0)	0
	Nonredirective Crash Cushions	G	3-40	1100C	62 (100.0)	0
		G	3-41	2270P	62 (100.0)	0
		G	3-42	1100C	62 (100.0)	5/15
		G	3-43	2270P	62 (100.0)	5/15
		G	3-44	2270P	62 (100.0)	20
		G	3-45	1500A	62 (100.0)	0

Table 9. Summary of Energy-Absorbing, Guardrail End Terminals with Dynamic Deflections

Type	Name	Manufacturer	Tangent/Flared	Length	Height	Flared Offset	Dynamic Deflection, in.										FHWA Approval Letter
							3-30	3-31	3-32	3-33	3-34	3-35	3-36	3-37	3-38	3-39	
Roadside Terminal	Bursting Energy Absorbing Terminal (BEAT)	Road Systems, Inc.	Tangent	14'	28"		73	57									CC-69
	Extruder Terminal (ET-Plus)	Trinity Highway Products, LLC	Tangent	37'-6"	27 3/4" or 31"	24"	214	457		11	37						CC-94
	Flared Energy-Absorbing Terminal (FLEAT)	Road Systems, Inc.	Flared	37'-6"	27 3/4"	30"-48"	302	690		33	70						CC-46 CC-61 CC-88
	Sequential Kinking Terminal (SKT)	Road Systems, Inc.	Tangent	37'-6"	27 3/4"	18"	NR	690	NR	NR	31						CC-40 CC-61 CC-88
	TREND 350 Flared	Trinity Highway Products, LLC	Flared	37'-6"	27 3/4" or 31"	48"	NR	NR	NR	NR	NR					NR	CC-123T
	Trinity SOFT-STOP Terminal	Trinity Highway Products, LLC	Tangent	37'-6"	31"		NR	548	212	24	139		102				CC-115
	Wyoming Box-Beam End Terminal (WY-BET)	Trinity Highway Products, LLC	Tangent	49'-2"	28"		113	162	361	112	63						CC-60
	X-Lite Terminal	Barrier Systems, Inc./Formet, Inc.	Both	37'-6"	27 5/8" or 31"	0"-48"	N/A	N/A			22	27					CC-120
	X-Tension Guardrail End Terminal	Barrier Systems, Inc.	Both	37'-6"	27 5/8" or 31"	0"-48"	15	NR	NR	NR	22	N/A		NR			CC-102
	Brakemaster 350	Energy Absorption Systems, Inc.	Tangent	31'-6"	27"		NR	NR	NR	NR	NR	NR					CC-41
Median Terminal	Bursting Energy Absorbing Terminal-Median (BEAT-MT)	Road Systems, Inc.	Tangent	32'-3 7/8"	28"												CC-69A
	Crash Cushion Attenuating Terminal (CAT-350)	Trinity Highway Products, LLC	Tangent	31'-3"	27 3/4"					NR							CC-33
	FLEAT Median Terminal (FLEAT-MT)	Road Systems, Inc.	Tangent	37'-6"	27 3/4"			NR									CC-46 CC-88E
	TREND 350 Median	Trinity Highway Products, LLC	Tangent	25'	27 3/4" or 31"		NR	NR									CC-122
	Wyoming Box-Beam End Terminal (WY-BET)	Trinity Highway Products, LLC	Tangent	49'-2"	28"		113	162	361	112	63						CC-60
	X-Tension Median Attenuator System (X-MAS)	Barrier Systems, Inc.	Tangent	37'-6"	28" or 31"		N/A	NR	NR								CC-102

4 CRASH CUSHIONS

A literature search was performed on existing crash cushion systems to investigate their potential use in new concepts for safely treating intersecting roadways. These situations often occur where there is limited space adjacent to a bridge end. Therefore, the overall dimensions and dynamic deflections were collected for existing crash cushions to determine their suitability for this application.

Crash cushions are designed to protect an errant vehicle from impacting a fixed object by gradually decelerating the vehicle to a safe stop or by redirecting the vehicle away from the obstacle. Crash cushions are typically anchored to the road surface, except for inertial barrier systems (e.g., sand barrels). For this research study, only crash cushion systems meeting the Test Level 3 of NCHRP Report No. 350 or MASH were investigated. These crash test conditions are summarized in Tables 7 and 8.

Crash cushions are categorized by two qualities: (1) gating versus non-gating and (2) redirective versus non-redirective. With a gating crash cushion, a vehicle impacting at an angle on the nose or the side of a crash cushion near the nose allows a vehicle to pass or gate through the crash cushion. A non-gating cushion prevents a vehicle from passing through the crash cushion even under impacts at the nose or on the side of a crash cushion near the nose but at an angle. With a redirective crash cushion, a vehicle impacting along the side of the crash cushion but downstream from the nose will be safely redirected back along traffic. A non-redirective system will capture the vehicle or let it pass through the barrier. For this study, a non-gating, redirective system could be advantageous if it would limit system interference when multiple safety treatments are used near one another.

FHWA resource charts for crash cushions served as an aid for field and design personnel in identifying and selecting barrier hardware [31]. These charts served as the basis for systems

shown in Tables 10 through 12. These lists consisted of all commonly available TL-3 crash cushion systems. The overall dimensions and dynamic deflections of these systems were found using the approval letters for End Treatments and Crash Cushions on the FHWA website [30]. The data were gathered from the listed approval letters or one of their derivatives. All commonly-used crash cushions are proprietary products.

Table 10. Non-Redirecting Crash Cushions and Dynamic Deflections

Style	Name	Manufacturer	Test Level	Width	Length	Height	Dynamic Deflection, in.						FHWA Approval Letter		
							3-38	3-40	3-41	3-42	3-43	3-44			
Non-Redirective, Gating	Absorb 350	Barrier Systems, Inc.	NCHRP 350 TL-2, TL-3	24"	VARIABLE 19'-4" (45 mph) to 32'-0" (60 mph)	32"	NR	NR	NR	NR	NR	NR	NR	NR	CC-66
	ACZ-350	Energy Absorption Systems, Inc.	TL-2, TL-3	20"	31'-7"	33"		106	218				67		CC-47
	Big Sandy	TraFFix Devices	TL-2, TL-3	Varies to fit site	VARIABLE (30 to 65 mph)	35" to 47"		N/A	N/A	N/A	N/A	N/A	N/A	N/A	CC-52
	CrashGuard	Plastic Safety Systems	TL-2, TL-3	Varies to fit site	VARIABLE (25 to 70 mph)	53"		NR	NR	NR	NR	NR	NR	NR	CC-97
	Energite	Energy Absorption Systems, Inc.	TL-2, TL-3	Varies to fit site	VARIABLE (30 to 65 mph)	32" to 36"		NR	NR	NR	NR	NR	NR	NR	CC-29
	Fitch	Energy Absorption Systems, Inc.	TL-2, TL-3	Varies to fit site	VARIABLE (30 to 65 mph)	33"		NR	NR	NR	NR	NR	NR	NR	CC-28
	SLED	TraFFix Devices	TL-2, TL-3	22 1/2"	25'-3"	42"		N/A	N/A	N/A	N/A	N/A	N/A	N/A	CC-114 CC-117
	NR = Test was performed but dynamic deflection was not reported N/A = Test was performed but dynamic deflection was reported as "N/A"														

5 TRUCK- AND TRAILER-MOUNTED ATTENUATORS

A literature search was performed on existing truck- and trailer-mounted attenuators (TMAs) to investigate their potential use in new concepts for safely treating intersecting roadways. These situations often occur where there is limited space adjacent to a bridge end. Therefore, the overall dimensions and dynamic deflections were collected for TMAs to determine their suitability for this application.

TMAs are a special type of crash cushion used to protect construction and maintenance personnel in work zones. These devices are essentially portable crash cushions, which are directly mounted onto the rear of a large truck or towed behind a vehicle as a trailer. The truck prevents vehicles from traversing the work site, while the TMA is used to reduce the severity of a rear-end impact. These devices may be used in moving operations, such as pavement marking, roadway sweeping, and maintenance activities in high-volume, high-speed areas, or at long-term, stationary construction sites [1].

TMAs are split into the following three classes of protective vehicles in work zones: shadow, barrier, and advance-warning trucks. A shadow vehicle is a moving truck traveling behind a moving operation, protecting the work site personnel from traffic approaching from the rear. Barrier vehicles are parked upstream from a work zone and are typically left unoccupied. Advance-warning trucks are also parked a considerable distance upstream from a moving or stationary operation, but they also display an arrow panel and other signs, as appropriate.

The overall dimensions and dynamic deflections of these systems were found using the approval letters for End Treatments and Crash Cushions on FHWA's website and are shown in Table 13 [30]. The data were gathered from the approval letters or one of their derivatives from FHWA website. The wide area of protection needed for protecting intersecting roadways would

likely require multiple TMA devices. None of the investigated systems were likely capable of being made wider without significant redesign of the device. In addition, the effects of using multiple units next to each other are unknown and would require testing to determine if this would be suitable.

Table 13. Truck- and Trailer-Mounted Attenuator Systems and Dynamic Deflections

Style	Name	Manufacturer	Length	Width	Height	Road Clearance	Weight	Dynamic Deflection, in.					FHWA Acceptance
								3-50	3-51	3-52	3-53	3-53	
Truck	Alpha 100K	Energy Absorption Systems, Inc.	100"	93"	22 1/2"	11'-13"	990 lb - 1200 lb	3.3	3.6				CC-39
	MPS-350	Trinity Highway Products	168"	70 11/16"	18 3/8"	12'-14"	1600 lb	NR	NR				CC-34
	RAM-100K	RENCO	132"	84"	22 1/2"		850 lb	2.1	1.7				CC-67
	Safe-Stop 180	Energy Absorption Systems, Inc.	170"	93"	50"	11'-13"	2080 lb	2.2	3.3	3.5	3.1		CC-78
	Scorpion	TraFFix Devices Inc.	166"	96"		12"	1975 lb	N/A	N/A	N/A	N/A		CC-65
	U-MAD 100K	Barrier Systems Inc.	129"	90"	28"	11'-13"	910 lb	NR	NR				CC-64
	Scorpion Trailer	TraFFix Devices Inc.	157"	96"	36"				N/A	N/A	N/A	N/A	CC-65
	Safe-Stop Trailer TMA	Energy Absorption Systems, Inc.	231"	93"	45"		2650 lb		NR	4.8	3.6		CC-78
	TTMA-100	Gregory, Safety By Design Co	276"	96"	31"	13"	1450 lb	3.077	5.132	N/A	N/A		CC-79 CC-90
	U-MAD Trailer 100K	Barrier Systems Inc.	129"	90"	40"		915 lb	NR	NR	1.3			CC-99 CC-103
Trailer	Vorteq	Energy Absorption Systems, Inc.	275"	92"	30 1/2"		1310 lb	2.9	4.3	4.9	4.7		CC-104

NR = Test was performed but dynamic deflection was not reported
N/A = Test was performed but dynamic deflection was reported as "N/A"

6 NET AND CABLE ATTENUATION SYSTEMS

A literature search was performed on existing net and cable attenuation systems to investigate their potential use in new concepts for safely treating intersecting roadways. These situations often occur where there is limited space adjacent to a bridge end. Therefore, the overall dimensions and dynamic deflections were collected for existing net and cable attenuation systems to determine their suitability for this application. In addition to overall system dimensions, their method of operation is also important. It is desirable that new concepts are long-term solutions to the problem with minimal maintenance required for operation.

There are several net attenuation systems available for the defense, aerospace, and highway safety industries. They shield work zones, capture runaway airplanes, and protect entrances to military bases. While there is no highway testing standard for net attenuation systems, many systems have been crash tested and received FHWA acceptance based on modified testing for crash cushions. Net attenuation systems from the security industry are often tested to SD-STD-02.01 [32] or ASTM International Designation F 2656-07 [33].

SD-STD-02.01 provided a range of specified levels of vehicle impact resistance required by the U.S. Department of State (DOS) and the Bureau of Diplomatic Security (DS) to select appropriate perimeter barriers and gates for use at DOS Facilities. This standard uses a 15,000-lb (6,800-kg) vehicle with different impact speeds to define performance ratings, as shown in Table 14.

Table 14. SD-STD-02.01 Impact Condition Designations for 15,000-lb (6,800-kg) Vehicle [32]

Nominal Impact Speed mph (kph)	Permissible Impact Speed Range mph (kph)	Kinetic Energy kip-ft (kJ)	Designation
50 (80)	47.0-56.9 (75.0+)	1,250 (1,695)	K12
40 (65)	38.0-46.9 (60.1-75.0)	800 (1,085)	K8
30 (50)	28.0-37.9 (45.0-60.0)	450 (610)	K4

ASTM F2656-07 provides a range of vehicle impact conditions, designations, and penetration performance levels that allow defense agencies to select passive perimeter barriers and active entry point barriers that are appropriate for their specific applications. This standard supersedes SD-STD-02.01 and attempts to address some of its shortcomings, such as lacking a range of vehicle types and tiered protection levels. These impact conditions are shown in Table 15.

Table 15. ASTM F 2656-07 Impact Condition Designations [33]

Test Vehicle	Nominal Mass lb (kg)	Nominal Test Velocity mph (km/h)	Kinetic Energy ft-kips (kJ)	Designation
Small Passenger Car (C)	2,430 (1,100)	40 (65)	131 (179)	C40
		50 (80)	205 (271)	C50
		60 (100)	295 (424)	C60
Pickup Truck (P)	5,070 (2,300)	40 (65)	273 (375)	PU40
		50 (80)	426 (568)	PU50
		60 (100)	613 (887)	PU60
Medium-Duty Truck (M)	15,000 (6,800)	30 (50)	451 (656)	M30
		40 (65)	802 (1110)	M40
		50 (80)	1250 (1680)	M50
Heavy Goods Vehicle (H)	65,000 (29,500)	30 (50)	1950 (2850)	H30
		40 (65)	3470 (4810)	H40
		50 (80)	5430 (7280)	H50

The dynamic deflection for a system on the anti-ram barrier list is referred to as penetration distance. This penetration distance is defined as the distance from the pre-impact,

inside edge of a barrier to the leading edge of the vehicle cargo bed [33]. These penetration ratings are shown in Table 16.

Table 16. ASTM F 2656-07 Penetration Rating System [33]

Designation	Dynamic Penetration Rating
P1	≤ 3.3 ft (1 m)
P2	3.31 to 23.0 ft (1.01 to 7 m)
P3	23.1 to 98.4 ft (7.01 to 30 m)
P4	98 ft (30 m) or greater

Many barriers meeting the ASTM F2656-07 standard can be found on the Department of Defense Anti-Ram barrier list [34]. The Anti-Ram barrier list provided some cable or net options for capturing vehicles, but it did not include systems with a P4 designation. Many of the barrier systems on that list are not recommended for safety treatments. Though some of the systems had dynamic deflections in the range of what was needed for this application, not all of them were suitable for highway installations. Passive, active, and mobile performance characteristics refer to how these systems function. Passive systems do not move, active systems can be lowered or moved to allow vehicles or personnel to pass through them, and mobile systems can be set up in temporary locations where entry points need to be controlled. Some systems, such as the Dragnet Vehicle Arresting Barrier, had both ASTM F2656-07 and NCHRP Report No. 350 approval. The overall dimensions and dynamic deflections of these systems were found using product manuals [35-43], approval letters for End Treatments and Crash Cushions on FHWA’s website [28], and/or the Anti-Ram barrier list. The data were gathered from the listed approval letters or one of their derivatives. These net and cable systems are shown in Table 17 .

7 DESIGN CRITERIA

7.1 Design Space Requirements

The Nebraska Department of Roads (NDOR) provided examples of intersections where an approved guardrail end terminal and Approach Guardrail Transition (AGT) could not be used to shield the bridge rail end adjacent to an intersecting roadway due to lack of space, as shown in Figure 11. From discussions with the Technical Advisory Committee (TAC), some specific site constraints were determined.

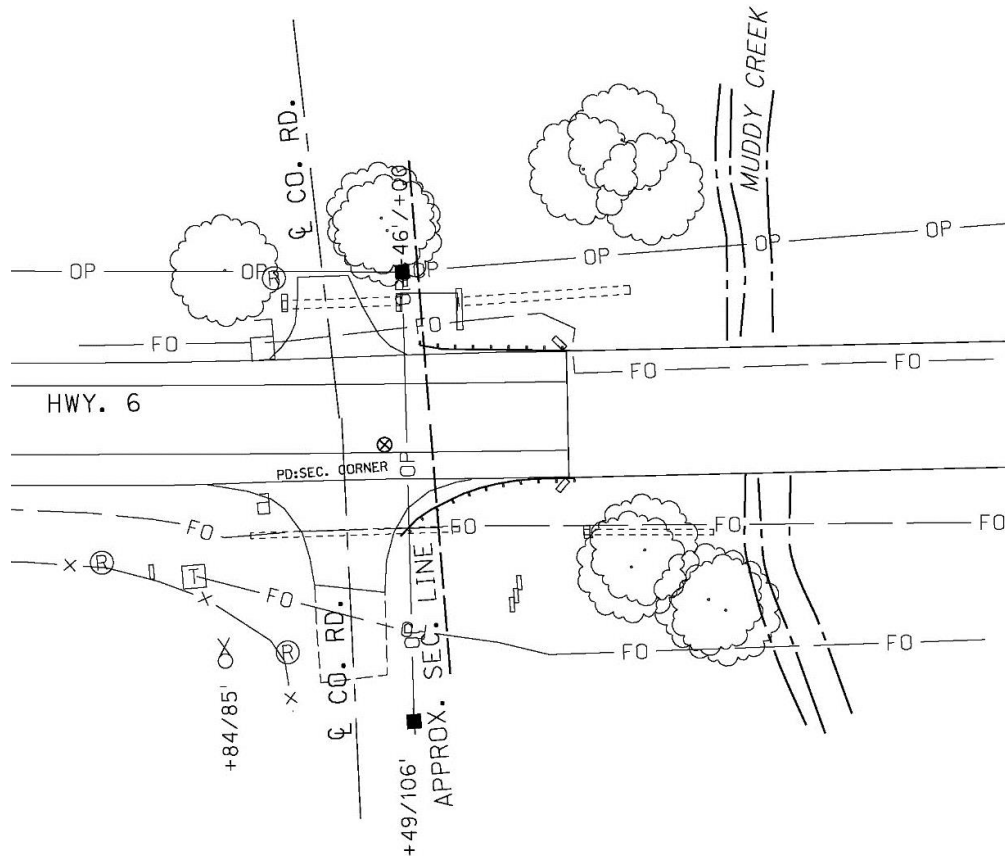


Figure 11. Example Intersection [44]

Typical intersection radii for these locations often range between 25 ft (7.6 m) and 50 ft (15.2 m). The bridge railing end is often located within 25 ft (7.6 m) from the intersection with

many locations having steep slopes beginning downstream from the bridge rail end. The bridge rail was assumed to be laterally offset 4 ft (1.2 m) away from the roadway edge. Also, the sponsor suggested that a clear-zone distance of 30 ft (9.1 m) should be assumed for all locations. These design details are shown in Figure 12.

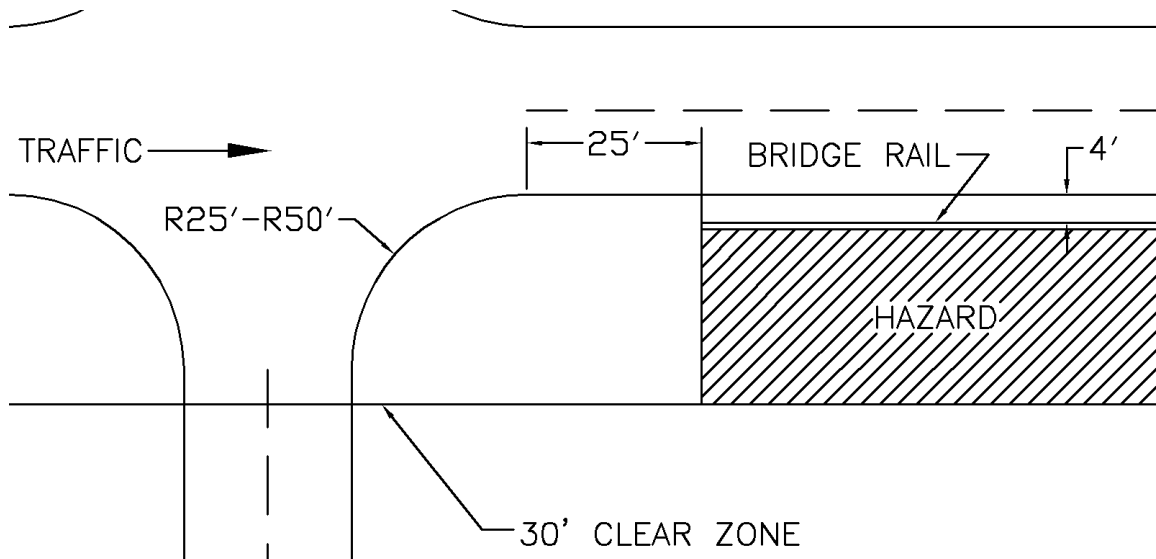


Figure 12. Site Constraints for New Impact Attenuation System

7.2 Impact Conditions Determined By Length of Need

When developing new ideas to treat these situations, it became apparent that different evaluation criteria were needed to compare the new concepts. Previous testing performed on short-radius guardrail systems was based on AASHTO bridge protection guidelines or modified crash cushion test matrices. The test matrix was adapted to the geometry of the guardrail systems, but it did not address all of the potential impacts possible near intersecting roadways.

The discrepancy between previous testing of short-radius guardrail systems and the actual impact conditions relative to bridges adjacent to intersecting roadways was discussed with NDOR sponsors. This discussion led to the determination to treat the intersection condition in a similar manner as used for general hazards found within the clear zone distance, as shown in

Figure 13. The hazard would extend perpendicular from the end of the bridge railing to the maximum clear zone distance, also shown in Figure 13. The area shielded would be determined with the runout length and LON from the RDG [1]. The upstream end of the bridge railing was used to define the beginning of the hazard, as steep slopes often begin at the end of the bridge railing. The length of need was determined using runout lengths suggested in the RDG (4th Ed.) for 60-mph (100-km/h) design speeds, as shown in Table 18. The resultant runout length for the system was 300 ft (91.4 m), assuming the ADT for the primary road would be 10,000 vehicles per day or greater, as shown in Figure 13. For 1,000 ADT and less, the runout length for the system would be only 200 ft (61.0 m), but for the purpose of this project, a higher ADT was assumed and deemed more conservative.

An alternative method was considered for determining the protected area, which assumed that vehicles could not traverse the area upstream from the secondary roadway. For this method, a line was drawn tangent to the radius opposite of the safety treatment and through a point to the back of the hazard. This approach may be applicable if a guardrail system was installed on the road upstream from the intersection. This third option decreased the coverage area required for new impact-attenuation systems, especially systems with very short intersection radii. Ultimately, the AASHTO RDG LON option was used to determine the protected or shielded area, as it better represented the worst-case scenario and would be largely consistent with state DOT design practice for treating roadside hazards. This conservative LON method does create a larger protected area, which is more difficult to shield. In the end, the sponsor decided that shielding that larger area was justified, given the treatment of other hazards.

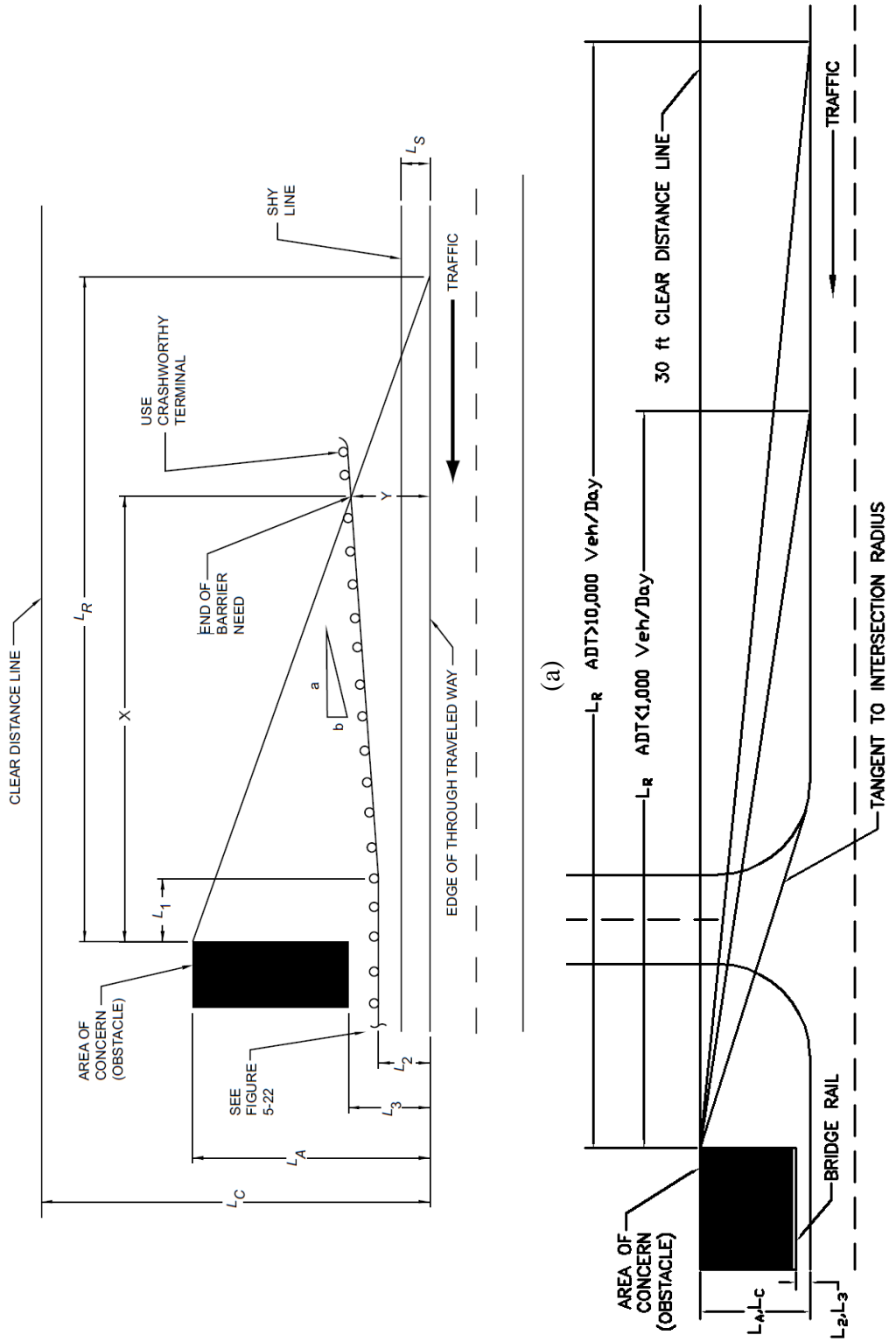


Figure 13. (a) Approach Guardrail with Variables [1], (b) Intersection Near Bridge with Variables

Table 18. Suggested Runout Length (L_R) for Barrier Design Given Traffic Volume (ADT) [1]

Design Speed mph (km/h)	Runout Length, L_R			
	Over 10,000 veh/day ft (m)	5,000 to 10,000 veh/day ft (m)	1,000 to 5,000 veh/day ft (m)	Under 1,000 veh/day ft (m)
80 (130)	470 (143)	430 (131)	380 (116)	330 (101)
70 (110)	360 (110)	330 (101)	290 (88)	250 (76)
60 (100)	300 (91)	250 (76)	210 (64)	200 (61)
50 (80)	230 (70)	190 (58)	160 (49)	150 (46)
40 (60)	160 (49)	130 (40)	110 (34)	100 (30)
30 (50)	110 (34)	90 (27)	80 (24)	70 (21)

7.3 Line of Sight Considerations

Intersections are designed so that their geometry and nearby obstacles or features do not create navigational problems for motorists that could result in traffic collisions. The sight distance, as defined in *Intersection Safety: A Manual for Local Rural Road Owners*, is the distance a motorist can see an approaching vehicle before their line of sight is blocked by an obstruction near the intersection [45]. The driver of a vehicle approaching or leaving an intersection requires an unobstructed view of the intersection with sufficient lengths along the intersecting roadway to anticipate and avoid potential collisions.

A barrier's height is an important consideration when considering new concepts. A system that is too tall reduces the sight distance for drivers on the secondary road turning onto the primary roadway. The *AASHTO Policy on Geometric Design of Highways and Streets* advises that roadside features should be less than 3.0 ft (0.91 m) above the road [46]. This criterion could be violated if the structure, such as a net, could be seen through. The area needed for this unobstructed view is called the Clear Sight Triangle, as shown in Figure 14. The Intersection Sight Distance (ISD) is measured along the major road beginning at a point that

coincides with the location of the minor road vehicle. The ISD is based on the following assumptions [45]:

- Stop control of the minor road approaches;
- Using driver eye and object heights associated with passenger cars;
- Both minor and major roads are considered at level grade;
- Considers a left-turn from the minor road as the worst-case scenario (i.e., requiring the most sight distance); and
- The major road is an undivided, two-way, two-lane roadway with no turn lanes.

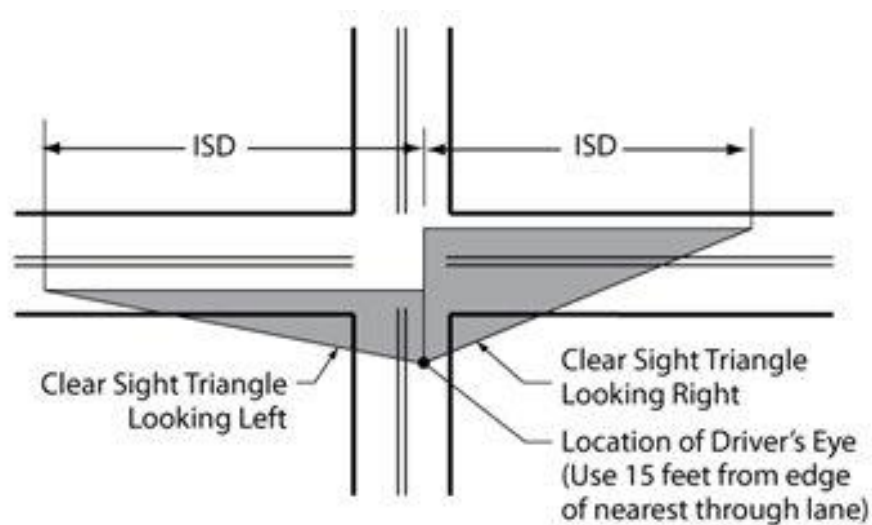


Figure 14. Clear Sight Distance Triangles for 4-Leg Stop-Controlled Intersections [45]

The Stopping Sight Distance (SSD) refers to the distance required for drivers to avoid potential collisions. Sight distances that exceed the recommended SSD, as shown in Table 19, are desirable.

Table 19. Sight Distance at Intersections [45]

Speed mph (km/h)	Stopping Sight Distance ft (m)	Design Intersection Sight Distance ft (m)
25 (40)	155 (47.2)	280 (85.3)
30 (48)	200 (61)	335 (102.1)
35 (56)	250 (76.2)	390 (118.9)
40 (64)	305 (93)	445 (135.6)
45 (72)	360 (109.7)	500 (152.4)
50 (80)	425 (129.5)	555 (169.2)
55 (89)	495 (150.9)	610 (185.9)
60 (97)	570 (173.7)	665 (202.7)
65 (105)	645 (196.6)	720 (219.5)

7.4 Preference for Existing Technologies

Preference was given to design concepts that utilized existing technologies in order to limit new hardware development for this project. An important consideration for this project was how well designs could be implemented into new concepts without interfering with the operation of another technology.

7.5 Other Considerations

Many locations that require a short-radius guardrail system have moderate to steep slopes inside the intersection radius. Though there are no specific criteria, it is desirable for new concepts to accommodate moderate slopes. These locations are often found in wetland areas. Thus, there are environments that limit the use of chemicals to control weeds and brush in those areas. As such, the protected area should allow access for mowers and other equipment to be used in the protected area. NDOR also indicated that it would be preferable if a guardrail system was not required along the secondary road.

8 DESIGN CONCEPTS

New design concepts were developed for treating bridge ends adjacent to intersecting roadways as well as to accommodate the design space and impact condition requirements. The concepts needed to address the design issues inherent to the current short-radius system, while improving impact performance and decreasing the overall system footprint.

A total of fifteen design concepts were identified in the initial brainstorming sessions.

They include:

- Concept A – Net Attenuator/End Terminal or Crash Cushion
- Concept B – Dual Bullnose
- Concept C – Bullnose with Sand Barrels
- Concept D – Bullnose
- Concept E – Two End Terminals with Secondary Energy-Absorbing Guardrail
- Concept F – Two Disconnected Guardrails
- Concept G – Cable or Net Attached Behind Two End Terminals
- Concept H – Energy Absorbers Between Impact Panel and Portable Concrete Barriers
- Concept I – Energy Absorbers, Rails, and Posts
- Concept J – Rubber Cylinders Between Impact Panel and Restoring Barrier
- Concept K – Sand Barrels with End Terminal or Crash Cushion
- Concept L – TMA(s) Between Two End Terminals
- Concept M – TMA(s) or Crash Cushion(s) with End Terminal
- Concept N – TMA between End Terminal and Bullnose
- Concept O – Bullnose with Net Attenuator

8.1 Concept A – Net Attenuator/End Terminal or Crash Cushion

Concept A used a net attenuator to span across the corner of the intersection with a TL-3 crashworthy end terminal and transition or a crashworthy crash cushion connected to the bridge rail, as shown in Figure 15. The net attenuator would be anchored near the secondary roadway and behind the crash cushion or guardrail end terminal. There are multiple methods of energy absorption available for net arrestors, including hydraulic shocks, fabric ripping, and metal bending.

One advantage of using a net attenuator is that there is a high probability for vehicle capture, redirection, or controlled stopping under a wide range of impact conditions due to the net's ability to capture and arrest vehicles at high impact angles and velocities. The net attenuator would seem likely to function on a moderate slope as well as eliminate the need for a guardrail system along the secondary roadway.

Many net attenuators are taller than the 36-in. (914-mm) maximum obstruction height that was provided as a design criterion. However, many nets are see-through and would not block the view of an oncoming vehicle or cause any sightline issues for vehicles entering the primary road. For impact events, interaction between the net and the end terminal or crash cushion is unknown and would require further investigation. The guardrail end terminal and AGT may be too long for most installations. Therefore, crash cushions with shorter system lengths and/or an integrated transition may be better suited for this application than guardrail end terminals. Concept A would not enclose any part of the protected area and would allow access to mowers and other equipment, thus increasing simplicity and ease of maintenance. There is also potential that the net could be laid down if maintenance personnel needed to mow or maintain the protected area.

One concern with this design is that a vehicle traveling parallel to the TL-3 traffic could pass behind the crash cushion and hit the anchorage of the net and not be captured. Thus, placement of the net ends or anchorages may be critical. A net would also need to be properly supported such that weather (i.e., snow wind, ice, etc.) or snow plows (i.e., thrown snow) would not knock it over. Because energy absorbers for most net attenuators are proprietary systems, they may be prohibitively expensive in current arrangements. Depending on the selected energy absorber, there may be field maintenance or inspections required to ensure their long-term performance. Some research and development would also be required to develop, modify, and integrate a net attenuator with an end terminal or crash cushion system before it is ready for highway use.

The stopping distances for many net attenuators are greater than the available space. To reduce stopping distances, most energy absorbers anchorages would need to develop higher resistive loads. However, this design concept met many of the design criteria and was chosen by the sponsor for further investigation.

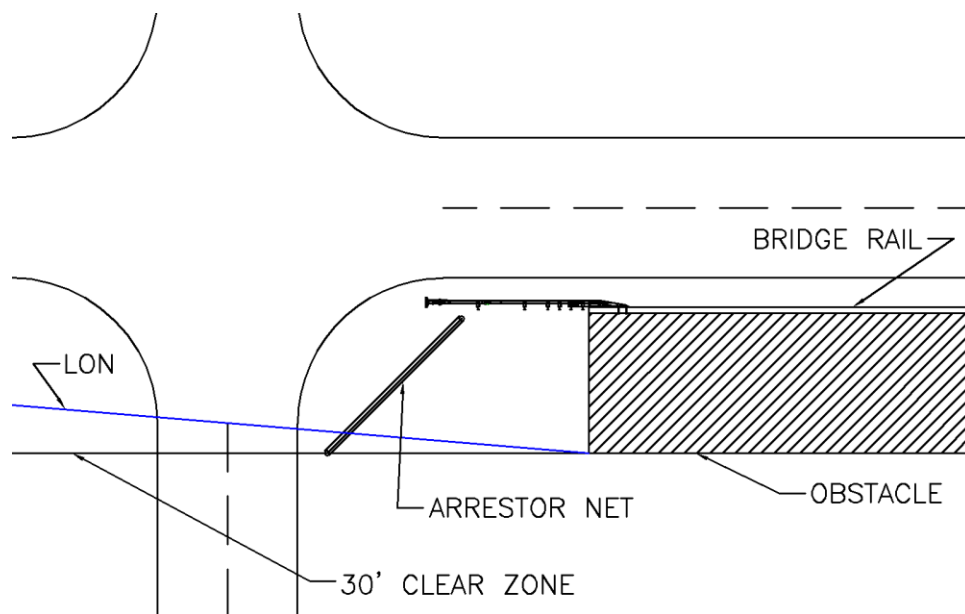


Figure 15. Concept A - Net Attenuator/End Terminal or Crash Cushion

8.2 Concept B – Dual Bullnose

Concept B used a wide bullnose to transition to the bridge rail as well as protect the corner area throughout to the clear zone. Bullnose guardrail systems often allow for more dynamic deflection than the available design space; therefore, another attenuation system is needed to stop an errant impacting vehicle, especially a pickup truck. Concept B uses a smaller, inner bullnose for additional energy absorption, as shown in Figure 16. The bullnose guardrail system shown for this system is lower than the 36-in. (914-mm) maximum height limit and would not cause any sight-line issues.

The advantages of this system would be that there is a continuous rail element wrapping around the entire system, and a vehicle would be unable to pass between the two systems. Bullnose guardrail systems have also been tested under NCHRP Report No. 350 TL-3 conditions and utilize many non-proprietary components, which could reduce the installation cost. Another benefit is that a bullnose uses three-beam guardrail elements that could be transitioned directly into the end of the bridge railing. This design also eliminated the need for a guardrail system along the secondary roadway.

The disadvantage of this concept is that adapting the bullnose to fit within this application may be difficult. Currently, bullnose guardrail systems require longer lengths to stop heavy passenger vehicles than allowed in the current design space. Therefore, the ‘stroke’ of the bullnose system would need to be reduced, thus requiring an additional form of energy absorption to stop the impacting vehicle. Shortening and widening a standard bullnose and an approved bridge rail transition into the bridge railing may cause the system to become too stiff to capture the small car and pickup truck vehicles noted within the MASH testing conditions. NDOR indicated that it would be difficult to grade the area to the end of the clear zone in many

locations. This concept would require a significant development effort, thus making it less desirable than other options that largely utilize existing hardware or technologies.

The installation of two different systems was not ideal due to the grading and extra hardware that would be required. Other designs that utilized staged energy absorption would have more favorable grading requirements, and the required hardware would be reduced. Concept B would also enclose two sections of the protected area and would not allow mowers and other equipment to easily access the area for maintenance. This concept would not likely accommodate a slope in the protected area. Though this design concept had the potential to work, other forms of energy absorption, such as a net or sand barrels, were seen as more favorable options.

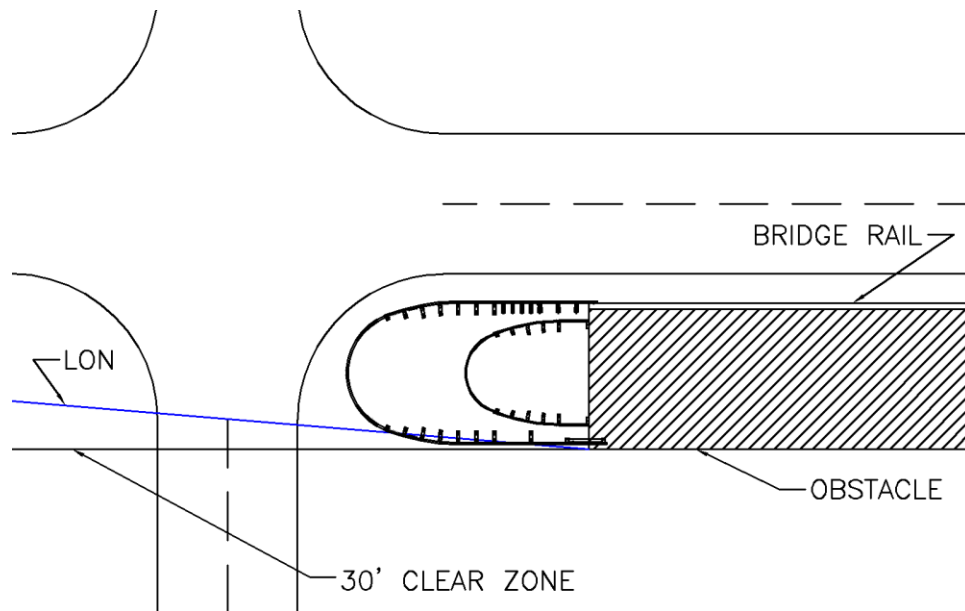


Figure 16. Concept B – Dual Bullnose

8.3 Concept C – Bullnose with Sand Barrels

Concept C used a wide bullnose to transition to the bridge rail as well as protect the corner area throughout the clear zone. Bullnose guardrail systems often allow for more dynamic

deflection than the available design space; therefore, another attenuation system is needed to stop an impacting vehicle. For this concept, sand barrels are placed inside the wide bullnose to provide a more efficient, staged energy dissipation, as shown in Figure 17. The bullnose guardrail system shown for this system is lower than the 36-in. (914-mm) maximum height limit and would not cause any sight-line issues.

The advantages of this system would be that there is a continuous rail element wrapping around the entire system, and a vehicle would be unable to pass between the two systems. Bullnose guardrail systems have also been tested under NCHRP Report No. 350 TL-3 conditions and utilize many non-proprietary components, which could reduce the installation cost. Another benefit is that a bullnose uses three-beam guardrail elements that could be transitioned directly into the end of the bridge railing. This design also eliminated the need for a guardrail system along the secondary roadway.

The disadvantage of this concept is that adapting the bullnose to fit within this application may be difficult. Currently, bullnose guardrail systems require longer lengths to stop heavy passenger vehicles than allowed in the current design space. Therefore, the 'stroke' of the bullnose system would need to be reduced, thus requiring an additional form of energy absorption to stop the impacting vehicle. Shortening and widening a standard bullnose and an approved bridge rail transition into the bridge railing may cause the system to become too stiff to capture the small car and pickup truck vehicles noted within the MASH testing conditions. NDOR indicated that it would be difficult to grade the area to the end of the clear zone in many locations. This concept would not likely accommodate a slope in the protected area. Maintenance of this system would be difficult, because mowers would need to be lifted over the top of the bullnose to maintain the enclosed area.

Sand barrels are an existing technology, relatively inexpensive, and can be installed in an array to provide staged energy absorption. Unfortunately, the 36-in. (914-mm) maximum height criterion limits the size of sand barrel that can be installed inside of a bullnose and still preserve sight-lines. Controlling weeds between the barrels could also be difficult, because the use of chemicals to treat weeds may be restricted depending on the location.

The installation of two different systems was not ideal due to the grading and extra hardware that would be required. Other designs that utilized staged energy absorption would have more favorable grading requirements, and the required hardware would be reduced. Concept B would also enclose two sections of the protected area and would not allow mowers and other equipment to easily access the area for maintenance. This design concept met much of the design criteria and was chosen by the sponsor for further investigation.

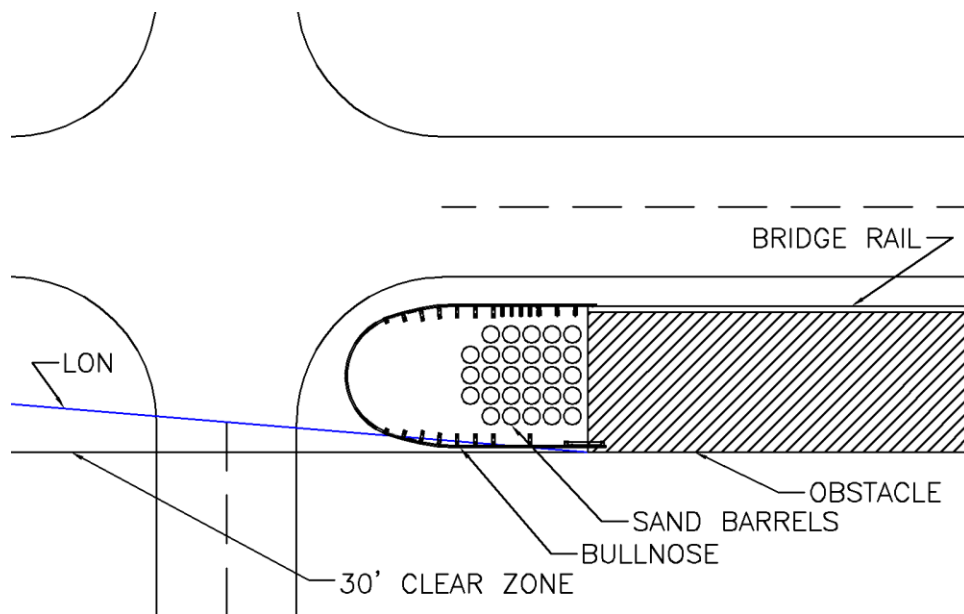


Figure 17. Concept C – Bullnose with Sand Barrels

8.4 Concept D - Bullnose

Concept D used a wide bullnose to both transition into the bridge rail and protect the corner of the intersection throughout the clear zone, as shown in Figure 18. One benefit of this system would be that there is a continuous rail element wrapping around the entire system, and the vehicle would be unable to pass through the system. Bullnose guardrail systems have also been tested under NCHRP Report No. 350 TL-3 conditions, though never at the width and length required for this concept. Another benefit is that a bullnose uses three-beam guardrail elements that could be transitioned directly into the end of the bridge rail. The bullnose guardrail system shown for this system is lower than the 36-in. (914-mm) maximum height limit and would not cause sight-line issues. This concept would not likely accommodate a slope in the protected area. This design concept also eliminated the need for a guardrail system along the secondary roadway.

The disadvantage of this concept is that adapting the bullnose to fit within this application may be difficult. Currently, bullnose guardrail systems require longer lengths to stop heavier passenger vehicles than allowed in the current design space. Therefore, the ‘stroke’ of the bullnose system would need to be reduced, thus requiring an additional form of energy absorption to stop the impacting vehicle. Shortening and widening a standard bullnose and an approved bridge rail transition into the bridge railing may cause the system to become too stiff to capture the small car and pickup truck vehicles noted within the MASH testing conditions. NDOR indicated that it would be difficult to grade the area to the end of the clear zone in many locations. Maintenance of this system would be difficult, because mowers would need to be lifted over the top of the bullnose to maintain the enclosed area. This concept would require a significant development effort. This concept would also require more space than allowed at most potential sites and thus was not chosen for further development.

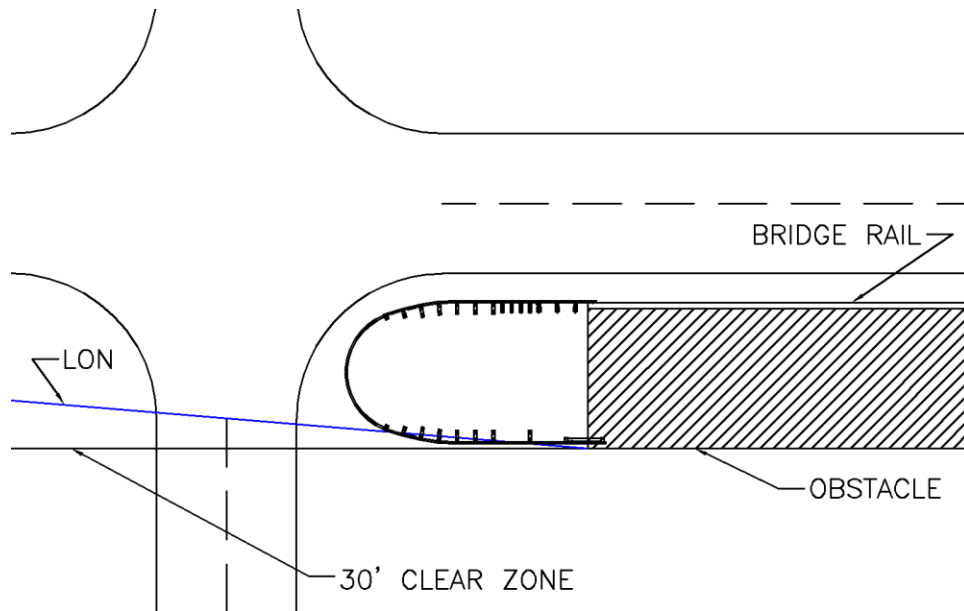


Figure 18. Concept D - Bullnose

8.5 Concept E – Two End Terminals with Secondary Energy-Absorbing Guardrail

Concept E used two guardrail end terminals, one along both the primary and secondary roadways, as shown in Figure 19. In between the end terminals, a secondary rail would be used to capture a vehicle traversing the corner of the intersection. This secondary guardrail would be fed through an energy-absorbing device, perhaps similar to some of the end terminal heads.

An advantage of this system is that the vehicle would be engaged sooner by having the nose of the system near the edge of the traveled way. This placement could reduce the deflection distance relative to the roadway and would reduce the footprint of the overall system. The guardrail system shown for this concept is lower than the 36-in. (914-mm) maximum height limit and would not cause any sight-line issues. Maintenance on this design would be comparable to current guardrail end terminal systems.

A disadvantage of this system is that it would require development of a new energy-absorption device, which violates the design criteria of using existing technologies. This concept

would require a significant development effort, thus making it less desirable than other options that better utilized existing hardware. An end terminal would be required on the secondary roadway, which violated the design criteria. This concept would not likely accommodate a slope in the protected area. The amount of development work required, and the need for a terminal on the secondary roadways, made this design less desirable than some of the other concepts.

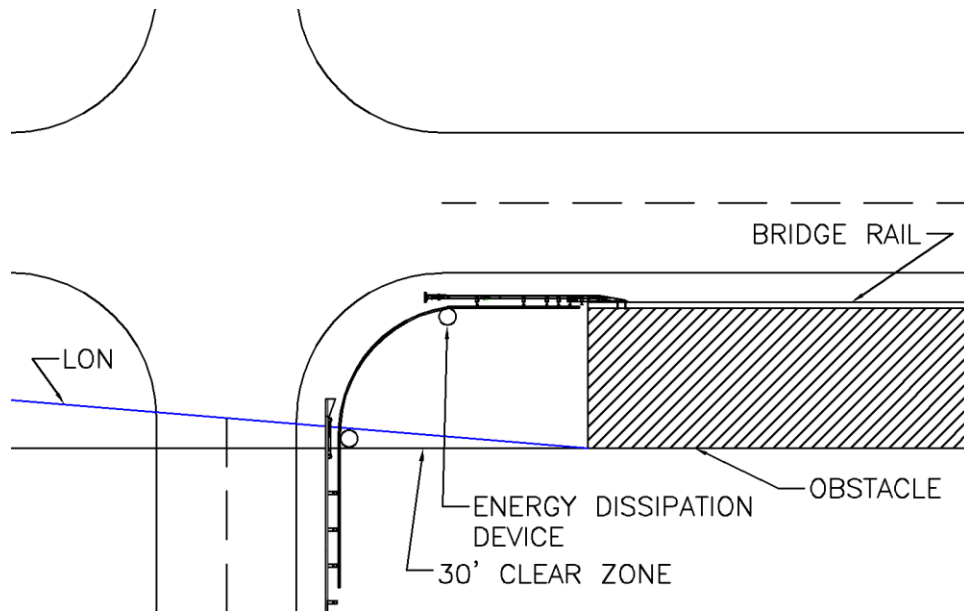


Figure 19. Concept E – Two End Terminals with Secondary Energy-Absorbing Guardrail

8.6 Concept F – Two Disconnected Guardrails

Concept F used two curved guardrail systems that partially wrapped around the corner with a transition section off the end of the bridge rail and with weaker posts in the corner. One concern with the use of a single guardrail system is that there needs to be a large distance upstream from the end of the bridge rail to stop and contain impacting vehicles in a stable manner. With two “stacked” systems, the required stopping distance may potentially be reduced due to increased energy dissipation without increasing the overall footprint of the system. The second guardrail system would be behind the primary system and is located in the region that

would capture the vehicle. Maintenance on this design would be comparable to current short-radius guardrail systems.

One of the major issues with short-radius designs was that the TL-3 side of the short-radius was too long to effectively transition into the bridge rail in the space available. Another issue was that the vehicle tended to yaw as the guardrail was pushed backward. Having two curved guardrail systems wrapped around one another, as shown in Figure 20, may allow the curved sections to pivot about different points and counteract each other, thus resulting in less vehicle yawing. The guardrail systems shown for this system would be lower than the 36-in. (914-mm) maximum height limit and would not cause any sight-line issues.

Although there were some benefits to this concept, a significant amount of research and development work would be required. This design concept would also require designing end terminals that could be placed inside the corner of the intersection. As the first guardrail is pushed backward, the posts could become tripping hazards when traversed by the impacting vehicles. With significant research and development required, it is less desirable than other options that better utilized existing hardware or technologies.

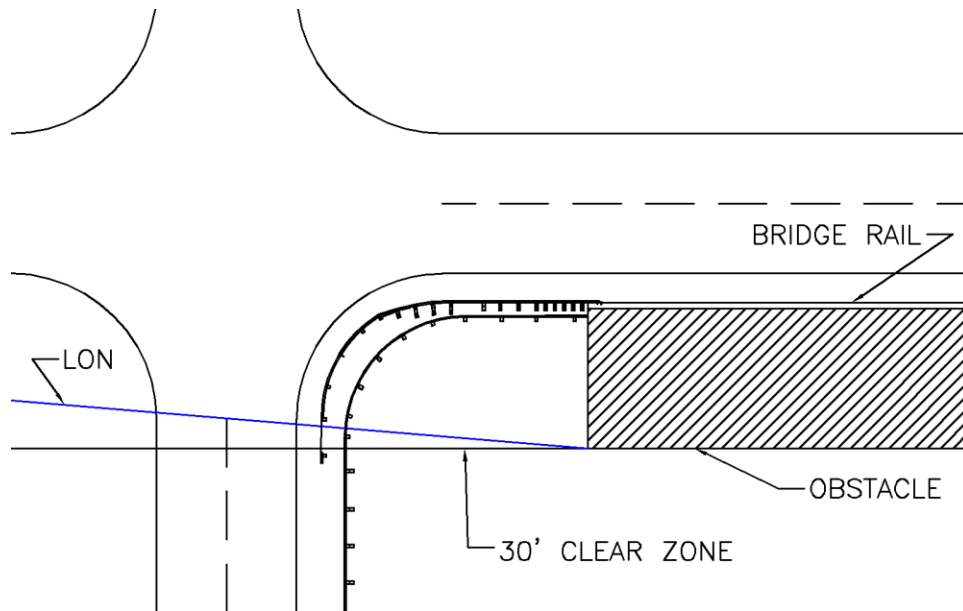


Figure 20. Concept F – Two Disconnected Guardrails

8.7 Concept G – Cable or Net Attached Behind Two End Terminals

Similar to Concept E, Concept G uses a guardrail end terminal along the primary and secondary roadways. Between the guardrail end terminals, a cable system would be used to capture a vehicle traversing the corner of the intersection, as shown in Figure 21. This cable system would be attached to the back of the posts of the end terminal or crash cushion systems. This attachment could come in the form of clips similar to those used in cable guardrail systems, or it may need to be something totally new.

The advantages of this system include engaging the vehicle sooner using a cable system near the edge of the traveled way. This placement could reduce the deflection distance relative to the roadway and the footprint of the overall system. The guardrail system shown for this concept was lower than the 36-in. (914-mm) maximum height limit and would not cause any sight-line issues. Maintenance on this design would be comparable to current end terminal systems.

Some of the disadvantages of this system are that it would require a new energy-absorbing clip or other device which would increase development time, which the design criteria of using existing technologies. Also, an end terminal would be required on the secondary roadway, which violated the design criteria. This concept would not likely accommodate a slope in the protected area. The required research and development work required and the need for a terminal on the secondary roadways made this design less desirable than some of the other concepts.

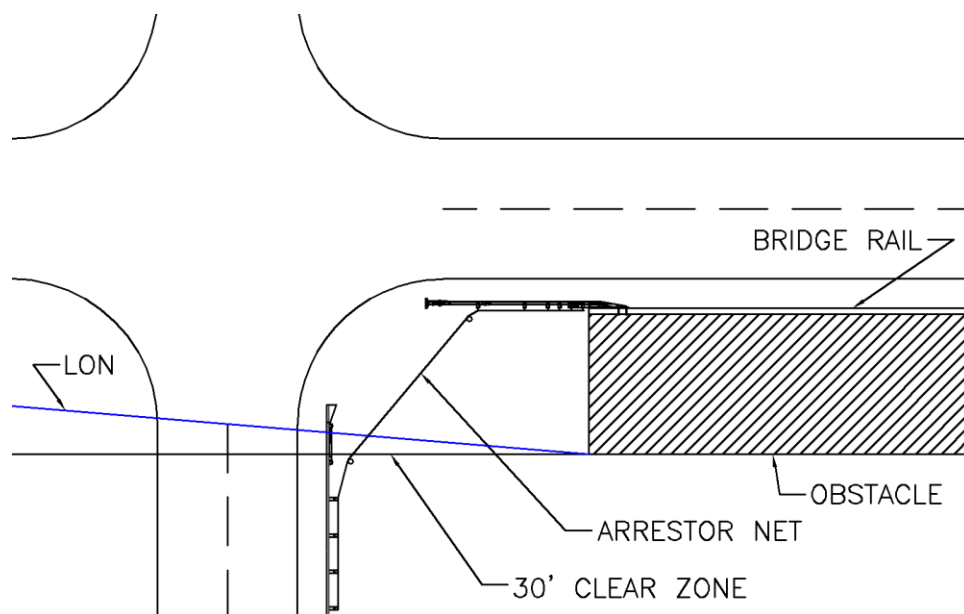


Figure 21. Concept G – Cable or Net Attached Behind Two End Terminals

8.8 Concept H – Energy Absorbers Between Impact Panel and Portable Concrete Barriers

Concept H, as shown in Figure 22, used many components to capture a vehicle, including an impact panel, energy absorbers, and portable concrete barriers (PCB). Concept H would be designed such that impacts on the primary side of the system would be redirected and impacts within the radius would be captured.

Advantages of this system include engaging the vehicle sooner by having the nose of the impact panel near the edge of the traveled way. This placement could reduce the deflection distance relative to the roadway and the footprint of the overall system. Another advantage is that it uses many components, such as portable concrete barriers and potentially sand barrels. For energy absorption, one option would be to use sand barrels, which are relatively inexpensive and can be installed in an array to provide staged energy absorption.

One of the disadvantages of this system is that it would likely require a concrete pad to support the portable concrete barriers, which would not be feasible in many situations. Though sand barrels are an existing technology, the chosen sizes would be limited to the 36-in. (914-mm) maximum height criterion needed to preserve sight-lines. Controlling weeds between the barrels would not be a major issue due to the required concrete pad. The amount of construction work required for implementing this concept made it less desirable than some of the other concepts. In some instances, it may actually be easier to move the problem intersection.

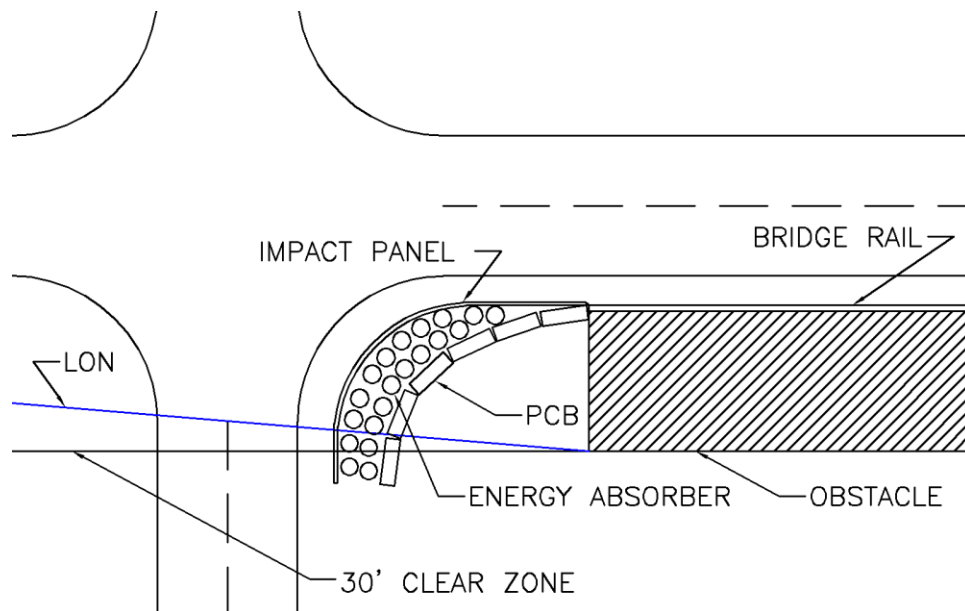


Figure 22. Concept H – Energy Absorbers Between Impact Panel and Temporary Concrete Barriers

8.9 Concept I – Energy Absorbers, Rails, and Posts

Concept I, as shown in Figure 23, used guardrails with posts and energy absorbers to redirect or capture the impacting vehicle. Concept I would be designed such that impacts on the primary side of the system would be redirected and impacts within the radius would be captured.

An advantage of this system is that the vehicle would be engaged sooner by having the nose of the rail element closer to the edge of the traveled way. This placement could reduce the deflection distance relative to the roadway and the footprint of the overall system.

One of the disadvantages of this system is that it would require development of a new energy-absorption component that attaches to the posts. This modification violates the design criteria of using existing technologies. This concept would require a significant development effort, making it less desirable than other options that better utilized existing hardware. This concept would not likely be able to accommodate a slope. The amount of development work required, and the need for a terminal on the secondary roadways, made this design less desirable than some of the other concepts. Maintenance of this system would be difficult, because mowers would need to be lifted over the top of the railing to maintain the enclosed area. This concept would require a significant development effort, thus making it less desirable than other options that better utilized existing hardware.

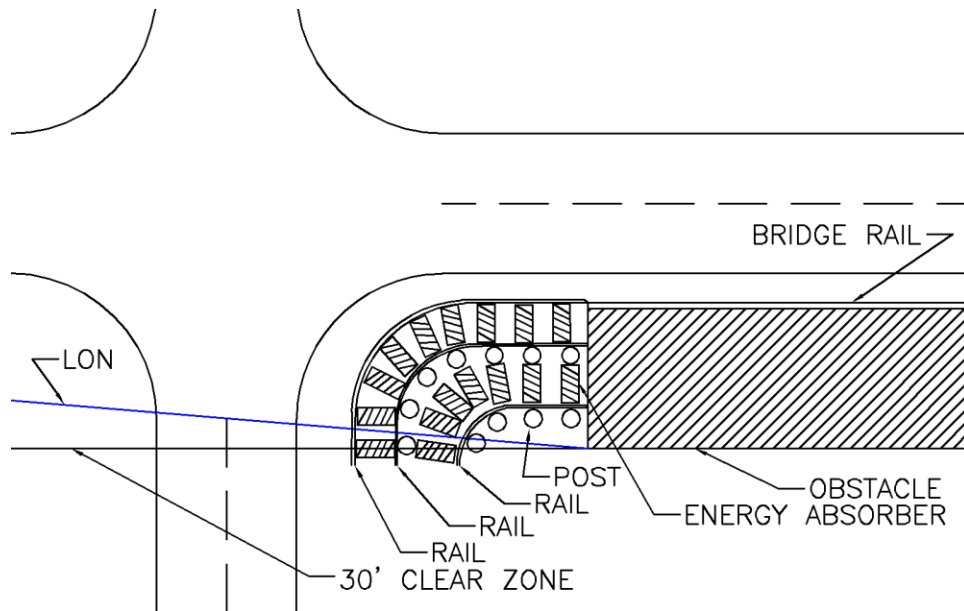


Figure 23. Concept I – Energy Absorbers, Rails, and Posts

8.10 Concept J – Rubber Cylinders Between Impact Panel and Restoring Barrier

Concept J, as shown in Figure 24, used rubber cylinders backed by a restoring barrier and covered by some form of skin to capture the impacting vehicle.

An advantage of this system would be that the vehicle would be engaged sooner by having the nose of the rail element closer to the edge of the traveled way. This placement could reduce the deflection distance relative to the roadway and the footprint of the overall system.

The restoring barrier would likely require a concrete pad to be placed in the corner, which was not feasible in most situations. Controlling weeds between the rubber cylinders could be difficult, because the use of chemicals to treat weeds may be restricted depending on the location. Another disadvantage was that it would require development of a new energy-absorbing restorable barrier. This modification violated the design criteria of using existing technologies. This concept would require significant research and development, thus making it

less desirable than other options that better utilized existing hardware. The amount of development work required made this design less desirable than some of the other concepts.

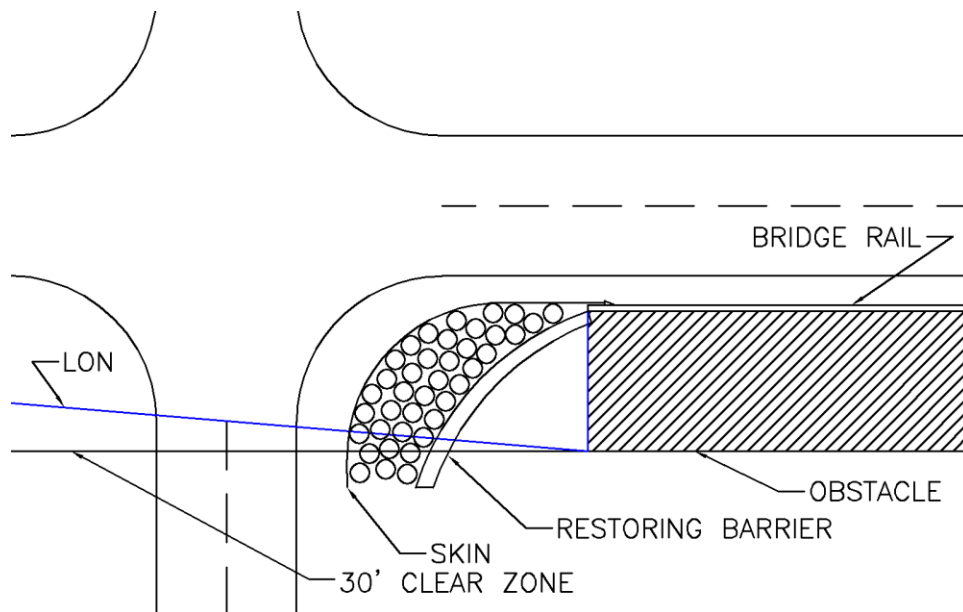


Figure 24. Concept J – Rubber Cylinders Between Impact Panel and Restoring Barrier

8.11 Concept K – Sand Barrels with End Terminal or Crash Cushion

Concept K, as shown in Figure 25, would use an end terminal or crash cushion to protect the bridge railing with a sand barrel array for capturing vehicles impacting in the radius. A large number of sand barrel modules would be required to protect the corner of the intersection. The height of some of the heavier modules can also create sightline issues.

The advantages of this system are that sand barrels are an existing technology, relatively inexpensive, and can be installed in an array to provide staged energy absorption. Unfortunately, the 36-in. (914-mm) maximum height criterion limits the size of sand barrel that can be installed inside bullnose systems and still preserve sight-lines. Although it is not the most aesthetically pleasing option, Concept K does use existing technologies.

A disadvantage of this system is that a flat pad may be required to support the barrels, which may not always be feasible. Controlling weeds between the barrels could be difficult, because the use of chemicals to treat weeds may be restricted depending on the location. NDOR indicated that it would be difficult to grade the area to the end of the clear zone in many locations. Given the use of existing technologies, this option would likely require less time and funds to develop than other options and was chosen by the sponsor for further investigation.

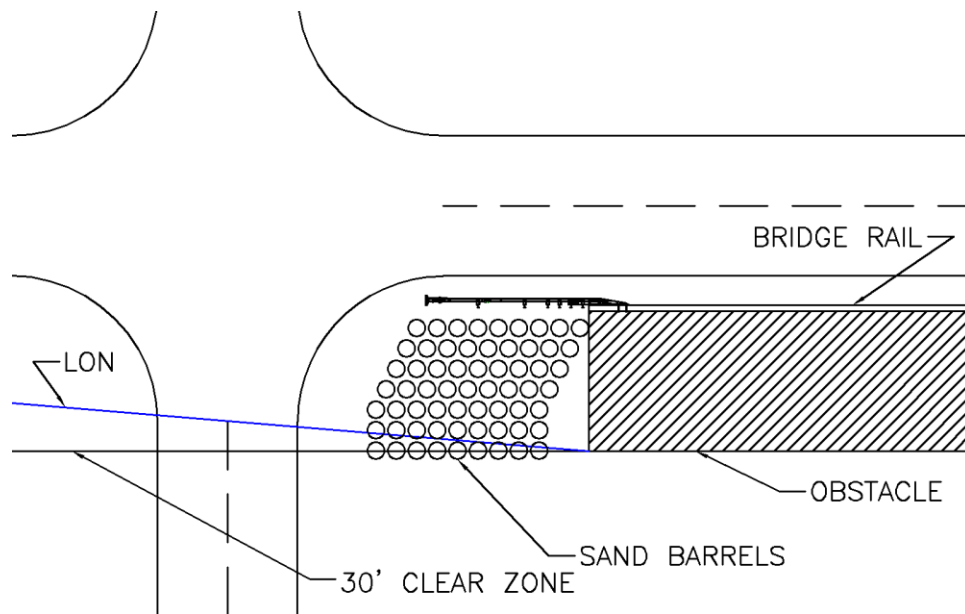


Figure 25. Concept K – Sand Barrels with End Terminal

8.12 Concept L – TMA(s) Between Two End Terminals

Concept L, as shown in Figure 26, used an end terminal/crash cushion for the bridge termination and an end terminal/crash cushion parallel that would redirect vehicles into sand barrels, crash cushions, or a truck-mounted attenuator. Vehicles would either impact the guardrail closest to the traffic side or be redirected into barrels, a crash cushion, or TMA due to the placement of a flared end terminal.

The advantage of this system is that TMAs, crash cushions, barrels, and end terminals are existing technologies and have been approved for highway use. Maintenance on this design would be comparable to current short-radius, end terminal, and crash cushion systems.

One disadvantage of this system is that it would require multiple proprietary systems that could be expensive to implement. Another disadvantage was that the effects of a vehicle impacting multiple different systems were unknown and would require research and development. This concept would not likely accommodate a slope in the protected area. Most importantly, the system would not shield the entire region that needed to be protected. For situations where the clear distance was much less, this concept could be a viable option. However, the amount of research and development for this concept made it less desirable than some of the other concepts.

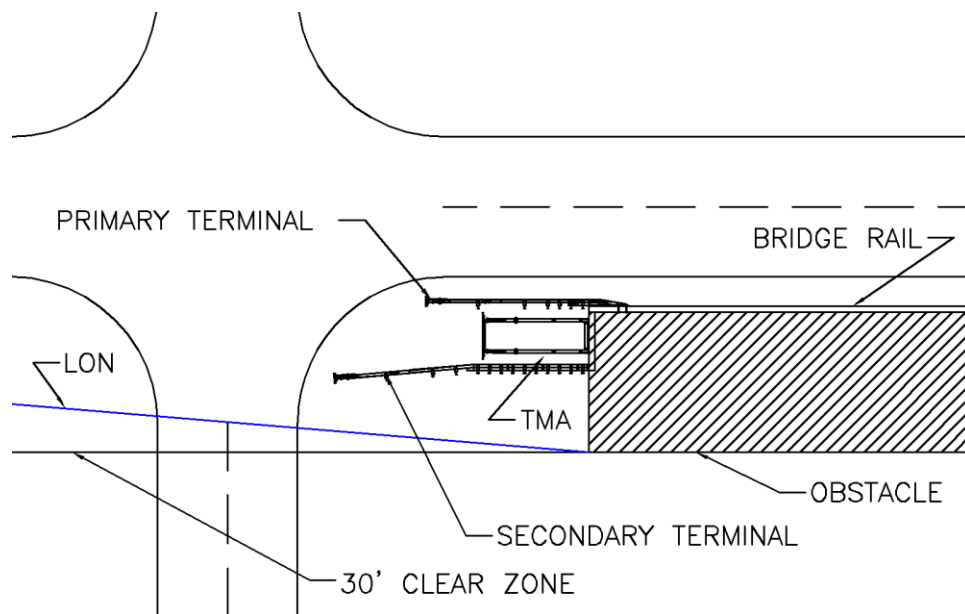


Figure 26. Concept L – Barrels, Crash Cushion, or TMA(s) Between Two End Terminals

8.13 Concept M - TMA(s) or Crash Cushion(s) with End Terminal

Concept M, as shown in Figure 27, used an end terminal or crash cushions with a Truck- or Trailer-Mounted Attenuator (TMA or TTMA) placed in the corner area of the intersection, as shown in Figure 27. This concept was desirable because of its potential use of currently existing hardware or technologies.

The advantage of this system is that TMAs, end terminals, and crash cushions are existing technologies and have been approved for highway use. Maintenance on this design would be comparable to current short-radius, end terminal, and crash cushion systems.

One disadvantage of this system is that it would require multiple proprietary systems that could be expensive to implement. Another disadvantage is that this system would require multiple TMA systems to effectively protect the entire area, which could be prohibitively expensive. Impacts involving multiple TMAs would require further research, development, and testing. This concept would not likely accommodate a slope in the protected area. The required research and development made this concept less desirable than some of the other concepts.

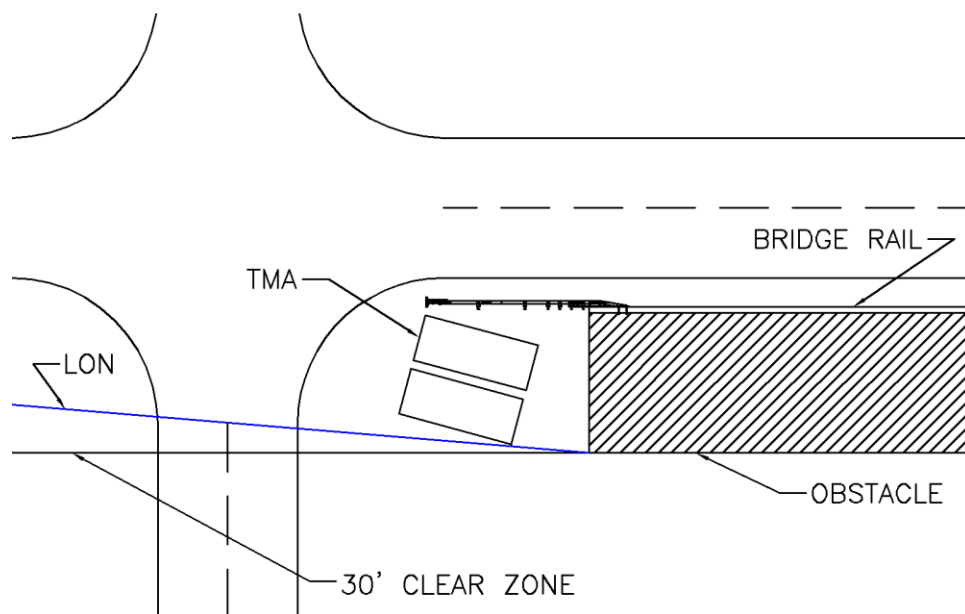


Figure 27. Concept M - TMA(s) or Crash Cushion(s) with End Terminal

8.14 Concept N – TMA between End Terminal and Bullnose

Concept N, as shown in Figure 28, is a variation of Concept L and uses an end terminal, TMA or TTMA, and a standard bullnose. With Concept L not being wide enough to protect the entire hazard, this concept attempted to increase the width by using a bullnose system instead of another guardrail end terminal.

The advantage of this system is that TMAs, end terminals or crash cushions, and bullnose guardrail systems are existing technologies and have been approved for highway use. Maintenance on this design would be comparable to current short-radius, end terminal, and crash cushion systems.

One major disadvantage of this system was that it would require multiple systems that could be expensive to implement. Impacts involving multiple TMAs would require further research, development, and testing. Although the nose of the bullnose was narrow and close in size to three-beam bullnose systems, approved systems are much longer than what is shown below. The required research and development work required made this concept less desirable than some of the other concepts.

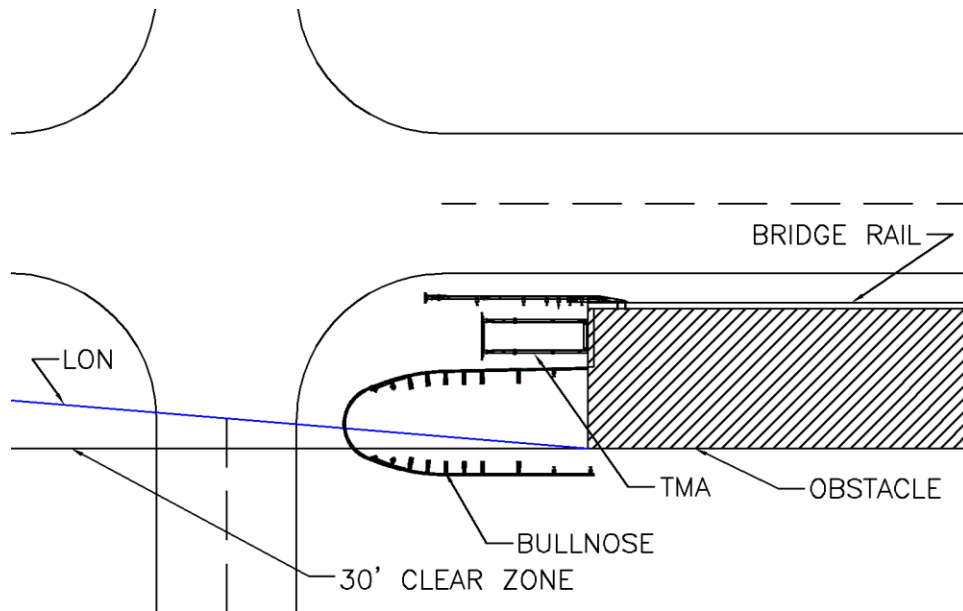


Figure 28. Concept N – TMA between End Terminal and Bullnose

8.15 Concept O – Bullnose with Net Attenuator

Concept O used a net attenuator enclosed by a wide bullnose to aid in capturing heavier vehicles that require extra energy absorption, as shown in Figure 29. Bullnose guardrail systems often allow for more dynamic deflection than allowed within the design space available. Therefore, another attenuation system was needed to stop an impacting vehicle. For this concept, a net attenuator, such as the Dragnet Vehicle Arresting Barrier, could be used to provide extra energy absorption. The bullnose guardrail system shown for this system is lower than the 36-in. (914-mm) maximum height limit and would not cause any sight-line issues.

The advantages of this system include a continuous rail element wrapping around the entire system where a vehicle would be unable to pass between two systems. Bullnose guardrail systems have also been tested under NCHRP Report No. 350 TL-3 conditions and utilize many non-proprietary components, which could reduce the installation cost. Another benefit is that a bullnose uses three-beam guardrail elements that could be transitioned directly into the end of the

bridge railing. This design also eliminated the need for a guardrail system along the secondary roadway. One advantage to using a net attenuator inside the bullnose is that there is a high probability of capture or controlled stopping under a wide range of impact conditions. Many net attenuators are taller than the 36-in. (914-mm) maximum height guideline in the design criteria. Because the net and bullnose would not block the view of an oncoming vehicle, this feature would not cause any sight-line issue.

A disadvantage of this system was that adapting the bullnose to fit this application would be difficult. End-on impacts into bullnose guardrail systems create long stopping distances, so a secondary absorption method was needed. Shortening and widening a standard bullnose that could safely transition into the bridge railing may cause the system to become too stiff to capture the small car and pickup truck vehicles noted within the MASH testing conditions. NDOR indicated that it would be difficult to grade the area all the way to the end of the clear zone in a real-world application. This concept would not likely accommodate a slope in the protected area, because both sides of the bullnose would need to be at the same level. Maintenance of this system would be difficult, because mowers would need to be lifted over the top of the bullnose to maintain the enclosed area.

Vehicle interaction between the net and bullnose systems during impacts is unknown and would require further investigation. Because the energy absorbers are proprietary systems, they could also be prohibitively expensive. Depending on the selected energy absorber, there may be maintenance required to ensure their performance in the field. Some research and development would be required to integrate a net attenuator and end terminal or crash cushion system. This concept met much of the design criteria and was chosen by the sponsor for further investigation.

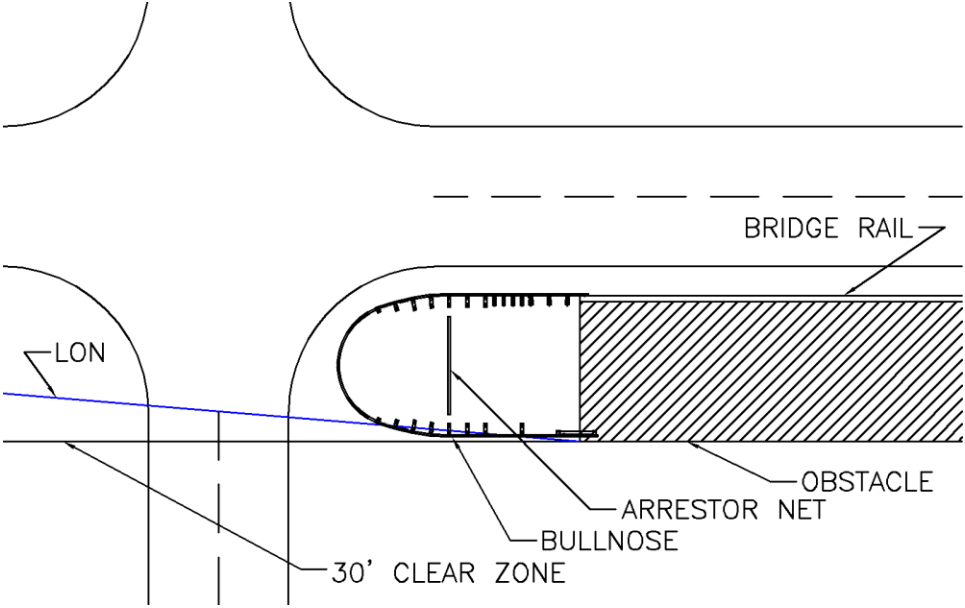


Figure 29. Concept O – Bullnose with Secondary Energy Absorber

9 RANKING AND SELECTION OF DESIGN CONCEPTS

MwRSF and Nebraska Department of Roads personnel met to narrow down the list of feasible concepts. Four main criteria were considered when ranking the design concepts: safety performance, maintenance and repair costs, development effort, and installation cost. From these discussions, the designs were ranked from most to least feasible. This information is shown in Table 20. During these discussions, three concepts were considered for further investigation into their feasibility: Concepts A, K, and C/O. Concepts C and O, which both used a secondary form of energy absorption enclosed by a bullnose, were later considered as one option. The other concepts were rejected for the following reasons:

- Concepts B, D, E, F, G, H, I, and J required significant research and development, thus making them less desirable than other options which better utilized existing components.
- Concept B was not pursued because the sand barrels and net attenuator used in Concepts C and O, respectively, were seen as more practical devices to provide secondary energy absorption.
- Concept D does not have enough space to safely stop an impacting vehicle.
- Concept F would require significant research and development. There is no guarantee that this system will capture the vehicle. The posts could become tripping hazards as well.
- Concepts L, M, and N would not shield the entire hazard. These concepts also utilized multiple different systems that have never been tested together. The repair cost was seen as high for these systems, because a vehicle could impact more than one system.

Concepts A, K, O, and C were the highest-ranking concepts and were chosen for further analysis and development to better determine their feasibility.

Table 20. Ranking of Design Concepts

Rank	Concept	Description	Safety Performance	Maintenance/Repair	Development Effort	Installation Cost	Overall Suitability
1	A	Net Attenuator	High	High	Medium	Medium	High
2	K	Sand Barrels with End Terminal	Medium-Low	Medium-Low	Low	Low	
3	O	Bullnose with Net Arrestor	High	Low	Medium	Medium-Low	High
4	C	Wide Bullnose with Sand barrels	High	Medium-Low	Medium	Medium-Low	
5	B	Dual Wide Bullnose	High	Low	Medium	Medium-Low	Medium
6	D	Wide Bullnose	High	Low	Medium	Low	
7	E	Two End Terminals with Secondary EA Guardrail	High-Medium	Low	High-Medium	Medium	Medium
8	F	Two Disconnected Guardrails	High-Medium	Low	High-Medium	Medium-Low	
9	G	Cable/Net Attached to Back of Posts with Clips	High-Medium	Low	High-Medium	Medium	Low
10	H	Energy Absorbers Between Impact Panel and Portable Concrete Barriers	Medium	Medium	High	High-Medium	
11	I	Energy Absorbers, Rails, and Posts	Medium	High-Medium	High	High-Medium	Low
12	J	Impact Panel ->Rubber Cylinders->Restoring Barriers	Medium	Medium	High	High-Medium	
13	L	TMA between Two End Terminals	Low	Low	Medium-Low	High-Medium	Low
14	M	TMA/CCs and End Terminal	Low	Low	High	High	
15	N	TMA between End Terminal and Bullnose	Low	Low	Medium-Low	High	

10 QUASI-STATIC TAPE COMPONENT TEST SETUP AND CONDITIONS

10.1 Purpose

To pursue the development of Concept A, the performance of several net attenuator components needed to be tested and evaluated. Impact Absorption, Inc., the manufacturer of the Dragnet Vehicle Arresting Barrier, provided a net attenuator system for testing purposes. For this net attenuator, the kinetic energy of an impacting vehicle is absorbed by bending steel straps back and forth through a series of pins that are housed in a stainless steel canister, herein referred to as an energy absorber. To evaluate the net attenuator's potential use for Concept A, the force level, energy absorbed, and the corresponding stopping distance of an impacting vehicle was required.

The total energy absorbed and stopping distance of the net attenuator was directly related to the force required to pull the steel strap through the pins. According to Impact Absorption Inc. the force levels were expected to be slightly less than 4,000 lb (17.8 kN). All quasi-static tests were conducted at the MwRSF Outdoor Proving Grounds in Lincoln, Nebraska.

10.2 Scope

Two quasi-static pull tests were conducted on the Dragnet energy absorber. The device was fixed at one end and pulled by a winch. The energy absorber and connection hardware were proprietary components, and thus, no material specifications, mill certifications, or certificates of conformity were provided.

10.3 Equipment and Instrumentation

The equipment and instrumentation that were utilized to collect and record the data during the quasi-static tests included force load cells, high-speed and standard-speed digital video cameras, and still cameras. The energy absorber, as shown in Figure 30, was mounted to

an anchored vehicle and pulled with a winch that was rated to 18,000 lbs (80 kN). Two 50-kip (222-kN) load cells were used to measure the force to pullout the steel tape. These load cells were not preloaded.

10.3.1 Test Jig

Chains were used to attach the load cells and energy absorbers to the anchored bogie vehicle, as shown in Figures 30 and 31. The front of the vehicle attached to the winch was also tied to the ground via a chain and bollard.



Figure 30. Dragnet Energy Absorber



Figure 31. Component Testing Setup, Test Nos. IRAS-1 and IRAS-2

10.3.2 Digital Photography

One AOS VITcam high-speed digital video camera and one GoPro digital video camera were used to document each test. The AOS high-speed camera had a frame rate of 125 frames per second and the GoPro digital video camera had a frame rate of 120 frames per second. Both cameras were placed laterally from the test setup, with a view perpendicular to the direction of tape pullout. A Nikon D3100 digital still camera was used to document pre- and post-test conditions for all tests.

10.3.3 Load Cells

Two load cells were used in-line with the energy absorber. The load cells were manufactured by Transducer Techniques and conformed to model no. TLL-50K with a load range up to 50,000 lb (222.4 kN). During testing, output voltage signals were sent from the load cells to a Keithly Metrabyte DAS-1802HC data acquisition board, acquired with Test Point software, and stored permanently on a personal computer. The data collection rate for the load cells was 10,000 samples per second (10,000 Hz).

10.4 Data Processing

The electronic transducer data obtained in dynamic testing was filtered using the SAE Class 60 Butterworth filter conforming to SAE J211/1 specifications [47]. The force transducer signal was extracted from the bulk of the data signals. A force vs. time curve was plotted for each test.

11 QUASI-STATIC TAPE COMPONENT TESTING RESULTS AND CONCLUSIONS

11.1 Results

A series of two component tests were conducted to evaluate the force required to pull out steel tape from the Dragnet energy absorbers. When the pulling force was initially applied to the energy absorbers, a noticeable peak in the force vs. time graph was achieved. The force readings taken from these tests were averaged so that they could be used for future simulations and analytical estimations of the Dragnet Vehicle Arresting Barrier. Further details on the individual tests are provided in subsequent sections of the report.

11.1.1 Test No. IRAS-1

In test no. IRAS-1, the energy absorber tape was pulled for a total of 141 in. (3581 mm) at an average velocity of 2.49 in/s (63.2 mm/s) by the winch. Although this velocity is much lower than the velocity during an impact scenario, it was the maximum velocity that could be achieved by the winch. As shown in Figure 32, the average force measured by the load cells was 3.812 kips and 3.814 kips (16.96 kN and 16.97 kN). As shown in Figure 33, the twisted steel tape from the energy absorber was caused by winch cable coiling as it reeled inward. During this test, initial slack in the system may have resulted in fluctuations in force levels measured by the load cells.

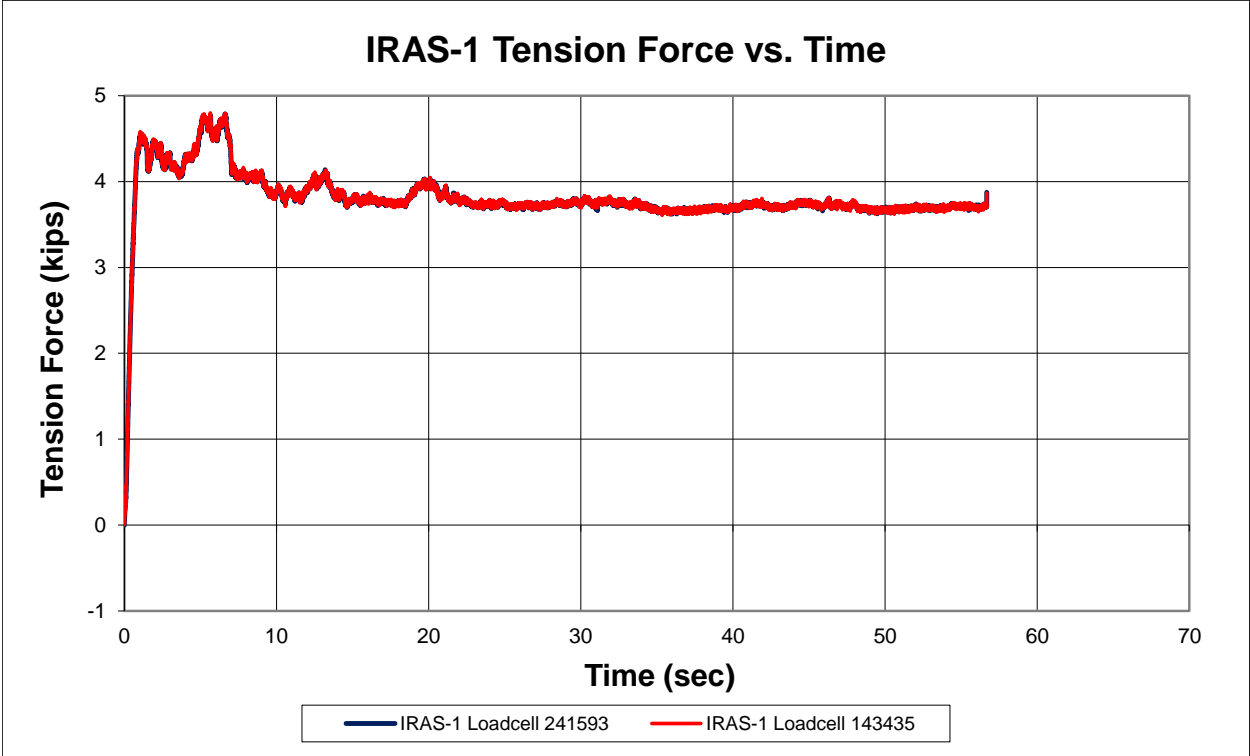


Figure 32. Tension Force vs. Time, Test No. IRAS-1

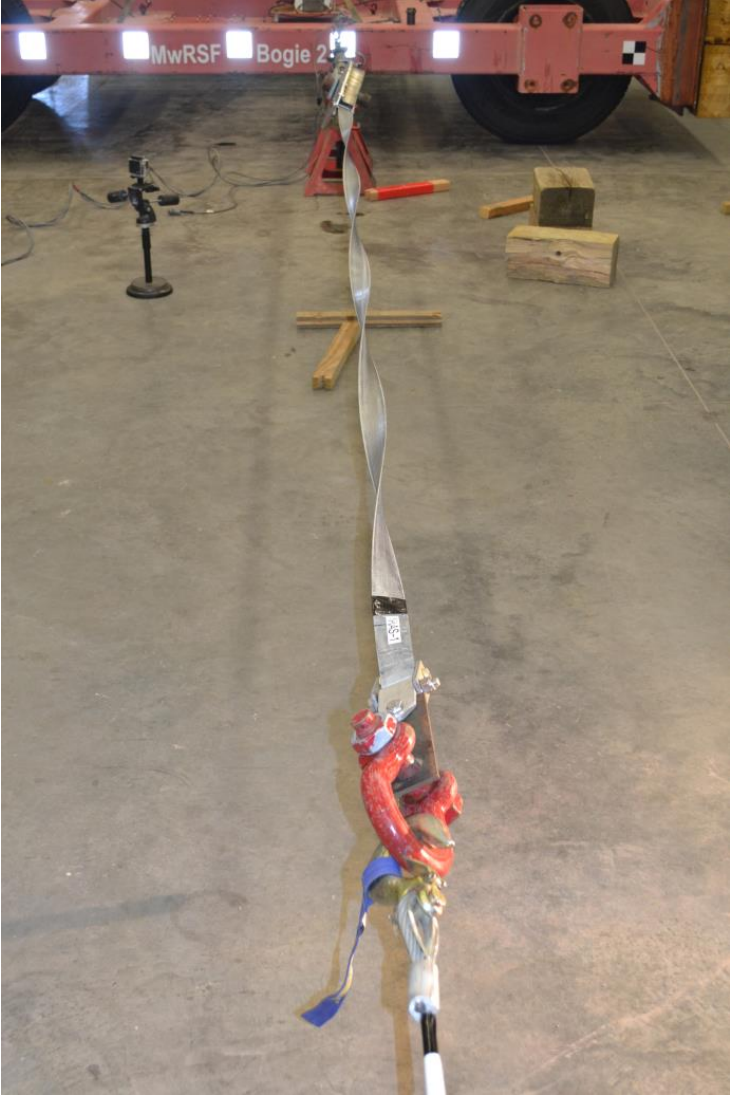


Figure 33. Energy Absorber Component Testing, Test No. IRAS-1

11.1.2 Test No. IRAS-2

In test no. IRAS-2, the energy absorber tape was pulled for a total of 144 in. (3658 mm) at an average velocity of 2.07 in/s (52.6 mm/s) by the winch. Although this velocity is much lower than the velocity during an impact scenario, it was the maximum velocity that could be achieved by the winch. As shown in Figure 34, the average force measured by the load cells was 3.893 kips and 3.889 kips (17.32 kN and 17.30 kN). As shown in Figure 35, the twisted steel tape from the energy absorber was caused by winch cable coiling as it reeled inward.

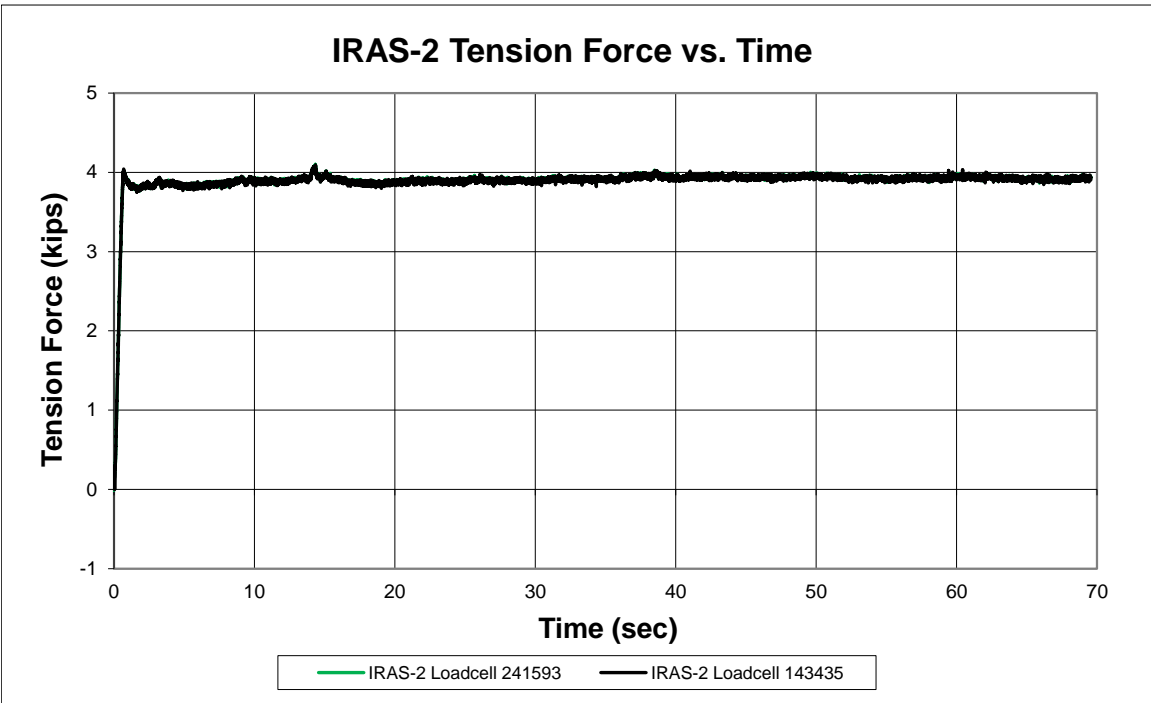


Figure 34. Tension Force vs. Time, Test No. IRAS-2



Figure 35. Energy Absorber Component Testing, Test No. IRAS-2

11.2 Discussion

The force to pull the tape out of the energy absorbers remained relatively constant during both tests. As a result, the average force of the energy absorbers for test nos. IRAS-1 and IRAS-2 was 3.81 kips and 3.89 kips (17.0 kN and 17.3 kN), respectively. Although the first test had high peak force during the beginning of the test, the force required to unreel the tape was relatively constant for both tests, as shown in Figure 36. The second test had a much smoother pull, and thus, the resistive force was relatively constant throughout.

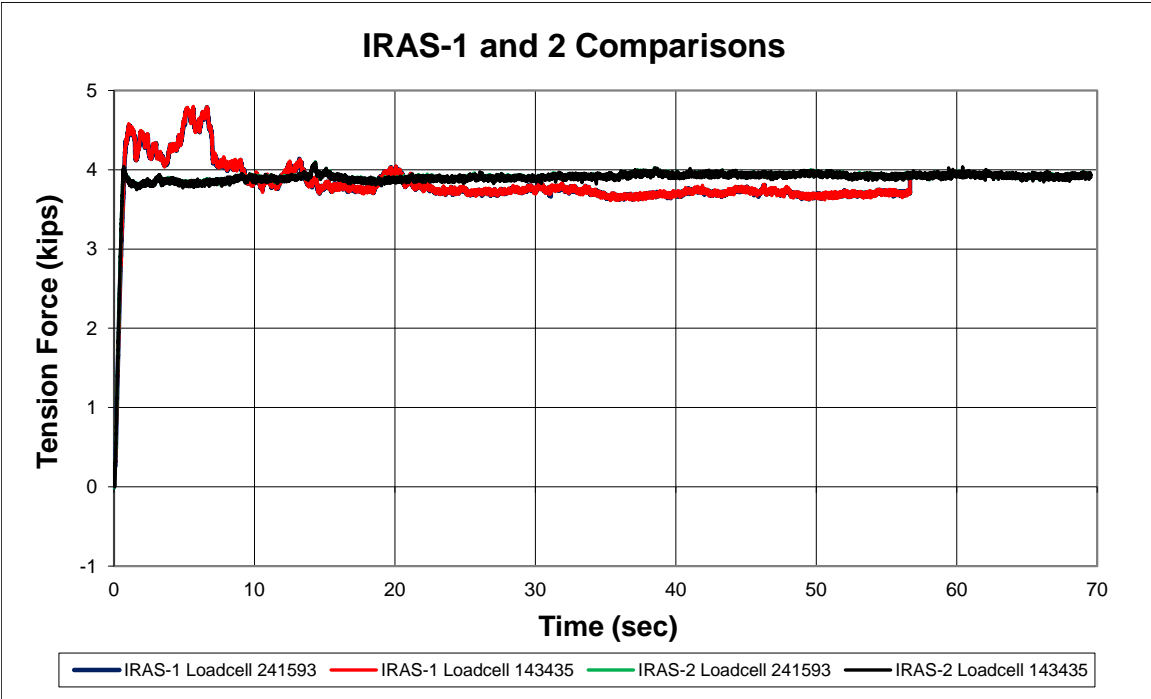


Figure 36. Pulling Force vs. Time Comparisons, Test Nos. IRAS-1 and IRAS-2

12 NET ATTENUATOR COMPONENT TESTING SETUP AND CONDITIONS

12.1 Purpose

Dynamic bogie tests were conducted on the Dragnet Vehicle Arresting Barrier. A standard Dragnet system uses one energy absorber per side, which is anchored to the ground, and produces stopping distances of 40.03 ft and 70.54 ft (12.2 m and 21.5 m) for NCHRP Report No. 350 test designation nos. 3-30 and 3-31 [48], respectively. The short distance between the end of the bridge railing and the beginning of the intersection requires the deflection of the standard net attenuator to be reduced. Impact Absorption, Inc. provided twenty-four energy absorbers for testing purposes. A net was also provided, which was designed to accommodate three standard energy absorbers per side. The average force measured in test no. IRAS-2 was 3,890 lb (17.3 kN), so three energy absorbers should have a combined resistive force of approximately 11,700 lb (52.0 kN) per side. The dynamic tests would demonstrate the potential for capturing and safely decelerating passenger vehicles using the Dragnet system at higher resistive forces and provide baseline data for further analytical and simulation studies. All dynamic tests were conducted at the MwRSF Outdoor Proving Grounds in Lincoln, Nebraska.

12.2 Scope

Four bogie tests were conducted on the Dragnet Vehicle Arresting Barrier with a total of six energy absorbers rated at 4,000 lb (17.8 kN) each. Three different target impact conditions were selected. All tests had a target impact velocity of 60.0 mph (96.6 km/h). Test condition 1 involved an impact at an angle of 90 degrees in the center of the net, which would serve as a baseline test for comparison with analytical and simulation estimates. Test condition 2 involved an impact at an angle of 90 degrees and offset from the center of the net by 12 ft (3,658 mm) to evaluate impacts very close to end of the net. Test condition 3 involved an impact at an angle of 60 degrees, and also offset by 12 ft (3,658 mm). This test would also evaluate the extents of the

net attenuator’s effective coverage area. The complete bogie test matrix is shown in Table 21. Material specifications, mill certifications, and certificates of conformity for the anchor plates are shown in Appendix A.

Table 21. Bogie Test Matrix

Test Condition	Impact Angle (Degrees)	Impact Velocity mph (km/h)	Offset From Center of Net in. (mm)
1	90	60.0 (96.6)	0
2	90	60.0 (96.6)	144 (3,658)
3	60	60.0 (96.6)	144 (3,658)

12.3 Equipment and Instrumentation

The equipment and instrumentation that was utilized to collect and record data during the dynamic bogie tests included a bogie, accelerometers, pressure tape switches, high-speed and standard-speed digital video cameras, and still cameras.

12.3.1 Vehicle Tow and Guidance System

A reverse-cable, tow system with a 1:2 mechanical advantage was used to propel the test vehicle. The distance traveled and tow vehicle speed were one-half those of the test vehicle. The test vehicle was released from the tow cable before impact with the net attenuator system. A digital speedometer on the tow vehicle increased the accuracy of the test vehicle impact speed.

12.3.2 Bogie

A rigid-frame bogie was used to impact the posts. A flat-front, detachable impact head was used in the testing. The bogie head was constructed of three 6-in. x 8-in. (152-mm x 203-mm) wood posts mounted horizontally to the front of the bogie with a 12-gauge (2.7-mm) steel sheet wrapping around the posts. The impact head was bolted to the bogie vehicle, creating a rigid frame with a flat impact face. The bogie with the impact head is shown in Figure 37. The

weight of the bogie with the addition of the mountable impact head was 5,090 lb (2,309 kg) for test nos. IRA-1 and IRA-2. The weight of the bogie for test nos. IRA-3 and IRA-4 was 5,259 lb (2,385 kg), which also included the weight of the accelerometers and other instrumentation equipment.



Figure 37. Rigid-Frame Bogie on Guidance Track

A pickup truck with a reverse-cable tow system was used to propel the bogie to a target impact speed of 60.0 mph (96.6 km/h). When the bogie approached the end of the guidance system, it was released from the tow cable, allowing it to be free-rolling when it impacted the post. A remote-control braking system was installed on the bogie, allowing it to be brought safely to rest after the test if the net did not capture the vehicle.

12.3.3 Accelerometers

Three environmental shock and vibration sensor/recorder systems were used to measure the accelerations in the longitudinal, lateral, and vertical directions. All of the accelerometers were mounted near the centers of gravity of the test vehicles. The electronic accelerometer data

obtained in dynamic testing was filtered using the SAE Class 60 and the SAE Class 180 Butterworth filters conforming to SAE J211/1 specifications [47].

The first accelerometer system was a two-arm piezoresistive accelerometer system manufactured by Endevco of San Juan Capistrano, California. Three accelerometers were used to measure each of the longitudinal, lateral, and vertical accelerations independently at a sample rate of 10,000 Hz. The accelerometers were configured and controlled using a system developed and manufactured by Diversified Technical Systems, Inc. (DTS) of Seal Beach, California. More specifically, data were collected using a DTS Sensor Input Module (SIM), Model TDAS3-SIM-16M. The SIM was configured with 16 MB SRAM and eight sensor input channels with 250 kB SRAM/channel. The SIM was mounted on a TDAS3-R4 module rack. The module rack was configured with isolated power/event/communications, 10BaseT Ethernet and RS232 communication, and an internal backup battery. Both the SIM and module rack were crashworthy. The “DTS TDAS Control” computer software program and a customized Microsoft Excel worksheet were used to analyze and plot the accelerometer data.

The second system, SLICE 6DX, was a modular data acquisition system manufactured by DTS. The acceleration sensors were mounted inside the body of the custom-built SLICE 6DX event data recorder and recorded data at 10,000 Hz to the onboard microprocessor. The SLICE 6DX was configured with 7 GB of non-volatile flash memory, a range of ± 500 g's, a sample rate of 10,000 Hz, and a 1,650 Hz (CFC 1000) anti-aliasing filter. The “SLICEWare” computer software program and a customized Microsoft Excel worksheet were used to analyze and plot the accelerometer data.

The third system, Model EDR-3, was a triaxial piezoresistive accelerometer system manufactured by Instrumented Sensor Technology, Inc. (IST) of Okemos, Michigan. The EDR-3 was configured with 256 kB of RAM, a range of ± 200 g's, a sample rate of 3,200 Hz, and a

1,120 Hz low-pass filter. The “DynaMax 1 (DM-1)” computer software program and a customized Microsoft Excel worksheet were used to analyze and plot the accelerometer data.

Test nos. IRA-1 and IRA-2 used DTS, DTS-SLICE, and EDR-3 accelerometers. For test nos. IRA-3 and IRA-4, two DTS-SLICE units were used in lieu of a DTS or EDR-3 accelerometer.

12.3.4 Rate Transducers

An angle rate sensor, the ARS-1500, with a range of 1,500 degrees/sec in each of the three directions (roll, pitch, and yaw) was used to measure the rates of rotation of the test vehicles. The angular-rate sensor was mounted on an aluminum block inside the test vehicle near the center of gravity and recorded data at 10,000 Hz to the SIM. The raw data measurements were then downloaded, converted to the proper Euler angles for analysis, and plotted. The “DTS TDAS Control” computer software program and a customized Microsoft Excel worksheet were used to analyze and plot the angular-rate sensor data.

A second angular-rate sensor system, the SLICE MICRO Triax ARS, with a range of 1,500 degrees/sec in each of the three directions (roll, pitch, and yaw) was used to measure the rates of rotation of the test vehicles. The angular-rate sensors were mounted inside the body of the custom-built SLICE 6DX event data recorder and recorded data at 10,000 Hz to the onboard microprocessor. The raw data measurements were then downloaded, converted to the proper Euler angles for analysis, and plotted. The “SLICEWare” computer software program and a customized Microsoft Excel worksheet were used to analyze and plot the angular-rate sensor data. For test nos. IRA-3 and IRA-4, only the DTS-SLICE data were used to measure the angular rate.

12.3.5 Speed Trap

For test nos. IRA-1 through IRA-4, a retroreflective optical sensor was used to determine the speed of the vehicle before impact. There were five targets spaced at 18-in. (457-mm) intervals along the side of the vehicle. Each target triggered an electronic timing signal to the data-acquisition system later used to calculate the vehicle speed.

12.3.6 Digital Photography

One AOS S-VIT 1531 high-speed digital video camera, three AOS X-PRI high-speed digital video cameras, two JVC standard-speed digital video cameras, and three GoPro Hero 3 digital video cameras were used to film test no. IRA-1. One AOS S-VIT 1531 high-speed digital video camera, two AOS X-PRI high-speed digital video cameras, and four GoPro Hero 3 digital video cameras were used to film test no. IRA-2. One AOS S-VIT 1531 high-speed digital video camera, two AOS X-PRI high-speed digital video cameras, one JVC standard-speed digital video cameras, and four GoPro Hero 3 digital video cameras were used to film test no. IRA-3. One AOS S-VIT 1531 high-speed digital video camera, two AOS X-PRI high-speed digital video cameras, one JVC standard-speed digital video cameras, and four GoPro Hero 3 digital video cameras were used to film test no. IRA-4. Camera details, camera operating speeds, lens information, and schematics of the camera locations relative to the system for test nos. IRA-1 through IRA-4 are shown in Figures 38 through 41.

The high-speed videos were analyzed using ImageExpress MotionPlus and RedLake MotionScope software programs. Actual camera speed and camera divergence factors were considered in the analysis of the high-speed videos. Nikon D3100 and Canon EOS 30D digital still cameras were used to document pre- and post-test conditions for all tests.

12.4 Data Processing

The electronic accelerometer data obtained in dynamic testing were filtered using the SAE Class 60 Butterworth filter conforming to SAE J211/1 specifications [47]. The pertinent acceleration signal was extracted from the bulk of the data signals. The processed acceleration data were then multiplied by the mass of the bogie to get the impact force using Newton's Second Law. Next, the acceleration trace was integrated to find the change in velocity versus time. Initial velocity of the bogie, calculated from the pressure tape switch data, was then used to determine the bogie velocity, and the calculated velocity trace was integrated to find the bogie's displacement. The trajectory of the vehicle was determined by processing rate gyro and accelerometer data.

No.	Type	Operating Speed (frames/sec)	Lens	Lens Setting
5	AOS X-PRI	500	Kowa 8mm	-
6	AOS X-PRI	500	Computar 12.5mm Fixed	-
7	AOS X-PRI	500	Nikon fixed 20mm	-
8	AOS S-VIT 1531	500	Nikon fixed 28mm	-
3	JVC – GZ-MC27u (Everio)	29.97		
4	JVC – GZ-MG27u (Everio)	29.97		
1	GoPro Hero 3	120		
2	GoPro Hero 3	120		
3	GoPro Hero 3	120		

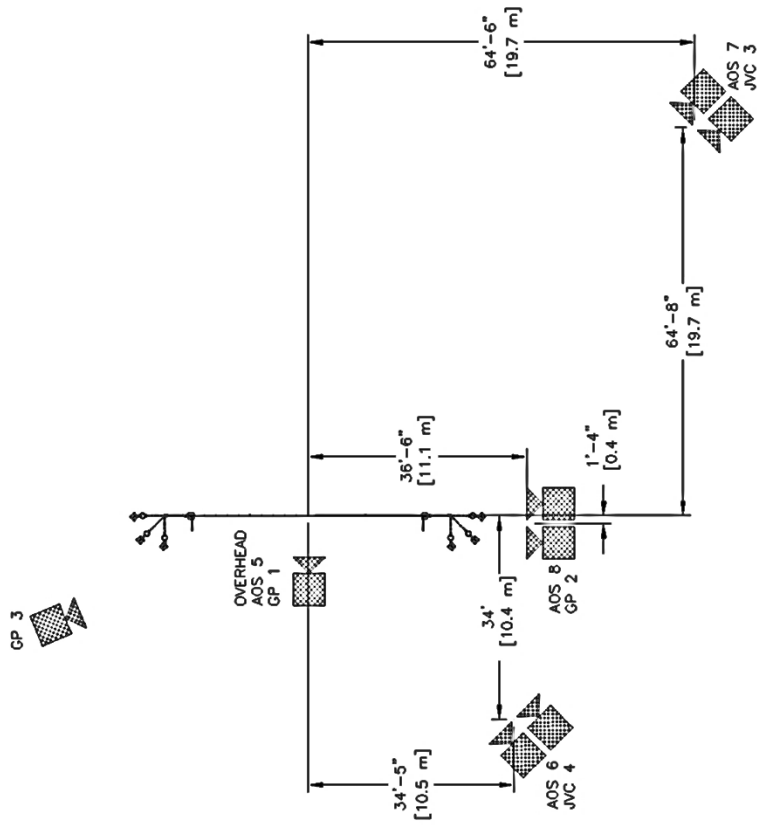


Figure 38. Camera Locations, Speeds, and Lens Settings, Test No. IRA-1

No.	Type	Operating Speed (frames/sec)	Lens	Lens Setting
5	AOS X-PRI	500	Kowa 8mm	-
6	AOS X-PRI	500	Nikon fixed 28mm	-
8	AOS S-VIT 1531	500	Nikon fixed 20mm	-
1	GoPro Hero 3	120		
2	GoPro Hero 3	120		
3	GoPro Hero 3	120		
4	GoPro Hero 3	120		

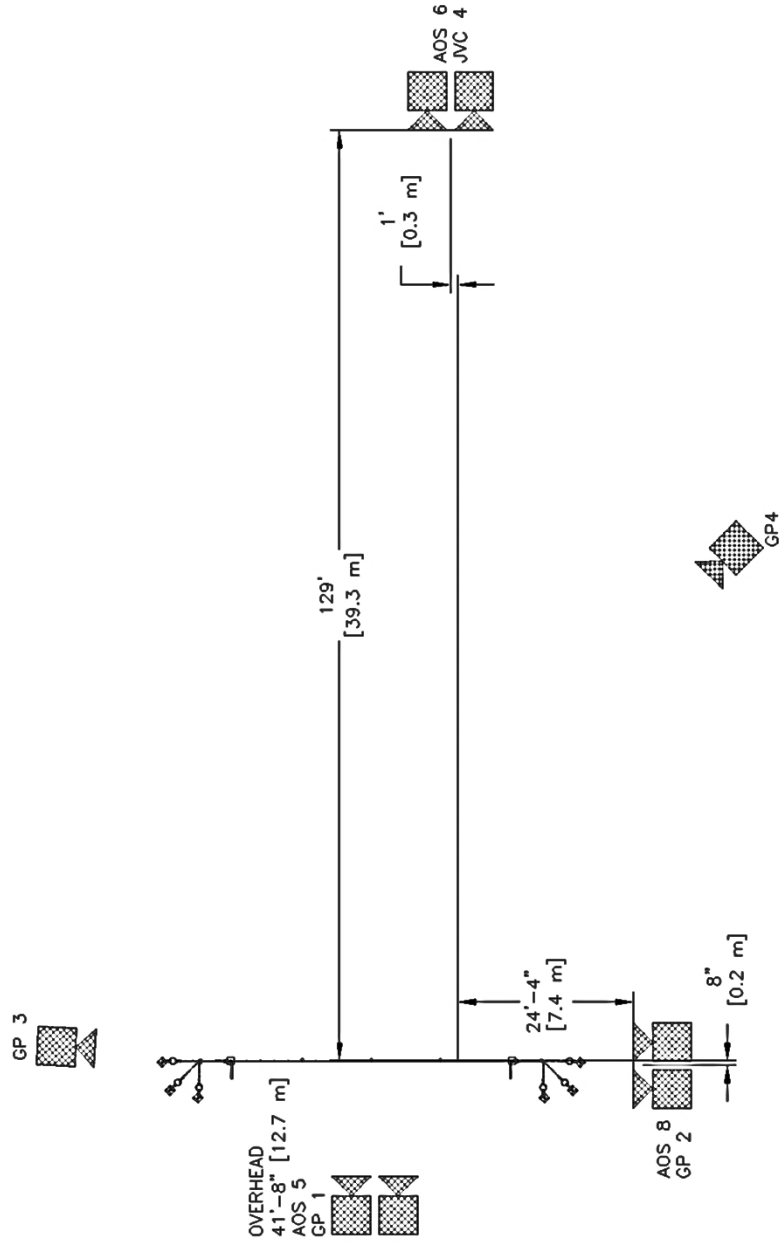


Figure 39. Camera Locations, Speeds, and Lens Settings, Test No. IRA-2

No.	Type	Operating Speed (frames/sec)	Lens	Lens Setting
5	AOS X-PRI	500	Kowa 8mm	-
6	AOS X-PRI	500	Nikon fixed 28mm	-
8	AOS S-VIT 1531	500	Nikon fixed 20mm	-
4	JVC – GZ-MG27u (Everio)	29.97		
1	GoPro Hero 3	120		
2	GoPro Hero 3	120		
3	GoPro Hero 3	120		
4	GoPro Hero 3	120		

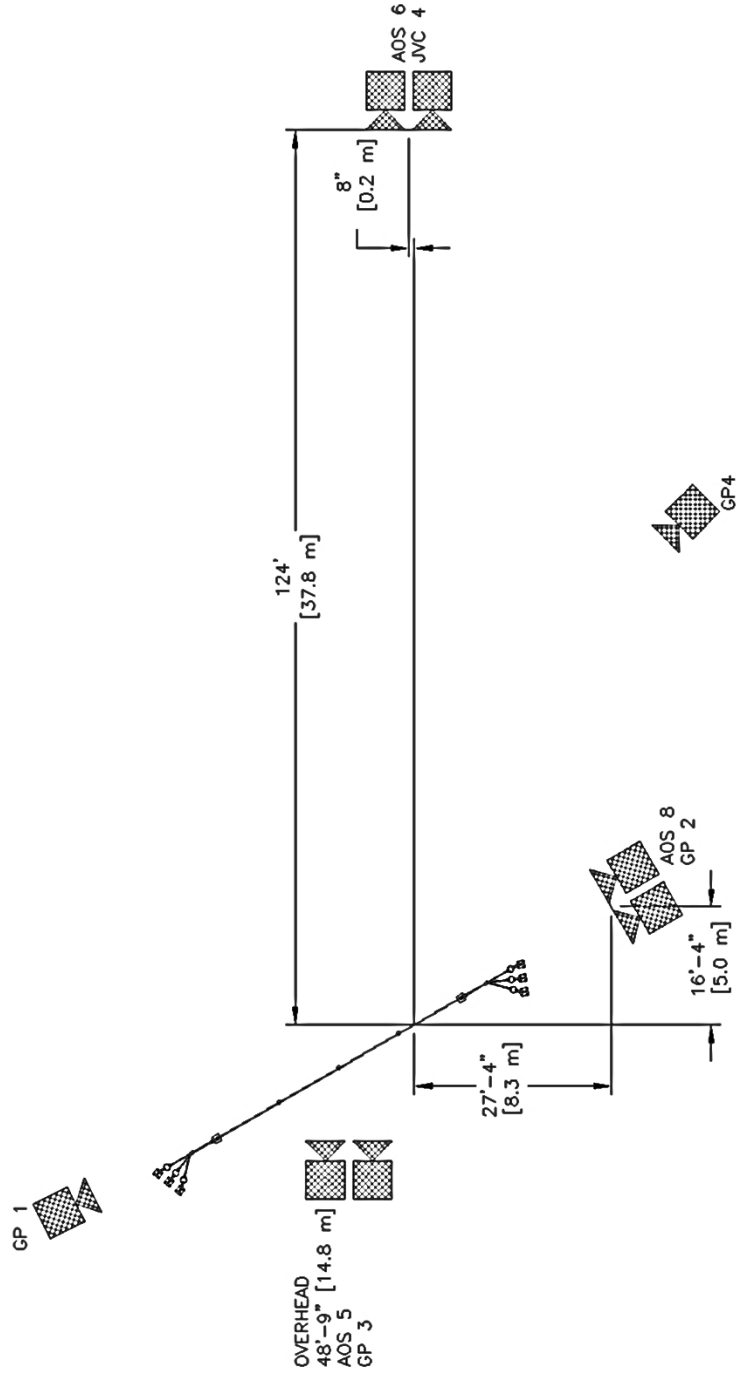


Figure 40. Camera Locations, Speeds, and Lens Settings, Test No. IRA-3

No.	Type	Operating Speed (frames/sec)	Lens	Lens Setting
5	AOS X-PRI	500	Kowa 8mm	-
6	AOS X-PRI	500	Nikon fixed 28mm	-
8	AOS S-VIT 1531	500	Nikon fixed 20mm	-
4	JVC – GZ-MG27u (Everio)	29.97		
1	GoPro Hero 3	120		
2	GoPro Hero 3	120		
3	GoPro Hero 3	120		
4	GoPro Hero 3	120		

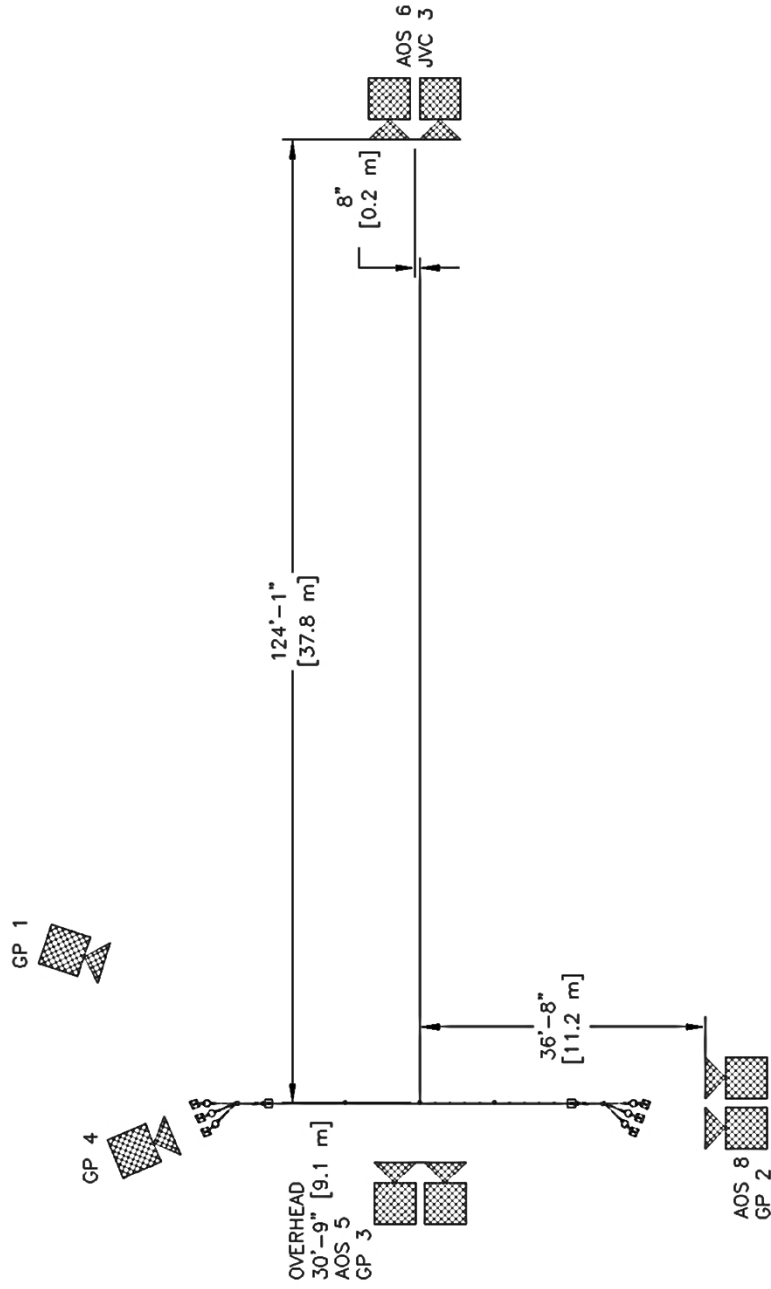


Figure 41. Camera Locations, Speeds, and Lens Settings, Test No. IRA-4

13 DESIGN DETAILS - TEST NOS. IRA-1 AND IRA-2

The net attenuation system for test nos. IRA-1 and IRA-2 consisted of a modified Dragnet Vehicle Arresting Barrier with three major components: a net, energy absorbers, and an anchorage system. The test installation was composed of six standard Dragnet energy absorbers with a modified net and anchorage system, as shown in Figures 42 through 60. Photographs of the test installations are shown in Figures 61 through 64. Material specifications, mill certifications, and certificates of conformity for the system materials are shown in Appendix A.

The 40-ft (12.2-m) wide net consisted of five horizontal $\frac{3}{8}$ -in. (10-mm) diameter steel cables with two steel plates at each end tying them together. Vertical steel plates were used to keep the cables from spreading apart and were attached with $\frac{1}{4}$ -in. (6-mm) bolts. A solid aluminum stand was used to support the center of the net, with two hollow aluminum posts supporting the net between the center post and end of the net. The ends of the net rested on wooden blocks with 42-in. (1,067-mm) long, $1\frac{1}{2}$ -in. by $1\frac{1}{2}$ -in. (38-mm by 38-mm) wooden posts used to prop it up vertically. The supports for the ends of the nets would not be suitable for long-term installations but were acceptable for testing purposes. Turnbuckles, eye nuts, and BCT Cable Anchors were used to connect the net assembly to the energy absorbers.

The energy absorbers contained a series of pins around which steel tape was bent back and forth as it was pulled through a stainless steel case. Each end of the net was attached to one end of the steel tape extending from each of the three energy absorbers on both sides. The anchorage system consisted of a 1-in. (25-mm) anchor hoop welded to a $\frac{3}{4}$ -in. (19-mm) steel plate. Four $\frac{3}{4}$ -in. (19-mm) diameter, 6-in. (152-mm) tapcon screws were used to attach the anchor plates to the tarmac.

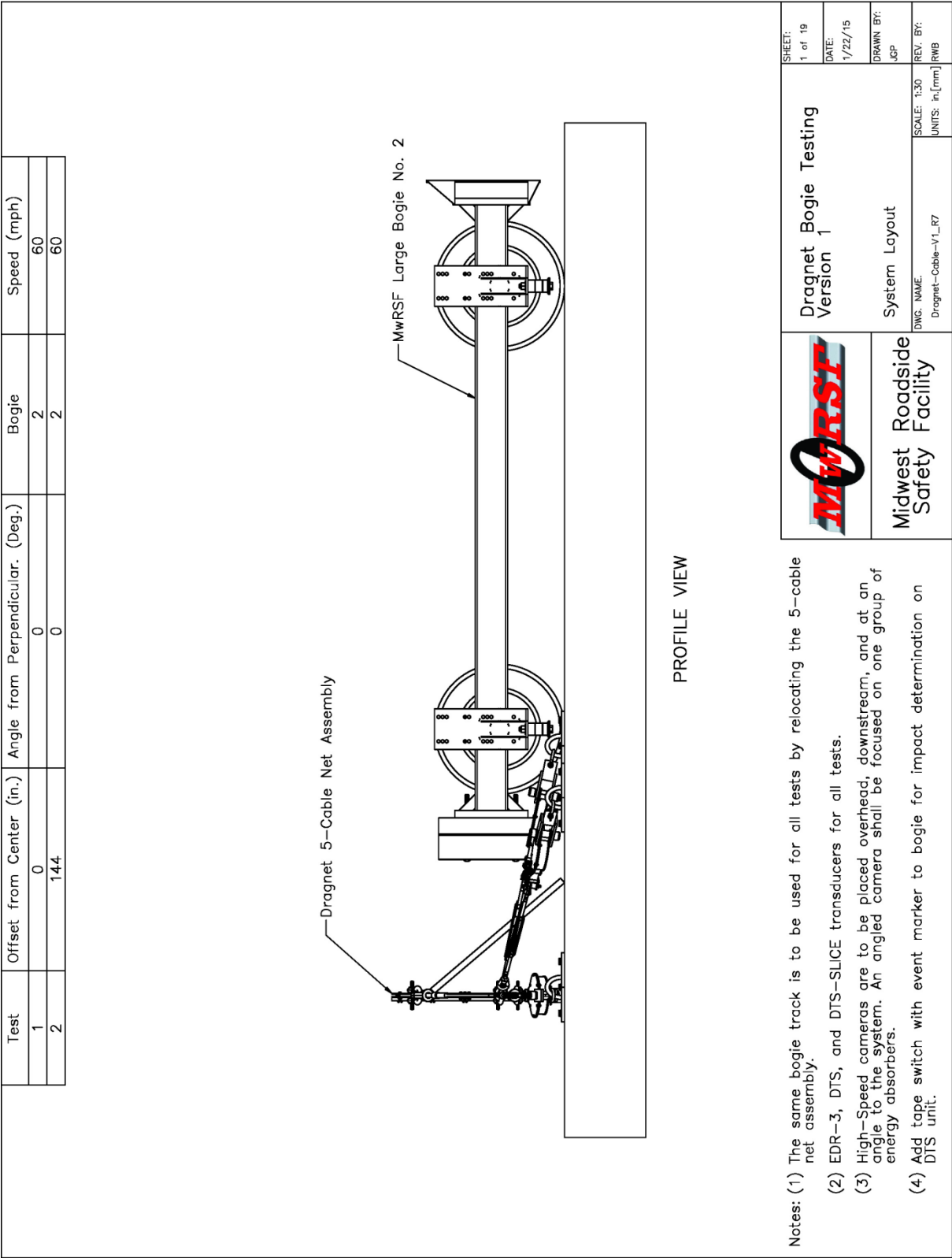


Figure 42. Bogie Test Installation, Test Nos. IRA-1 and IRA-2

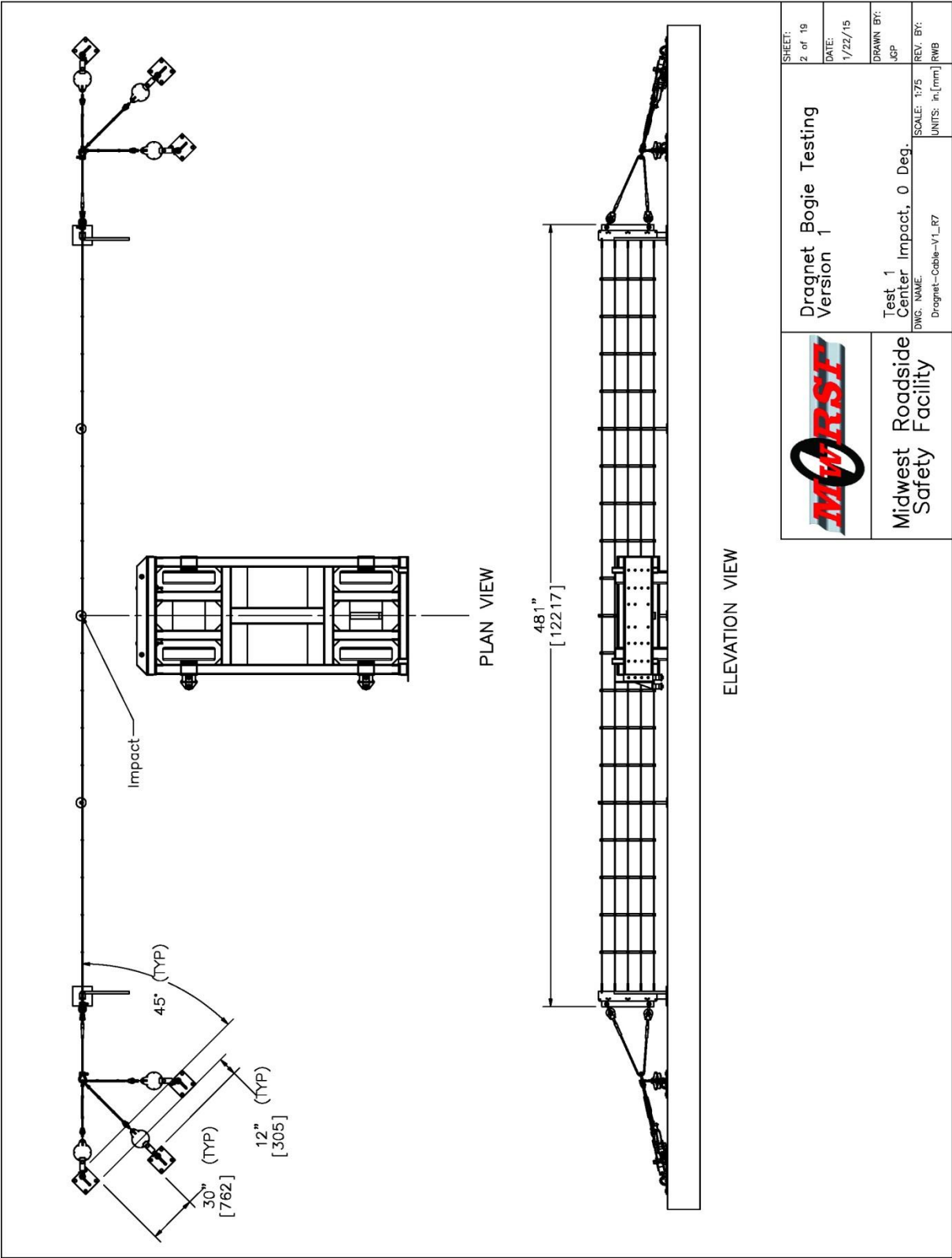


Figure 43. 0 Deg. Central Impact, Test No. IRA-1

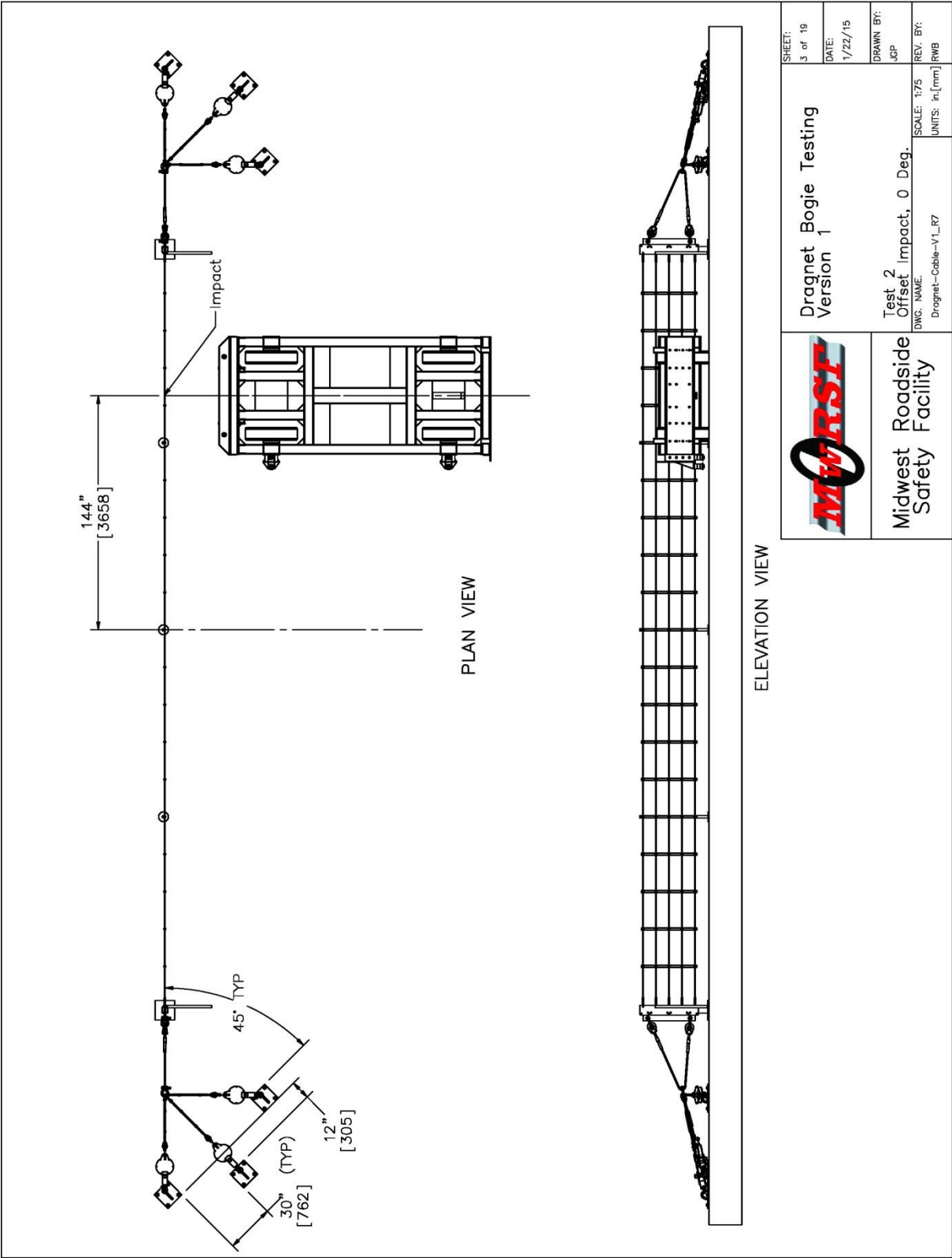
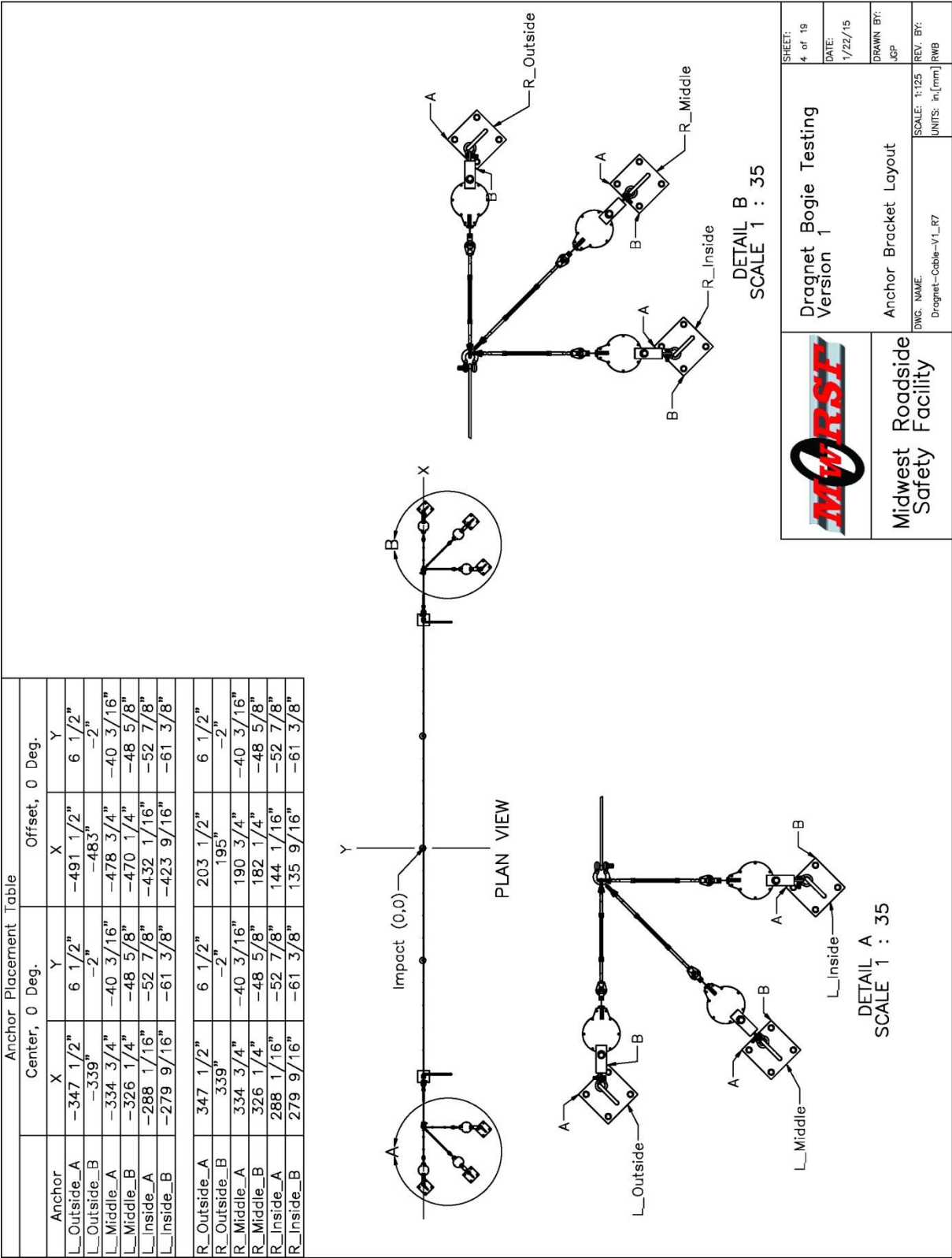


Figure 44. 0 Deg. Offset Impact, Test No. IRA-2



**Midwest
Safety
Facility**

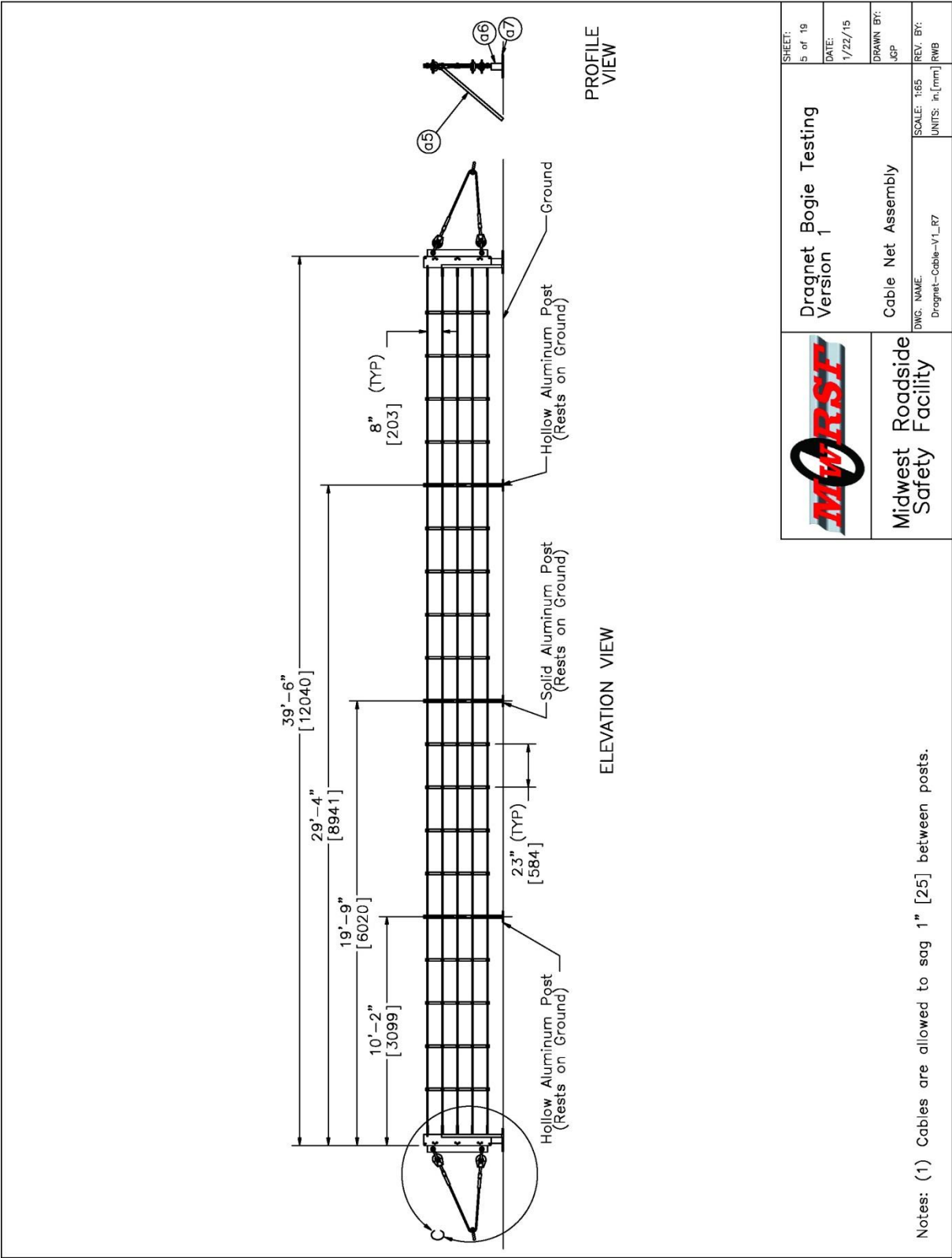
Dragnet Bogie Testing
Version 1


Anchor Bracket Layout

DWG. NAME: Dragnet-Cable-V1_R7
SCALE: 1:125
UNITS: in, [mm]

SHEET: 4 of 19
DATE: 1/22/15
DRAWN BY: JCP
REV. BY: RWB

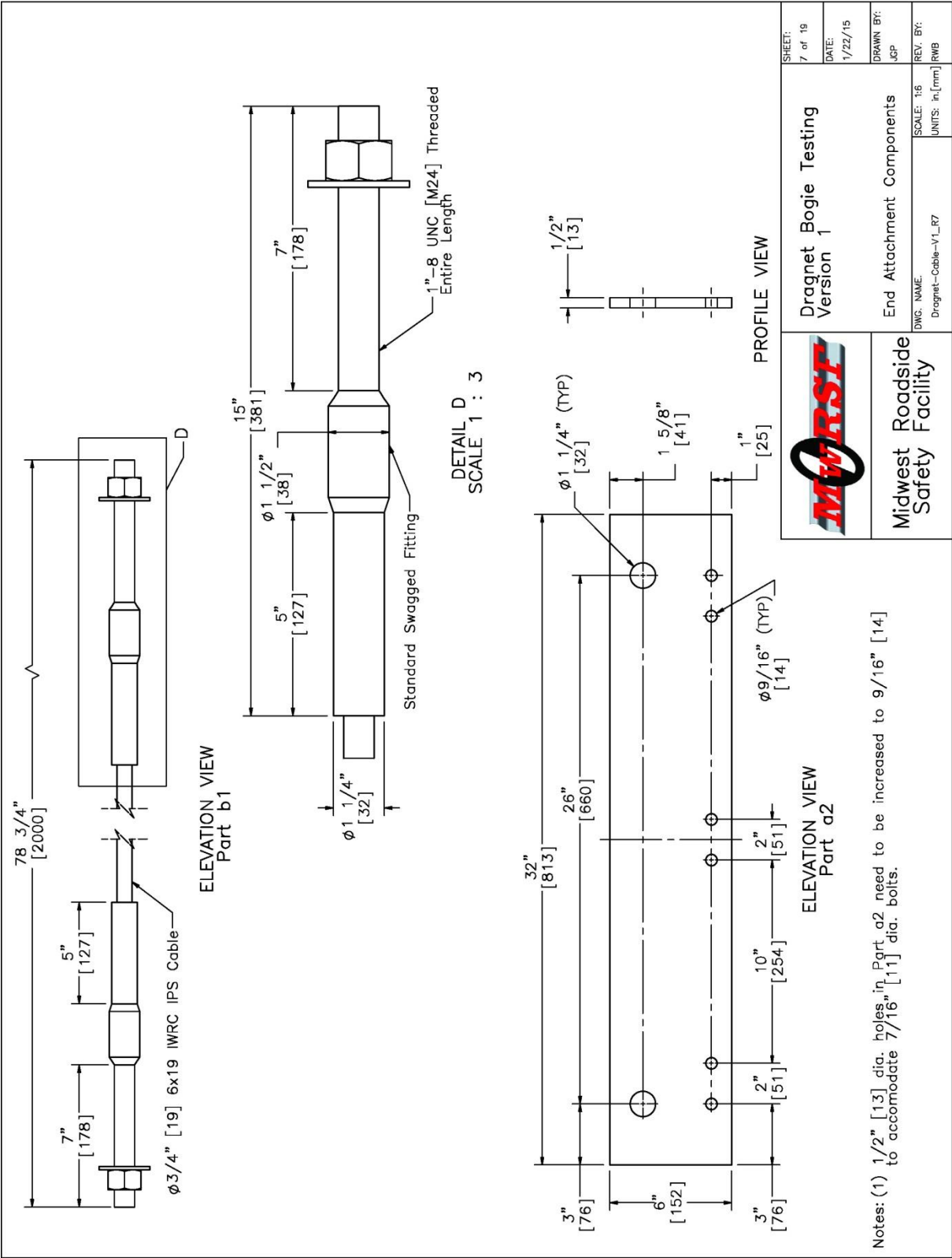
Figure 45. Anchor Bracket Layout, Test Nos. IRA-1 and IRA-2



	Dragnet Bogie Testing Version 1	SHEET: 5 of 19
	Cable Net Assembly	DATE: 1/22/15
DWG. NAME: Dragnet-Cable-V1_R7	SCALE: 1:65 UNITS: in, [mm]	DRAWN BY: JCP
Midwest Roadside Safety Facility	REV. BY: RWB	

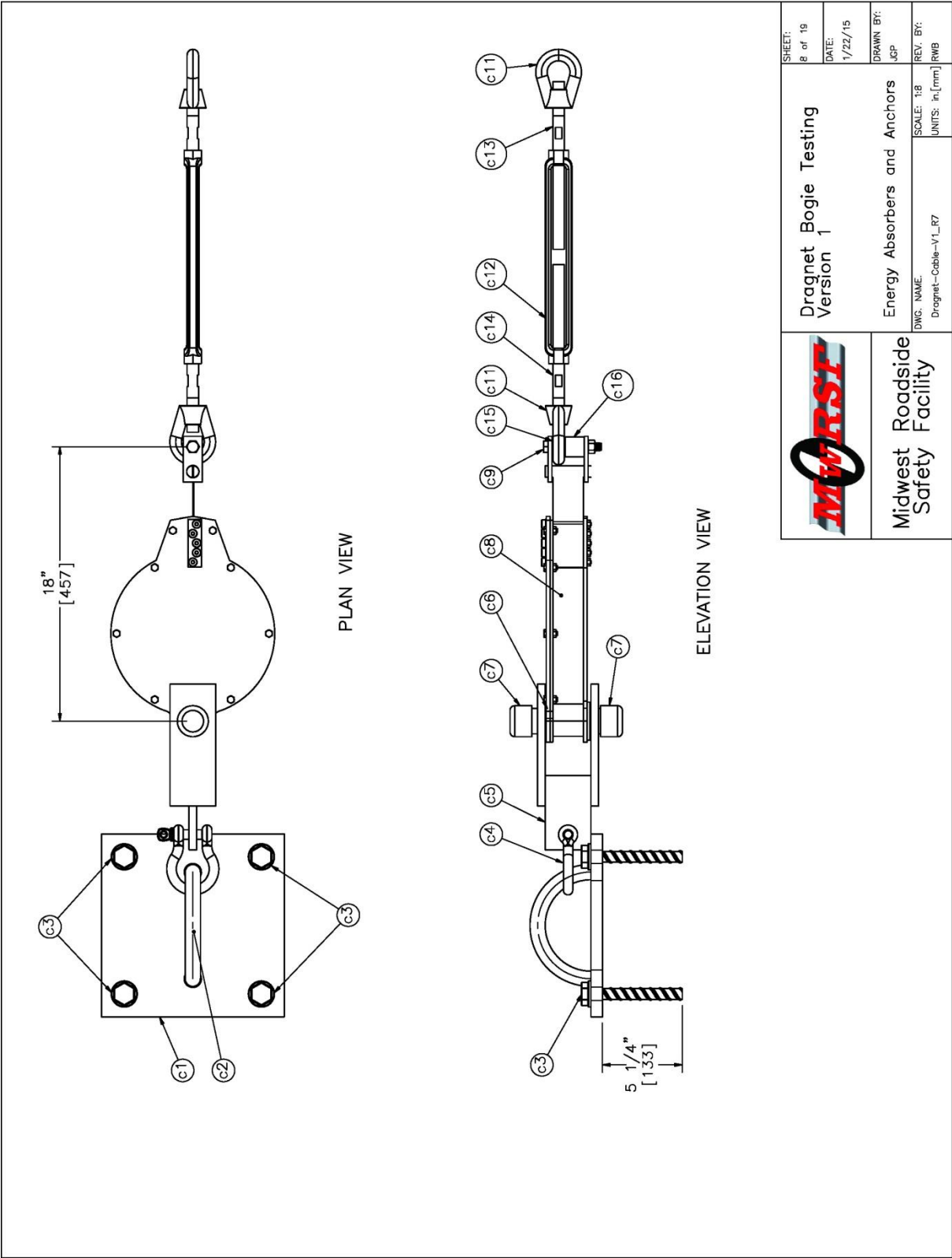
Notes: (1) Cables are allowed to sag 1" [25] between posts.

Figure 46. Cable Net Assembly, Test Nos. IRA-1 and IRA-2



Notes: (1) 1 1/2" [13] dia. holes in Part a2 need to be increased to 9/16" [14] to accommodate 7/16" [11] dia. bolts.

Figure 48. End Attachment Components, Test Nos. IRA-1 and IRA-2




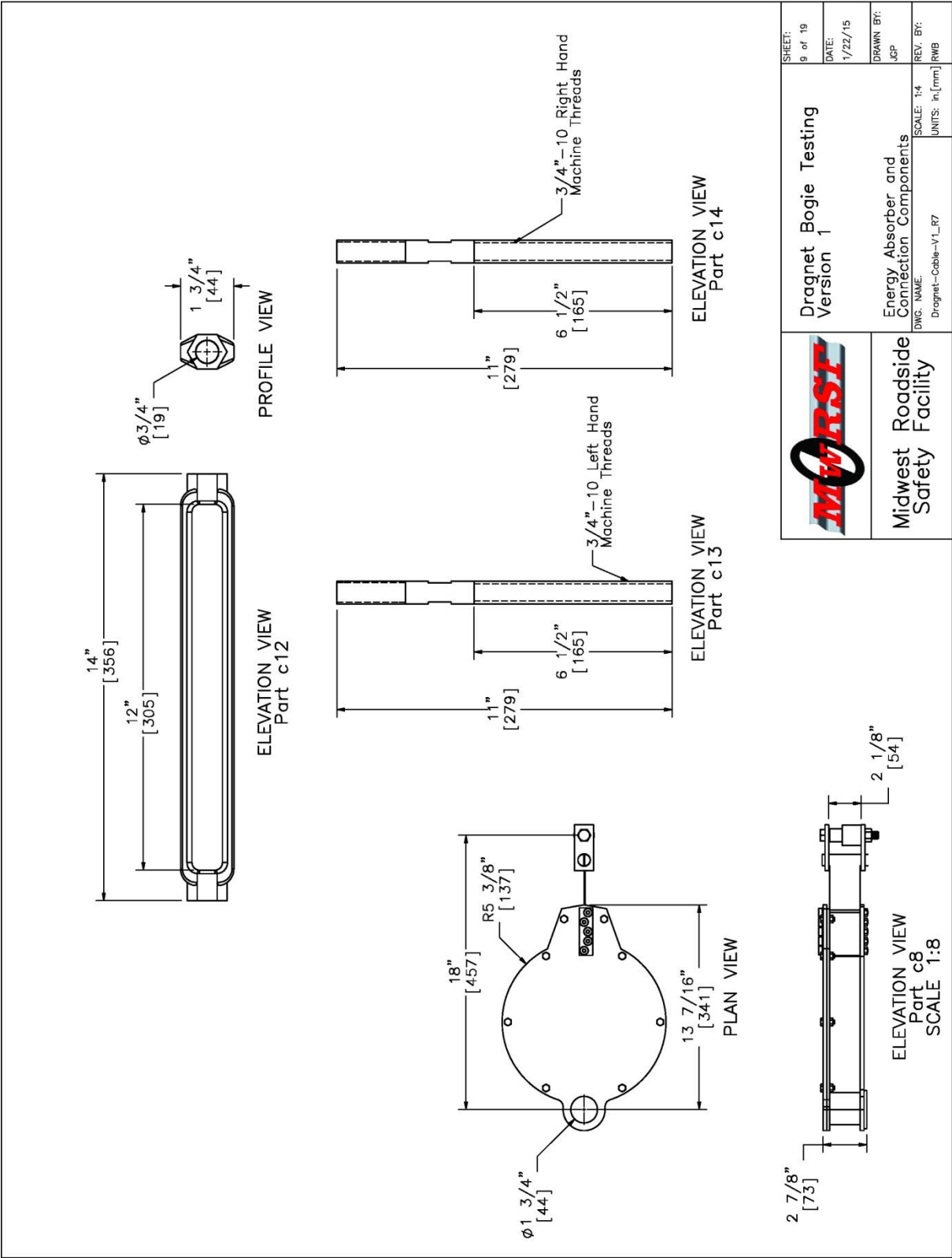
	Dragnet Bogie Testing Version 1	SHEET: 8 of 19
	Energy Absorbers and Anchors DWG. NAME: Dragnet-Cable-V1_R7	DATE: 1/22/15
Midwest Roadside Safety Facility	SCALE: 1:8 UNITS: in, [mm]	DRAWN BY: JCP
		REV. BY: RWB

Figure 49. Energy Absorbers and Anchors, Test Nos. IRA-1 and IRA-2




	Dragnet Bogie Testing Version 1	SHEET: 9 of 19 DATE: 1/22/15 DRAWN BY: JCP REV. BY: RWB SCALE: 1:4 UNITS: in, [mm]
	Midwest Roadside Safety Facility	Energy Absorber and Connection Components DWG. NAME: DragNet-Cable-V1_R7

Figure 50. Energy Absorber and Connection Components, Test Nos. IRA-1 and IRA-2

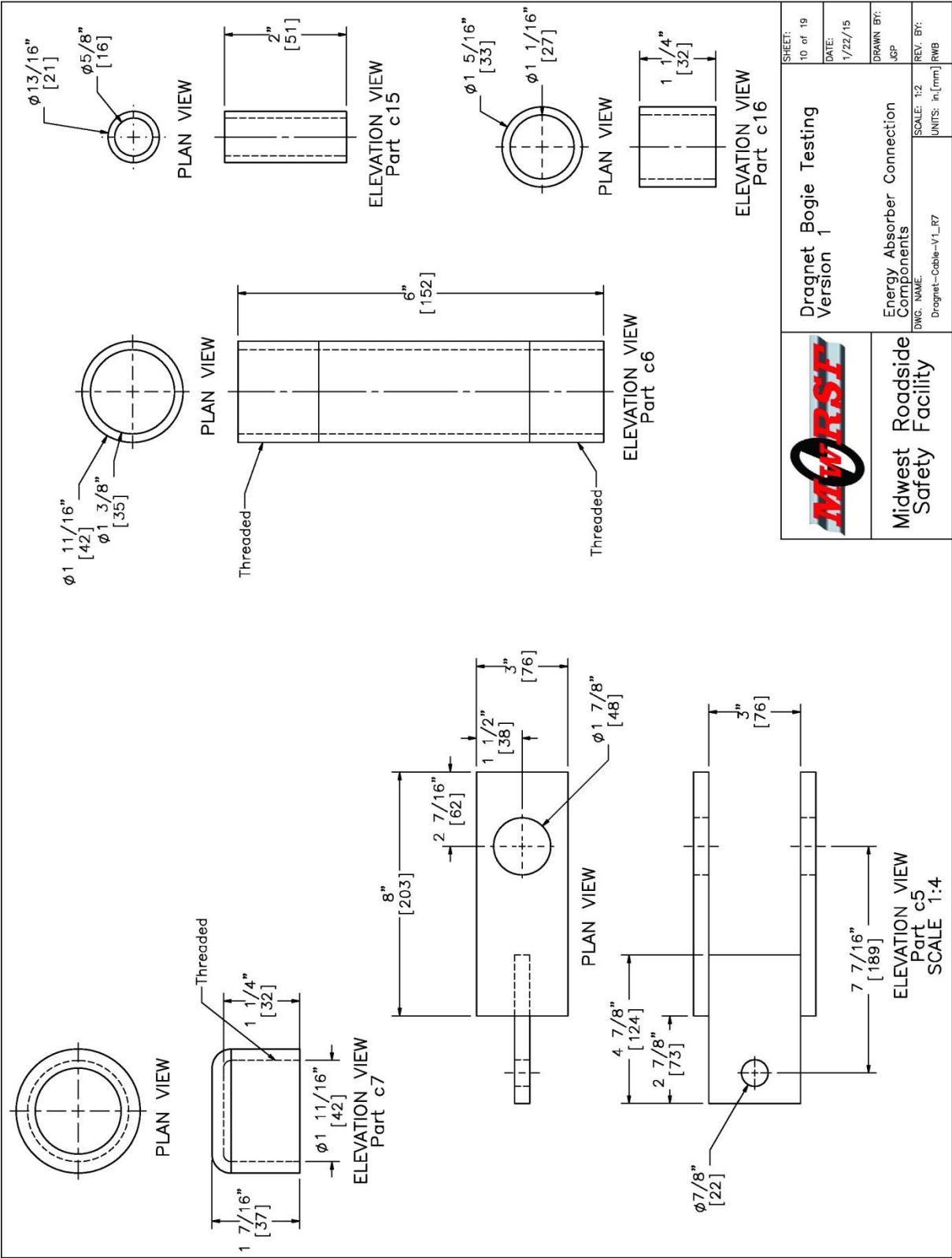


Figure 51. Energy Absorber Connection Components, Test Nos. IRA-1 and IRA-2

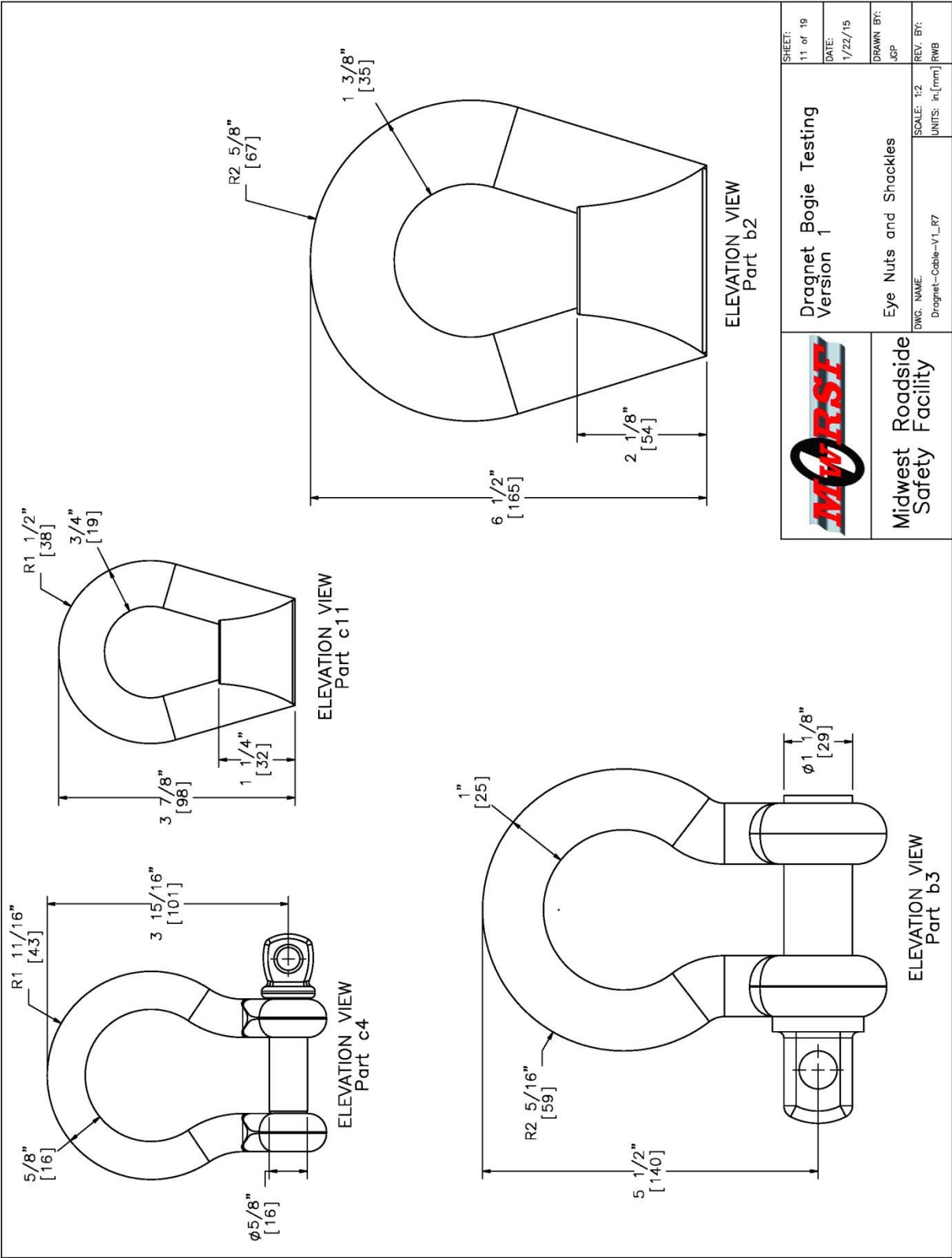


Figure 52. Eye Nuts and Shackles, Test Nos. IRA-1 and IRA-2

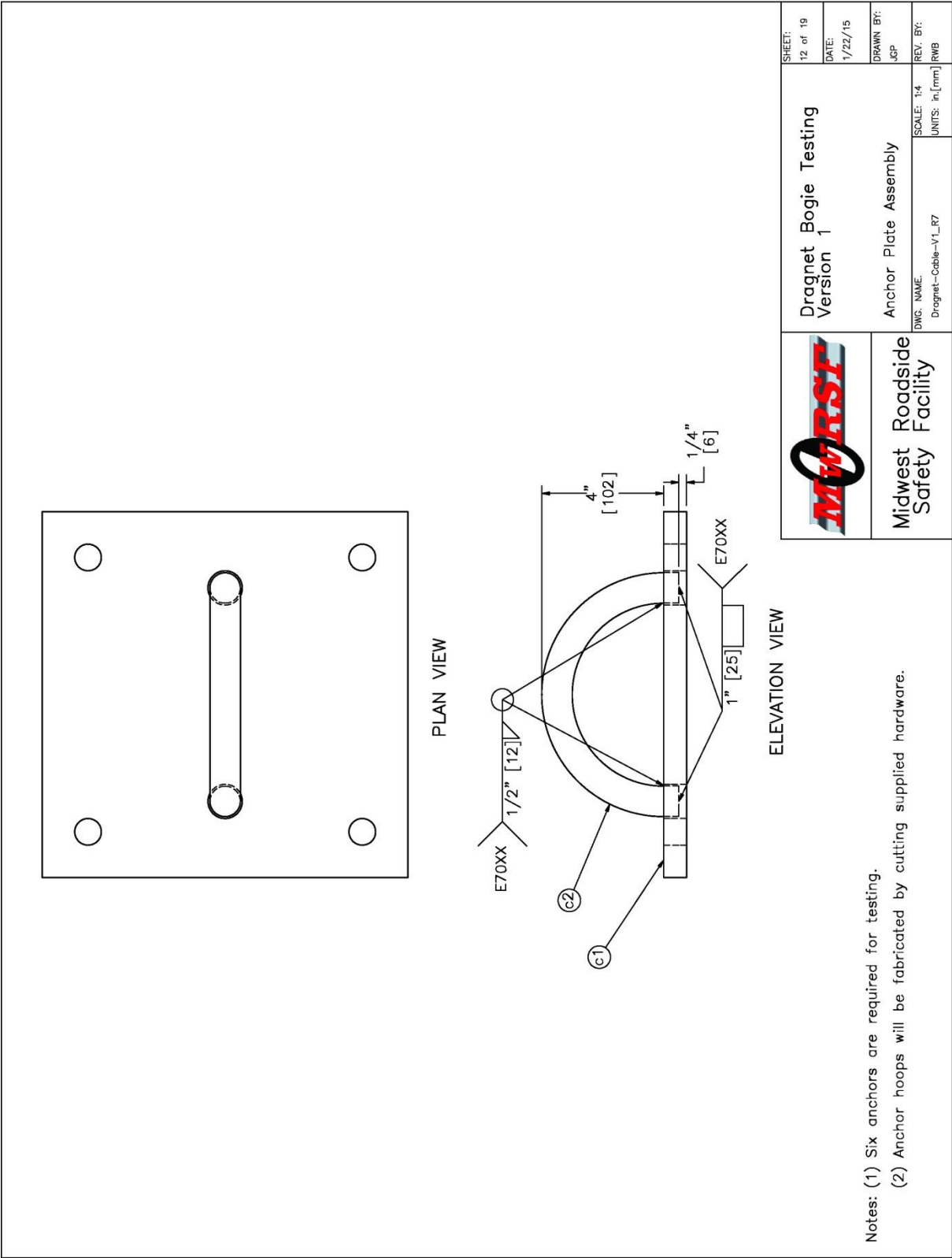


Figure 53. Anchor Plate Assembly, Test Nos. IRA-1 and IRA-2

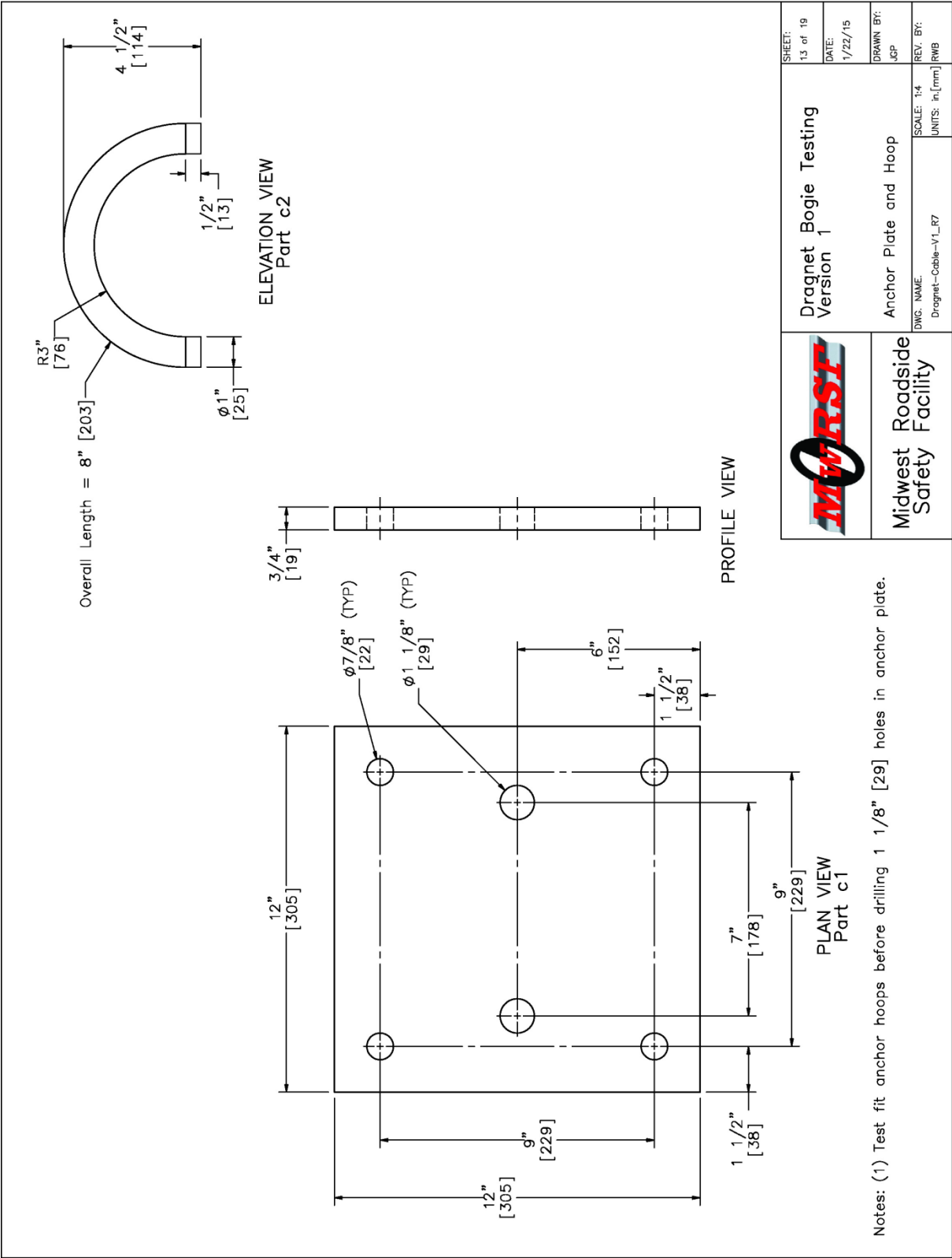


Figure 54. Anchor Plate and Hoop, Test Nos. IRA-1 and IRA-2

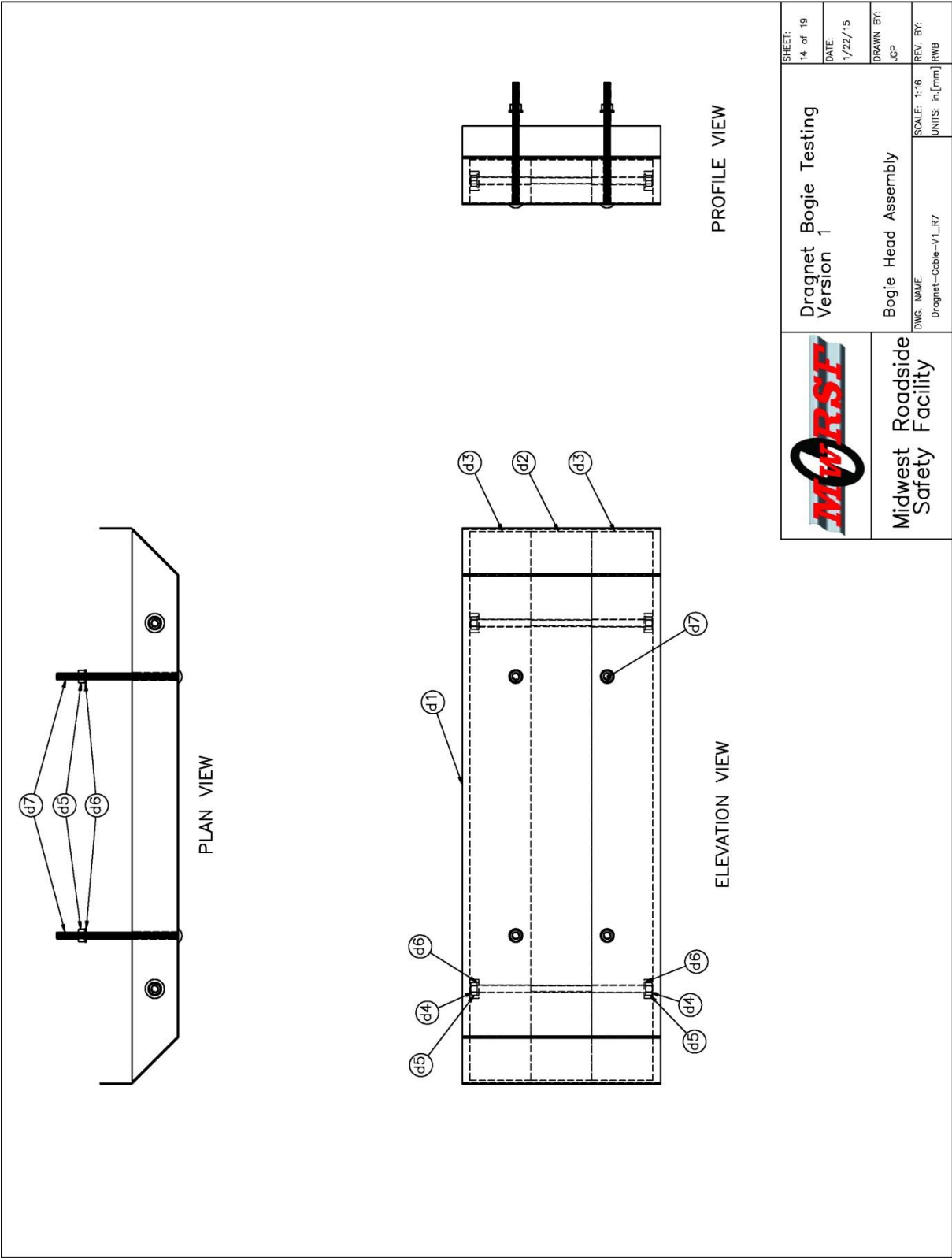
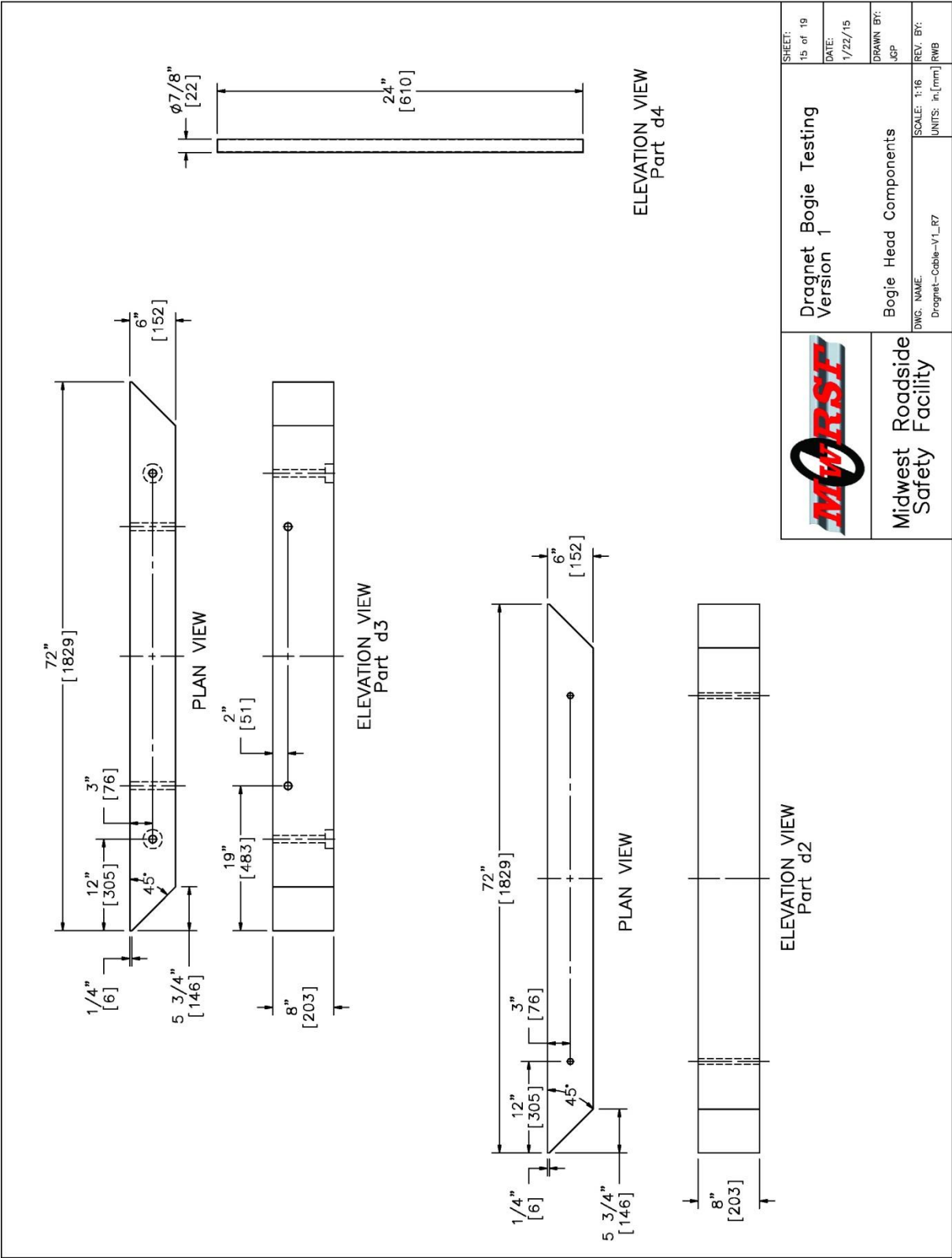


Figure 55. Bogie Head Assembly, Test Nos. IRA-1 and IRA-2




	Dragnet Bogie Testing Version 1	SHEET: 15 of 19 DATE: 1/22/15 DRAWN BY: JCP REV. BY: RWB
	Bogie Head Components DWG. NAME: Dragnet-Cable-V1_R7	SCALE: 1:16 UNITS: in, [mm]

Figure 56. Bogie Head Components, Test Nos. IRA-1 and IRA-2

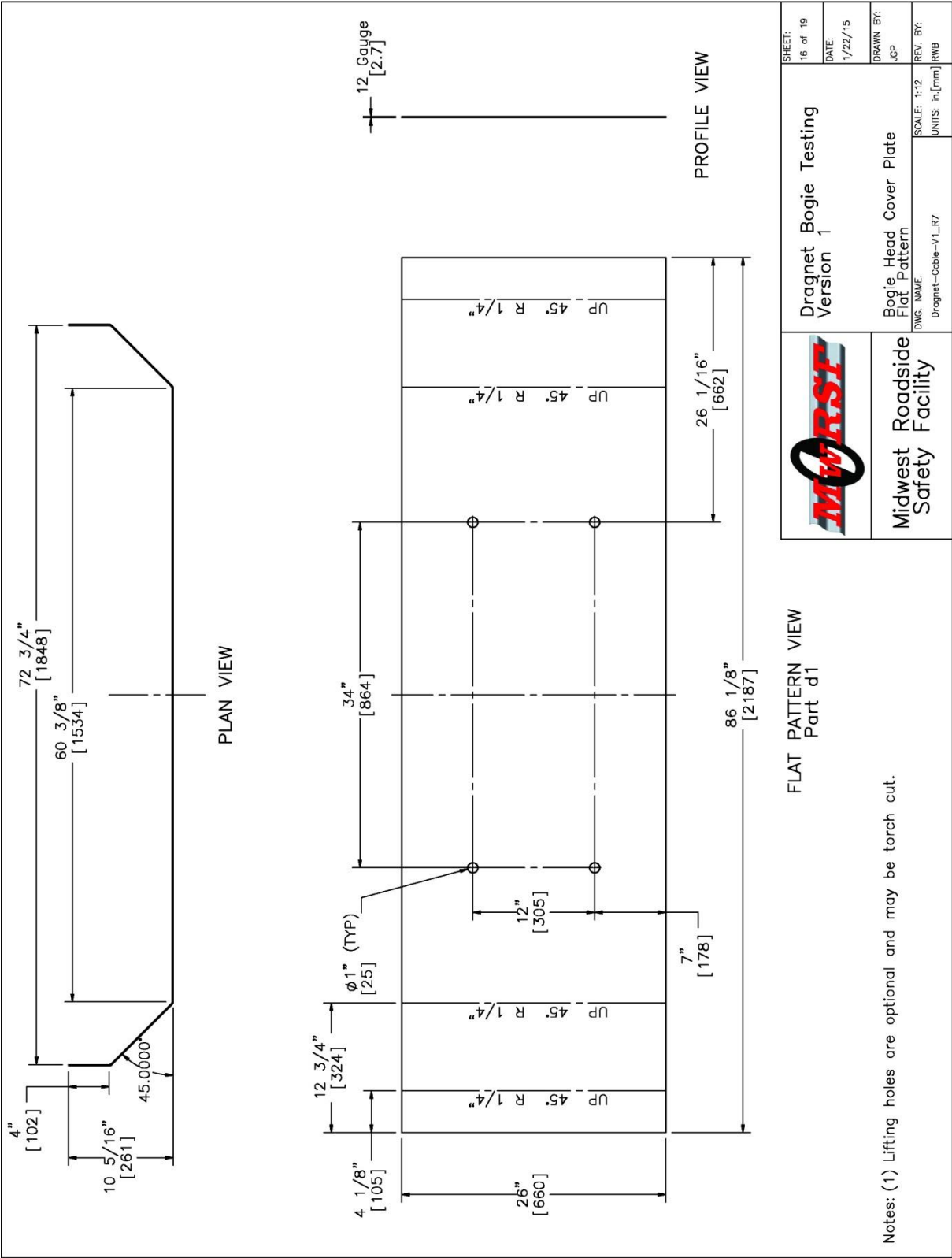


Figure 57. Bogie Head Cover Plate, Flat Pattern, Test Nos. IRA-1 and IRA-2

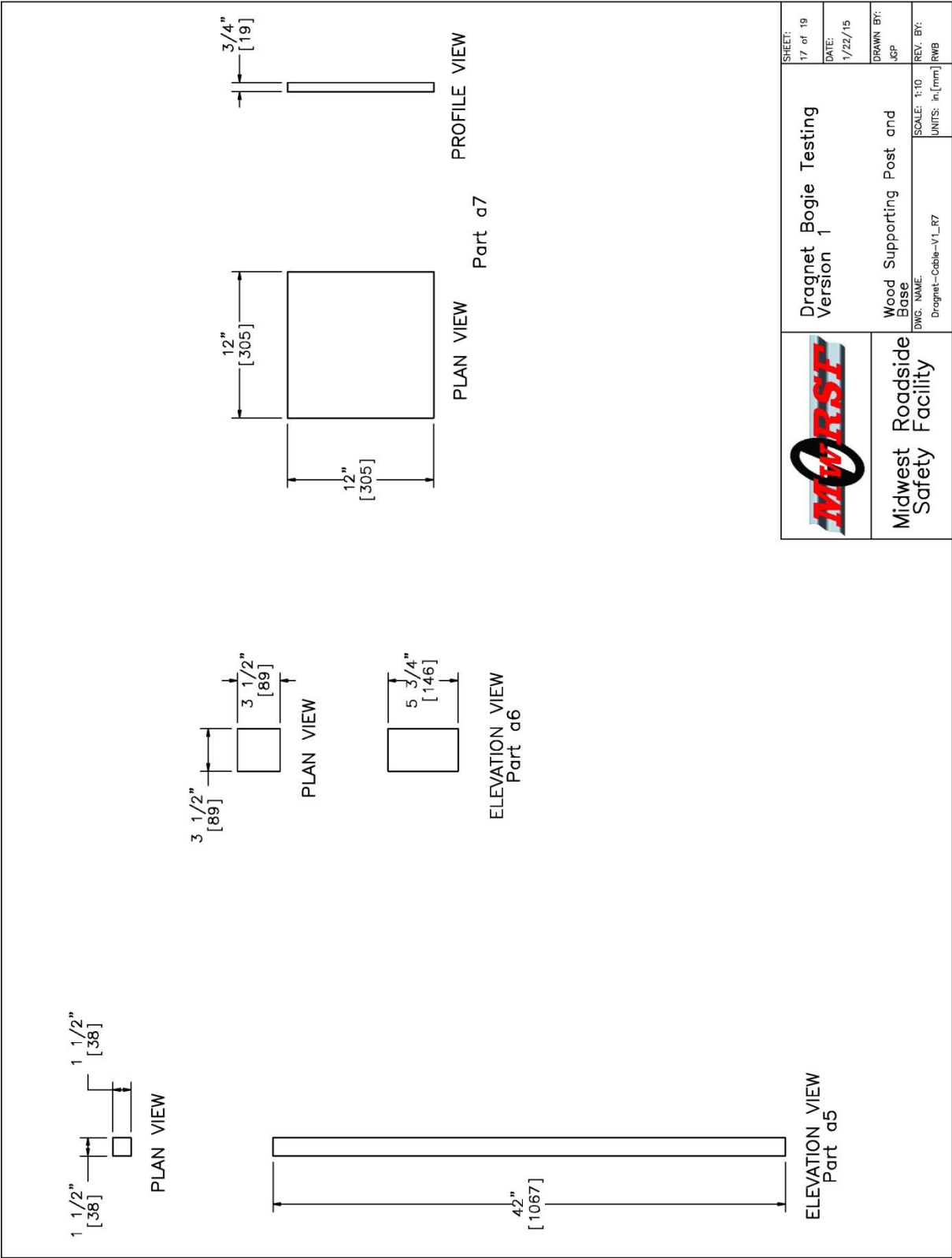


Figure 58. Wood Supporting Post and Base, Test Nos. IRA-1 and IRA-2

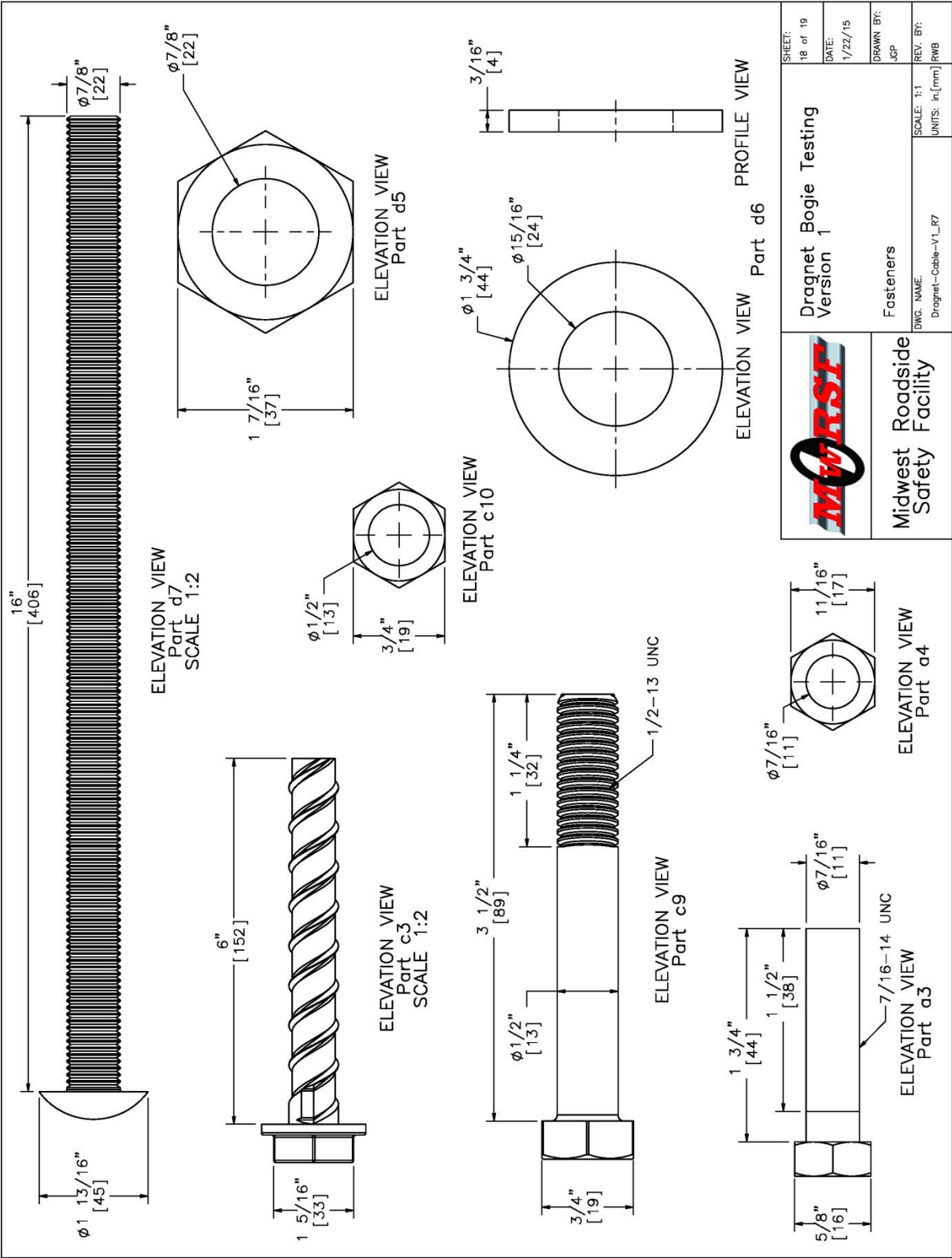


Figure 59. Fasteners, Test Nos. IRA-1 and IRA-2

Item No.	Qty.	Description	Material Specification	Comment
a1	1	Dragnet 5-Cable Net Assembly	Donated, No Material Certifications	-
a2	2	1/2"x6"x32" [13x152x813] Attachment Plate	ASTM A36	-
a3	12	7/16" [11] Dia. UNC, 1 3/4" [44] Long Hex Bolt	SAE J429 Gr. 5	-
a4	12	7/16" [11] Dia. UNC Heavy Hex Nut	ASTM A563 DH	-
a5	2	2"x2" [51x51], 42" [1067] Long Wooden Post	Wood	-
a6	2	4"x4" [102x102], 5 3/4" [146] Long Wooden Block	Wood	-
a7	2	12"x12"x3/4" [305x305x19] Post Base	Plywood	-
b1	2	BCT Cable Anchor Assembly (Includes Nuts & Washers)	3/4" [19] Dia. 6x19 IWRC IPS Galv. Wire Rope	FCA01
b2	4	1 1/2" [38] Dia. Oval Eye Nut	-	**3274T48
b3	6	1" [25] Dia. Shackles	-	**3663T46
c1	6	12"x12"x3/4" [305x305x19] Anchor Plate	ASTM A36	-
c2	6	1" [25] Dia. Anchor Hoop	Donated, No Material Specification	-
c3	24	3/4" [19] Dia., 6" [152] Long Wedge Bolt	Power Fasteners	-
c4	6	5/8" [16] Dia. Shackles	Donated, No Material Specification	**3663T43
c5	6	Dragnet Transition Piece	Donated, No Material Specification	-
c6	6	1 1/4" [32] Dia., 6" [152] Long Schedule 40 Pipe	Donated, No Material Specification	-
c7	12	1 1/4" [32] Dia., Schedule 40 Pipe Cap	Donated, No Material Specification	-
c8	6	Dragnet Energy Absorber 4,500 lb [20 kN]	Donated, No Material Certifications	-
c9	6	1/2" [13] UNC, 3 1/2 [89] Long Hex Bolt	SAE J429 Gr. 5	-
c10	6	1/2" [13] Dia. UNC Hex Nut	ASTM A325DH	Manuf. Supplied
c11	12	3/4" [19] Dia. UNC Oval Eye Nut	-	**3274T44
c12	6	3/4" [19] Dia. UNC, 14" [356] Turnbuckle	Not Specified	-
c13	6	3/4" [19] Dia. UNC, 11" [279] Left-Hand Threaded Rod	ASTM A449	-
c14	6	3/4" [19] Dia. UNC, 11" [279] Right-Hand Threaded Rod	ASTM A449	-
d1	1	86 1/8"x26"x12 Gauge [2187x660x2.7] Bogie Head Plate	ASTM A36	-
d2	1	6"x8"x72" [152x203x1829] Post	SYP Grade No. 1	-
d3	2	6"x8"x72" [152x203x1829] Post	SYP Grade No. 1	-
d4	2	7/8" [22] Dia. UNC, 24" [610] Long Threaded Rod	ASTM A449	-
d5	8	7/8" [22] Dia. UNC Heavy Hex Nut	ASTM A563 DH	-
d6	8	7/8" [22] Dia. Hardened Round Washer	ASTM F436	-
d7	4	7/8" [22] Dia. UNC, 16" [406] Long Round Head Bolt	ASTM A449	-

** McMaster-Carr part no. used for general dimensions.


	Dragnet Bogie Testing Version 1	SHEET: 19 of 19 DATE: 1/22/15 DRAWN BY: JCP REV. BY: RWB SCALE: 1:384 UNITS: in, [mm]
	Bill of Materials DWG. NAME: Dragnet-Cable-V1_R7	

Figure 60. Bill of Materials, Test Nos. IRA-1 and IRA-2



Figure 61. Test Installation, Test No. IRA-1



Figure 62. Test Installation, Test No. IRA-1



Figure 63. Test Installation, Test No. IRA-2



Figure 64. Test Installation, Test No. IRA-2

14 NET ATTENUATOR COMPONENT TEST NO. IRA-1

14.1 Test No. IRA-1

The 5,090-lb (2,309-kg) bogie vehicle impacted the net arrestor at a speed of 60.4 mph (97.2 km/h) in the center of the net at an angle of 90 degrees. Sequential photographs are shown in Figures 65 through 70. Documentary photographs of the crash test are shown in Figures 71 and 72.

14.2 Weather Conditions

Test no. IRA-1 was conducted on December 12, 2013 at approximately 3:00 p.m. The weather conditions, as per the National Oceanic and Atmospheric Administration (station 14939/LNK), were reported and are shown in Table 22.

Table 22. Weather Conditions, Test No. IRA-1

Temperature	32° F
Humidity	64%
Wind Speed	9 mph
Wind Direction	200° from True North
Sky Conditions	Clear
Visibility	10 Statute Miles
Pavement Surface	Dry
Previous 3-Day Precipitation	0 in.
Previous 7-Day Precipitation	0.20 in.

14.3 Test Description

Initial vehicle impact was to occur in the center of the net, as shown in Figure 73. Although the actual point of impact could not be determined from examining the post-test damage of the system, analysis of the crash test videos showed that the bogie did appear to impact in the center of the net. The vehicle had a maximum dynamic deflection of 44.2 ft (13.5 m) downstream from the point of impact and a lateral movement of 1.3 ft (0.4 m). The maximum

dynamic deflection was determined using accelerometer traces to calculate the planar trajectory. The deflection could not be verified with overhead video analysis because of skewed cameras. The innermost energy absorber on the left side of the system failed 120 ms after impact occurred. Near the end of the test, the vehicle yawed to the right, as a result of the failed energy absorber. The vehicle trajectory and final position are shown in Figure 74.

14.4 System Damage

Damage to the net attenuator was minimal, as shown in Figures 75 through 77. The innermost energy absorber on the left side of the system failed 120 ms after impact occurred. The failure was likely caused by excessive whipping that occurred with both inside energy absorbers of the system. As shown in Figures 67 and 70, the 1-in. (25-mm) shackle that connected the energy absorbers to the assembly initially moved upstream and towards the center of the net. This motion caused the innermost energy absorbers to compress and rotate away from impact. As the innermost energy absorber on the left side was pulled tight, the steel tape ruptured at the connection between the tape and the turnbuckles, as shown in Figure 76. Although the inside energy absorbers on both sides of the net exhibited the same motion, only the left absorber had a failure. One factor that could have influenced this failure was the direction the tape was wrapped around the bracket. The amount of tape pulled from each energy absorber is shown in Table 23. A bolt used to connect an energy absorber to the net was bent, as shown in Figure 77.

Table 23. Energy-Absorber Tape Pullout, Test No. IRA-1

Side	Location	Pullout Distance	
		ft	m
Right	Outside	20.71	6.31
	Middle	23.21	7.07
	Inside	23.54	7.18
Left	Outside	30.23	9.21
	Middle	32.04	9.77
	Inside	0.50	0.15

The net assembly deformed around the bogie vehicle. The hollow aluminum posts that supported the net had fractured at the bottom mounting bolt hole used to attach the bottom cable, approximately 8 in. (203 mm) above the ground, as shown in Figure 77. The solid aluminum center post was also bent at the same location. The end plates, cables, and vertical cable spreaders had minimal damage and were able to be reused.

14.5 Vehicle Damage

The damage to the bogie vehicle was minimal, as shown in Figure 77. The damage to the vehicle was isolated to the top and bottom of the bogie impact head. Denting and scraping were observed on the top and bottom of the bogie impact head.

14.6 Occupant Risk

The calculated occupant impact velocities (OIVs) and maximum 0.010-sec occupant ridedown accelerations (ORAs) in both the longitudinal and lateral directions are shown in Table 24. Note that the OIVs and ORAs were within the suggested limits provided in MASH, although the velocity was slightly less than a MASH TL-3 tests and the mass of the bogie vehicle was slightly higher than the MASH 2270P vehicle. The calculated THIV, PHD, and ASI values are also shown in Table 24. The recorded data from the accelerometers and the rate transducers are shown graphically in Appendix B.

Table 24. Summary of OIV, ORA, THIV, PHD, and ASI Values, Test No. IRA-1

Evaluation Criteria		Transducer			MASH Limits
		EDR-3	DTS	SLICE	
OIV ft/s (m/s)	Longitudinal	17.16 (5.23)	18.24 (5.56)	18.47 (5.63)	≤ 40 (12.2)
	Lateral	0.10 (0.03)	0.07 (0.02)	0.69 (0.21)	≤40 (12.2)
ORA g's	Longitudinal	3.08	4.00	3.86	≤ 20.49
	Lateral	1.45	1.95	2.03	≤ 20.49
MAX. ANGULAR DISPL. deg.	Roll	NA	1.82	-3.36	≤75
	Pitch	NA	-0.42	1.25	≤75
	Yaw	NA	46.41	47.66	not required
THIV ft/s (m/s)		NA	18.31 (5.58)	18.5 (5.64)	not required
PHD g's		NA	4.42	4.10	not required
ASI		0.26	0.36	0.33	not required

14.7 Discussion

The analysis of the test results for test no. IRA-1 showed that the net attenuator adequately captured the 5,090-lb (2,309-kg) bogie vehicle and brought it to rest. There were neither detached elements nor fragments from the net which showed potential for undue hazard to other traffic. One of the energy absorber straps fractured at the beginning of the test, resulting in asymmetric loading on the test vehicle. This asymmetric loading caused the vehicle to yaw to the right. The test vehicle did not penetrate or ride over the net attenuator and remained upright during and after the collision.

The occupant risk values for the bogie vehicle were assumed to be equivalent for the 2270P truck. Estimations for the 1100C and 1500A MASH vehicles were calculated using the

Occupant Risk Estimation procedure discussed in Appendix G of MASH [3]. The procedure consisted of integrating the CFC 180-filtered, longitudinal acceleration trace from test no. IRA-1 to obtain the force-deflection characteristics of the net attenuator. The force-deflection data was then applied to the 1100C and 1500A vehicles to obtain the OIV and ORA estimate, as shown in Table 25. Note that the OIV and ORA estimates for both vehicles were below MASH limits, and higher-force energy absorbers could be used without issue for small cars. Further details of these estimations are located in Appendix B.

Table 25. 1100C and 1500A Displacement, OIV, and ORA Estimations, Test No. IRA-1

Vehicle	Mass lb (kg)	Velocity mph (km/h)	OIV Estimation ft/s (m/s)	ORA Estimation g's	Maximum Deflection ft (m)
1100C	2,425 (1,100)	62.14 (100.00)	25.69 (7.83)	7.69	25.9 (7.9)
1500A	3,307 (1,500)	62.14 (100.00)	22.91 (6.98)	5.36	33.1 (10.1)



0.000 sec



0.600 sec



0.240 sec



0.900 sec



0.300 sec



1.200 sec



0.480 sec



1.500 sec

Figure 65. Sequential Photographs, Test No. IRA-1



0.000 sec



0.240 sec



0.480 sec



0.720 sec



0.960 sec



1.200 sec



0.000 sec



0.240 sec



0.480



0.720 sec



0.960 sec



1.200 sec

Figure 66. Additional Sequential Photographs, Test No. IRA-1



0.000 sec



0.120 sec



0.036 sec



0.180 sec



0.046 sec



0.240 sec



0.060 sec



0.360 sec

Figure 67. Additional Sequential Photographs, Test No. IRA-1



0.000 sec



0.252 sec



0.504 sec



0.756 sec



1.008 sec



1.261 sec



0.000 sec



0.126 sec



0.252 sec



0.378 sec



0.504 sec



0.630 sec

Figure 68. Additional Sequential Photographs, Test No. IRA-1



0.000 sec



0.600 sec



0.070 sec



0.900 sec



0.140 sec



1.200 sec



0.300 sec



1.500 sec

Figure 69. Additional Sequential Photographs, Test No. IRA-1



0.020 sec



0.100 sec



0.050 sec



0.120 sec



0.070 sec



0.130 sec



0.080 sec



0.140 sec

Figure 70. Additional Sequential Photographs, Test No. IRA-1

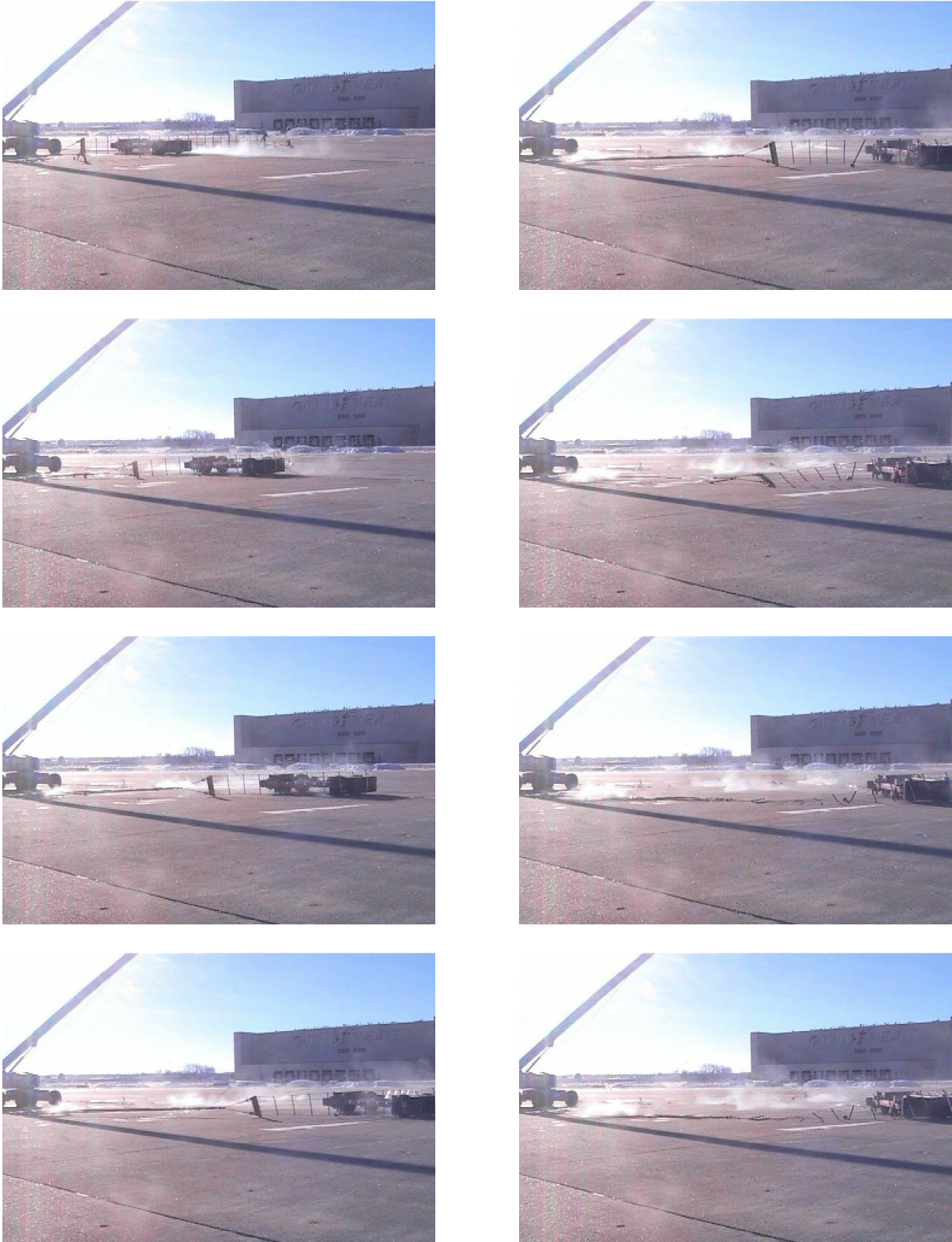


Figure 71. Documentary Photographs, Test No. IRA-1



Figure 72. Documentary Photographs, Test No. IRA-1



Figure 73. Impact Location, Test No. IRA-1



Figure 74. Vehicle Final Position and Trajectory Marks, Test No. IRA-1

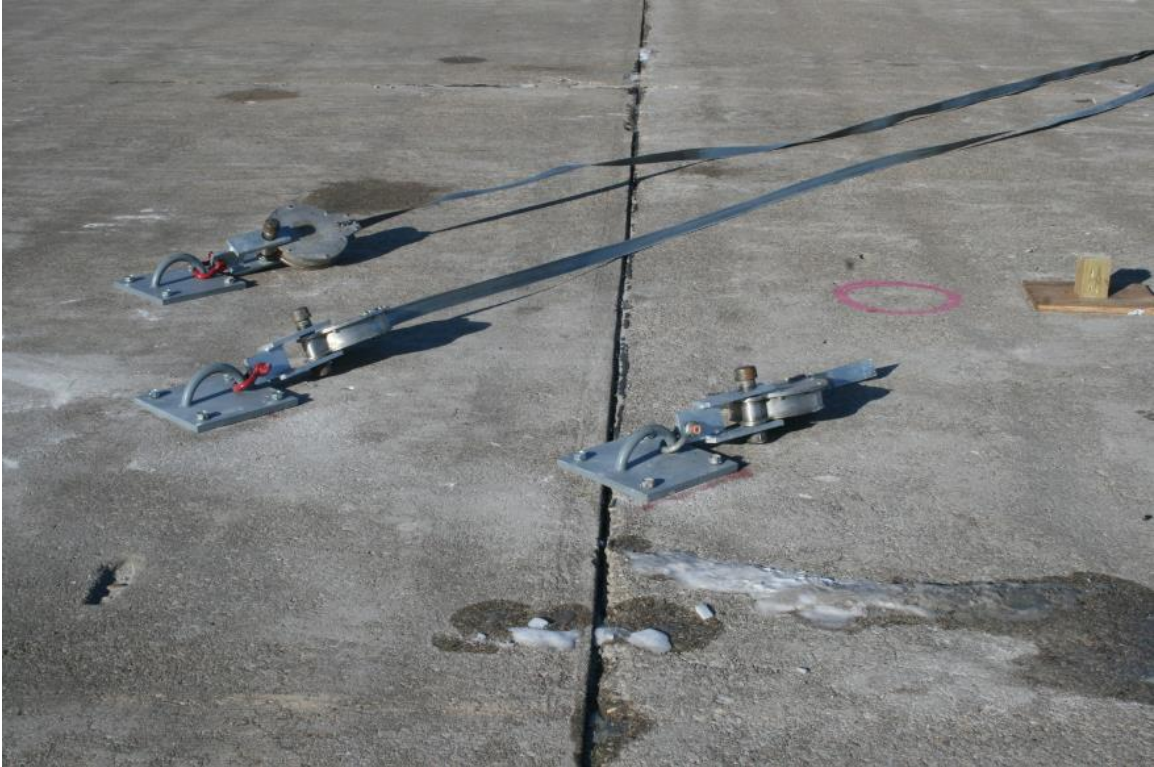


Figure 75. System Damage, Test No. IRA-1



Figure 76. System Damage – Fractured Energy Absorber Tape, Test No. IRA-1

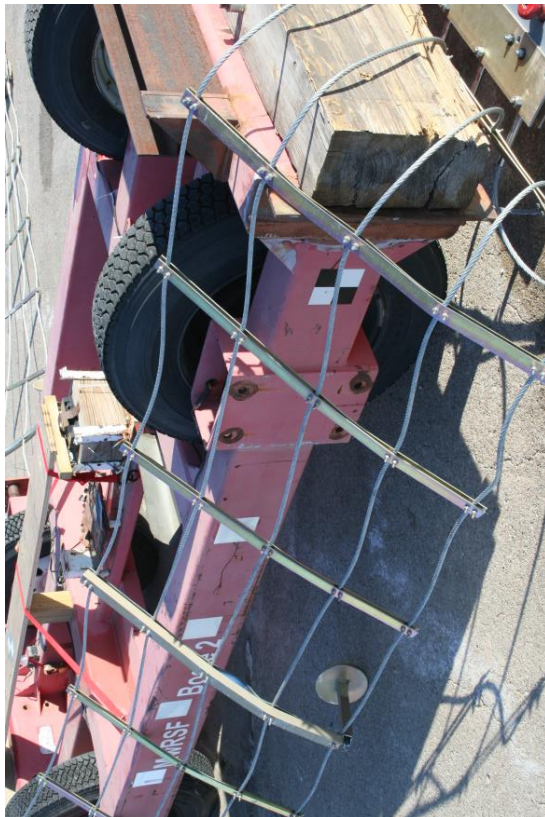


Figure 77. System Damage, Test No. IRA-1

15 NET ATTENUATOR COMPONENT TEST NO. IRA-2

15.1 Test No. IRA-2

The 5,090-lb (2,309-kg) bogie vehicle impacted the net arrestor at a speed of 59.9 mph (96.4 km/h) and an angle of 90 degrees, offset 12 ft (3.7 m) to the right from the center of the net. All components of the net were reused from the previous test, except for the vertical posts that support the net, which were replaced with lightweight steel shelving posts. The energy absorbers from the previous test were also replaced with unused units. Sequential photographs are shown in Figures 78 through 82.

15.2 Weather Conditions

Test no. IRA-2 was conducted on December 13, 2013 at approximately 3:00 p.m. The weather conditions, as per the National Oceanic and Atmospheric Administration (station 14939/LNK), were reported and are shown in Table 26.

Table 26. Weather Conditions, Test No. IRA-2

Temperature	28° F
Humidity	78%
Wind Speed	10 mph
Wind Direction	40° from True North
Sky Conditions	Clear
Visibility	6 Statute Miles
Pavement Surface	Dry
Previous 3-Day Precipitation	0 in.
Previous 7-Day Precipitation	0 in.

15.3 Test Description

Initial vehicle impact was to occur in the 12-ft (3.7-m) offset to the right from the center of the net, as shown in Figure 83. Although the actual point of impact could not be determined from examining the post-test damage of the system, analysis of the crash test videos showed that

the bogie did appear to impact the intended location. The vehicle had a maximum dynamic deflection of 41.0 ft (12.5 m) downstream from the point of impact and a lateral movement of 0.43 ft (0.13 m). The maximum dynamic deflection was determined using accelerometer traces to calculate the planar trajectory. The deflection could not be verified with overhead video analysis, because of skewed cameras. The innermost energy absorber on the left side of the system failed 150 ms after impact occurred. Near the end of the test, the vehicle yawed to the right. The vehicle trajectory and final position are shown in Figure 84.

15.4 System Damage

Damage to the net attenuator was minimal, as shown in Figures 85 through 87. The innermost energy absorber on the left side of the system failed 150 ms after impact occurred. The failure was likely caused by excessive whipping that occurred with both inside energy absorbers of the system. As shown in Figures 80 and 82, the 1-in. (25-mm) shackle that connected the energy absorbers to the assembly initially moved upstream and towards the center of the net. This motion caused the innermost energy absorbers to compress and rotate away from impact. As the innermost energy absorber on the left side was pulled tight, the steel tape ruptured at the connection between the tape and the turnbuckles, as shown in Figure 86. Although both the inside energy absorbers on both sides of the net exhibited the same motion, only the left absorber had a failure. One factor that could have influenced this failure was the direction the tape was wrapped around the bracket. One of the $7/16$ -in. (11-mm) bolts that attached the ends of the net to the energy absorbers fractured in shear. The amount of tape pulled from each energy absorber is shown in Table 27.

Table 27. Energy-Absorber Tape Pullout, Test No. IRA-2

Side	Location	Pullout Distance	
		ft	m
Right	Outside	25.52	7.78
	Middle	28.58	8.71
	Inside	29.63	9.03
Left	Outside	23.50	7.16
	Middle	25.06	7.64
	Inside	0.50	0.15

The net assembly deformed around the bogie vehicle. The light-weight steel posts that supported the net had fractured at the bottom mounting bolt hole used to attach the bottom cable, approximately 8 in. (203 mm) above the ground, as shown in Figures 85 through 87. The solid aluminum center post was also bent at the same location. The steel post on the right side of the system fractured at the center cable location where it was folded over the top of the bogie head. The end plates, cables, and vertical cable spreaders had minimal damage and were able to be reused.

15.5 Vehicle Damage

The damage to the vehicle was minimal, as shown in Figure 87. The damage to the vehicle was isolated to the top and bottom of the bogie impact head, where denting and scraping were observed.

15.6 Occupant Risk

The calculated occupant impact velocities (OIVs) and maximum 0.010-sec occupant ridedown accelerations (ORAs) in both the longitudinal and lateral directions are shown in Table 28. Note that the OIVs and ORAs were within the suggested limits provided in MASH, although the velocity was slightly less than a MASH TL-3 test, and the mass of the bogie vehicle was slightly higher than the MASH 2270P vehicle. The calculated THIV, PHD, and ASI values are

also shown in Table 28. The recorded data from the accelerometers and the rate transducers are shown graphically in Appendix C.

Table 28. Summary of OIV, ORA, THIV, PHD, and ASI Values, Test No. IRA-2

Evaluation Criteria		Transducer			MASH Limits
		EDR-3	DTS	SLICE	
OIV ft/s (m/s)	Longitudinal	17.76 (5.41)	17.98 (5.48)	18.49 (5.63)	≤ 40 (12.2)
	Lateral	0.89 (0.27)	1.64 (0.50)	0.48 (0.15)	≤40 (12.2)
ORA g's	Longitudinal	3.53	3.79	3.99	≤ 20.49
	Lateral	1.59	2.12	1.81	≤ 20.49
MAX. ANGULAR DISPL. deg.	Roll	NA	2.81	-6.42	≤75
	Pitch	NA	-1.203	2.34	≤75
	Yaw	NA	59.66	61.12	not required
THIV ft/s (m/s)		NA	18.11 (5.52)	18.53 (5.65)	not required
PHD g's		NA	3.99	4.14	not required
ASI		0.33	0.37	0.37	not required

15.7 Discussion

The analysis of the test results for test no. IRA-2 showed that the net attenuator adequately captured the 5,090-lb (2,309-kg) bogie vehicle and brought it to rest. There were neither detached elements nor fragments from the net which showed potential for undue hazard to other traffic. One of the energy absorber straps fractured at the beginning of the test, resulting in asymmetric loading on the test vehicle. This asymmetric loading caused the vehicle to yaw to

the right. The test vehicle did not penetrate or ride over the net attenuator and remained upright during and after the collision.

The occupant risk values for the bogie vehicle were assumed to be equivalent for the 2270P truck. Estimations for the 1100C and 1500A MASH vehicles were calculated using the Occupant Risk Estimation procedure discussed in Appendix G of MASH [3]. The procedure consisted of integrating the CFC 180-filtered, longitudinal acceleration trace to obtain the force-deflection characteristics of the net attenuator. The force-deflection data was then applied to the 1100C and 1500A vehicles to obtain the OIV and ORA estimates, as shown in Table 29. Note that the OIV and ORA estimates for both vehicles were below MASH limits, and higher-force energy absorbers could be used without issue for small cars. Further details of these estimations are located in Appendix C.

Table 29. 1100C and 1500A Displacement, OIV, and ORA Estimations, Test No. IRA-2

Vehicle	Mass lb (kg)	Velocity mph (km/h)	OIV Estimation ft/s (m/s)	ORA Estimation g's	Maximum Deflection ft (m)
1100C	2,425 (1,100)	62.14 (100.00)	26.75 (8.15)	8.33	23.1 (7.0)
1500A	3,307 (1,500)	62.14 (100.00)	23.18 (7.06)	5.78	30.4 (9.2)



0.000 sec



0.1050 sec



0.350 sec



1.400 sec



0.700 sec



1.750 sec

Figure 78. Sequential Photographs, Test No. IRA-2



0.000 sec



0.350 sec



0.700 sec



0.1050 sec



0.1400 sec



1.750 sec



0.000 sec



0.100 sec



0.200



0.300 sec



0.400 sec

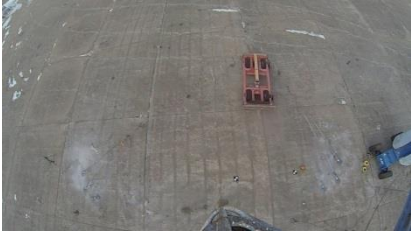


0.500 sec

Figure 79. Additional Sequential Photographs, Test No. IRA-2



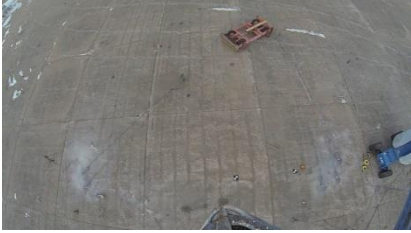
0.000 sec



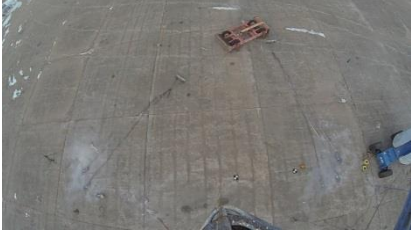
0.378 sec



0.756 sec



1.134 sec



1.513 sec



1.891 sec



0.000 sec



0.067 sec



0.134 sec



0.202 sec



0.269 sec



0.336 sec

Figure 80. Additional Sequential Photographs, Test No. IRA-2



0.000 sec



0.252 sec



0.504 sec



0.756 sec



1.008 sec



1.261 sec



0.000 sec



0.101 sec



0.202 sec



0.303 sec



0.403 sec



0.504 sec

Figure 81. Additional Sequential Photographs, Test No. IRA-2



0.025 sec



0.126 sec



0.050 sec



0.143 sec



0.084 sec



0.151 sec



0.118 sec



0.160 sec

Figure 82. Additional Sequential Photographs, Test No. IRA-2



Figure 83. Impact Location, Test No. IRA-2



Figure 84. Vehicle Final Position and Trajectory Marks, Test No. IRA-2



Figure 85. System Damage, Test No. IRA-2



Figure 86. System Damage – Fractured Energy Absorber Tape, Test No. IRA-2



Figure 87. System and Vehicle Damage, Test No. IRA-2

16 DESIGN DETAILS - TEST NOS. IRA-3 AND IRA-4

The net attenuation system for test nos. IRA-3 and IRA-4 consisted of the same modified Dragnet Vehicle Arresting Barrier with a different energy absorber orientation. During test nos. IRA-1 and IRA-2, the inside energy absorbers were compressed immediately after impact, as shown in Figure 82. As the bogie traveled farther into the system, the energy absorbers became taut and began to feed the steel tape. This behavior resulted in a whipping action that caused the inside energy absorbers on the left side of the system to rupture after impact.

The anchorage system was modified to help reduce the likelihood that inner energy absorbers would compress when the bogie impacted the net. As shown in Figures 88 through 106, the angle between the energy absorbers was reduced from 45 degrees to 22.5 degrees. With this change, the inside and middle energy absorbers were moved more in-line with the net and farther from the center. Photographs of the test installation are shown in Figures 107 through 110.

Most of the components from previous tests were reused for test nos. IRA-3 and IRA-4. Unused energy absorbers were used for each test. The hollow aluminum posts that supported the net were repaired with light-weight steel shelving to splice between the fractured halves of the posts. In test no. IRA-2, one of the $\frac{7}{16}$ -in. (11-mm) bolts that attached the ends of the net to the energy absorbers fractured. For test nos. IRA-3 and IRA-4 the $\frac{7}{16}$ in. (11-mm) fasteners were increased to $\frac{1}{2}$ -in. (13-mm) diameter. Material specifications, mill certifications, and certificates of conformity for the system materials are shown in Appendix A.

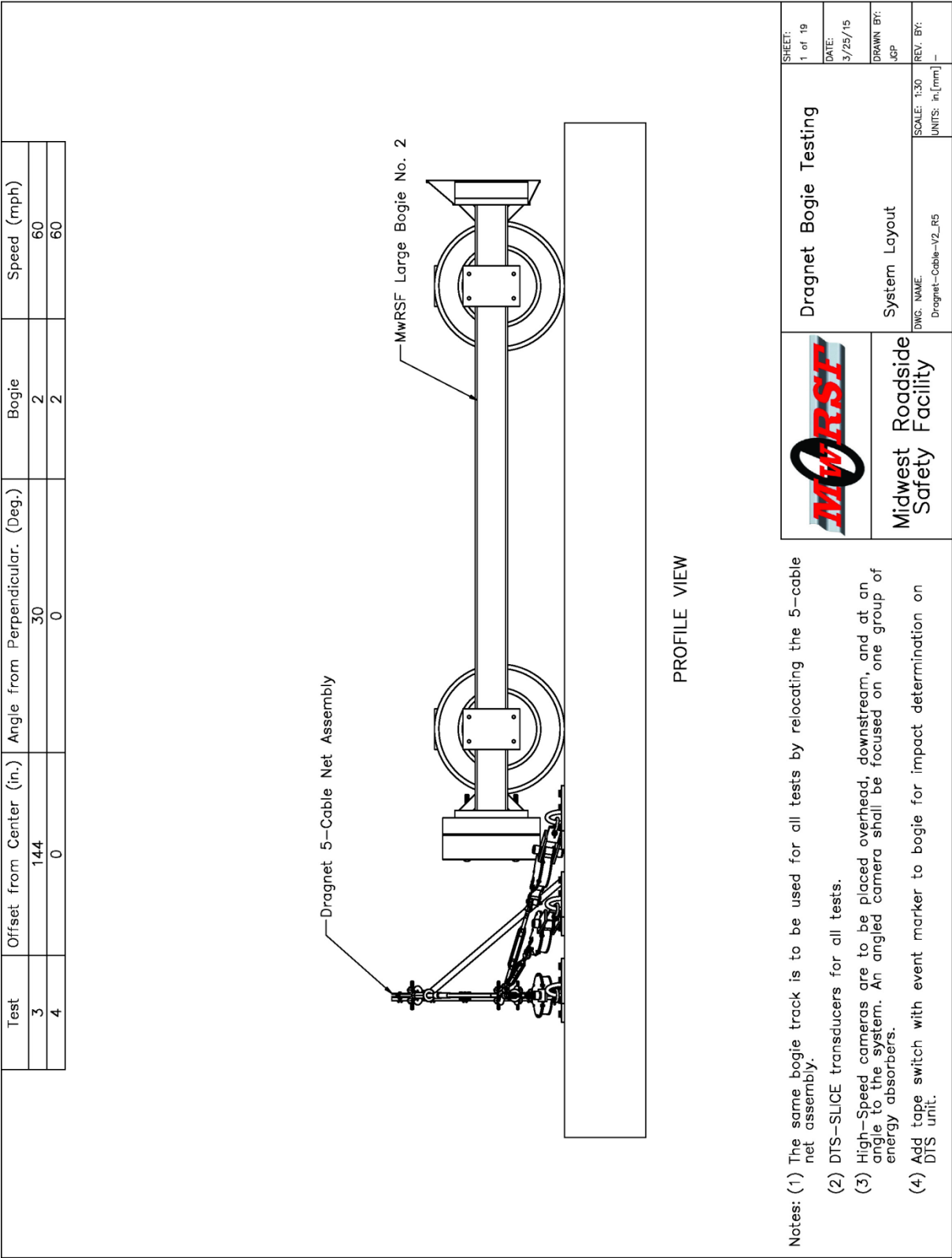
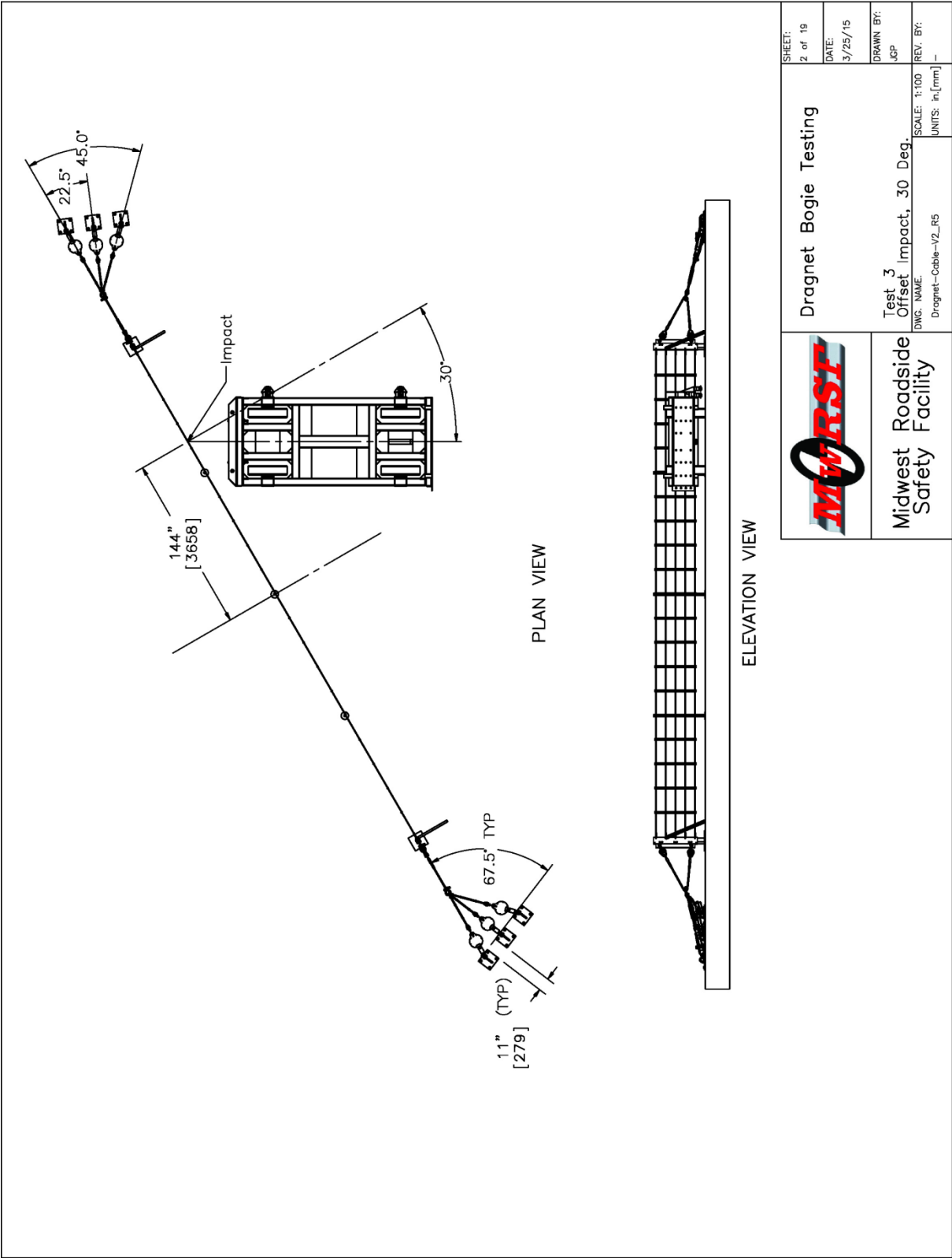


Figure 88. Bogie Test Installation, Test Nos. IRA-3 and IRA-4




	Dragnet Bogie Testing	SHEET: 2 of 19
	Test 3 Offset Impact, 30 Deg. DWG. NAME: Dragnet-Cable-V2_RS SCALE: 1:100 UNITS: in, [mm]	DATE: 3/25/15
Midwest Roadside Safety Facility	DRAWN BY: JCP	REV. BY:

Figure 89. Offset Impact, 30 Deg. From Perpendicular, Test No. IRA-3

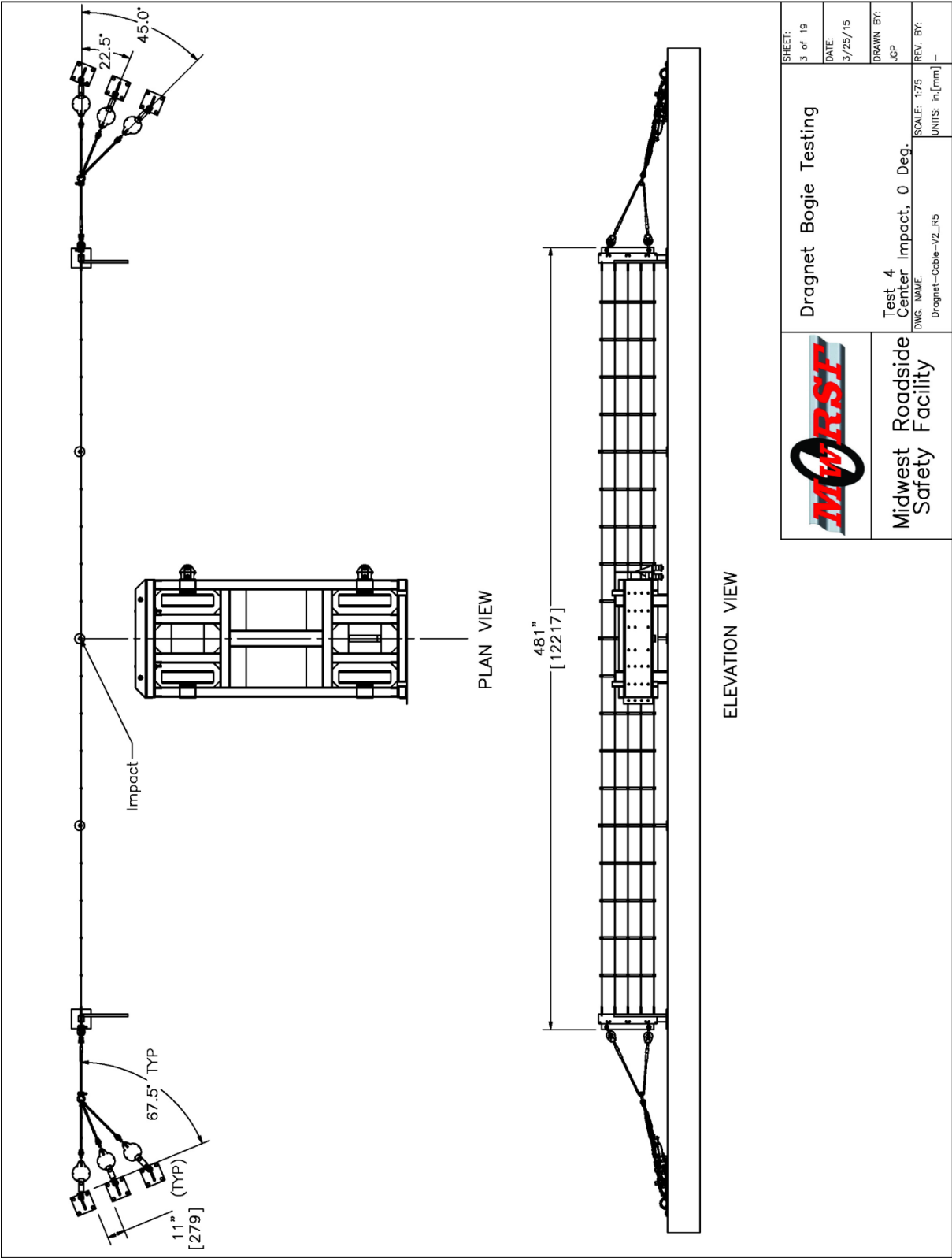


Figure 90. Center Impact, 0 Deg. From Perpendicular, Test No. IRA-4

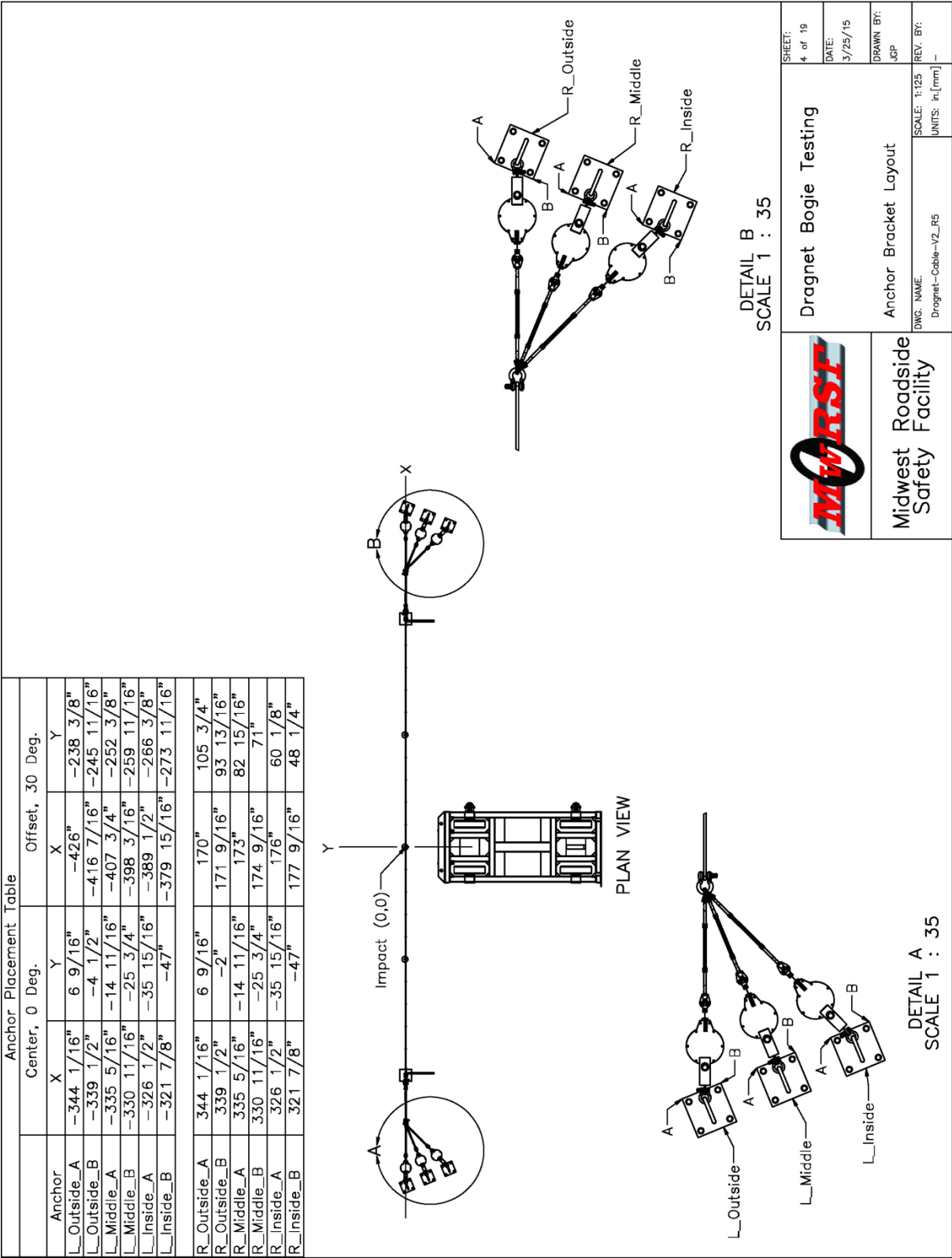
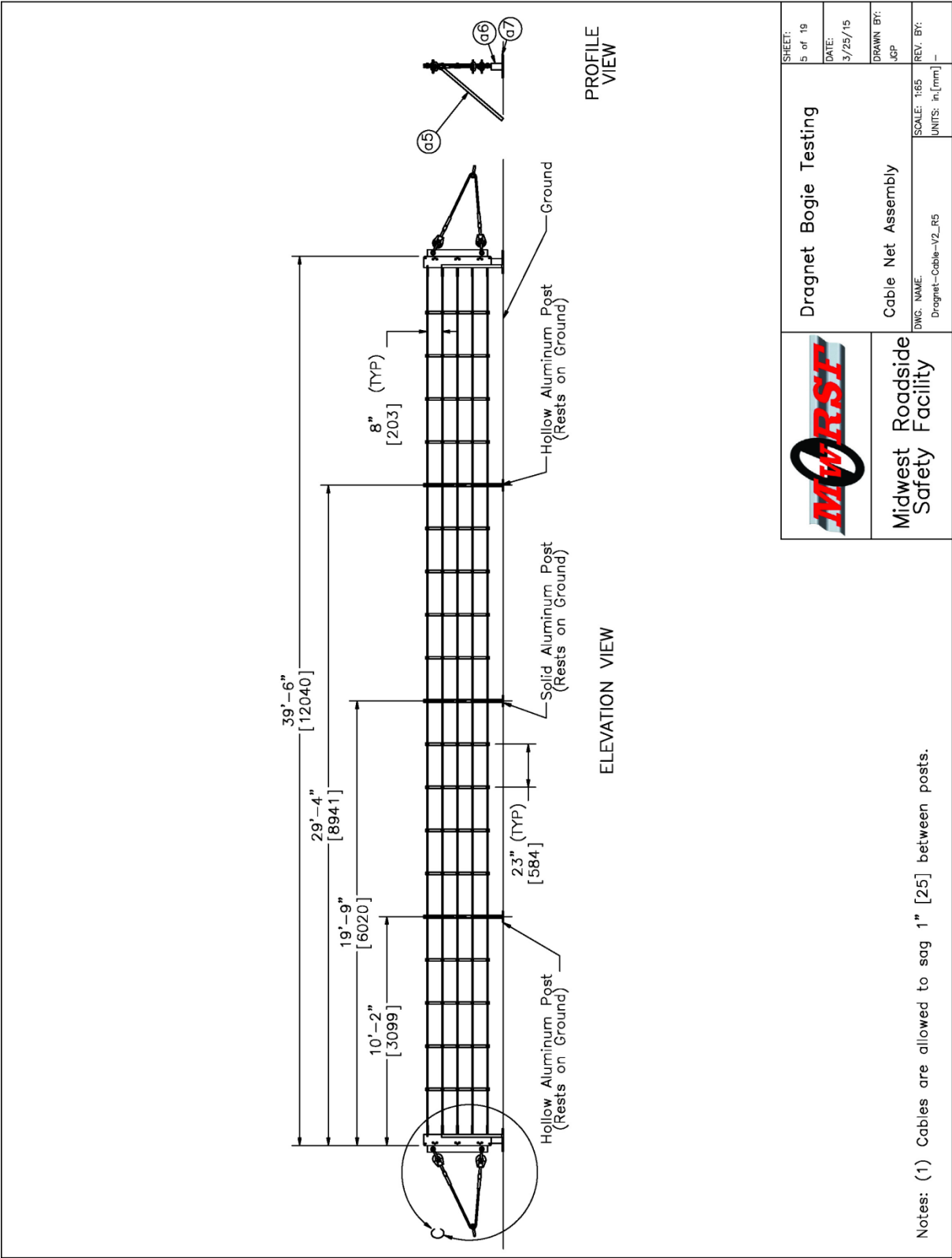



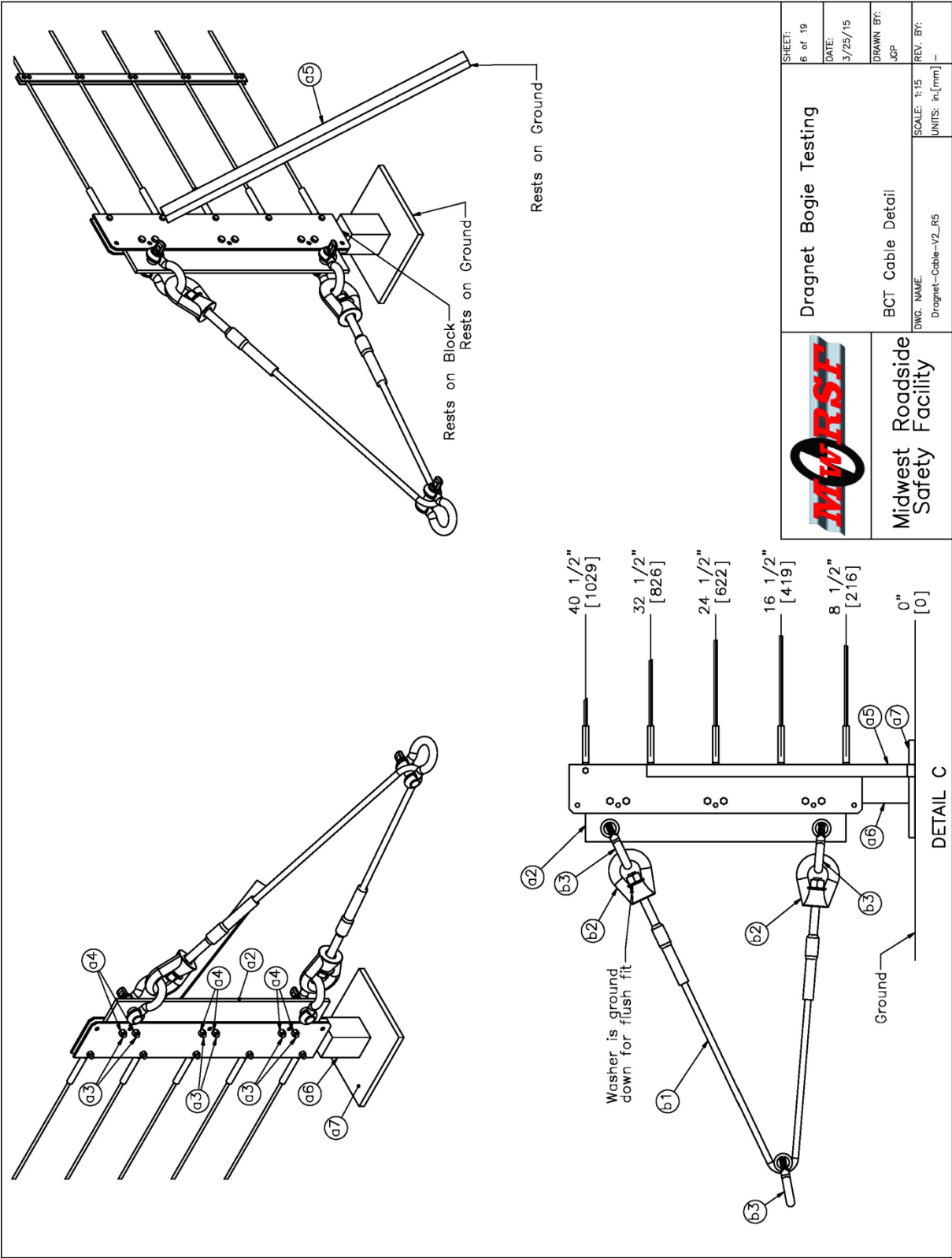
Figure 91. Anchor Bracket Layout, Test Nos. IRA-3 and IRA-4



	Dragnet Bogie Testing		SHEET: 5 of 19
	Cable Net Assembly		DATE: 3/25/15
DWG. NAME: Dragnet-Cable-V2_IR5		SCALE: 1:65 UNITS: in, [mm]	DRAWN BY: JCP
			REV. BY:

Notes: (1) Cables are allowed to sag 1" [25] between posts.

Figure 92. Cable Net Assembly, Test Nos. IRA-3 and IRA-4




 Midwest Roadside Safety Facility	Dragnet Bogie Testing	SHEET: 6 of 19
	BCT Cable Detail	DATE: 3/25/15
DWG. NAME: Dragnet-Cable-V2_RS	SCALE: 1:15 UNITS: in, [mm]	DRAWN BY: JCP
		REV. BY: —

Figure 93. BCT Cable Detail, Test Nos. IRA-3 and IRA-4

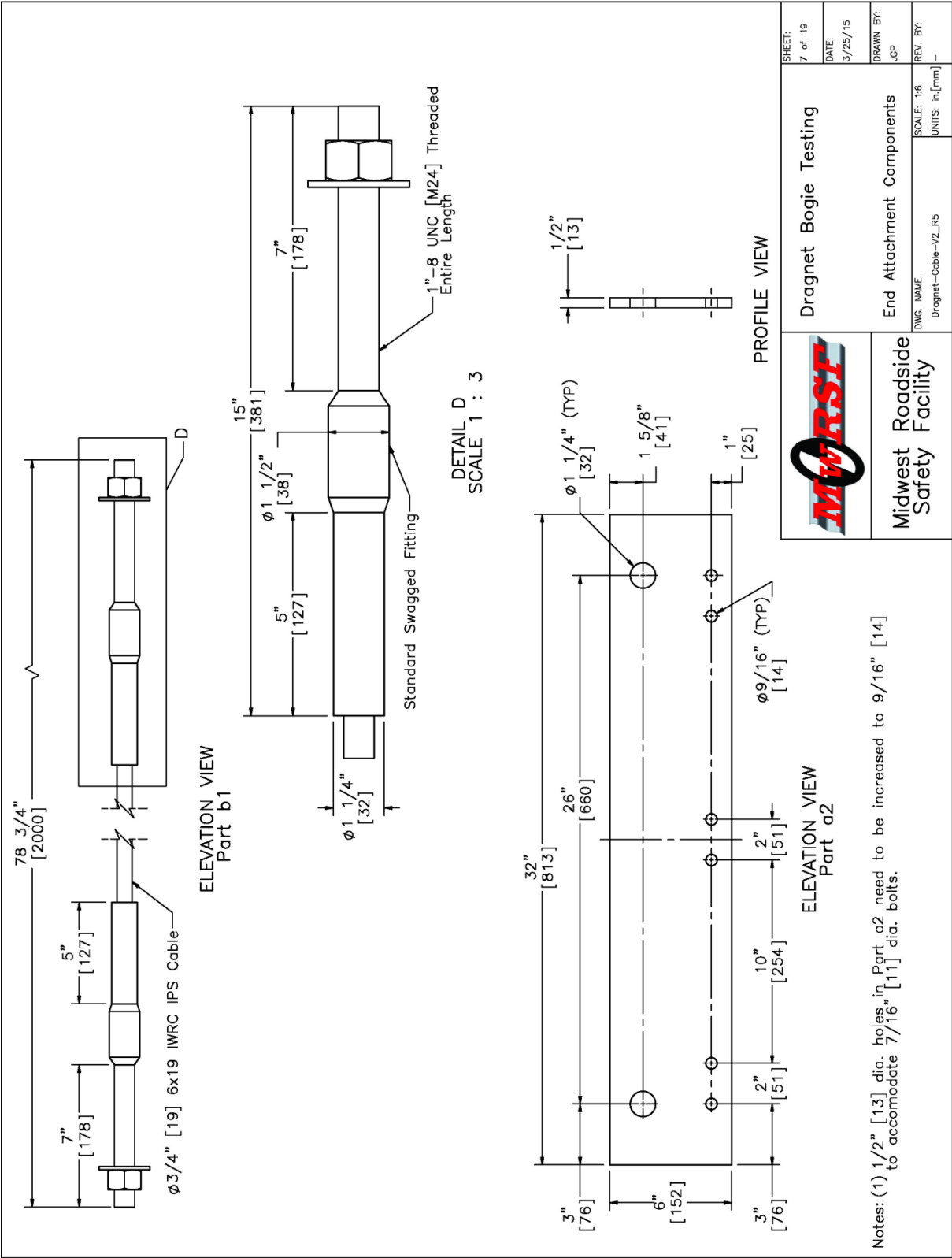


Figure 94. End Attachment Components, Test Nos. IRA-3 and IRA-4

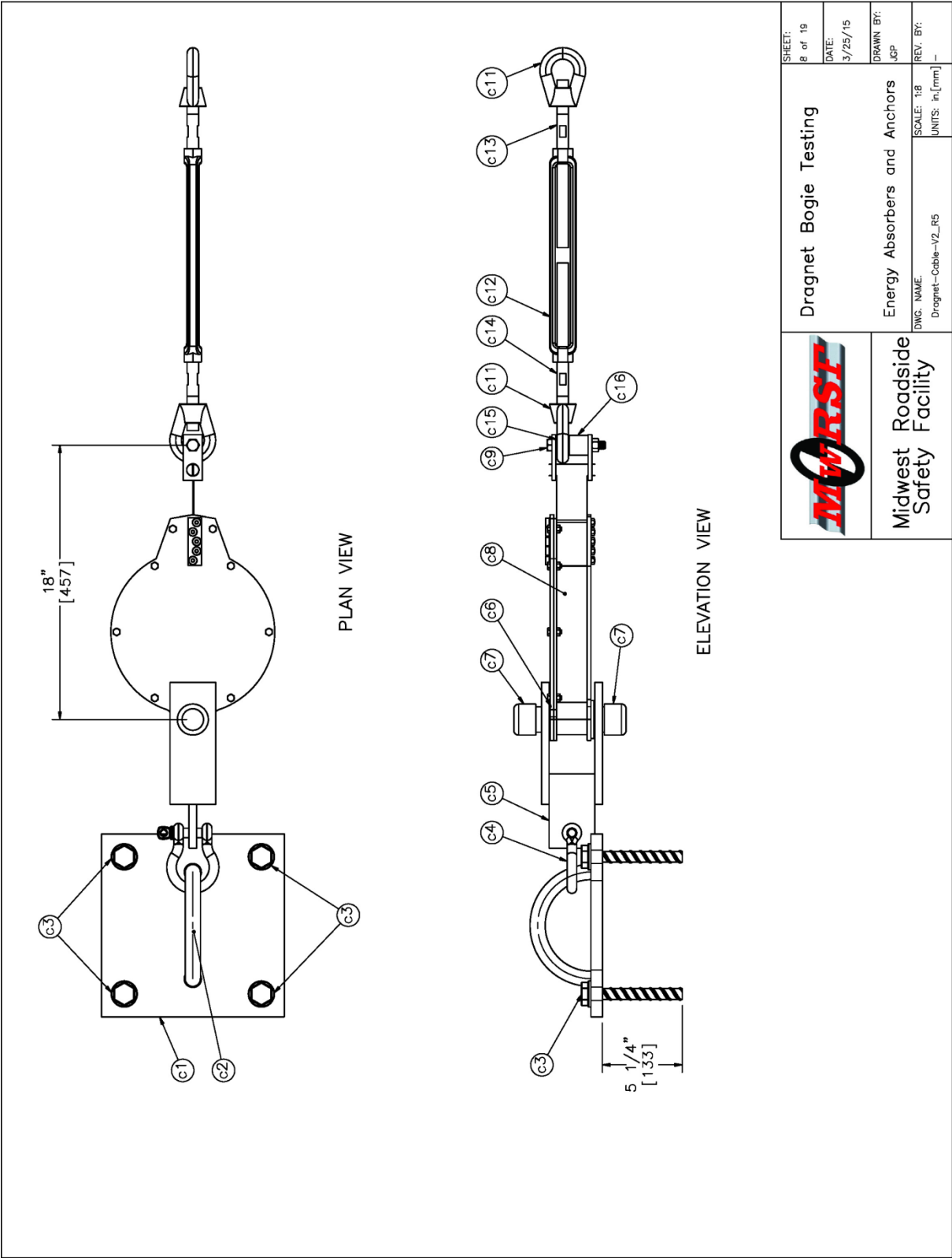
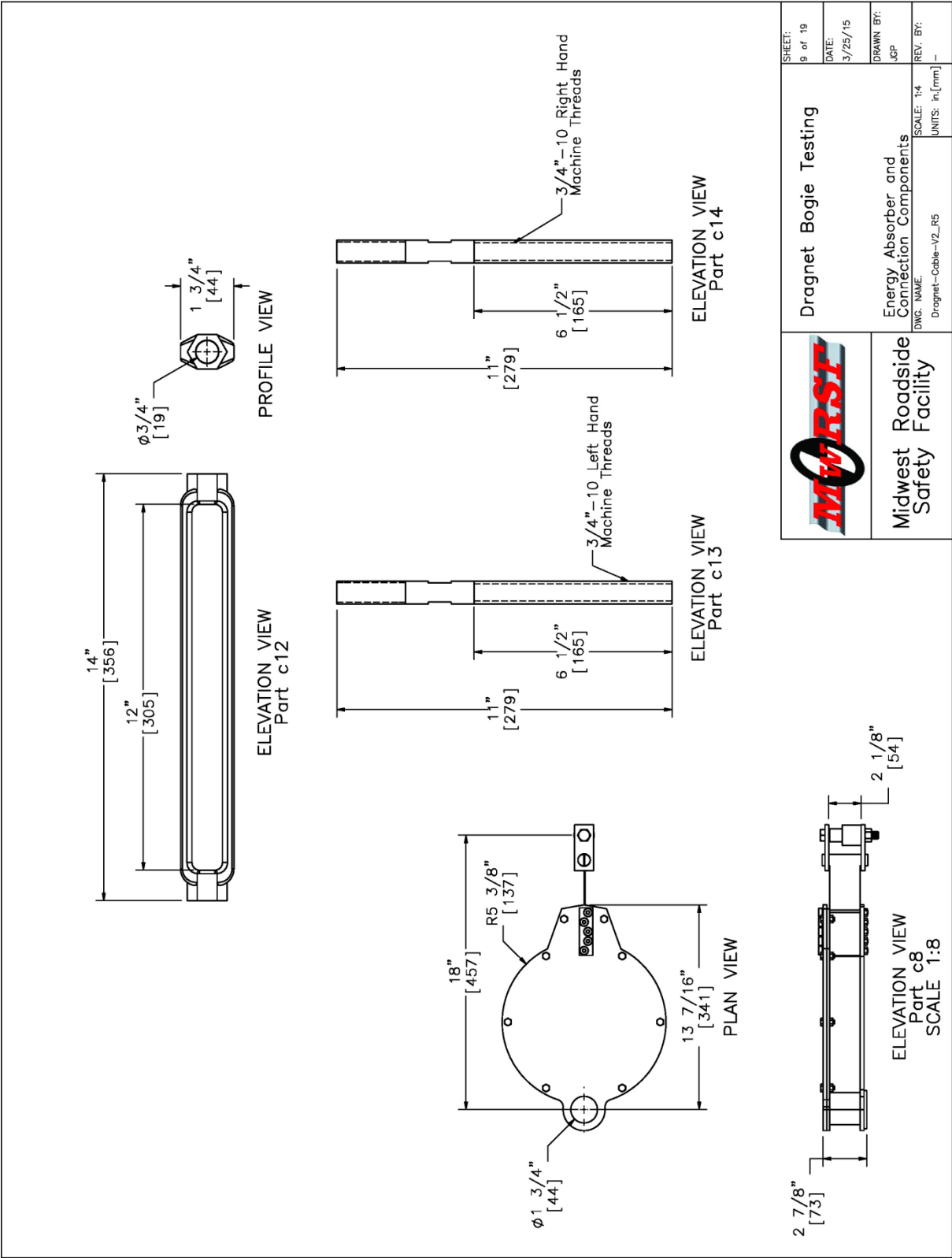
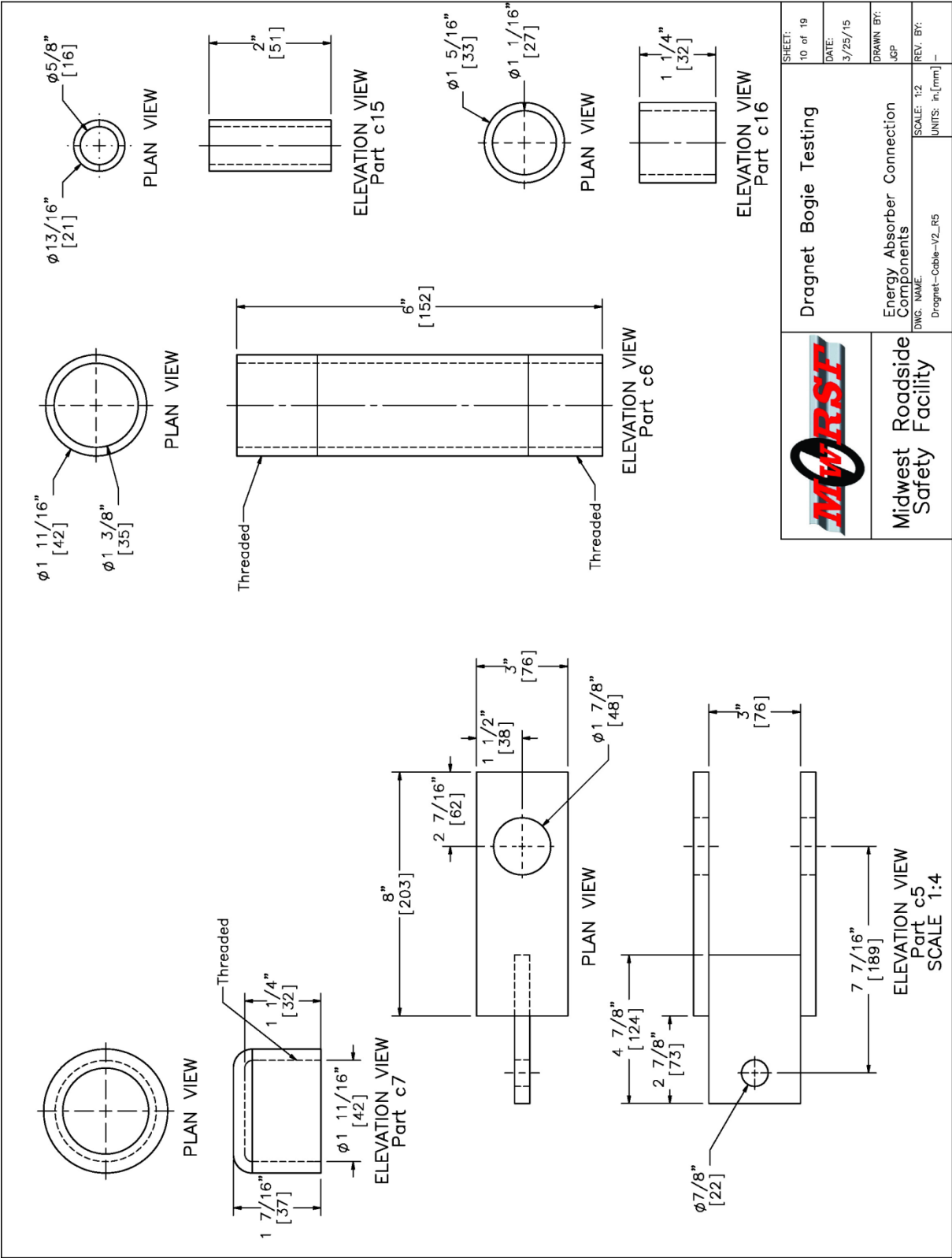


Figure 95. Energy Absorbers and Anchors, Test Nos. IRA-3 and IRA-4



	Dragnet Bogie Testing	SHEET: 9 of 19 DATE: 3/25/15 DRAWN BY: JCP REV. BY:
	Energy Absorber and Connection Components DWG. NAME: Dragnet-Cable-V2_R5 SCALE: 1:4 UNITS: in, [mm]	MIDWEST SAFETY FACILITY

Figure 96. Energy Absorber and Connection Components, Test Nos. IRA-3 and IRA-4




 Midwest Roadside Safety Facility	Dragnet Bogie Testing	SHEET: 10 of 19 DATE: 3/25/15 DRAWN BY: JGP REV. BY: — SCALE: 1:2 UNITS: in, [mm]
	Energy Absorber Connection Components DWG. NAME: Dragnet-Cable-V2_R5	

Figure 97. Energy Absorber Connection Components, Test Nos. IRA-3 and IRA-4

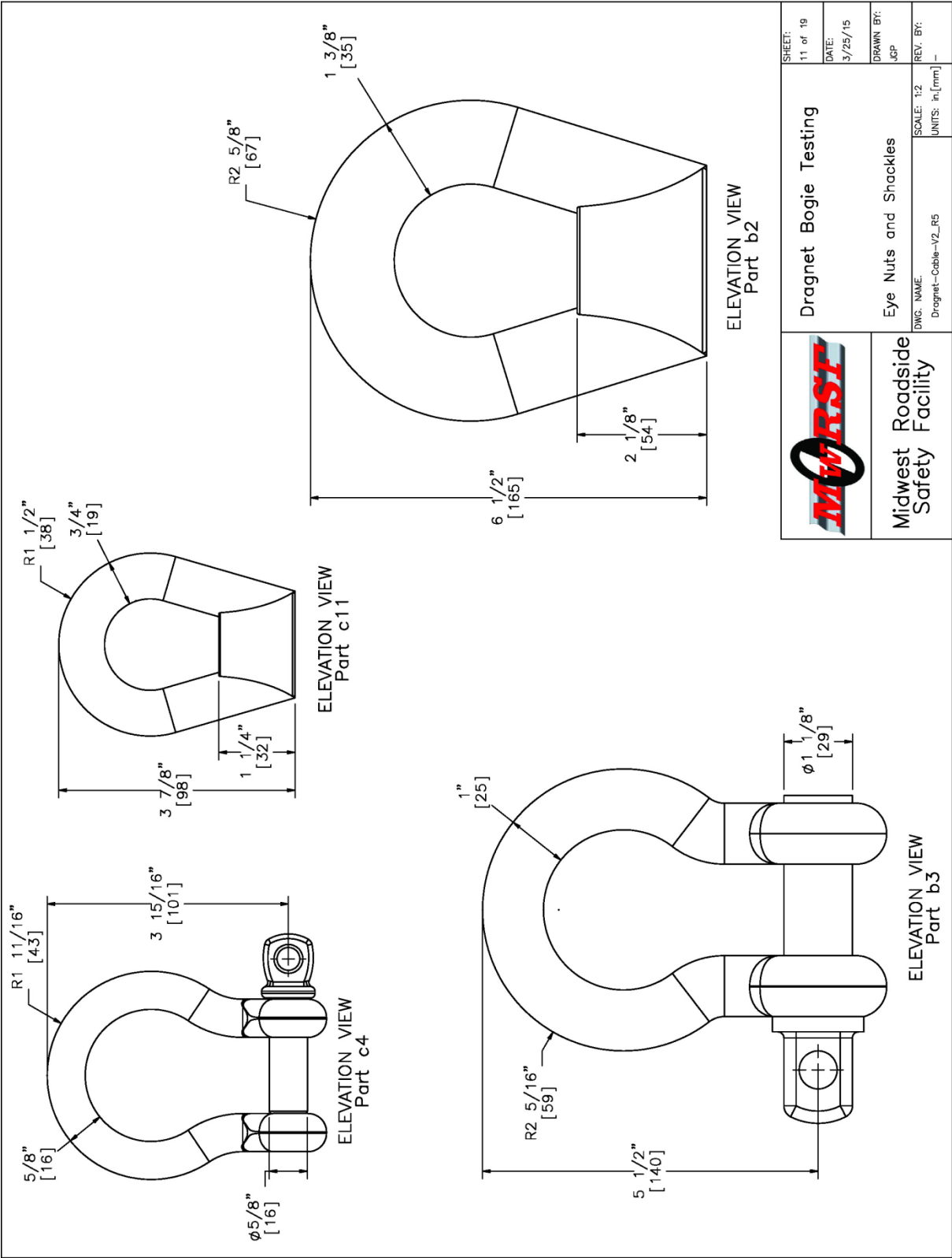
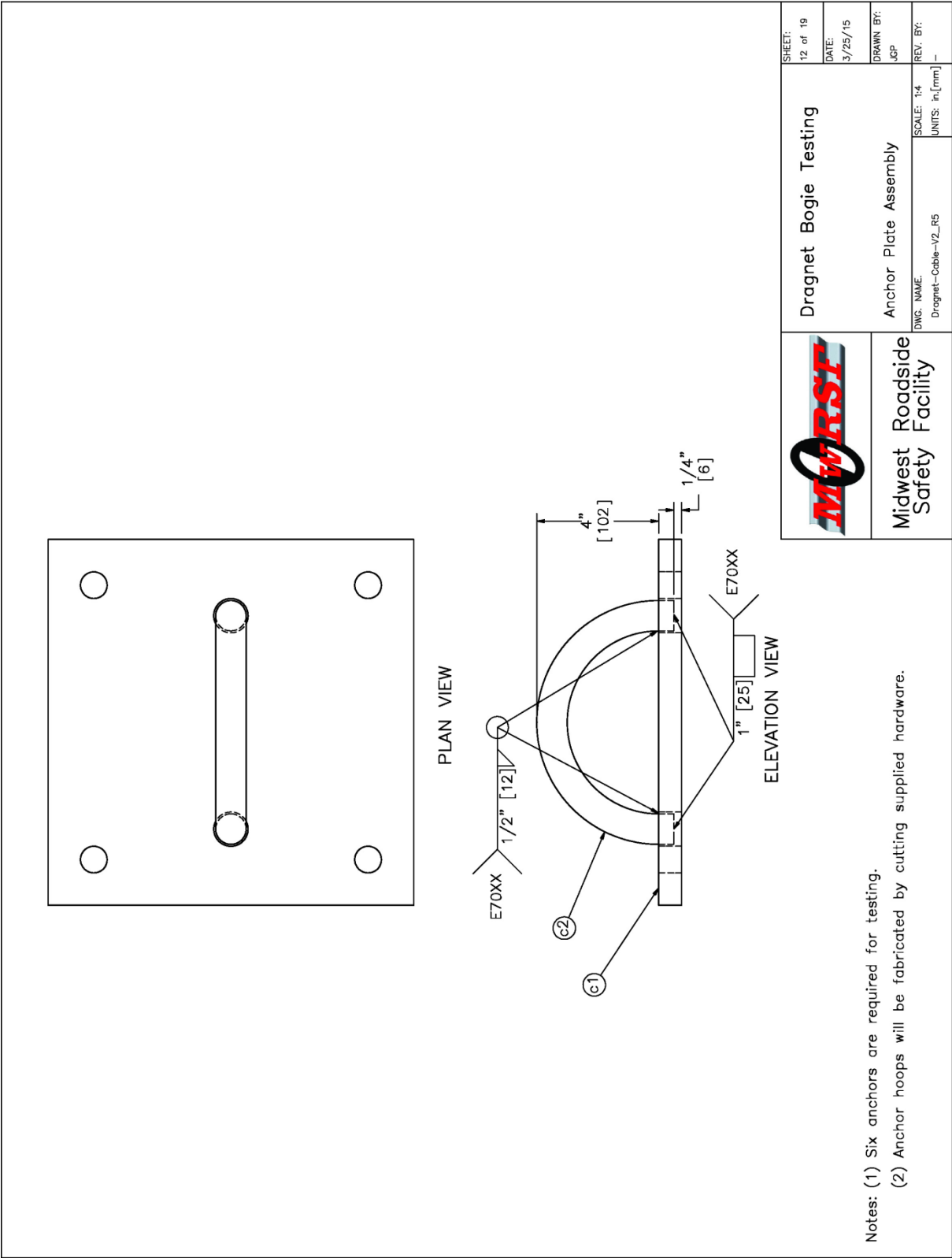
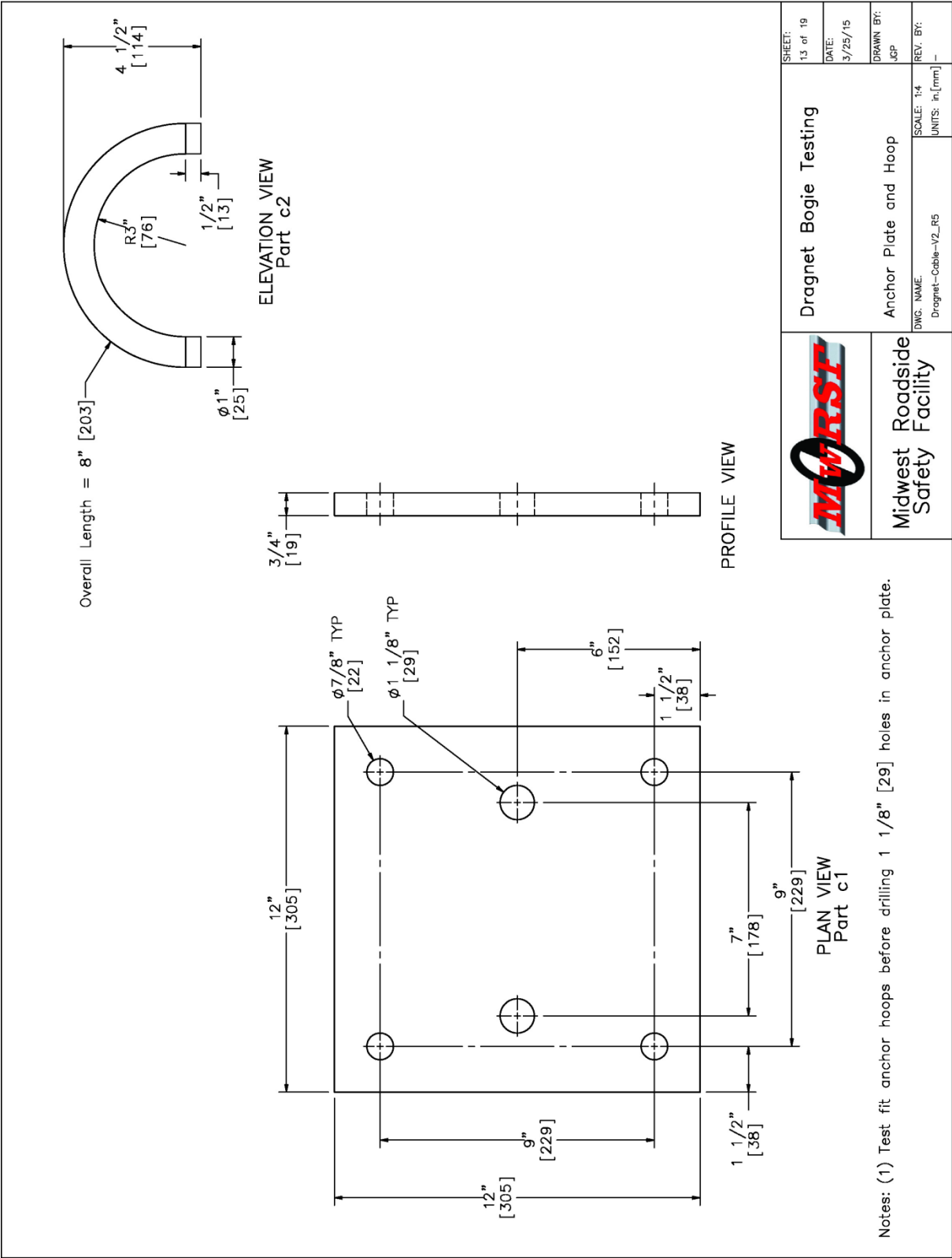


Figure 98. Eye Nuts and Shackles, Test Nos. IRA-3 and IRA-4



Notes: (1) Six anchors are required for testing.
 (2) Anchor hoops will be fabricated by cutting supplied hardware.

Figure 99. Anchor Plate Assembly, Test Nos. IRA-3 and IRA-4




	Dragnet Bogie Testing	SHEET: 13 of 19 DATE: 3/25/15 DRAWN BY: JCP REV. BY:
	Anchor Plate and Hoop	SCALE: 1:4 UNITS: in, [mm]
DWG. NAME: Dragnet-Cable-V2_IRS		REV. BY:

Figure 100. Anchor Plate and Hoop, Test Nos. IRA-3 and IRA-4

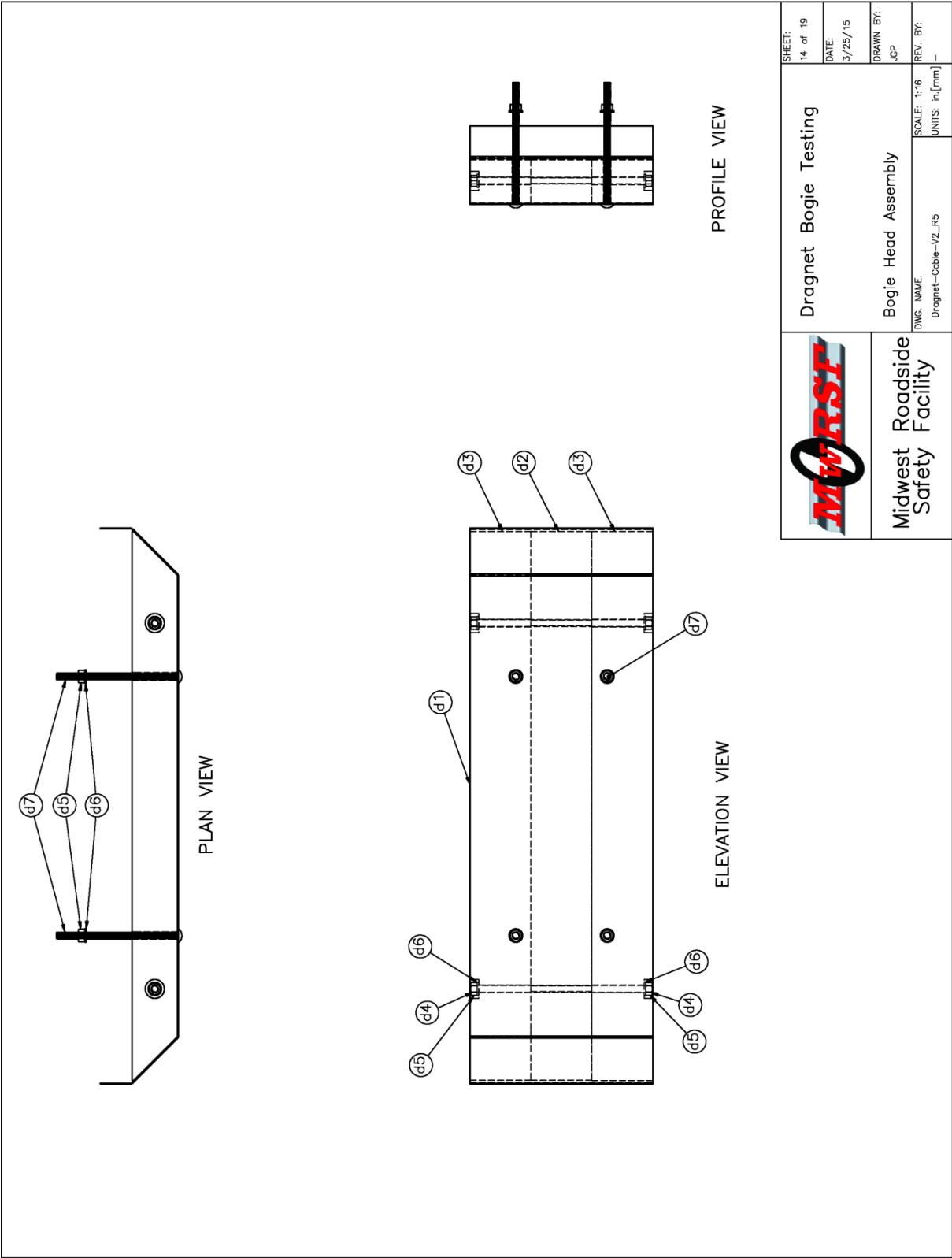


Figure 101. Bogie Head Assembly, Test Nos. IRA-3 and IRA-4

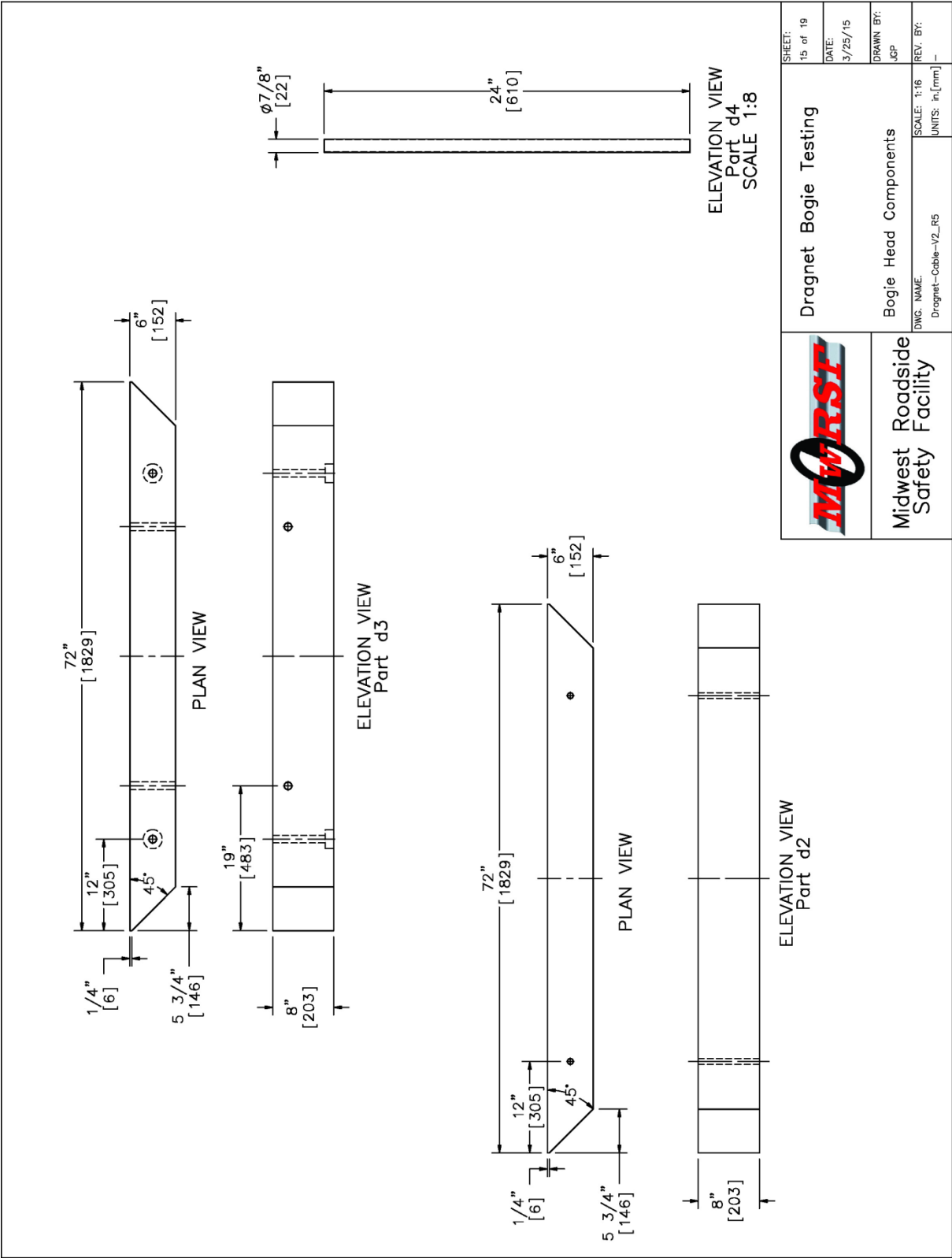


Figure 102. Bogie Head Components, Test Nos. IRA-3 and IRA-4

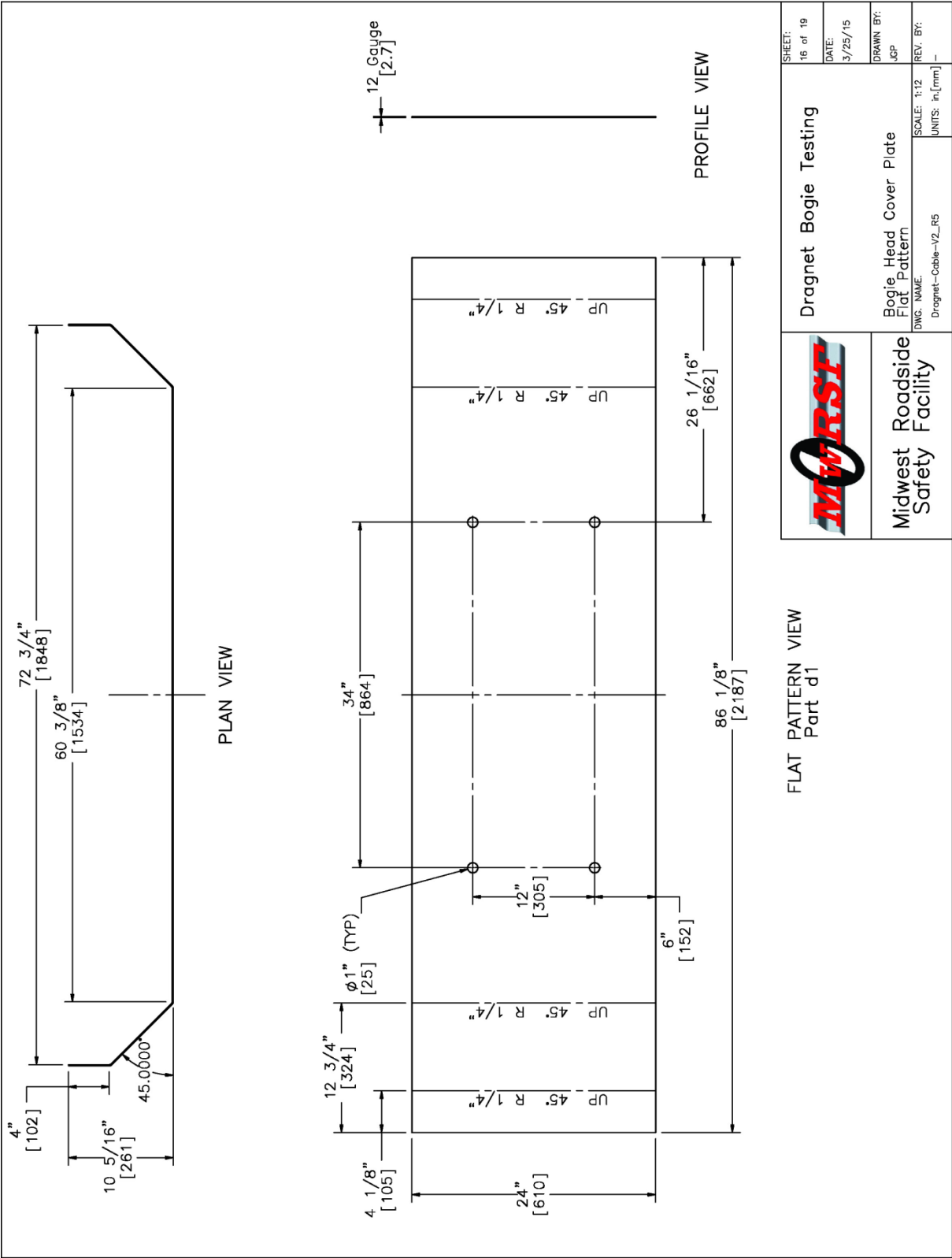


Figure I03. Bogie Head Cover Plate, Flat Pattern, Test Nos. IRA-3 and IRA-4

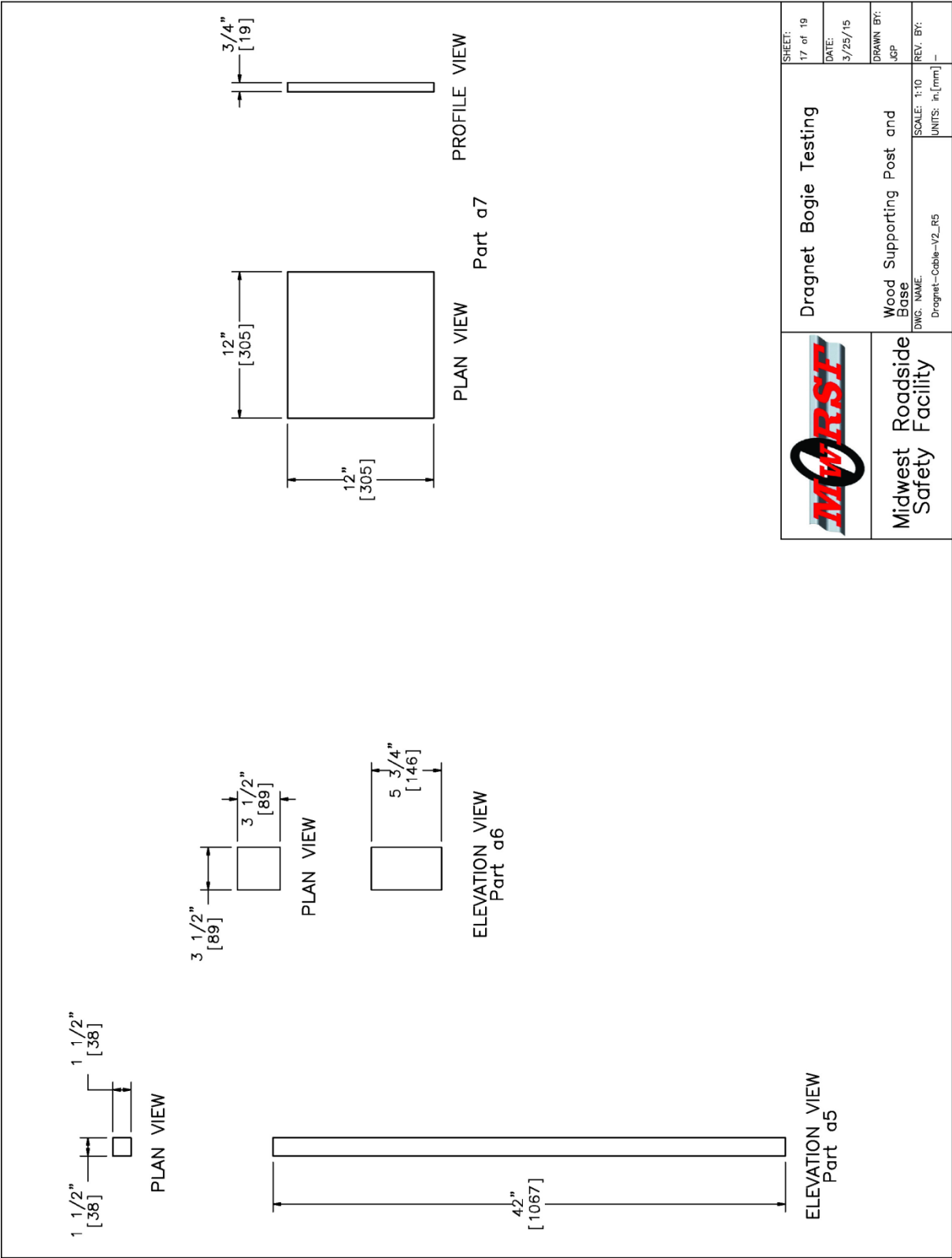


Figure I04. Wood Supporting Post and Base, Test Nos. IRA-3 and IRA-4

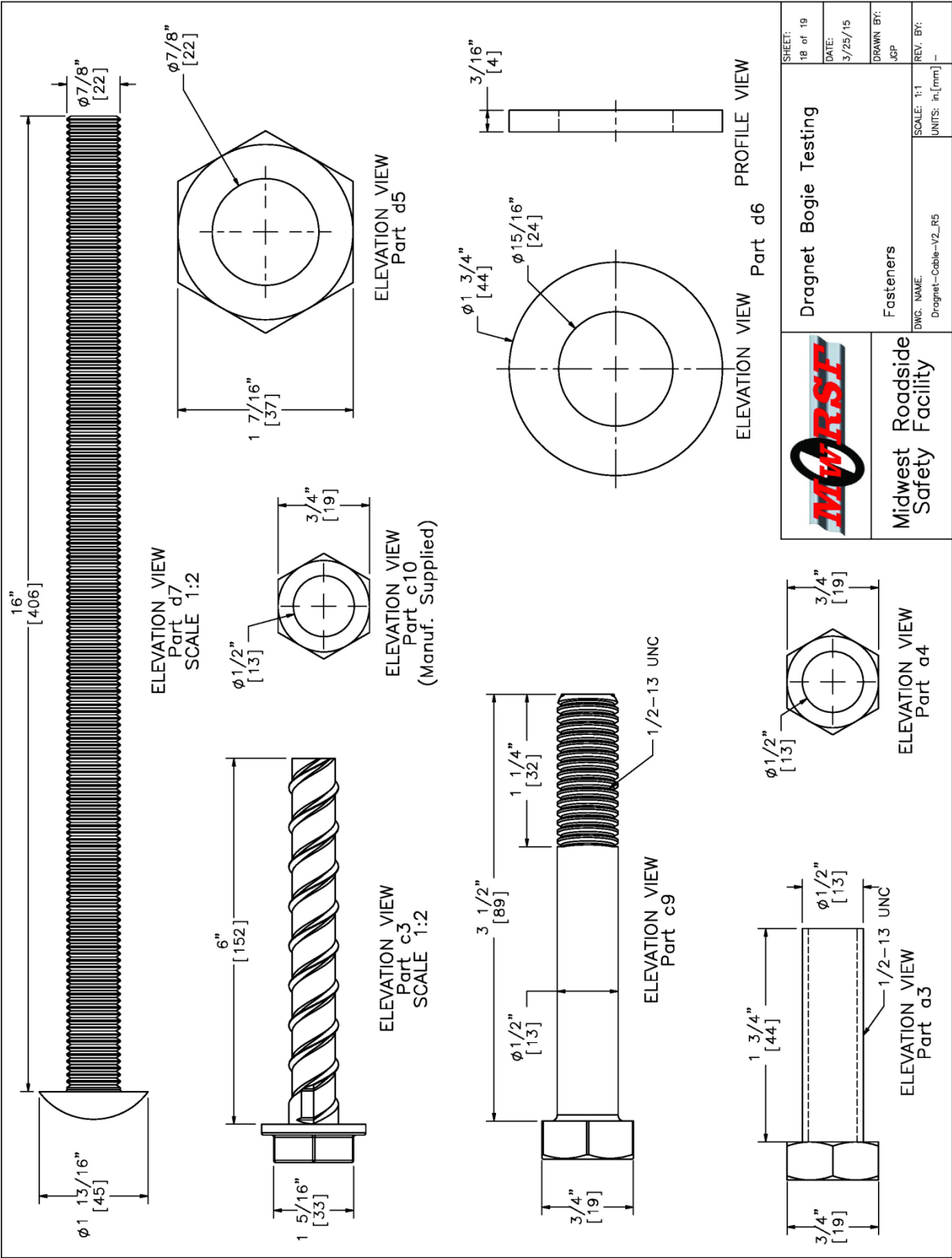


Figure I05. Fasteners, Test Nos. IRA-3 and IRA-4

Item No.	Qty.	Description	Material Specification	Comment
a1	1	Dragnet 5-Cable Net Assembly	Donated, No Material Certifications	-
a2	1/2"x6"x32"	[13x152x813] Attachment Plate	ASTM A36	-
a3	1/2" [13]	Dia. UNC, 1 3/4" [44] Long Hex Bolt	SAE J429 Gr. 5	-
a4	1/2" [13]	Dia. UNC Heavy Hex Nut	ASTM A563 DH	-
a5	2"x2"	[51x51], 42" [1067] Long Wooden Post	Wood	-
a6	4"x4"	[102x102], 5 3/4" [146] Long Wooden Block	Wood	-
a7	12"x12"x3/4"	[305x305x19] Post Base	Plywood	-
b1	2	BCT Cable Anchor Assembly (Includes Nuts & Washers)	3/4" [19] Dia. 6x19 IWRC IPS Galv. Wire Rope	FCA01
b2	4	1 1/2" [38 Dia.] Oval Eye Nut	-	**3274T48
b3	6	1" [25] Dia. Shackles	-	**3663T46
c1	6	12"x12"x3/4" [305x305x19] Anchor Plate	ASTM A36	-
c2	6	1" [25] Dia. Anchor Hoop	Donated, No Material Specification	-
c3	24	3/4" [19] Dia., 6" [152] Long Wedge Bolt	Power Fasteners	-
c4	6	5/8" [16] Dia. Shackles	Donated, No Material Specification	**3663T43
c5	6	Dragnet Transition Piece	Donated, No Material Specification	-
c6	6	1 1/4" [32] Dia., 6" [152] Long Schedule 40 Pipe	Donated, No Material Specification	-
c7	12	1 1/4" [32] Dia., Schedule 40 Pipe Cap	Donated, No Material Specification	-
c8	6	Dragnet Energy Absorber 4,500 lb [20 kN]	Donated, No Material Certifications	-
c9	6	1/2" [13] UNC, 3 1/2 [89] Long Hex Bolt	SAE J429 Gr.5	-
c10	6	1/2" [13] Dia. UNC Hex Nut	ASTM A325DH	Manuf. Supplied
c11	12	3/4" [19] Dia. UNC Oval Eye Nut	-	**3274T44
c12	6	3/4" [19] Dia. UNC, 14" [356] Turnbuckle	Not Specified	-
c13	6	3/4" [19] Dia. UNC, 11" [279] Left-Hand Threaded Rod	ASTM A449	-
c14	6	3/4" [19] Dia. UNC, 11" [279] Right-Hand Threaded Rod	ASTM A449	-
c15	6	1/2" [13] Dia. Schedule 40 Pipe, 2" [51] Long	ASTM A500	-
c16	6	1" [25] Dia. Schedule 40 Pipe, 1 1/4" [32] Long	ASTM A500	-
d1	1	86 1/8"x28"x12 Gauge [2187x711x2.7] Bogie Head Plate	ASTM A36	-
d2	1	6"x8"x72" [152x203x1829] Post	SYP Grade No. 1	-
d3	2	6"x8"x72" [152x203x1829] Post	SYP Grade No. 1	-
d4	2	7/8" [22] Dia. UNC, 24" [610] Long Threaded Rod	ASTM A449	-
d5	8	7/8" [22] Dia. UNC Heavy Hex Nut	ASTM A563 DH	-
d6	8	7/8" [22] Dia. Hardened Round Washer	ASTM F436	-
d7	4	7/8" [22] Dia. UNC, 16" [406] Long Round Head Bolt	ASTM A449	-
<p>** McMaster-Carr part no. used for general dimensions.</p>				


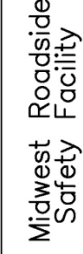
	Dragnet Bogie Testing	SHEET: 19 of 19
		DATE: 3/25/15
Bill of Materials DWG. NAME: Dragnet-Cable-V2_R5		DRAWN BY: JCP
SCALE: 1:384 UNITS: in, [mm]		REV. BY: -

Figure 106. Bill of Materials, Test Nos. IRA-3 and IRA-4



Figure 107. Test Installation, Test No. IRA-3



Figure 108. Test Installation, Test No. IRA-3



Figure 109. Test Installation, Test No. IRA-4

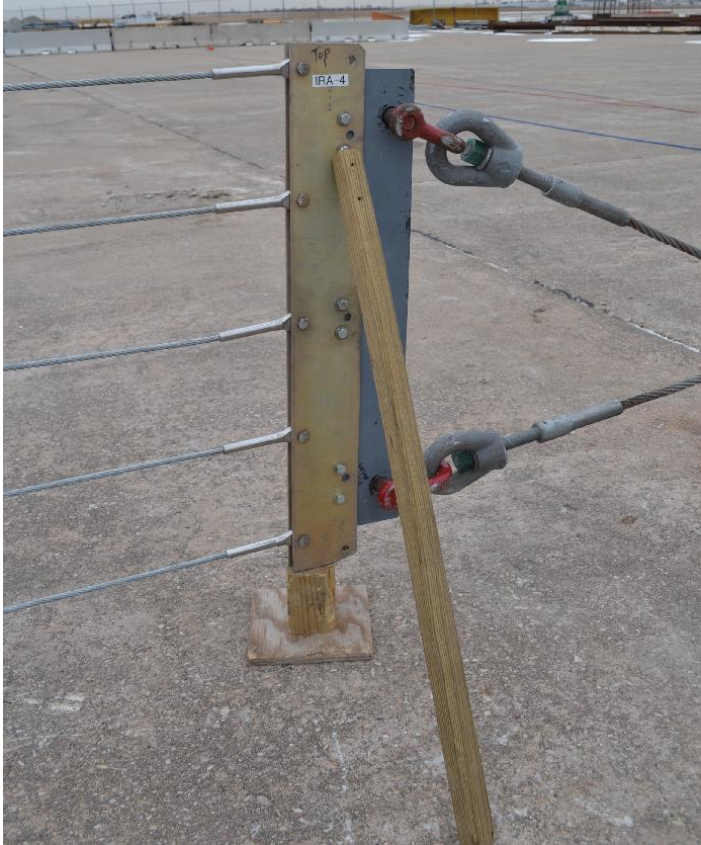


Figure 110. Test Installation, Test No. IRA-4

17 NET ATTENUATOR COMPONENT TEST NO. IRA-3

17.1 Test No. IRA-3

The 5,259-lb (2,385-kg) bogie vehicle impacted the net arrestor at a speed of 58.0 mph (93.3 km/h) and an angle of 60 degrees, offset 12 ft (3.7 m) to the right from the center of the net. All components of the net, except for the vertical posts supporting the net, were reused from test no. IRA-2. The vertical posts supporting the net were replaced with lightweight steel shelving posts. The $\frac{7}{16}$ -in. (11-mm) diameter fasteners that attached the ends of the net to the energy absorbers were replaced with $\frac{1}{2}$ -in. (13-mm) diameter fasteners. The energy absorbers from the previous test were also replaced with unused units. Sequential photographs are shown in Figures 111 through 114. Documentary photographs of the crash test are shown in Figure 115.

17.2 Weather Conditions

Test no. IRA-3 was conducted on February 3, 2014 at approximately 11:00 a.m. The weather conditions, as per the National Oceanic and Atmospheric Administration (station 14939/LNK), were reported and are shown in Table 30.

Table 30. Weather Conditions, Test No. IRA-3

Temperature	29° F
Humidity	51%
Wind Speed	14 mph
Wind Direction	210° from True North
Sky Conditions	Overcast 80%
Visibility	10 Statute Miles
Pavement Surface	Dry
Previous 3-Day Precipitation	0.02 in.
Previous 7-Day Precipitation	0.05 in.

17.3 Test Description

Initial vehicle impact was to occur in the center of the net, as shown in Figure 116. Although the actual point of impact could not be determined from examining the post-test damage of the system, analysis of the crash test videos showed that the bogie did appear to impact the intended location. The vehicle had a maximum dynamic deflection of 33.0 ft (10.1 m) downstream from the point of impact with a lateral movement of 18.0 ft (5.5 m), resulting in a total displacement of 37.6 ft (11.5 m). The maximum dynamic deflection was determined using accelerometer traces to calculate the planar trajectory. The deflection could not be verified with overhead video analysis because of skewed cameras. The vehicle yawed slightly to the left during the test. The vehicle trajectory and final position are shown in Figure 117.

17.4 System Damage

Damage to the net attenuator was minimal, as shown in Figures 118 and 119. The innermost energy absorbers did not experience the excessive whipping that occurred in test nos. IRA-1 and IRA-2, and all energy absorbers functioned as designed. The amount of tape pulled from each energy absorber is shown in Table 23.

Table 31. Energy-Absorber Tape Pullout, Test No. IRA-3

Side	Location	Pullout Distance	
		ft	m
Right	Outside	22.60	6.89
	Middle	21.08	6.43
	Inside	18.79	5.73
Left	Outside	23.33	7.11
	Middle	24.00	7.32
	Inside	24.29	7.40

The net assembly deformed around the bogie vehicle. The lightweight steel post on the right side of the system fractured at the bottom mounting bolt for the bottom cable, approximately 8 in. (203 mm) above the ground and at the center cable location where it was folded over the top of the bogie head, as shown in Figure 118. The cables and vertical cable spreaders had minimal damage and were able to be reused.

17.5 Vehicle Damage

The damage to the vehicle was minimal, as shown in Figure 119. The damage to the vehicle was isolated to the top and bottom of the impact head, where denting and scraping were observed.

17.6 Occupant Risk

The calculated occupant impact velocities (OIVs) and maximum 0.010-sec occupant ridedown accelerations (ORAs) in both the longitudinal and lateral directions are shown in Table 32. Note that the OIVs and ORAs were within the suggested limits provided in MASH, although the velocity was slightly less than a MASH TL-3 tests and the mass of the bogie vehicle was slightly higher than the MASH 2270P vehicle. The calculated THIV, PHD, and ASI values are also shown in Table 32. The recorded data from the accelerometers and the rate transducers are shown graphically in Appendix D.

Table 32. Summary of OIV, ORA, THIV, PHD, and ASI Values, Test No. IRA-3

Evaluation Criteria		Transducer		MASH Limits
		DTS SLICE-1	DTS SLICE-2	
OIV ft/s (m/s)	Longitudinal	19.24 (5.86)	19.31 (5.89)	≤ 40 (12.2)
	Lateral	0.20 (0.06)	0.16 (0.05)	≤40 (12.2)
ORA g's	Longitudinal	4.64	4.68	≤ 20.49
	Lateral	1.87	2.00	≤ 20.49
MAX. ANGULAR DISPL. deg.	Roll	1.22	1.74	≤75
	Pitch	-0.71	1.01	≤75
	Yaw	8.02	7.12	not required
THIV ft/s (m/s)		18.43 (5.62)	18.58 (5.66)	not required
PHD g's		4.93	5.03	not required
ASI		0.38	0.38	not required

17.7 Discussion

The analysis of the test results for test no. IRA-3 showed that the net attenuator adequately captured the 5,259-lb (2,385-kg) bogie vehicle and brought it to rest. There were neither detached elements nor fragments from the net which showed potential for undue hazard to other traffic. The test vehicle did not penetrate or ride over the net attenuator and remained upright during and after the collision.

The occupant risk values for the bogie vehicle were assumed to be equivalent for the 2270P truck. Estimations for the 1100C and 1500A MASH vehicles were calculated using the Occupant Risk Estimation procedure discussed in Appendix G of MASH [3]. The procedure consisted of integrating the CFC 180-filtered, longitudinal acceleration trace to obtain the force-

deflection characteristics of the net attenuator. The force-deflection data was then applied to the 1100C and 1500A vehicles to obtain the OIV and ORA estimates, as shown in Table 33. Note that the OIV and ORA estimates for both vehicles were below MASH limits, and higher-force energy absorbers could be used without issue for small cars. Further details of these estimations are located in Appendix D.

Table 33. 1100C and 1500A Displacement, OIV, and ORA Estimations, Test No. IRA-3

Vehicle	Mass lb (kg)	Velocity mph (km/h)	OIV Estimation ft/s (m/s)	ORA Estimation g's	Maximum Deflection ft (m)
1100C	2,425 (1,100)	62.14 (100.00)	26.09 (7.95)	8.97	24.4 (7.4)
1500A	3,307 (1,500)	62.14 (100.00)	23.18 (7.07)	7.72	30.0 (9.2)

The test represented a worst-case scenario, where a vehicle impacts very near the end of the net. This test proved that a vehicle could be safely captured very close to the end of the net. If the forces from the energy absorbers were increased, it would be expected that the lateral forces on the vehicle from the net would also increase and could potentially cause the vehicle to yaw even more.

By changing the anchorage location of the energy absorbers, the innermost energy absorber was no longer perpendicular to the net and was not compressed as much as in test nos. IRA-1 and IRA-2. It is therefore recommended that future installations should also anchor the energy absorbers as close to parallel with the net as practical, also considering that extra clearance is needed to allow the energy absorbers to rotate without interference in angled impacts where the energy absorbers need to go beyond perpendicular with the system.



0.000 sec



0.720 sec



0.240 sec



0.960 sec



0.480 sec



1.200 sec

Figure 111. Sequential Photographs, Test No. IRA-3



0.000 sec



0.240 sec



0.480 sec



0.720 sec



0.960 sec



1.200 sec



0.000 sec



0.080 sec



0.160 sec



0.2400 sec



0.320 sec



0.400 sec

Figure 112. Additional Sequential Photographs, Test No. IRA-3



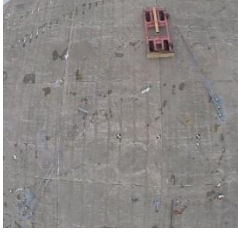
0.000 sec



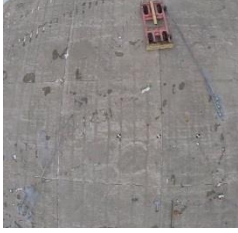
0.202 sec



0.403 sec



0.605 sec



0.807 sec



1.008 sec



0.000 sec



0.118 sec



0.235 sec



0.353 sec



0.471 sec



0.588 sec

Figure 113. Additional Sequential Photographs, Test No. IRA-3



0.000 sec



0.067 sec



0.134 sec



0.202 sec



0.269 sec



0.336 sec



0.000 sec



0.067 sec



0.134 sec



0.336 sec



0.403 sec



0.538 sec

Figure 114. Additional Sequential Photographs, Test No. IRA-3



Figure 115. Documentary Photographs, Test No. IRA-3



Figure 116. Impact Location, Test No. IRA-3



Figure 117. Vehicle Final Position and Trajectory Marks, Test No. IRA-3



Figure 118. System Damage, Test No. IRA-3



Figure 119. System and Vehicle Damage – Fractured Support Post, Test No. IRA-3

18 NET ATTENUATOR COMPONENT TEST NO. IRA-4

18.1 Test No. IRA-4

The 5,259-lb (2,385-kg) bogie vehicle impacted the net arrestor at a speed of 59.5 mph (95.8 km/h) in the center of the net at an angle of 90 degrees. All components of the net, except for one of the vertical posts supporting the net, were reused from test no. IRA-3. This vertical post was replaced with a lightweight steel shelving post. The energy absorbers from the previous test were also replaced with unused units. Sequential photographs are shown in Figures 120 through 123. Documentary photographs of the crash test are shown in Figure 124.

18.2 Weather Conditions

Test no. IRA-4 was conducted on February 3, 2014 at approximately 2:00 p.m. The weather conditions, as per the National Oceanic and Atmospheric Administration (station 14939/LNK), were reported and are shown in Table 34.

Table 34. Weather Conditions, Test No. IRA-4

Temperature	29° F
Humidity	49%
Wind Speed	7 mph
Wind Direction	190° from True North
Sky Conditions	Overcast 75%
Visibility	10 Statute Miles
Pavement Surface	Dry
Previous 3-Day Precipitation	0.02 in.
Previous 7-Day Precipitation	0.05 in.

18.3 Test Description

Initial vehicle impact was to occur in the center of the net, as shown in Figure 125. The actual point of impact could not be determined from examining the post-test damage of the system, but analysis of the crash test videos showed that the bogie did appear to impact a few

inches left of the center of the net. As the vehicle was traveling down the bogie track, the bogie began bouncing down the pipe track, bending it as shown in Figure 127. Although the vehicle was bouncing down the track, the effect on the vehicle’s velocity and impact angle was negligible. The vehicle had a maximum dynamic deflection of 42.2 ft (12.9 m) downstream from the point of impact with a lateral movement of 1.82 ft (0.55 m). The maximum dynamic deflection was calculated using the planar trajectory spreadsheets. The deflection could not be verified with overhead video analysis because of skewed cameras. The test vehicle yawed slightly to the right. The vehicle trajectory and final position are shown in Figure 126.

18.4 System Damage

Damage to the net attenuator was minimal, as shown in Figures 127 through 130. The outermost energy absorber on the right side of the system failed 720 ms after impact occurred. The failure occurred when the net went slack and then was suddenly loaded again. The amount of tape pulled from each energy absorber is shown in Table 35.

Table 35. Energy-Absorber Tape Pullout, Test No. IRA-4

Side	Location	Pullout Distance	
		ft	m
Right	Outside	19.94	6.08
	Middle	22.29	6.79
	Inside	23.25	7.09
Left	Outside	23.21	7.07
	Middle	24.81	7.56
	Inside	26.04	7.94

The net assembly deformed around the bogie vehicle. The hollow aluminum posts that supported the net had fractured at the bottom mounting bolt for the bottom cable, approximately 8 in. (203 mm) above the ground, as shown in Figures 127 through 130. The cables and vertical cable spreaders had minimal damage and were capable of being reused.

18.5 Vehicle Damage

The damage to the vehicle was minimal, as shown in Figure 126. The damage to the vehicle was isolated to the top and bottom of the impact head, where denting and scraping were observed.

18.6 Occupant Risk

The calculated occupant impact velocities (OIVs) and maximum 0.010-sec occupant ridedown accelerations (ORAs) in both the longitudinal and lateral directions are shown in Table 36. Note that the OIVs and ORAs were within the suggested limits provided in MASH, although the velocity was slightly less than a MASH TL-3 tests and the mass of the bogie vehicle was slightly higher than the MASH 2270P vehicle. The calculated THIV, PHD, and ASI values are also shown in Table 36. The recorded data from the accelerometers and the rate transducers are shown graphically in Appendix E.

Table 36. Summary of OIV, ORA, THIV, PHD, and ASI Values, Test No. IRA-4

Evaluation Criteria		Transducer		MASH Limits
		DTS SLICE-1	DTS SLICE-2	
OIV ft/s (m/s)	Longitudinal	18.34 (5.59)	18.47 (5.63)	≤ 40 (12.2)
	Lateral	1.71 (0.52)	1.88 (0.57)	≤40 (12.2)
ORA g's	Longitudinal	4.88	4.98	≤ 20.49
	Lateral	1.15	1.31	≤ 20.49
MAX. ANGULAR DISPL. deg.	Roll	1.22	1.74	≤75
	Pitch	-0.71	1.01	≤75
	Yaw	8.02	7.12	not required
THIV ft/s (m/s)		18.43 (5.62)	18.58 (5.66)	not required
PHD g's		4.93	5.03	not required
ASI		0.37	0.38	not required

18.7 Discussion

The analysis of the test results for test no. IRA-4 showed that the net attenuator adequately captured the 5,259-lb (2,385-kg) bogie vehicle and brought it to rest. There were neither detached elements nor fragments from the net which showed potential for undue hazard to other traffic. The test vehicle did not penetrate or ride over the barrier and remained upright during and after the collision.

The occupant risk values for the bogie vehicle were assumed to be equivalent for the 2270P truck. Estimations for the 1100C and 1500A MASH vehicles were calculated using the Occupant Risk Estimation procedure discussed in Appendix G of MASH [3]. The procedure

consisted of integrating the CFC 180-filtered, longitudinal acceleration trace to obtain the force-deflection characteristics of the net attenuator. The force-deflection data was then applied to the 1100C and 1500A vehicles to obtain the OIV and ORA estimates shown in Table 33. Note that the OIV and ORA estimates for both vehicles were below MASH limits, and higher-force energy absorbers could be used without issue for small cars. Further details of these estimations are located in Appendix E.

Table 37. 1100C and 1500A Displacement, OIV, and ORA Estimations, Test No. IRA-4

Vehicle	Mass lb (kg)	Velocity mph (km/h)	OIV Estimation ft/s (m/s)	ORA Estimation g's	Maximum Deflection ft (m)
1100C	2,425 (1,100)	62.14 (100.00)	26.23 (8.00)	7.83	26.9 (8.2)
1500A	3,307 (1,500)	62.14 (100.00)	22.81 (6.95)	6.28	32.7 (10.0)

This test had the same target impact conditions as IRA-1 and would serve as a baseline for which to compare and validate simulations and analytical predictions. By changing the anchorage location of the energy absorbers, the innermost energy absorber was no longer perpendicular to the net and was not compressed as much as observed in test nos. IRA-1 and IRA-2. It is therefore recommended that future installations should also anchor the energy absorbers as close to parallel with the net as practical, also considering that extra clearance is needed to allow the energy absorbers to rotate without interference in angled impacts where the energy absorbers need to go beyond perpendicular with the system.



0.000 sec



0.720 sec



0.240 sec



0.960 sec



0.480 sec



1.200 sec

Figure 120. Sequential Photographs, Test No. IRA-4



0.000 sec



0.240 sec



0.480 sec



0.720 sec



0.960 sec



1.200 sec



0.000 sec



0.080 sec



0.160 sec



0.240 sec



0.320 sec



0.400 sec

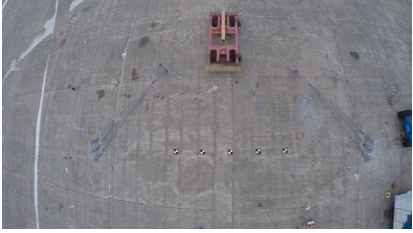
Figure 121. Additional Sequential Photographs, Test No. IRA-4



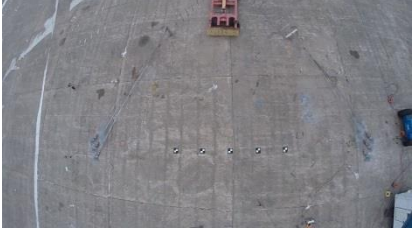
0.000 sec



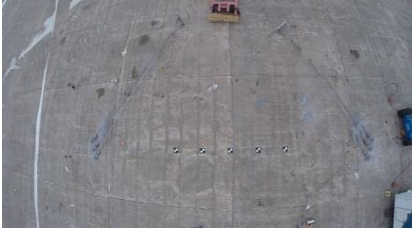
0.202 sec



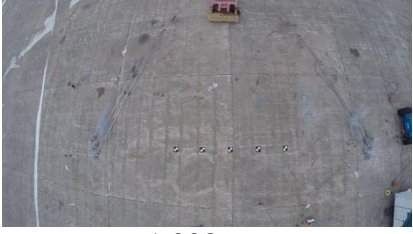
0.403 sec



0.605 sec



0.807 sec



1.008 sec



0.000 sec



0.202 sec



0.403 sec



0.605 sec



0.807 sec



1.008 sec

Figure 122. Additional Sequential Photographs, Test No. IRA-4



0.000 sec



0.235 sec



0.471 sec



0.706 sec



0.941 sec



1.176 sec



0.000 sec



0.067 sec



0.134 sec



0.202 sec



0.471 sec



1.008 sec

Figure 123. Additional Sequential Photographs, Test No. IRA-4

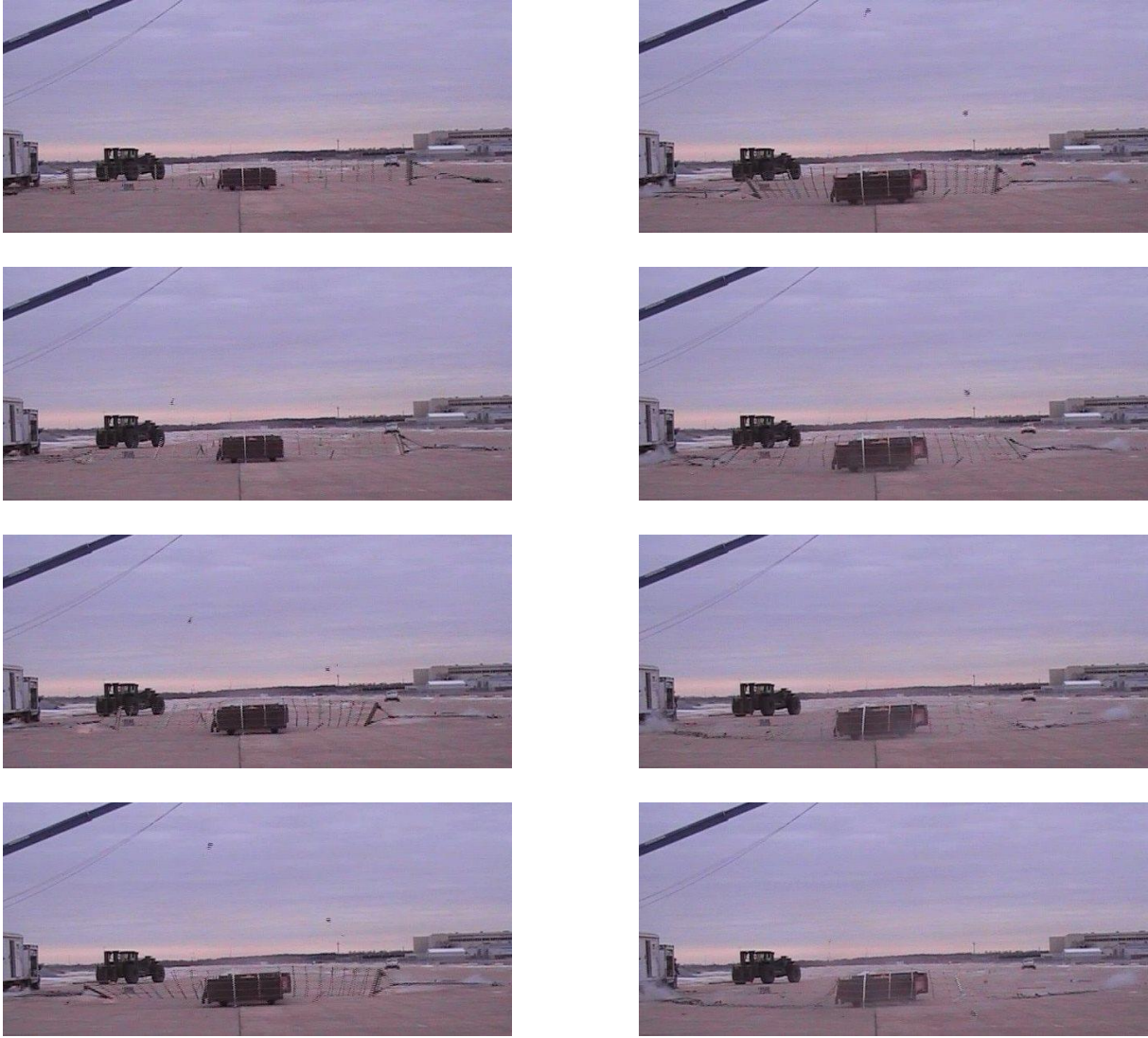


Figure 124. Documentary Photographs, Test No. IRA-4

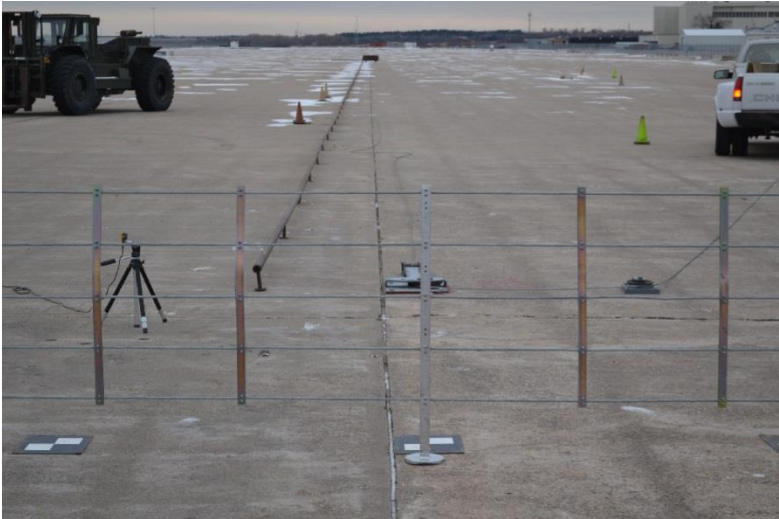


Figure 125. Impact Location, Test No. IRA-4



Figure 126. Vehicle Final Position and Trajectory Marks, Test No. IRA-4



Figure 127. System Damage, Test No. IRA-4



Figure 128. System Damage, Test No. IRA-4



Figure 129. System Damage, Test No. IRA-4



Figure 130. System Damage, Test No. IRA-4

19 EVALUATION OF NET ATTENUATOR PERFORMANCE

Testing on the modified Dragnet Vehicle Arresting Barrier showed that it could be a viable option for use in Concept A. The bogie vehicle was successfully captured in test nos. IRA-1 through IRA-4. There were neither detached elements nor fragments from the net which showed potential for undue hazard to other traffic. The test vehicles were captured by the net without any issues and remained upright during and after the collisions. Even though the net is taller than the 36-in. (914-mm) height criterion, the net can easily be seen through and would not cause sight-line issues.

The prototype net attenuator system used existing technologies, and most of its components were reusable. The anchorage systems could be placed near the primary and secondary roads where the ground is level. Although the area in front of the net needs to be flat, this concept could likely accommodate a moderate slope behind it. Some research and development would be required to integrate a net attenuator with either an end terminal or crash cushion system. Interior support posts may need to be embedded in soil instead of supported on tarmac. Mowing operations would be simpler than many concepts due to the absence of enclosed regions within the protected area.

The stopping distances ranged from 37.6 ft (11.5 m) in test no. IRA-3 to 44.2 ft (13.5 m) in test no. IRA-4. A stopping distance of 30 ft (9.1 m) was desired for Concept A, but the net could be modified to accommodate the shorter stopping distance. Higher-capacity energy absorbers would result in higher occupant risk values but shorter stopping distances. After analysis, the actual and estimated occupant risk values showed that this concept was feasible due to values below the MASH limits, as shown in Tables 38 and 39. Although the stopping distance

could be reduced to 30 ft (9.1 m) or less, this system might still require more space than what is available at some field locations.

Table 38. Occupant Risk Summary, Test Nos. IRA-1 through IRA-4

Test No.	Vehicle	Mass lb (kg)	Velocity mph (km/h)	OIV ft/s (m/s)	ORA g's
IRA-1	Bogie	5,090 (2,309)	60.39 (97.19)	18.24 (5.56)	4.00
IRA-2	Bogie	5,090 (2,309)	59.86 (96.34)	17.98 (5.48)	3.79
IRA-3	Bogie	5,259 (2,385)	58.03 (93.39)	19.24 (5.86)	4.64
IRA-4	Bogie	5,259 (2,385)	59.46 (95.69)	18.34 (5.59)	4.88

Table 39. Estimated Occupant Risk for 1100C and 1500A Vehicles, Test Nos. IRA-1 through IRA-4

Test No.	Vehicle	Mass lb (kg)	Velocity mph (km/h)	Estimated OIV ft/s (m/s)	Estimated ORA g's
IRA-1	1100C	2,425 (1,100)	62.14 (100.00)	25.69 (7.83)	7.69
	1500A	3,307 (1,500)	62.14 (100.00)	22.91 (6.98)	5.36
IRA-2	1100C	2,425 (1,100)	62.14 (100.00)	26.75 (8.15)	8.33
	1500A	3,307 (1,500)	62.14 (100.00)	23.18 (7.06)	5.78
IRA-3	1100C	2,425 (1,100)	62.14 (100.00)	26.09 (7.95)	8.97
	1500A	3,307 (1,500)	62.14 (100.00)	23.18 (7.07)	7.72
IRA-4	1100C	2,425 (1,100)	62.14 (100.00)	26.23 (8.00)	7.83
	1500A	3,307 (1,500)	62.14 (100.00)	22.81 (6.95)	6.28

During test nos. IRA-1 and IRA-2, the innermost energy absorber on the left side of the systems failed 120 ms and 150 ms after impact occurred, respectively. The failures were likely caused by excessive whipping that occurred with both inside energy absorbers of the system. As shown in Figures 67 and 70, the 1-in. (25-mm) shackle that connected the energy absorbers to the assembly initially moved upstream and towards the center of the net. This motion caused the innermost energy absorbers to compress and rotate away from impact. As the innermost energy

absorber on the left side was pulled tight, the steel tape ruptured at the connection between the tape and the turnbuckles, as shown in Figure 76. Although the inner energy absorbers on both sides of the net exhibited the same motion, only the left absorbers had a failure. One factor that could have influenced this failure was the direction the tape was wrapped around the bracket.

The solution to this whipping action was to reduce the angle between the energy absorbers and the net from 0, 45, and 90 degrees to 0, 22.5, and 45 degrees. This modification moved the energy absorbers closer together and had the added benefit of reducing the pad area that was needed for each side of the installation. This issue could be eliminated altogether if one energy absorber on each side of the system was used instead of multiple units. With a smaller anchorage footprint, there would be reduced risk for the energy absorbers to cross over each other in high-angle impacts such as test no. IRA-3. To allow the energy absorbers to rotate without interacting with one another, the outermost energy absorber should be installed in-line with the net, with all other energy absorbers installed on the impact side.

During test no. IRA-4, the outermost energy absorber on the right side of the system failed 720 ms after impact occurred. This failure was likely caused by the net going slack momentarily and then being immediately loaded again, or a combination of both. One possible solution to this problem could be to make sure that the energy absorbers are not attached to the net at a single point, as they were during test nos. IRA-1 through IRA-4. One possible reason for the net going slack is that the energy absorbers tip over on their sides as they rotate about the anchorage point. This behavior exposes an edge that sticks into the ground as they rotate about the anchor hoop. Instead of sliding across the ground, they tend to skip over the pavement. This skipping could cause momentary losses in tension. Uneven loading could magnify the effects of stress concentrations that occurred when the turnbuckles were close together toward the end of the test. One benefit of having the energy absorbers spaced farther apart is that the turnbuckles

that attached the energy absorbers to the net would be farther apart and less likely to interact with one another.

Testing on the prototype net attenuator system showed that it would be a viable design concept. In all of the tests, the net successfully captured the vehicle and would likely be able to accommodate moderate slopes behind the system. The stopping distance was greater than desired but could likely be decreased without adverse effects to occupant safety. Some research and development was still required for this system, but most of the components already existed.

20 DEVELOPMENT OF NET ATTENUATOR MODEL

20.1 Methodology

A finite element model of a prototype net attenuator system was developed to further investigate its performance for treatment of bridge rails adjacent to intersecting roadways. These simulations were performed using LS-DYNA to serve as a comparison to physical component testing and analytical calculations. LS-DYNA is a transient, nonlinear finite element analysis computer program that has been widely used in analysis and design of roadside safety hardware as well as the study of vehicular impact events [49]. A finite element model could be used to investigate different energy absorber capacities and to continue the development of Concept A. The development of a simulation model of a modified Dragnet Vehicle Arresting Barrier and some of its components are detailed herein. This simulation model was developed to represent the actual system used in test no. IRA-4, as shown in Figure 131.



Figure 131. Modified Dragnet Vehicle Arresting Barrier, Test No. IRA-4

20.2 Bogie Model

A heavy bogie vehicle model, shown in Figure 132, was used as the impacting vehicle during the development of the net attenuator model. The steel frame of the bogie model was rigid

and had the same mass and material properties as the bogie used in test no. IRA-4. The bogie head geometry was identical to the bogie head used in test nos. IRA-1 through IRA-4 and was rigidly tied to the bogie frame. Dimensions of the bogie head are shown in Figure 57. Nodal masses were added to the rigid frame to match the test weight of 5,259 lb (2,385 kg).

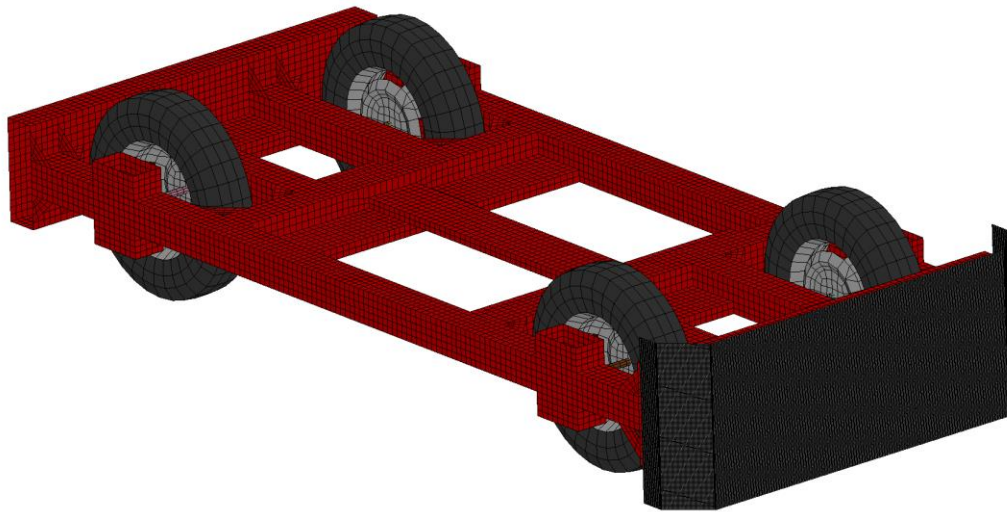


Figure 132. Bogie Finite Element Model

20.3 Modified Dragnet Vehicle Arresting Barrier Model

20.3.1 Energy Absorbers

Ideally, the energy absorbers would be modeled using the actual geometry in static and dynamic component testing programs. Simulating the energy absorption mechanism and cyclic plastic bending would result in a more complex model, thus requiring material properties that were unavailable and additional time to validate the model. Updating the overall simulation to investigate different energy absorber forces would likely be difficult as well as time-consuming. Instead of modeling the energy-absorption mechanism, a simplified component was selected to provide the same resistive force as the energy absorbers.

To accomplish this goal, a discrete element was chosen and general non-linear spring material with a simplified force-deflection curve was used for each of the six energy absorbers.

This method was beneficial, because it could be easily modified to investigate other energy absorber force levels, would be more efficient in regards to simulation time, and could accurately represent the function of the energy absorbers.

The average tensile force measured in test no. IRAS-2 was used, because the loading from that test was more consistent than in test no. IRAS-1. The simulation was performed with an energy absorber force of 3,920 lb (17.4 kN) instead of the value of 3,890 lb (17.3 kN) from test no. IRAS-2. This change resulted in a 0.77 percent increase in energy-absorber force, although this would have a negligible effect on the stopping distance or occupant risk values. The force of the energy absorber, as shown in Figure 133, was increased from 0 to 3,920 lb (17.4 kN) over the first 3.94 in. (100 mm) of extension and then remained constant for the rest of the displacement. Although overcoming the initial static friction would initially result in higher forces, it was neglected due to resistive vehicle forces being low initially from the shallow angles immediately after impact.

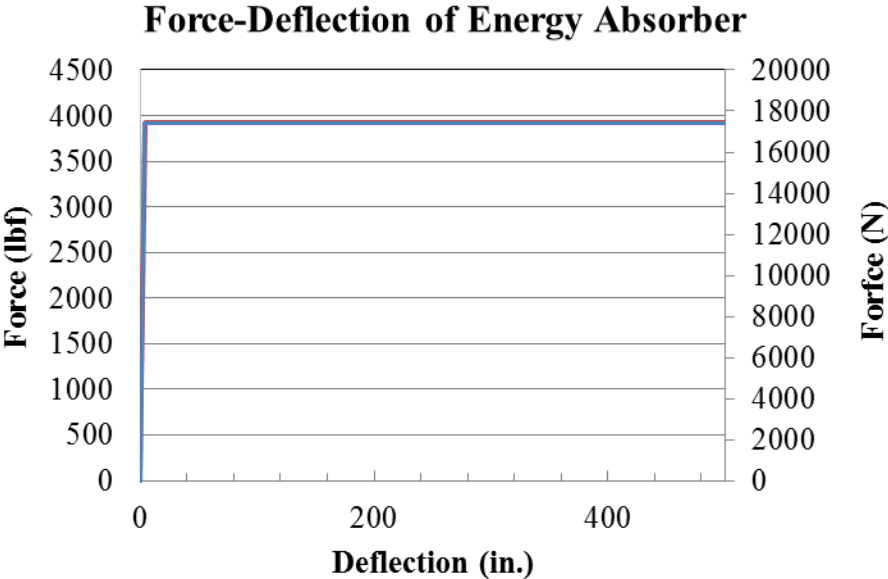


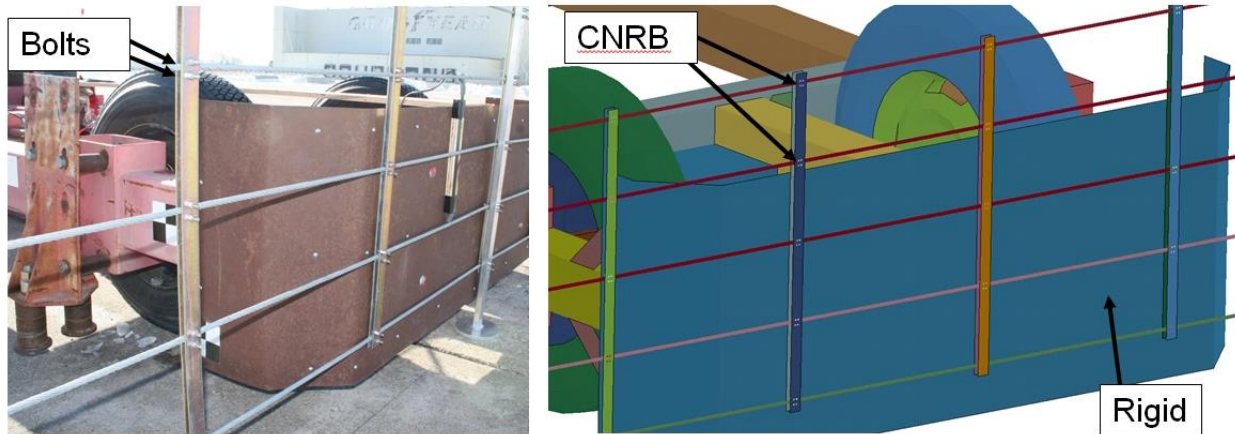
Figure 133. Force vs. Deflection of Energy Absorbers

20.3.2 Cable Net

Five horizontal $\frac{3}{8}$ -in. (10-mm) diameter cables were used in the net for the physical test and were modeled using beam elements. Previously, MwRSF researchers had developed an advanced material model for use with cable guardrails [50]. This material model used a user-defined axial force-strain, moment curvature, and torque-twist rate curves and Belytschko-Schwer beam element formulation. The cable was modeled using 0.50-in. (12.7-mm) long single beam elements along the length of the rope. Because the exact wire rope that was used during testing remained unknown when the model was developed, the parameters from the $\frac{3}{4}$ -in. (19-mm) cable used in the original cable model were scaled to the $\frac{3}{8}$ -in. (10-mm) diameter cable used in the net. An automatic node-to-surface contact with a soft option equal to 1 was used to control the interaction between the cables, cable spreaders, and the bogie head.

20.3.3 Cable Spreaders

Nineteen pairs of cable spreaders were attached on the front and back of the cables on 23-in. (584-mm) centers. They prevented the cables from separating during an impact and aided in clamping the front of the vehicle. A piecewise-linear plasticity material model was used with fully-integrated, Belytschko-Tsay shell elements that had the same geometry, mass, and material properties of the vertical spreaders that were used during testing. In test no. IRA-4, the cable spreaders were attached to the cables via bolts and nuts above and below each cable. For simulation purposes, attachment of the spreaders to the wire rope was accomplished using Constrained Nodal Rigid Bodies (CNRB). Four nodes on each cable spreader and one node from the cable made up each connection. There were five connections per pair of cable spreaders. This configuration differed from the actual attachment, as shown in Figure 134.



(b) (b)
Figure 134. Connection of Cable Spreaders: (a) Actual and (b) Simulation

Using the nodal rigid body effectively splits the cable into individual segments between each rigid attachment. This configuration prevents the spreaders from sliding or twisting independent of the cable. With the components tied together instead of the cable twisting inside of the spreaders, the entire connection was twisted. A better method of attachment would be to model the clamping force from the bolts and allow the spreaders to slide along the cable, which better represents the behavior observed in test no. IRA-4. The contact between the cables and cable spreaders may have been difficult to replicate and unstable in the simulation model. Although the connection had issues, it was unlikely to cause large errors in the final displacement of the net, because most of the kinetic energy of the test should be dissipated by the energy absorbers.

20.3.4 Net End Conditions

For the actual test, the net end plates were resting on top of a wooden block and propped upright by a stick. In the simulation, the net was just sitting in space and unsupported, which was reasonable as the stands only support the net prior to impact and are not structurally significant. Instead of using two net end plates to sandwich the ends of the horizontal wire ropes as used in

the test, one layer of rigid shell elements with an equivalent mass and section modulus was used. The ends of the net cables were attached to nodes along the edges of the net endplates. The 3/4-in. (19-mm) diameter cable that connects the energy absorbers to the net end plates used the same element formulation and material model as the cables composing the net. However, the cable properties were adjusted for the increased size. For each side, all three nonlinear discrete elements of the energy absorbers and the net end cable were attached to one node in the approximate position of their connection in the actual test. In test nos. IRA-1 through IRA-4, the energy absorbers and end cable were attached using a shackle and eye nuts, as shown in Figure 135. Although the modeled and actual connections differed, it would not have a significant effect on the maximum displacement of the bogie vehicle. The final model is shown in Figure 136.

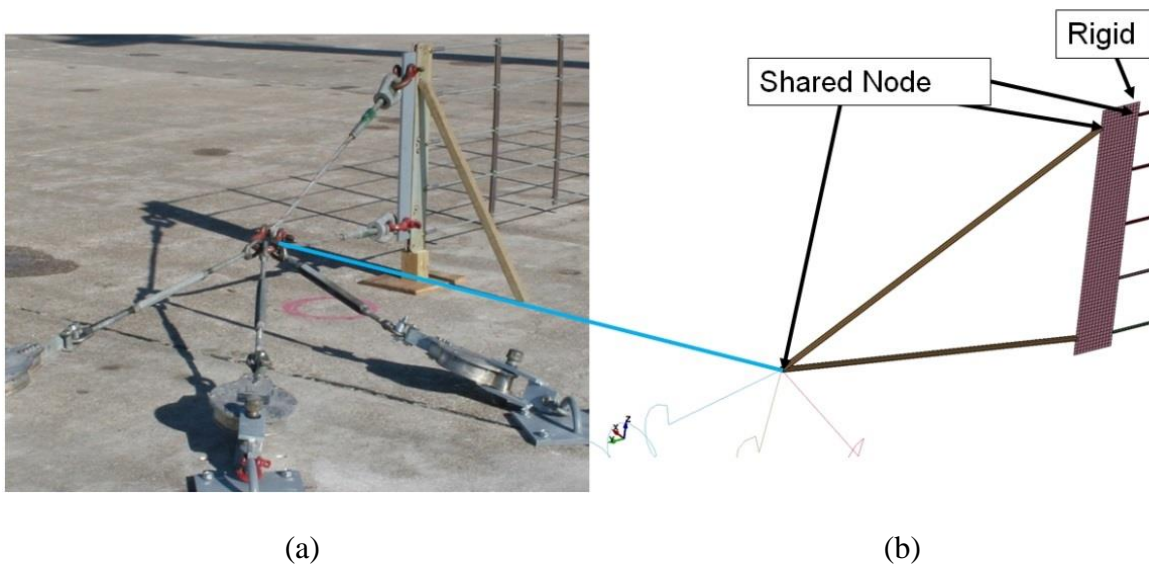


Figure 135. Energy Absorber and Net Connection: (a) Actual and (b) Simulation

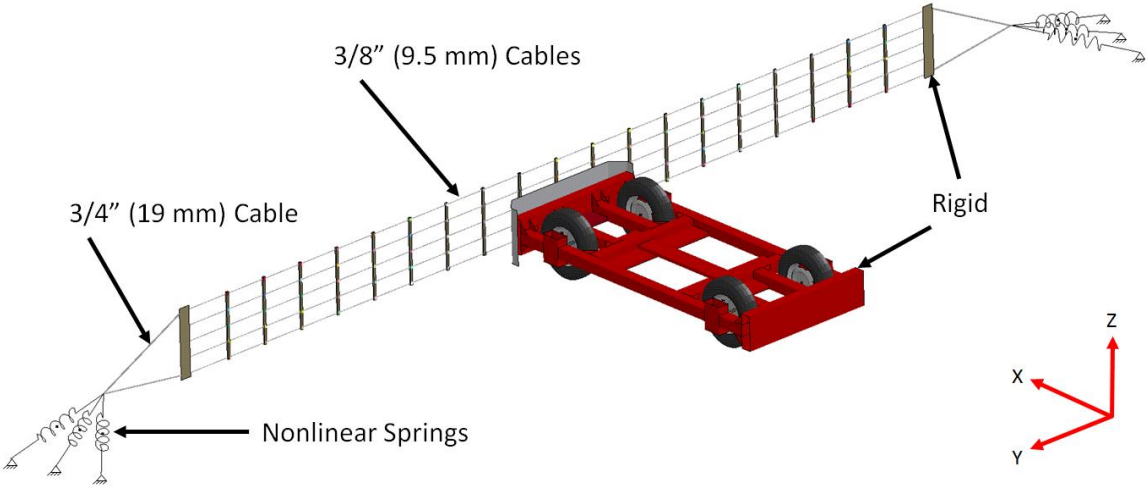


Figure 136. Final Model Setup

21 SIMULATION OF TEST NOS. IRA-3 AND IRA-4

21.1 Correlation Between Baseline Model and Full-Scale Crash Test No. IRA-4

The baseline model of the net attenuator was simulated using the conditions in test no. IRA-4. This test was chosen as the baseline, because the 90-degree impact into the center of the net was a simpler configuration than the offset and angled impacts in test nos. IRA-2 and IRA-3. Test no. IRA-1 was not used, because one of the energy absorbers failed during testing. The baseline simulation used a 5,259-lb (2,385-kg) bogie vehicle model with an initial velocity of 59.46 mph (95.69 km/h) and an angle of 90 degrees. The bogie vehicle impacted the center of the net, as shown in Figure 137. In addition to a visual analysis, the velocity profiles, maximum net deflections, and occupant risk values were used to evaluate the baseline simulations.

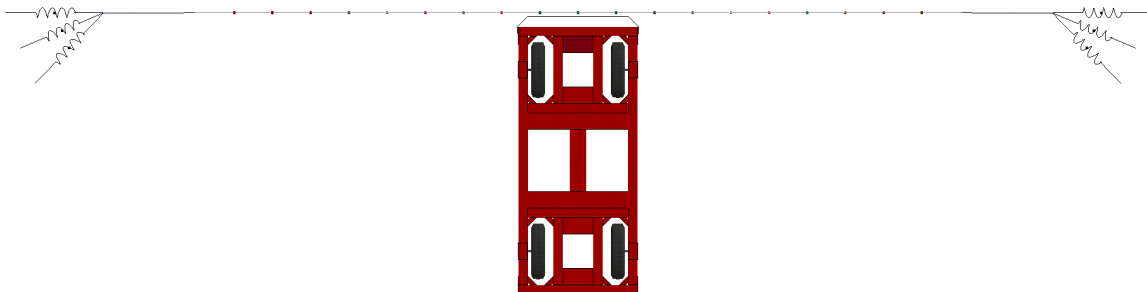


Figure 137. Simulation of Test No. IRA-4

The simulation results were compared with the results from test no. IRA-4. Test no. IRA-4 also consisted of a 5,259-lb (2,385-kg) bogie vehicle impacting at a speed of 59.46 mph (95.69 km/h) and an angle of 90 degrees. The net attenuator in this test safely captured the bogie vehicle and had a maximum dynamic deflection of 42.2 ft (12.9 m) downstream from the point of impact.

Comparison of the baseline model with the bogie crash test found that the baseline model provided good correlation with the bogie test and was appropriate for use in evaluation of the dynamic deflection of the prototype net attenuator system.

21.1.1 Graphical Comparison

Sequential images of test no. IRA-4, along with the corresponding baseline simulation, are presented in Figures 138 and 139. The IRA-4 baseline model accurately captured vehicle and system behavior exhibited in the bogie crash test. The vehicle in the simulation did have a slightly higher maximum displacement of 44.29 ft (13.50 m), compared with 42.2 ft (12.90 m) in test no. IRA-4. For test no. IRA-4, the bogie vehicle impacted the net attenuator at a slight angle and offset to the left of center of the net. This condition caused the bogie vehicle to yaw slightly to the right. The bogie vehicle in the simulation model did not yaw.



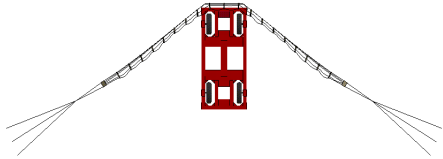
0.000 sec



0.000 sec



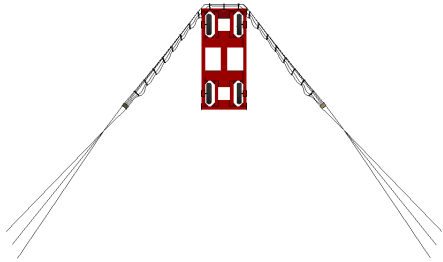
0.200 sec



0.200 sec



0.400 sec



0.400 sec

Figure 138. Test No. IRA-4 and LS-DYNA Simulation Sequentials



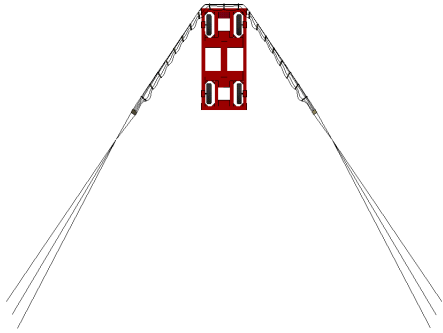
0.600 sec



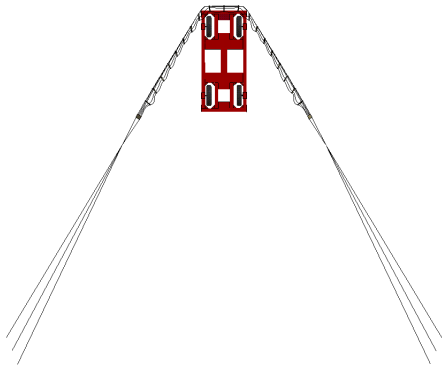
0.800 sec



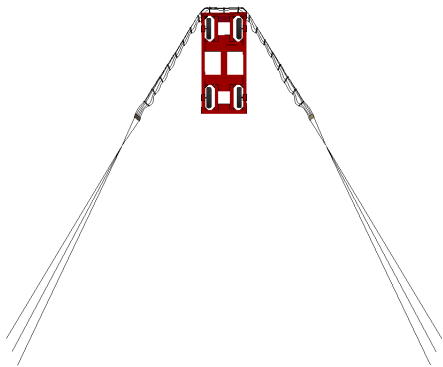
1.000 sec



0.600 sec



0.800 sec



1.000 sec

Figure 139. Test No. IRA-4 and LS-DYNA Simulation Sequentials

21.1.2 Velocity Profiles

Velocity profiles from onboard transducers were compared between the bogie in the baseline simulations and test no. IRA-4, as shown in Figure 140. The longitudinal velocity of the simulation closely matched the bogie test. The simulation over-predicted the stopping distance, resulting in a stopping time of 885 ms, versus 847 ms in test no. IRA-4. In both the test and the simulation, the bogie vehicles rolled backwards after reaching their maximum dynamic deflection.

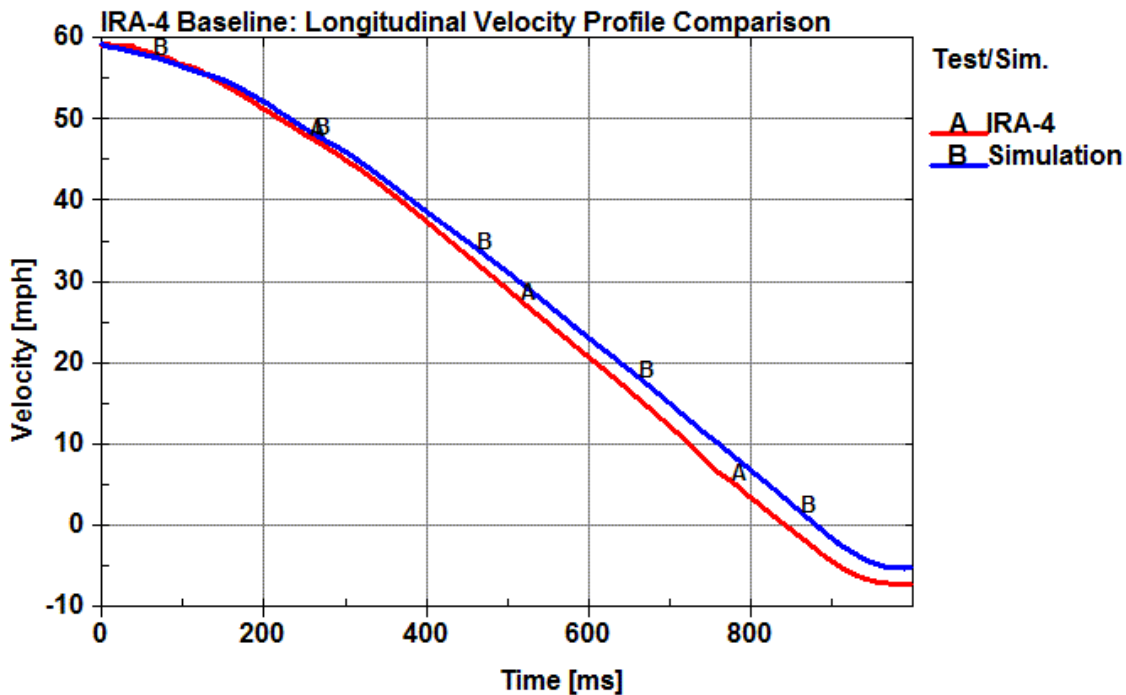


Figure 140. Velocity Profiles – Baseline Simulation and Test No. IRA-4

21.1.3 Occupant Risk

The calculated occupant impact velocities (OIVs) and maximum 0.010-sec occupant ridedown accelerations (ORAs) in both the longitudinal and lateral directions are shown in Table 40. Note that the OIVs and ORAs were within the suggested limits provided in MASH, although the velocity was slightly less than a MASH TL-3 test, and the mass of the bogie vehicle was

slightly higher than the MASH 2270P vehicle. The longitudinal occupant impact velocity between the simulation and the physical crash test was comparable; however, the longitudinal ORA was under-predicted by 19.9 percent. Further details of these predictions are located in Appendix F.

Table 40. Comparison of OIV and ORA Values, Baseline Simulation and Test No. IRA-4

Evaluation Criteria		Baseline Simulations	Test No. IRA-4 Transducers		MASH Limits
			DTS SLICE-1	DTS SLICE-2	
OIV ft/s (m/s)	Longitudinal	17.67 (5.39)	18.34 (5.59)	18.47 (5.63)	≤ 40 (12.2)
	Lateral	0.01 (0.002)	1.71 (0.52)	1.88 (0.57)	≤40 (12.2)
ORA g's	Longitudinal	3.91	4.88	4.98	≤ 20.49
	Lateral	0.08	1.15	1.31	≤ 20.49

21.1.4 Discussion of Test No. IRA-4

Several metrics, including a visual analysis and comparisons between velocity profiles, maximum net attenuator deflections, and occupant risk values, were used to evaluate the baseline net attenuator model. It was determined that the baseline simulation produced results that were comparable with bogie crash test no. IRA-4. There were no vehicle instabilities associated with either the baseline simulation or test no. IRA-4. The maximum deflections and occupant impact velocity were comparable between the simulation and the physical crash test, although there was less correlation with the occupant ridedown accelerations. During the physical component test, the bogie vehicle impacted the net slightly off-center with a slight angle, which could have had a minor effect on the stopping distance and occupant risk values.

21.2 Correlation Between Baseline Model and Full-Scale Crash Test No. IRA-3

The baseline model of the net attenuator was modified to investigate test no. IRA-3. The net was offset 12 ft (3.7 m) to the left from the center of the net and rotated 30 degrees. The same 5,259-lb (2,385-kg) bogie vehicle model from the baseline simulation was used with an impact velocity of 58.03 mph (93.39 km/h) from that was measured in no. IRA-3. The bogie vehicle and net model are shown in Figure 141. In addition to a visual analysis, the velocity profiles, maximum net deflections, and occupant risk values were used to evaluate this simulation.

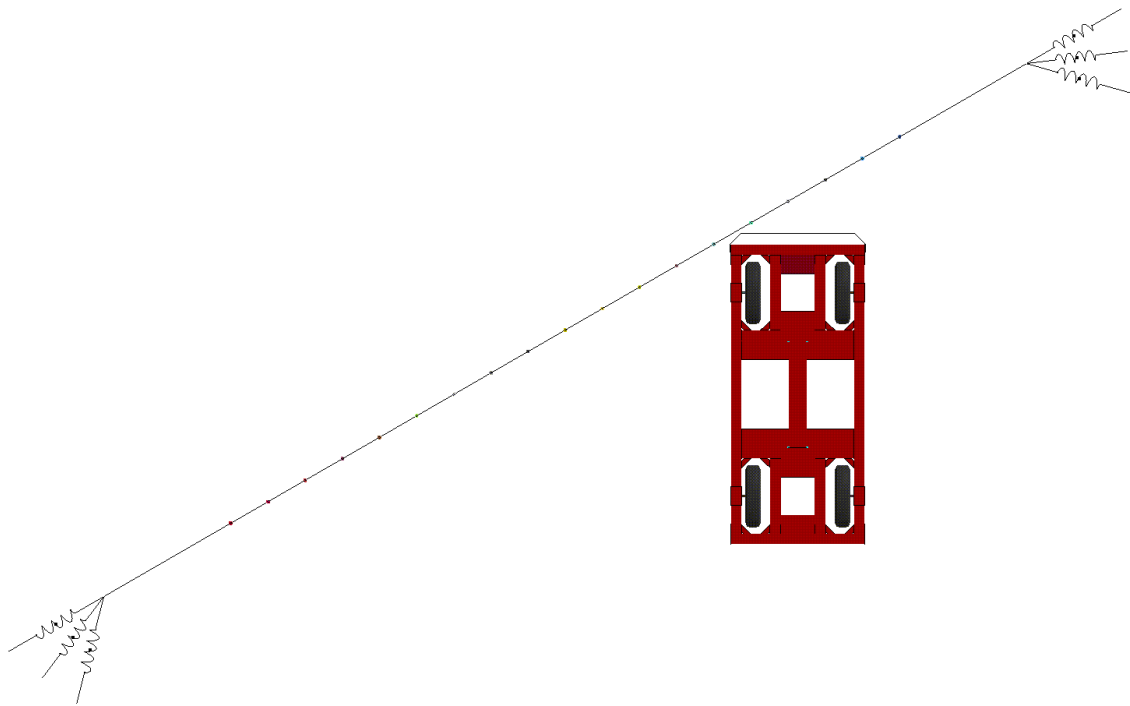


Figure 141. Simulation of Test No. IRA-3

The net attenuator in test no. IRA-3 safely captured the bogie vehicle and had a maximum dynamic deflection of 37.6 ft (12.9 m) downstream from the point of impact. A comparison of the angled simulation model with bogie test no. IRA-3 revealed that the simulation did not provide a good correlation with the bogie test. Thus, future work is required

before the model could be used to evaluate the dynamic deflection of angled impacts into the prototype net attenuator system.

21.2.1 Graphical Comparison

Sequential images of test no. IRA-3 and the corresponding baseline simulation are presented in Figures 142 and 143. The bogie vehicle was captured in test no. IRA-3 but not in the angled simulation. As shown in the sequential images, the bogie vehicle began to yaw to the left as it contacted the net. Even though all of the energy absorbers had the same force vs. deflection characteristics, the difference in angle between the left and right energy absorbers and the direction of travel caused an imbalance in the lateral forces on the vehicle. This imbalance caused the vehicle to yaw to the left in the direction of the higher lateral forces. The maximum simulated front-end bogie deflection as it rotated out of the system was 38.0 ft (11.6 m), compared with 37.6 ft (11.5 m) in test no. IRA-3.



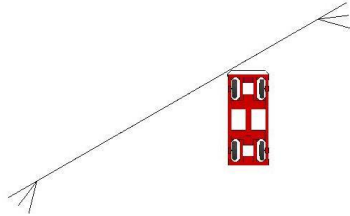
0.000 sec



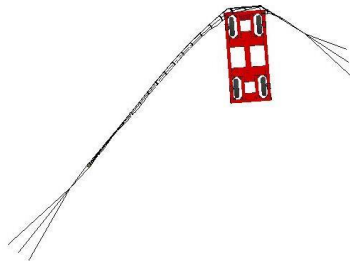
0.200 sec



0.400 sec



0.000 sec



0.200 sec



0.400 sec

Figure 142. Test No. IRA-3 and LS-DYNA Simulation Sequentials



0.600 sec



0.800 sec



1.000 sec



0.600 sec



0.800 sec



1.000 sec

Figure 143. Test No. IRA-3 and LS-DYNA Simulation Sequentials

21.2.2 Velocity Profiles

Resultant velocity profiles from onboard transducers were compared between the bogie vehicle in the baseline simulations and test no. IRA-3, as shown in Figure 144. The vehicle in test no. IRA-3 was stopped in 780 ms, before it began to roll backwards. In the simulation, the bogie vehicle was sliding sideways when the simulation ended after 1000 ms.

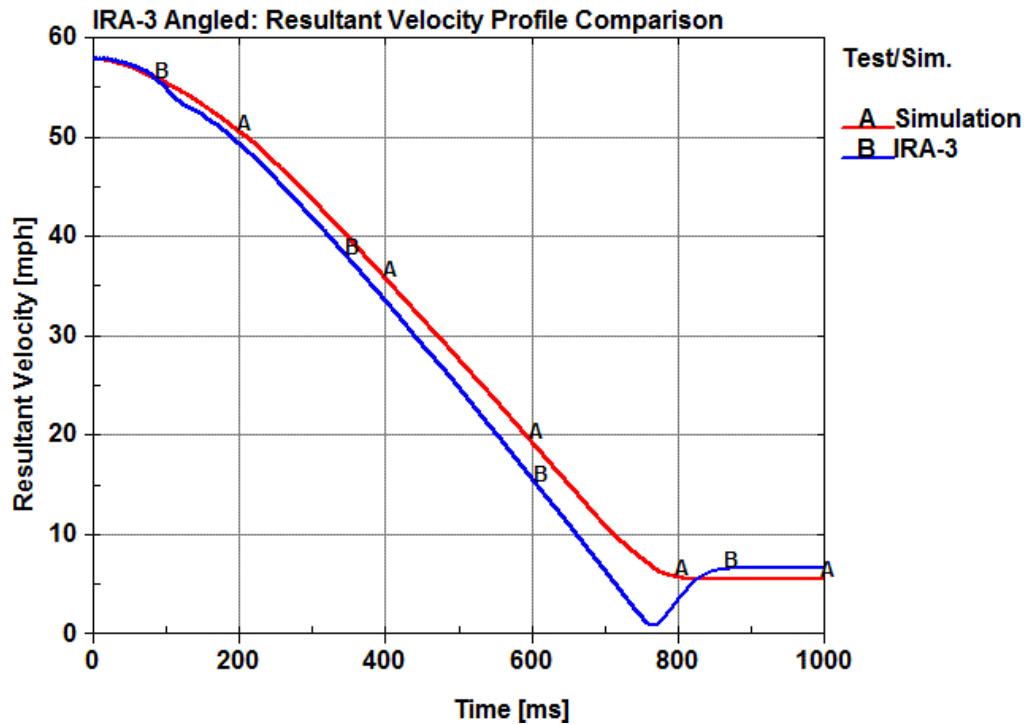


Figure 144. Velocity Profiles – Baseline Simulation and Test No. IRA-3

21.2.3 Occupant Risk

The calculated occupant impact velocities (OIVs) and maximum 0.010-sec occupant ridedown accelerations (ORAs) in both the longitudinal and lateral directions are shown in Table 41. Note that the OIVs and ORAs were within the suggested limits provided in MASH, although the velocity was slightly less than a MASH TL-3 test, and the mass of the bogie vehicle was slightly higher than the MASH 2270P vehicle. The occupant impact velocity between the simulation and the physical crash test was comparable; however, the longitudinal ORA was

under-predicted by 16.5 percent. If the vehicle model in the simulation had a shorter stopping distance, the longitudinal ORA would be increased. Further details of these predictions are located in Appendix F.

Table 41. Comparison of OIV and ORA Values, Baseline Simulation and Test No. IRA-4

Evaluation Criteria		Baseline Simulations	Test No. IRA-3 Transducers		MASH Limits
			DTS SLICE-1	DTS SLICE-2	
OIV ft/s (m/s)	Longitudinal	18.44 (5.62)	19.24 (5.86)	19.31 (5.89)	≤ 40 (12.2)
	Lateral	0.4 (0.12)	0.20 (0.06)	0.16 (0.05)	≤40 (12.2)
ORA g's	Longitudinal	3.98	4.64	4.68	≤ 20.49
	Lateral	0.65	1.87	2.00	≤ 20.49

21.2.4 Discussion of Test No. IRA-3

Several metrics, including a visual analysis and comparisons between velocity profiles, maximum net attenuator deflections, and occupant risk values, were used to evaluate the baseline net attenuator model. It was determined that the angled simulation did not adequately capture the behavior of the vehicle in test no. IRA-3. The bogie vehicle in the simulation yawed to the left as it hit the net. The coefficient of friction between the tires and the ground was low, which allowed the vehicle to yaw without much resistance. There was very little sliding between the net and the bogie head. The model did not produce results that were comparable with bogie crash test no. IRA-3. There were no vehicle instabilities in test no. IRA-3, but the vehicle did rotate out of the system in the simulation.

21.3 Discussion

The simulations of the net attenuator system indicated successful performance with the 5,259-lb (2,385-kg) bogie vehicle. However, there were modeling assumptions and physical test details that resulted in discrepancies between the simulation and the bogie test. Using constrained nodal rigid bodies for the cable-to-spreader attachment is different than the physical crash test. In the physical crash test, the vertical spreaders deformed and slid along the cable when the bogie impacted the net. In the simulation model, the vertical spreaders could not slide. Although this may be insignificant in terms of the final displacement for a central impact, it did have an influence in the capturing of a vehicle in an angled test. With a better vertical spreader and cable modeling connection, the baseline and angled simulations could be used in future testing to investigate the performance of the system when there is a slope behind the net. The connection may be as simple as using beam elements with the characteristics of the bolts used in the physical component testing.

The average force level from test no. IRAS-2 was used to prescribe a constant force for the nonlinear discrete element, which proved to be an acceptable assumption given the close correlation with the maximum system displacements. In future simulations, a parameter study could be performed to determine the maximum allowable energy absorber force for a given net width. If new energy absorbers were developed, average force levels from quasi-static testing could be used to estimate the maximum dynamic deflection.

There were multiple instances in this model where shared nodes were used to connect rigid components instead of modeling the physical components, such as shackles or eye nuts. Thus, the model presented herein was only suitable for impacts into the net where the vehicle would not interact with these connections. The influence of these connections could become more important with impacts closer to the sides of the net.

This model would be useful for future investigations into the net attenuator concept. Future simulations could involve slopes, higher energy forces, and more complex vehicle models.

22 NET ATTENUATOR ANALYSIS

An analytical method exists to estimate the performance of the Dragnet net attenuator system [51]. This method was modified to further investigate performance of the prototype net attenuator system when configured with different energy-absorber load capacities. As such, this method could be used to estimate the maximum dynamic deflection of the system using different vehicles, net widths, and energy absorber capacities.

22.1 Methodology

In 1969, TTI completed testing on the Dragnet Vehicle Arresting System [51], with energy absorbers similar in operation to those used in quasi-static test nos. IRAS-1 and IRAS-2 and bogie test nos. IRA-1 through IRA-4. Equations were developed to help select an appropriate energy-absorber tension force and length of tape required for a given vehicle mass and speed. The equations were derived for the simplified case of an angular or perpendicular impact into the center of the net. For treatment of bridge rail ends near intersecting roadways, many different impact scenarios are possible. Therefore, it was desirable to rederive those equations for investigating, for any impact location or angle.

The maximum dynamic deflection was estimated using an energy balance of the initial kinetic energy of the vehicle and the work done on the vehicle by the resistive force of the energy absorbers. Although the energy absorber force was assumed to be constant, the force on the vehicle is a function of the distance traveled in the system.

The following assumptions were used:

- all of the kinetic energy is absorbed by the energy absorbers,
- the energy absorbers provide a constant resistive force,
- the vehicle is assumed to travel in a straight line following the initial trajectory,

- the effective length of the net is considered as the distance between the anchorage points,
- no sliding occurs between the front of the vehicle and the net, and
- no stretching occurs in the net.

A general overhead view of the system is shown in Figure 136.

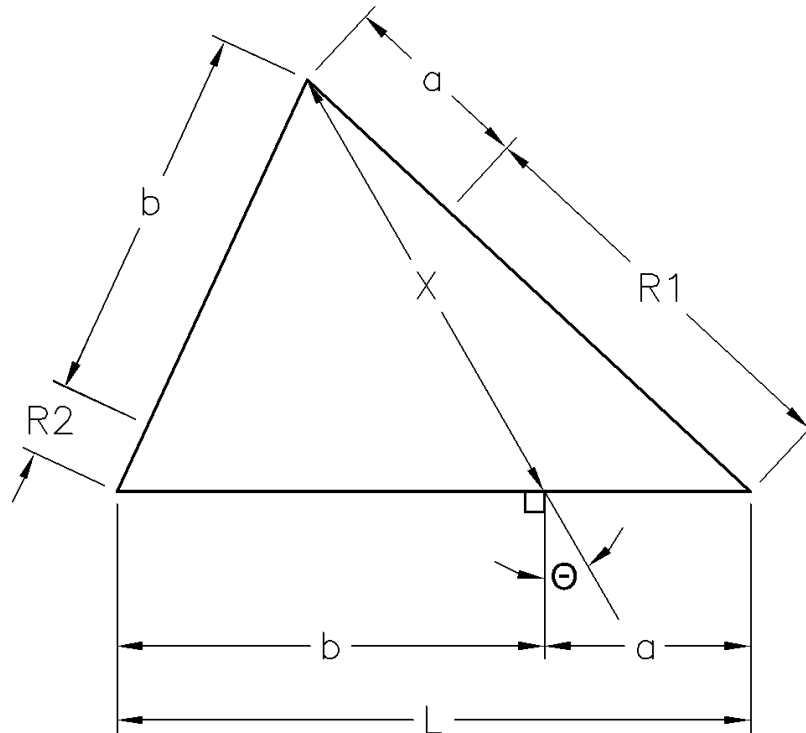


Figure 145. Net Attenuator Analytical Method and FBD setup

In Figure 145:

- L = Effective length of net ($a + b$) (ft)
- T = Energy absorber constant tension force (lb)
- θ = Angle of impact from perpendicular (deg)
- R_1 = Length of tape pulled from right energy absorber (ft)
- R_2 = Length of tape pulled from left energy absorber (ft)
- X = Travel distance of vehicle after engaging net (ft)

F_{R1} = Force component from right energy absorber acting opposite of vehicle trajectory (lb)

F_{R2} = Force component from left energy absorber acting opposite of vehicle trajectory (lb)

F_t = ($F_{R1} + F_{R2}$) or total force acting opposite of vehicle trajectory (lb)

W = Weight of vehicle (lb)

v = Initial velocity of vehicle (ft/s)

g = Acceleration due to gravity (32.174 ft/s²)

G = Acceleration on vehicle (g's)

KE = Kinetic energy of vehicle (ft-lb)

The force on the vehicle is a function of the vehicle's position in the system. Distances a and b are determined from the initial impact point in the system. To determine the amount of tape pulled out of each energy-absorber, R_1 and R_2 , the Pythagorean Theorem is used:

$$(R_1 + a)^2 = (a + X \cdot \sin \theta)^2 + (X \cdot \cos \theta)^2 \quad (1)$$

$$(R_2 + b)^2 = (b - X \cdot \sin \theta)^2 + (X \cdot \cos \theta)^2 \quad (2)$$

Then R_1 and R_2 can then be calculated:

$$R_1 = (a^2 + X^2 + 2aX \cdot \sin \theta)^{\frac{1}{2}} - a \quad (3)$$

$$R_2 = (b^2 + X^2 - 2bX \cdot \sin \theta)^{\frac{1}{2}} - b \quad (\text{For } X > 2b \cdot \sin \theta) \quad (4)$$

$$R_2 = 0 \quad (\text{For } X \leq 2b \cdot \sin \theta) \quad (5)$$

Note: ($2b \cdot \sin \theta$) is derived from Law of Sines

For X in terms of R_1 or R_2 :

$$X = (a^2 \cdot \sin^2 \theta + R_1^2 + 2bR_1)^{\frac{1}{2}} - a \cdot \sin \theta \quad (6)$$

The vehicle's kinetic energy is related to the theoretical total strap pullout by:

$$KE = \frac{Wv^2}{2g} = T(R_{1max} + R_{2max}) \quad \text{For } \theta \neq 0 \quad (7)$$

Forces F_{R1} and F_{R2} are the components of the energy absorber tension force T that are parallel to the vehicle's path and resist the movement. The forces that are perpendicular to the vehicle's path are neglected, and the trajectory is a straight line. In actual impact, unbalanced lateral forces would tend to cause the vehicle to yaw.

$$F_{R1} = T \left(\frac{X + a \cdot \sin \theta}{R_1 + a} \right) = \frac{T(X + a \cdot \sin \theta)}{(a^2 + X^2 + 2aX \cdot \sin \theta)^{\frac{1}{2}}} \quad (8)$$

$$F_{R2} = T \left(\frac{X - b \cdot \sin \theta}{R_2 + b} \right) = \frac{T(X - b \cdot \sin \theta)}{(b^2 + X^2 - 2bX \cdot \sin \theta)^{\frac{1}{2}}} \quad (9)$$

The total force on the vehicle can then be found by combining these component forces, as shown in Figure 146:

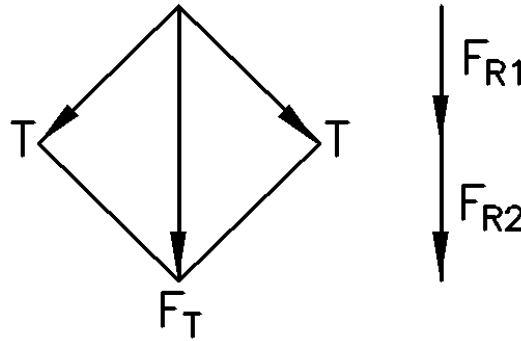


Figure 146. Free-Body-Diagram of the Vehicle

$$F_T(X) = F_{R1} + F_{R2} \quad (10)$$

$$F_T(X) = T \left(\frac{(X + a \cdot \sin \theta)}{(a^2 + X^2 + 2aX \cdot \sin \theta)^{\frac{1}{2}}} + \frac{(X - b \cdot \sin \theta)}{(b^2 + X^2 - 2bX \cdot \sin \theta)^{\frac{1}{2}}} \right) \quad (11)$$

For $X > 2b \cdot \sin \theta$

$$F_T(X) = T \left(\frac{(X + a \cdot \sin \theta)}{(a^2 + X^2 + 2aX \cdot \sin \theta)^{\frac{1}{2}}} \right) \quad (12)$$

For $X \leq 2b \cdot \sin \theta$

Assuming that all of the vehicle's kinetic energy is absorbed by the energy absorber,
then:

$$KE = \frac{Wv^2}{2g} = \int_0^{X_{max}} F_T dx \quad (13)$$

$$= T \int_0^{X_{max}} \left(\frac{X + a \cdot \sin \theta}{(a^2 + X^2 + 2aX \cdot \sin \theta)^{\frac{1}{2}}} \right) dx + T \int_{2b \cdot \sin \theta}^{X_{max}} \left(\frac{X - b \cdot \sin \theta}{(b^2 + X^2 - 2bX \cdot \sin \theta)^{\frac{1}{2}}} \right) dx$$

For $X > 2b \cdot \sin \theta$

Integration of the Equation 14 by parts requires the following:

$$u = (a^2 + X^2 + aX \cdot \sin \theta)$$

$$v = (b^2 + X^2 - bX \cdot \sin \theta)$$

$$du = (2X + 2a \cdot \sin \theta) dx$$

$$dv = (2X - 2b \cdot \sin \theta) dx$$

Therefore:

$$KE = \frac{Wv^2}{2g} = \frac{T}{2} \int_{u_i}^{u_f} u^{-\frac{1}{2}} du + \frac{T}{2} \int_{v_i}^{v_f} v^{-\frac{1}{2}} dv$$

$$= \frac{T}{2} \left(2u^{\frac{1}{2}} + 2v^{\frac{1}{2}} \right)_{initial}^{final}$$

$$= T \left((a^2 + X^2 + 2aX \cdot \sin \theta)^{\frac{1}{2}} \Big|_0^{X_{max}} + (b^2 + X^2 - 2bX \cdot \sin \theta)^{\frac{1}{2}} \Big|_{2b \cdot \sin \theta}^{X_{max}} \right)$$

$$= T \left((a^2 + X_{max}^2 + 2aX_{max} \cdot \sin \theta)^{\frac{1}{2}} + (b^2 + X_{max}^2 - 2bX_{max} \cdot \sin \theta)^{\frac{1}{2}} - a - b \right)$$

Or:

$$KE = \frac{Wv^2}{2g} = T \left((a^2 + X_{max}^2 + 2aX_{max} \cdot \sin \theta)^{\frac{1}{2}} \right. \quad (14)$$

$$\left. + (b^2 + X_{max}^2 - 2bX_{max} \cdot \sin \theta)^{\frac{1}{2}} - a - b \right)$$

For $X > 2b \cdot \sin \theta$

$$KE = \frac{Wv^2}{2g} = T \left((a^2 + X_{max}^2 + 2aX_{max} \cdot \sin \theta)^{\frac{1}{2}} - a \right) \quad (15)$$

$$\text{For } X \leq 2b \cdot \sin \theta$$

Note that the expression for total energy is obtained by integrating $F_T dx$ is equal to $T \times (R_1 + R_2)$. The theoretical stopping distance (X) can then be determined algebraically by solving for (X_{max}). Equations (14) and (15), when solved for X , yield the stopping distance in Equations (16) and (17):

$$\begin{aligned} X_{max} = & (\text{sqrt}((-64a^2g^3T^3v^2W \cdot \sin(\theta) - 16ag^2T^2v^4W^2 \cdot \sin(\theta) \\ & + 64b^2g^3T^3v^2W \cdot \sin(\theta) + 16bg^2T^2v^4W^2 \cdot \sin(\theta))^2 \\ & - 4(64a^2bg^3T^3v^2W + 16a^2g^2T^2v^4W^2 + 64ab^2g^3T^3v^2W \\ & + 48abg^2T^2v^4W^2 + 8agTv^6W^3 + 16b^2g^2T^2v^4W^2 \\ & + 8bgTv^6W^3 + v^8W^4)(-32a^2g^4T^4 \cdot \cos(2\theta) - 32a^2g^4T^4 \\ & - 64abg^4T^4 \cdot \cos(2\theta) - 64abg^4T^4 - 64ag^3T^3v^2W \\ & - 32b^2g^4T^4 \cdot \cos(2\theta) - 32b^2g^4T^4 - 64bg^3T^3v^2W \\ & - 16g^2T^2v^4W^2)) + 64a^2g^3T^3v^2W \cdot \sin(\theta) + 16ag^2T^2v^4W^2 \\ & \cdot \sin(\theta) - 64b^2g^3T^3v^2W \cdot \sin(\theta) - 16bg^2T^2v^4W^2 \\ & \cdot \sin(\theta)) / (2(-32a^2g^4T^4 \cdot \cos(2\theta) - 32a^2g^4T^4 - 64abg^4T^4 \\ & \cdot \cos(2\theta) - 64abg^4T^4 - 64ag^3T^3v^2W - 32b^2g^4T^4 \cdot \cos(2\theta) \\ & - 32b^2g^4T^4 - 64bg^3T^3v^2W - 16g^2T^2v^4W^2)) \end{aligned} \quad (16)$$

$$\begin{aligned} X_{max} = & \left(-\text{sqrt}(64a^2g^4T^4 \cdot \sin^2(\theta) - 16g^2T^2(v^4(-W^2) - 4agTv^2W)) \right. \\ & \left. - 8ag^2T^2 \cdot \sin(\theta) \right) / (8g^2T^2) \end{aligned} \quad (17)$$

(When only one energy absorber is engaged during an angled impact)

The theoretical maximum G-force on the vehicle for a given energy absorber force (T) occurs when both energy absorbers are directly opposing the motion of the vehicle. The deceleration of the vehicle can approach this maximum when L is small relative to the stopping distance:

$$F_{R_1} = F_{R_2} = T \quad (18)$$

$$G_{max} = \frac{2T}{W} \quad (19)$$

The deceleration of the vehicle at any distance X is then:

$$G(X) = \frac{T}{W} \left(\frac{(X + a \cdot \sin \theta)}{(a^2 + X^2 + 2aX \cdot \sin \theta)^{\frac{1}{2}}} + \frac{(X - b \cdot \sin \theta)}{(b^2 + X^2 - 2bX \cdot \sin \theta)^{\frac{1}{2}}} \right) \quad (20)$$

22.2 Comparison of Original and New Analytical Technique

Previous test data was used to verify the new equations for calculating the deceleration of the vehicle and the stopping distance. Six full-scale crash tests were performed by TTI [51] during the initial test of the Dragnet system. Two tests were conducted on the “DRAGNET Work ZoNet” to obtain NCHRP Report No. 350 TL-3 approval [48]. The original equations found in the report published by TTI [51] and a Dragnet product manual [52] could not provide enough information to calculate the stopping distance and deceleration of the vehicle directly from equations. A comparison of the actual test data, original calculations, and new equations is shown in Table 42. The simplified equations for calculating the stopping distance with a perpendicular impact into the center of the net and the deceleration of the vehicle for a perpendicular impact that could be offset from the center are noted below.

$$X_{max} = \sqrt{\left(\frac{WV^2}{4gT}\right) \left(\frac{WV^2}{4gT} + L\right)} \quad (21)$$

$$G(X) = \left(\frac{T}{W}\right) \left(\frac{X}{\sqrt{(X^2 + a^2)}} + \frac{X}{\sqrt{X^2 + b^2}}\right) \quad (22)$$

Table 42. Comparison of Dragnet System with Analytical Calculations

Test Ref.	Test No.	Inputs for Analytical Equations					Deflection				Deceleration		
		Θ Impact Angle Deg.	T Tape Force kip (kN)	L Net Width ft (m)	W Weight lb (kg)	v Velocity ft/s (m/s)	Actual ft (m)	Original ³ ft (m)	New ⁵ ft (m)	Actual g/s	Original ⁴ g/s	New ⁵ g/s	
51	4A	0	25.0 (111.2)	33.0 (10.1)	1460 (662)	61.6 (18.8)	8.4 (2.6)	7.73 (2.36)	7.73 (2.36)	16	14.53	14.53	
	4B	0	25.0 (111.2)	33.0 (10.1)	4300 (1950)	88.0 (26.8)	18.4 (5.6)	21.18 (6.46)	21.18 (6.46)	16	9.17	9.17	
	4C	30	25.0 (111.2)	33.0 (10.1)	1620 (735)	70.4 (21.5)	12.9 (3.9)	7.6 ² (2.32)	10.45 (3.18)	13	N/A	14.61	
	4D	30	25.0 (111.2)	33.0 (10.1)	4520 (2050)	79.2 (24.1)	22.0 (6.7)	20.2 ² (6.2)	20.30 (6.19)	8	N/A	8.52	
	4E	0	12.5 (55.6)	33.0 (10.1)	3760 (1706)	82.1 (25.0)	26.0 (7.9)	27.73 (8.45)	27.73 (8.45)	7	5.71	5.71	
	4F ¹	30	12.5 (55.6)	33.0 (10.1)	3880 (1760)	90.9 (27.7)	29.0 (8.8)	29.5 ² (9.0)	33.36 (10.17)	5	N/A	5.85	
48	01-7629-001	0	4.5 (20.0)	38.0 (11.6)	4410 (2000)	85.5 (26.1)	70.5 (21.5)	72.31 (22.04)	72.31 (22.04)	2.4	1.99	1.99	
	01-7629-002	0	4.5 (20.0)	38.0 (11.6)	1810 (821)	94.0 (28.7)	40.0 (12.2)	42.60 (12.98)	42.60 (12.98)	3.9	4.64	4.64	
1. Test vehicle was not stopped by the net attenuator [51]													
2. Not calculated, reference text measured from graph [51]													
3. Calculated using Equation 22 unless otherwise noted (1969 method [51])													
4. Calculated using Equation 23 unless otherwise noted (method found in product manual [52])													
5. Calculated using Equations 17 and 21 presented in this document													

The new equations were able to calculate stopping distances and decelerations in all cases whereas previously, no equations were available for certain impact conditions. The new general equations provided the same values as the previous equations, except that they can accommodate a wide range of impact conditions. Both methods had good correlation with the test data and were suitable for making estimates for higher-capacity energy absorbers.

22.3 Analysis of Test Nos. IRA-3 and IRA-4

The verified equations were incorporated into an Excel spreadsheet program to calculate the maximum deflection and deceleration for impacts at any angle or location within the system. The analytical method could be used to closely determine the dynamic deflection, and peak decelerations could be predicted. Data from test nos. IRA-3 and IRA-4 were used, because both tests had all six energy absorbers working for most of the impact event. The deceleration on the vehicle increases as the vehicle travels farther into the system; therefore, the maximum ORA value occurred at the end of the event. Occupant impact velocity was not considered for this analysis, because the forces on the vehicle were initially much lower than end terminal or crash cushion systems, and the test was unlikely to violate the limits in MASH [3].

The effective length of the net was considered to be the distance between anchorage points of the middle energy absorbers on the left and right side of the net attenuator, as shown in Figure 147. The effective widths of version 1 (test nos. IRA-1 and IRA-2) and version 2 (test nos. IRA-3 and IRA-4) of the system were 55 ft - 4 ⁹/₁₆ in. (16.9 m) and 55 ft - 10 ⁵/₈ in. (17.0 m), respectively. Version 1 would be able to accommodate a wider range of angled impacts without the energy absorbers crossing over one another, but during component testing some of the innermost energy absorbers' tapes were rupturing. Version 2 alleviated these problems by decreasing the angle between the net and the energy absorbers, thus reducing the range of impact angles but increasing reliability. The inner- and outermost energy absorbers would contribute the

most and least, respectively, to the force applied to the vehicle when all energy absorbers are engaged. The middle energy absorber was assumed to be the average of both. This configuration does not exactly represent the conditions of test. The relative contribution of each energy absorber would change as deflection increased.

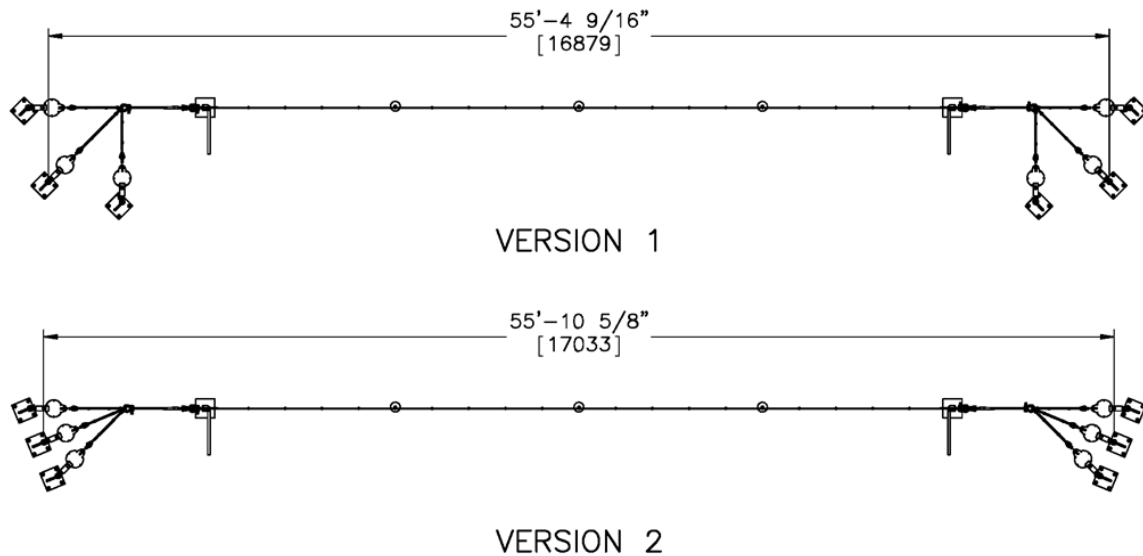


Figure 147. Effective Length of Versions 1 and 2

22.3.1 Analysis of Test No. IRA-3

The analytical model was compared against accelerometer data from test no. IRA-3, as shown in Table 43. The input parameters that were used in the analytical solution of test no. IRA-3 are shown in Table 43, while a graphical representation of the results are shown in Figure 148.

Table 43. Input Parameters for Analytical Solution of IRA-3

Test No.	Net Width L ft (m)	Offset a ft (m)	Impact Angle Θ Deg	Tape Force T lbf (kN)	Weight W lb (kg)	Velocity v ft/s (m/s)	Gravity Constant ft/s ² (m/s ²)
IRA-3	55.88 (17.03)	15.94 (4.859)	-30	11,700 (52.0)	5,259 (2,385)	85.11 (25.94)	32.174 (9.81)

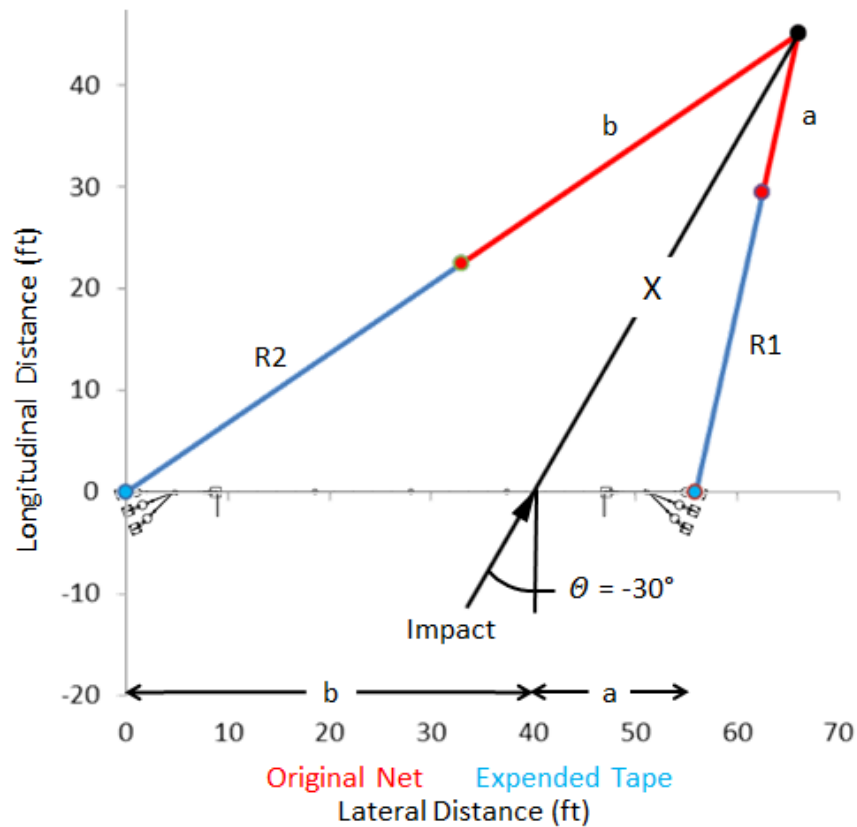


Figure 148. Analytical Solution for Test No. IRA-3

The analytical method calculated a maximum deflection of 50.5 ft (15.4 m), compared to 37.6 ft (11.5 m) in test no. IRA-3. The calculated ORA in the longitudinal direction for the analytical solution, simulation, and test no. IRA-3 were 4.13 g's, 4.02 g's, and 4.64 g's, respectively. A comparison of the accelerations of the analytical model and physical crash test are shown in Figure 149. The analytical solution under-predicted the accelerations on the vehicle

and over-predicted the stopping distances. It should be noted that the vehicle was not captured in the angled simulation and had begun to yaw out of the system when the simulation ended.

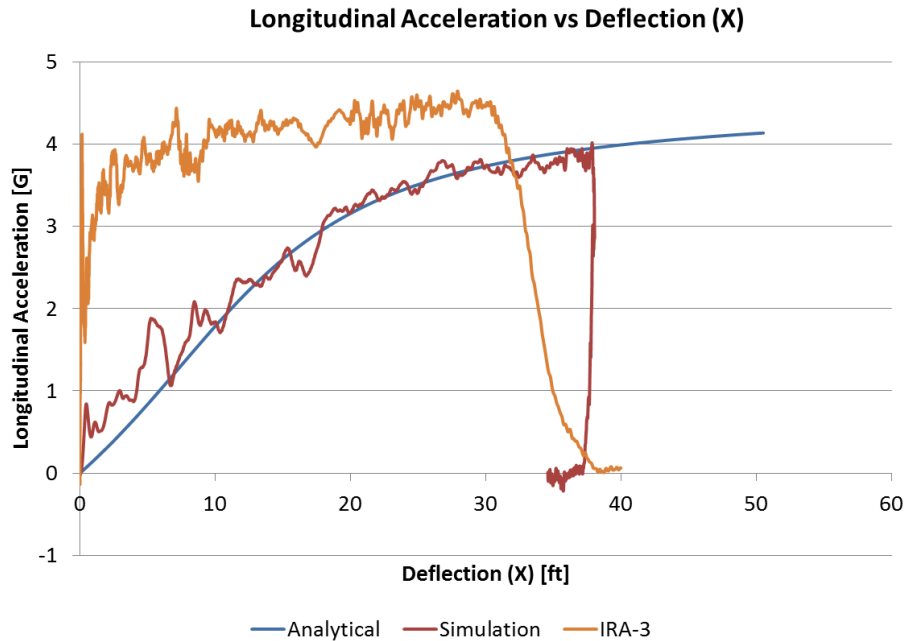


Figure 149. Analytical Model, Angled Simulation, and Test No. IRA-3 Accelerations

The discrepancies between the analytical model and the physical crash test are likely due to some of the assumptions of the analytical solution. When the vehicle impacted the net, it was assumed that the net would not slide along the front of the vehicle. The implications were that during an angled impact, one end of the net would be slack until the vehicle had traveled a sufficient distance into the system for the net to be taut again. During test no. IRA-3, the net slid along the front face of the impact head until both energy absorbers were engaged. With both energy absorbers engaged sooner in the event, the increased force on the vehicle caused higher decelerations and a shorter stopping distance. The analytical method made poor estimates of the stopping distance and the accelerations on the vehicle. The estimated stopping distance was 34 percent greater than the physical crash test. The calculated peak acceleration was only 11 percent

less than that of the actual test, but because the acceleration on the vehicle is a function of the distance X , the acceleration cannot be considered a good estimate.

22.3.2 Analysis of Test No. IRA-4

The analytical model was compared against full-scale crash test no. IRA-4. The input parameters that were used in the analytical solution of test no. IRA-4 are shown in Table 44, while a graphical representation of the results is shown in Figure 150.

Table 44. Input Parameters for Analytical Solution of IRA-4

Test	Net Width L ft (m)	Offset a ft (m)	Impact Angle Θ Deg	Tape Force T lbf (kN)	Weight W lb (kg)	Velocity v ft/s (m/s)	Gravity Constant g ft/s ² (m/s ²)
IRA-4	55.8 (17.0)	27.9 (8.5)	0	11,700 (52.0)	5,259 (2,385)	87.21 (26.58)	32.174 (9.81)

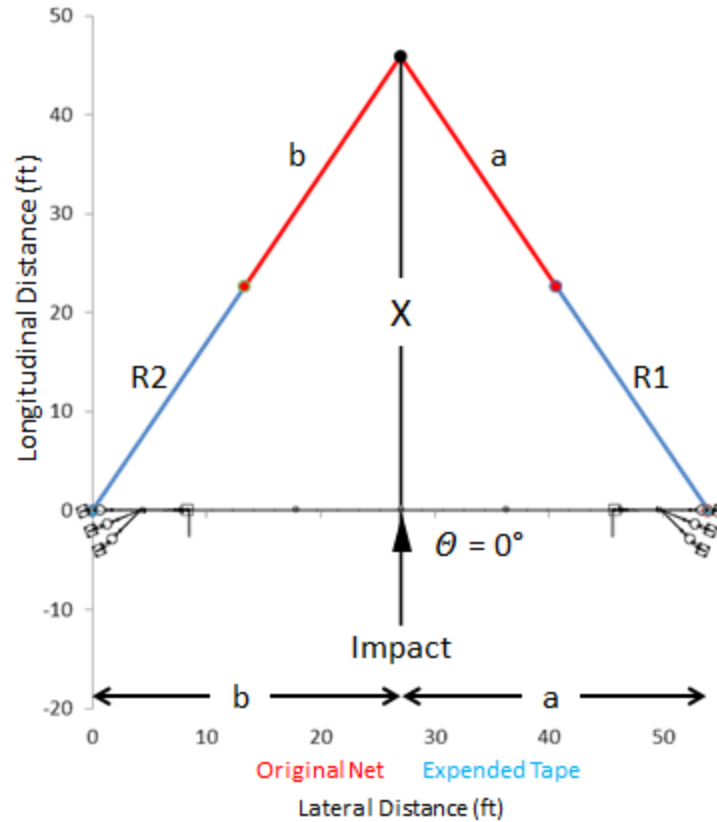


Figure 150. Analytical Solution for Test No. IRA-4

The analytical model calculated a maximum deflection of 46.6 ft (14.2 m), compared to 42.2 ft. (12.9 m) and 44.29 ft (13.50 m) for the physical crash test and simulation, respectively. The calculated ORA in the longitudinal direction for the analytical model, test no. IRA-4, and baseline simulation were 3.84 g's, 4.88 g's, and 3.91 g's, respectively. A comparison of the accelerations of the analytical model, simulation, and physical crash test is shown in Figure 151. For this central, perpendicular impact, there was much better correlation between the analytical method, physical component test, and simulation. The analytical method provided a conservative estimate of the maximum dynamic deflection and under-predicted the peak decelerations of test no. IRA-4.

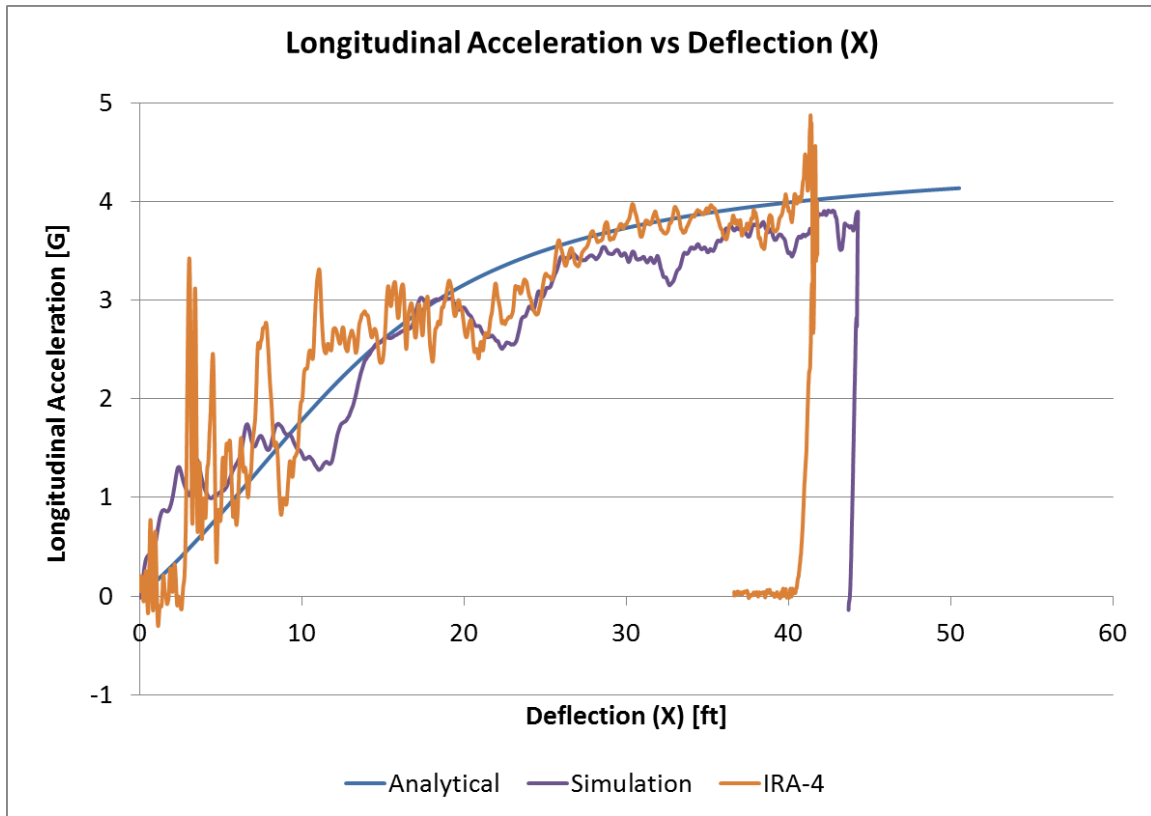


Figure 151. Analytical Model, Baseline Simulation, and Test No. IRA-4 Accelerations

22.4 Discussion

This analysis assumed that the vehicle was a point mass, and no consideration was given for the vehicle's geometry. In the model, the vehicle is represented by a point mass. Accounting for the width of the vehicle reduces the effective width of the net. Thus, the component forces on the vehicle would be higher, causing higher deceleration values and shorter stopping distances. Accounting for a vehicle's width would add considerable complexity to the equations presented in this report. For the scenarios considered in this report, the net width was much greater than the vehicle width. Thus, the effects on the stopping distance and accelerations would be minimal. However, these effects should be considered in future analyses of the prototype net attenuator system.

When assuming that the net would not slide along the front of the bogie in angled impacts, the vehicle will be closer to one of the energy absorbers than another at impact, thus causing one energy absorber to be slack and not contributing to the force on the vehicle until the vehicle is farther into the system. In an actual system, the net would likely slide along the face of the vehicle until both energy absorbers were engaged. This behavior was not considered in this analysis but would be necessary to accurately estimate stopping distances and decelerations in angled and offset impacts.

The estimate for the central, perpendicular impact in test no. IRA-4 was conservative for maximum dynamic deflection of the net but under-predicted the longitudinal ORA. The estimate for maximum dynamic deflection in the offset, angled impact in test no. IRA-3 was off by 34 percent. The maximum longitudinal deceleration calculated with the analytical method for test no. IRA-3 was only 11 percent less than that observed in the physical crash test. Because the calculated acceleration is a function of X , the acceleration likely would have been much lower had the vehicle not traveled as far into the system.

23 IMPACT ANALYSIS FOR INERTIA BARRIERS

Sand inertial barrels, sometimes referred to as inertia barriers or modules, are used in conjunction with an end terminal or crash cushion in Concept K. To evaluate Concept K and develop potential configurations, a plan was needed to analyze large arrays of sand barrels. The large area that needed to be protected, in addition to multiple potential impact locations and angles, required the development of non-standard, sand barrel configurations. While the *Roadside Design Guide* provided a methodology for analyzing inertia barrier impacts, guidelines for partial barrel impacts or multiple barrel interactions prevalent in large arrays were not discussed [1].

23.1 Inertia Barrier Analysis for Head-On Impacts

The *Roadside Design Guide* [1] outlines a method for analyzing head-on impacts where sand barrels are used to protect a narrow concrete barrier end or other hazard. A typical situation where a vehicle impacts the nose of an array with all of the barrels inside the path of the vehicle is shown in Figure 152. As the vehicle travels through the system, each new contacted barrel is considered a distinct impact event. When multiple barrels are contacted at the same time, the mass of the barrels is combined to form the same impact event.

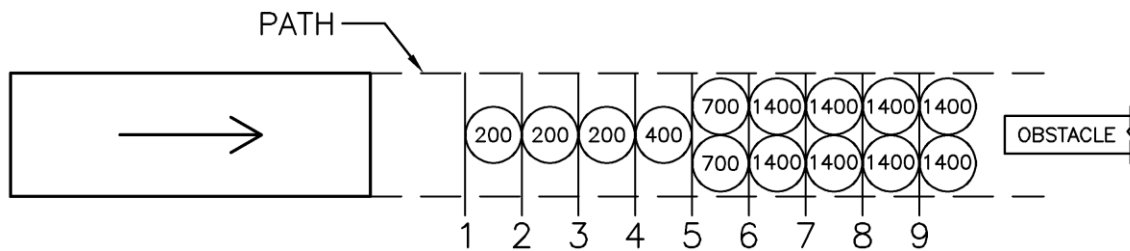


Figure 152. Typical Sand Barrel System [1]

Although other factors influence energy dissipation during an impact event, simple momentum transfer is used as the basis for predicting a system's performance. This analysis is discussed in the RDG and reproduced here [1]. Using the conservation of momentum principle:

Where:

- M_v = Mass of vehicle (lb)
- M_1 = Mass of sand in first contacted barrel (lb)
- M_n = Mass of sand in the n th impacted container(s)
- V_0 = Original impact velocity (ft/s)
- V_1 = Velocity after first impact (ft/s)
- V_n = Velocity after n th impact (ft/s)

$$M_v V_0 = M_v V_1 + M_1 V_1 \quad (23)$$

This equation can be rearranged such that:

$$V_1 = \frac{M_v V_0}{M_v + M_1} \quad (24)$$

The combined momentum of the vehicle and the sand after impact is assumed to be effectively equal to the momentum of the vehicle just before impact with the next barrel(s). This assumption implies that after the front of the vehicle has passed over the original location of the module, the sand has been completely dispersed and no longer contributes to absorbing the kinetic energy. Applying this in a sequential manner for each row of sand barrels impacted, the vehicle's speed after its n th impact is:

$$V_n = \frac{M_v V_{n-1}}{M_v + M_n} \quad (25)$$

For each row of sand barrels impacted, the deceleration distance is equal to the diameter of the barrel. The frangible plastic of the barrel breaks apart as it is struck by the vehicle. Frequently, the maximum deceleration in g 's is desired for an estimate of the occupant risk from

ridedown decelerations. The 1977 AASHTO *Guide for Selecting, Locating, and Designing Traffic Barriers* suggests a 12-g maximum average acceleration for crash cushions [53]. This limit is considered common practice for designing sand barrel systems and was used in lieu of the MASH ridedown acceleration limit of 20.49 g's [3]. Average acceleration is used in this analysis, because it is assumed that the velocity of the vehicle is immediately reduced after an impact with a barrel. This sudden drop in velocity would result in infinite, nonphysical accelerations that could not be used for assessing occupant risk. The average acceleration, a , and time between each impact event, t , can be calculated:

Where:

l_n = Deceleration distance for n th impact (ft)

a_n = Deceleration rate for n th impact (ft/s²)

g = Acceleration of gravity (32.174 ft/s²)

G_n = Deceleration rate for n th impact (G's)

t = Duration of n th event (s)

$$a_n = \frac{V_{n-1}^2 - V_n^2}{2l_n} \quad (26)$$

$$G_n = \frac{a_n}{g} \quad (27)$$

$$t_n = \frac{V_{n-1} - V_n}{a_n} \quad (28)$$

Other important criteria include the theoretical Occupant Impact Velocity (OIV) and Occupant Ridedown Acceleration (ORA). These criteria represent the hypothetical velocity and acceleration of an unbelted occupant upon impact with an interior surface. These values were estimated using the procedure outlined in MASH and the velocities and accelerations described above [3].

Theoretically, a vehicle will not be stopped using the conservation of momentum. For this reason, common practice is to design systems such that the velocity is reduced to below 10 mph (16 km/h) after the last module has been impacted. Manufacturers often recommend placing another row of heavy barrels beyond the point at which the vehicle's velocity is reduced to less than 10 mph (16 km/h), although this is not required [1]. In non-standard barrel configurations or angled impacts, some of the modules may only be partially impacted. A procedure for this scenario was not outlined in the RDG.

23.2 Analyzing Inertia Barrier Impacts - General Form

This section describes a method developed for analyzing more complex sand barrel arrays that accounts for barrels only partially struck by a vehicle and adjusts for a wide array of impact conditions. The method uses the same basic principles described previously, but modifications consider the discrete contributions of the mass of each impacted or partially impacted barrel.

Consider the large sand barrel array shown in Figure 153. A 2270P vehicle, represented as a rectangle, impacts the barrels with an assumed linear trajectory. Although the shape for many commercially available modules varies, this analysis considers all barrels to be perfect cylinders with a diameter of 36 in. (914 mm) and spaced 6 in. (152 mm) apart.

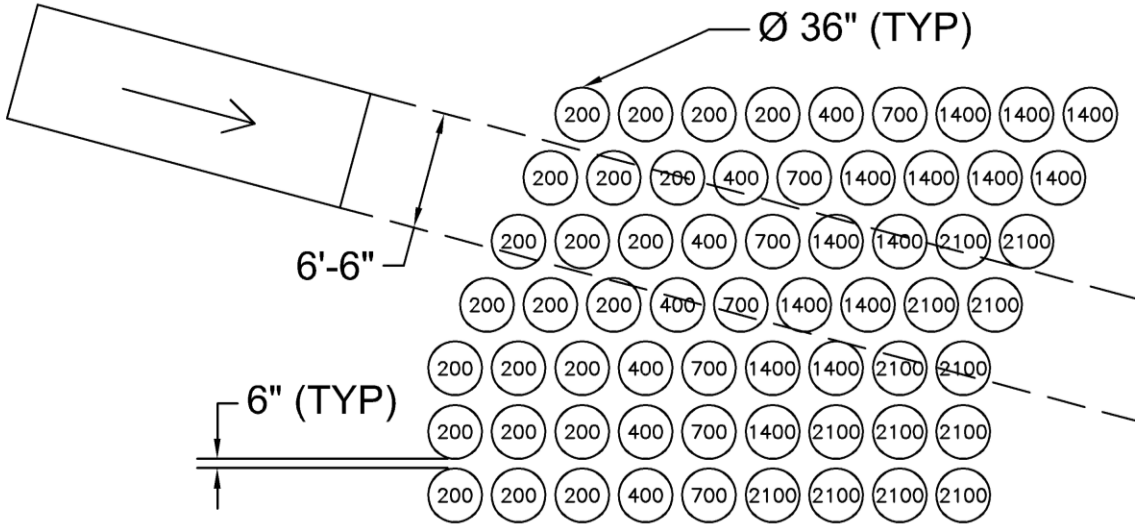


Figure 153. Large Sand Barrel Array

The contribution of each impacted barrel to momentum transfer needs to be determined. Because sand barrels are made of frangible plastic, the vehicle breaks apart the barrel and accelerates the sand and barrel fragments in all directions. For partial impacts, only the mass inside of the vehicle's path is assumed to contribute to momentum transfer, as shown in Figure 154.

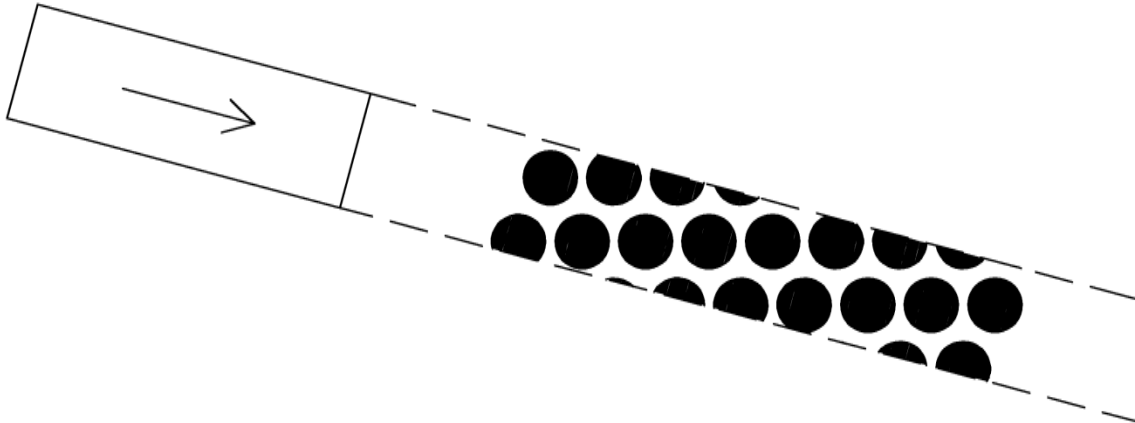


Figure 154. Effective Masses of Each Impacted Barrel

Each impact with a barrel is considered a unique event, as shown in Figure 155. The deceleration distance for each event is equal to either the distance between impact events or the length of contact with the barrel, whichever is less. The “length of contact” refers to the distance the vehicle interacts with the barrel. As shown in Figure 156, the length of contact is equal to the diameter of the barrel when the center of a module is inside the vehicle’s path (A and B). If the center of the module is outside of the path, then the length of contact is equal to the chord length of the split module (C).

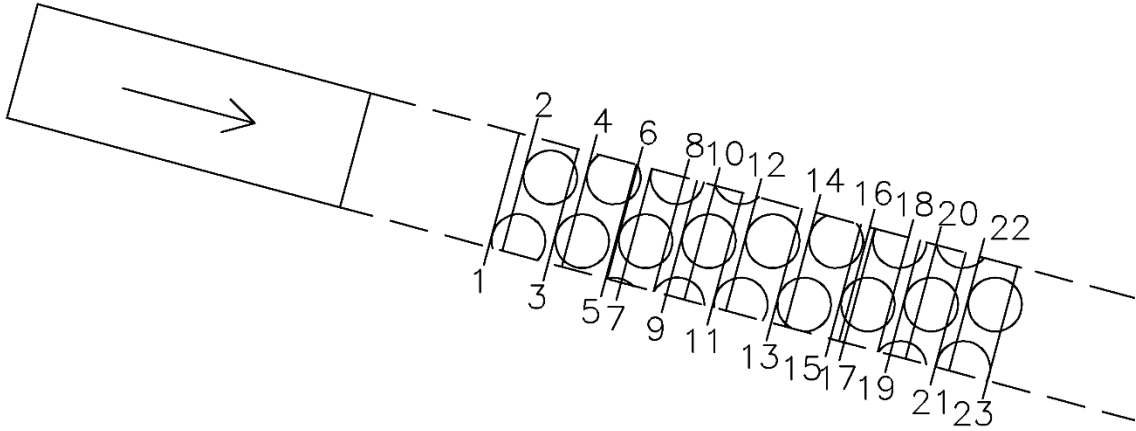


Figure 155. Impact Order and Deceleration Distance

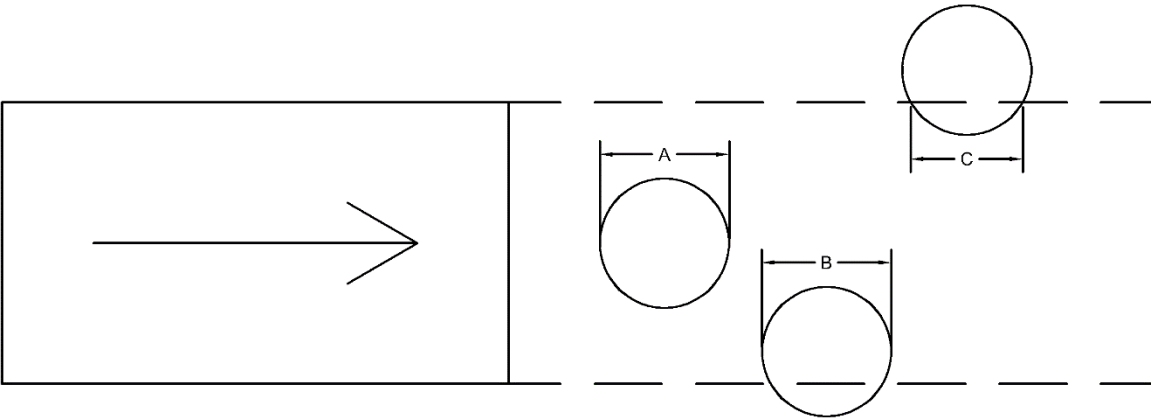


Figure 156. Length of Contact Description

The mass for impact event n is all of the mass that is located between impact n and impact $n+1$, as shown in Figure 157. Thus, not all of a barrel's mass would necessarily contribute to energy absorption during the same impact event.

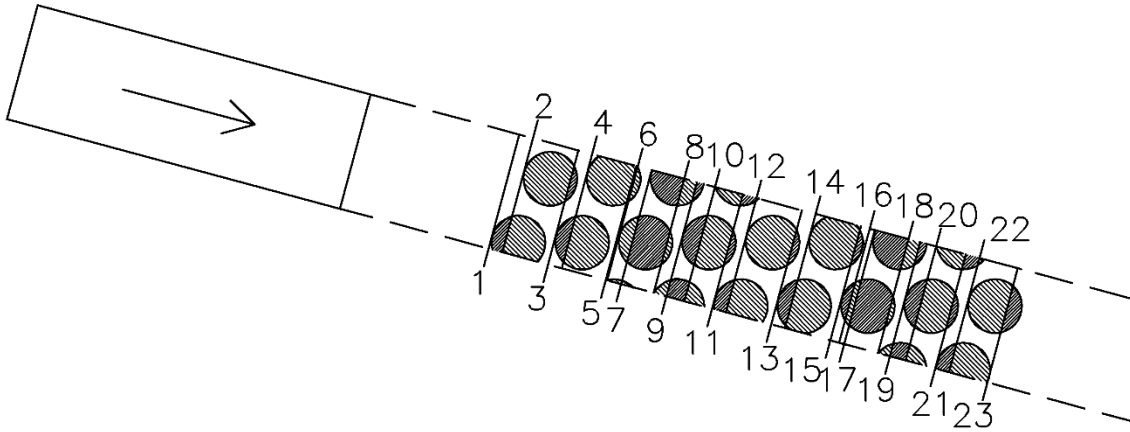


Figure 157. Mass Distribution Between Impact Events

23.2.1 Mass Distribution

Multiple methods for distributing mass between the impact events were considered. The mass of each barrel that is inside the path of the vehicle can be determined algebraically for all barrels that are impacted or partially impacted. Between each impact event, there may be one or more barrels that are contributing to momentum transfer. The barrels are split between each impact event. The mass of each barrel segment can be determined using the area of each barrel segment, dividing it by the total area of the barrel that lies inside the vehicle's path, and then multiplying it by the mass of the barrel that lies inside the path.

The first step in analyzing each impact event is to determine the amount of sand inside the vehicle's path:

Where:

$$D = \text{Diameter of sand barrel (ft)}$$

$$X_T = \text{Total area of sand barrel (ft}^2\text{)}$$

- X = Area of sand barrel inside of path (ft²)
- X_l = Area of circle with diameter equal to length of contact (ft²)
- K = Area of partially impacted sand barrel bisected by path (ft²)
- K_b = Area segment defined by diameter equal to length of contact and a width
- h = Distance from path to center of sand barrel (ft)
- c = Chord length of partially impacted sand barrel (ft)
- b = Distance of bisection from circle edge (ft)
- L_n = Distance from front of vehicle to impact point on barrel (ft)
- M_{X_T} = Total mass of sand barrel X (lb)
- M_X = Mass of sand barrel X contributing to momentum transfer (lb)
- M_n = Mass at impact event n (lb)

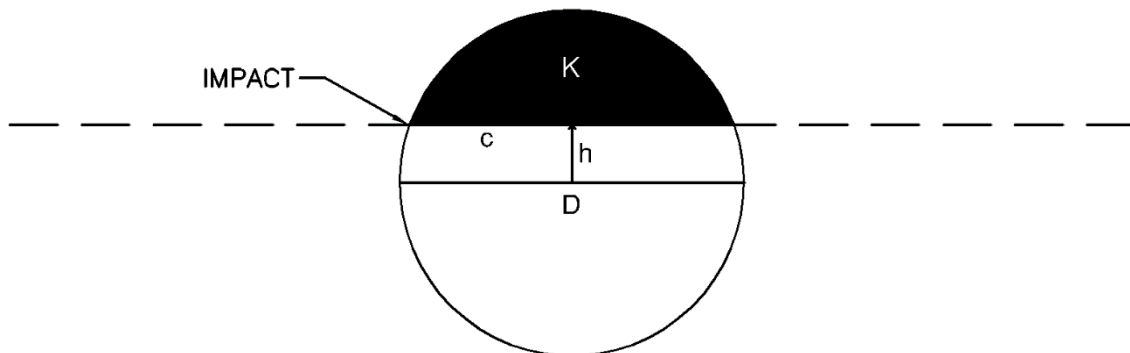


Figure 158. Details of Partially Impacted Sand Barrel

For barrel area, X_T :

$$X_T = \frac{\pi D^2}{4} \quad (29)$$

The distance from the path to the center h can be used to determine the area of a bisected circle. If the center of the module is inside the vehicle's path:

$$K_i = \frac{D^2}{4} \left(\pi - \cos^{-1} \left(\frac{2h}{D} \right) \right) + h \sqrt{\frac{D^2}{4} - h^2} \quad (30)$$

The area of the barrel segment if the center of the module is outside the vehicle's path:

$$K_o = \frac{D^2}{4} \cos^{-1} \left(\frac{2h}{D} \right) - h \sqrt{\frac{D^2}{4} - h^2} \quad (31)$$

And the chord length c is:

$$c = \sqrt{\frac{D^2}{4} - h^2} \quad (32)$$

The effective mass of the impacted sand barrel is thus:

$$\text{Full impact: } M_X = M_{X_T} \quad (33)$$

$$\text{Partial Impact, center inside path: } M_X = \left(\frac{K_i}{A} \right) M_{X_T} \quad (34)$$

$$\text{Partial impact, center outside path: } M_X = \left(\frac{K_o}{A} \right) M_{X_T} \quad (35)$$

The mass calculations for the first seven impacts of the large sand barrel array example are shown in Figure 159 and depicted in the following equations. For this example, barrel A corresponded with impact event no. 1, barrel B with impact event no. 2, and so on. Mass M_A was the mass of barrel A inside the vehicle's path, M_B , the mass of barrel B inside the vehicle's path, and so on. Mass M_1 was the sum of all sand barrel masses located between impact event no. 1 and 2, M_2 , the sum of all sand barrel masses between impact event no. 2 and 3, and so on.

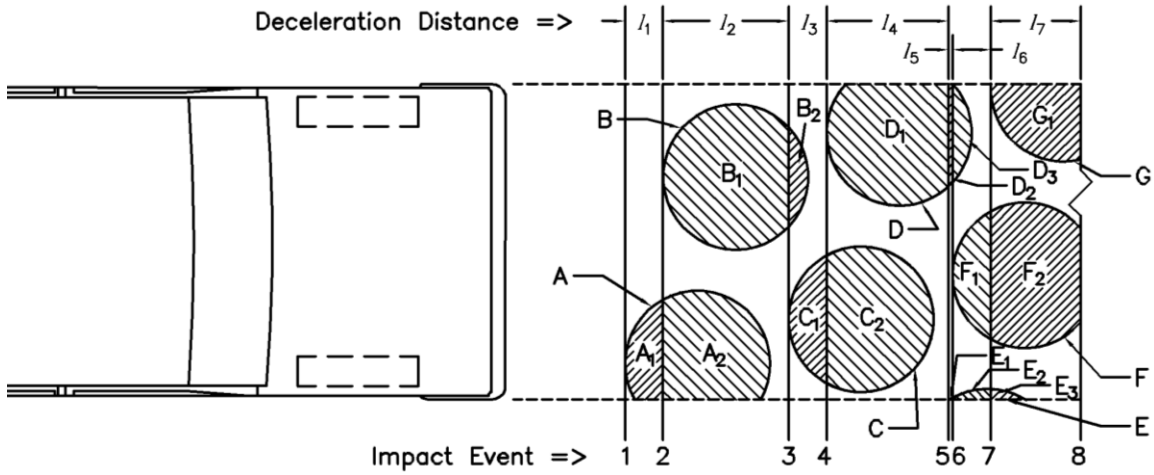


Figure 159. Mass Distribution Between Impact Events

$$M_1 = \left(\frac{A_1}{A}\right) M_A \quad (36)$$

$$M_2 = \left(\frac{B_1}{B}\right) M_B + \left(\frac{A_2}{A}\right) M_A \quad (37)$$

$$M_3 = \left(\frac{C_1}{C}\right) M_C + \left(\frac{B_2}{B}\right) M_B \quad (38)$$

$$M_4 = \left(\frac{D_1}{D}\right) M_D + \left(\frac{C_2}{C}\right) M_C \quad (39)$$

$$M_5 = \left(\frac{E_1}{E}\right) M_E + \left(\frac{D_2}{D}\right) M_D \quad (40)$$

$$M_6 = \left(\frac{F_1}{F}\right) M_F + \left(\frac{E_2}{E}\right) M_E + \left(\frac{D_3}{D}\right) M_D \quad (41)$$

$$M_7 = \left(\frac{G_1}{G}\right) M_G + \left(\frac{F_2}{F}\right) M_F + \left(\frac{E_3}{E}\right) M_E \quad (42)$$

23.2.1.1 Ideal Mass Distribution

Ideally, the exact area for each split barrel segment would be calculated algebraically. For large sand barrel arrays, this results in many calculations. A more efficient method for calculating the area would be to use a CAD program to find all of the bisected areas. Whether the areas of the barrel segments are calculated algebraically or with CAD, the mass of each barrel segment can be determined using the area of each barrel segment, dividing it by the total area of

the barrel that lies inside the vehicle's path, and then multiplying it by the mass of the barrel that lies inside the path. Two different cases are geometrically represented in Figure 160, where segment area X_1 and X_2 are divided by area X to provide a ratio. The first case is where the individual sections are only split once. The scenario in Case 2 occurs when a section is taken out of the middle of the circle. Both of the cases shown in Figure 160 have a portion of the barrel that is outside of the path of the vehicle and does not contribute to the mass calculation.

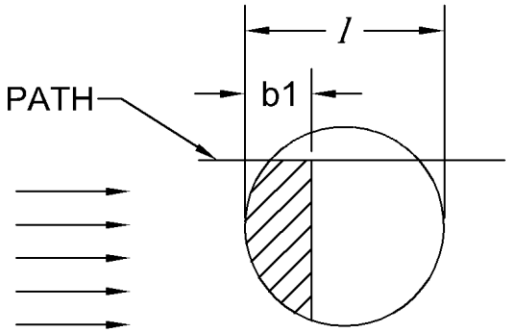
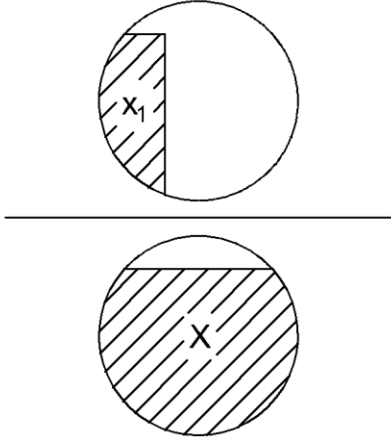
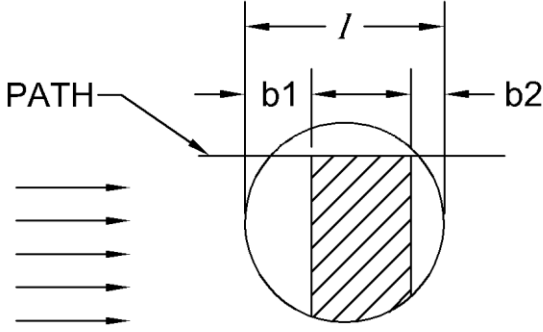
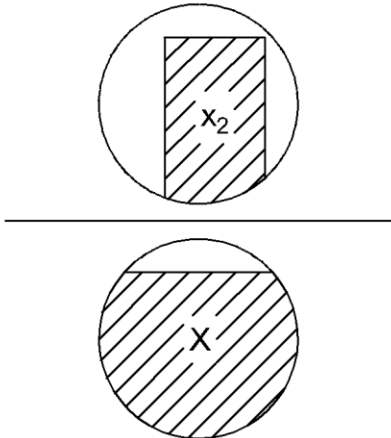
Impact Scenario	Mass Ratio (Ideal Distribution)
<p>Case 1: The impacted section is taken from the edge of the module.</p> 	
<p>Case 2: The impacted section is taken from the middle of the module.</p> 	

Figure 160. Ideal Mass Distribution

23.2.1.2 Mass Distribution by Linear Approximation

Although the exact area for each split barrel can be calculated algebraically or by using a drafting program for each instance, this task is often time-consuming. Instead of trying to

calculate each individual area, a simpler method is to assume that the effective mass of each barrel is evenly distributed along the length of contact l with the barrel.

The location of the center of each barrel is known. Knowing the center position of the barrel relative to the impact events allows the masses to be split among the different impact events. A geometric representation of this approximation is shown in Figure 161. The hatched areas for Cases 1 and 2 represent a section of a barrel that is contributing to the mass at some impact event. In Case 1, the width of the first barrel section is divided by the overall length of contact to calculate the mass ratio. In Case 2, the width of the middle barrel segment is divided by the overall length of contact. The distance that the vehicle is in contact with the barrel is used instead of the diameter of the barrel in partial impacts where the center of the barrel is outside the vehicle's path.

If the vehicle passes through the entire barrel before the next barrel is struck:

$$\frac{L_{n+1} - L_n - l_n}{l_n} (M_n) \quad (43)$$

If barrel(s) $n+1$ are struck before the vehicle has passed completely over barrel n :

$$\frac{L_{n+1} - L_n}{l_n} (M_n) \quad (44)$$

The mass from previous barrels $n-u$ are included in the same fashion if:

$$(L_{n-u} + l_{n-u}) \geq L_N \quad (45)$$

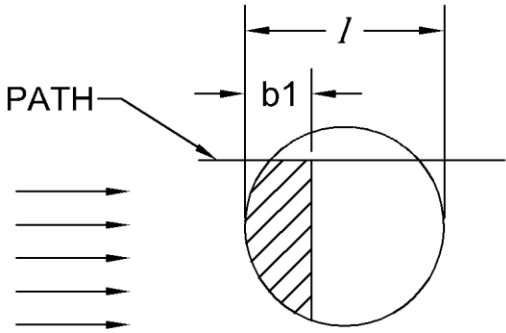
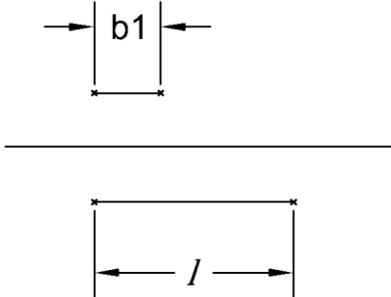
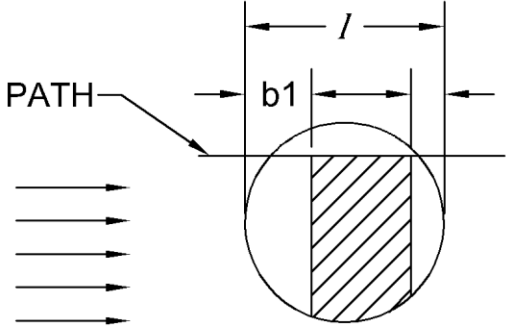
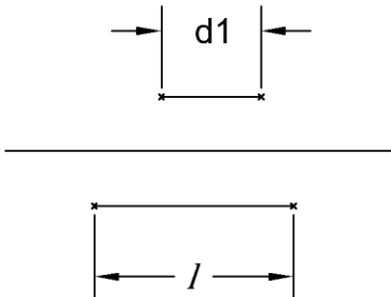
Impact Scenario	Mass Ratio (Linear Approx.)
<p>Case 1: The impacted section is taken from the edge of the module.</p> 	
<p>Case 2: The impacted section is taken from the middle of the module.</p> 	<p>$d1 = l - b1 - b2$</p> 

Figure 161. Linear Mass Distribution Approximation

Using this approximation method will overestimate the mass for small sections near the edge of the circle, resulting in larger-than-expected velocity drops. These drops can occur over relatively small deceleration distances, which can create spikes in the average acceleration which exceed the 12-g limit.

23.2.1.3 Mass Distribution by Partial Areas Approximation

The linear approximation method was an effective first step, but it had potential for unrealistic spikes in acceleration. Therefore, a more refined method was needed. The mass ratio can be approximated using the center position of the barrel relative to the impact events. The mass ratio of each cut section is estimated by dividing the area of the cut section by the area of a circle with a diameter equal to the deceleration distance l_n of the barrel, as geometrically shown in Figure 162.

The hatched areas for Cases 1 and 2 represent a section of a barrel that is contributing to the mass at some impact event. In Case 1, the width of the first barrel section and the length of contact were used to calculate the area K_{b1} . This area is then divided by the area of a circle equal to the length of contact of X_l and multiplied by the mass of the barrel inside the path of the vehicle. In Case 2, a section out of the middle of the barrel was needed. First, area X_2 is calculated by subtracting the areas to the left and right of the middle section. This area is then divided by the area of a circle equal to the length of contact of X_l and multiplied by the mass of the barrel inside the path of the vehicle. The overall length of contact is used, because for situations where the center of the barrel is outside the path of the vehicle, the length of contact is less than the diameter of the barrel.

For Case 1:

$$M_{X_1} = \frac{K_{b_1}}{X_l} \cdot M_X \quad (46)$$

$$K_{b_n} = \frac{l_n^2}{4} \cos^{-1} \left(\frac{l_n - 2b_n}{l_n} \right) - \left(\frac{l_n}{2} - b_n \right) \cdot \sqrt{l_n \cdot b_n - b_n^2} \quad (47)$$

For Case 2:

$$M_{X_2} = \frac{X_l - K_{b_1} - K_{b_2}}{X_l} \cdot M_n \quad (48)$$

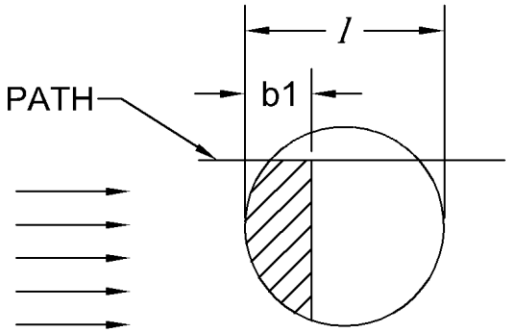
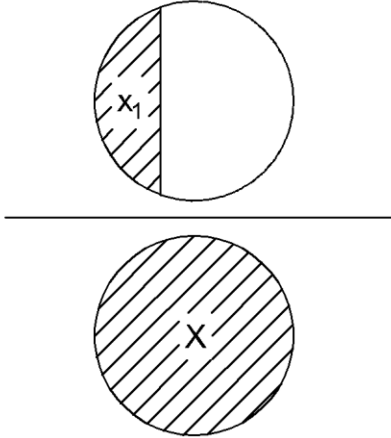
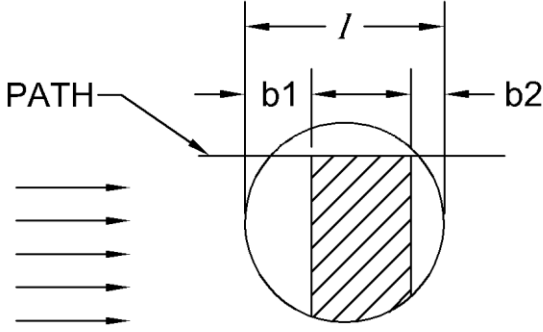
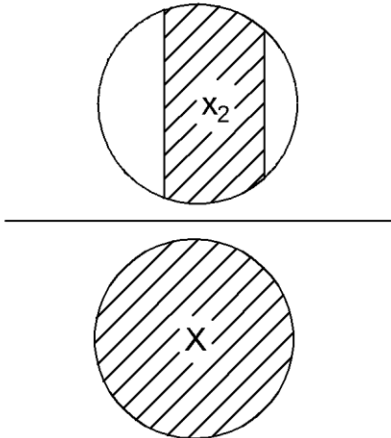
Impact Scenario	Mass Ratio (Partial Areas Approx.)
<p>Case 1: The impacted section is taken from the edge of the module.</p> 	
<p>Case 2: The impacted section is taken from the middle of the module.</p> 	

Figure 162. Partial Areas Mass Distribution Approximation

23.2.2 Comparison of Mass Distribution Methods

The large sand barrel array shown in Figure 153 had a variety of fully and partially impacted barrels and was used to compare the different mass distribution techniques, as shown in Table 45. The areas of the segmented barrels were calculated using a 2D CAD program to determine the ideal mass distribution program, while the linear approximation and partial areas approximation were incorporated into a spreadsheet program. All three techniques had the same total impacted mass. However, the partial areas distribution had an average absolute error of only 1.85 percent, and the linear method had an average absolute error of 17.12 percent. All three techniques for distributing masses provided identical results for the head-on impact shown in Figure 152.

Table 45. Mass Distribution Method Comparison

Impact Event	Ideal		Linear Approximation			Partial Areas Approximation		
	lb	kg	lb	kg	Absolute Error	lb	kg	Absolute Error
1	36.09	16.37	42.07	19.08	16.57%	33.51	15.20	7.15%
2	308.72	140.03	291.89	132.40	5.45%	311.30	141.20	0.84%
3	57.73	26.18	79.22	35.93	37.23%	57.73	26.18	0.00%
4	316.39	143.51	297.69	135.03	5.91%	318.48	144.46	0.66%
5	4.70	2.13	5.06	2.30	7.71%	4.39	1.99	6.60%
6	61.58	27.93	79.79	36.19	29.55%	59.74	27.10	2.99%
7	218.39	99.06	194.39	88.17	10.99%	218.72	99.21	0.15%
8	68.35	31.00	85.89	38.96	25.65%	70.54	31.99	3.19%
9	191.19	86.72	198.52	90.05	3.83%	187.70	85.14	1.83%
10	346.16	157.01	309.66	140.46	10.54%	346.01	156.95	0.04%
11	167.29	75.88	208.25	94.46	24.48%	160.04	72.59	4.33%
12	1038.62	471.11	984.83	446.71	5.18%	1047.05	474.93	0.81%
13	347.84	157.78	458.80	208.11	31.90%	346.63	157.23	0.35%
14	2324.60	1054.42	2184.49	990.87	6.03%	2331.07	1057.36	0.28%
15	259.88	117.88	406.60	184.43	56.46%	254.62	115.49	2.03%
16	144.96	65.75	139.80	63.41	3.56%	144.93	65.74	0.02%
17	1634.56	741.42	1468.60	666.14	10.15%	1641.16	744.42	0.40%
18	370.01	167.83	464.96	210.90	25.66%	384.55	174.43	3.93%
19	851.04	386.03	932.83	423.12	9.61%	825.85	374.60	2.96%
20	1971.16	894.10	1749.61	793.61	11.24%	1968.74	893.01	0.12%
21	628.02	284.86	786.23	356.63	25.19%	611.09	277.19	2.69%
22	2702.00	1225.61	2561.00	1161.65	5.22%	2726.77	1236.84	0.92%
23	465.49	211.14	584.62	265.18	25.59%	464.16	210.54	0.29%
Total Mass	14514.78	6583.79	14514.78	6583.79		14514.78	6583.79	
Average Error					17.12%			1.85%

A barrel can be split by both the path of the vehicle and other impact events. To calculate the actual area of each split segment, there are many possible distribution scenarios that must be considered, as the barrel can be segmented based on two axes. Both the linear and partial areas methods calculate the mass distribution using one axis, drastically reducing the number of scenarios to calculate the mass distribution. The partial areas method provided a close approximation to the ideal distribution with an absolute error of less than 1.85 percent.

23.2.3 Spreadsheet Procedure

Using the general form for analyzing inertia barrier impacts with large sand barrel arrays would be time-consuming if performed with hand calculations. A more practical way to apply this method is to implement it into a spreadsheet program. The sand barrel layout can be described in two-dimensional (2D) Cartesian coordinates with an (x,y) pair describing the center position of each module with some mass. In addition to locating the modules in 2D space, a vehicle and path are also needed. For the vehicle, four nodes are used to represent the corners of a vehicle model, as shown in Figure 163.

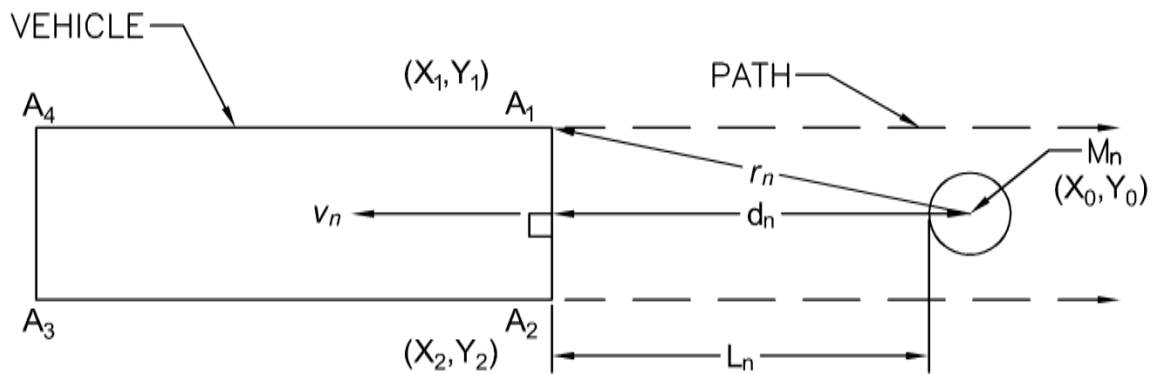


Figure 163. Simple Vehicle Model and Sand Barrel

In Figure 163:

\vec{v}_n = Direction vector through center of vehicle

\vec{r}_n = Vector from center of barrel to point A₁ on the front of vehicle

d_n = Distance from center of barrel to front of vehicle

Using this model, the distance, d_n , from the front of the vehicle to the center of a barrel can be used to determine the impact order. To find the distance from the vehicle to each barrel, a direction vector, \vec{v} , passing through the center of the sand barrel and perpendicular to the front of the vehicle, is created by the line between points A_1 and A_2 :

$$\vec{v}_n = \begin{bmatrix} y_2 - y_1 \\ -(x_2 - x_1) \end{bmatrix} \quad (49)$$

Next, a vector is drawn from M_n to point A_1 :

$$\vec{r} = \begin{bmatrix} x_1 - x_0 \\ y_1 - y_0 \end{bmatrix} \quad (50)$$

Finally, the length of the projection of \vec{r} on to \vec{v} yields the distance from the center of the n th sand barrel to the front of the vehicle, d_n :

$$d_n = \frac{(x_1 - x_0)(y_2 - y_1) + (y_1 - y_0)(x_1 - x_2)}{\sqrt{(y_2 - y_1)^2 + (x_2 - x_1)^2}} \quad (51)$$

This process can then be used to find the distance to all of the modules in the system. The distance, L_n , to the front of the vehicle is:

$$L_n = d_n - \frac{c}{2} \quad (52)$$

When the center of a sand barrel is inside the path of the vehicle, the chord length is:

$$c = D \quad (53)$$

Similarly, the module's distance from the left and right sides of the vehicle's path can be determined using (A_4, A_1, M_n) and (A_3, A_2, M_n) , respectively. Calculating the distances from the left and right sides of the vehicle path would allow logic conditions to determine whether or not a module is in the path of the vehicle and if the barrel was fully impacted or partially impacted.

23.2.4 Large Sand Barrel Array Example Calculations

The large sand barrel array shown in Figure 153 was used as a representative system to evaluate the spreadsheet procedure described in the previous section. With this program, each of the 36-in. (914-mm) diameter sand barrels had a unique mass and (x, y) coordinate, as shown in Figure 164. Sand barrel masses were limited to standard sizes of 200 lb (91 kg), 400 lb (182 kg), 700 lb (318 kg), 1,400 lb (636), and 2,100 lb (955 kg) [1]. The partial areas mass distribution method was used in this program, because it provided a good approximation of the mass distribution and was much simpler to implement than trying to calculate each individual mass.

Using the equations defined previously, the position of the vehicle relative to the barrels was used to determine the impact event order and the relative mass contribution of each impacted barrel. The impact event order and mass, as well as velocity calculation, average deceleration, and occupant impact velocity calculations, are presented in Table 42 and graphically shown in Figure 165.

The duration and velocity of each event were used to determine the theoretical occupant impact time of 0.15 seconds. The OIV was 24.5 ft/s (7.5 m/s), which was below the 40 ft/s (12.2 m/s) limit in MASH [3]. The ORA was 7.97 g's, which was below the 12-g average deceleration limit for sand barrel analysis. As shown in Table 42, when the vehicle's velocity was reduced to below 14.67 ft/s (4.5 m/s), the vehicle would be allowed to impact a rigid barrier [1]. In this analysis, the vehicle was considered to be stopped after the velocity was reduced to less than 14.67 ft/s (4.5 m/s).

This analysis verified that the partial areas approximation could be implemented into a spreadsheet program and that the relevant calculations could be made quickly. This spreadsheet program could be later used to investigate many different layouts and impact conditions to determine a suitable sand barrel configuration for intersecting roadways.

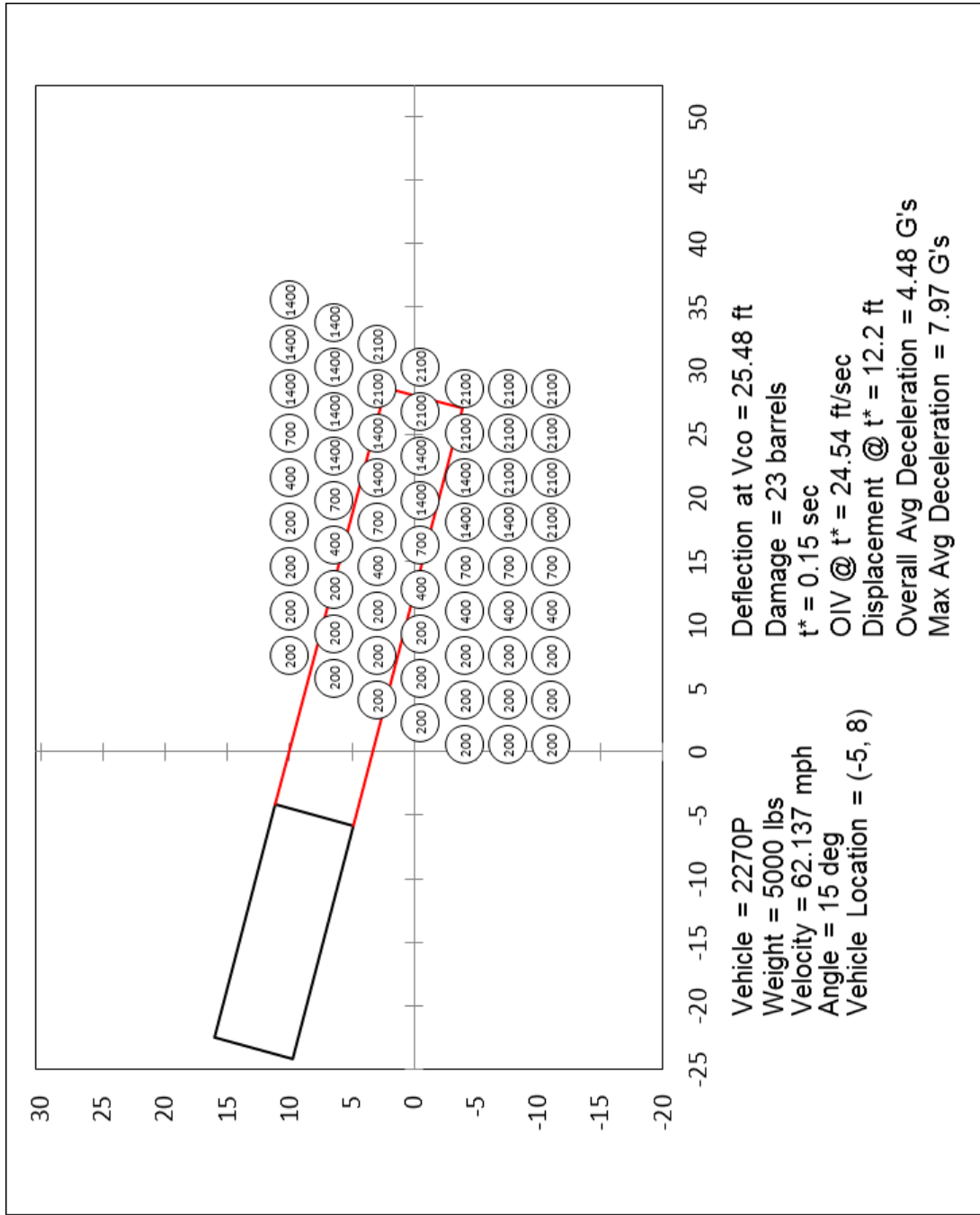


Figure 164. Inertia Barrier Example Summary

Table 46. Inertia Barrier Example Calculations

Impact Order	Sand Weight Per Impact (lbs)	Initial Velocity V_{n-1} (ft/s)	Final Velocity V_n (ft/s)	Deceleration Distance (ft)	Impact Distance (ft)	Average Deceleration (g/s)	Event Time (sec)	OIV (ft/s)	OD (in.)
1	33.51	91.13	90.53	3.00	0.78	2.1832	0.0086	0.000	0.000
2	311.30	90.53	85.22	3.00	2.60	5.5818	0.0295	0.607	0.063
3	57.73	85.22	84.25	3.00	0.78	3.2654	0.0093	5.913	2.159
4	318.48	84.25	79.20	3.00	2.52	5.0913	0.0308	6.885	2.924
5	4.39	79.20	79.13	1.59	0.08	2.1597	0.0010	11.930	7.333
6	59.74	79.13	78.20	3.00	0.78	2.9122	0.0100	12.000	7.477
7	218.72	78.20	74.92	3.00	1.86	4.1995	0.0243	12.934	9.025
8	70.54	74.92	73.88	2.91	0.74	3.2610	0.0099	16.212	13.744
9	187.70	73.88	71.21	3.00	1.02	5.9307	0.0140	17.254	15.801
10	346.01	71.21	66.60	2.54	1.58	6.2470	0.0229	19.927	19.151
11	160.04	66.60	64.53	3.00	0.78	5.3656	0.0120	24.536*	25.902
12	1047.05	64.53	53.36	3.00	2.60	7.8851	0.0440	26.601	29.722
13	346.63	53.36	49.90	3.00	0.78	7.0760	0.0152	37.775	49.687
14	2331.07	49.90	34.03	3.00	2.60	7.9714	0.0619	41.235	57.206
15	254.62	34.03	32.38	3.00	0.49	3.4993	0.0146	57.101	99.597
16	144.93	32.38	31.47	0.46	0.30	3.0370	0.0093	58.750	109.923
17	1641.16	31.47	23.69	3.00	1.93	3.4601	0.0699	59.663	116.607
18	384.55	23.69	22.00	2.77	0.67	1.7955	0.0293	67.440	173.144
19	825.85	22.00	18.88	3.00	0.91	2.1879	0.0443	69.132	197.444
20	1968.74	18.88	13.55**	2.76	1.69	1.5905	0.1042	72.251	235.859
21	611.09	13.55	7.81**	3.00	0.78	0.7489	0.0612	77.586	332.917
22	2726.77	12.07	7.15**	3.00	2.18	0.6027	0.2197	79.061	391.015
23	464.16	7.81	7.15**	0.20	0.20	0.7730	0.0267	83.322	610.713
* Occupant Impact Velocity									
** Velocity 10 mph cutoff (14.67 ft/s)									

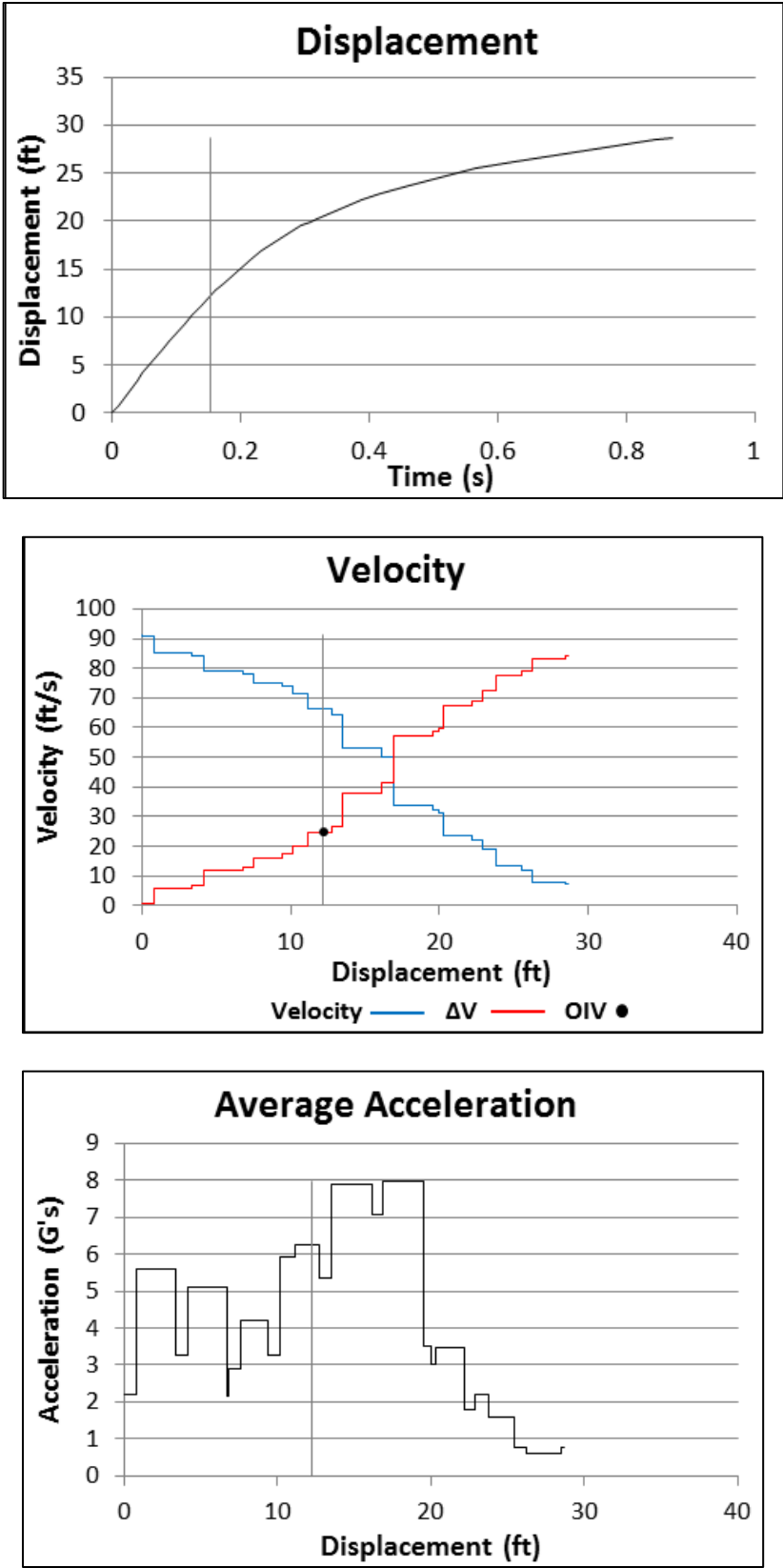


Figure 165. Inertia Barrier Example Displacement, Velocity, and Average Acceleration

24 COMBINED END TERMINAL AND SAND BARREL IMPACTS

An analytical method for considering impacts into sand barrel arrays with either an end terminal or crash cushion was developed to further investigate the feasibility of Concept K. Many end terminals and crash cushions are designed such that their occupant risk values are close to the limits defined in NCHRP Report No. 350 or MASH in order to reduce their overall length. Concept K would require sand barrels and an end terminal or crash cushion to be placed very near one another, thus creating the potential that both systems would be engaged at the same time. If both systems were impacted simultaneously, the occupant risk limits may be exceeded. The large sand barrel array example from the previous chapter is shown in Figure 166, laterally offset from an end terminal by 2 ft (610 mm). In this arrangement, the end terminal and only one row of sand barrels could be impacted.

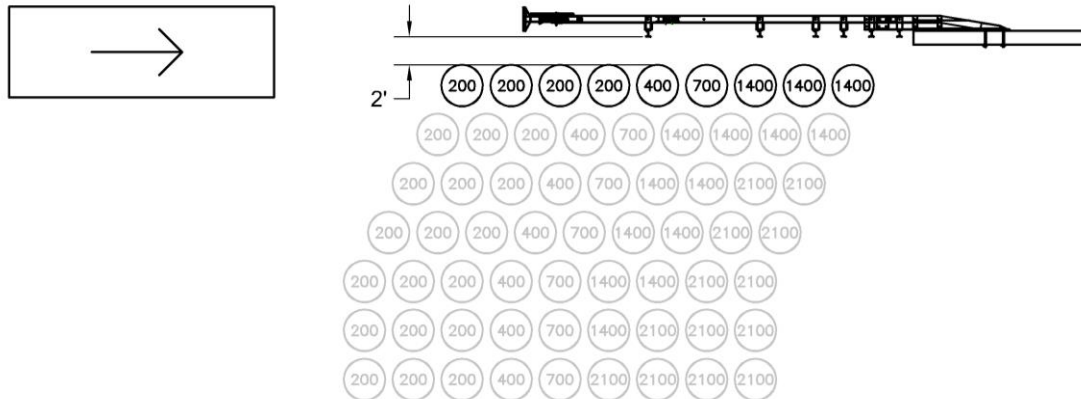


Figure 166. Combined Crash Cushion and Sand Barrel Array

24.1 Analysis

In an impact with an energy-absorbing guardrail end terminal, the acceleration of the impact head, followed by the deformation of the rail element as the head is pushed down the rail, dissipates the majority of the energy. During the initial impact, the vehicle contacts and

accelerates the terminal head, fracturing the first post, and often releases the tension in the rail. As the vehicle and terminal head reach the same velocity, the terminal head is driven down the guardrail, dissipating energy through rail deformation and/or post fracture. The vehicle either comes to rest in contact with the end terminal or has a post-impact trajectory with possible subsequent impacts.

A technique used for accident reconstruction of end terminal impacts, first developed by Coon, was modified for this application to include the effect of sand barrels adjacent to the terminal [54]. In this technique, the conservation of momentum theory is used for the initial impact with the terminal head. The collision can be considered perfectly plastic, with the head traveling with the vehicle after it is struck. For high-speed frontal impacts, the coefficient of restitution is relatively low. This implies that almost all of the kinetic energy is transformed into crush energy and that there is little elasticity to a frontal vehicle impact. Since the coefficient of restitution is relatively small, conservation of momentum is used, and the elastic restoration of vehicle crush during impact with the terminal head may be neglected.

The average force levels provided by several end terminals are shown in Table 47. The ranges of force levels were determined in Coon's work through reconstruction of full-scale crash testing and, when available, the examination of corresponding accelerometer traces from test reports. Since the forces from the post fracture and head acceleration of the system are inherently included in the accelerometer trace, they do not need to be accounted for individually.

Table 47. Average End Terminal Forces [54]

End Terminal	Head Mass lb (kg)	Average Force kip (kN)
BEAT	130 (59)	20 (87) to 27.5 (122.5) [Stage 1]
BEAT-MT		
BEAT-SSCC		29 (129) [Stage 2]
BEST-350	275 (125)	18.7 (83.4) to 22.5 (100)
ET-2000	268 (122)	12 (53.4) to 12.3 (54.5)
ET-2000 PLUS	175 (79)	
FLEAT-350, MT	120 (54.5)	13.5 (60.2) to 15 (67)
REGENT	46 (21)	N/A
SKT-350	172 (78)	7.1 (31.6) to 11.3 (50.1)
WY-BET	125 (57)	18 (80.1) [Stage 1]
WY-BET (MB)		35 (155) [Stage 2]

An example of a vehicle impacting both a row of sand barrels and an end terminal is shown in Figure 167. In this scenario, the vehicle strikes multiple sand barrels before striking the end terminal. Impacts with the sand barrels result in an immediate drop in velocity through momentum transfer. After the end terminal is struck, the inertia of the end terminal head and the resistive force of the end terminal head as it moves along the rail cause an additional change in velocity. To account for both sand barrel impacts and end terminal forces, the velocity needs to be calculated after each impact V_n and at the instant before the next impact V_n' from the velocity drop caused by the end terminal force.

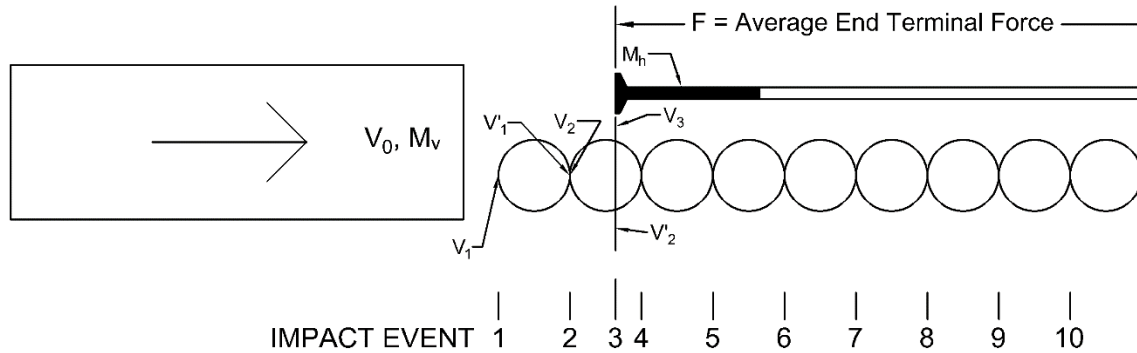


Figure 167. Combined Sand Barrel and End Terminal Impact Scenario

For the example shown in Figure 167, sand barrel impacts upstream from the end terminal could be treated using the same conservation of momentum procedure discussed in the previous chapter. After rearranging the conservation of momentum equations, they could be applied in a sequential manner for each sand barrel impacted upstream from the end terminal. When the vehicle impacts the end terminal, there is an initial drop in velocity when the head is accelerated from rest. Upon impact, the masses of the vehicle and the end terminal head are combined, and the decreased velocity of the end terminal head and vehicle can be determined using the conservation of momentum. After the end terminal is struck and the head is traveling down the guardrail, the principle of Work-Energy is implemented. The force levels to deform guardrail sections within end terminals were considered to be relatively constant in this analysis. The amount of time between impact event n and $n+1$ is calculated using the initial velocity and the distance between impacts x . The width of the vehicle was not considered for this analysis, because it was assumed that the end terminal and one row of sand barrels would be fully impacted. Assuming no gap between the barrels, the number of calculations required was reduced and would not raise occupant risk concerns.

If a vehicle impacts sand barrels before the end terminal is impacted, then the equations for calculating the velocity drop after each impact as well as the average deceleration of the bogie vehicle are as follows:

Where:

M_v = Mass of vehicle (lb)

M_n = Mass of sand in n th impacted barrel (s)

M_h = Mass of end terminal head (lb)

V_n = Vehicle velocity after n th impact (ft/s)

V_n' = Vehicle velocity at instant before impact $n+1$ (ft/s)

a_n = Average acceleration from sand barrel and end terminal head impact (ft/s²)

a_{et} = Acceleration due to end terminal force

a_T = Combined end terminal acceleration and average acceleration from sand barrels

g = Acceleration of gravity (32.174 ft/s²)

G = Deceleration (g's)

t = Time of event (s)

F = Average resistive force of end terminal system (lbf)

x_n = Longitudinal position within system (ft)

$$V_n = \frac{M_v V_{n-1}}{M_v + M_n} \quad (54)$$

The velocity V_n' the instant before impact $n+1$ is the same as V_n :

$$V_n' = V_n \quad (55)$$

The average acceleration on the vehicle only depends on the sand barrel impacts:

$$a_n = \frac{V_{n-1}^2 - V_n^2}{2l_n} \quad (56)$$

$$G_n = \frac{a_n}{g} \quad (57)$$

The duration of the impact event is:

$$t_n = \frac{V_{n-1} - V_n}{a_n} \quad (58)$$

If the next impact is with another sand barrel, then the cycle will repeat using the previous four equations. In this analysis, the end terminal head sticks to the vehicle after it is impacted and adds to the overall mass. If the end terminal is impacted, the following equations are to be used:

$$V_n = \frac{(M_v + M_h) \cdot V'_{n-1}}{M_v + M_h + M_n} \quad (59)$$

There is now a velocity drop after the impact with the head or sand barrels, as well as a drop in velocity:

$$V'_n = V_n + a \cdot t_{n \text{ to } n+1} \quad (60)$$

$$a_n = \frac{V_{n-1}^2 - V_n^2}{2x_{n \text{ to } n+1}} \quad (61)$$

$$a_{et} = \frac{Fg}{M_v + M_h} \quad (62)$$

$$a_T = a_n + a_{et} \quad (63)$$

$$t_{n \text{ to } n+1} = \frac{-V_n + \sqrt{V_n^2 - \left(4 \cdot \left(\frac{a}{2}\right) \cdot (-x_{n \text{ to } n+1})\right)}}{a} \quad (64)$$

24.2 Limitations of Procedure

The reconstruction procedure is based on an ideally functioning, energy-absorbing end terminal [54]. In cases where the guardrail does not deform as planned, force levels may be significantly different. Thus, this procedure is limited to cases where the guardrail properly feeds. However, this analysis was sufficient as an analytical tool.

25 WIDE BULLNOSE CONCEPT – ANALYTICAL MODEL

25.1 Bullnose with Secondary Energy Absorption

Thrie-beam bullnose systems are often too long to install within the available space near most interesting roadways. To use a thrie-beam bullnose system to safely capture and decelerate a vehicle in the limited space near intersecting roadways, a secondary energy-absorption method would be needed to reduce the system length. For secondary energy absorption, a net attenuator or sand barrel system could be configured inside the bullnose area, as shown in Figure 168.

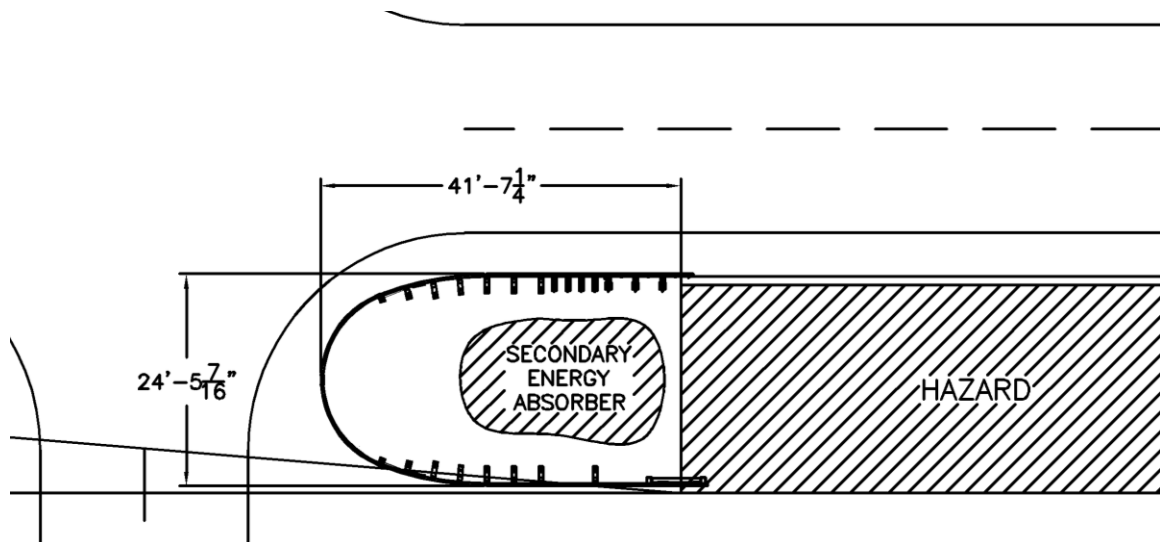


Figure 168. Bullnose with Secondary Energy Absorber System

The analysis of Concepts C and O can be performed using similar methods to the combined sand barrel and energy-absorbing terminal analysis described previously. Bullnoses were not covered in the scope of the accident reconstruction effort performed by Coon et al. [54]. Thus, the average force of a bullnose had to be determined using experimental test data. MwRSF had previously completed testing on a Universal Steel-Post Bullnose system, as shown in Figure 169, which could be applicable for this analysis [25].

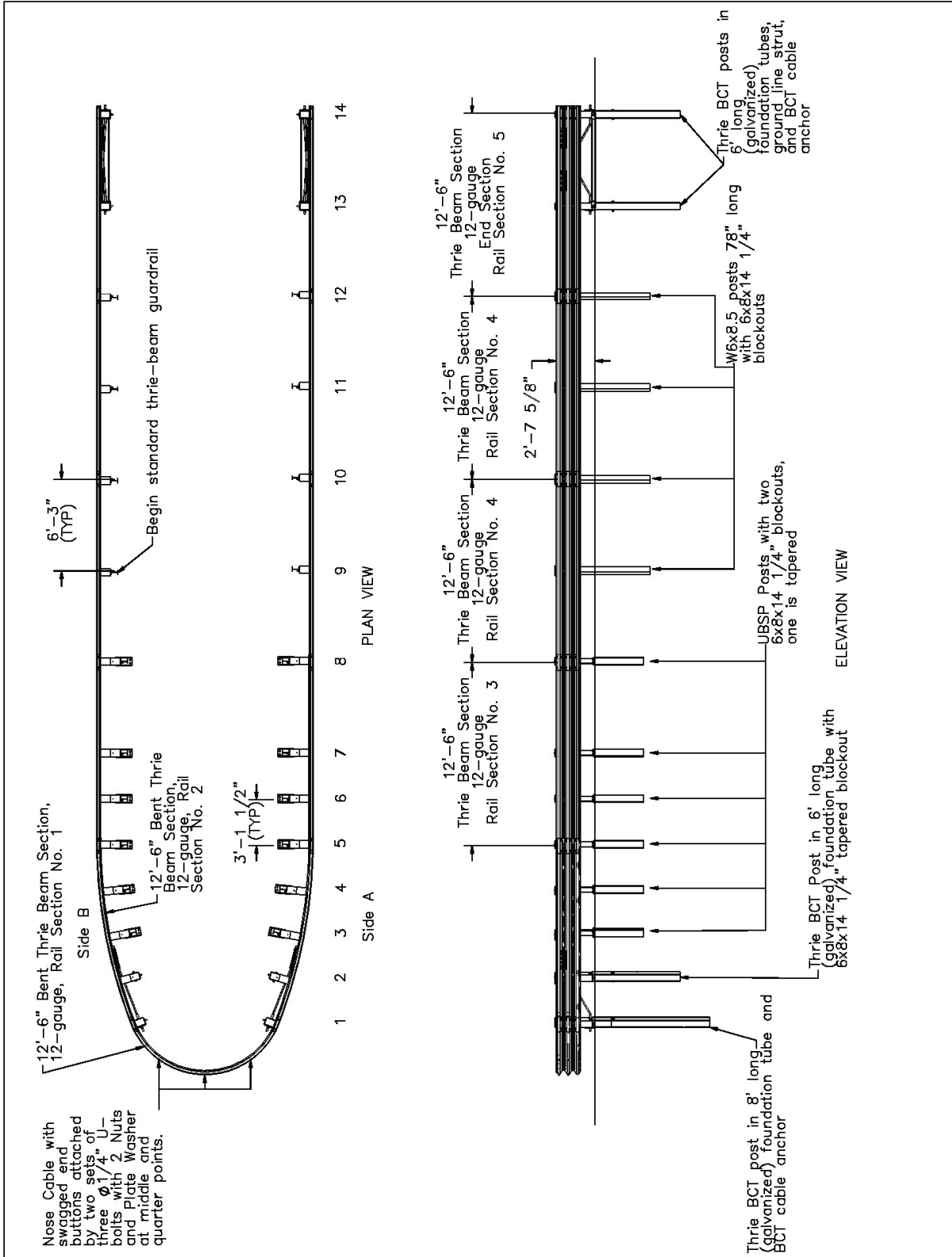


Figure I69. USPBN-4 Bullnose Dimensions [25]

In this test, a 4,429-lb (2,009-kg) pickup truck impacted the bullnose median barrier at a speed of 64.5 mph (103.8 km/h) and an angle of 0 degrees. The impact point was located with the center of the vehicle aligned with the center of the bullnose [25]. The maximum dynamic deflection in the test was 56 ft - 1 in. (17.1 m) downstream from the point of impact. This system was much narrower than the bullnose needed for Concepts C and O. As the bullnose width increased, it was expected that the average crush force would slightly decrease, thus resulting in an overall increase in stopping distance.

25.2 Determine Average Resistive Force of Bullnose

The average resistive force on the vehicle was determined using the average crushing force on the vehicle by calculating the area underneath the force vs. deflection curve, as shown in Figure 170, which was based on the CFC 60-filtered longitudinal acceleration. The area under the force vs. deflection curve, or work done, was calculated using the trapezoidal rule. The final summation of this energy could then be divided by the total distance.

Where:

x_n = Displacement at t_n (ft)

V_n = Velocity at time t_n (ft/s)

E_n = Energy absorbed at time t_n (lb)

F_{avg} = Resistive force acting on vehicle (lbf)

$$x_n = \frac{1}{2}(t_n - t_{n-1}) \cdot (V_n + V_{n+1}) + \sum_{i=0}^{n-1} x_i \quad (65)$$

$$E_n = \frac{1}{2}(x_n - x_{n-1}) \cdot (F_n + F_{n-1}) + \sum_{i=0}^{n-1} E_i \quad (66)$$

$$F_{avg} = \frac{E_{final}}{x_{final}} \quad (67)$$

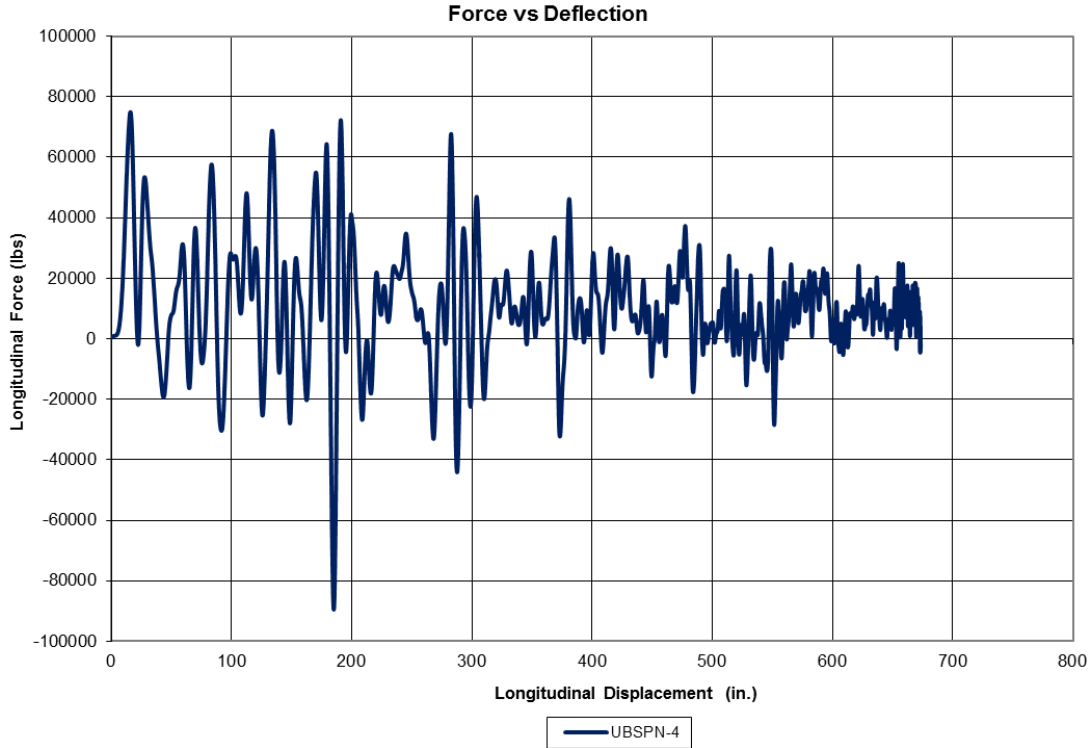


Figure 170. Force vs Displacement – Test No. USPBN-4

Using this method, the average crushing force was 10,957 lbf (48.7 kN), based on the CFC60-filtered longitudinal acceleration. In order to verify the method used to find the average crush force, a simple work-energy analysis was performed to determine an estimated system deflection using the calculated average force :

Where:

- V_o = Initial velocity at time t_n (ft/s)
- x_{final} = Total displacement of the bogie vehicle (ft)
- W = Weight of vehicle (lb)
- g = Gravitational constant (32.174 ft/s²)

$$x_{final} = \frac{WV_o^2}{2gF} \tag{68}$$

The test vehicle had a weight of 4,429 lb (2,009 kg) and an initial velocity of 64.5 mph (103.8 km/h). The force calculated from the energy equations was 10,957 lbf (48.7 kN), which yielded an estimated final deflection of 56.17 ft (17.12 m), which was very close to the actual dynamic deflection of 56.08 ft (17.09 m). Because of the close comparison with the actual and estimated deflection using the force from the energy equation, this force was used for analysis.

25.3 Combined Bullnose and Sand Barrel System

The procedure for analyzing the combined bullnose and sand barrel concept was the same as that used for analyzing impacts into guardrail end terminals and sand barrels. For this analysis, however, there would be no situations where the vehicle would impact sand barrels before engaging the bullnose, and only the combined analysis would be performed.

25.4 Bullnose and Net Attenuator System

The combined bullnose and net arrestor concept used a similar procedure for analyzing impacts into guardrail end terminals and sand barrels. For this analysis, however, there would be no situations where the vehicle would impact only sand barrels as the vehicle would impact the bullnose system before the net arrestor was struck. The equations from the previous chapters were simplified for this analysis. Head-on impacts at 0 degrees were assumed for this situation.

Table 48 summarizes the equations that were used, where:

- n = Impact event number
- V_n = Velocity at impact event n (ft/s)
- $V_{n'}$ = Velocity immediately before impact $n+1$ (ft/s)
- L = Width of net (ft)
- T = Tension force from energy absorbers (lbf)
- F_{avg} = Resistive force acting on vehicle (lbf)
- F_{avg} = Resistive force acting on vehicle (lbf)
- M_v = Mass of vehicle (lb)

- M_n = Mass impacted at event n (lb)
 a_{net} = Acceleration from net forces (g's)
 a_{et} = Acceleration from end terminal forces (g's)
 a_T = Total acceleration from both systems (g's)
 g = Gravitational constant (32.174 ft/s²)

Table 48. Calculation Procedure for Impacts Into Combined Bullnose and Sand Barrel System

Only Bullnose Impact	Bullnose and Net Arrestor	
$M_v V_{n-1} = M_v V_n + M_1 V_n$	$M_v V_{n-1} = M_v V_n + M_1 V_n$	(69)
$V_n = \frac{M_v V_{n-1}}{M_v + M_n}$	$V_n = \frac{(M_v + M_h) \cdot V'_{n-1}}{M_v + M_h + M_n}$	(70)
$V'_n = V_n + a_{et} \cdot t_{n \text{ to } n+1}$	$V'_n = V_n + [(a_{et} + a_{net}) \cdot t_{n \text{ to } n+1}]$	(71)
$a_{et} = \frac{Fg}{M_v + M_h}$	$a_{et} = \frac{Fg}{M_v + M_h}$	(72)
$a_{net} = 0$	$a_{net} = \left(\frac{T}{W}\right) \cdot (2x_n) \cdot \sqrt{\left(\frac{L}{2}\right)^2 + (x_n)^2}$	(73)
$a_T = a_{net} + a_{et}$	$a_T = a_{net} + a_{et}$	(74)
$t_{n \text{ to } n+1} = \frac{-V_n + \sqrt{V_n^2 - \left(4 \cdot \left(\frac{a_T}{2}\right) \cdot (-x_{n \text{ to } n+1})\right)}}{a}$	$t_{n \text{ to } n+1} = \frac{-V_n + \sqrt{V_n^2 - \left(4 \cdot \left(\frac{a_T}{2}\right) \cdot (-x_{n \text{ to } n+1})\right)}}{a}$	(75)

25.5 Limitations of procedure

The reconstruction procedure is based on ideally functioning, energy-absorbing end terminals or crash cushions [54]. Note that force levels could be significantly higher in angled impacts on the nose or impacts that are offset more to one side. For this analysis, only centerline impacts on the nose and parallel to the system were considered. However, this analytical approach should be sufficient to determine the feasibility of the concept.

26 POTENTIAL LAYOUTS

26.1 Introduction

This chapter presents potential layouts for the net attenuator, inertia barrier, and bullnose concepts. The analysis techniques presented earlier were used to provide the general dimensions required for each system. A summary of the design, operational, and constructability concerns can be found in Table 50.

26.2 Concept A – Net Attenuator/End Terminal or Crash Cushion

26.2.1 Estimating Net Widths

The width of the required net attenuator was determined by examining the smallest available space for a new attenuation system. Narrower net installations will cause higher decelerations than wider nets and provide a worst-case scenario. For the layout shown in Figure 171, a net system of approximately 35 ft (10.7 m) was needed to cover the distance between the end terminal and the edge of the 30-ft (9.1-m) clear zone. After discussions with the manufacturer of the Dagnet Vehicle Arresting Barrier, it was believed that the number of energy absorbers could be reduced to one or two on each side of the net.

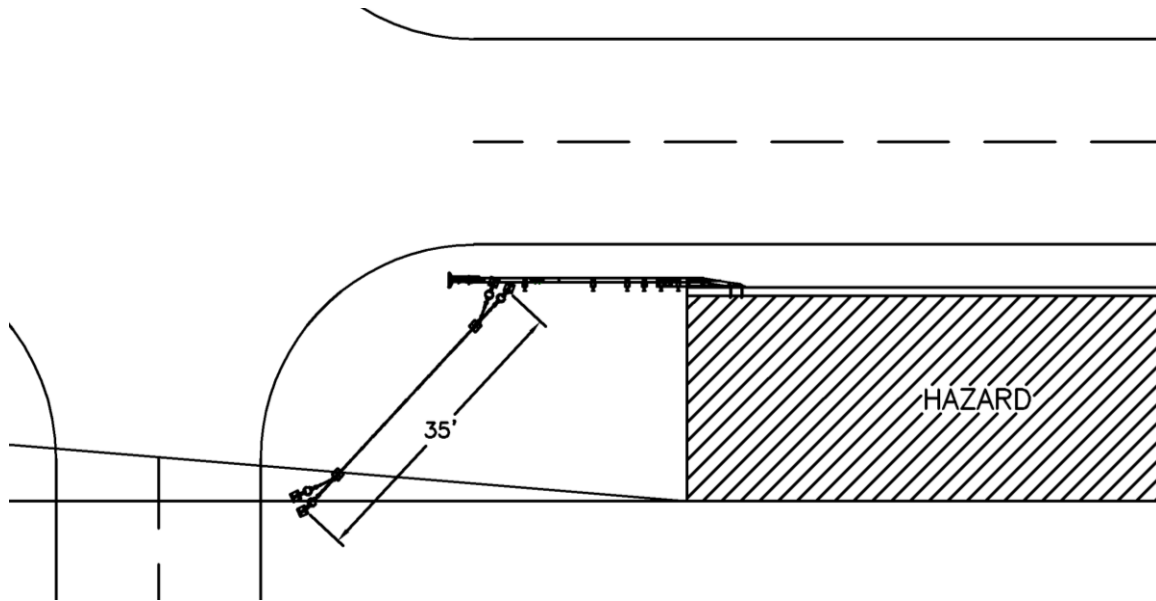


Figure 171. Potential Layout for Net Attenuator

Placement of the energy absorbers and anchorages is critical to the overall performance of the safety treatment. The energy absorbers and anchorages should be placed as close as practical to the end terminal or crash cushion without adversely affecting the operation of either system. The Length-of-Need (LON) of the end terminal or crash cushion is also an important consideration. Many end terminal systems have a LON downstream from the third post location. To prevent vehicles from striking the hazard (i.e., impacting between the end terminal head and the LON), the net must be anchored downstream from the LON. Moving the net anchorages downstream from the corner of the intersection can increase the distance required to stop a vehicle. For this reason, non-gating, redirective crash cushion systems would be advantageous, because they would limit the interference between multiple safety treatments when used at the same location.

26.2.2 Predicting Deflections with MASH Vehicles

The analytical method was used to investigate the performance of the prototype net attenuator system with different energy absorber capacities. This investigation was limited to

central, perpendicular impacts into the net due to the poor correlation of the performance estimates for offset, angled impact events. With an impact velocity of 62.14 mph (100.0 km/h), the stopping distance and maximum deceleration could be estimated for the 1100C and 2270P MASH vehicles, as shown in Table 49. All impacts were perpendicular to the center of a 35-ft (10.7-m) wide net. The goal was to stop 2270P vehicles in a minimum distance without causing ORA concerns with the lighter 1100C vehicle. OIV was not considered for this analysis, because the forces on 1100C vehicles are initially much lower for net impacts than for impacts with end terminal or crash cushion systems, and the test was not likely to violate the limits in MASH [3]. The analytical method tended to overestimate system deflection and underestimate occupant ridedown acceleration.

Table 49. Predicted Distance and Peak Deceleration for 1100C and 2270P Vehicles

Vehicle Designation	Vehicle Mass lb (kg)	Energy Absorber Force kip (kN)	Vehicle Deflection ft (m)	Peak Deceleration g's
1100C	2,425 (1,100)	4.5 (20.0)	49.3 (15.0)	3.50
		9.0 (40.0)	30.2 (9.2)	6.42
		18.0 (80.1)	19.5 (5.9)	11.05
		25.0 (111.2)	16.1 (4.9)	13.95
2270P	5,000 (2,268)	4.5 (20.0)	87.5 (26.6)	1.77
		9.0 (40.0)	50.4 (15.4)	3.40
		18.0 (80.1)	30.8 (9.4)	6.26
		25.0 (111.2)	24.9 (7.6)	8.18

For all cases, the predicted peak decelerations were less than the MASH-allowable limit of 20.49 g's. To reduce the stopping distance to 30 ft (9.1 m) or less, the system requires at least an 18.0-kip (80.1-kN) combined energy-absorber force on each side of the system. Although none of the theoretical peak decelerations approached 20.49 g's, energy absorber forces should be limited to prevent other issues such as excessive vehicle yawing in angled impacts. This

analysis did not account for any vehicle deformation and assumed that the energy absorber force remained constant throughout the impact event. Even with favorable anchorage locations, the vehicle could still travel, requiring more area than available in the shortest installations.

26.2.3 Potential Layout for Net Attenuator Concept

Assuming that longitudinal vehicle deflections for the net attenuator system can be reduced to 30 ft (9.1 m) or less, the grading suggestions for the potential net layout are shown in Figure 172. The ground leading up to the net system and surrounding the end terminal or crash cushion would need to be a 10:1 slope or flatter. Immediately behind the net, an 8:1 to 3:1 longitudinal or lateral slope could potentially be accommodated, although research and development is needed to confirm feasibility. The net and anchorage system should be placed as close as practical to the slope break point to allow the energy absorbers to rotate freely, with the strap in contact with the ground as the impacting vehicles traverse the area below the anchorage points. Beyond the intended vehicle stopping distance, 4 ft (1.2 m) wide or greater, 2:1 or flatter fill slope is suggested before a vertical drop is reached. These grading suggestions would be evaluated in a Phase II study.

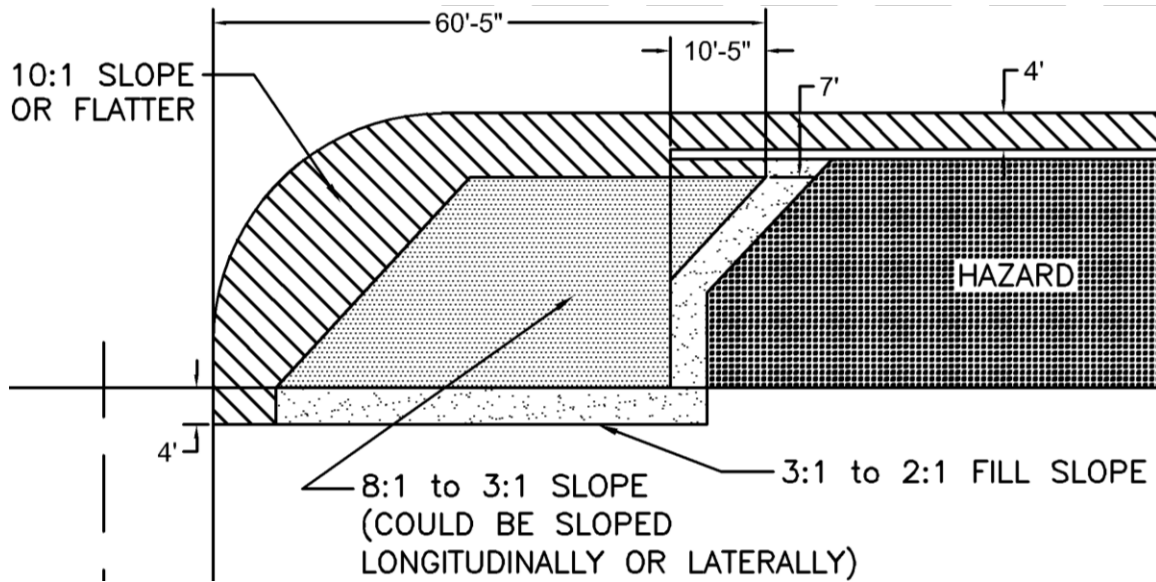


Figure 172. Potential Layout for Net Attenuator System

26.2.4 Net Attenuator Concept Discussion

To reduce net attenuator deflections to 30 ft (9.1 m) or less, the combined force of the energy absorbers on each side of the system should be greater than or equal to 18 kips (80.1 kN). The predicted maximum deflections for 1100C and 2270P vehicles were 19.5 ft (5.9 m) and 30.8 ft (9.4 m), respectively. These values are considered to be conservative, as the analytical method considers that only the energy absorbers are dissipating the kinetic energy of the impacting vehicle. In reality, rolling resistance, friction forces, and vehicle crush would dissipate energy. As the resistive force of the energy absorbers increase, it is likely that vehicles impacting at an angle may experience greater instabilities. For this reason, when the Dragnet System was first tested in 1969, the researchers suggested that the resistive force not exceed 12,500 lb (55.6 kN). The project team opined that an energy absorber tensile force of 8,000 lbf (35.6 kN) or less would provide acceptable stopping characteristics with energy absorbers mounted flush with the ground [51].

The height of the net is also an important factor for achieving acceptable system performance, as noted in the original testing performed on the Dagnet Vehicle Arresting Barrier [51]. The researchers noted that the net should be approximately 4 ft (1.2 m) tall, because a 3-ft (0.91-m) tall net failed to completely capture the front end of the vehicle. If the net is not tall enough, it will not grab the front end of the vehicle and could be pulled underneath it, thus allowing the vehicle to override the system.

One design challenge involves the possibility for a vehicle to pass between the net and the end terminal. Placement of the energy absorbers near the upstream end of the guardrail end terminal may result in system interference with the function of the end terminal. Thus, retesting of the guardrail end terminal system may be required if the energy absorbers degrade end terminal performance. Further development of this concept would also require collaboration with end terminal and crash cushion manufacturers. Non-gating, redirective crash cushion or end terminal systems would be preferred to limit the interference between the systems. Overall, the performance of this concept makes it suitable for further development.

26.3 Concept K – Sand Barrels with End Terminal or Crash Cushion

The general inertia barrier analysis and the combined barrel and end terminal impact analysis were used to develop potential barrier layouts. Sand barrel systems often use a row of sand barrels beyond the point where the velocity of the vehicle is reduced to less than 10 mph (16 km/hr). The extra row of barrels may be challenging in this configuration due to the presence of steep slopes. Further, design layouts for barrels should ensure that vehicles do not impact multiple rows of sand barrels when also impacting the head of the guardrail end terminal.

26.3.1 Potential Layouts for Sand Barrel Concept

For the combined sand barrel and crash cushion concept, the BEAT-SSCC was selected for the crash cushion due to its short length and crashworthy transition to rigid bridge rail. The

combined sand barrel and crash cushion impact analysis indicated that the row of barrels placed laterally behind the crash cushion should be offset several feet. The two rows closest to the primary roadway utilized barrels that weighed 1,400 lb (635 kg) or less, since most 2,100-lb (953-kg) sand barrels were excessively tall and would cause sight-line issues. However, the sand barrel offset and restricted mass increased the overall footprint of the array. An impact analysis of the combined sand barrel and crash cushion system can be found in Appendix G.

26.3.1.1 Barrel Layout with Standard Spacing

The first potential layout assumed a standard 6-in. (152-mm) distance between the barrels, as shown in Figure 173. Many different configurations and barrel masses were investigated in order to reduce the overall footprint and required number of barrels. As part of the combined sand barrel and crash cushion analysis, four impact scenarios were considered for the 1100C and 2270P MASH vehicles at 62.14 mph (100 km/h):

- 1) 15 degree impact upstream from the end terminal head,
- 2) 15 degree impact into center of array,
- 3) 0 degree impact into first two rows of barrels, and
- 4) 5 degree impact in-line with the LON.

A full analysis of this combination system can be found in Appendix G.

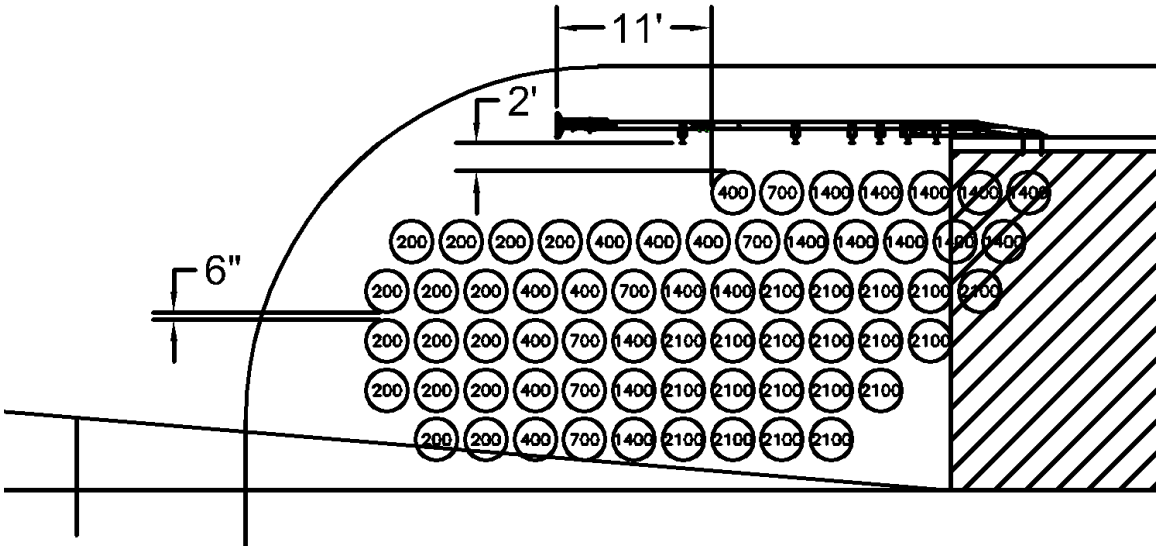


Figure 173. Standard-Spacing Sand Barrel Array

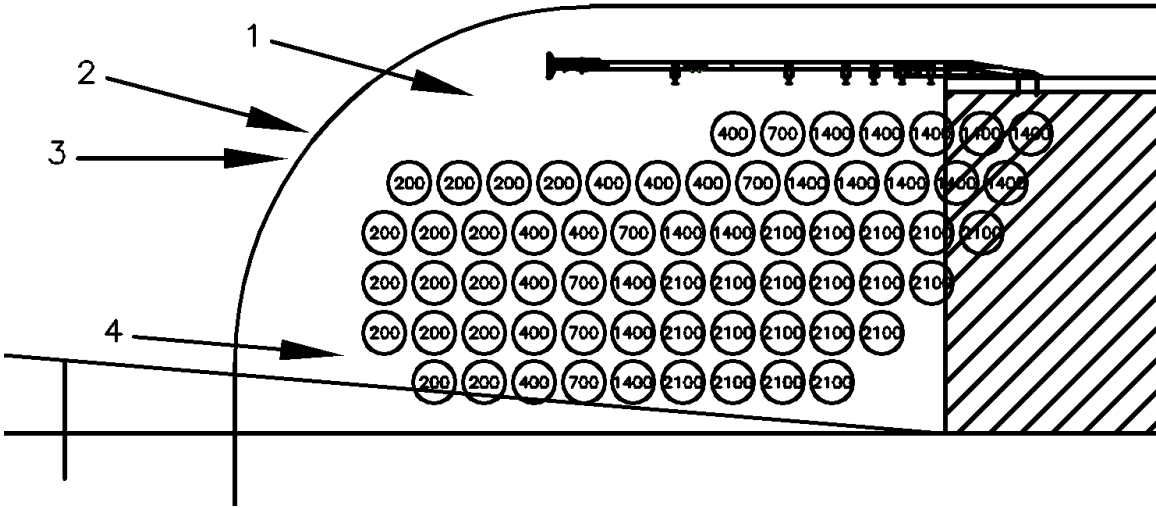


Figure 174. 1100C and 2270P Impact Scenarios for Standard-Spacing Sand Barrel Array

This general configuration provided acceptable performance, but the use of 65 barrels with 6-in. (152-mm) spacing seemed excessive. It was conceived that an increased spacing using heavier barrels would more feasibly protect the same area.

26.3.1.2 Barrel Layout with Mixed Spacing

To reduce the number of barrels required for this concept, heavier barrels were spaced farther apart. The mixed layout used a barrel spacing which ranged between 6 in. and 18 in. (152 mm and 457 mm), as shown in Figure 175. Gaps larger than 18 in. between the barrels may cause issues with small vehicles, because they may pass mostly in between two lighter barrels and then hit a heavier barrel at a greater speed, raising ORA and OIV concerns.

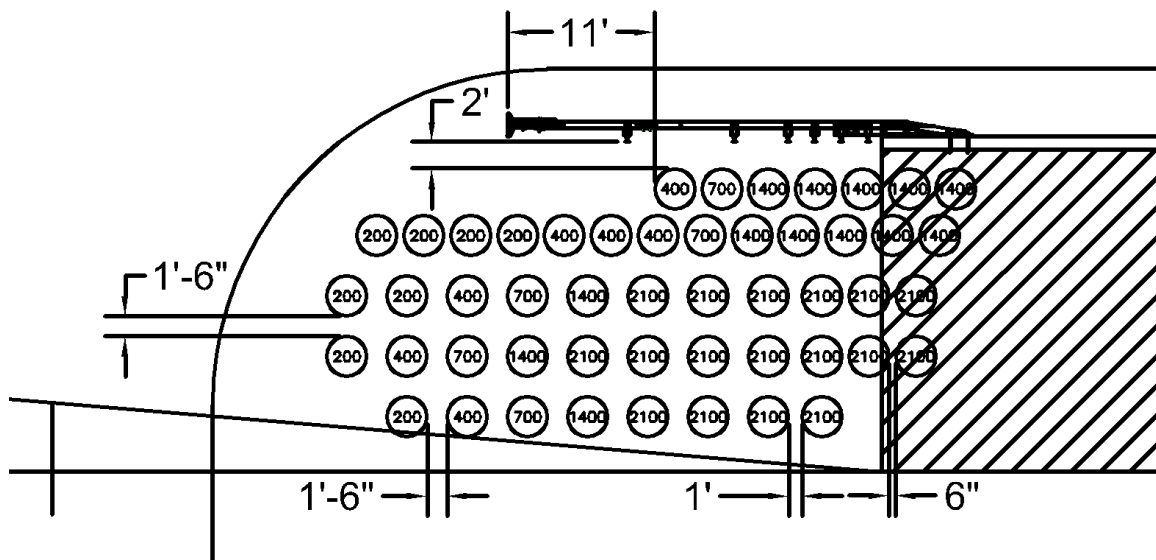


Figure 175. Mixed-Spacing Sand Barrel Array

Using a mixed-spacing barrel concept reduced the number of barrels from 65 to 50, which would improve maintenance between the barrels. In addition, the increased space between barrels would decrease the likelihood that adjacent barrels contribute to momentum transfer in actual impacts as well as provide more space for sand to disperse. As part of the combined sand barrel and crash cushion analysis, four impact scenarios were considered for the 1100C and 2270P MASH vehicles at 62.14 mph (100 km/h):

- 1) 15 degree impact upstream of end terminal head,
- 2) 15 degree impact into center of array,

- 3) 0 degree impact into first two rows of barrels, and
- 4) 5 degree impact in-line with LON.

A full analysis of this combination system can be found in Appendix G.

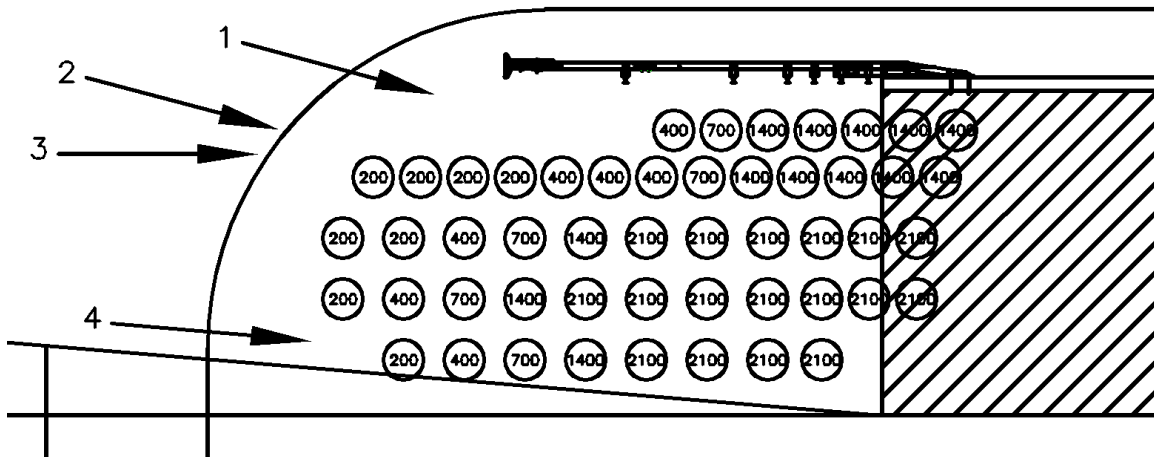


Figure 176. 1100 C and 2270P Impact Scenarios for Mixed-Spacing Sand Barrel Array

26.3.2 Grading Requirements

Using these potential layouts, suggested grading requirements for the standard- and mixed-spacing systems were considered, as shown in Figures 177 and 178. The system with mixed spacing concepts reduced the number of barrels required from 65 to 50. Both concepts required more space than was available for the smallest protected areas. The sand barrels and end terminal or crash cushion systems generally require 10:1 or flatter slopes. Beyond the footprint of the sand barrels, the system should utilize a 4-ft (1.2-m) wide or greater buffer region consisting of a 3:1 or flatter fill slope before any steeper slopes are considered.

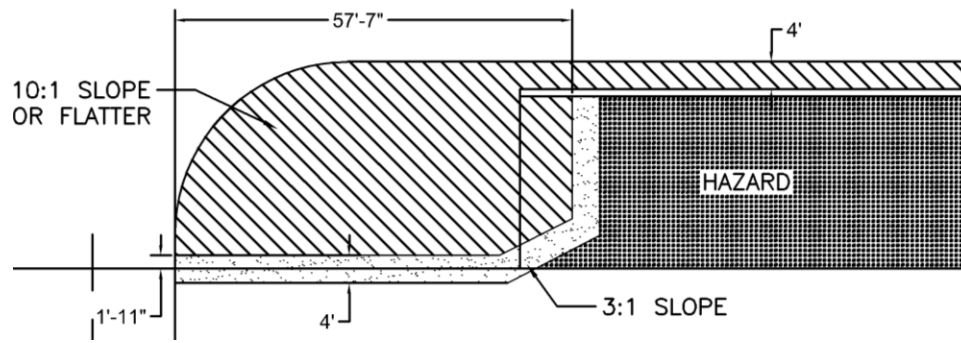


Figure 177. Sand Barrel Grading Suggestions for Standard-Spacing Systems

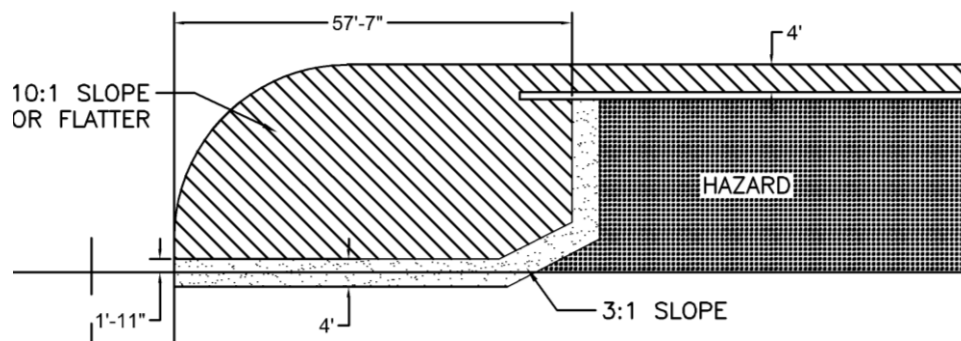


Figure 178. Sand Barrel Grading Suggestions for Mixed-Spacing Systems

26.3.3 Sand Barrel Concept Discussion

A general inertia barrier analysis was used to evaluate a combination sand barrel array with an end terminal or crash cushion for safely treating hazards present at intersecting roadways and shielding bridge railings. A sand barrel array using a standard spacing of 6 in. (152 mm) would require 65 barrels. Alternatively, heavier barrier masses in combination with increased spacing would allow fewer barrels to be used to shield the same area. A spacing of 6 in. to 18 in. (152 mm to 457 mm) proved to provide acceptable performance while also reducing the number of barrels to 50. The BEAT-SSCC was selected for the crash cushion and sand barrel analysis. However, various crash cushion or guardrail end terminal systems could provide acceptable safety performance. The combined sand barrel and end terminal impact analysis indicated that

the row of barrels placed immediately behind the end terminal should be offset by several feet. This concept has not been recommended for further development, due to grading requirements as well as the significant number of sand barrels required to shield the hazard.

26.4 Concept C and O – Bullnose with Secondary Energy Absorption

Both thrie-beam bullnose systems considered for this concept were approximately 42 ft (12.8 m) long and 24 ft – 5 in. (7.4 m) wide. The bullnose system was assumed to have an average crush force of 10,960 lb (48.8 kN). This analysis was also performed using a force reduction factor of 75 percent with an average crush force of 8,220 lb (36.6 kN) in order to determine if a wider bullnose system would be weaker.

26.4.1 Concept O – Bullnose with Net Arrestor Potential Layout

A thrie-beam bullnose system with a net attenuator placed inside is shown in Figure 179. The net attenuator was assumed to be 17 ft (5.2 m) wide and placed 21 ft – 1 ¼ in. (6.4 m) behind the nose section. This net location was chosen based on the estimated LON for the bullnose. A total energy-absorber force of 13,500 lb (60.1 kN) was assumed at each end of the net. This capacity could be accomplished by using three energy absorbers vertically mounted to a post or a single modified, high-capacity unit. An impact analysis of the combined sand barrel and crash cushion system can be found in Appendix G.

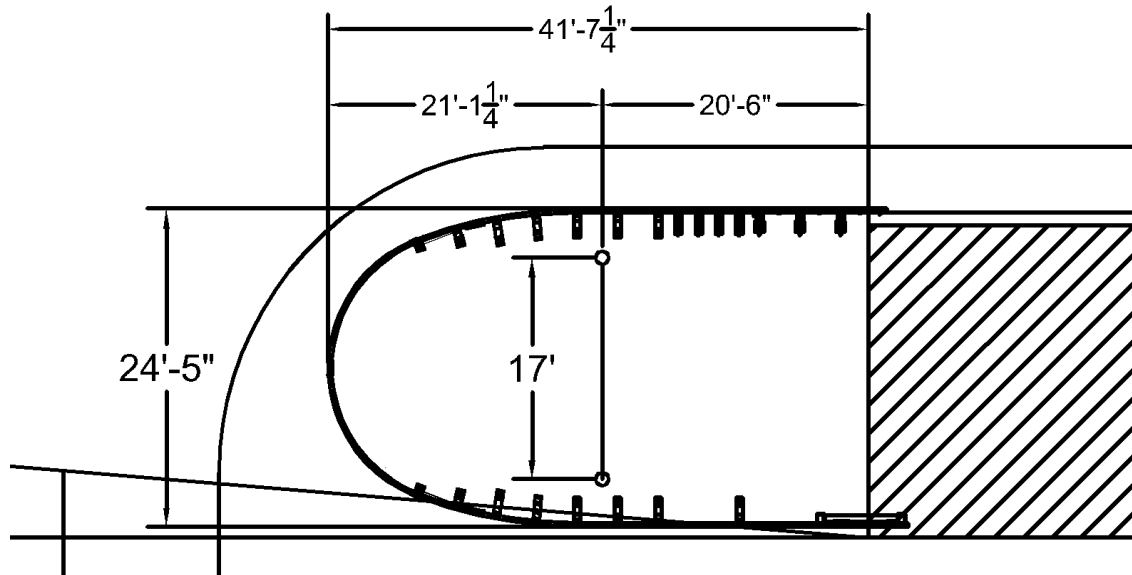


Figure 179. Bullnose and Net Attenuator Concept

26.4.2 Concept C – Bullnose with Sand Barrels Potential Layout

A three-beam bullnose system with sand barrels placed inside it is shown in Figure 180. A 3x4 array of sand barrels placed 21 ft – 1 1/4 in. (6.4 m) behind the nose section was considered for this concept. This sand barrel array location was chosen based on the estimated LON for the bullnose. For this analysis, it was assumed that two rows of barrels would be engaged simultaneously. An impact analysis of the combined sand barrel and end terminal concept can be found in Appendix G.

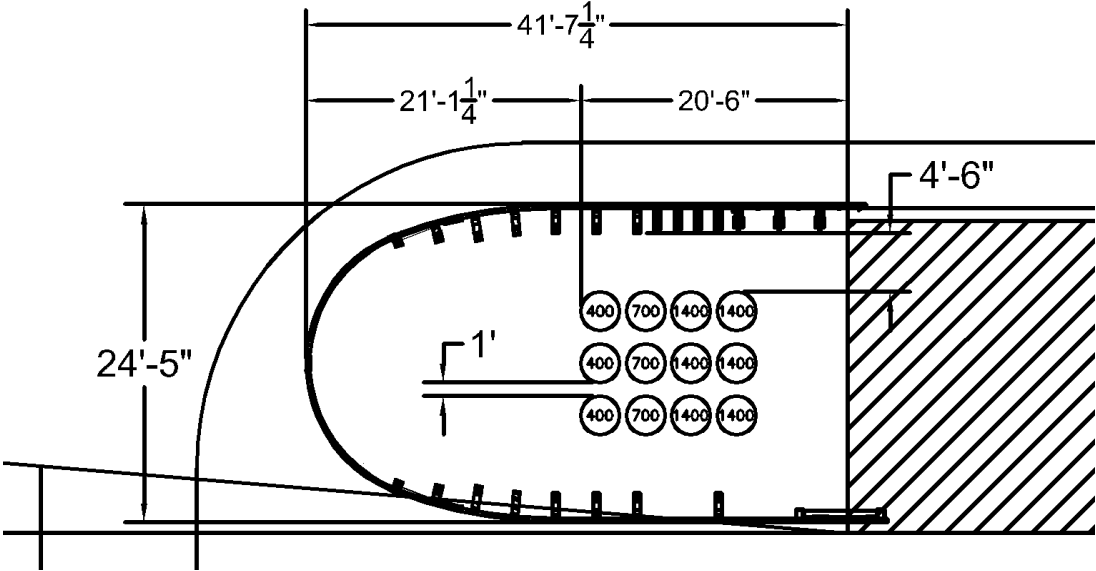


Figure 180. Bullnose and Sand Barrel Array Concept

26.4.3 Grading Requirements

The suggested grading requirements, as shown in Figure 181, were identical for the combined thrie-beam bullnose system with secondary energy-absorption. Both concepts required slightly more space than was available for the smallest protected areas. The area occupied inside and in front of the bullnose would require 10:1 or flatter slopes. Beyond the foot-print of the bullnose, the grading should utilize a 4 ft (1.2 m) wide or greater buffer region consisting of 3:1 or flatter fill slope before any steeper slopes are considered.

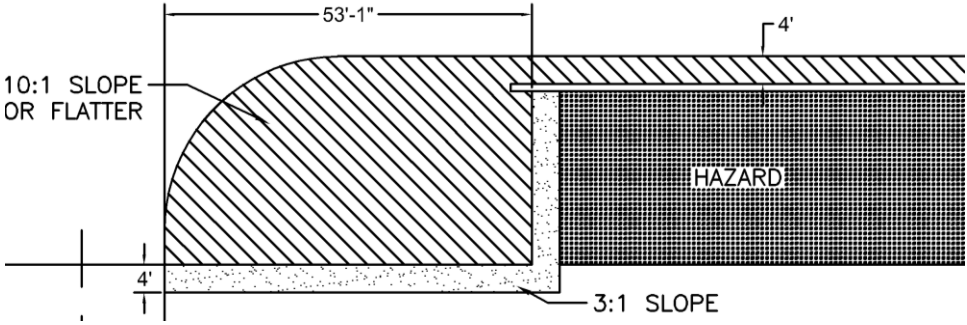


Figure 181. Grading Suggestions for Thrie-Beam Bullnose Concepts

26.4.4 Combined Bullnose Concept Discussion

The impact analysis for these concepts indicated that a vehicle could be safely stopped inside the available space. One advantage for this concept pertains to the continuous rail element wrapping around the entire system, thus preventing a vehicle from passing between systems. Second, bullnose guardrail systems have also been tested under NCHRP Report No. 350 TL-3 conditions and utilize many non-proprietary components, which could reduce installation cost. Another benefit is that bullnose systems use three-beam guardrail elements that could be transitioned directly into the end of the bridge railing. This concept also eliminated the use of a guardrail system along the secondary roadway.

The resistive force, safety performance, and vehicle stopping distance of the three-beam bullnose system shown requires that the net or sand barrels be placed sufficiently back from the nose section to reduce concerns for increased occupant risk for 1100C passenger vehicles. NDOR also indicated that it would be difficult to grade the protected area to meet the needs for satisfactory bullnose performance. Maintenance concerns would exist as equipment would need to be lifted over the top of the bullnose to mow the enclosed area.

One advantage for using a net attenuator inside the bullnose is that there is a high probability to capture and stop passenger vehicles under a wide range of impact conditions. However, it would be difficult to incorporate the combined bullnose system with realistic site constraints. Again, maintenance concerns exist, as equipment would need to be lifted over the top of the bullnose to mow the enclosed area.

Sand barrels are an existing technology, relatively inexpensive, and can be installed in an array to provide staged energy absorption. Unfortunately, the 36-in. (914-mm) maximum height criterion limits the sand barrels that can be installed within a bullnose system and still preserve sight lines.

The interaction between the net attenuator and bullnose system during impact events is unknown and would require further investigation. Because the energy absorbers are proprietary systems, they may be cost-prohibitive if current units are used. Significant research and development would be required to integrate a net attenuator with an end terminal or crash cushion system. Again, this concept would require significant site grading for the three-beam bullnose system.

26.5 Concept Recommendations Summary

The net attenuator concept was perceived to be the simplest combined system and deemed most likely to accommodate small to moderate fill slopes within the protected area. A net attenuator does not cause the sight-line concerns associated with some of the heavier sand barrel arrays. The net attenuator and crash cushion investigated also used currently available technologies. The sand barrel array concepts and the bullnose concept would require significant grading that is impractical at most locations.

Table 50. Design, Operational, and Constructability Challenges for Potential Layouts

Concept	Design	Operational	Constructability
Net Attenuator	<ul style="list-style-type: none"> Need higher force energy absorbers to stop vehicles in 30 ft or less Net attenuator would require more space than available at smaller sites, road may need to be moved Anchorage of net attenuators would require design and consideration for integration with the end terminal or crash cushion Need to use frangible posts or lightweight wood to support net 	<ul style="list-style-type: none"> Except for expended tape, most major components are reusable Does not create site line issues Mowing and landscaping simple 	<ul style="list-style-type: none"> Overall the “cleanest” installation Energy absorbers are proprietary and costs are unknown Area in front of net needs to be flat, area past the net could accommodate small to moderate slopes
Bullnose with Secondary Energy Absorber	<ul style="list-style-type: none"> Bullnose required for this setup would need to be shorter and wider than any currently available system Need to design and evaluate transition section Energy absorbers would need to be anchored downstream of redirective section of bullnose 	<ul style="list-style-type: none"> Mowers would have to be lifted over top of bullnose to maintain enclosed area Height of sand barrels could cause site line issues 	<ul style="list-style-type: none"> Bullnose systems are non-proprietary and include a crash cushion and bridge transition The protected area would need to be flat, requiring grading out to clear zone and capture area
Sand Barrels	<ul style="list-style-type: none"> Least amount of development work among different concepts Vehicles impacting sand barrels and end terminal would need to be investigated 	<ul style="list-style-type: none"> Landscaping and mowing would be difficult Height of sand barrels could cause site line issues Sand barrels would require more space than available at smaller sites, road may need to be moved 	<ul style="list-style-type: none"> The protected area would need to be flat, requiring grading out to clear zone and capture area 50+ barrels required to bring truck to stop

27 SUMMARY, CONCLUSIONS, AND RECOMMENDATIONS

The research effort described herein detailed the design, analysis, and bogie testing of concepts for a MASH-compliant attenuation system for use near intersecting roadways and utilizing as small of a footprint for the device as possible. The effort began with a review of existing short-radius, end terminal, crash cushion, net attenuation, and truck- and trailer-mounted attenuation systems. Design criteria for the new system for treatment of intersecting roadways were investigated including design space requirements, determination of the required protection envelope based on length-of-need and runout length, sight line concerns, and other operational and maintenance issues. It was noted during development of the design criteria that the potential for impacts some distance down the secondary roadway needed to be considered based on potential vehicle trajectories, and that the existing crash test matrix used previously for short-radius type systems may need to be adjusted to account for these impacts.

The researchers developed a variety of design concepts to meet these design criteria that could potentially be used in lieu of the short-radius systems that are currently available and/or in place. With input from the project sponsor, three concepts were selected for further development: (1) a net attenuator with approved end terminal or crash cushion, (2) an array of sand barrels with approved end terminal or crash cushion, and (3) a wide bullnose with a secondary energy absorber enclosed.

27.1 Net Attenuator with End Terminal or Crash Cushion

In order to evaluate the net attenuator concept, several components needed to be tested and evaluated. Two quasi-static component tests were performed on the energy absorbers used in the Dragnet Vehicle Arresting Barrier in order to investigate the force required to feed steel tape from an energy absorber drum. The force vs. deflection results were then used in future analytical and simulation investigations.

Four component tests were performed on a combination of selected components from a Dragnet Vehicle Arresting Barrier. To evaluate the potential to accommodate increased net energy absorber forces, three standard Dragnet energy absorbers were installed on each side of the net in order to evaluate vehicle capture. This arrangement produced a nominal resistive force of 11,700 lb (52.0 kN) per side. The dynamic tests demonstrated the successful capture and safe deceleration of vehicles using Dragnet hardware under higher resistive forces. These findings also provided baseline data for use in future analytical and simulation investigations.

Test no. IRA-1 consisted of a 5,090-lb (2,309-kg) bogie vehicle impacting the net arrestor prototype at a speed of 60.4 mph (97.2 km/h) and an angle of 90 degrees, in the center of the net. The bogie vehicle was safely and smoothly captured. There were neither detached elements nor fragments from the net which showed potential for undue hazard to other traffic. The vehicle had a maximum dynamic deflection of 44.2 ft (13.5 m) downstream from the point of impact and a lateral movement of 1.3 ft (0.4 m). One of the energy absorber straps on the left side of the system fractured at the beginning of the test, resulting in asymmetric loading on the test vehicle. This asymmetric loading caused the vehicle to yaw to the right. The failure was likely caused by excessive whipping that occurred to both inside energy absorbers of the system.

Test no. IRA-2 consisted of a 5,090-lb (2,309-kg) bogie vehicle impacting the net arrestor prototype at a speed of 59.9 mph (96.4 km/h) and an angle of 90 degrees, offset to the right from the center of the net. The bogie vehicle was safely and smoothly captured. There were neither detached elements nor fragments from the net which showed potential for undue hazard to other traffic. The vehicle had a maximum dynamic deflection of 41.0 ft (12.5 m) downstream from the point of impact and a lateral movement of 0.43 ft (0.13 m). As observed in test no. IRA-1, one of the energy absorber straps on the left side of the system fractured at the beginning of the test, resulting in asymmetric loading on the test vehicle. This asymmetric loading caused the vehicle

to yaw to the right. The failure was likely caused by excessive whipping that occurred to both inside energy absorbers of the system. With a second failure in the same location, the researchers decided that this issue required further investigation.

When the vehicle impacted the net, the energy absorbers that were mounted perpendicular to the net had initially compressed. As the vehicle tracked through the system and the innermost energy absorber on the left side was pulled tight, the steel tape ruptured at the connection between the tape and the turnbuckles. Even though the inside energy absorber on each side of the net exhibited the same motion, only the left absorber had a failure. The solution to this problem was to mitigate the compression behavior by reducing the angle between the three energy absorbers from 45 degrees to 22.5 degrees. With this change, the inside and middle energy absorbers were moved more in-line with the net and farther away from the center of the net.

Test no. IRA-3 consisted of a 5,259-lb (2,385-kg) bogie vehicle impacting the net arrestor prototype at a speed of 58.0 mph (93.3 km/h) 12 ft (3.7 m) and an angle of 60 degrees, offset to the right from the center of the net. The bogie vehicle was safely and smoothly captured. There were neither detached elements nor fragments from the net which showed potential for undue hazard to other traffic. The vehicle had a maximum dynamic deflection of 33.0 ft (10.1 m) downstream from the point of impact and a lateral movement of 18.0 ft (5.5 m), resulting in a total displacement of 37.6 ft (11.5 m). This test showed the net arrestor could safely capture the vehicle in impacts near the edge of the net.

Test no. IRA-4 consisted of a 5,259-lb (2,385-kg) bogie vehicle impacting the net arrestor prototype at a speed of 59.5 mph (95.8 km/h) and an angle of 60 degrees, in the center of the net. The bogie vehicle was safely and smoothly captured. There were neither detached elements nor fragments from the net which showed potential for undue hazard to other traffic. The vehicle had

a maximum dynamic deflection of 42.2 ft (12.9 m) downstream from the point of impact and a lateral movement of 1.82 ft (0.55 m). This test was a repeat of test no. IRA-1 and would serve as a baseline comparison to analytical and simulation predictions.

Testing on selected components of the modified Dragnet Vehicle Arresting Barrier showed potential for use in protecting hazards near intersecting roadways. The concept used existing technologies, which were largely reusable. The anchorage systems could be placed near the primary and secondary roads where the ground is mostly level. Although the area in advance of the net needs to be mostly flat, this concept could likely accommodate moderate slopes behind it. Some research and development work would be required to integrate a net attenuator with either a guardrail end terminal or crash cushion system. Interior support posts for the net may need to be embedded in the ground, as most protected areas will not have a concrete or asphalt pad to support the posts and the net system. Mowing operations would be more manageable with this concept due to the absence of an enclosed area. There is also potential that the net could be laid down if maintenance personnel needed to mow or maintain the protected area.

A finite element model of the prototype net attenuator system that was evaluated in test nos. IRA-1 through IRA-4 was also developed to further investigate the viability of the concept. LS-DYNA computer simulations were performed to serve as a comparison to results obtained from physical component tests and analytical methods. During the simulation investigation, the simulation demonstrated similar deflections and velocities to the physical testing, but generated lower ORA values. Thus, the simulation model could be useful for future investigations into the viability of the net attenuator concept. Future simulations could involve slopes, higher energy absorber forces, and more complex vehicle models.

An analytical method was also developed to further investigate the net attenuator system's performance when configured with different energy absorber load capacities. The

analytical method was used to estimate maximum dynamic deflections and maximum accelerations using different vehicles but could include varying net widths and energy-absorber forces. Comparison of the analytical method with centered, perpendicular impacts with the physical tests found that it produced results similar to the simulation model, in that the deflections tended to be conservative, and the ORA values were under predicted. The analytical method was less accurate, but still conservative for angled impacts away from the center of the net. The analytical method was deemed suitable for conservative estimation of system deflections or for calculating a resistive force to provide a desired stopping distance.

To reduce net attenuator deflections below 30 ft (9.1 m) or less, the combined resistive force of the energy absorbers on each side of the system should be greater than or equal to 18 kips (80.1 kN). The predicted maximum deflections, for the 1100C and 2270P vehicle were 19.5 ft (5.9 m) and 30.8 ft (9.4 m), respectively. These vehicle displacements can be considered upper limits for the maximum deflection as friction, rolling resistance, and vehicle crush were not considered. As the resistive force of the energy absorbers increase, vehicles impacting at angles may potentially experience some instability, especially as slopes are introduced behind the net.

For the combination net attenuator and end terminal concept, one concern pertains to the possibility for a vehicle to pass between the end of the net and the head of the guardrail end terminal. Another concern relates to the potential for the energy absorbers to interfere with the end terminal and degrade its safety performance. Due to these concerns, additional full-scale crash testing may be required on the combined prototype or even on the end terminal when vehicle contact with the net attenuator anchorages could occur. Further research and development of this concept would likely require collaboration with the manufacturer of the selected end terminal or crash cushion. Note that the use of a non-gating, redirective crash cushion or end terminal system would limit the potential interference between the systems as

well as the propensity for the impacting vehicle to pass between the systems. A net attenuator and end terminal/crash cushion concept does not cause sight-line issues that were associated with higher-mass sand barrels.

The net attenuator concept and end terminal/crash cushion appeared to be least complex, used existing technologies, and the most likely to accommodate small to moderate slopes behind the system. The investigation of this system deemed it suitable for further research and development.

27.2 Sand Barrels with End Terminal or Crash Cushion

A general inertia barrier analysis was used to determine an array of sand barrels that could safely treat hazards present at intersecting roadways when used in combination with an end terminal or crash cushion. An array using a standard spacing of 6 in. (152 mm) could require up to 65 barrels. Spreading the sand barrels out in combination with higher masses would allow fewer barrels to be used to shield the same area. Using a spacing of 6 in. to 18 in. (152 mm to 457 mm) proved to provide acceptable performance while also reducing the number of barrels to 50. The BEAT-SSCC was used for the end terminal and sand barrel analysis. However, other crash cushion or end terminal systems could provide acceptable performance. The impact analysis of the combined sand barrel and end terminal system indicated that the row of barrels placed immediately behind the end terminal should be offset several feet. In general, this concept was not recommended for further research and development, due to the significant grading that would be required over the array footprint and the excessive number of sand barrels required to safely shield the hazard.

27.3 Bullnose with Secondary Energy Absorption

The analysis of the thrie-beam bullnose concepts indicated that a vehicle could be safely stopped inside the available space using a secondary form of energy absorption. The advantages

of this system would be that there is a continuous rail element wrapping around the entire system, thus preventing a vehicle from passing in between systems. Thrie-beam bullnose guardrail systems have been tested under NCHRP Report No. 350 TL-3 conditions and utilize many non-proprietary components, which could reduce installation costs. The bullnose system uses thrie-beam rail elements, which can be more easily transitioned into the buttress end of bridge railings.

The secondary energy absorption system, either a net attenuator or sand barrels, must be placed far enough behind the nose of the bullnose to prevent the 1100C vehicle from engaging both systems simultaneously, as this could cause occupant risk concerns. Shortening and widening a standard bullnose and an approved bridge rail transition into the bridge railing may cause the system to become too stiff to capture the small car and pickup truck used under MASH testing conditions. NDOR indicated that it would be impractical to grade the protected area to the end of the clear zone for many locations. Since bullnose systems are enclosed, mowers would need to be lifted over the top of the rail to maintain the enclosed area.

When using a net attenuator system inside the bullnose, there exists increased probability for safe capture or controlled stopping under a wide range of impact conditions. However, it may be challenging to incorporate such a system into the existing footprint where significant grading would be required. Sand barrels are an existing technology, relatively inexpensive, and can be installed in an array to provide staged energy absorption. Unfortunately, the 36-in. (914-mm) maximum height criterion limits the size of sand barrel that can be installed inside of a bullnose and still preserve sight lines.

The interaction between a net attenuator and bullnose system during vehicular impacts remains unknown and would require further research and development. The energy absorbers are proprietary systems, so they may be prohibitively expensive if not modified to reduce the

number of energy absorbers. This concept was not recommended for further research and development, due to the grading required for the current bullnose system.

27.4 Recommendations for Future Research

A combination of engineering analysis, computer simulation, and dynamic component testing were used to evaluate the three design concepts denoted previously. All three systems demonstrated potential for use in the treatment of intersecting roadways. However, the hybrid end terminal/crash cushion and sand barrel attenuator and the hybrid bullnose system both posed greater operational and constructability concerns due to their complexity and relatively large footprint. Thus, the hybrid end terminal/crash cushion and net attenuator was selected for further study based on its potential safety performance, its relatively clean design and ease of maintenance, and the potential to accommodate moderate slopes behind the system.

Based on the analysis and testing detailed herein, the hybrid end terminal/crash cushion and net attenuator system had several areas in need of further development. First, dynamic component testing of the proposed Dragnet attenuator found that the current force levels were insufficient to maintain stopping distances near the desired length of 30 ft (9.1 m). In fact, component testing with three standard Dragnet energy absorbers on each side of the system resulted in deflections over 40 ft (12.2 m). Thus, redesign of the net attenuator system will be required to increase the resistive force and shorten the stopping distances. This will likely require redesign of the energy-absorbing drums, the capture net, and the anchorage of the energy absorbers. Additionally, it was desired that the hybrid end terminal/crash cushion and net attenuator attempt to accommodate moderate slopes. Thus, additional research is needed to determine what slopes can be safely used with the revised net attenuator. This initial phase of the research considered a variety of end terminal and crash cushion systems, but additional research is needed to determine what other systems are optimal based on their geometry and shielding of

the bridge rail end. Finally, additional research is needed to determine the exact layout of the hybrid end terminal/crash cushion and net attenuator system in order to ensure that the two systems function properly when used together.

Thus, the current research results indicated a potential for an alternative treatment for intersecting roadways to meet the MASH safety criteria. However, further research is needed to complete the design and prepare it for full-scale crash testing and evaluation to MASH TL-3.

28 REFERENCES

1. *Roadside Design Guide*, American Association of State Highway and Transportation Officials (AASHTO), Issue 4, Washington, D.C., 2011.
2. Ross, H.E., Sicking, D.L., Zimmer, R.A., and Michie, J.D., *Recommended Procedures for the Safety Performance Evaluation of Highway Features*, National Cooperative Highway Research Program (NCHRP) Report No. 350, Transportation Research Board, Washington, D.C., 1993.
3. *Manual for Assessing Safety Hardware (MASH)*, American Association of State Highway and Transportation Officials (AASHTO), Washington, D.C., 2009.
4. Abu-Odeh, A.Y., McCaskey, K., Bligh, R.P., Menges, W.L., and Kuhn, D.L., *Crash Test and MASH TL-3 Evaluation of the TxDOT Short Radius Guardrail*, Final Report to the Texas Department of Transportation, Report No. 0-6711-1, Texas Transportation Institute, Texas A&M University, College Station, Texas, March 2015.
5. Michie, J.D., *Recommended Procedures for the Safety Performance Evaluation of Highway Appurtenances*, National Cooperative Highway Research Program (NCHRP) Report No. 230, Transportation Research Board, Washington, D.C., March 1981.
6. Mayer, J.B., *Full-Scale Crash Testing of Approach Guardrail for Yuma County Public Works Department*, Final Report, Project No. 06-2111, Southwest Research Institute, San Antonio, Texas, 1989.
7. *Guide Specifications for Bridge Railings*, American Association of State Highway Transportation Officials (AASHTO), Washington, D.C., 1989.
8. *Curved W-Beam Guardrail Installations at Minor Roadway Intersections*, Federal Highway Administration (FHWA), U.S. Department of Transportation, Technical Advisory T5040.32, April 13, 1992.
9. Bronstad, M.E., Calcote, L.R., Ray, M.H., and Mayer, J.B., *Guardrail-Bridge Rail Transition Designs*, Volume I, Report No. FHWA/RD-86/178, Southwest Research Institute, San Antonio, Texas, April 1988.
10. Ross, H.E. Jr., Bligh, R.P., and Parnell, C.B., *Bridge Railing End Treatments at Intersecting Streets and Drives*, Report No. FHWA TX-91/92-1263-1F, Texas Transportation Institute, College Station, Texas, November 1992.
11. Bligh, R.P., Ross, H.E. Jr., and Alberson, D.C., *Short-Radius Thrie-Beam Treatment for Intersecting Streets and Drives*, Final Report to the Texas Department of Transportation, Report No. FHWA/TX-95/1442-1F, Texas Transportation Institute, Texas A&M University, College Station, Texas, November 1994.

12. Bielenberg, R.W., Reid, J.D., Faller, R.K., Rohde, J.R., Sicking, D.L., and Keller, E.A., *Concept Development of a Short-Radius Guardrail System for Intersecting Roadways*, Final Report to the Midwest States Regional Pooled Fund, Midwest Research Report No. TRP-03-100-00, Midwest Roadside Safety Facility, University of Nebraska-Lincoln, Lincoln, Nebraska, September 2000.
13. Bielenberg, R.W., Faller, R.K., Holloway, J.C., Reid, J.D., Rohde, J.R., and Sicking, D.L., *Phase II Development of a Short-Radius Guardrail for Intersecting Roadways*, Final Report to the Midwest States Pooled Fund Program, MwRSF Research Record No. TRP-03-137-03, Midwest Roadside Safety Facility, University of Nebraska-Lincoln, Lincoln, Nebraska, 2003.
14. Stolle, C.S., Polivka, K.A., Bielenberg, R.W., Reid, J.D., Faller, R.K., Rohde, J.D., and Sicking, D.L., *Phase III Development of a Short-Radius Guardrail for Intersecting Roadways*, Final Report to the Midwest States Pooled Fund Program, MwRSF Research Report No. TRP-03-183-07, Midwest Roadside Safety Facility, University of Nebraska-Lincoln, Lincoln, Nebraska, August 2007.
15. Stolle, C.S., Polivka, K.A., Bielenberg, R.W., Reid, J.D., Faller, R.K., Rohde, J.D., and Sicking, D.L., *Phase IV Development of a Short-Radius Guardrail for Intersecting Roadways*, Final Report to the Midwest States Pooled Fund Program, MwRSF Research Report No. TRP-03-199-08, Midwest Roadside Safety Facility, University of Nebraska-Lincoln, Lincoln, Nebraska, February 2008.
16. Button, J.W., Buth, E., and Olson, R.M., *Crash Tests of Five-Foot Radius Plate Beam Guardrail*, Final Report to the Minnesota Department of Transportation, Texas Transportation Institute, Texas A&M University, College Station, Texas, June 1975.
17. Parks, D.M., Stoughton, R.L., Stoker, J.R., and Nordlin, E.F., *Vehicular Crash Tests of Four Bullnose Traffic Barrier Designs*, Final Report to the California Department of Transportation, Caltrans Report No. FHWA-CA-DOT-TL-6392-5-76-35, California Department of Transportation, Sacramento, California, June 1976.
18. Robertson, R.G., and Ross, H.E. Jr., *Colorado Median Barrier End Treatment Tests*, Final Report to the Colorado Department of Transportation, TTI Research Report No. CDOH-TTI-R-81-2, Texas Transportation Institute, Texas A&M University, College Station, Texas, May 1981.
19. Bronstad, M.E., Ray, M.H., Mayer, J.B. Jr., and Brauer, S.K., *Median Barrier Terminals and Median Treatments: Volume I*, Final Report to the Federal Highway Administration, SwRI Research Report No. FHWA/RD-88/004, Southwest Research Institute, San Antonio, Texas, October 1987.
20. Bielenberg, R.W., Faller, R.K., Reid, J.D., Sicking, D.L., Rohde, J.R., and Keller, E.A., *Concept Development of a Bullnose Guardrail System for Median Applications*, Final Report to the Midwest States Regional Pooled Fund Program, Midwest Research Report No. TRP-03-73-98, Midwest Roadside Safety Facility, University of Nebraska-Lincoln, Lincoln, Nebraska, May 1998.

21. Bielenberg, R.W., Reid, J.D., Faller, R.K., Sicking, D.L., Rohde, J.R., Keller, E.A., and Holloway, J.C., *Phase II Development of a Bullnose Guardrail System for Median Applications*, Final Report to the Midwest States Regional Pooled Fund Program, Midwest Research Report No. TRP-03-78-98, Midwest Roadside Safety Facility, University of Nebraska-Lincoln, Lincoln, Nebraska, December 1998.
22. Bielenberg, R.W., Reid, J.D., Faller, R.K., Rohde, J.R., Sicking, D.L., Keller, E.A., Holloway, J.C., and Supencheck, L., *Phase III Development of a Bullnose Guardrail System for Median Applications*, Final Report to the Midwest States Regional Pooled Fund Program, Midwest Research Report No. TRP-03-95-00, Midwest Roadside Safety Facility, University of Nebraska-Lincoln, Lincoln, Nebraska, June 2000.
23. Arens, S.W., Sicking, D.L., Faller, R.K., Reid, J.D., Bielenberg, R.W., Rohde, J.R., and Lechtenberg, K.A., *Investigating the Use of a New Breakaway Steel Post*, Letter Report to the Midwest States Regional Pooled Fund Program, Midwest Research Report No. TRP-03-218-09, Midwest Roadside Safety Facility, University of Nebraska-Lincoln, Lincoln, Nebraska, August 2009.
24. Arens, S.W., Sicking, D.L., Faller, R.K., Reid, J.D., Bielenberg, R.W., Rohde, J.R., and Lechtenberg, K.A., *Investigating the Use of a New Universal Breakaway Steel Post*, Final Report to the Midwest States Regional Pooled Fund Program, Midwest Research Report No. TRP-03-281-09, Midwest Roadside Safety Facility, University of Nebraska-Lincoln, Lincoln, Nebraska, August 2009.
25. Schmidt, J.D., Sicking, D.L., Faller, R.K., Reid, J.D., Bielenberg, R.W., and Lechtenberg, K.A., *Investigating the Use of a New Breakaway Steel Post – Phase 2*, Final Report to the Midwest States Regional Pooled Fund Program, Midwest Research Report No. TRP-03-230-10, Midwest Roadside Safety Facility, University of Nebraska-Lincoln, Lincoln, Nebraska, August 2010.
26. Abu-Odeh, A., and Kim, K., *Evaluation of Existing T-Intersection Guardrail Systems for Equivalency with NCHRP Report No. 350 TL-2 Test Conditions*, Final Report to the Roadside Safety Research Pooled Fund Program, TTI Research Report No. 405160-10, Texas Transportation Institute, Texas A&M University, College Station, Texas, August, 2010.
27. Dobrovolny, C.S., and Brackin, M.S., *Best Practices for Barrier Protection of Bridge Ends*, Final Report to the Roadside Safety Research Pooled Fund Program, TTI Research Report No. 405160-38, Study No. TPF-5(114), Texas Transportation Institute, Texas A&M University, College Station, Texas, February, 2014.
28. Roadway Departure Technology Transfer, Resource Charts, Roadside Terminals, Federal Highway Administration, Washington, DC, Available: < http://safety.fhwa.dot.gov/roadway_dept/policy_guide/road_hardware/resource_charts/road_sideterminals.pdf>, Updated October 2012, Accessed: October 3, 2014.
29. Roadway Departure Technology Transfer, Resource Charts, Median Terminals, Federal Highway Administration, Washington, DC, Available: < <http://safety.fhwa.dot.gov/>

roadway_dept/policy_guide/road_hardware/resource_charts/medianterminals.pdf>, Updated September 2012, Accessed: October 3, 2014.

30. List of Geometric and Roadside Design Acceptance Letters, Longitudinal Barriers, Federal Highway Administration, Washington, DC, Available: < http://safety.fhwa.dot.gov/roadway_dept/policy_guide/road_hardware/listing.cfm?code=cushions>, Accessed: October 3, 2014.
31. Roadway Departure Technology Transfer, Resource Charts, Crash Cushions, Federal Highway Administration, Washington, DC, Available: < http://safety.fhwa.dot.gov/roadway_dept/policy_guide/road_hardware/resource_charts/crashcushions.pdf>, Updated October 2012, Accessed: October 3, 2014.
32. “Test Method for Vehicle Crash Testing of Perimeter Barriers and Gates”, Department of State Bureau of Diplomatic Security, Washington, D.C., March 2003.
33. ASTM International Designation F2656-07, 2007, “Standard Test Method for Vehicle Crash Testing of Perimeter Barriers,” ASTM International, West Conshohocken, PA, 2007, DOI: 10.1520/F2656-07, www.astm.org.
34. Department of Defense Anti-Ram Vehicle Barrier List, US Army Corps of Engineers, Omaha, NE, Available: <http://www.usace.army.mil/Portals/2/docs/Protection/DOD_Anti-Ram_Vehicle_Barriers_January_20141.pdf> Accessed: October 31, 2014.
35. Anti-Ram Cable Fence, NEU Security Services, Austin, TX, Available: <<http://www.neusecurity.com/pdf/Anti-Ram-Cable-Fence.pdf>> Accessed: October 31, 2014.
36. Cable Based Restraint Barrier, NEU Security Services, Austin, TX, Available: <http://www.neusecurity.com/pdf/Cable_based_restraint_barrier-NSS.pdf> Accessed: October 31, 2014.
37. GRAB-300 Barrier, Future Net Security Solutions, Franklin, TN, Available: <<http://futurenetsecurity.com/specifications/specification-GRAB-300.pdf>> Accessed: October 31, 2014.
38. Xtreme Mobile Barrier, Future Net Security Solutions, Franklin, TN, Available: <<http://futurenetsecurity.com/cut-sheets/xmb.pdf>> Accessed: October 31, 2014.
39. Gibraltar Anti-Ram Crash Fence, Gibraltar, Marble Falls, TX, Available: <<http://www.gibraltarus.com/anti-ram-vehicle-barriers/anti-ram-cable-fence>> Accessed: October 31, 2014.
40. Quick Connect Barrier, Barrier1 Systems, Inc., Greensboro, NC, Available: <<http://www.barrier1.us/brochures/qcb.pdf>> Accessed: October 31, 2014.
41. RSS-2015 Electric Cable Trap, RSSI, Panama City, FL, Available: <<http://www.rssi.com/downloads/docs/RSS-2015%20CutSheet.pdf>> Accessed: October 31, 2014.

42. SW1200 Post & Cable Passive Barrier System, Future Net Security Systems, Franklin, TN, Available: <<http://futurenetsecurity.com/cut-sheets/sw1200.pdf>> Accessed: October 31, 2014.
43. VA-Net-300, Barrier 1 System, Inc., Greensboro, NC, Available: <<http://barrier1.us/brochures/Vehicle%20Arrestor%20-%20Net%20Based%20Active%20Barrier.pdf>> Accessed: October 31, 2014.
44. Site drawings provided by the Nebraska Department of Roads in an email.
45. Intersection Safety: A Manual for Local Rural Road Owners, Federal Highway Administration, Washington, DC, Available: <http://safety.fhwa.dot.gov/local_rural/training/fhwasal108/ch3.cfm> Accessed: March 21, 2015.
46. *A Policy On Geometric Design of Highways and Streets 4th Ed.*, American Association of State Highway and Transportation Officials (AASHTO), Washington, D.C., 2001.
47. Society of Automotive Engineers (SAE), *Instrumentation for Impact Test – Part 1 – Electronic Instrumentation*, SAE J211/1 MAR95, New York City, NY, July, 2007.
48. Federal Highway Administration, Acceptance Letter CC-70, November 28, 2000. Retrieved from: <http://safety.fhwa.dot.gov/roadway_dept/policy_guide/road_hardware/barriers/pdf/cc-70.pdf> [2014, August 18].
49. Hallquist, J.O. *LS-DYNA Keyword User's Manual – LS-DYNA R7.1*, Livermore Software Technology Corporation, Livermore, California, May 26, 2014.
50. Stolle, C.S., Reid, J.D., and Lechtenberg, K.A., *Development of Advanced Finite Element Material Model for Cable Barrier Wire Rope*, Final Report to the Mid-America Transportation Center, MwRSF Research Report No. TRP-03-137-03, Midwest Roadside Safety Facility, University of Nebraska-Lincoln, Lincoln, Nebraska, 2010.
51. Hirsch, T. J., Hayes, G. G., and Ivey, D. L., *Dragnet Vehicle Arresting System*, Technical Memorandum 505-4, Progress Memorandum on Contract No. CPR-11-5851, U.S. Department of Transportation, Federal Highway Administration, Bureau of Public Roads, Texas Transportation Institute, Texas A&M University, College Station, Texas, February 1969.
52. *The Dragnet Vehicle Arresting System*, Product Manual, Roadway Safety Service, Inc., Ronkonkoma, New York, 1995.
53. *Guide for Selecting, Locating, and Designing Traffic Barriers*, American Association of State Highway and Transportation Officials (AASHTO), Washington, D.C., 1977.
54. Coon, B. A., *Development of Crash Reconstruction Procedures for Roadside Safety Appurtenances*, Doctoral Dissertation, School, University of Nebraska-Lincoln, August, 2003.

29 APPENDICES

Appendix A. Material Specifications

METALLURGICAL TEST REPORT



SPS Coil Processing Tulsa
5275 Bird Creek Ave.
Port of Catoosa, OK 74015

PAGE 1 of 1
DATE 09/04/2013
TIME 11:16:04
USER WILLIAMR

Dragnet Project Plates 1/2" and 3/4"
R# 14-0204

13716
Warehouse 0040
401 New Century Parkway
New Century KS 66031

S
H
I
P
T
O

S
O
L
D
T
O

Order	Material No.	Description	Quantity	Weight	Customer Part	Customer PO	Ship Date
40209023-0010	701672120TM	1/2 72 X 120 A36 TEMPERPASS STPLPL	8	9,801.600			09/04/2013

Heat No.	Vendor	Material	Weight	Customer Part	Customer PO	Ship Date							
A307682	SEVERSTAL COLUMBUS	8 EA 9,801.600 LB	9,801.600			09/04/2013							
Batch 0002553602													
Carbon	Phosphorus	Sulphur	Nickel	Chromium	Molybdenum	Boron	Copper	Aluminum	Titanium	Vanadium	Columbium	Nitrogen	Tin
0.1900	0.0300	0.0140	0.0400	0.0600	0.0100	0.0001	0.1000	0.0300	0.0020	0.0030	0.0010	0.0066	0.0050

Chemical Analysis		Mechanical/ Physical Properties	
DOMESTIC		MILL SEVERSTAL COLUMBUS	
Elong		Charpy	
73416.000	36.20	0	0
71202.000	33.30	0	0
Yield		Charpy Dr	
49559.000	0	NA	NA
47760.000	0	NA	NA
Rckwl		Charpy Sz	
0	0		
Grain		Temperature	
0.000	0.000		
0.000	0.000		

THE CHEMICAL, PHYSICAL, OR MECHANICAL TESTS REPORTED ABOVE ACCURATELY REFLECT INFORMATION AS CONTAINED IN THE RECORDS OF THE CORPORATION.

Figure A-1. Material Certifications, Test Nos. IRA-1 through IRA-4

MILL TEST CERTIFICATE

1700 HOLT RD N.E.
Tuscaloosa, AL 35404-1000
800-827-8872



NUCOR STEEL TUSCALOOSA, INC.

Load Number	Tally	Mill Order Number	PO NO Line NO	Part Number	Certificate Number	Prepared															
T040265	00000000516331	N-123795-007	4500208906 7		1433792-1	08/22/2013 20:28															
Grade																					
Order Description: A36, 0.7500 IN x 72.000 IN x 240.000 IN Quality Plan Description: A36/SA36/A70936: ASTM A36-08/ASME SA36-03/A709-36-10																					
Customer:																					
Sold TO: STEEL & PIPE SUPPLY CO., INC. Gardner KS Ship TO: Kansas City Warehouse New Century KS																					
Shipped Item	Heat/Slab Number	Certified By	C	Mn	P	S	Si	Cu	Ni	Cr	Mo	Cb	V	Al	Ti	N2	B	Ca	Sn	CEV	Test
3H1457E	B3U7752-03 ***	B3U7752	0.19	0.86	0.014	0.008	0.05	0.23	0.09	0.07	0.020	0.000	0.001	0.032	0.001	0.009	0.0000	0.0035	0.009	0.37	
3H1488B	B3U7757-01 ***	B3U7757	0.19	0.88	0.012	0.007	0.07	0.21	0.08	0.06	0.027	0.000	0.002	0.035	0.001	0.009	0.0001	0.0035	0.009	0.37	
Shipped Item	Certified By	Heat Number	Yield ksi	Tensile ksi	Y/T %	ELONGATION %		Bend	Hard	Charpy Impacts (ft-lbs)			Shear %			Test					
						2"	8"	OK?	HB	Size mm	1	2	3	Avg	1	2	3	Avg		Temp	
3H1457E	S3H1457FTT	B3U7752 ***	53.2	73.0	72.9	36.2															
3H1457E	S3H1457MTT	B3U7752 ***	51.8	68.0	76.2	36.2															
3H1488B	S3H1488FTT	B3U7757 ***	52.4	71.4	73.4	33.0															
3H1488B	S3H1488MTT	B3U7757 ***	51.1	67.0	76.3	37.7															

Items: 2 PCS: 9 Weight: 33079 LBS

Mercury has not come in contact with this product during the manufacturing process nor has any mercury been used by the manufacturing process. Certified in accordance with EN 10204 3.1. No weld repair has been performed on this material. CERTIFIED IN ACCORDANCE WITH EN 10204 3.1 B* NACE MR0175 Annex 2.1.2 compliant. Manufactured to a fully killed fine grain practice. NUTEMPER TEMPER PASSED plate from coil
ISO 9001:2008 Registered, PED Certified

***** indicates Heats melted and Manufactured in the U.S.A.

We hereby certify that the product described above passed all of the tests required by the specifications.

Quilin Yu
Dr. Quilin Yu - Metallurgist

Figure A-2. Material Certifications, Test Nos. IRA-1 through IRA-4

Appendix B. Accelerometer and Rate Transducer Data Plots, Test No. IRA-1

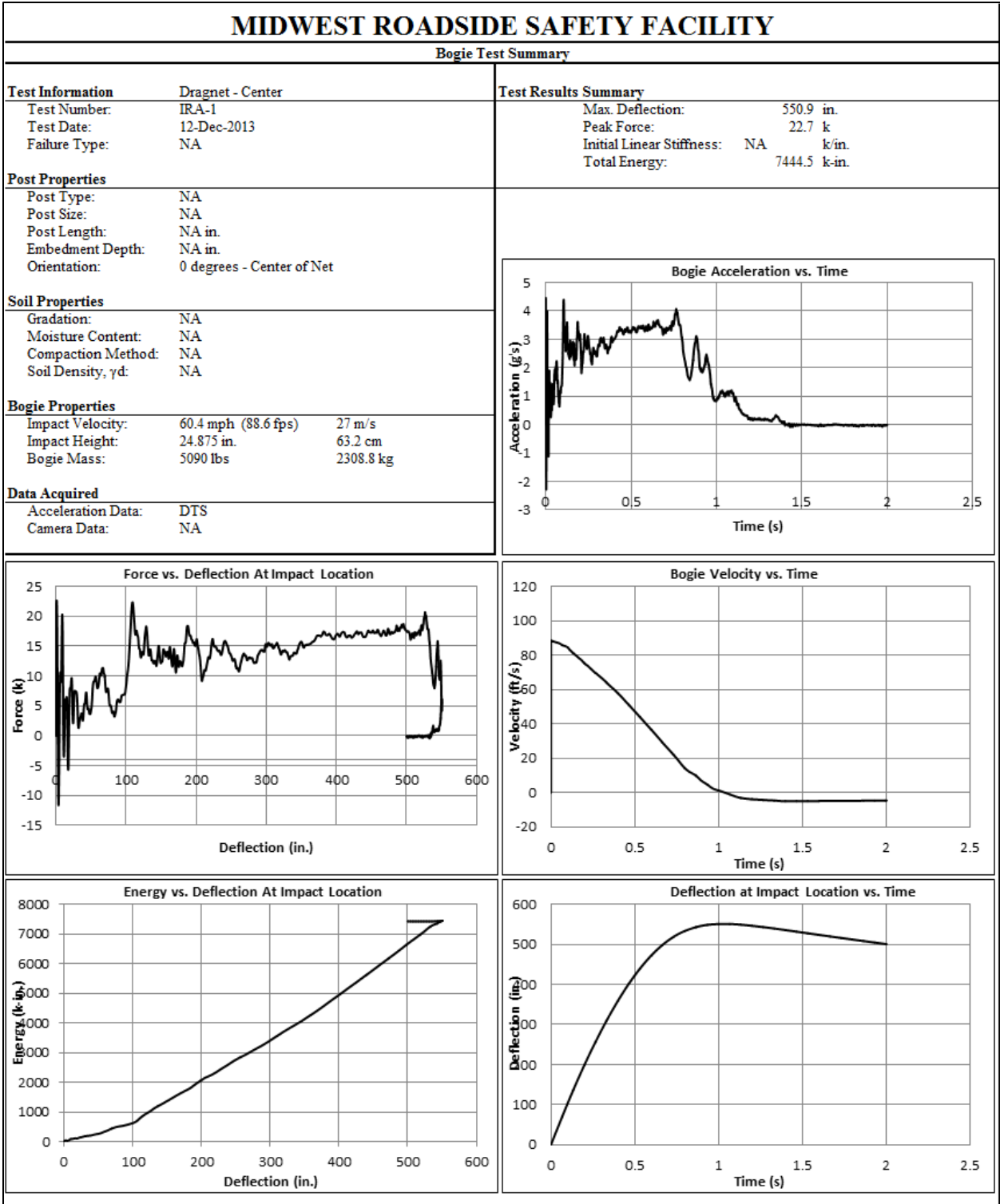


Figure B-1. Test No. IRA-1 Results (DTS) [English Units]

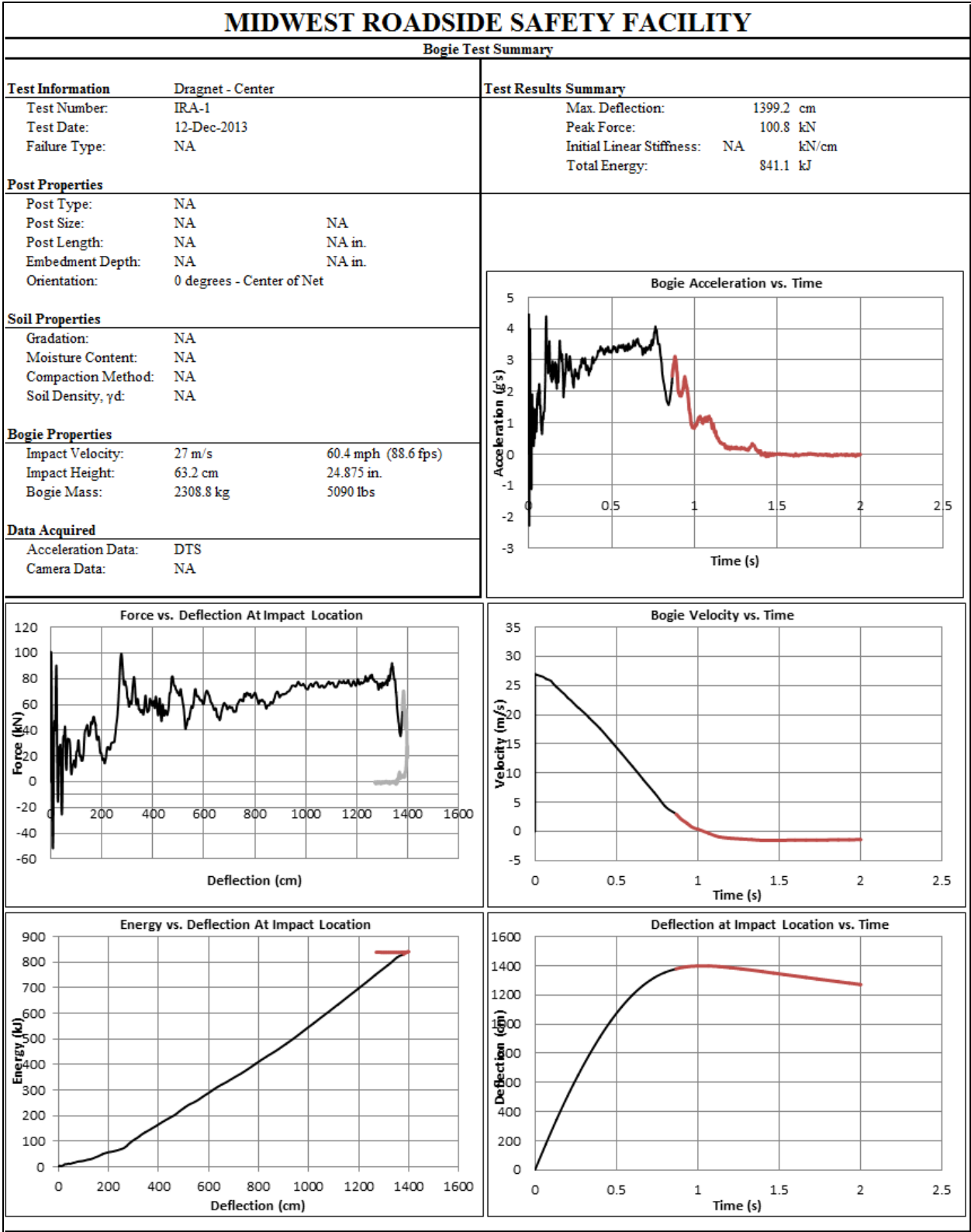


Figure B-2. Test No. IRA-1 Results (DTS) [Metric Units]

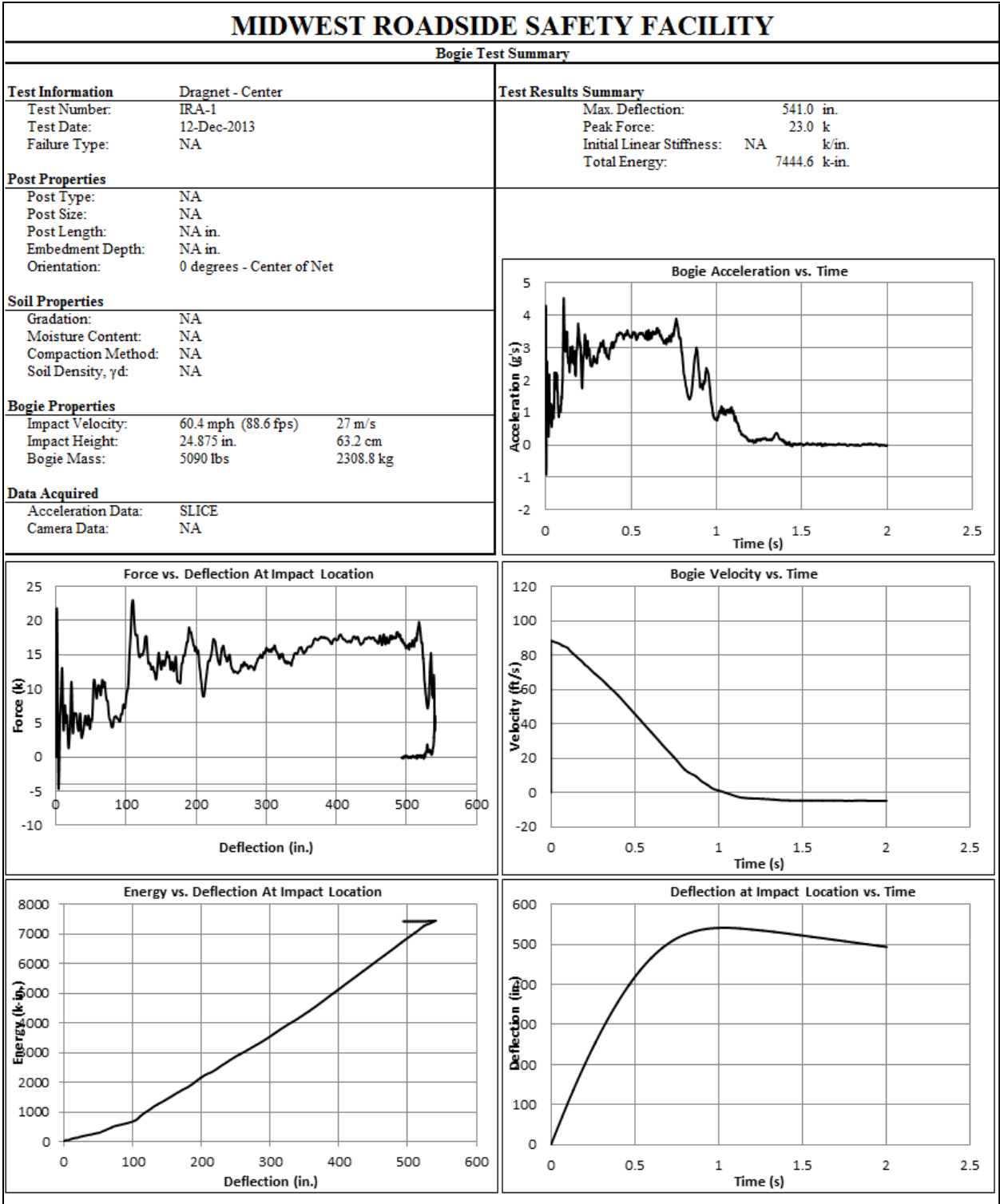


Figure B-3. Test No. IRA-1 Results (DTS-SLICE) [English Units]

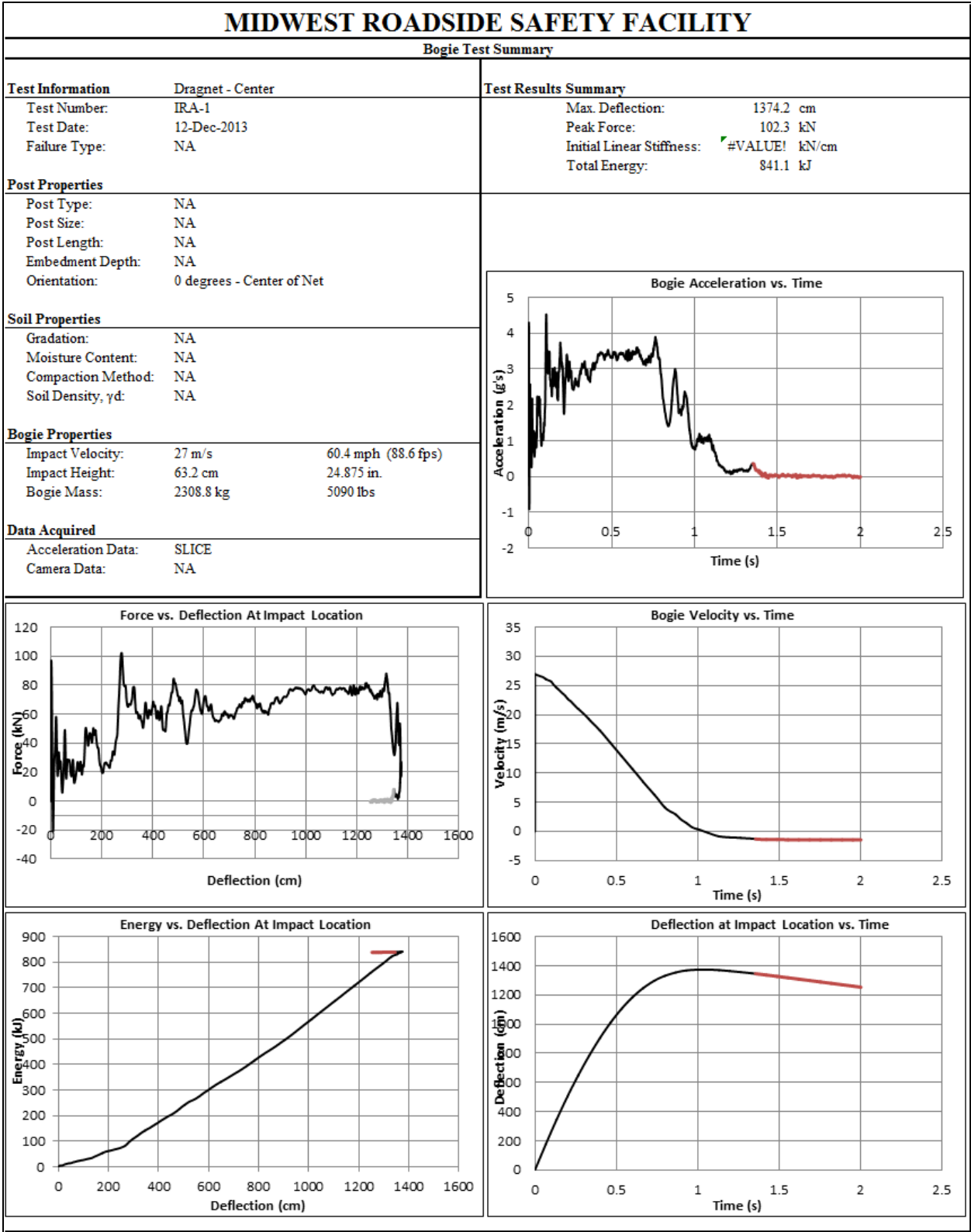


Figure B-4. Test No. IRA-1 Results (DTS-SLICE) [Metric Units]

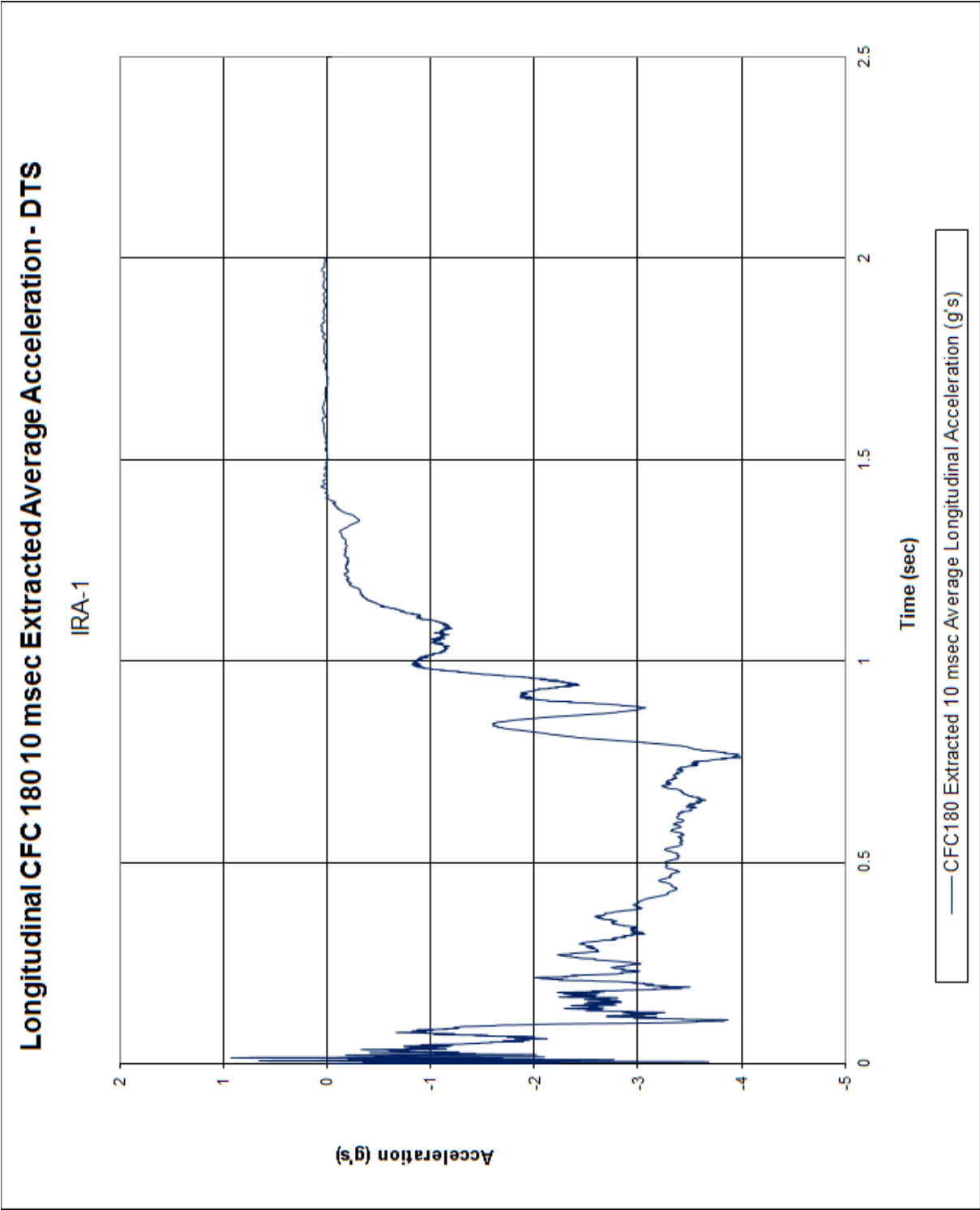


Figure B-5. 10-ms Average Longitudinal Deceleration (DTS), Test No. IRA-1

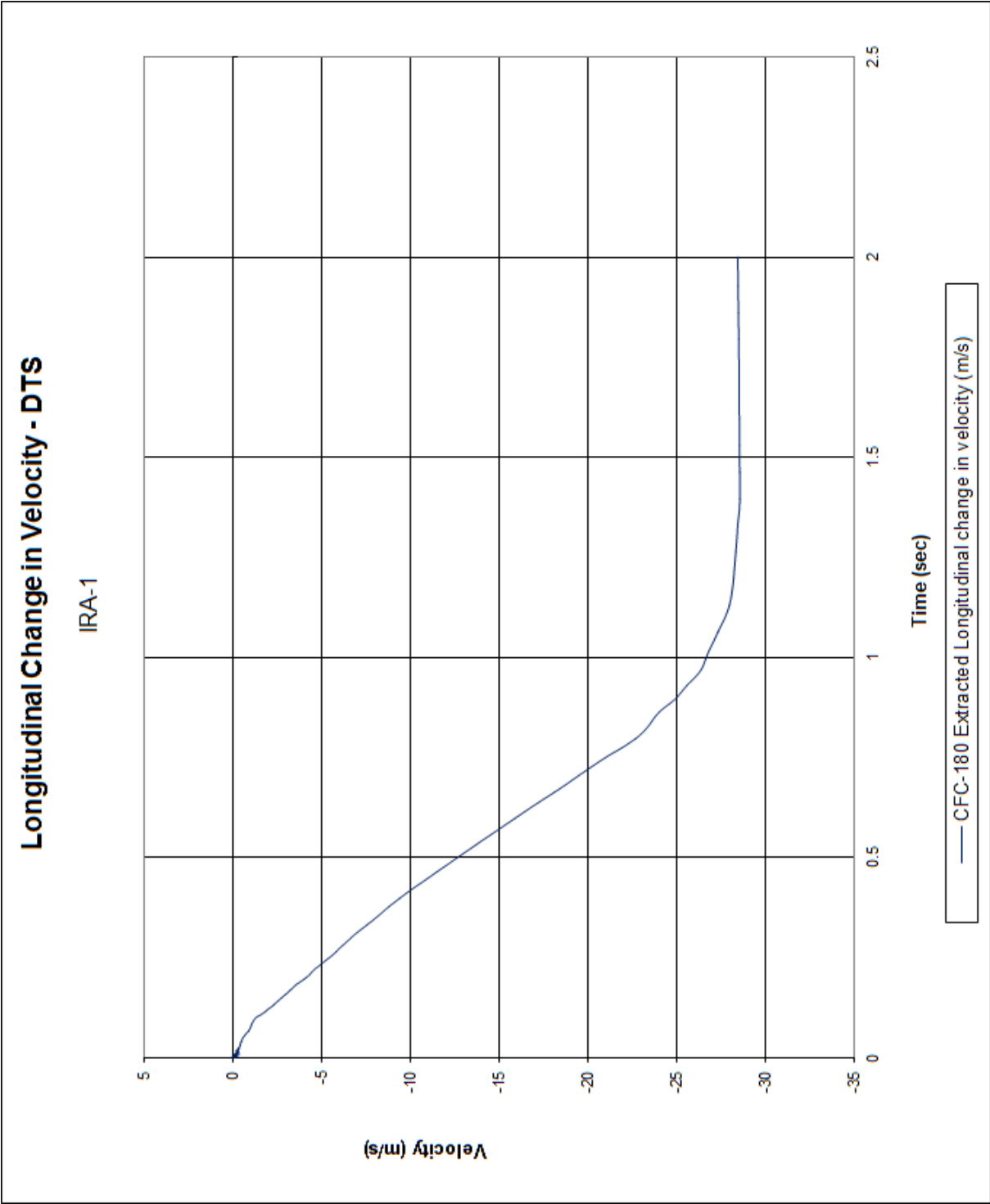


Figure B-6. Longitudinal Occupant Impact Velocity (DTS), Test No. IRA-1

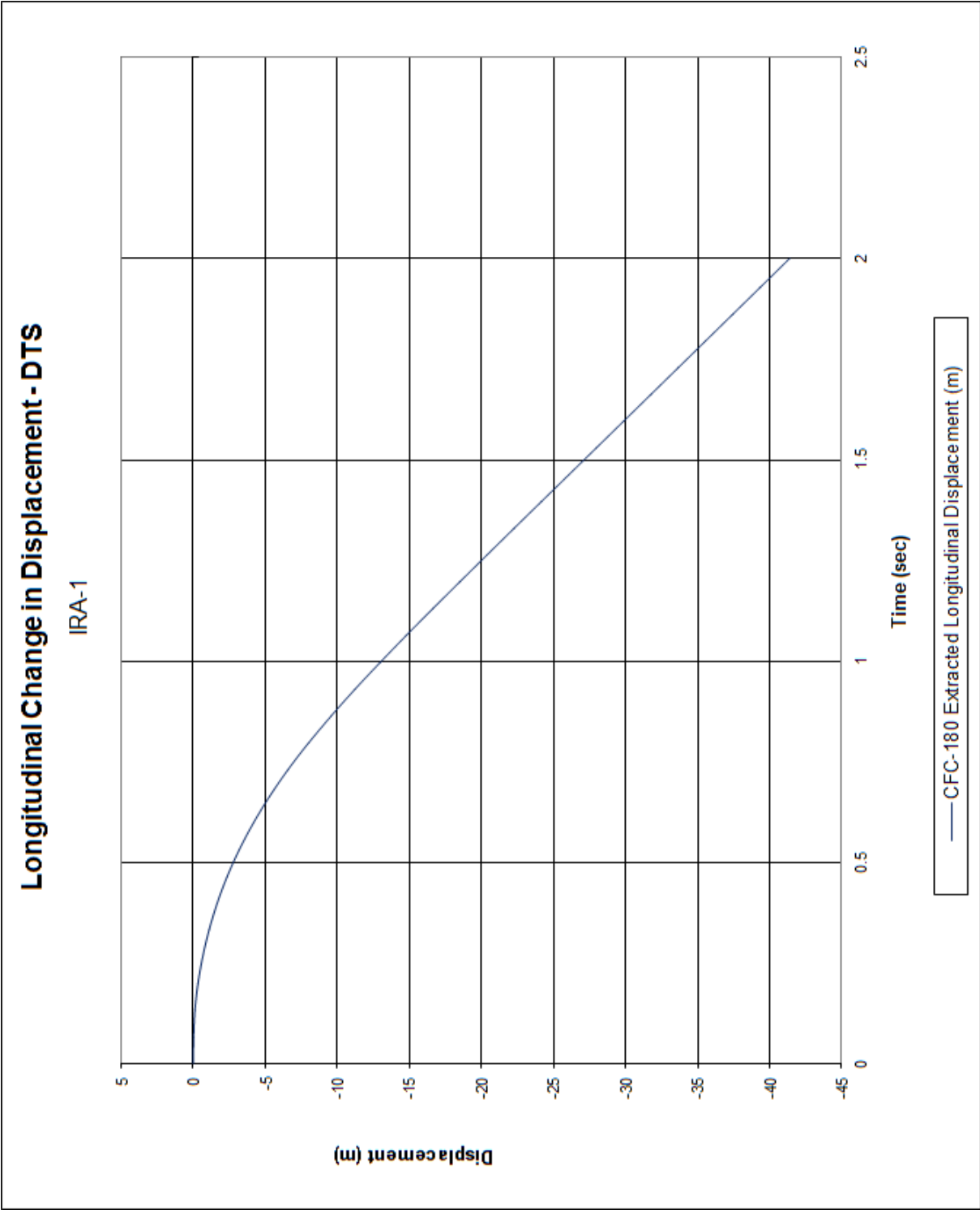


Figure B-7. Longitudinal Occupant Displacement (DTS), Test No. IRA-1

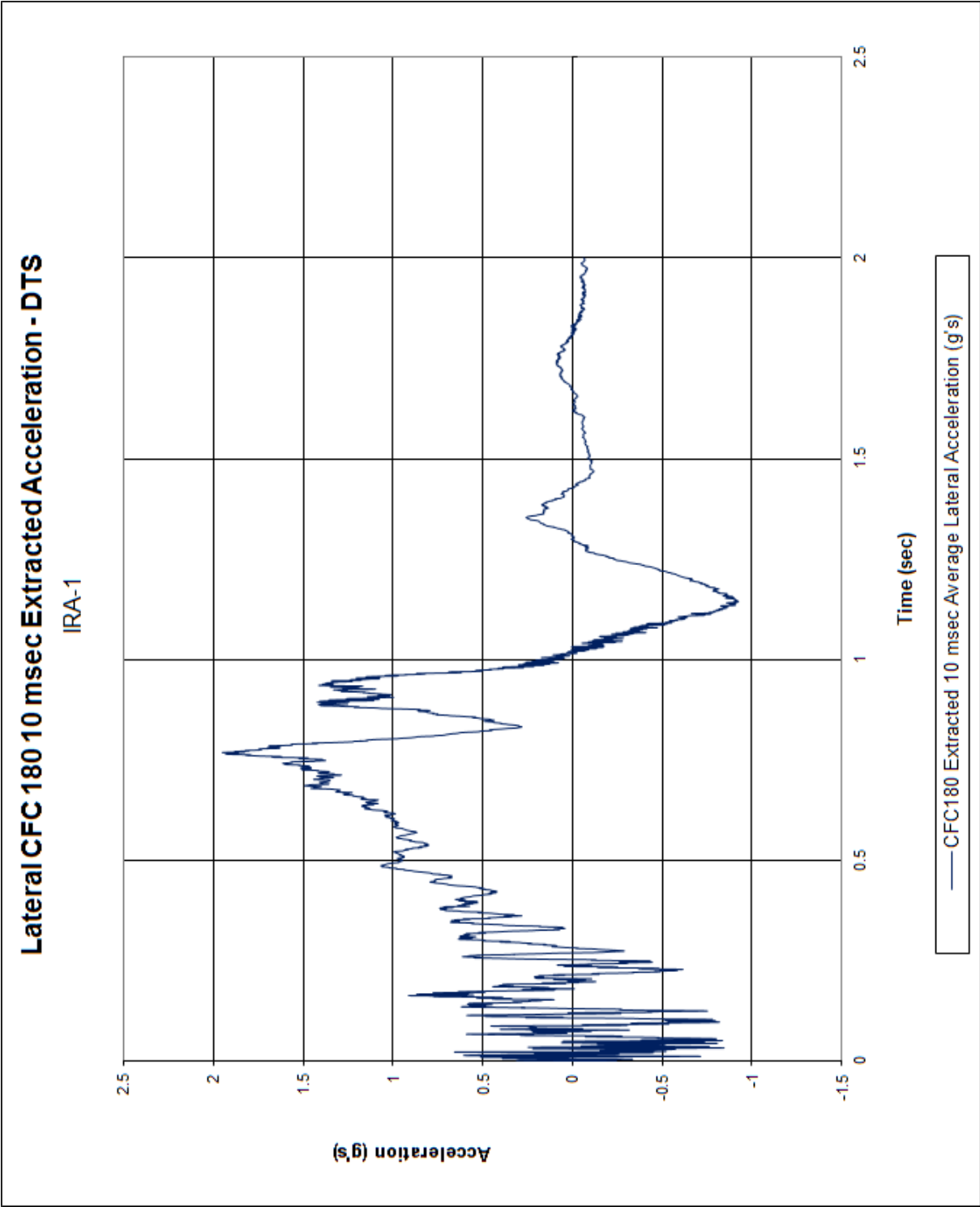


Figure B-8. 10-ms Average Lateral Deceleration (DTS), Test No. IRA-1

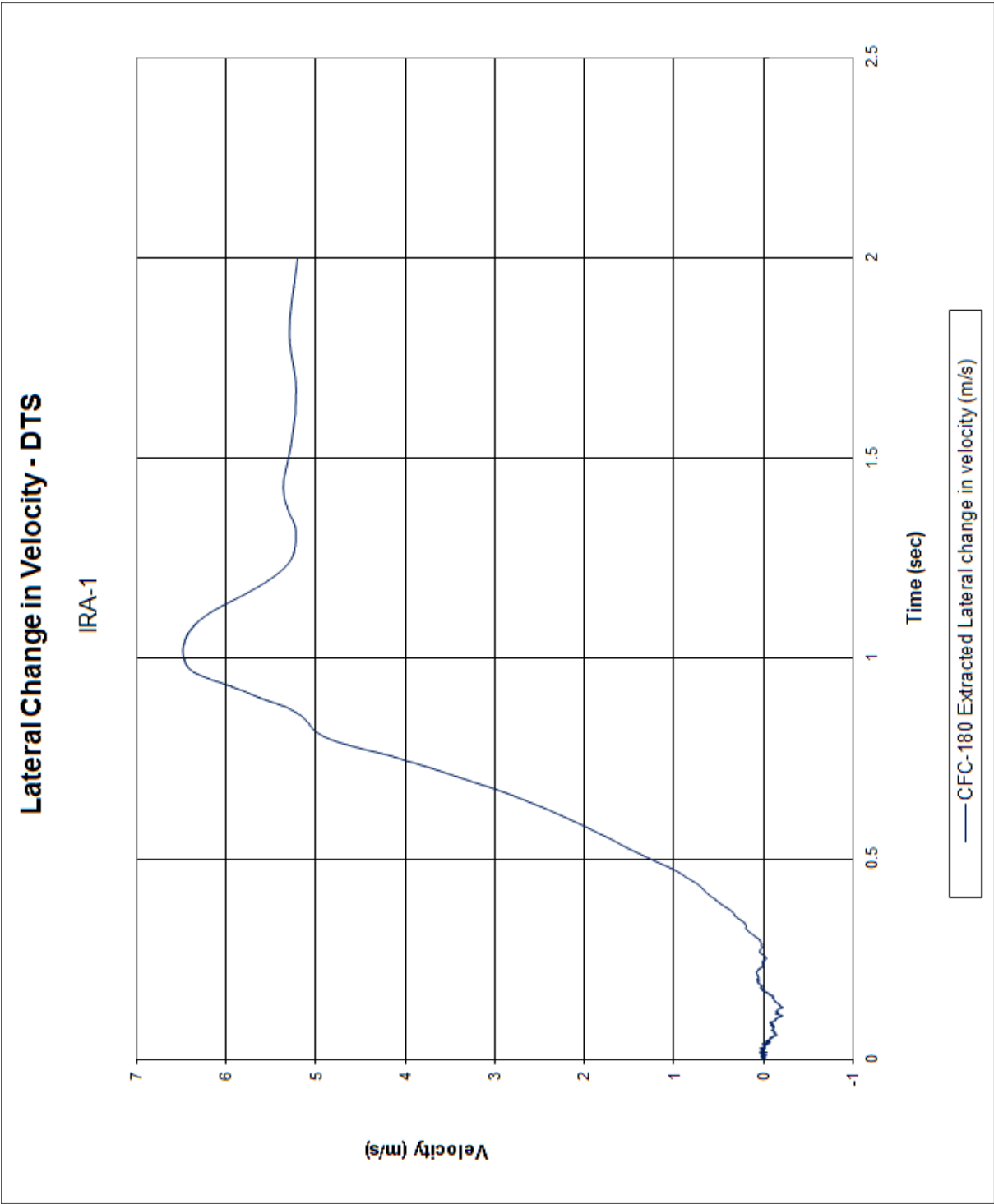


Figure B-9. Lateral Occupant Impact Velocity (DTS), Test No. IRA-1

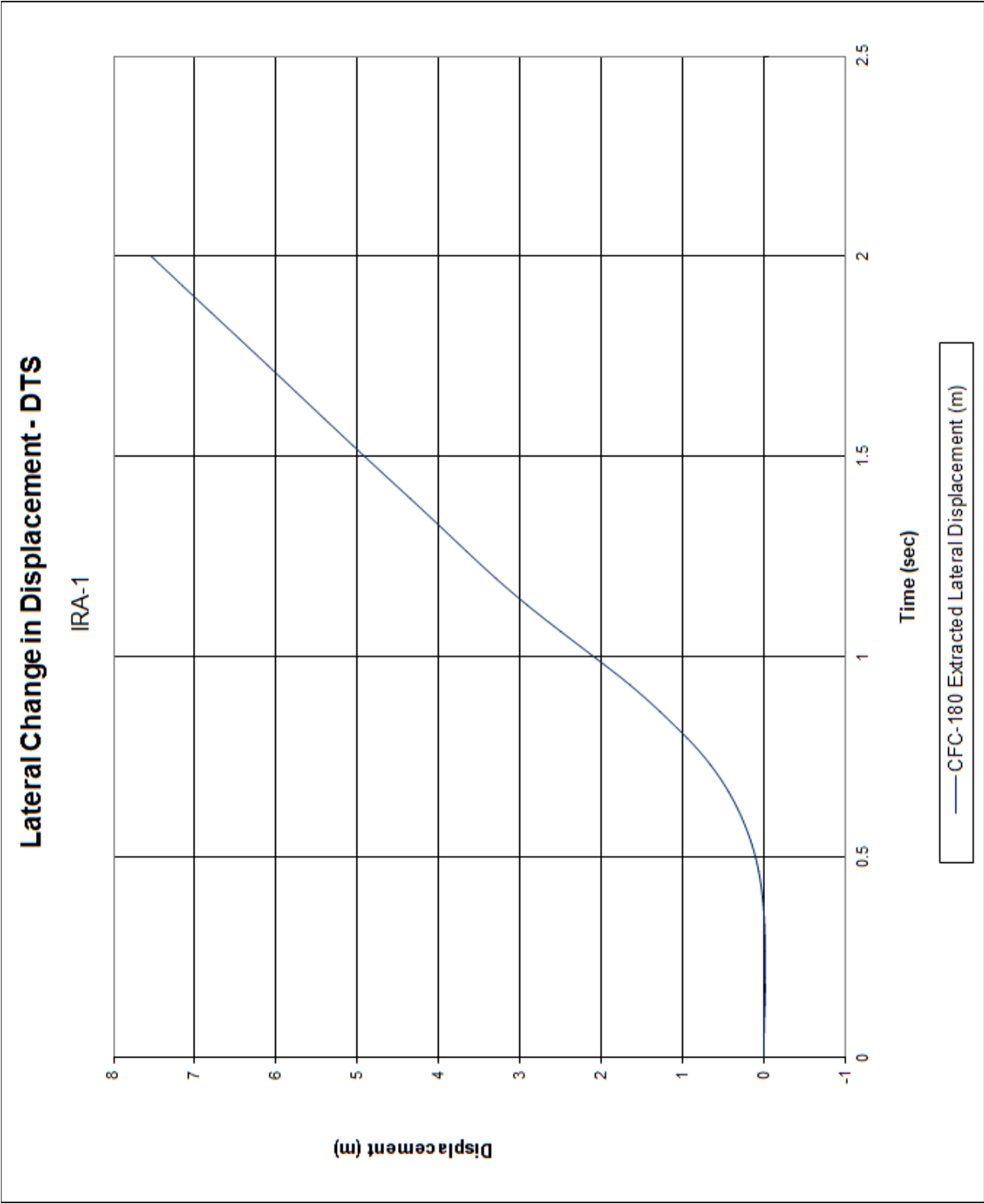


Figure B-10. Lateral Occupant Displacement (DTS), Test No. IRA-1

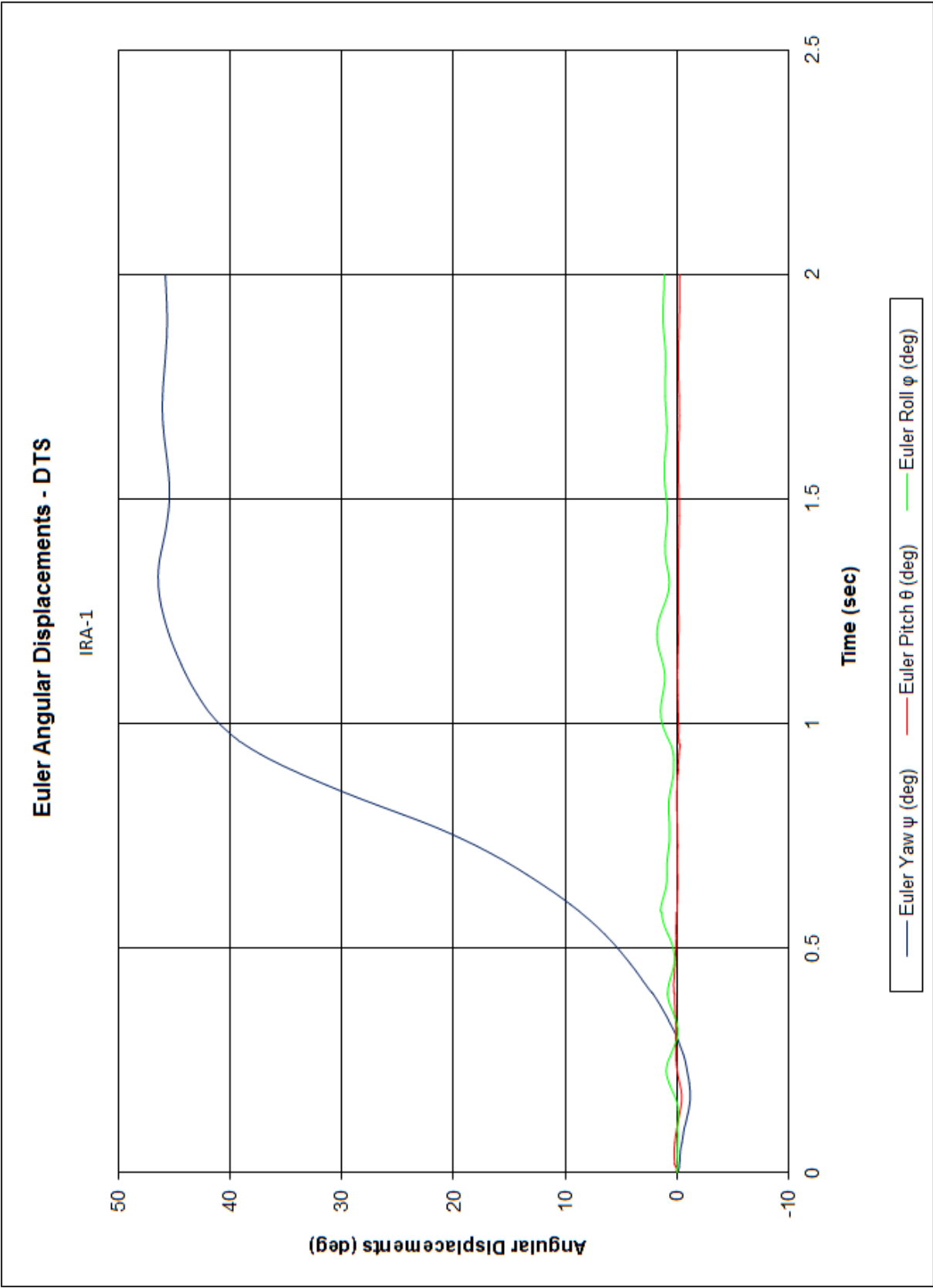


Figure B-11. Vehicle Angular Displacements (DTS), Test No. IRA-1

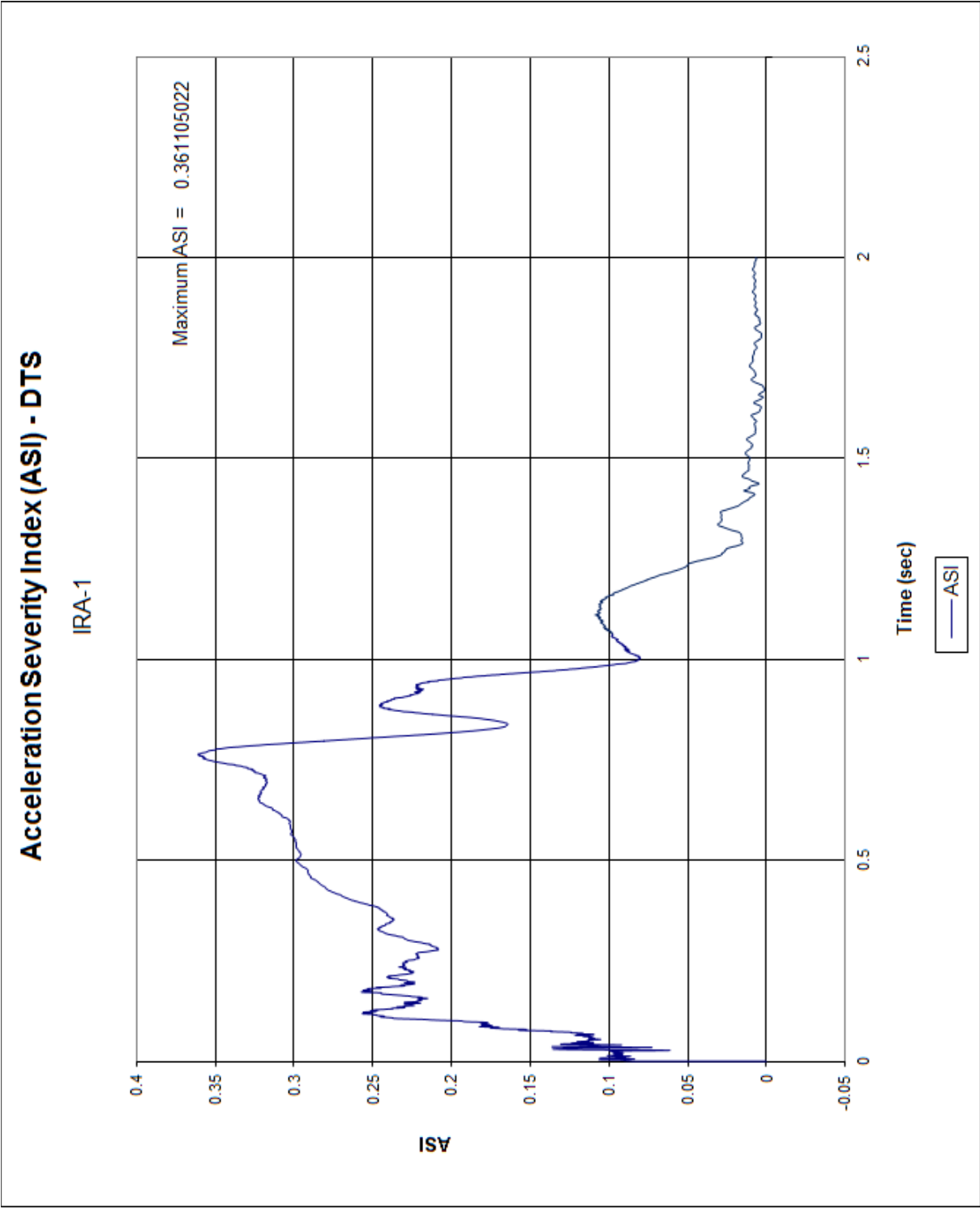


Figure B-12. Acceleration Severity Index (DTS), Test No. IRA-1

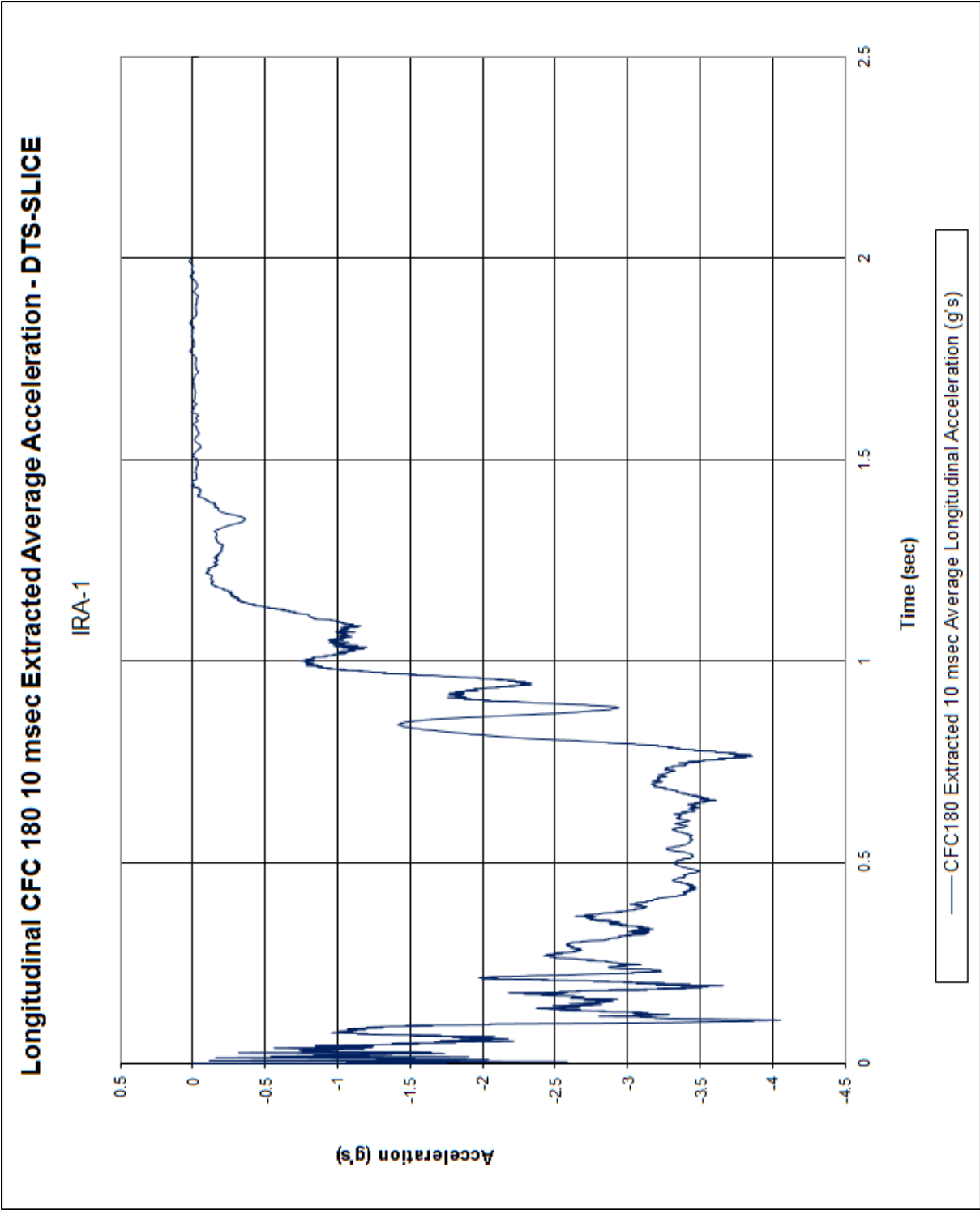


Figure B-13. 10-ms Average Longitudinal Deceleration (DTS-SLICE), Test No. IRA-1

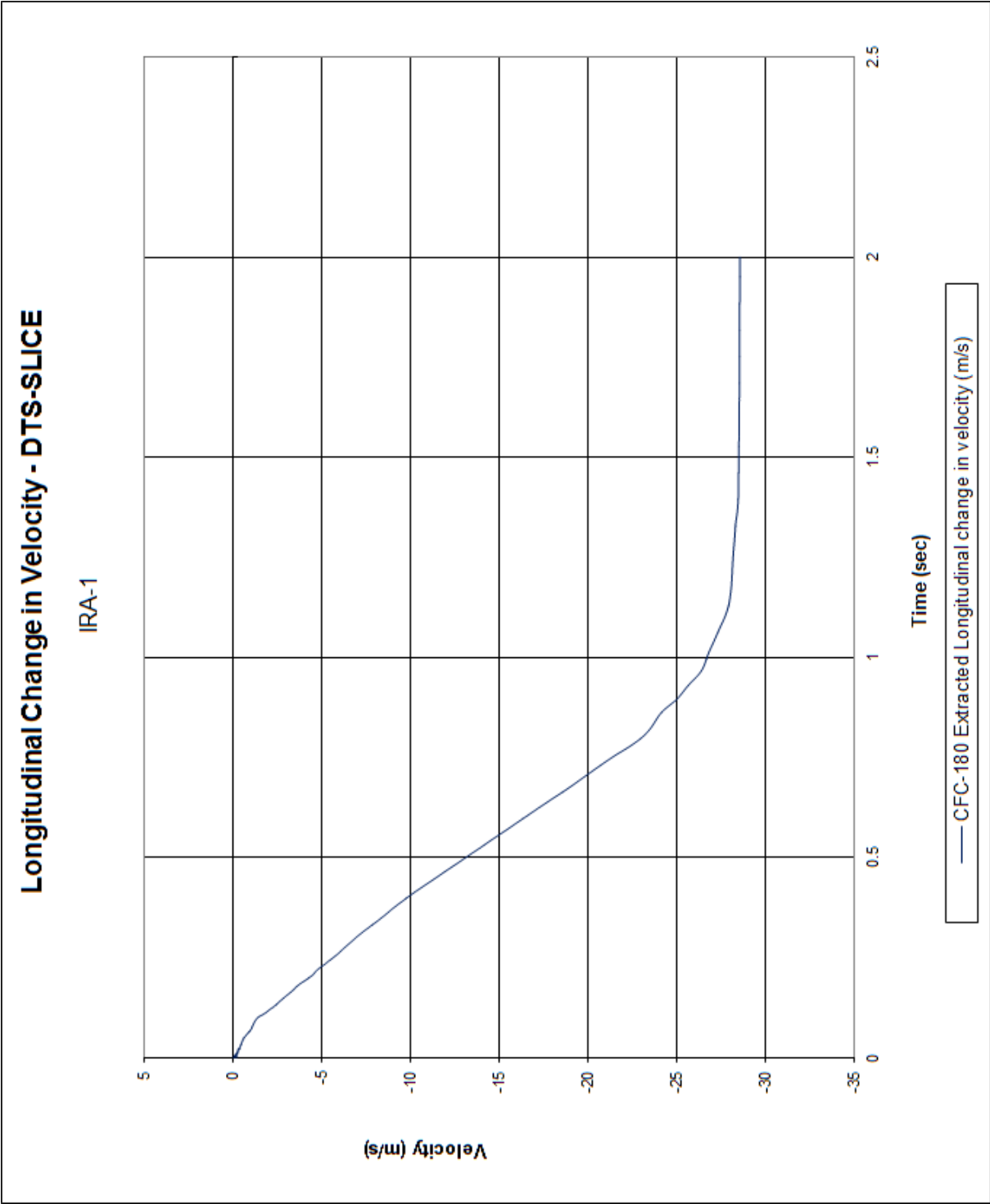


Figure B-14. Longitudinal Occupant Impact Velocity (DTS-SLICE), Test No. IRA-1

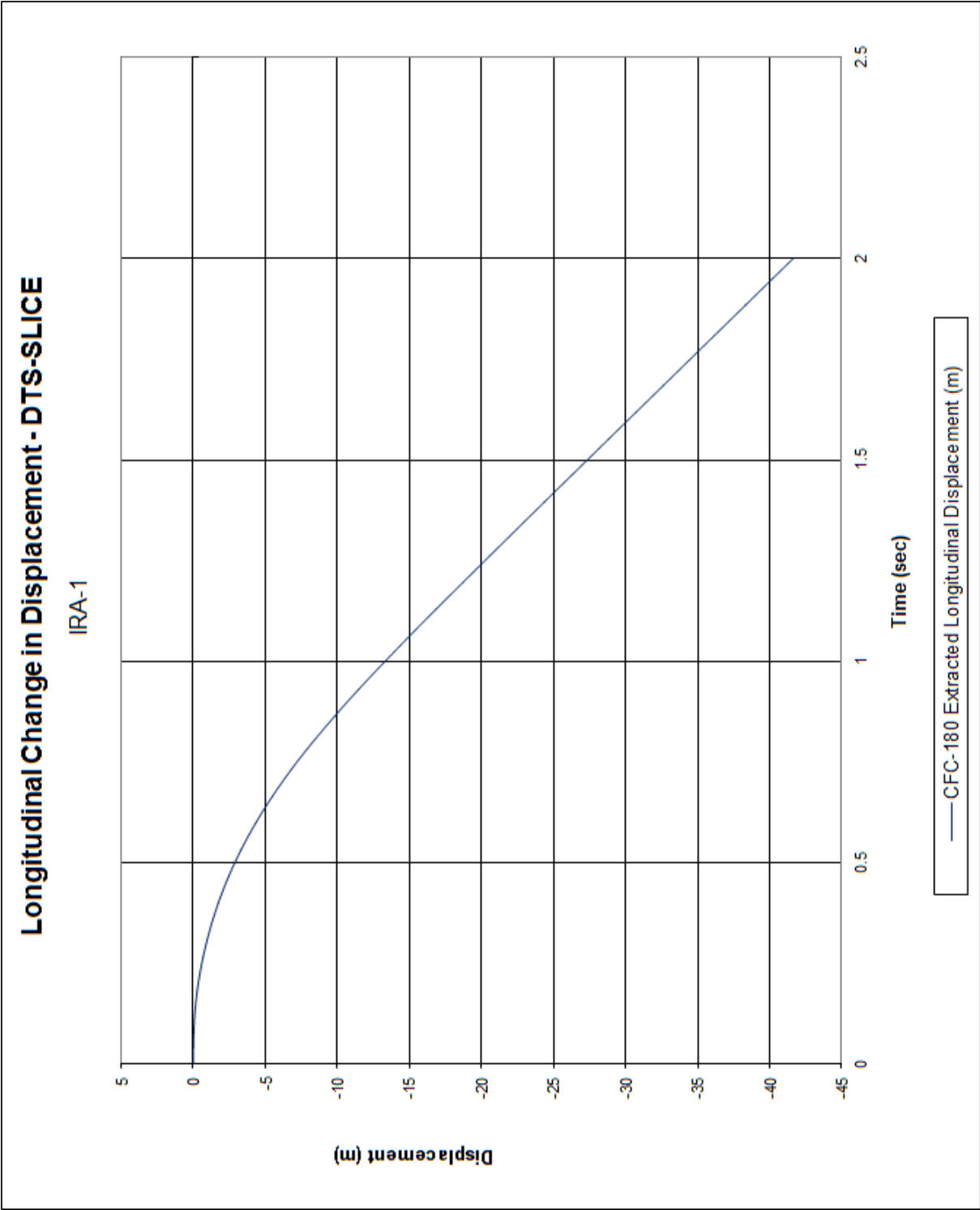


Figure B-15. Longitudinal Occupant Displacement (DTS-SLICE), Test No. IRA-1

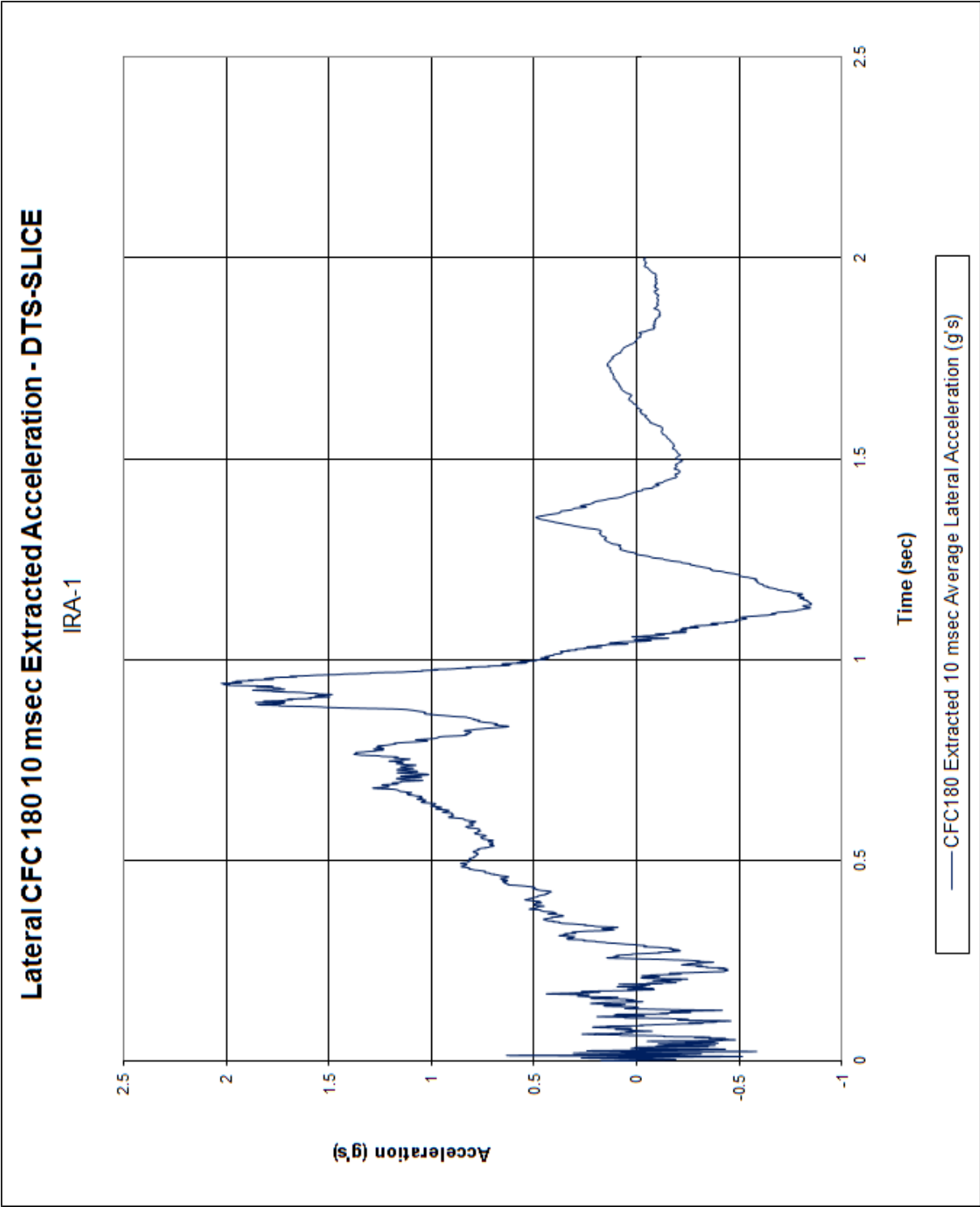


Figure B-16. 10-ms Average Lateral Deceleration (DTS-SLICE), Test No. IRA-1

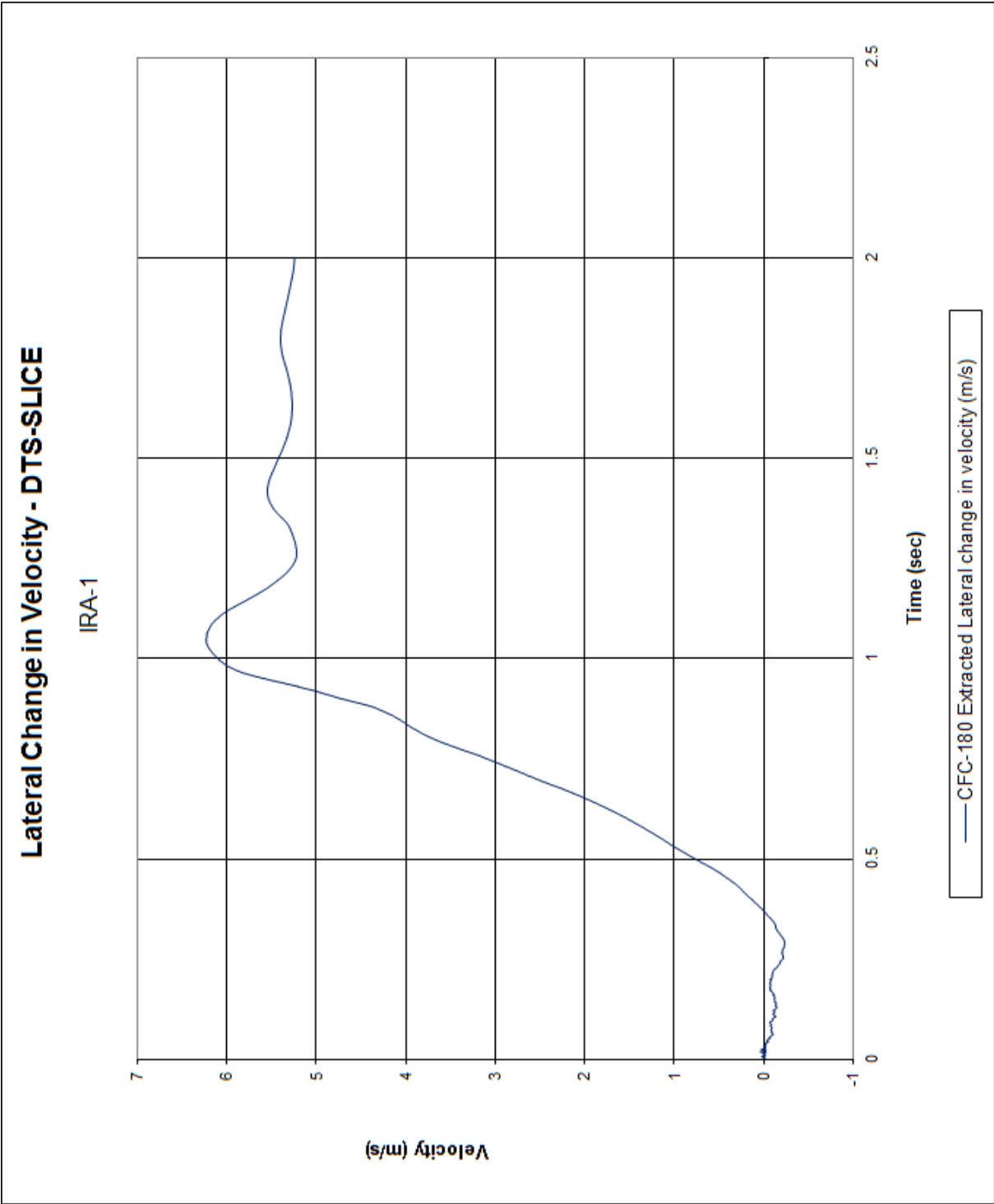


Figure B-17. Lateral Occupant Impact Velocity (DTS-SLICE), Test No. IRA-1

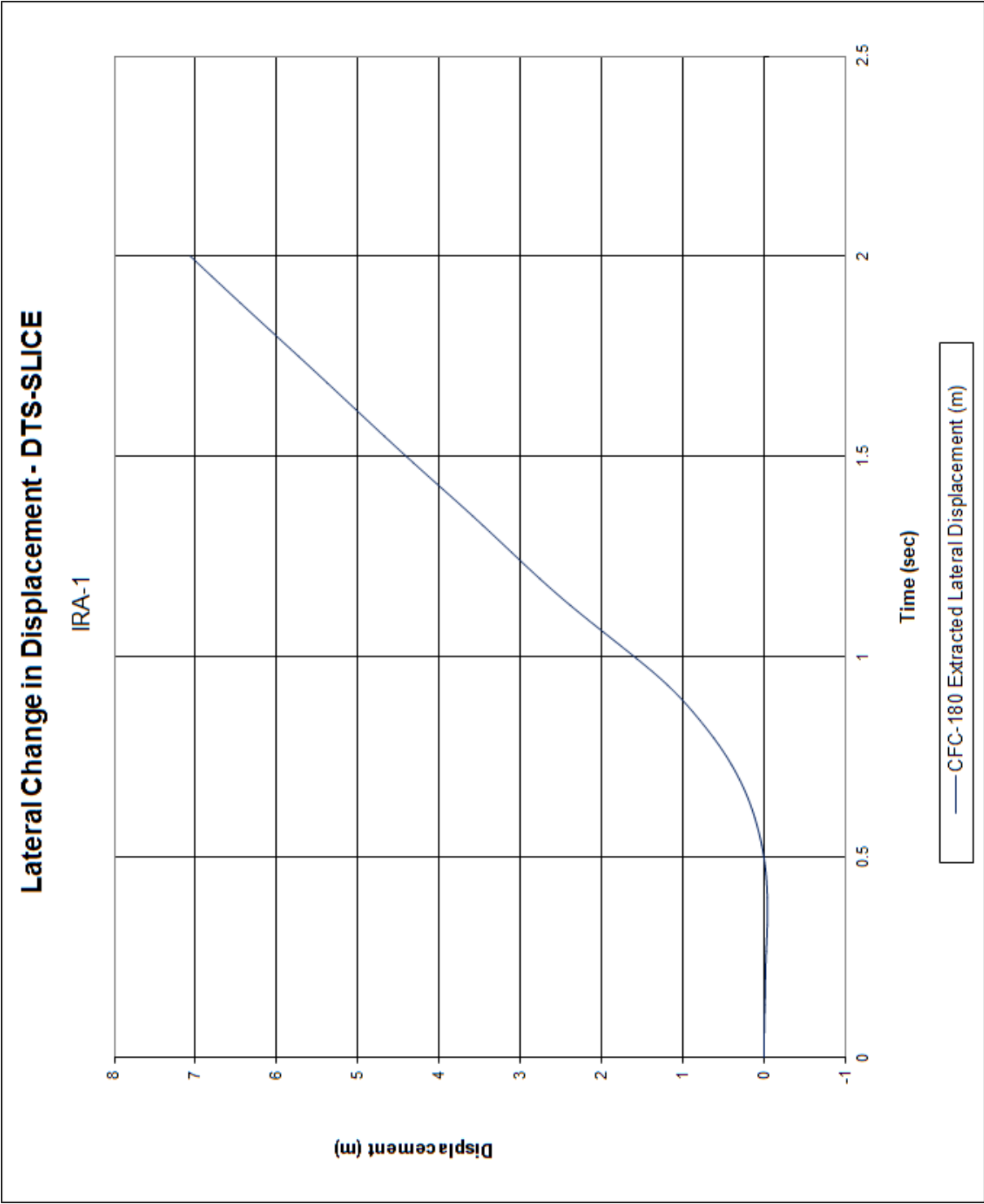


Figure B-18. Lateral Occupant Displacement (DTS-SLICE), Test No. IRA-1

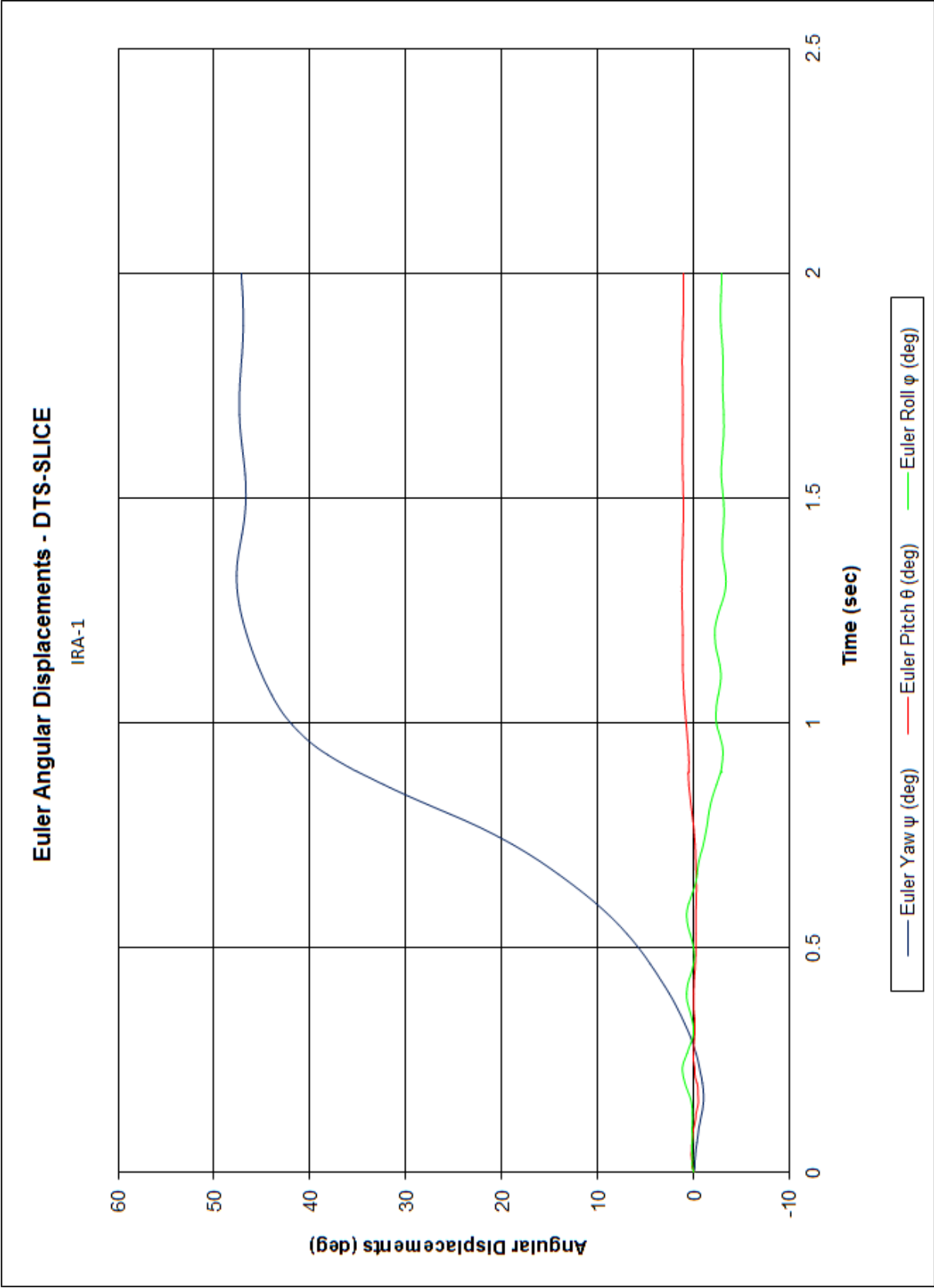


Figure B-19. Vehicle Angular Displacements (DTS-SLICE), Test No. IRA-1

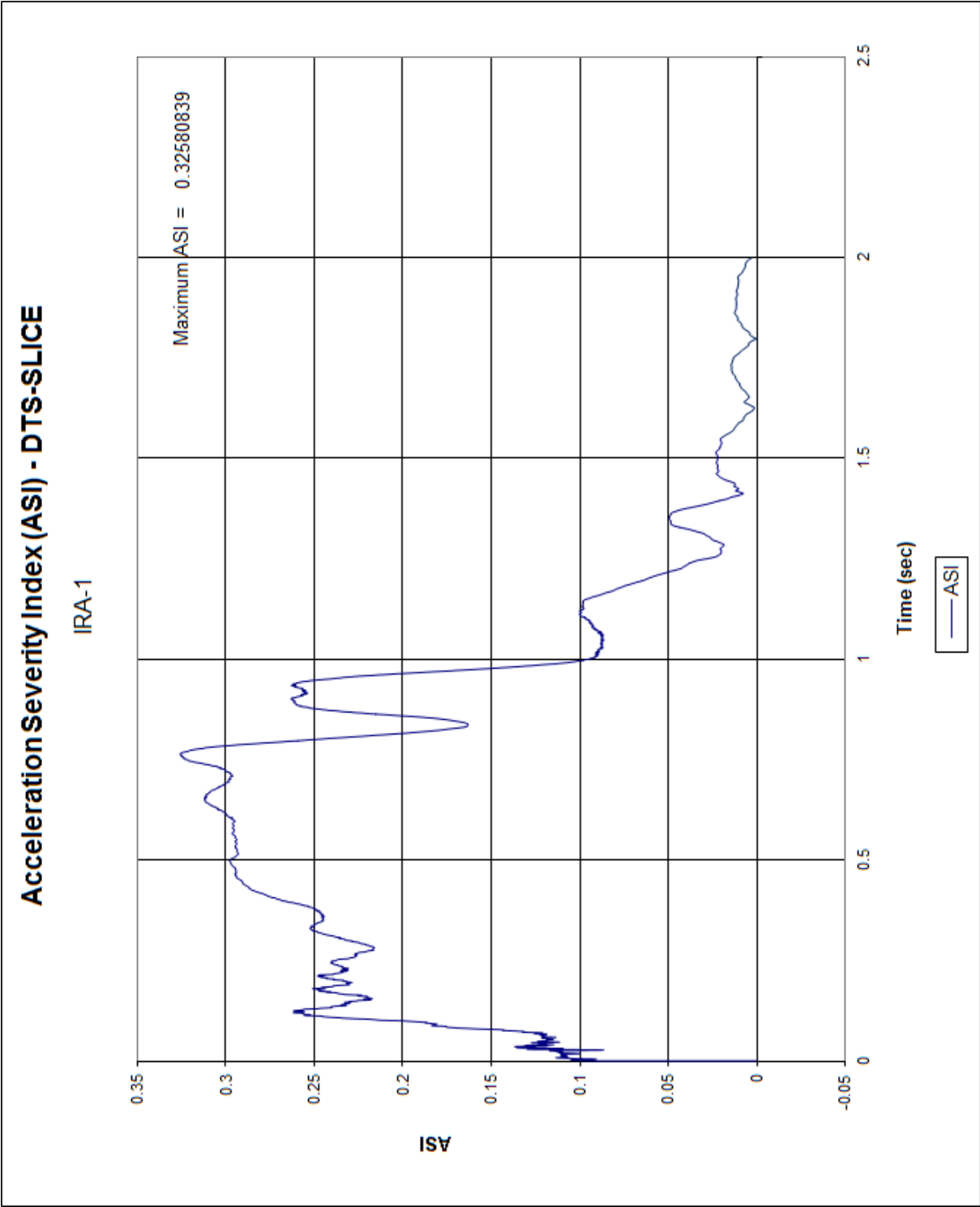


Figure B-20. Acceleration Severity Index (DTS-SLICE), Test No. IRA-1

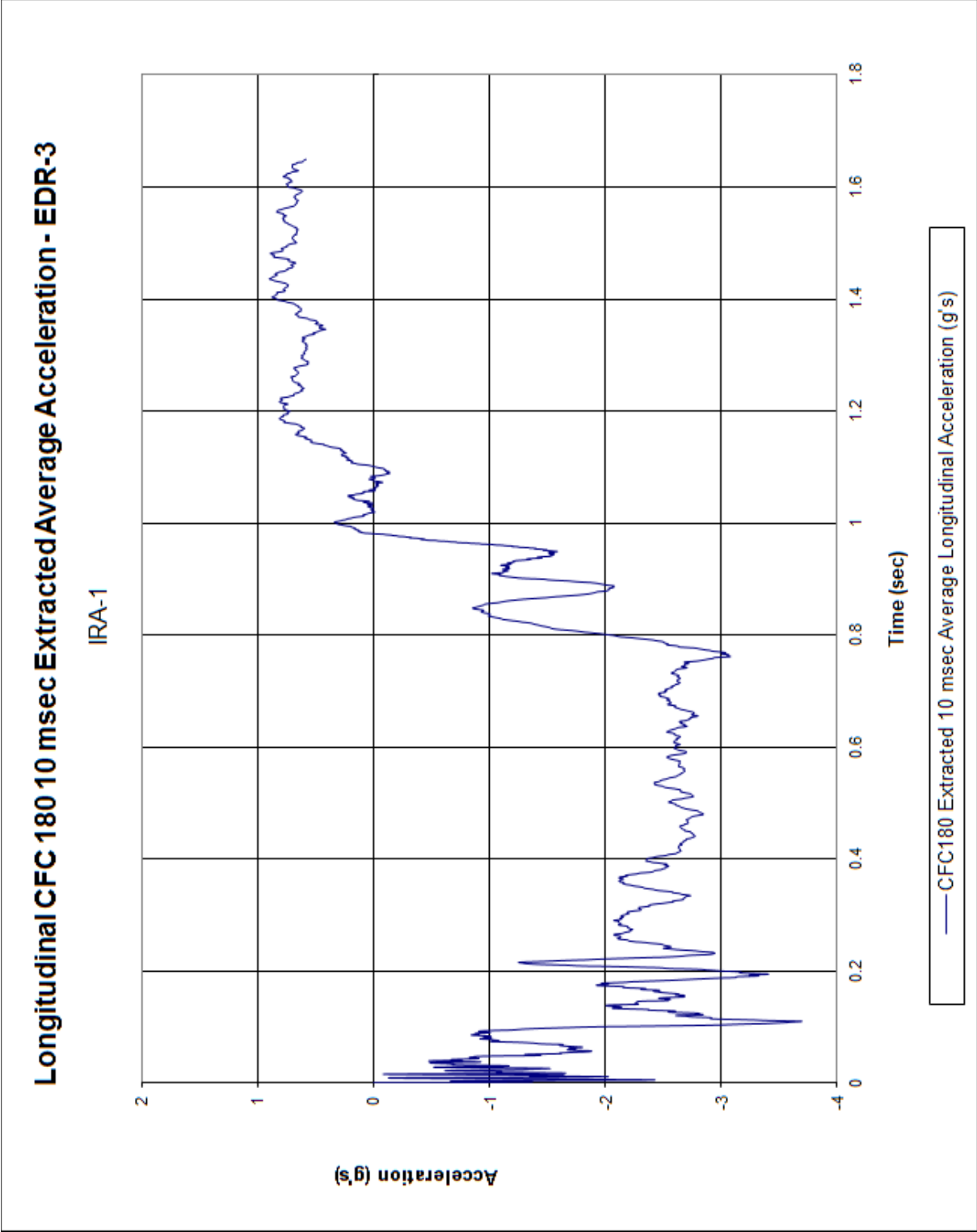


Figure B-21. 10-ms Average Longitudinal Deceleration (EDR-3), Test No. IRA-1

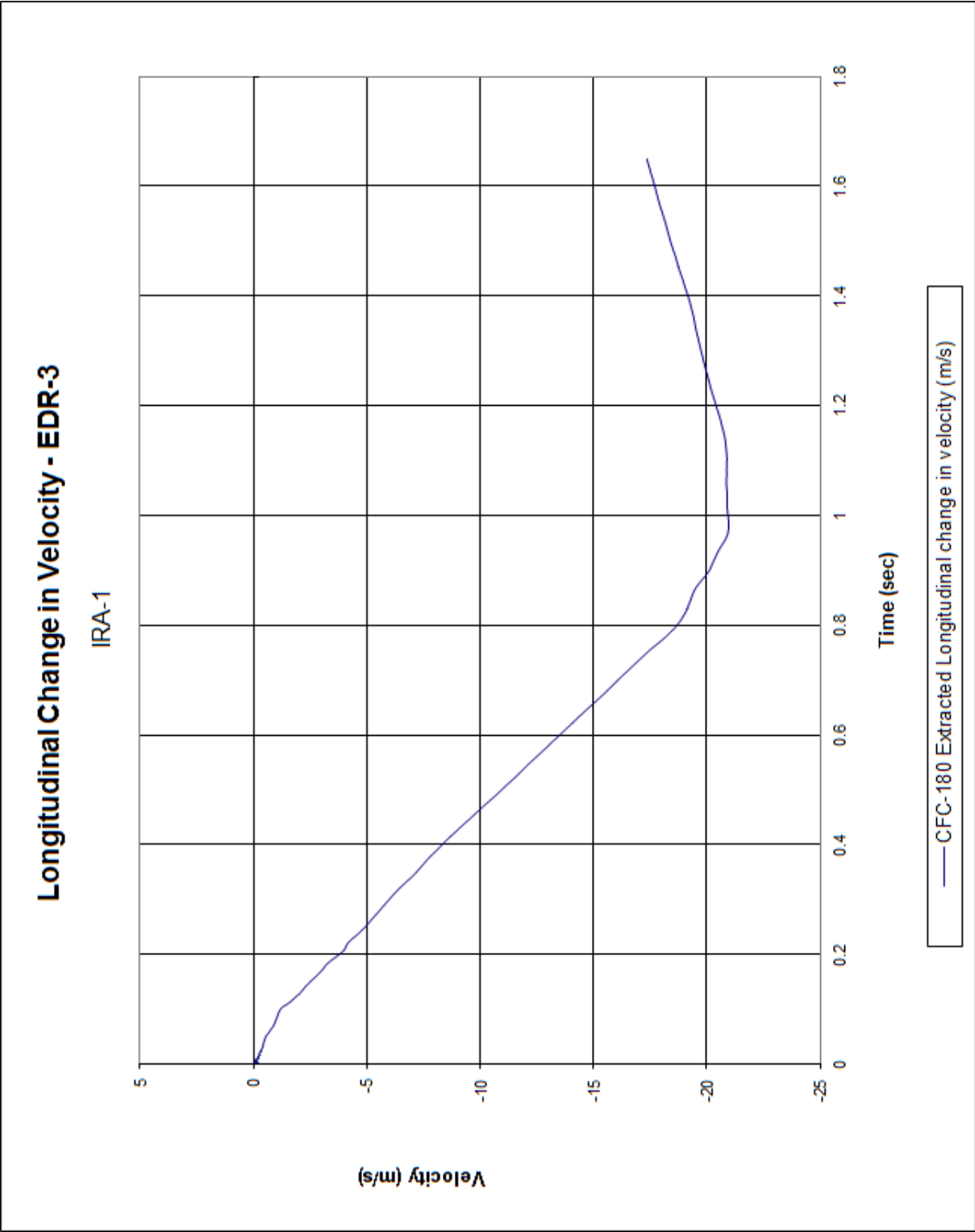


Figure B-22. Longitudinal Occupant Impact Velocity (EDR-3), Test No. IRA-1

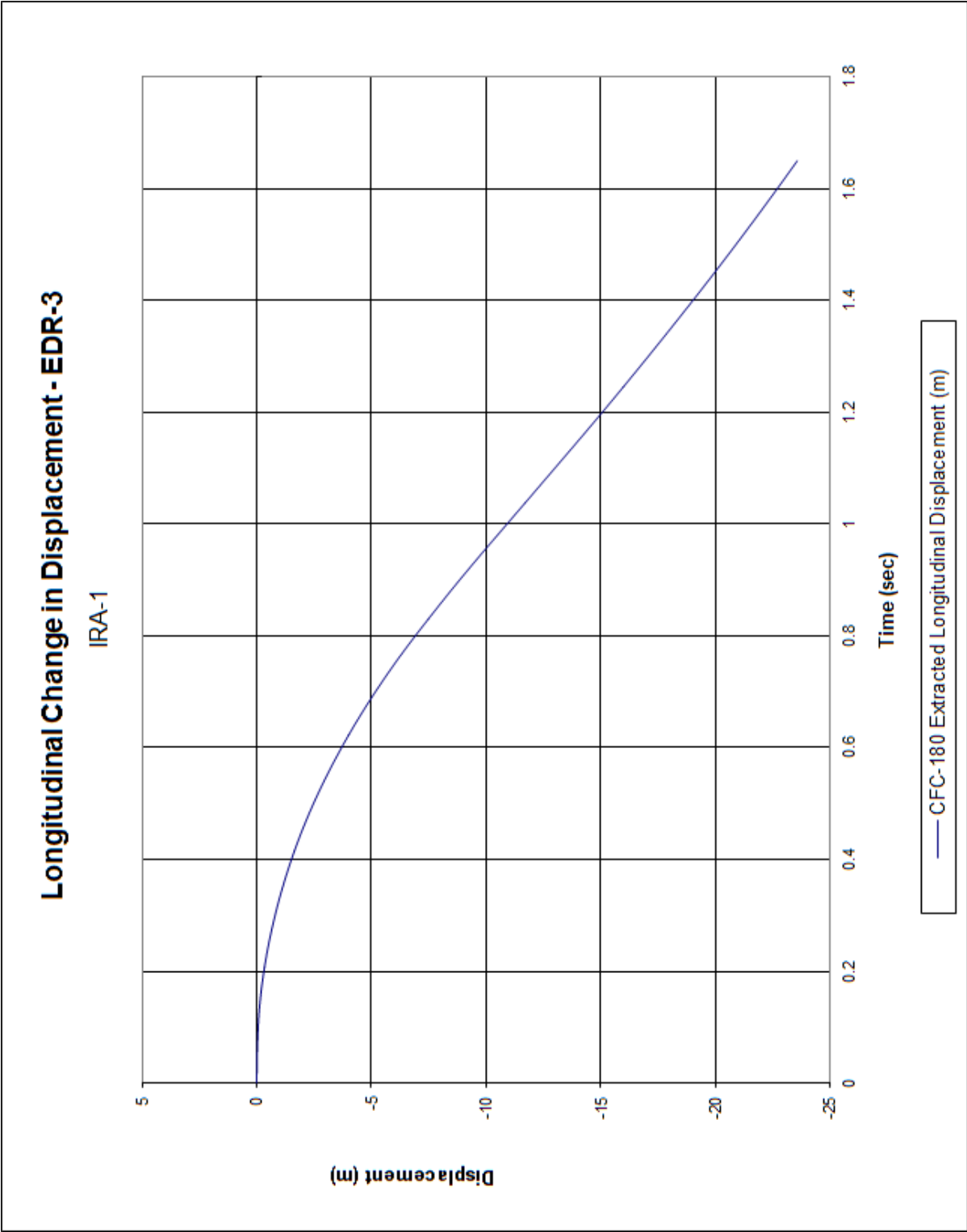


Figure B-23. Longitudinal Occupant Displacement (EDR-3), Test No. IRA-1

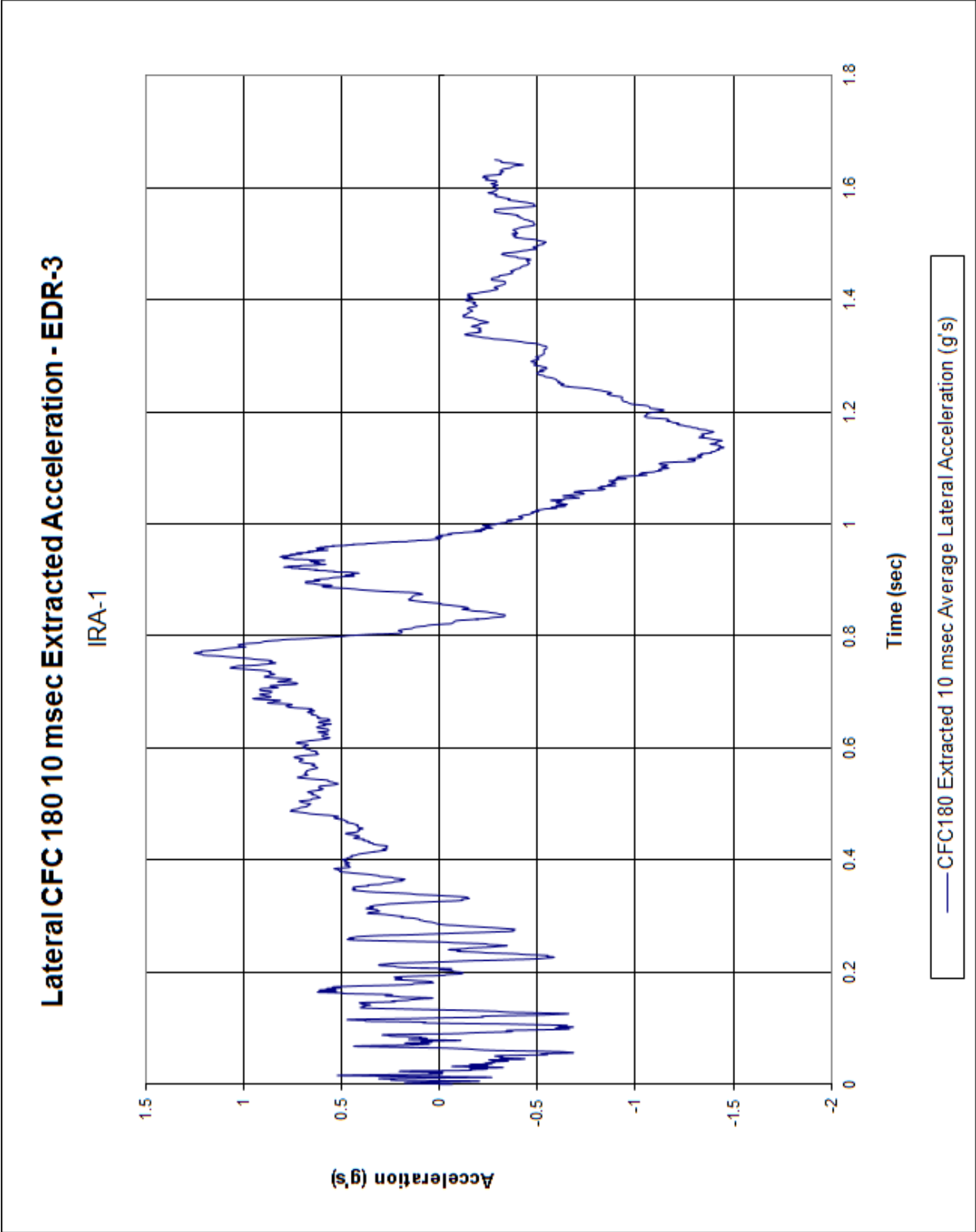


Figure B-24. 10-ms Average Lateral Deceleration (EDR-3), Test No. IRA-1

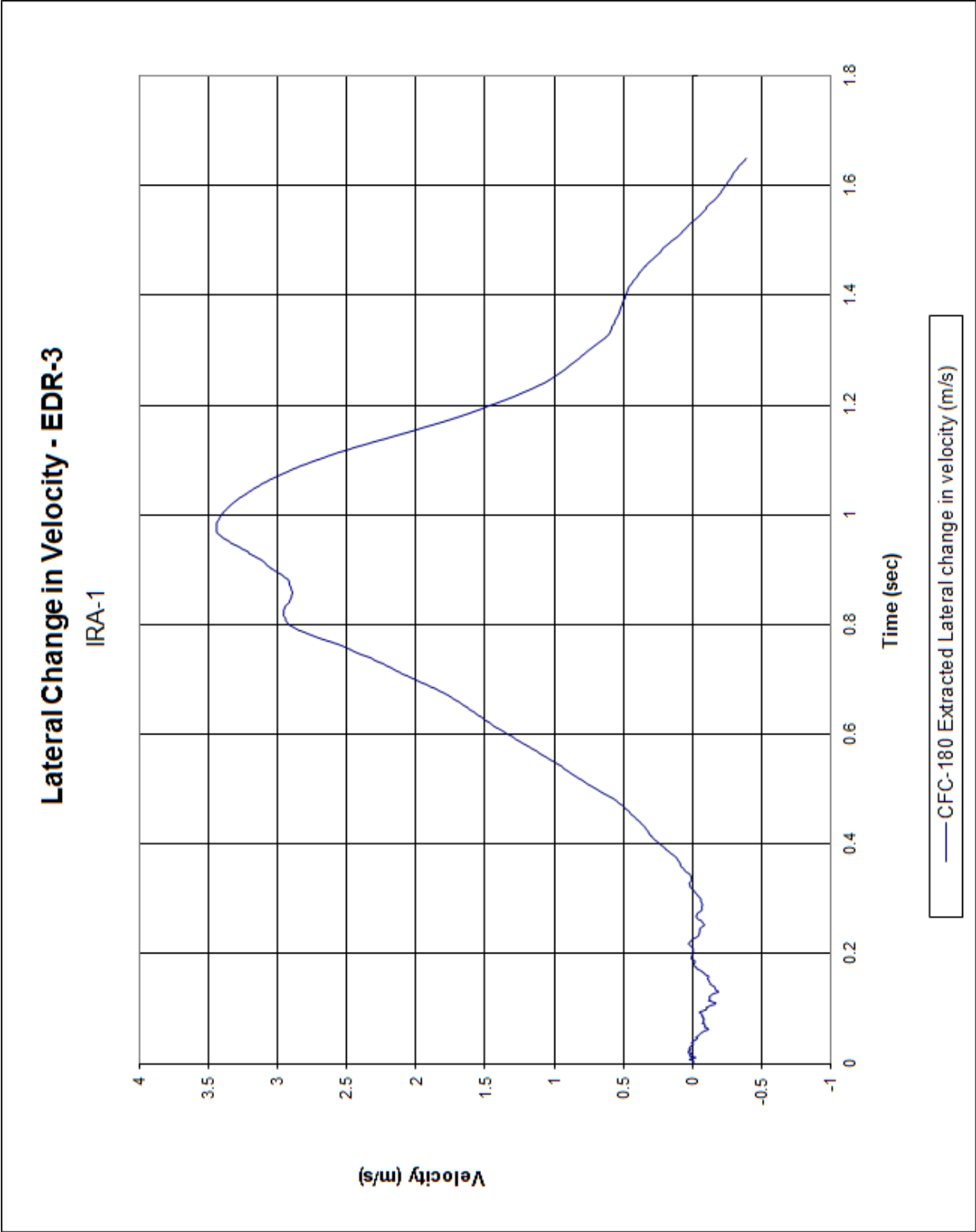


Figure B-25. Lateral Occupant Impact Velocity (EDR-3), Test No. IRA-1

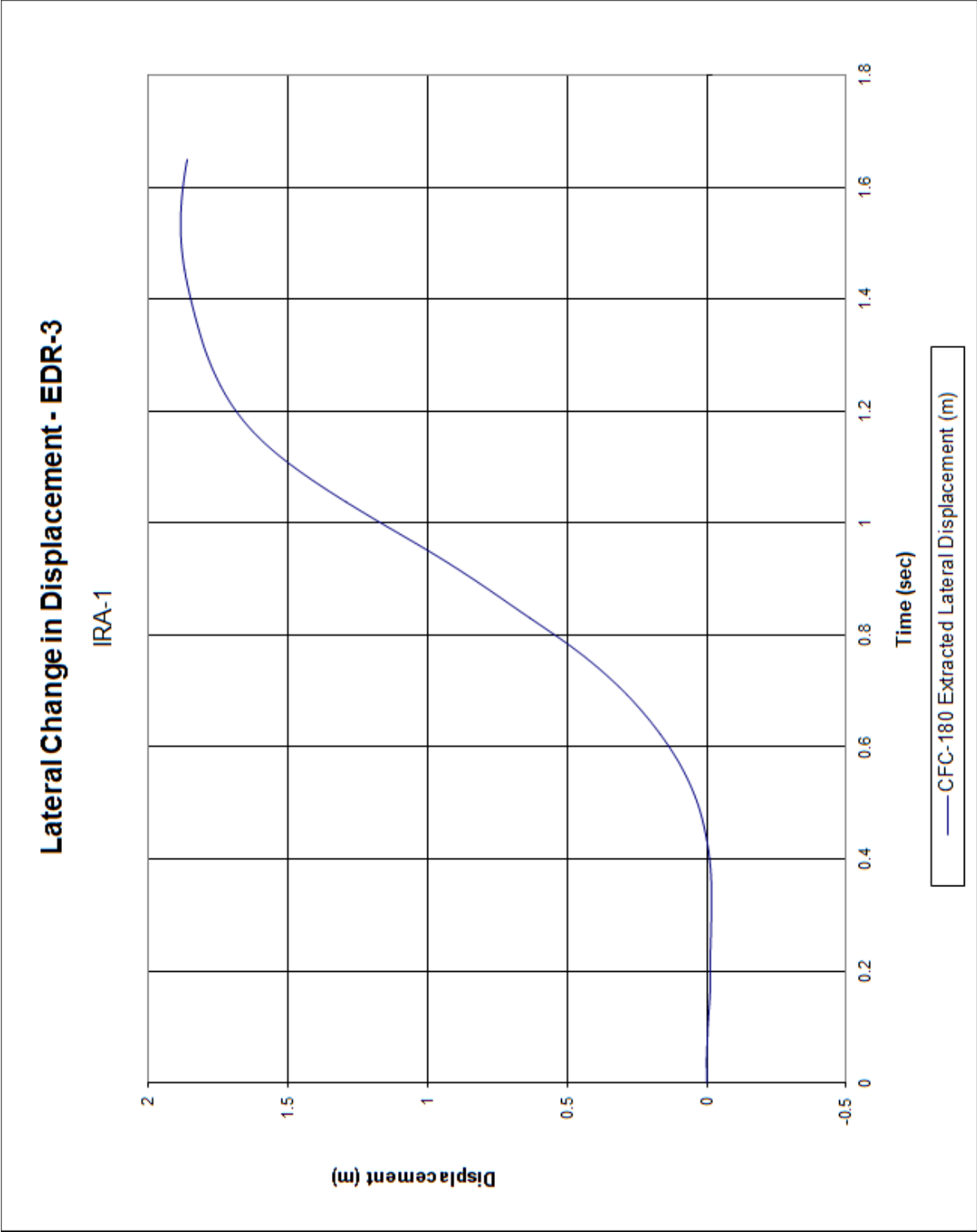


Figure B-26. Lateral Occupant Displacement (EDR-3), Test No. IRA-1

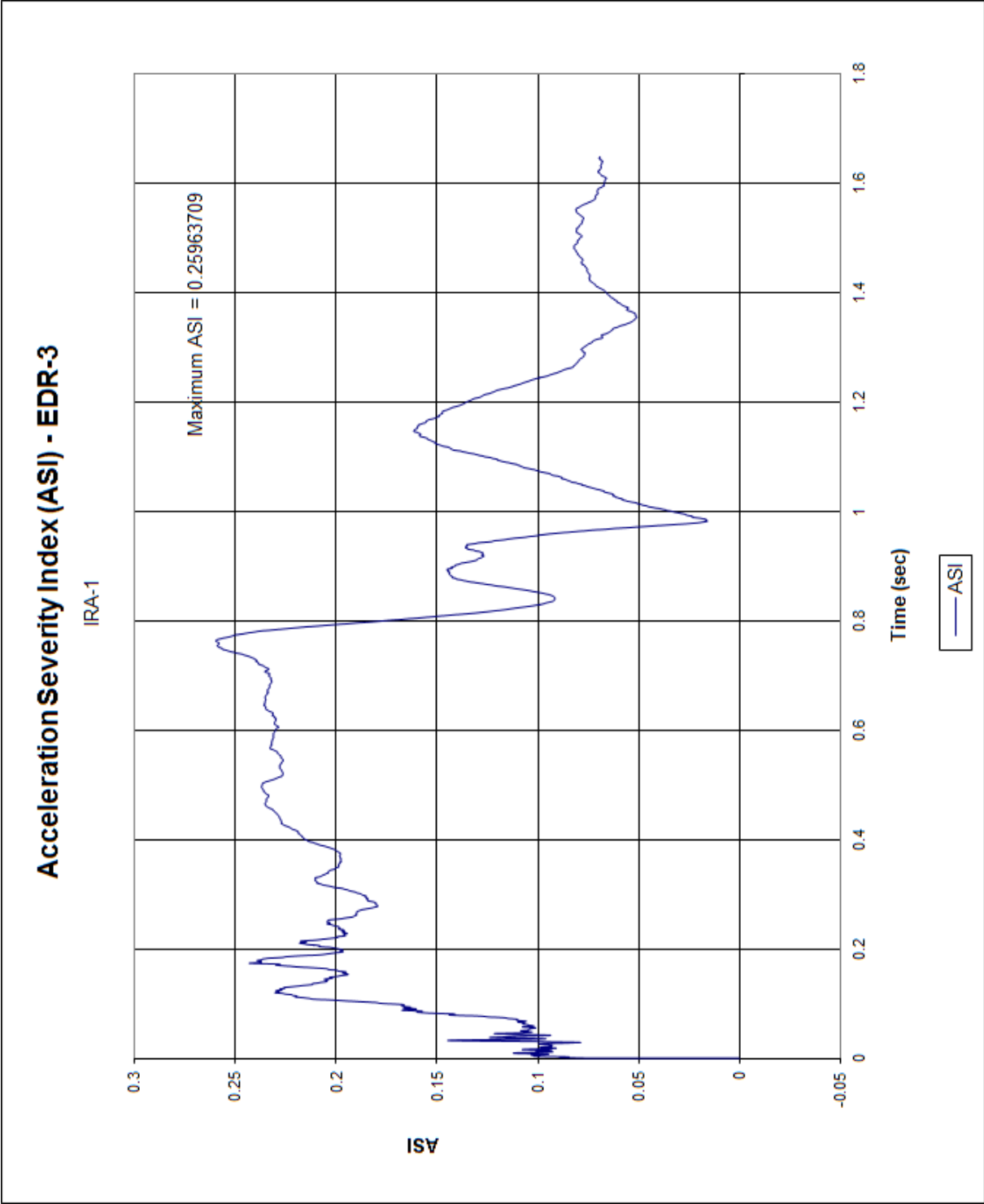


Figure B-27. Acceleration Severity Index (EDR-3), Test No. IRA-1

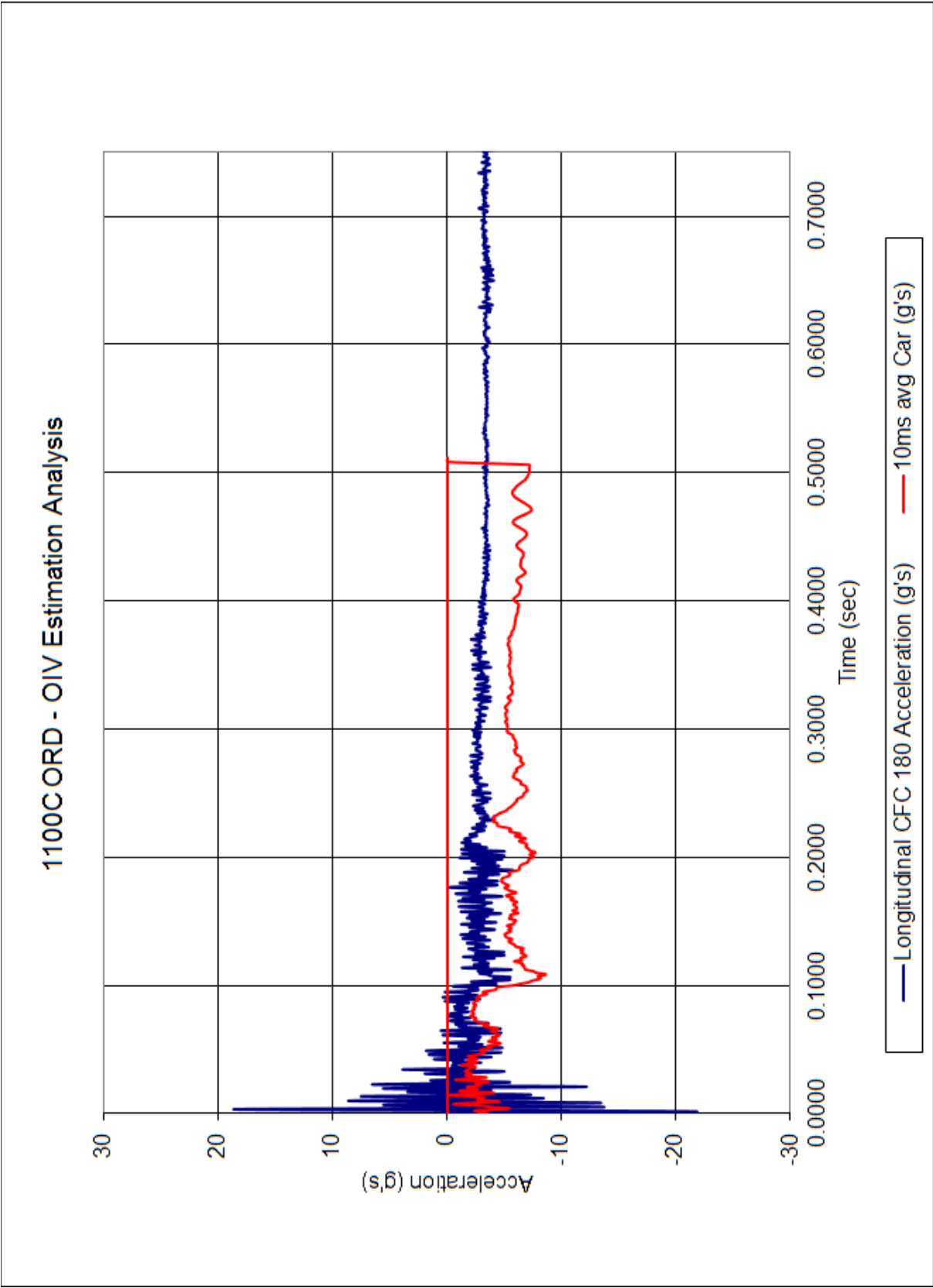


Figure B-28. 1100C ORD-OIV Estimation, Test No. IRA-1

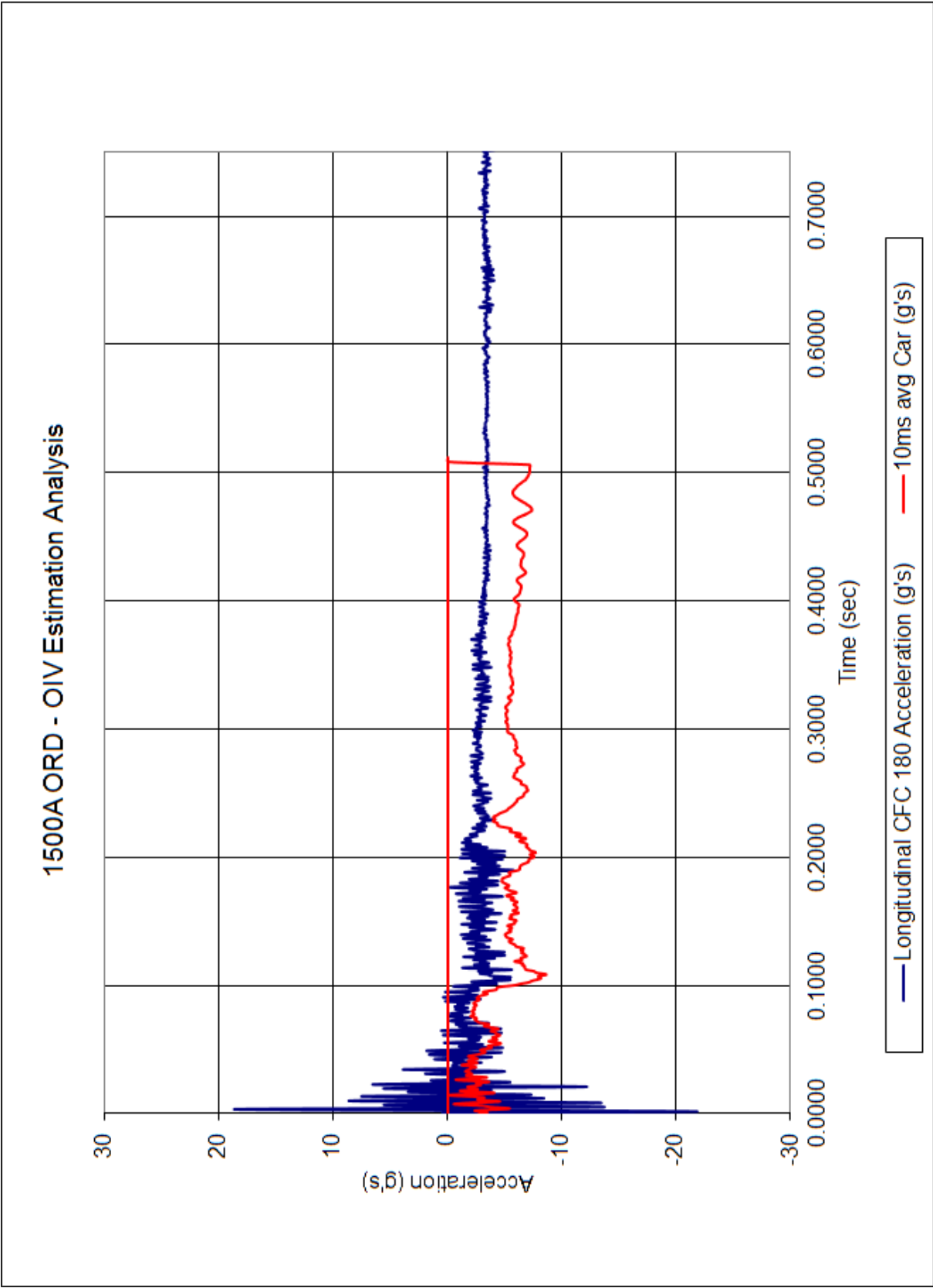


Figure B-29. 1500A ORD-OIV Estimation, Test No. IRA-1

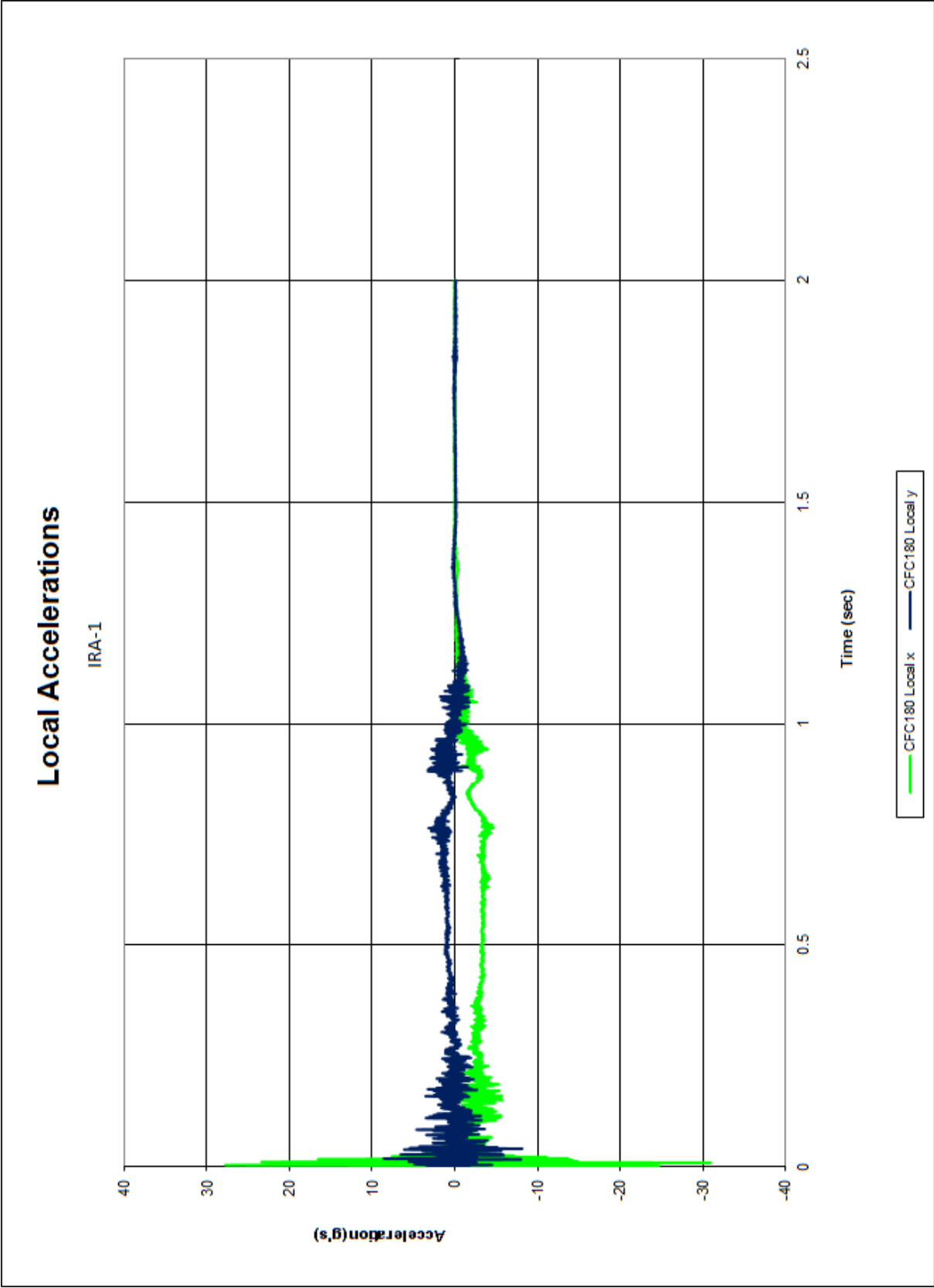


Figure B-30. Local Accelerations, Test No. IRA-1

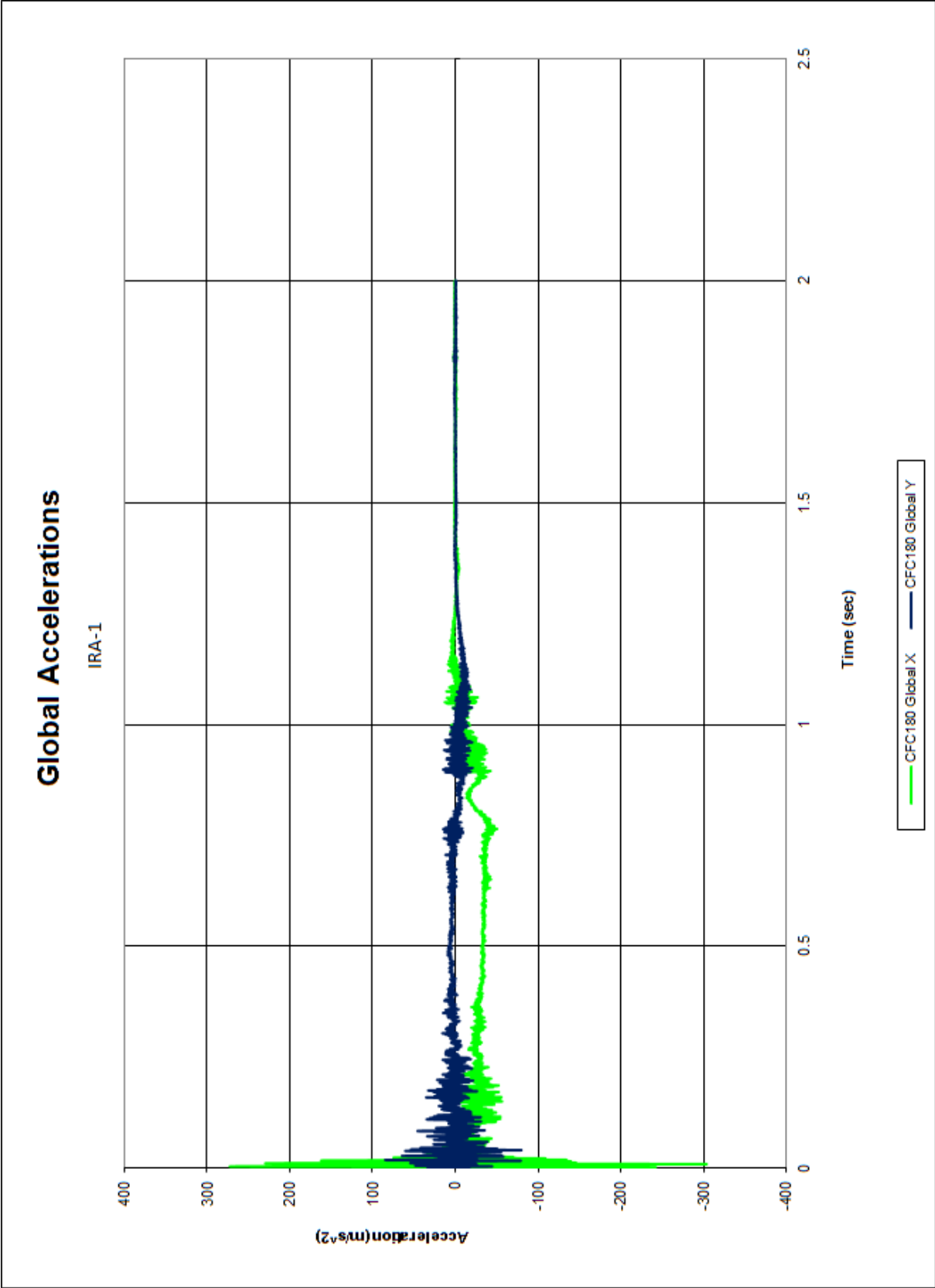


Figure B-31. Global Accelerations, Test No. IRA-1

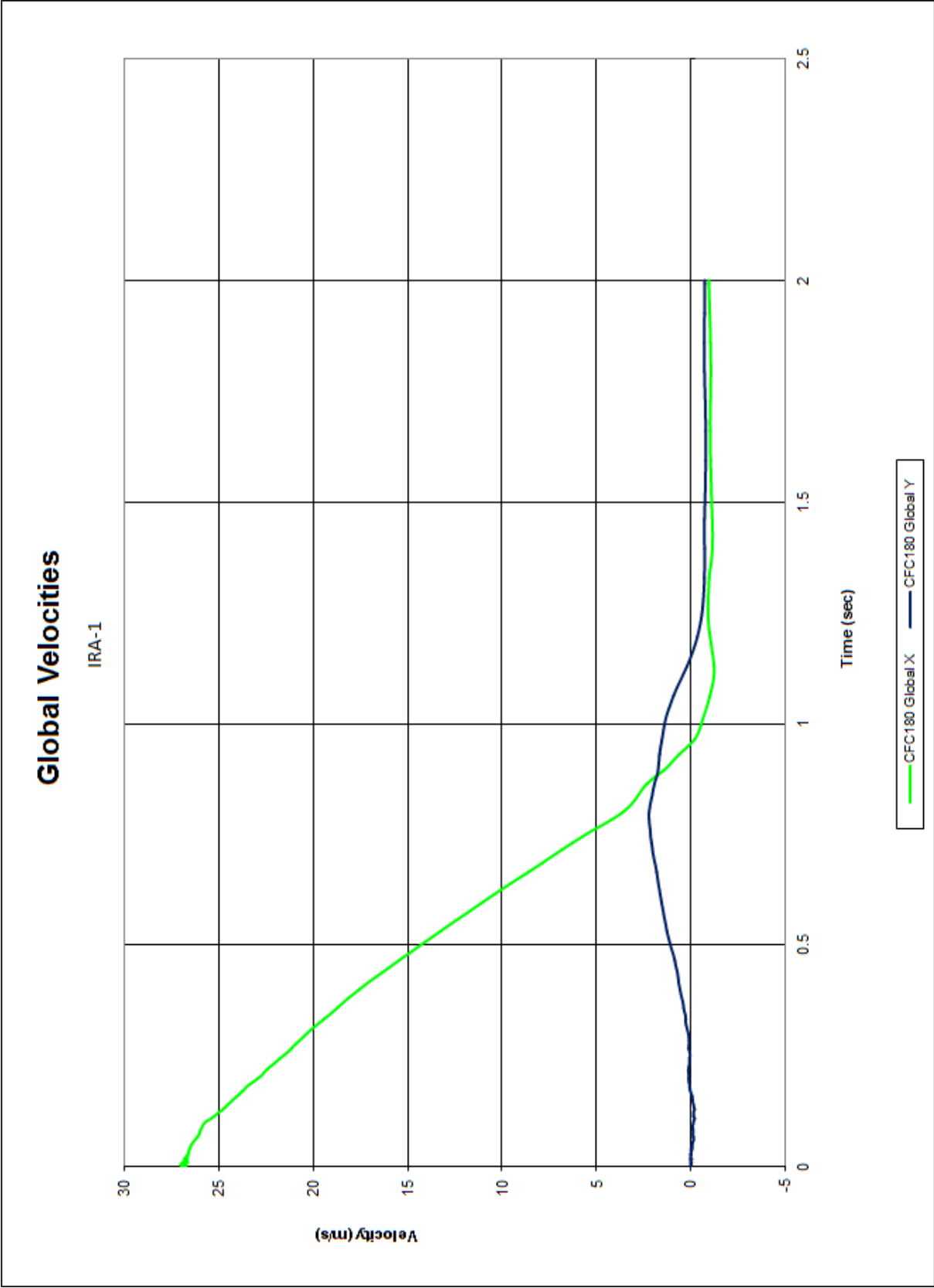


Figure B-32. Global Velocities, Test No. IRA-1

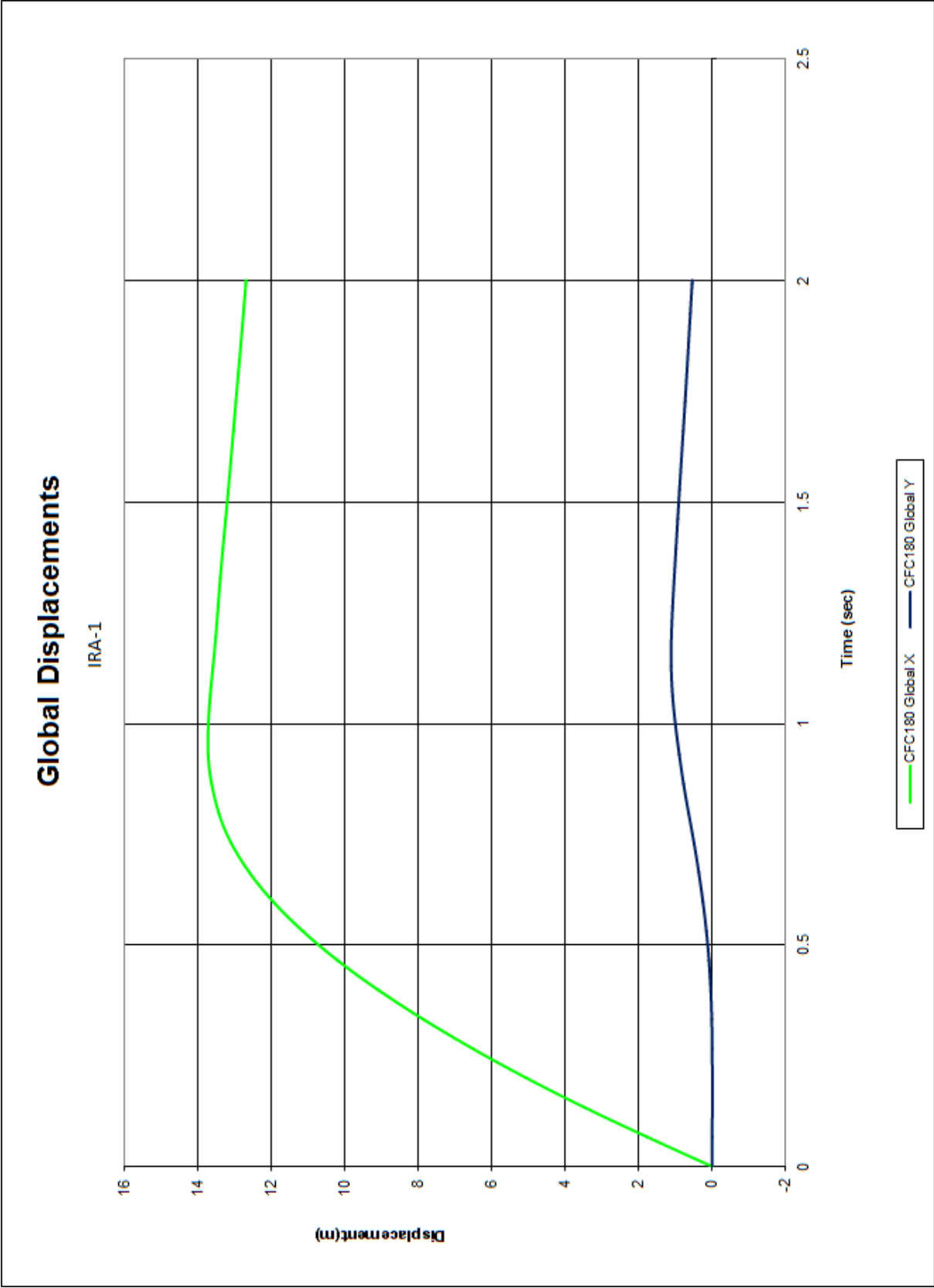


Figure B-33. Global Displacements, Test No. IRA-1

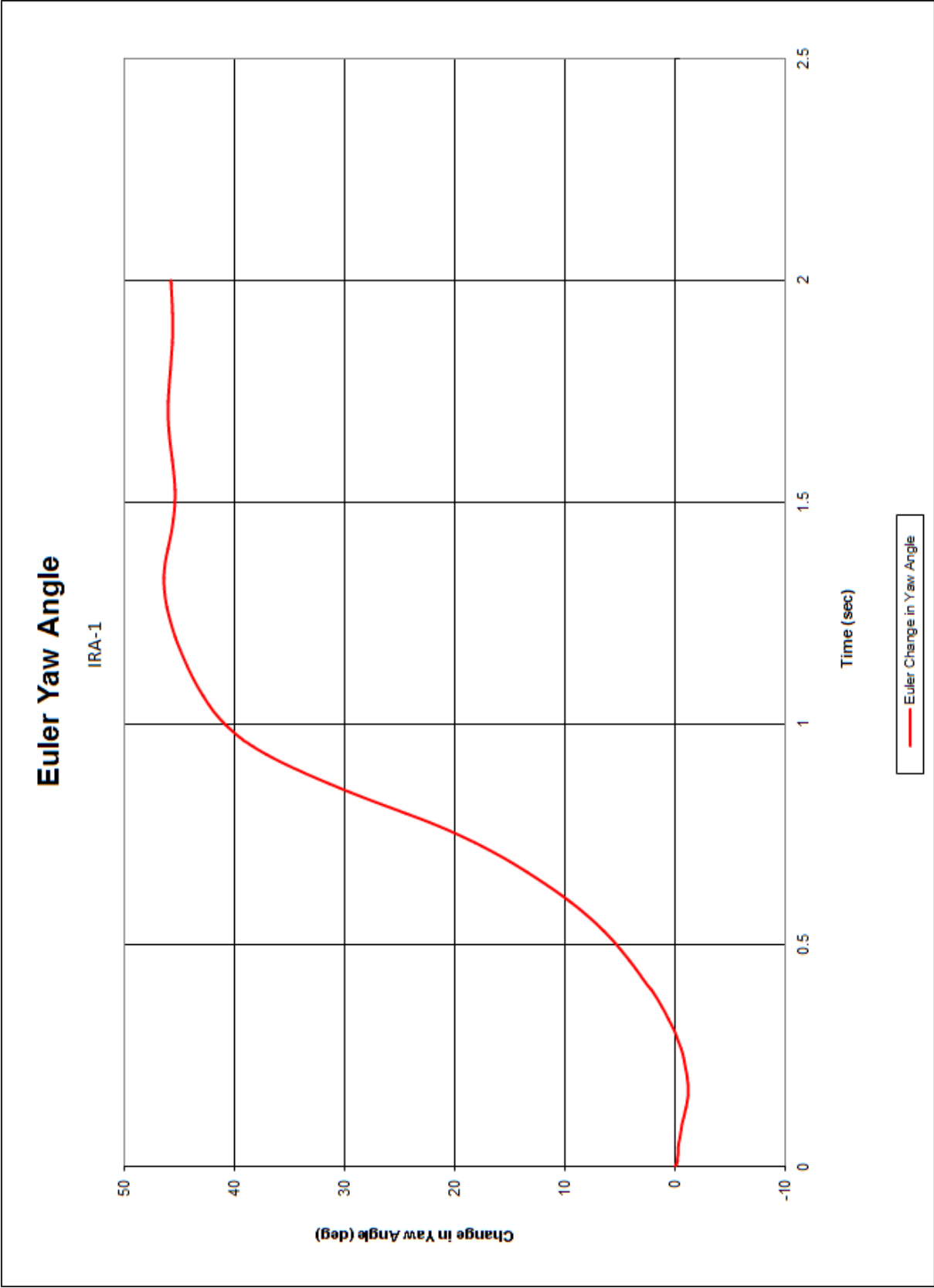


Figure B-34. Euler Yaw Angle, Test No. IRA-1

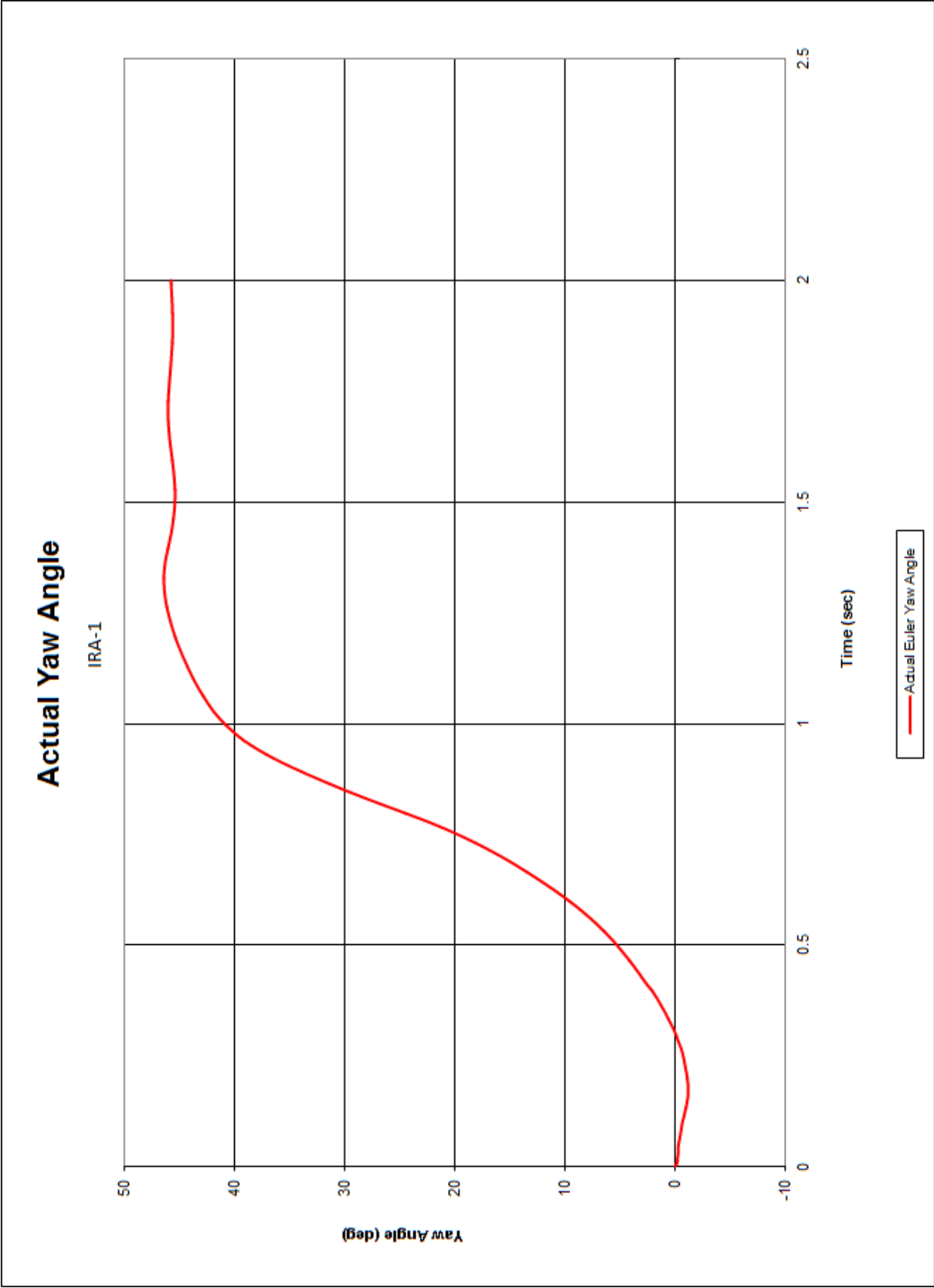


Figure B-35. Actual Yaw Angle, Test No. IRA-1

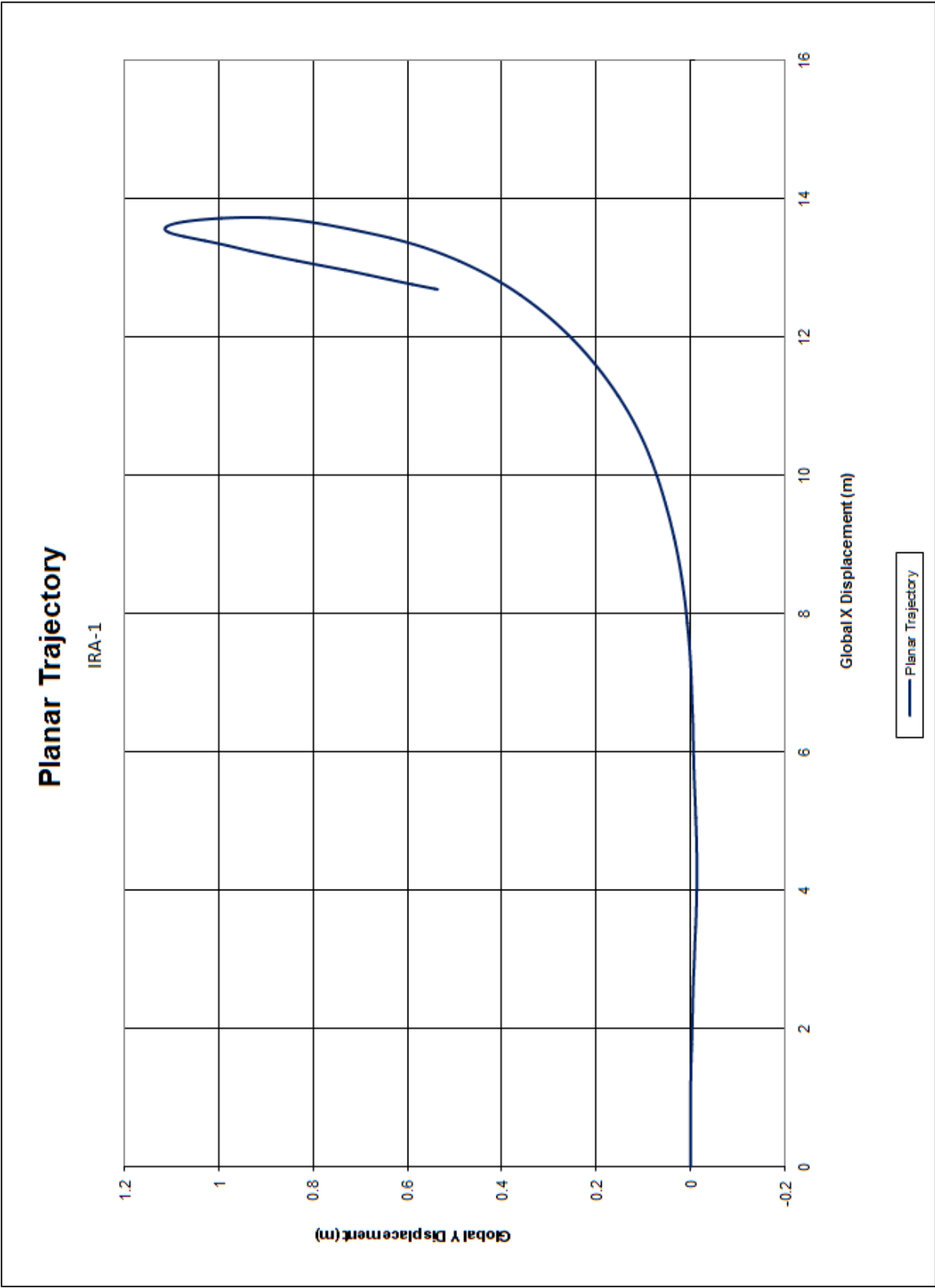


Figure B-36. Planar Trajectory, Test No. IRA-1

Appendix C. Accelerometer and Rate Transducer Data Plots, Test No. IRA-2

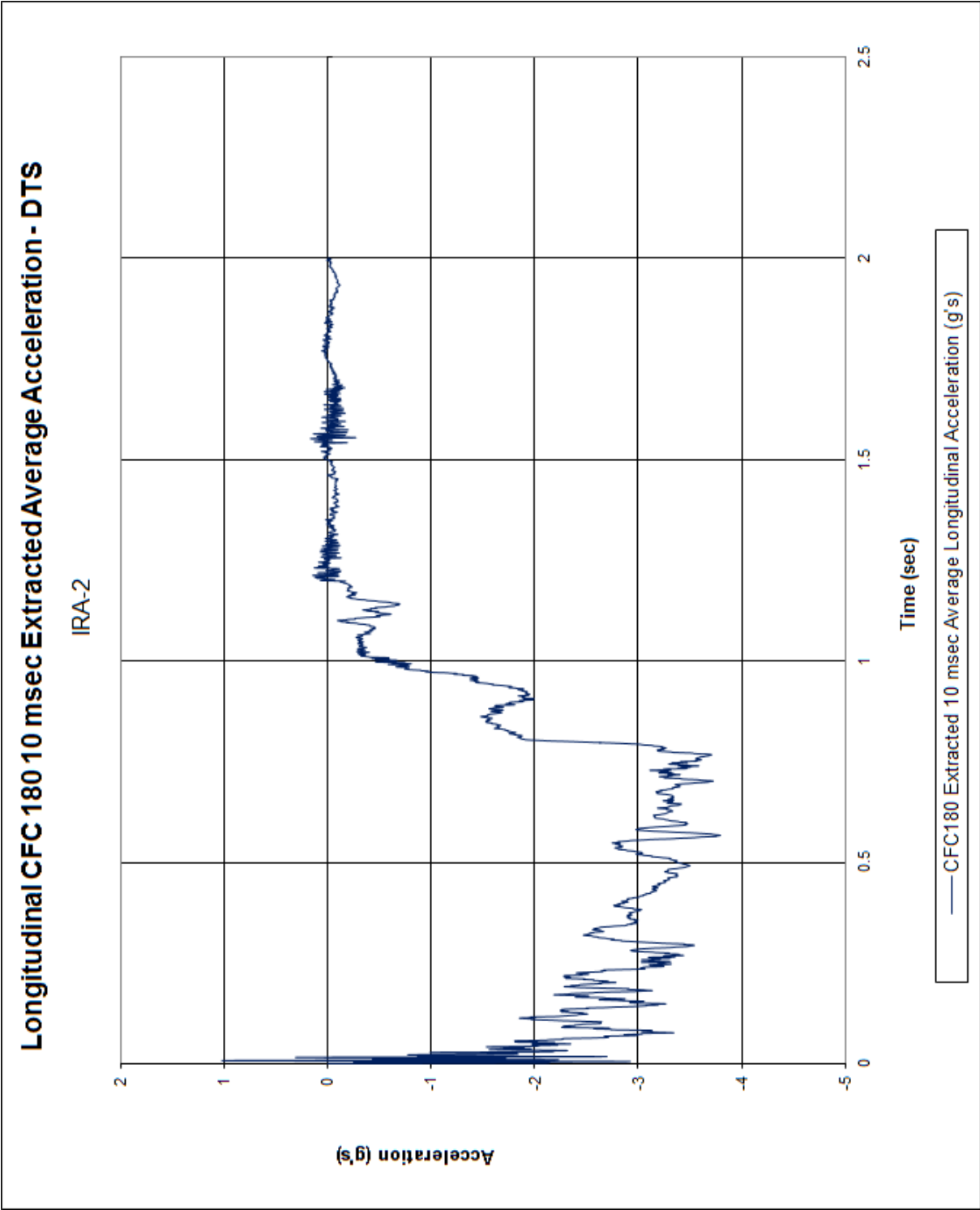


Figure C-1. 10-ms Average Longitudinal Deceleration (DTS), Test No. IRA-2

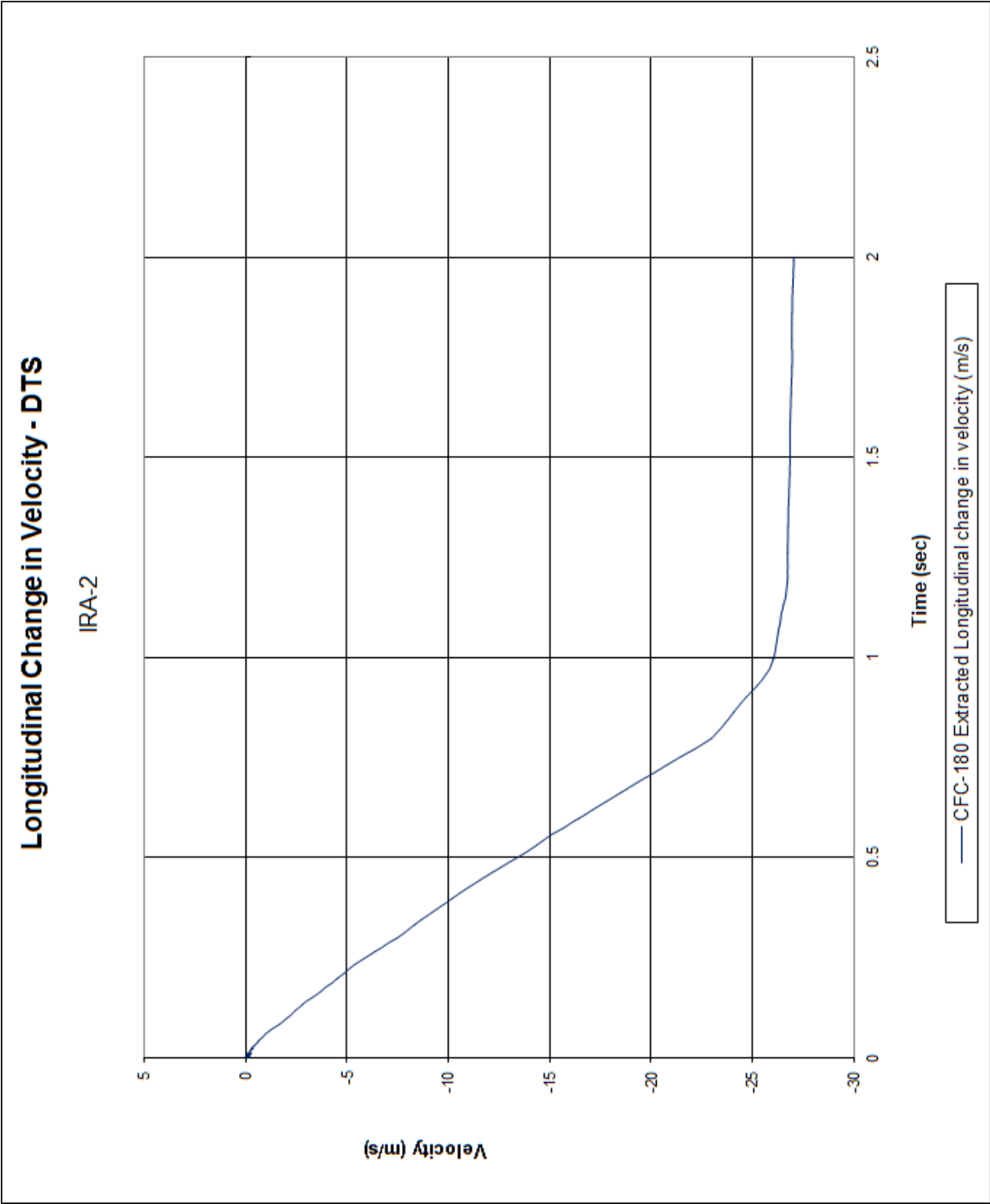


Figure C-2. Longitudinal Occupant Impact Velocity (DTS), Test No. IRA-2

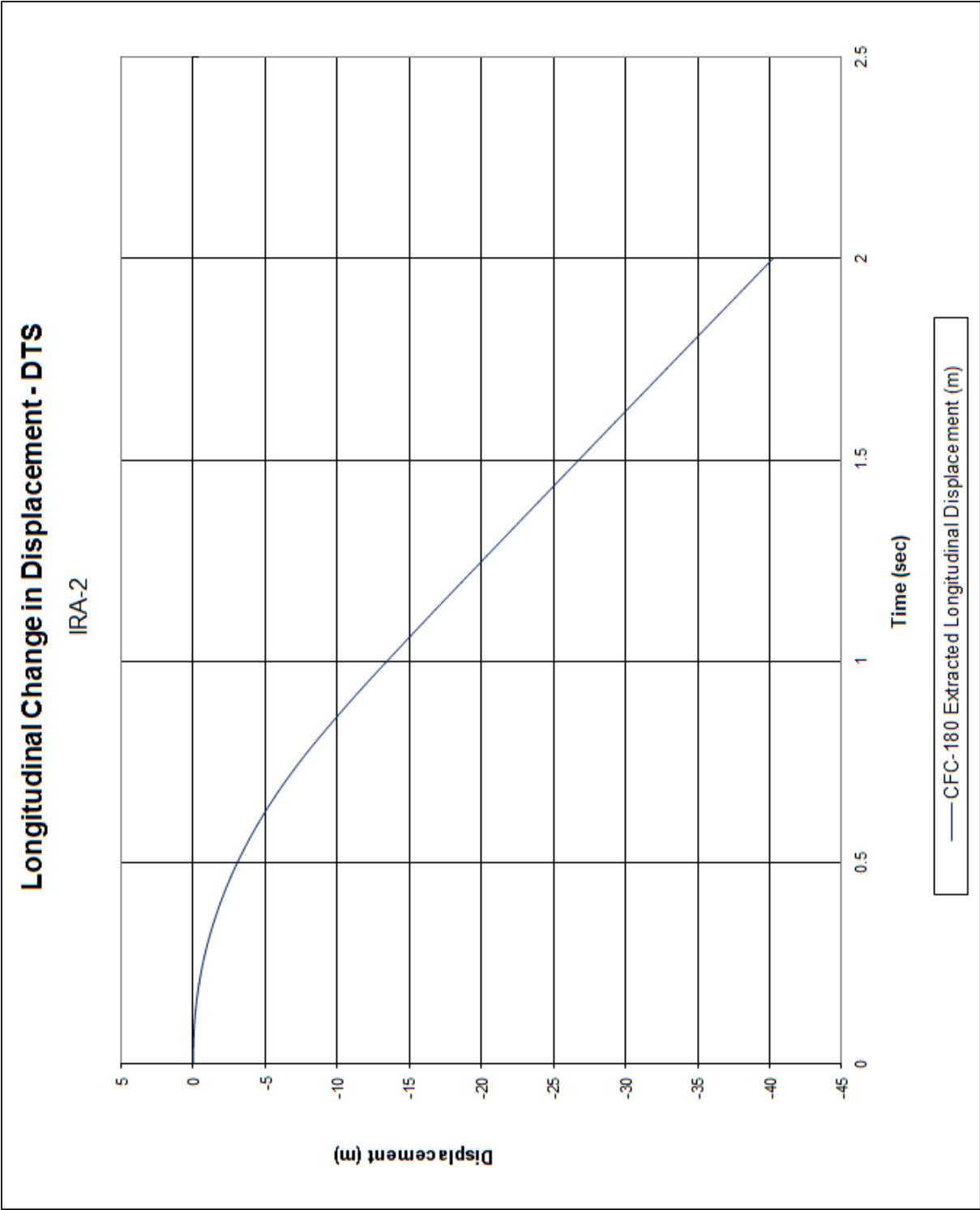


Figure C-3. Longitudinal Occupant Displacement (DTS), Test No. IRA-2

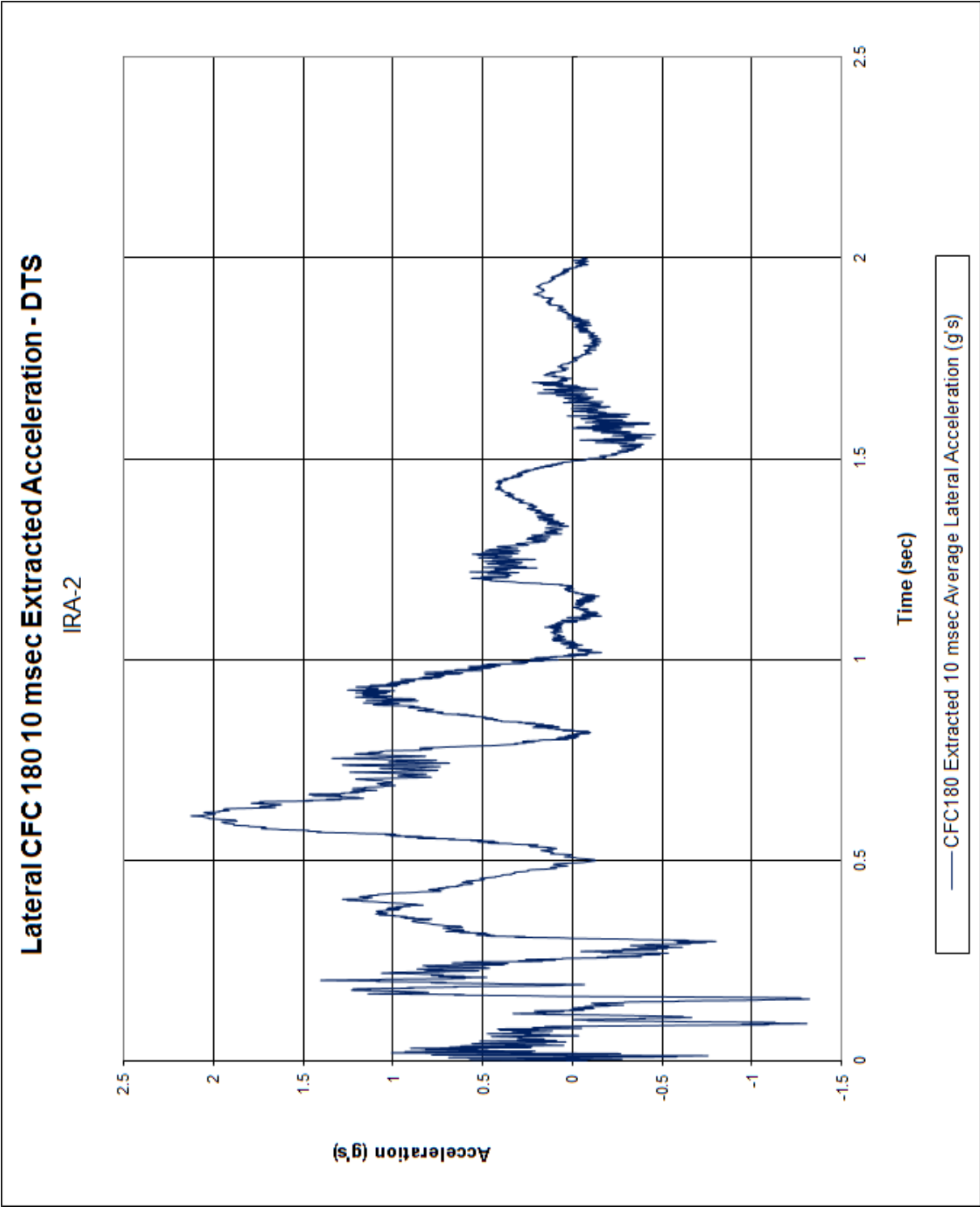


Figure C-4. 10-ms Average Lateral Deceleration (DTS), Test No. IRA-2

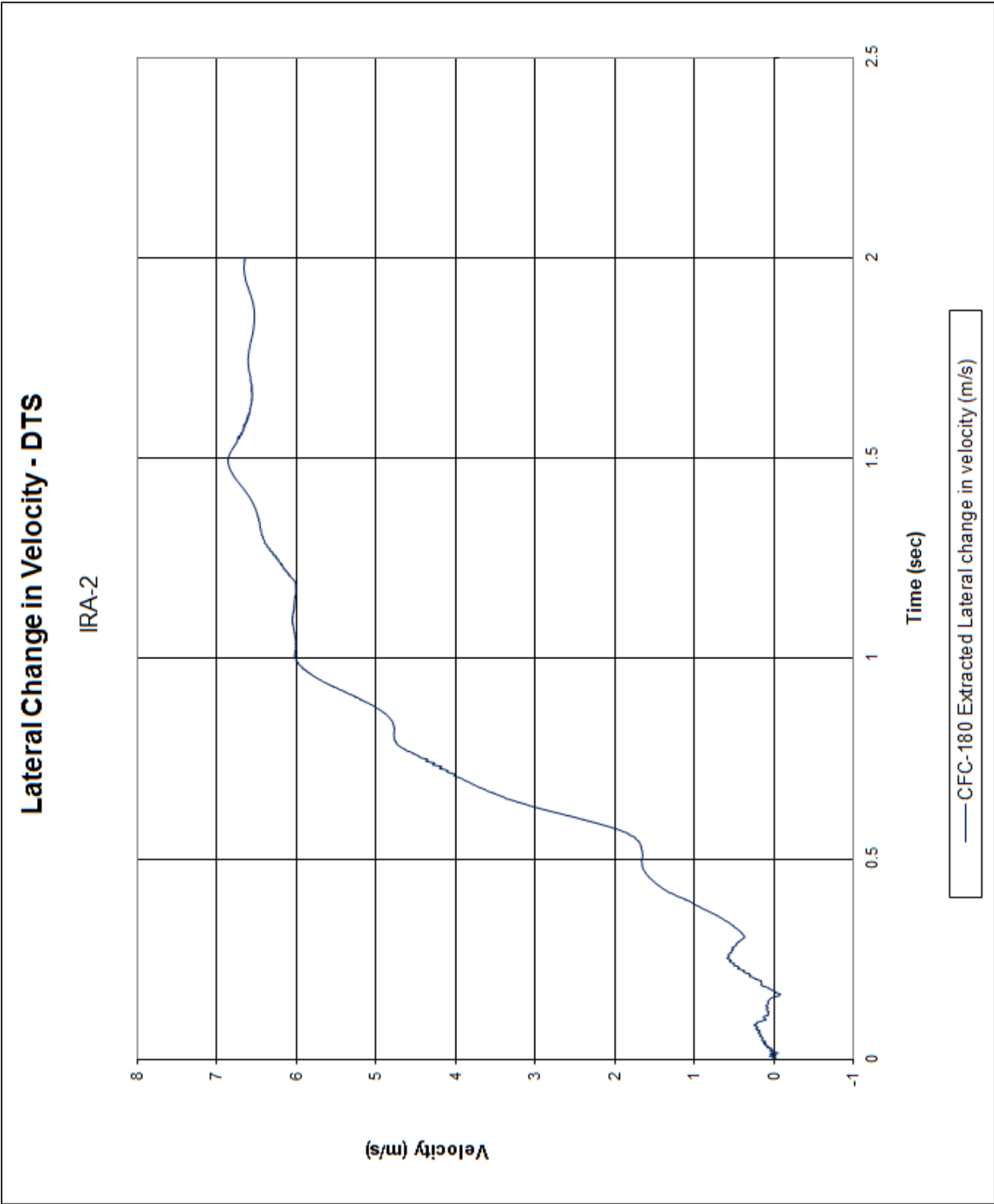


Figure C-5. Lateral Occupant Impact Velocity (DTS), Test No. IRA-2

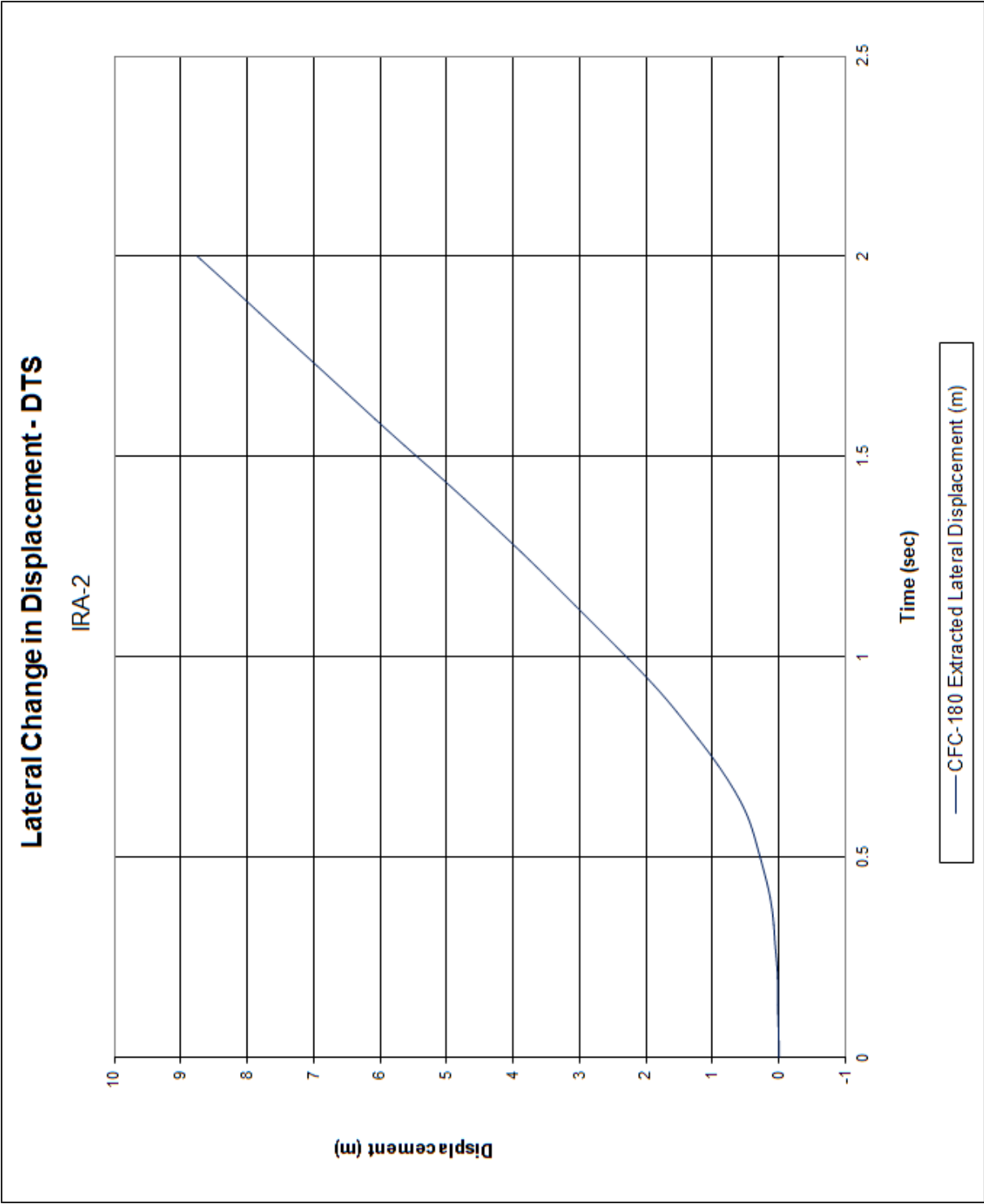


Figure C-6. Lateral Occupant Displacement (DTS), Test No. IRA-2

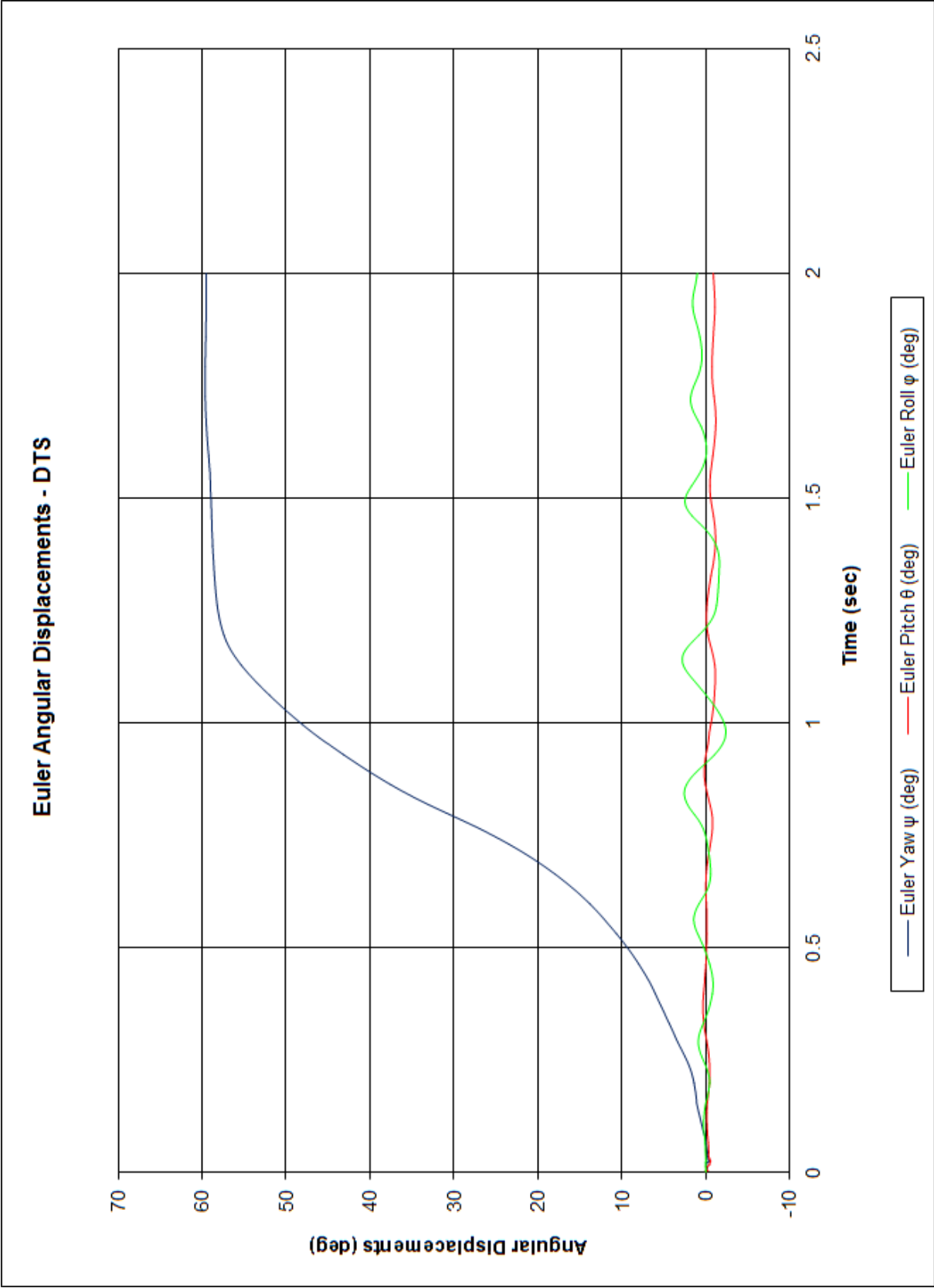


Figure C-7. Vehicle Angular Displacements (DTS), Test No. IRA-2

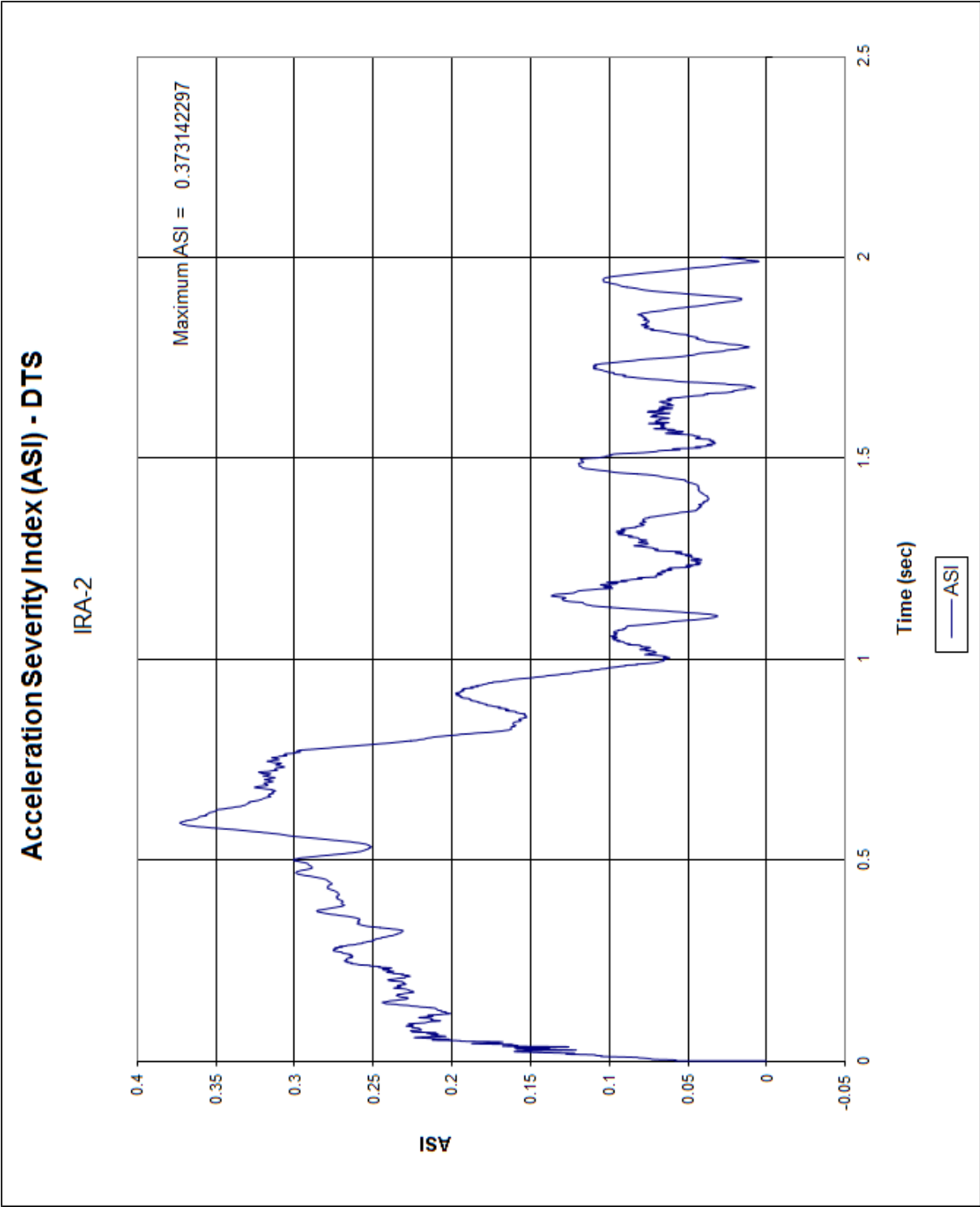


Figure C-8. Acceleration Severity Index (DTS), Test No. IRA-2

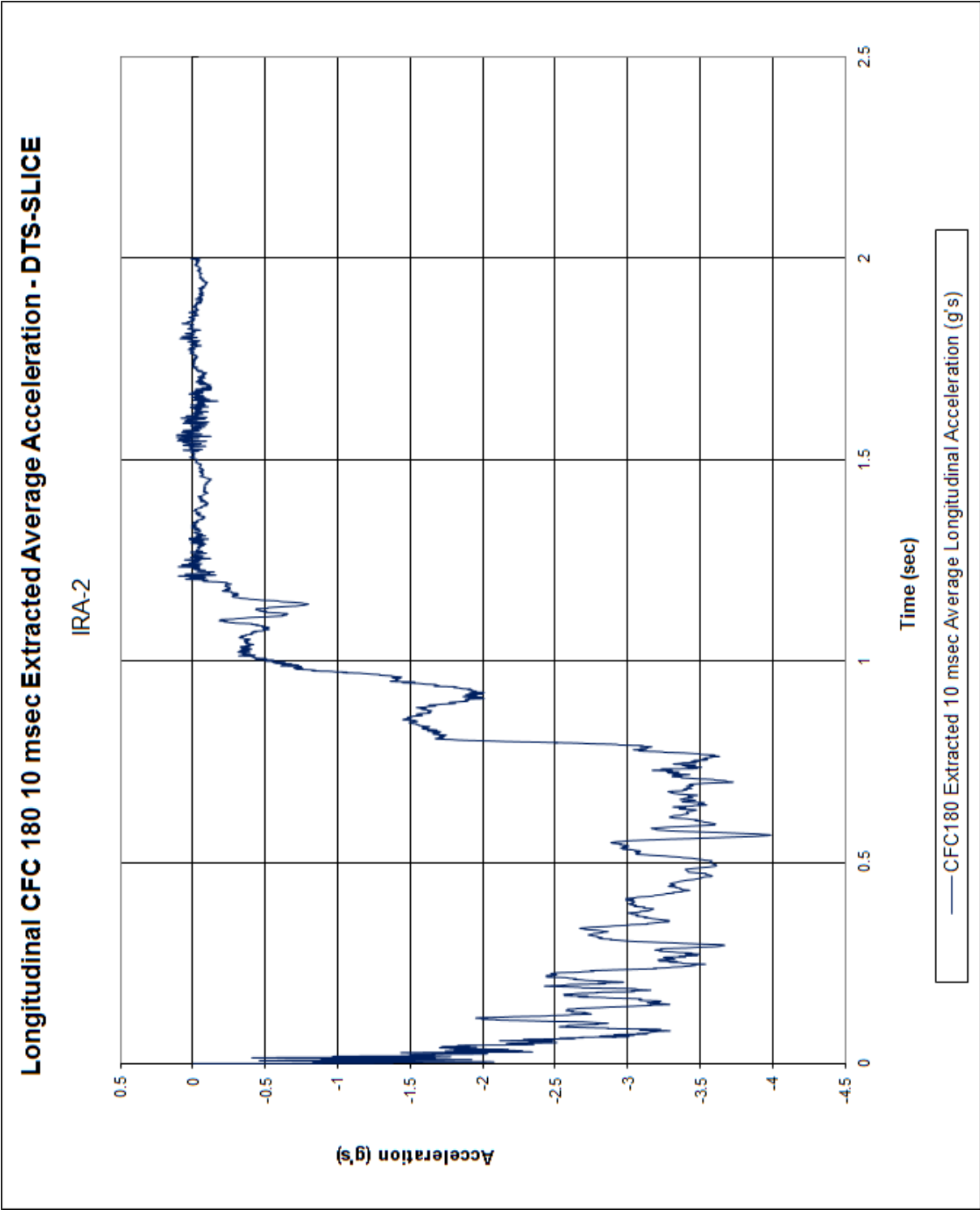


Figure C-9. 10-ms Average Longitudinal Deceleration (DTS-SLICE), Test No. IRA-2

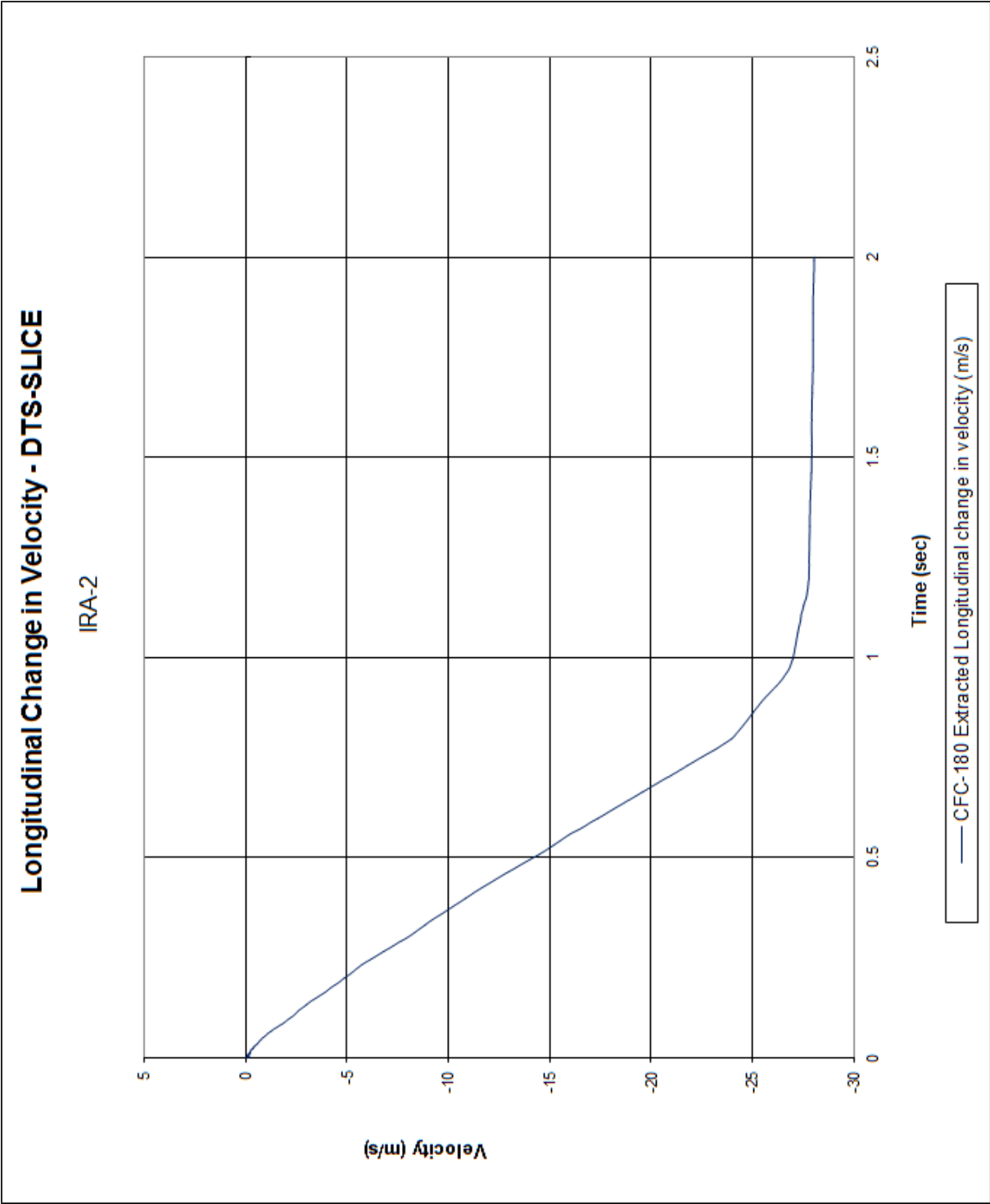


Figure C-10. Longitudinal Occupant Impact Velocity (DTS-SLICE), Test No. IRA-2

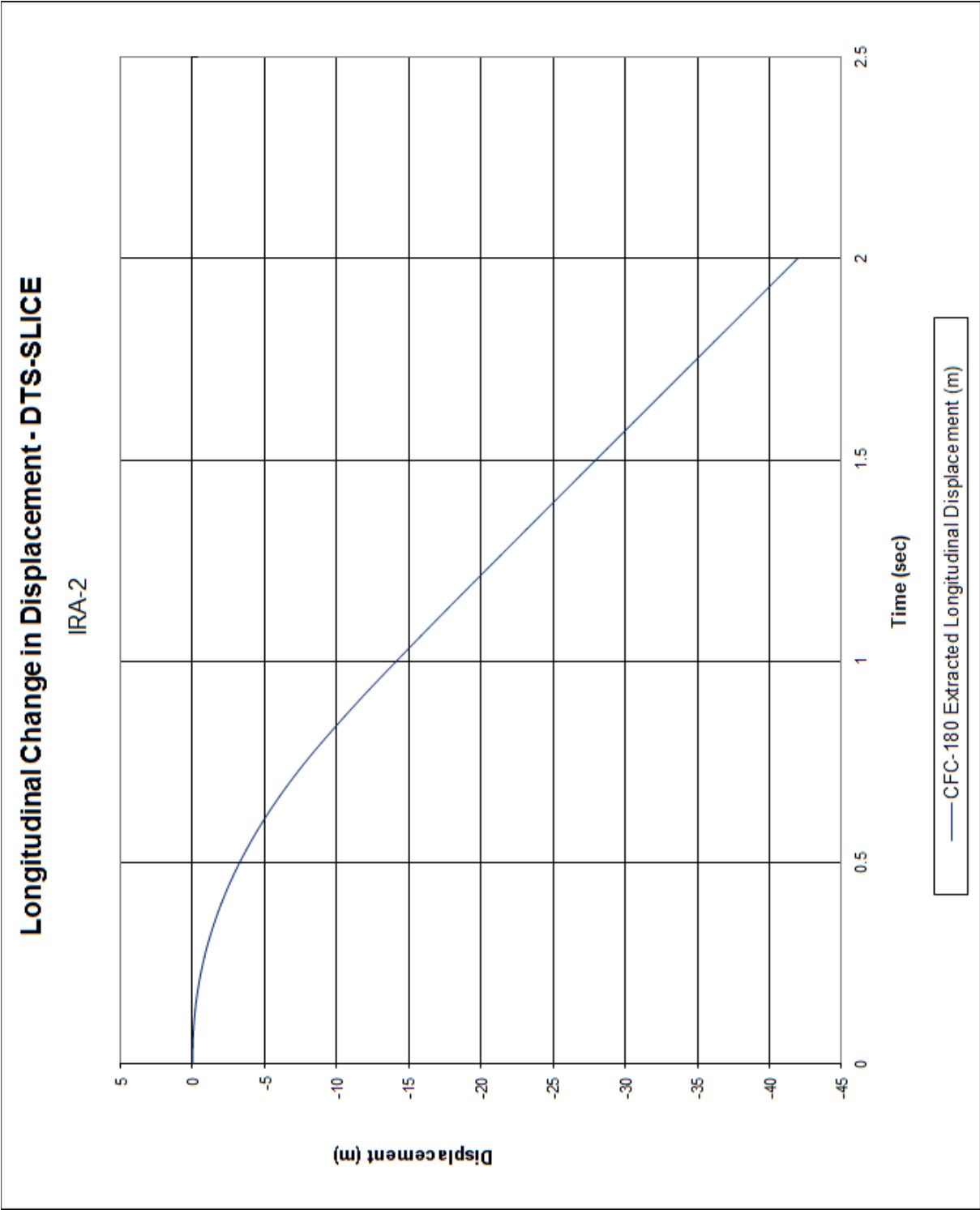


Figure C-11. Longitudinal Occupant Displacement (DTS-SLICE), Test No. IRA-2

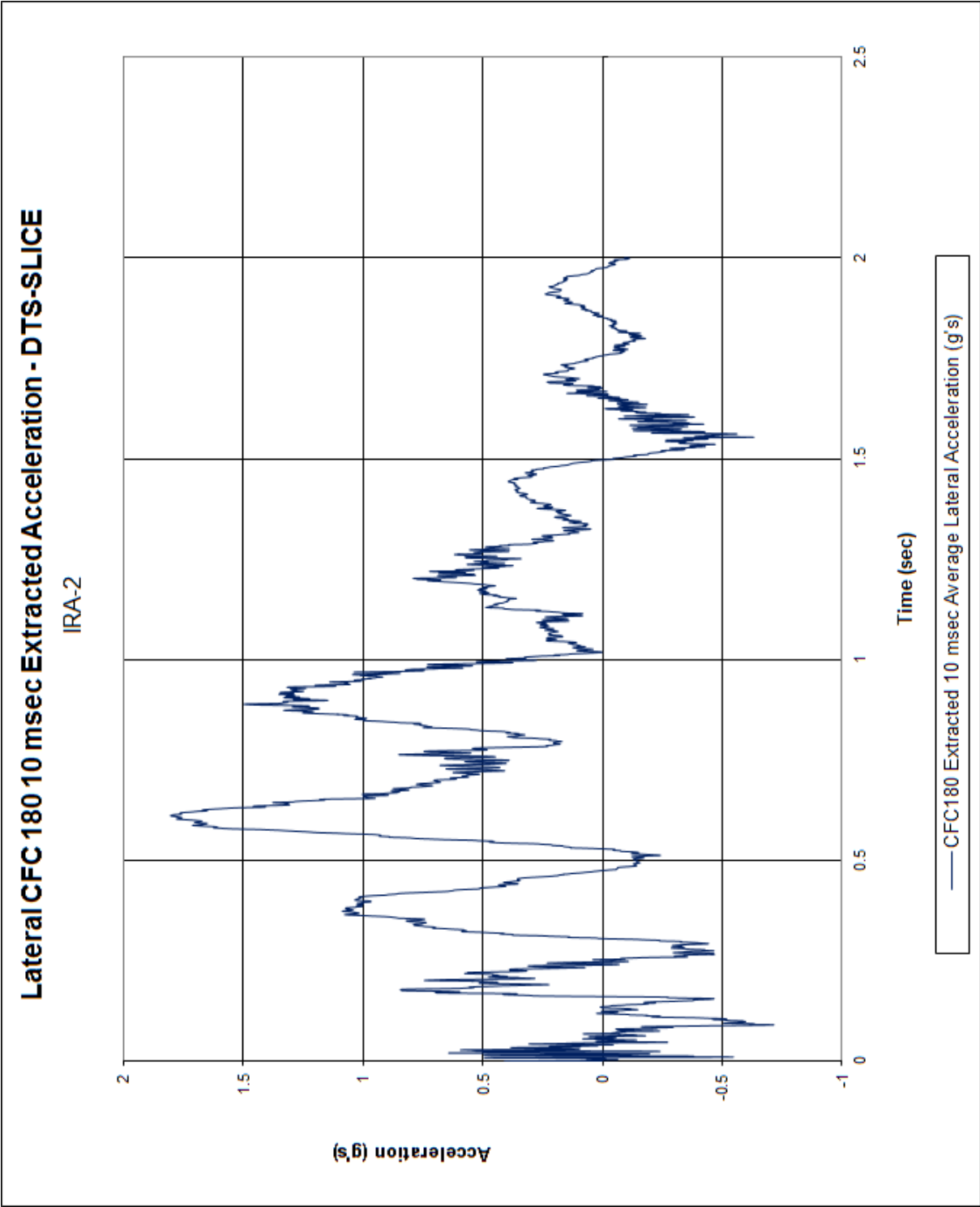


Figure C-12. 10-ms Average Lateral Deceleration (DTS-SLICE), Test No. IRA-2

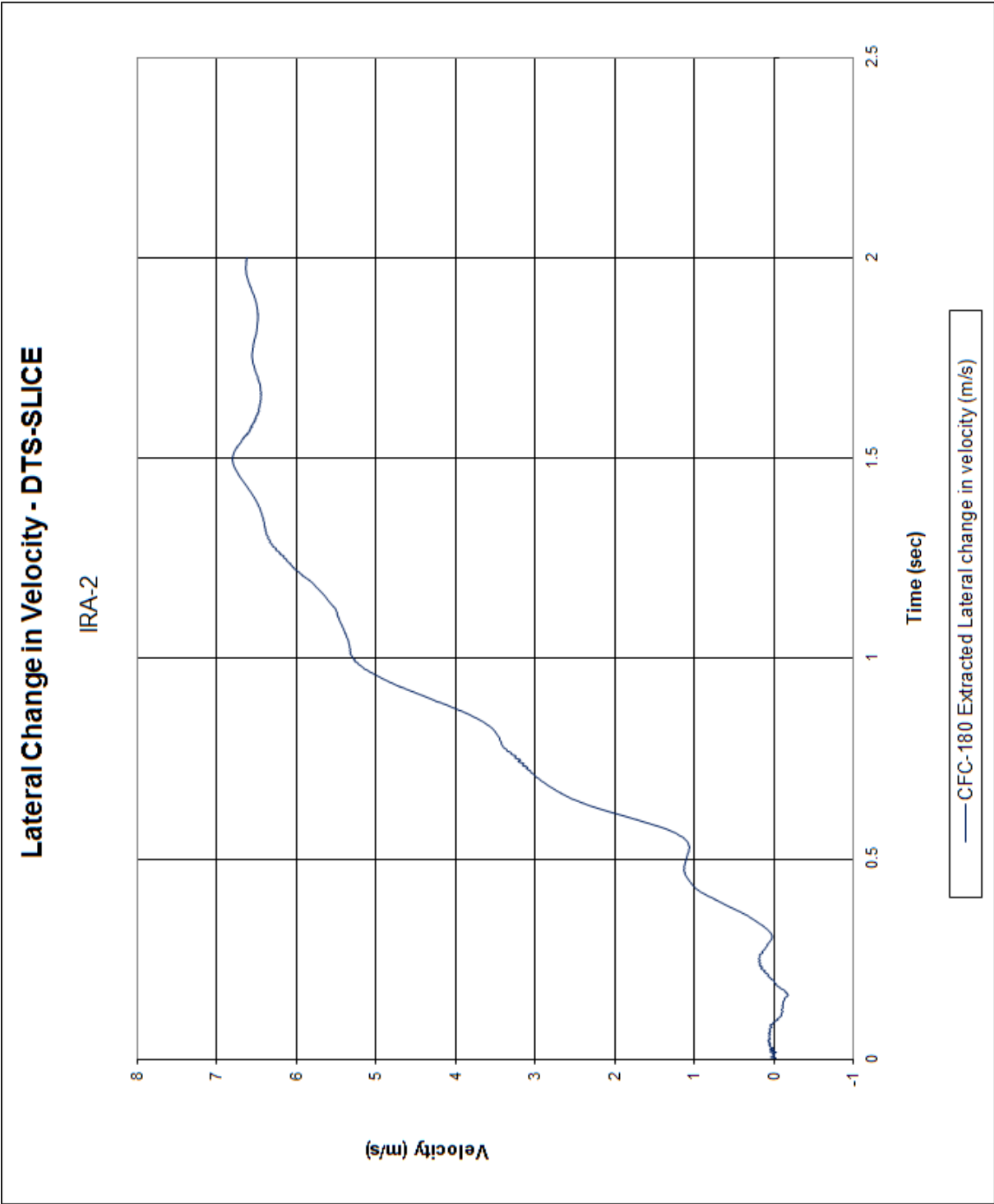


Figure C-13. Lateral Occupant Impact Velocity (DTS-SLICE), Test No. IRA-2

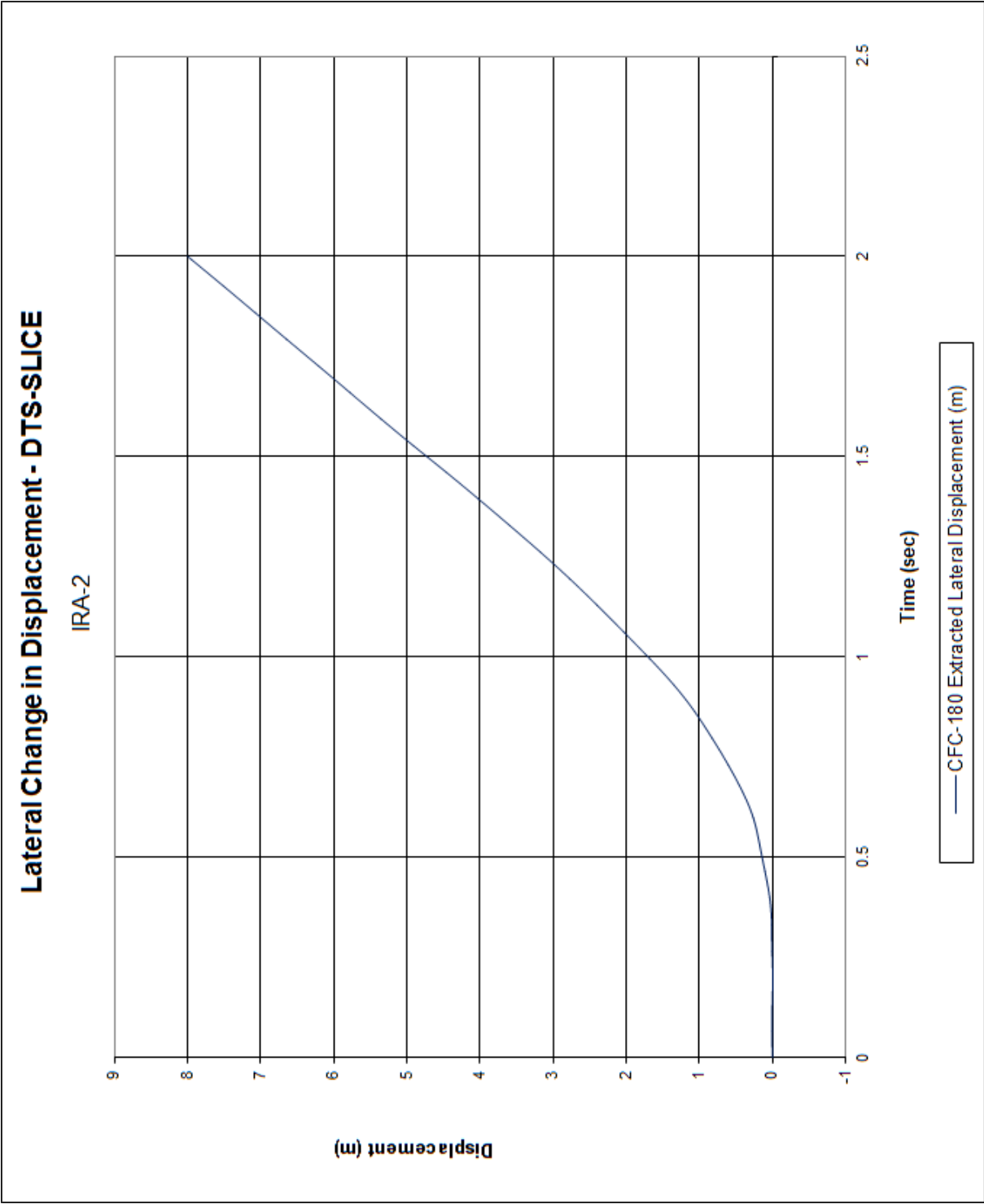


Figure C-14. Lateral Occupant Displacement (DTS-SLICE), Test No. IRA-2

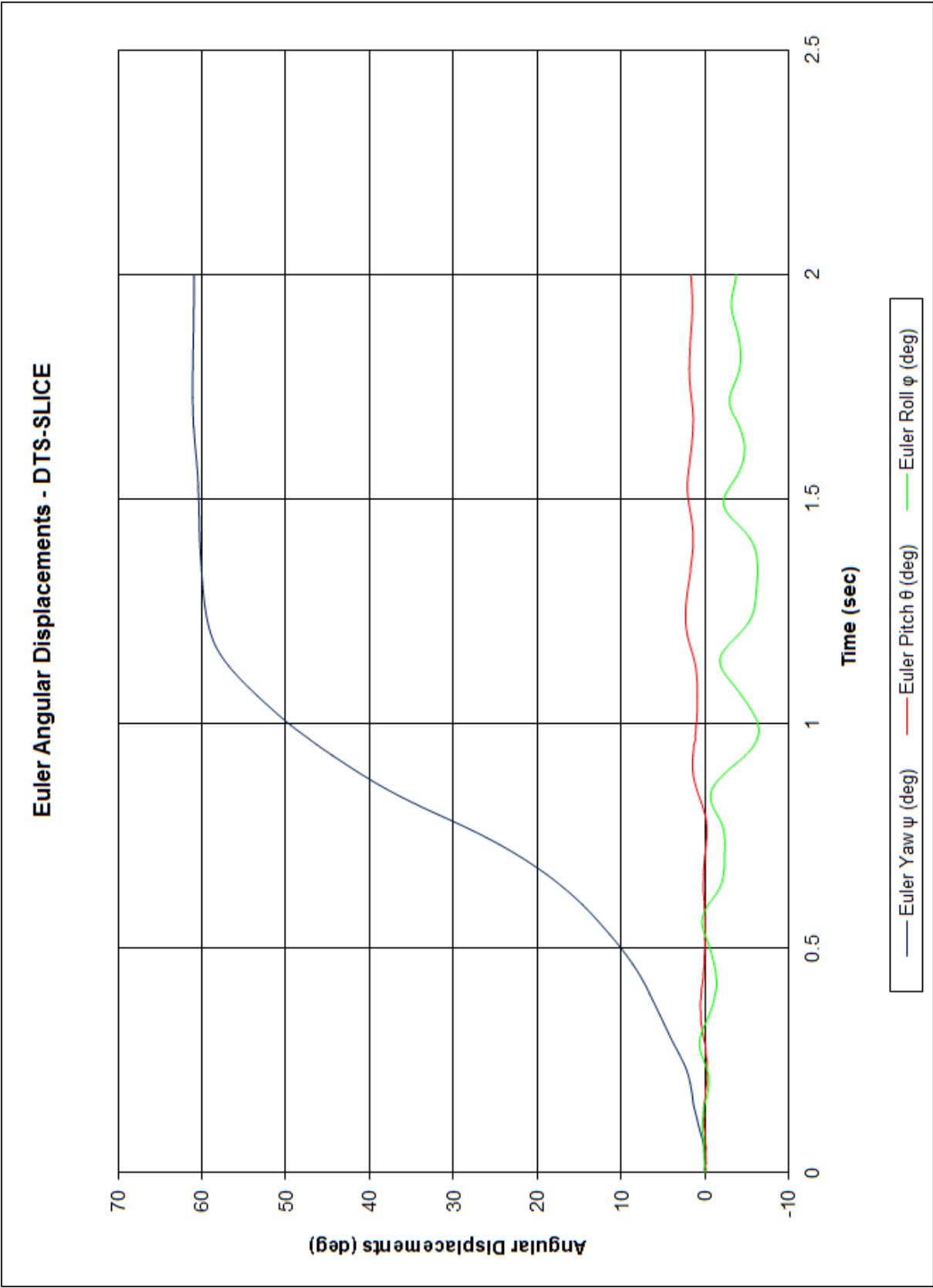


Figure C-15. Vehicle Angular Displacements (DTS-SLICE), Test No. IRA-2

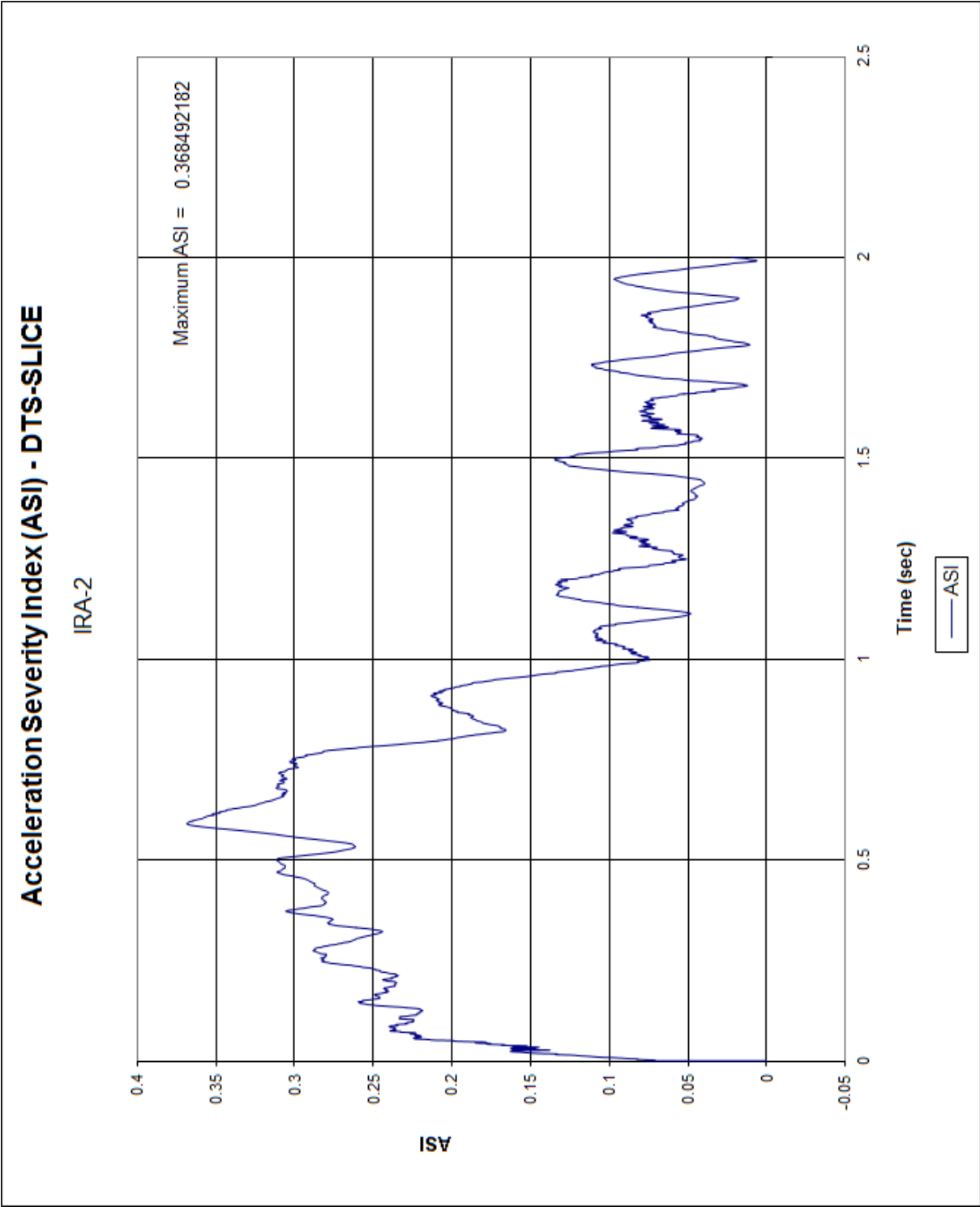


Figure C-16. Acceleration Severity Index (DTS-SLICE), Test No. IRA-2

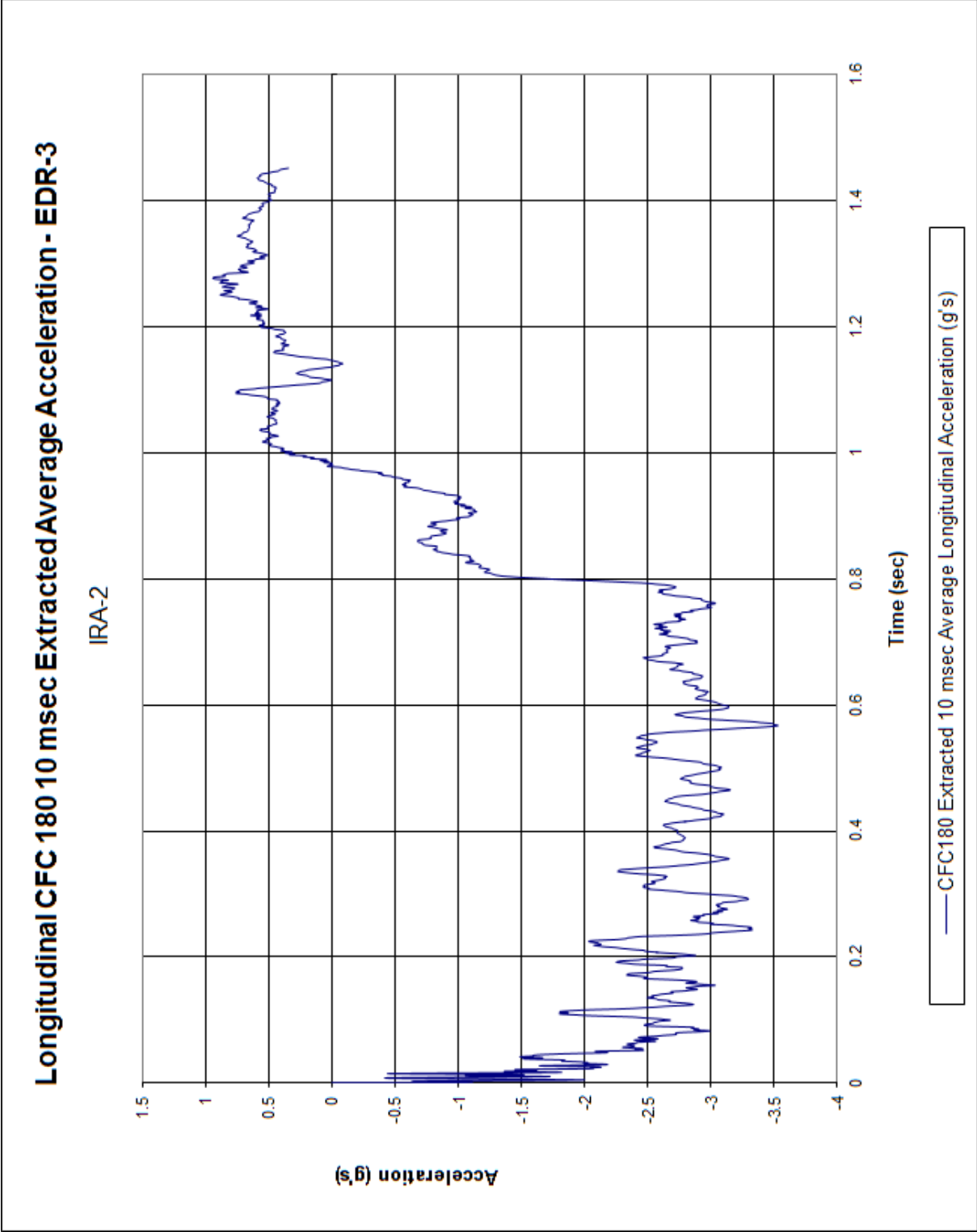


Figure C-17. 10-ms Average Longitudinal Deceleration (EDR-3), Test No. IRA-2

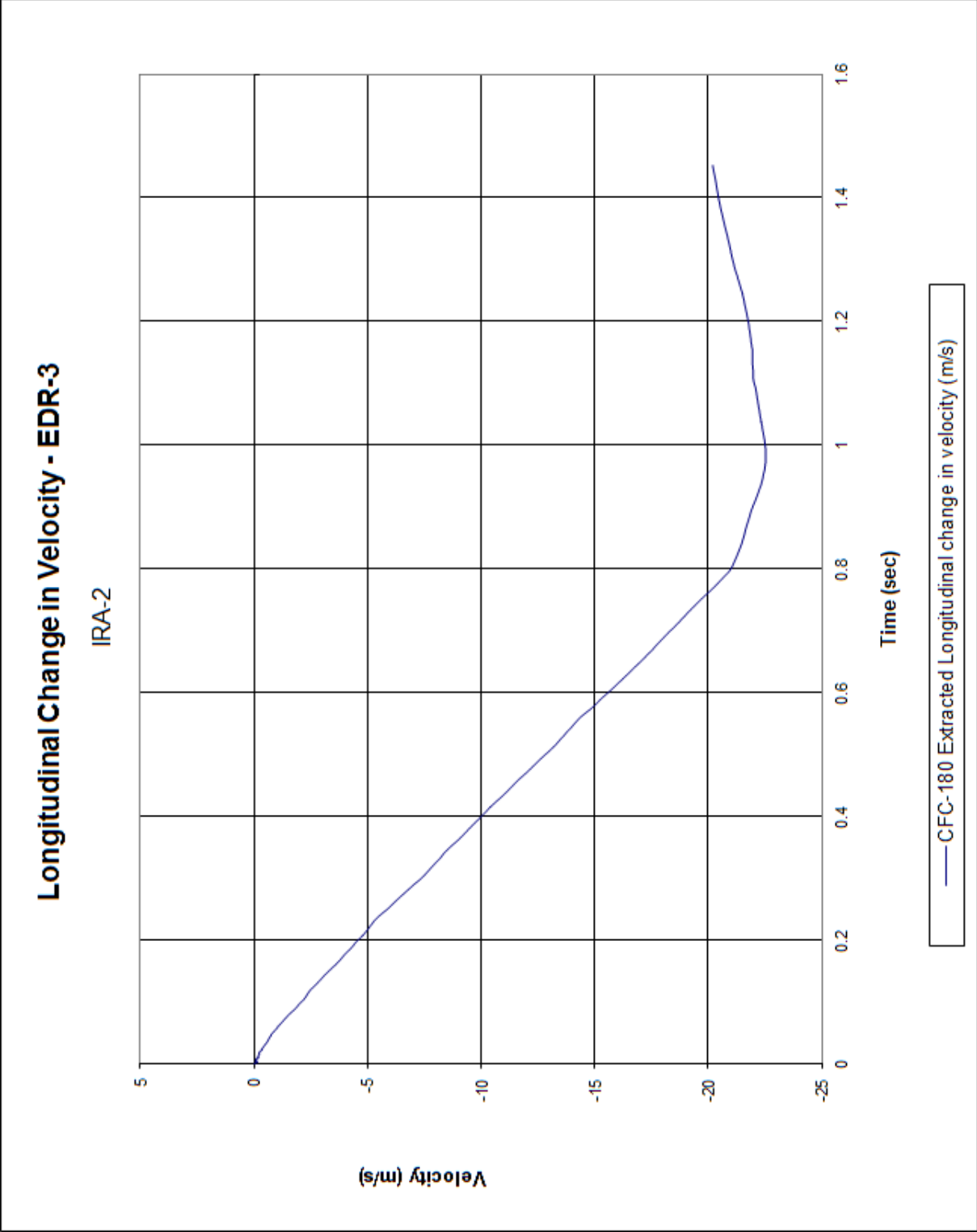


Figure C-18. Longitudinal Occupant Impact Velocity (EDR-3), Test No. IRA-2

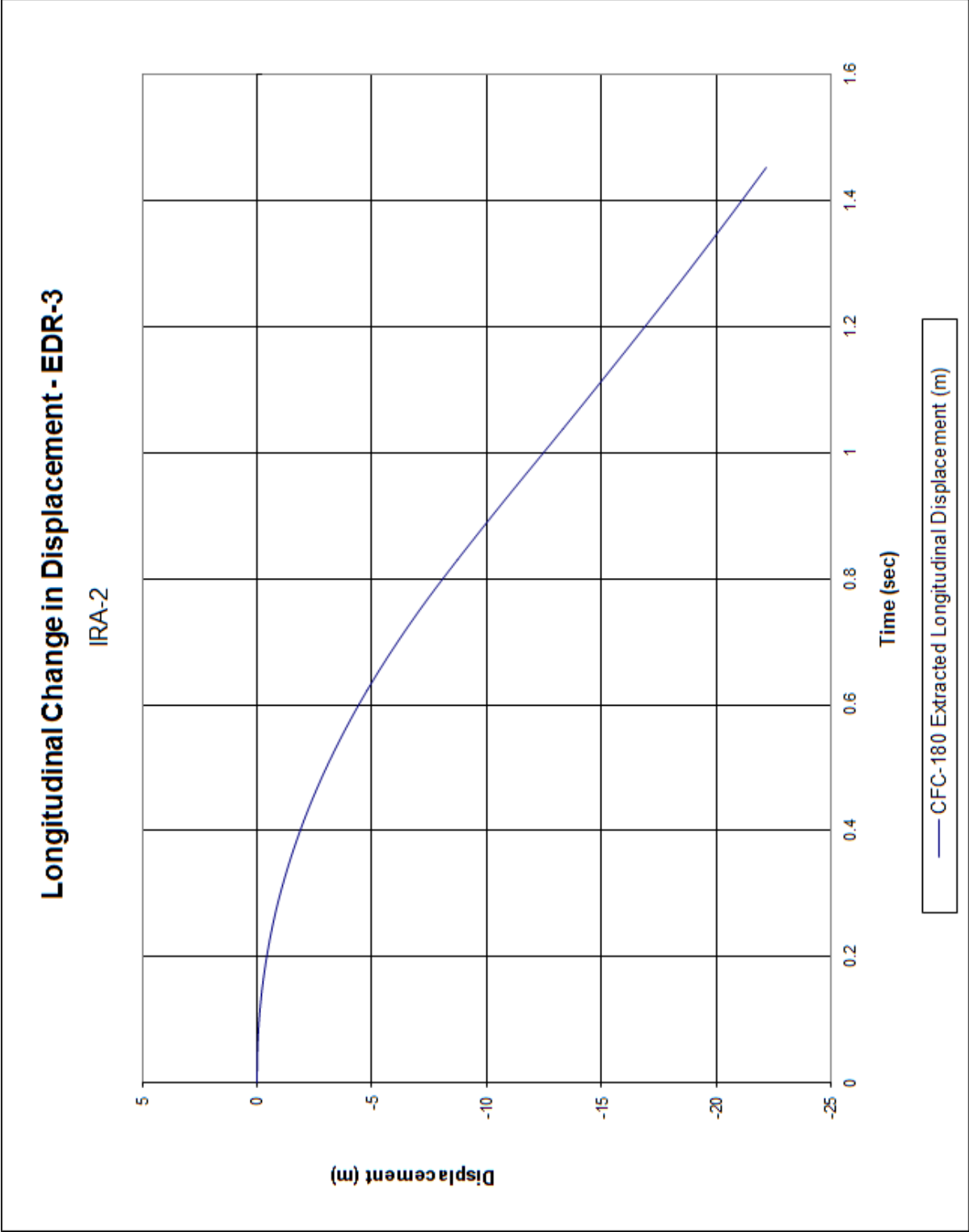


Figure C-19. Longitudinal Occupant Displacement (EDR-3), Test No. IRA-2

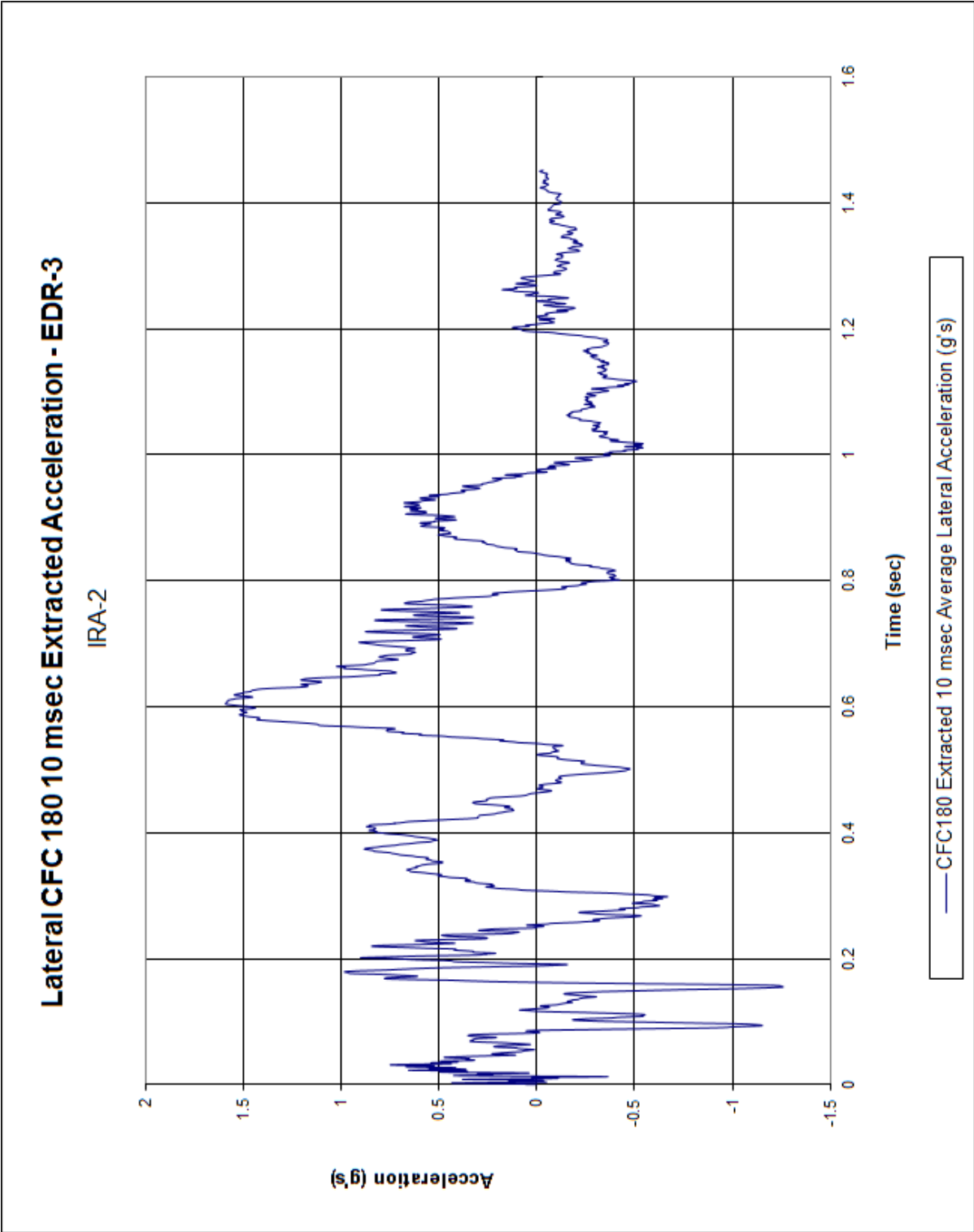


Figure C-20. 10-msec Average Lateral Deceleration (EDR-3), Test No. IRA-2

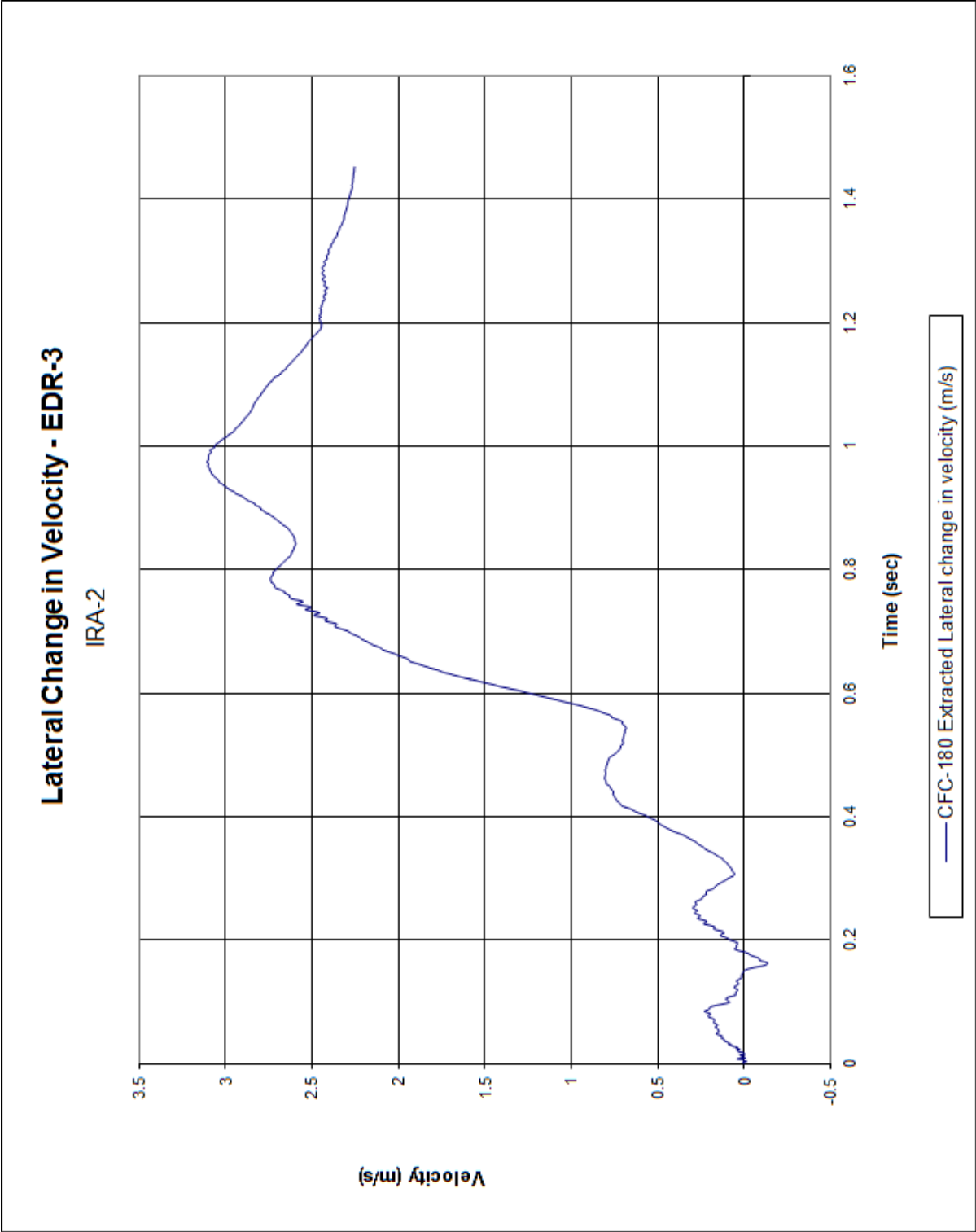


Figure C-21. Lateral Occupant Impact Velocity (EDR-3), Test No. IRA-2

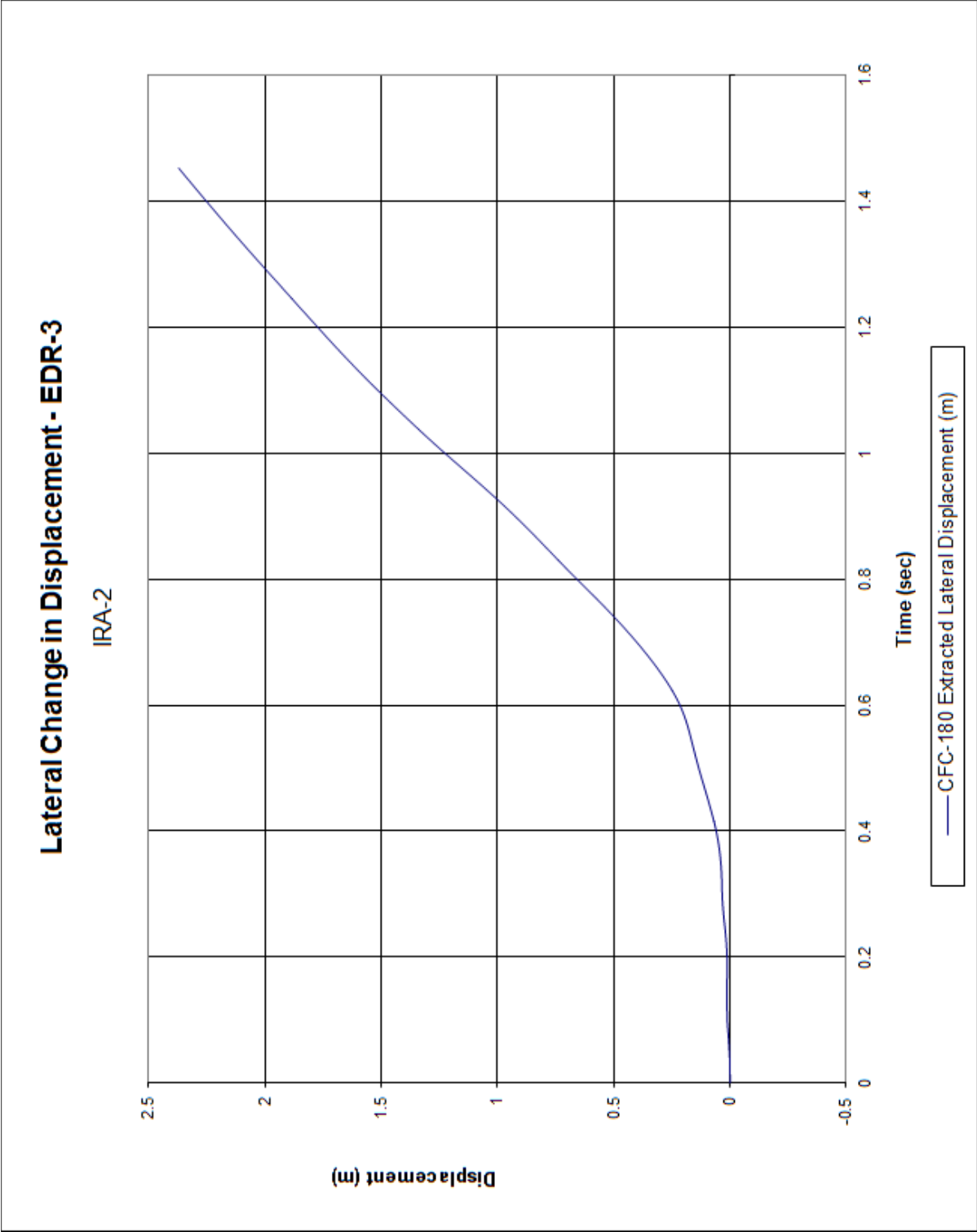


Figure C-22. Lateral Occupant Displacement (EDR-3), Test No. IRA-2

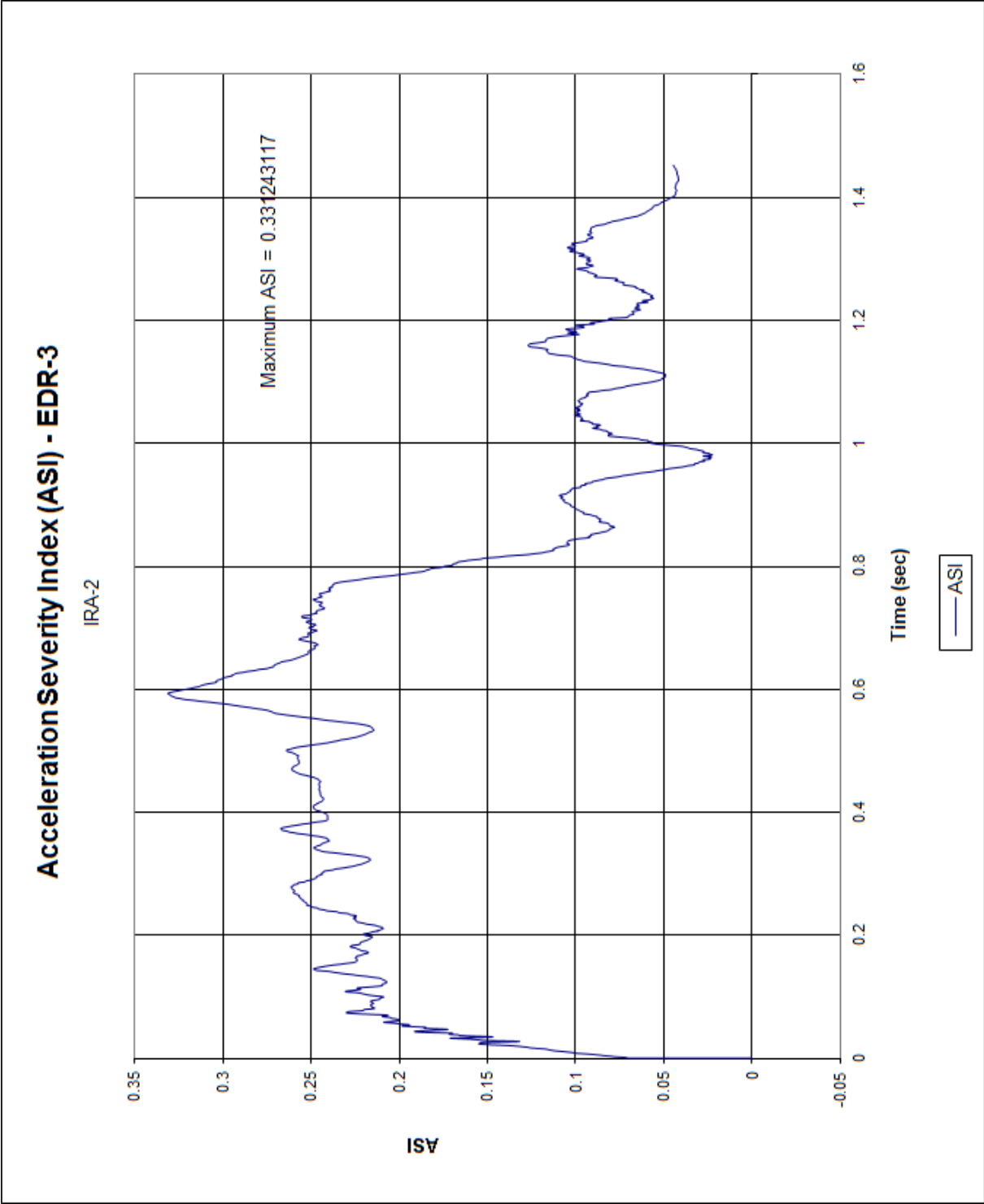


Figure C-23. Acceleration Severity Index (EDR-3), Test No. IRA-2

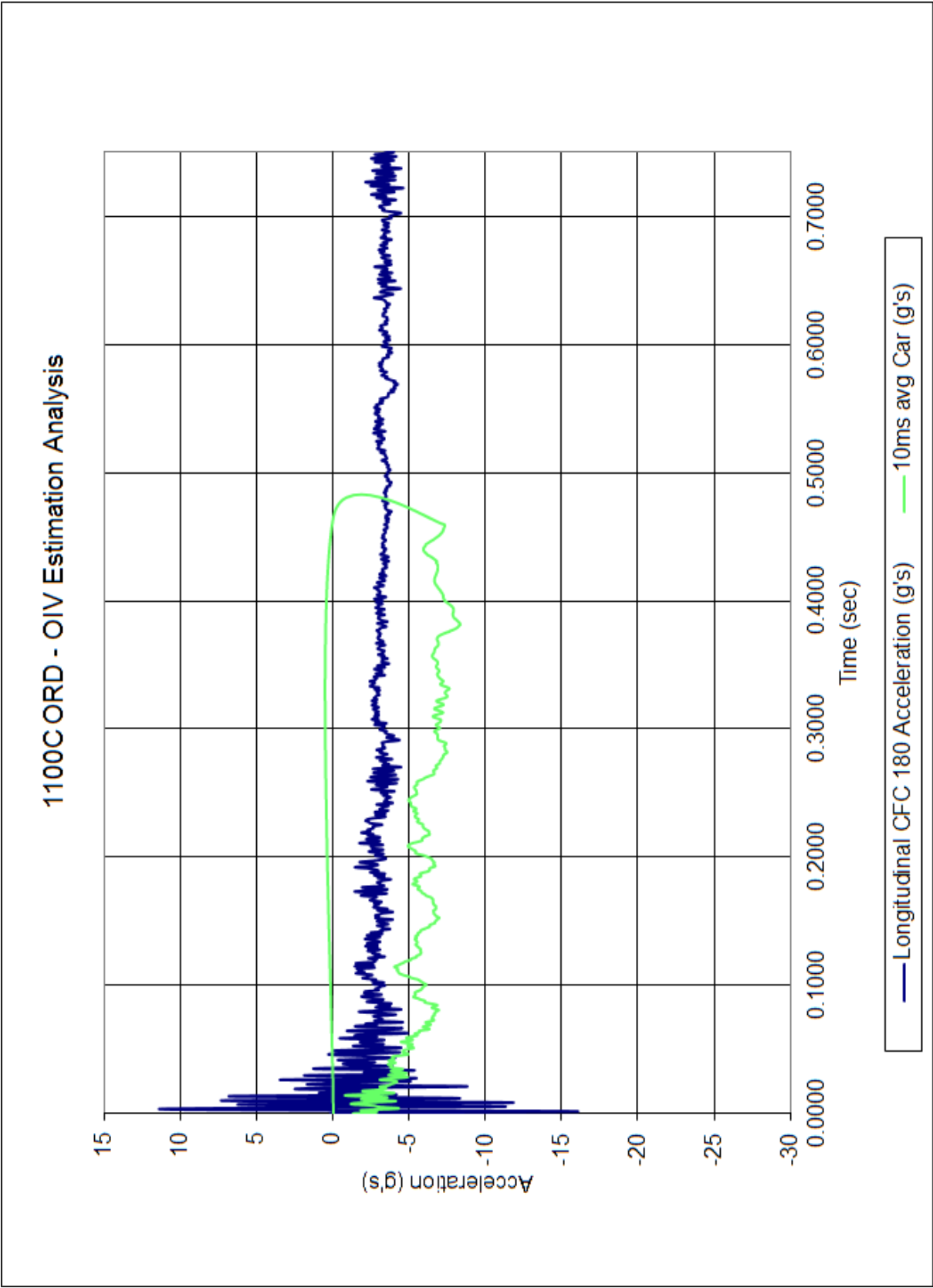


Figure C-24. 1100C ORD-OIV Estimation, Test No. IRA-2

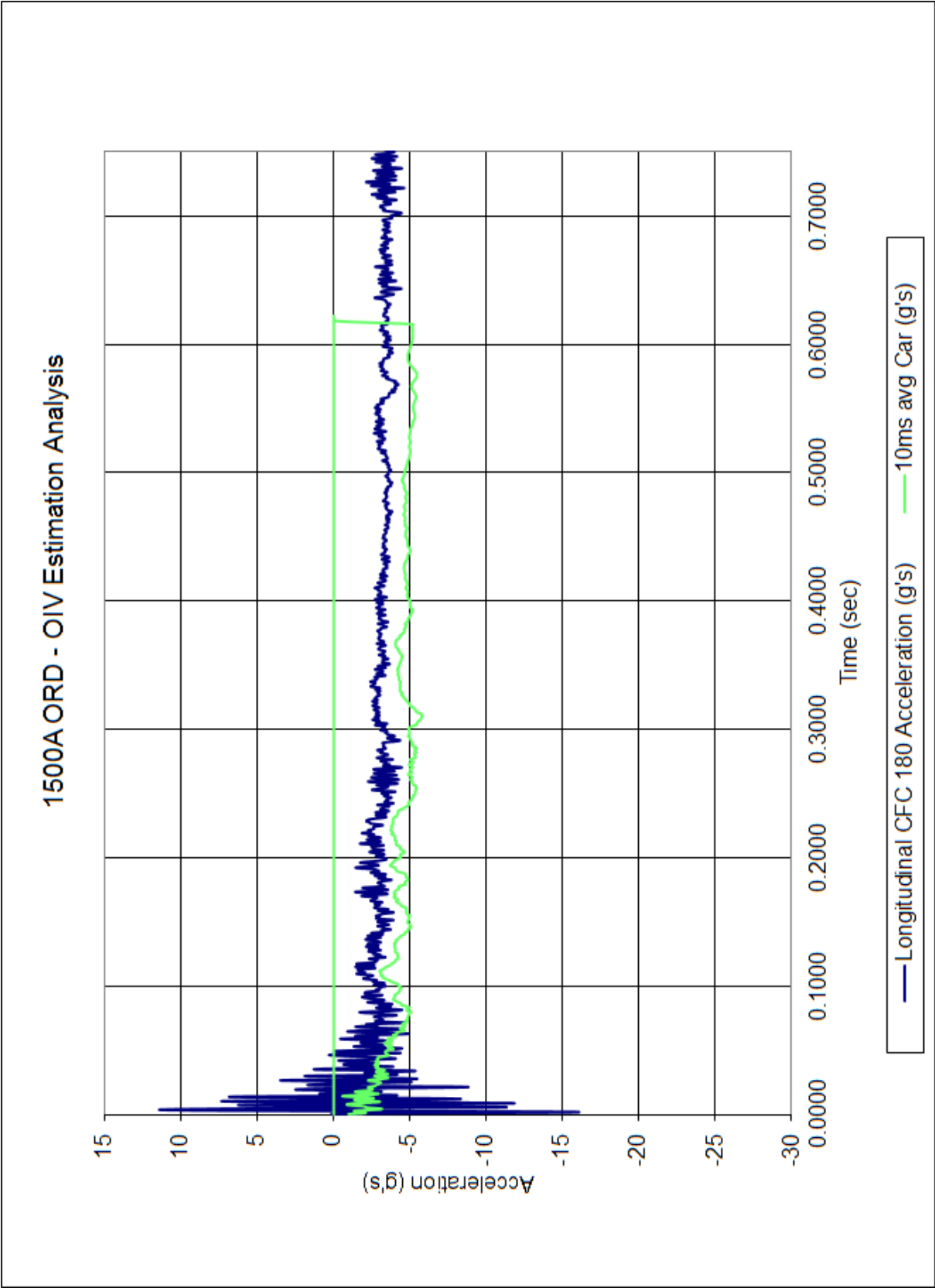


Figure C-25. 1500A ORD-OIV Estimation, Test No. IRA-2

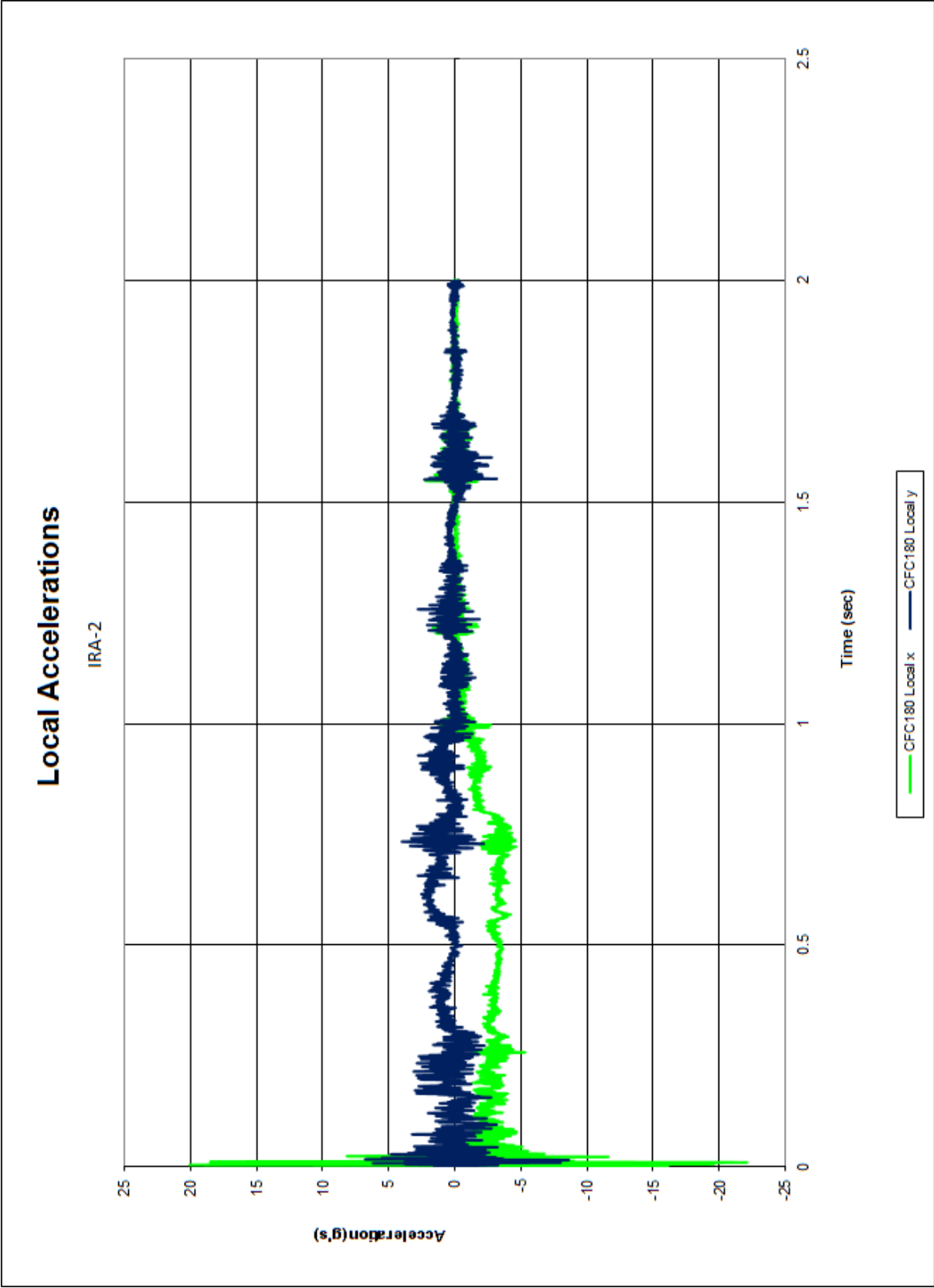


Figure C-26. Local Accelerations, Test No. IRA-2

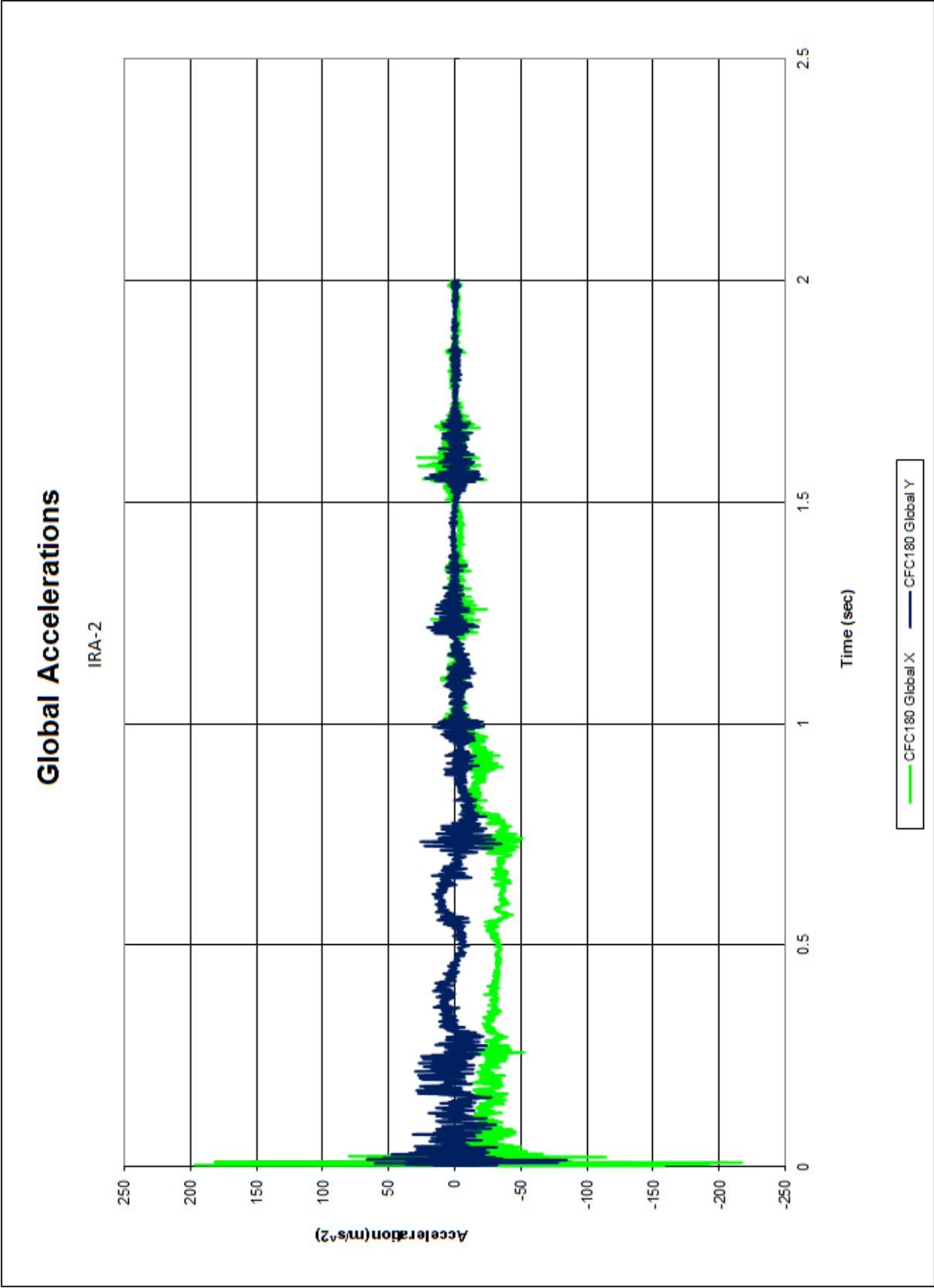


Figure C-27. Global Accelerations, Test No. IRA-2

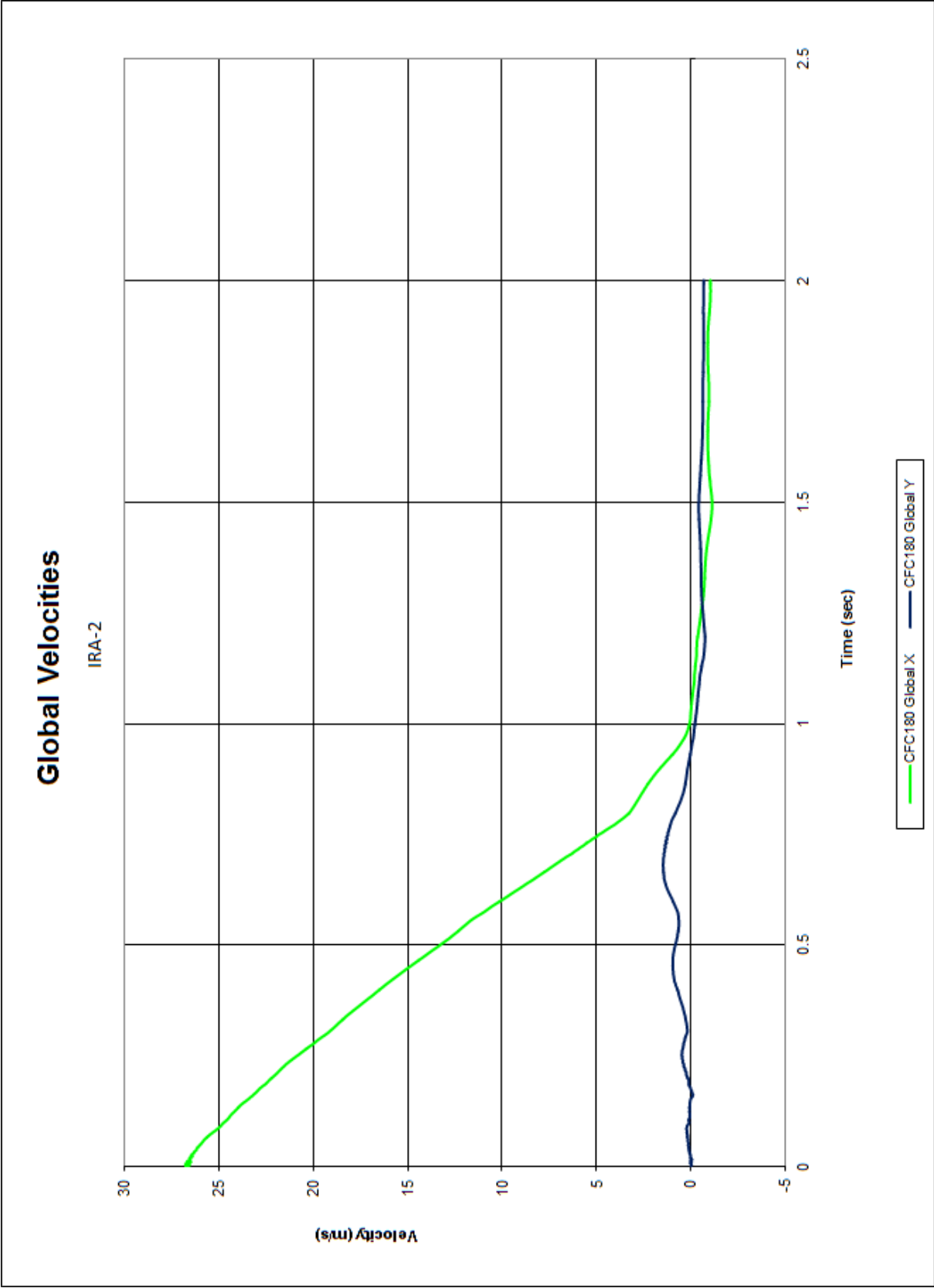


Figure C-28. Global Velocities, Test No. IRA-2

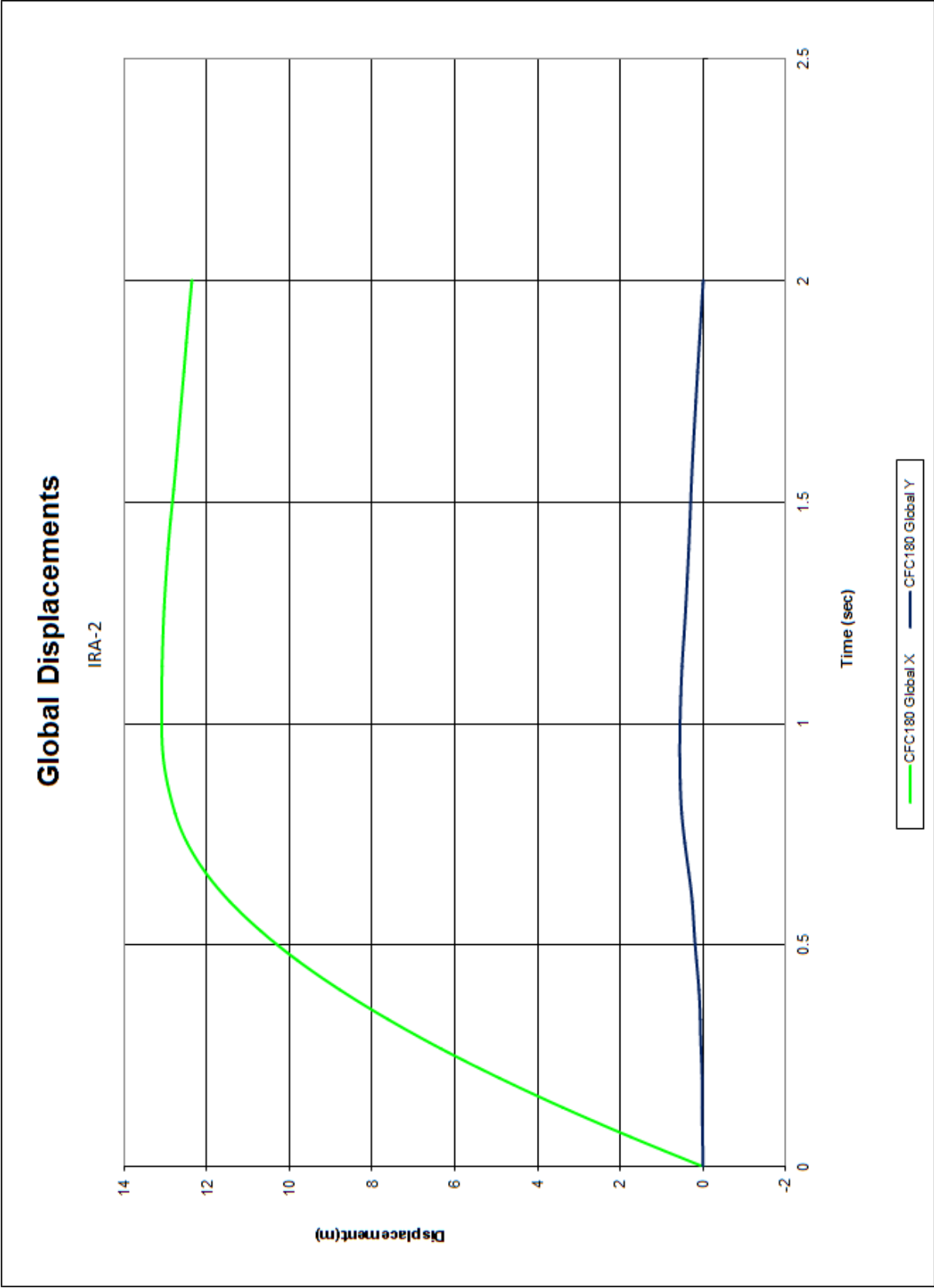


Figure C-29. Global Displacements, Test No. IRA-2

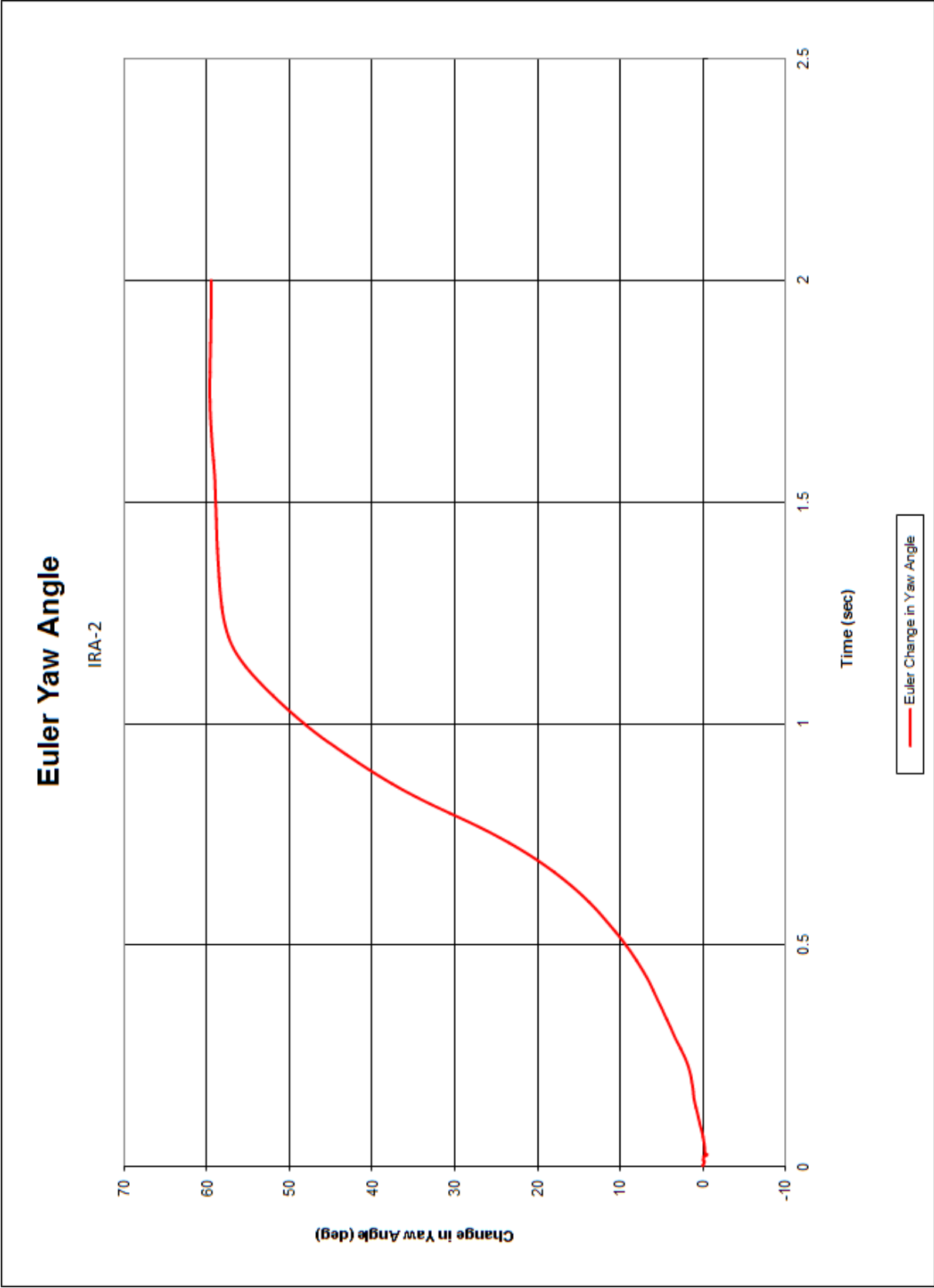


Figure C-30. Euler Yaw Angle, Test No. IRA-2

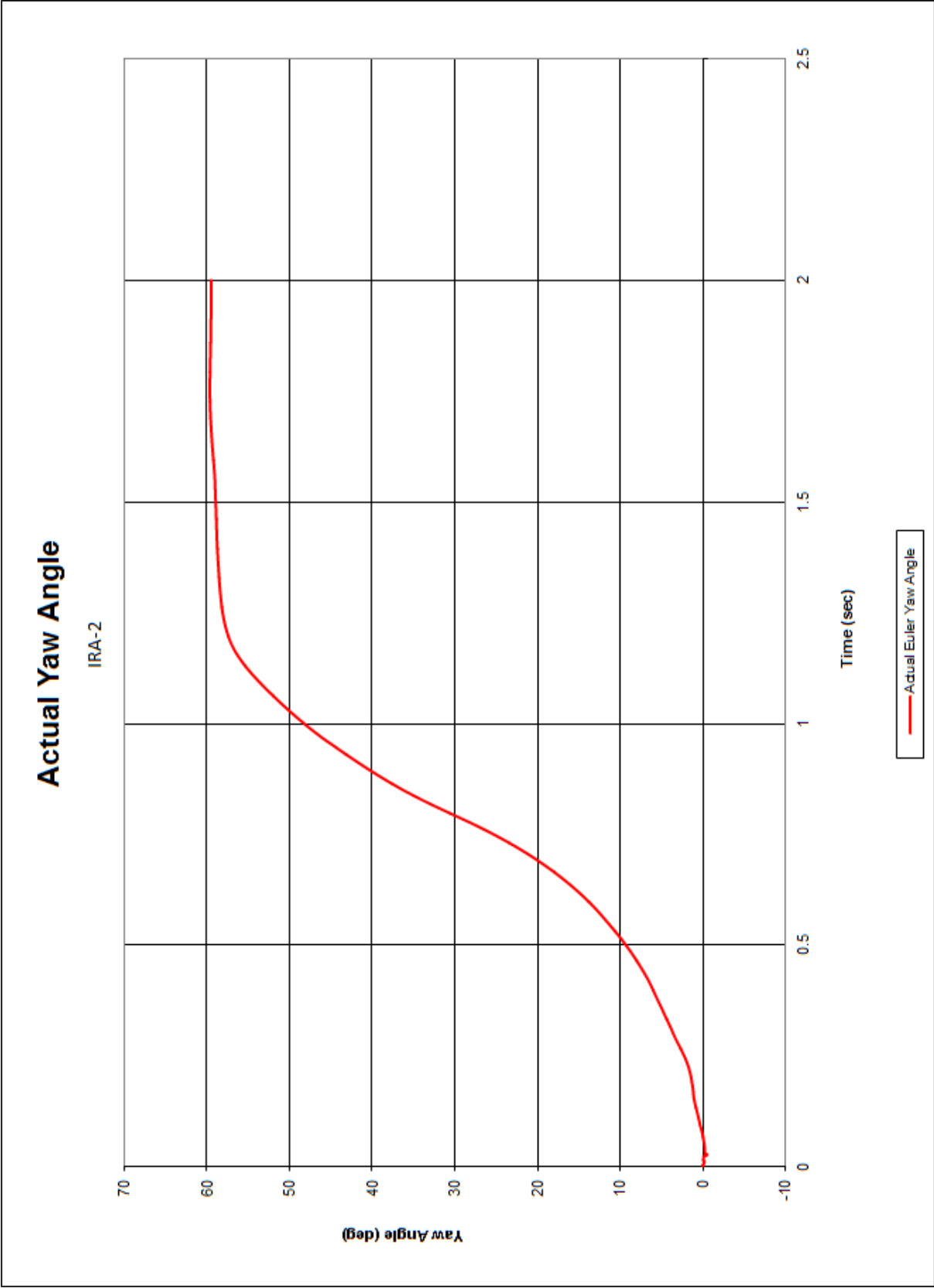


Figure C-31. Actual Yaw Angle, Test No. IRA-2

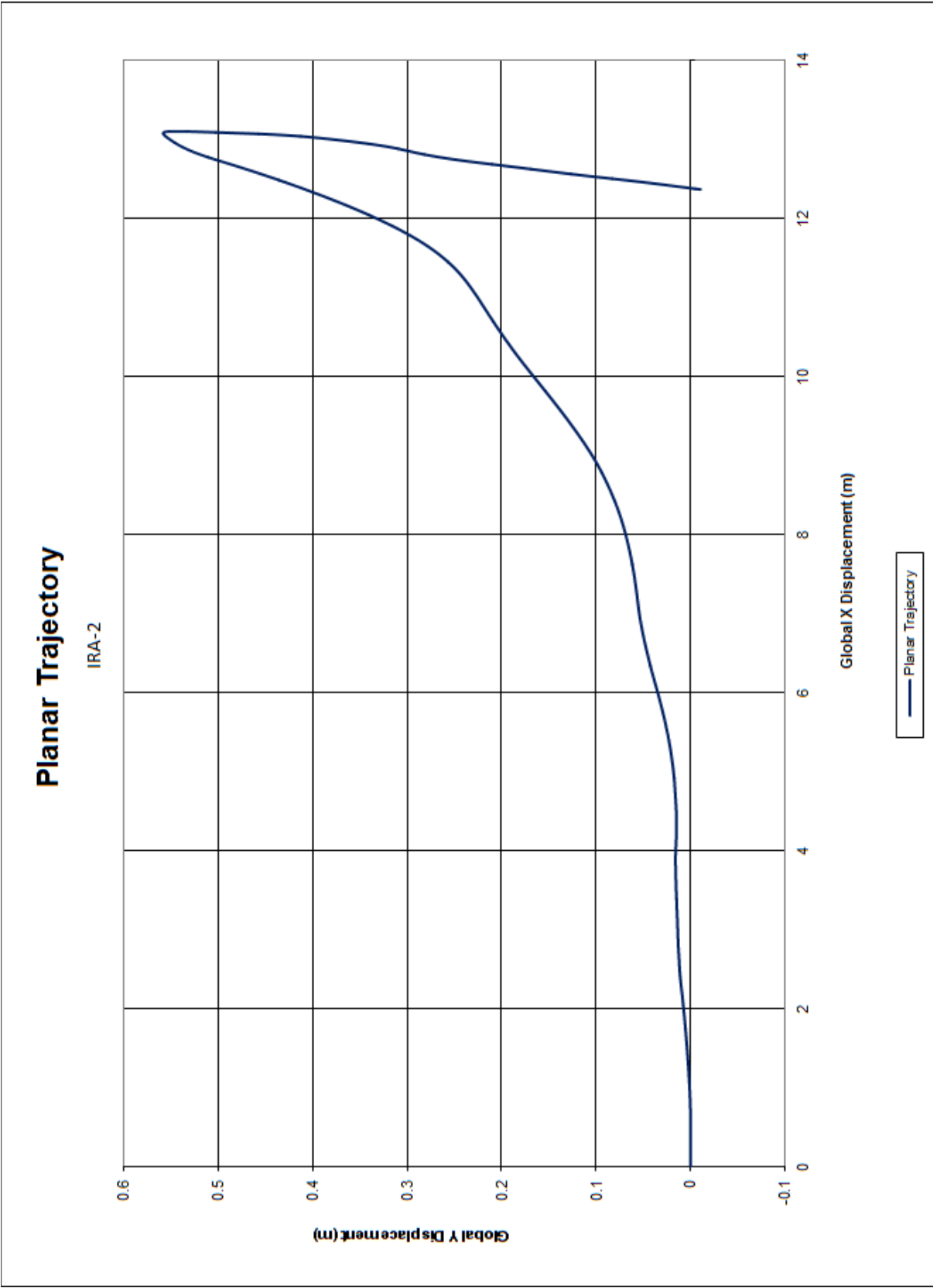


Figure C-32. Planar Trajectory, Test No. IRA-2

Appendix D. Accelerometer and Rate Transducer Data Plots, Test No. IRA-3

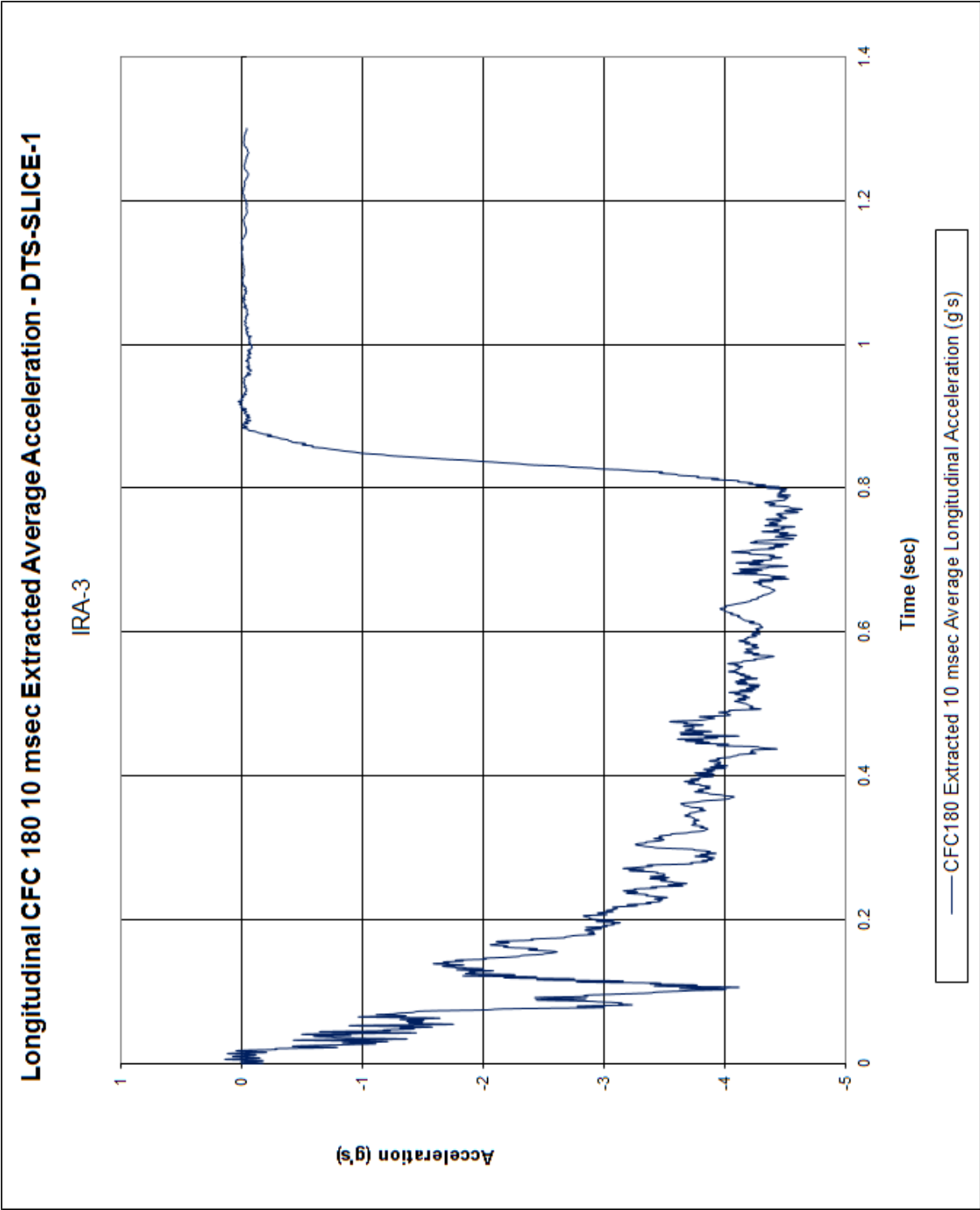


Figure D-1. 10-ms Average Longitudinal Deceleration (DTS-SLICE-1), Test No. IRA-3

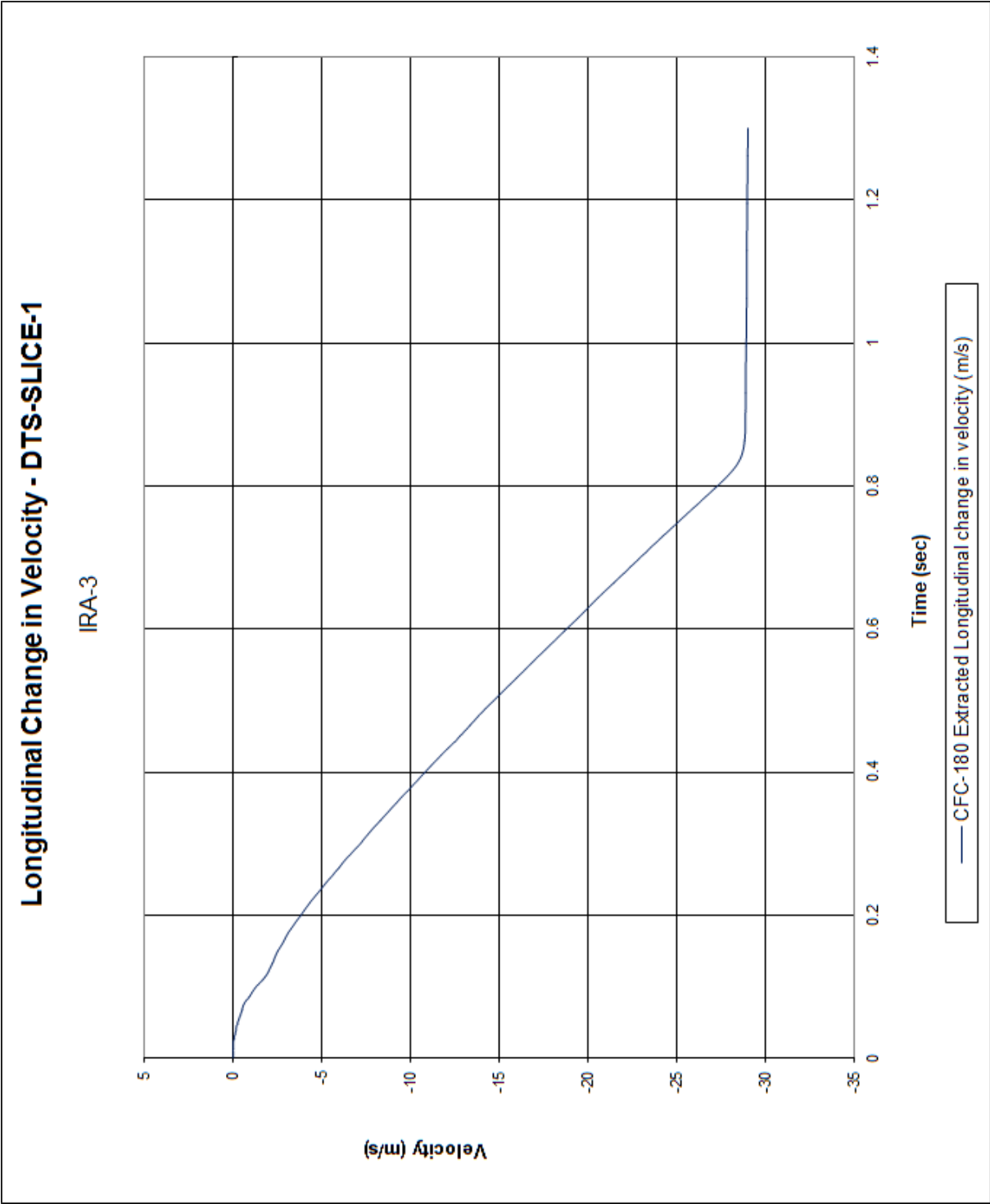


Figure D-2. Longitudinal Occupant Impact Velocity (DTS-SLICE-1), Test No. IRA-3

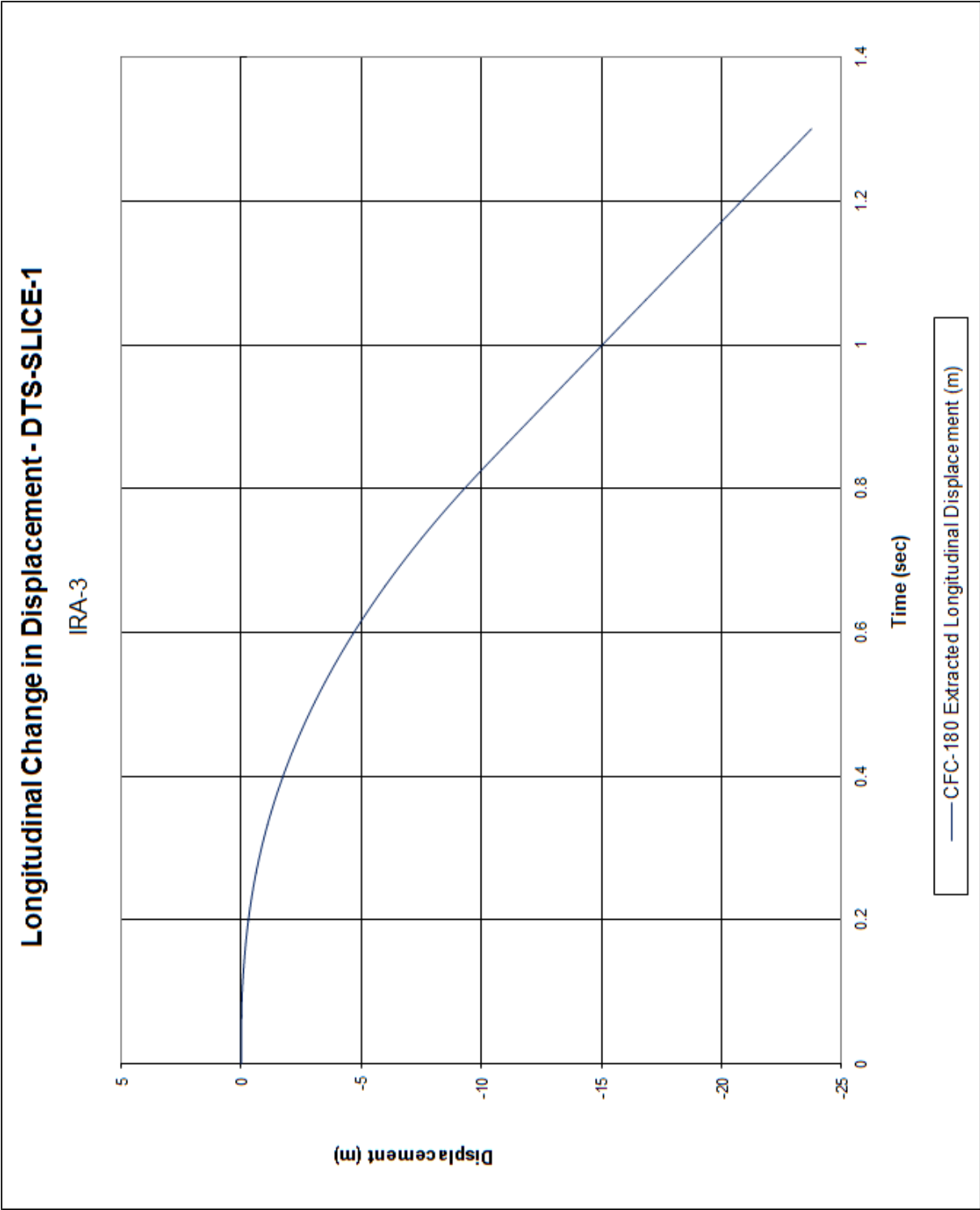


Figure D-3. Longitudinal Occupant Displacement (DTS-SLICE-1), Test No. IRA-3

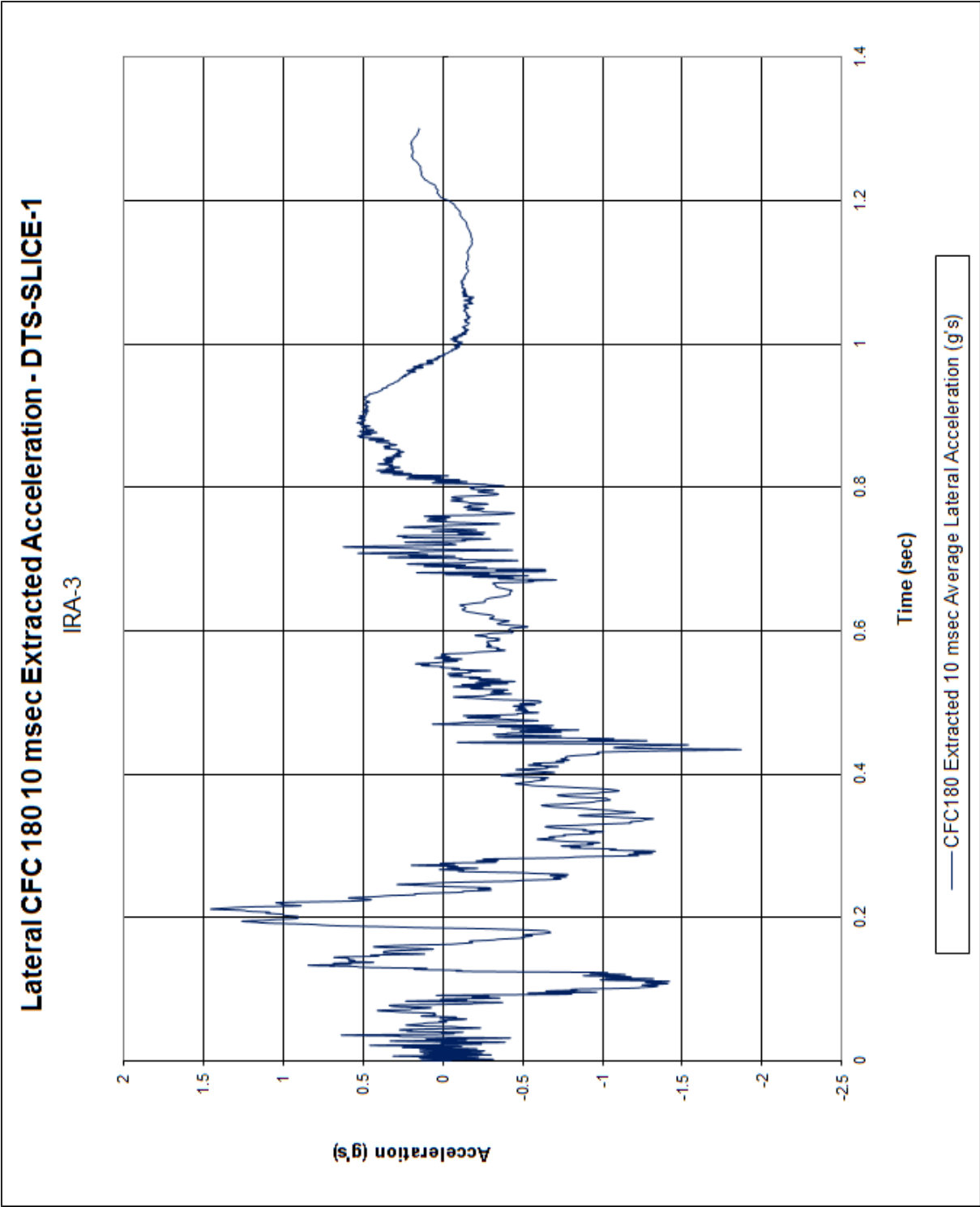


Figure D-4. 10-ms Average Lateral Deceleration (DTS-SLICE-1), Test No. IRA-3

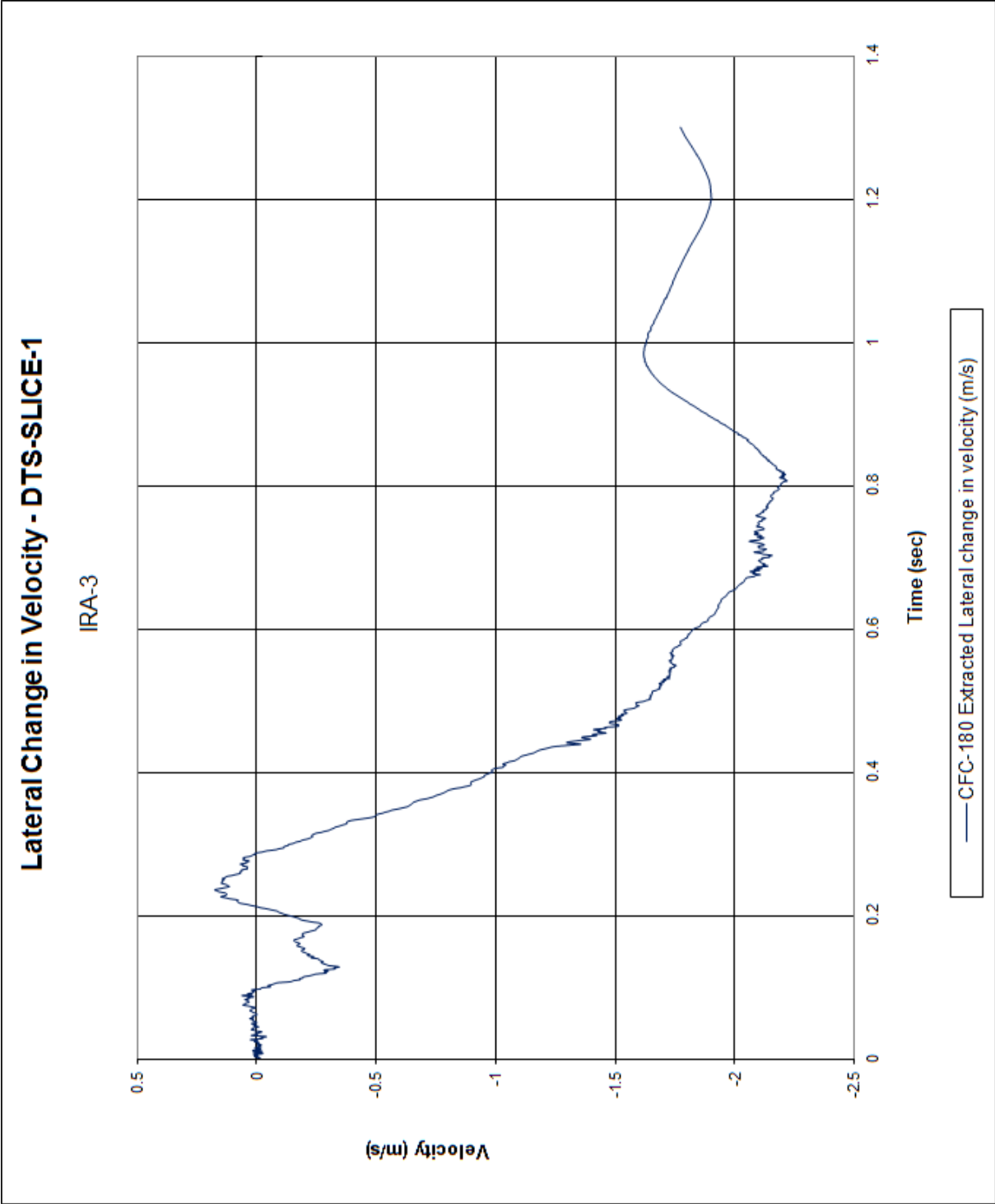


Figure D-5. Lateral Occupant Impact Velocity (DTS-SLICE-1), Test No. IRA-3

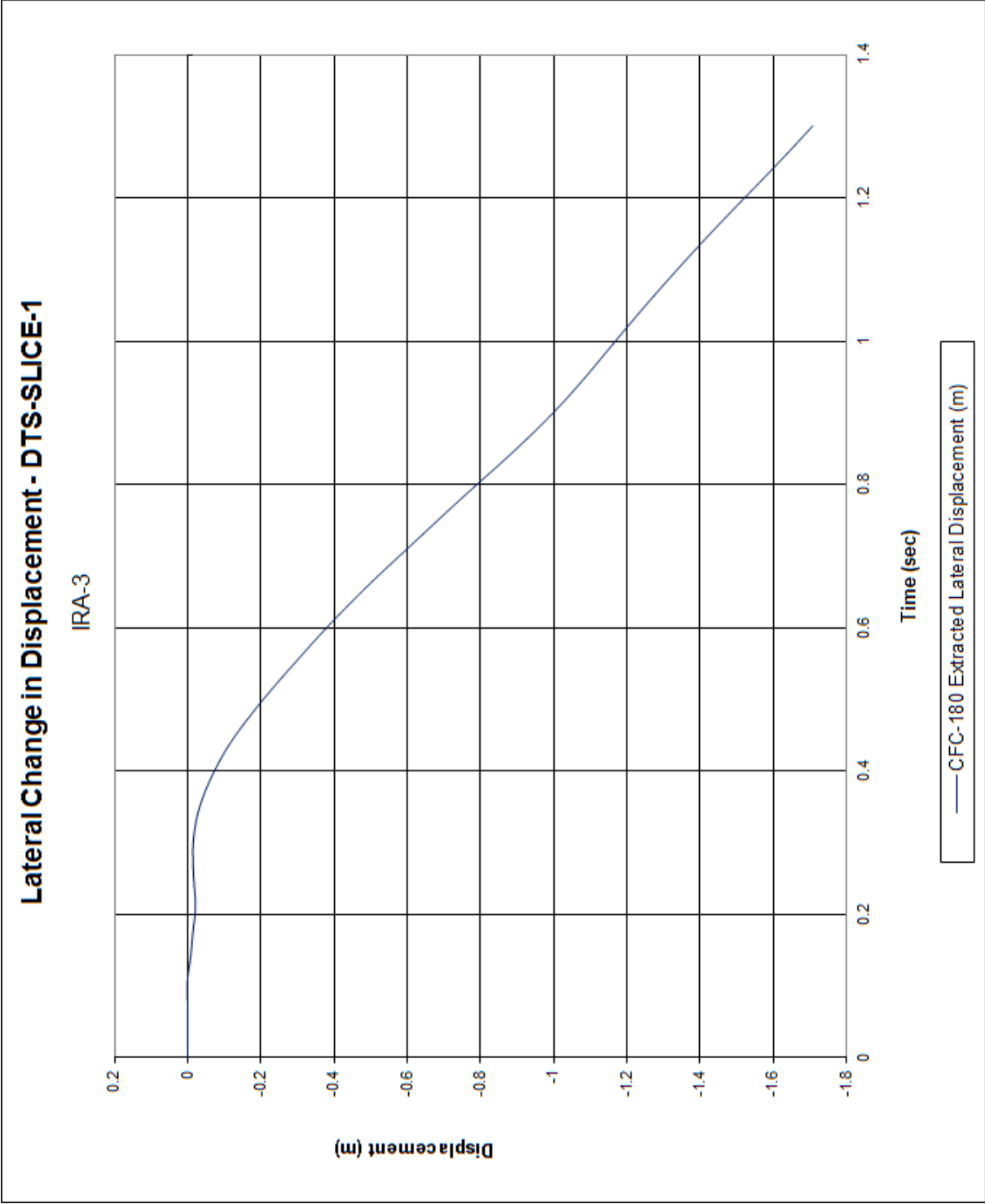


Figure D-6. Lateral Occupant Displacement (DTS-SLICE-1), Test No. IRA-3

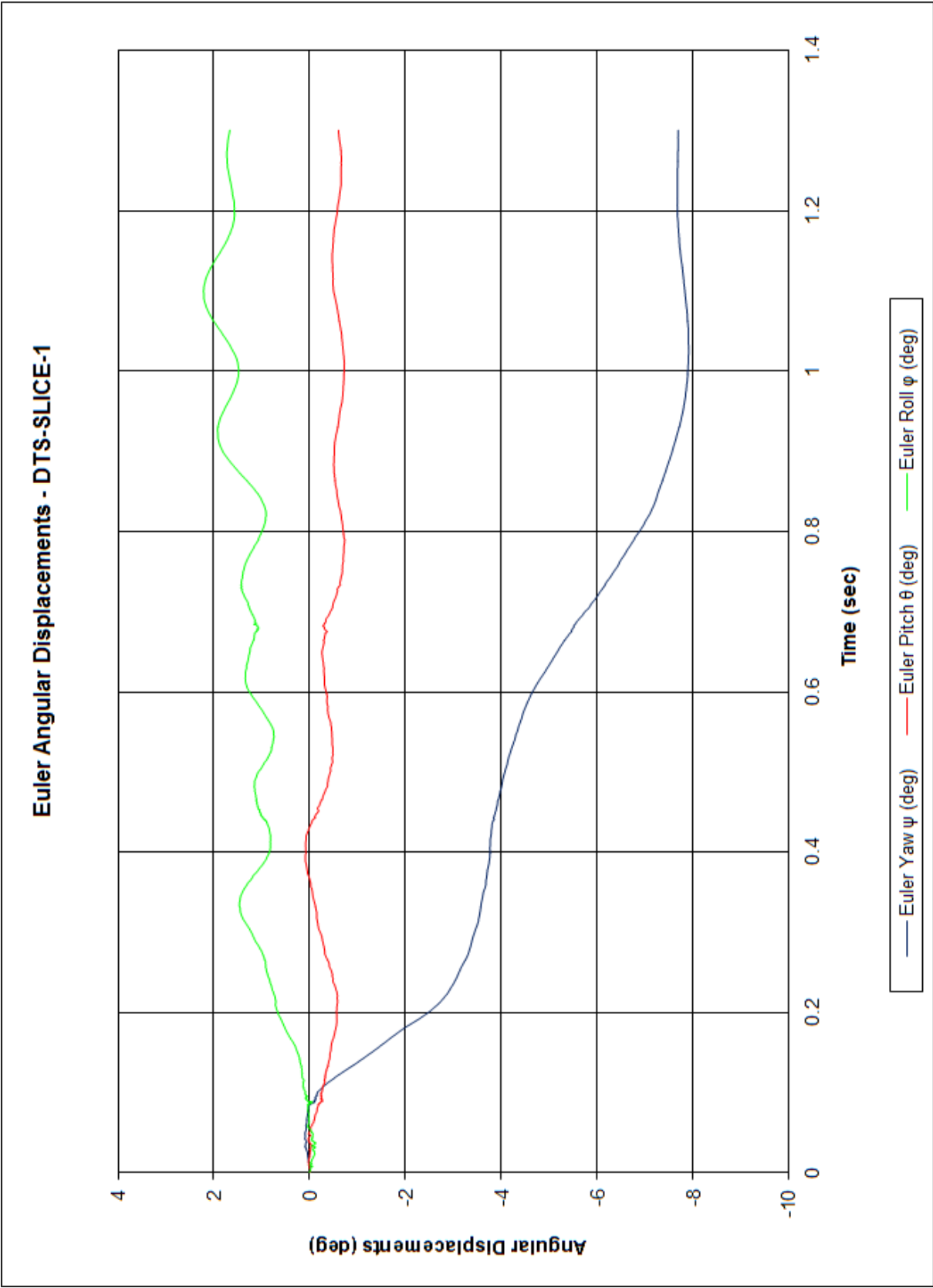


Figure D-7. Vehicle Angular Displacements (DTS-SLICE-1), Test No. IRA-3

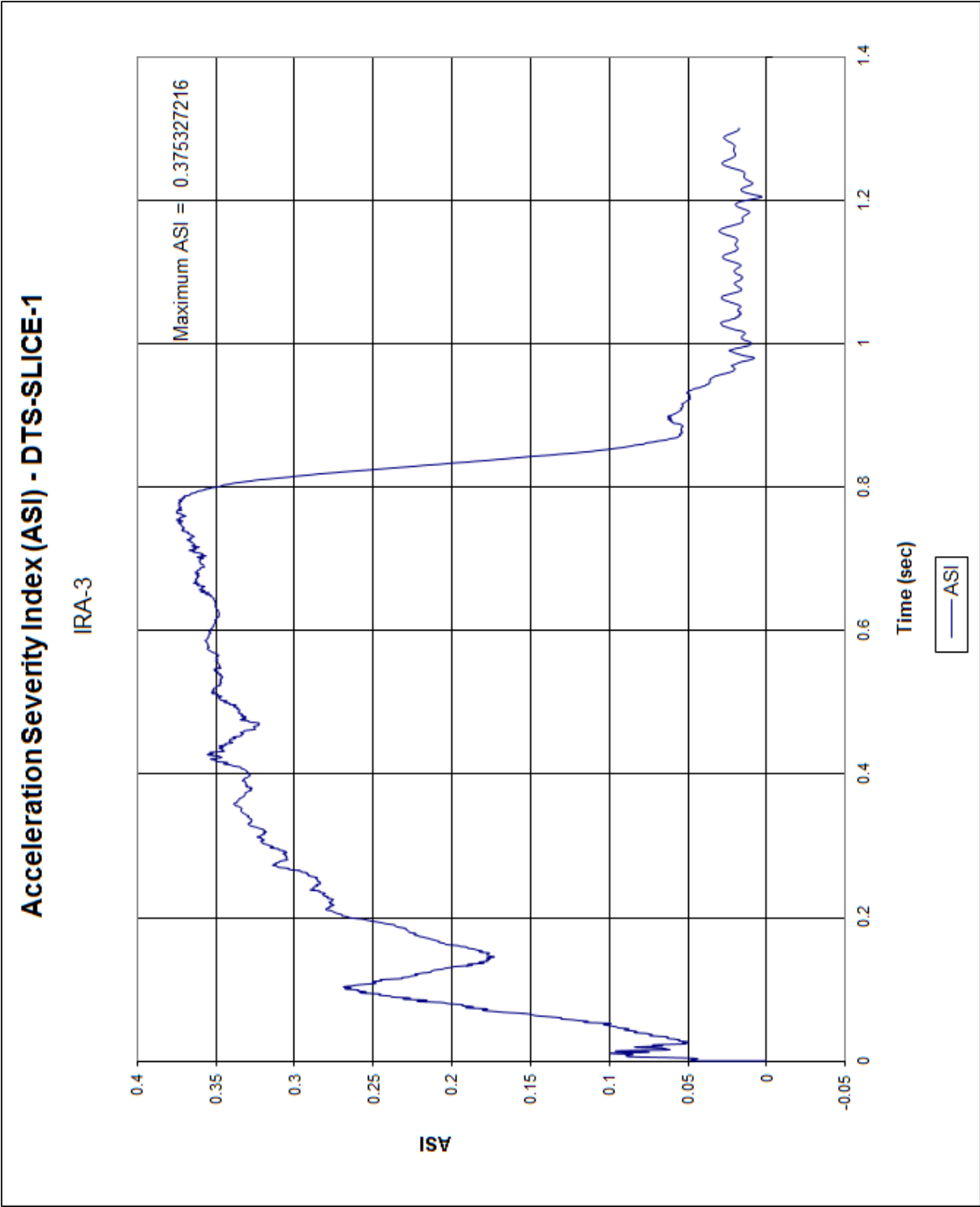


Figure D-8. Acceleration Severity Index (DTS-SLICE-1), Test No. IRA-3

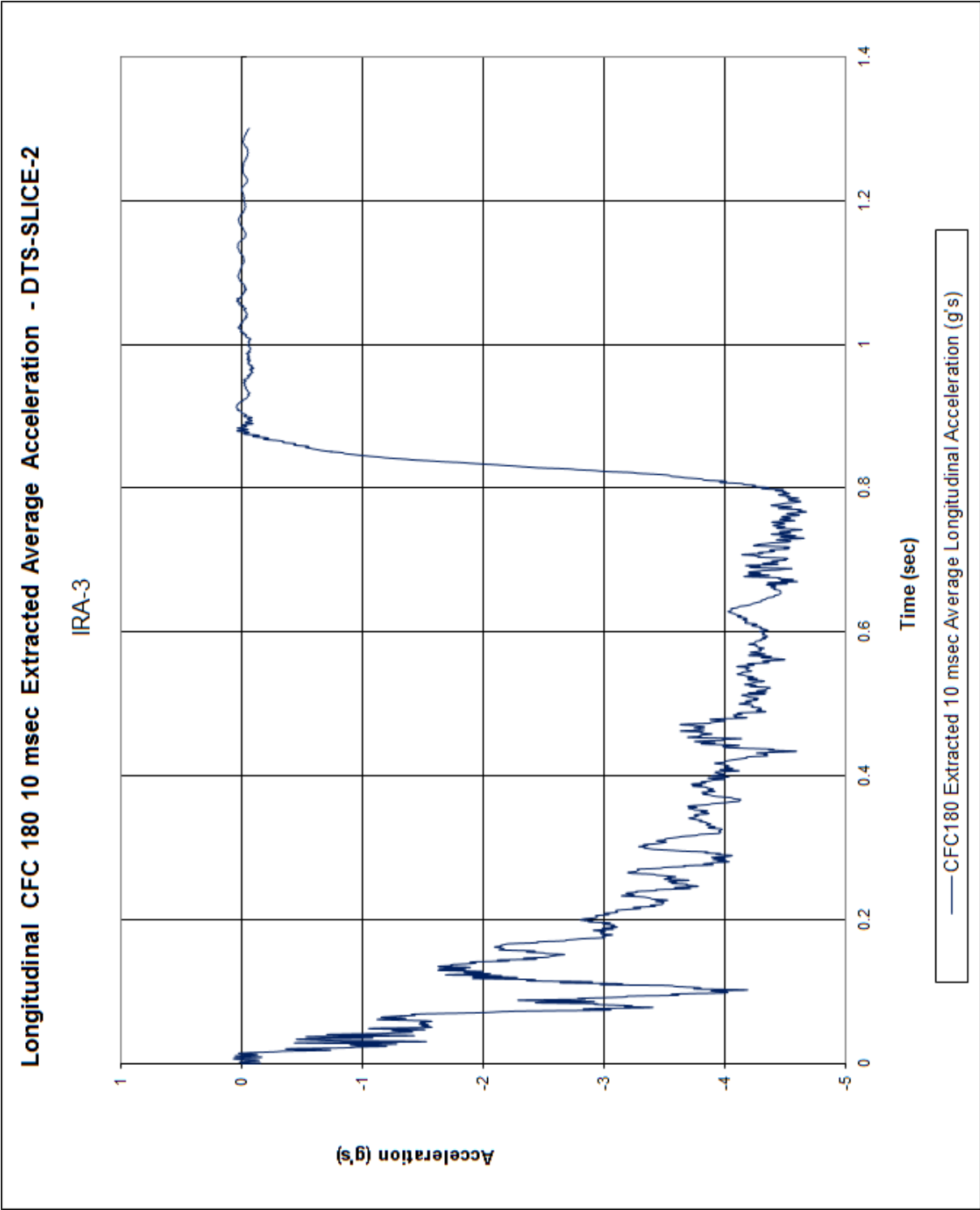


Figure D-9. 10-ms Average Longitudinal Deceleration (DTS-SLICE-2), Test No. IRA-3

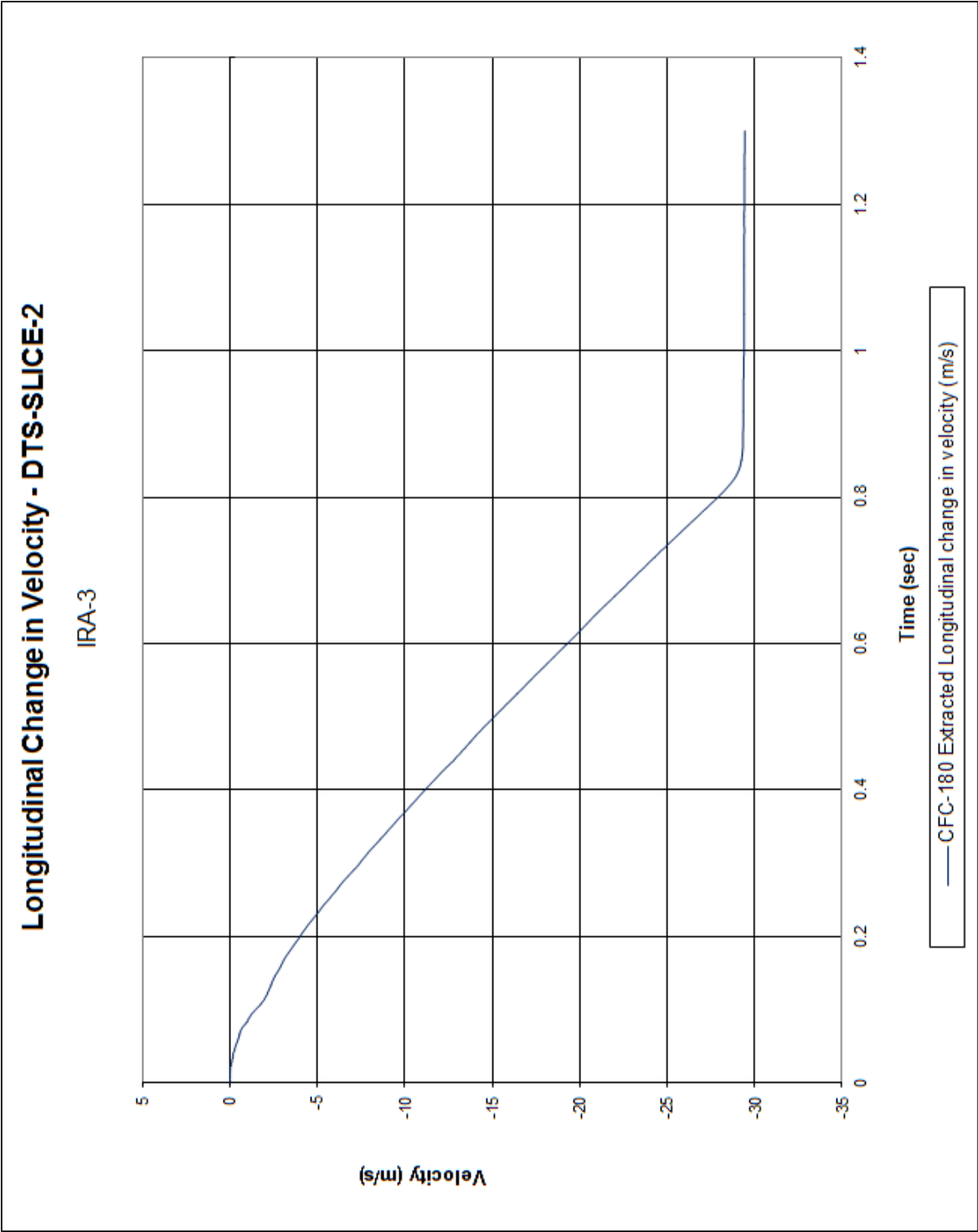


Figure D-10. Longitudinal Occupant Impact Velocity (DTS-SLICE-2), Test No. IRA-3

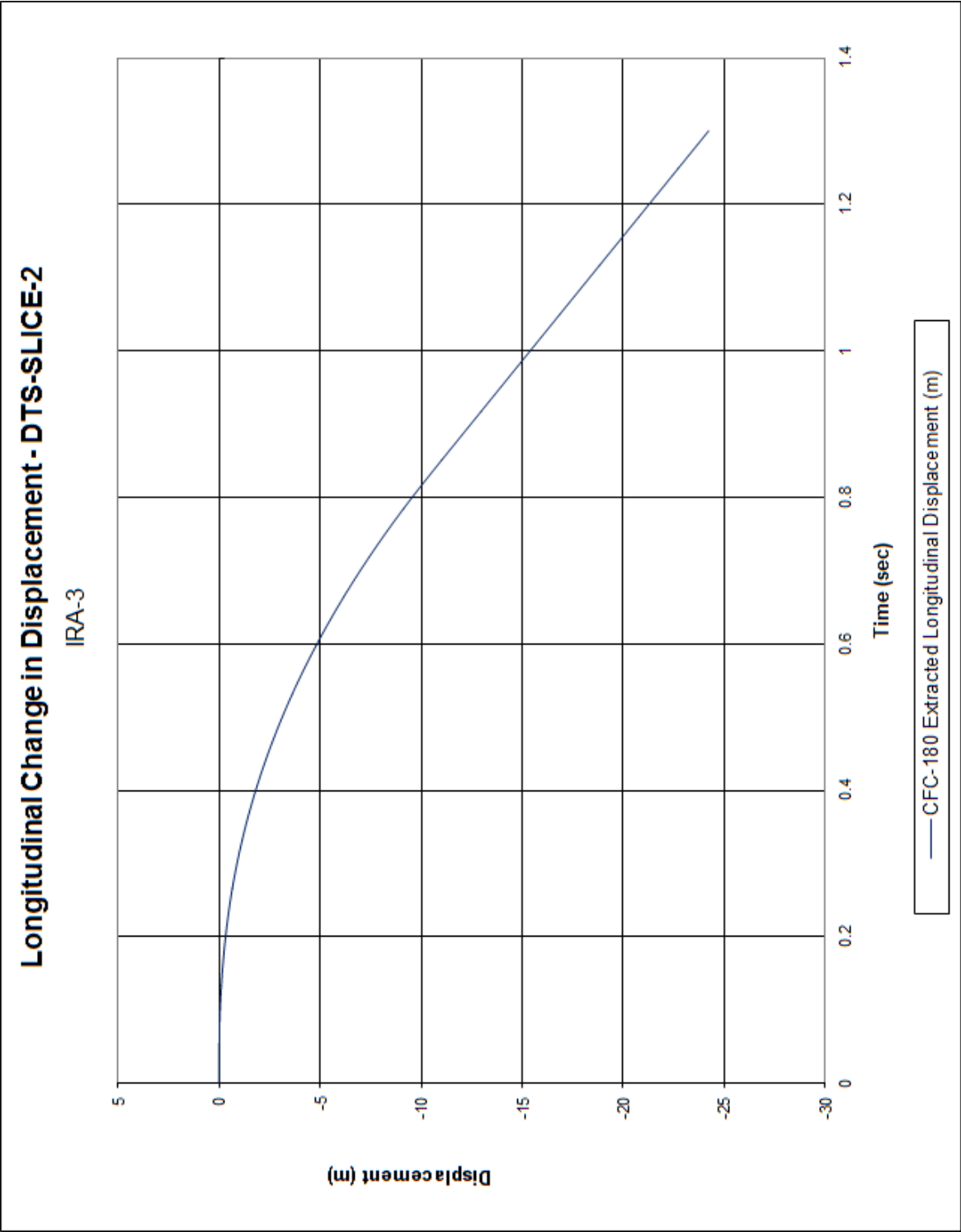


Figure D-11. Longitudinal Occupant Displacement (DTS-SLICE-2), Test No. IRA-3

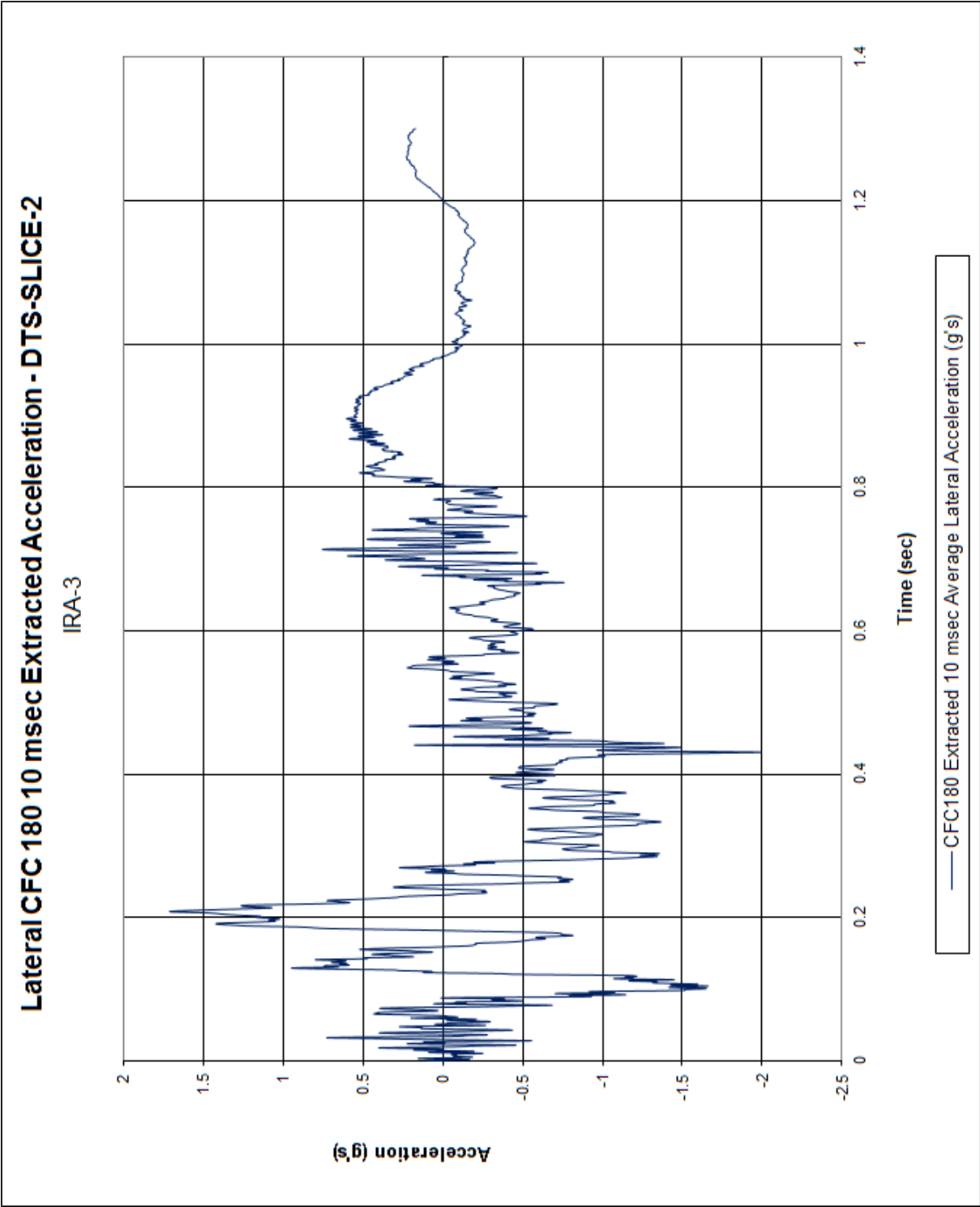


Figure D-12. 10-ms Average Lateral Deceleration (DTS-SLICE-2), Test No. IRA-3

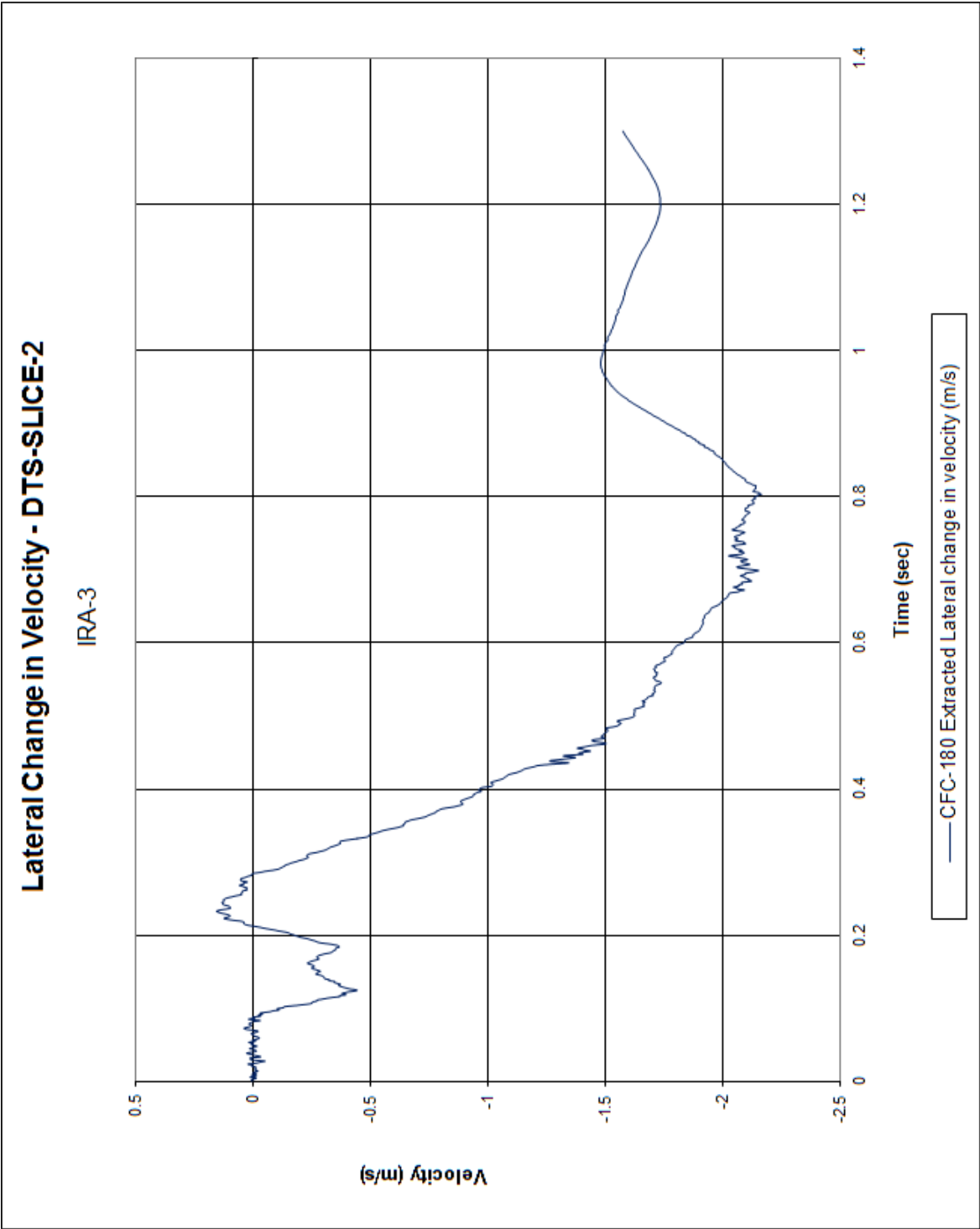


Figure D-13. Lateral Occupant Impact Velocity (DTS-SLICE-2), Test No. IRA-3

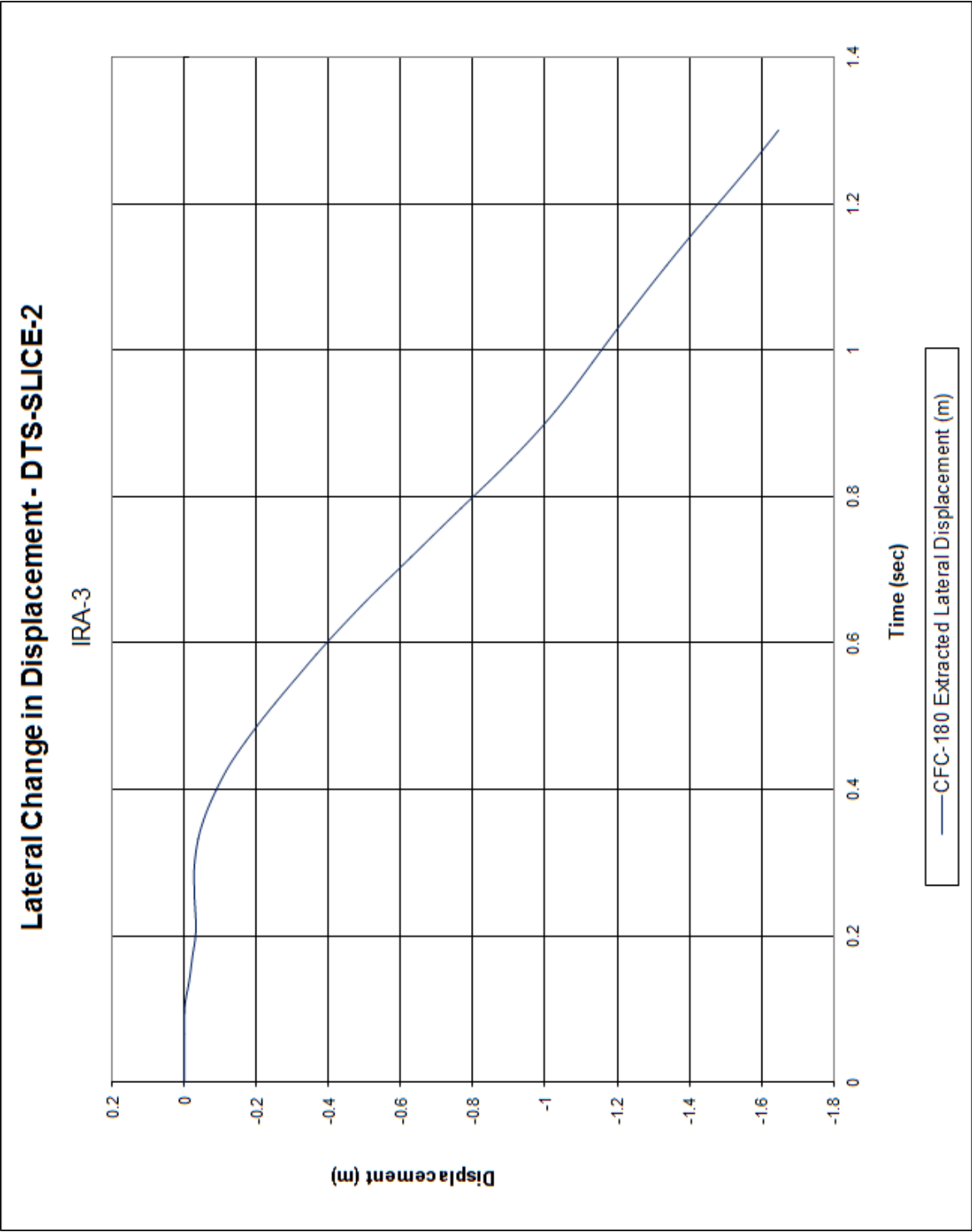


Figure D-14. Lateral Occupant Displacement (DTS-SLICE-2), Test No. IRA-3

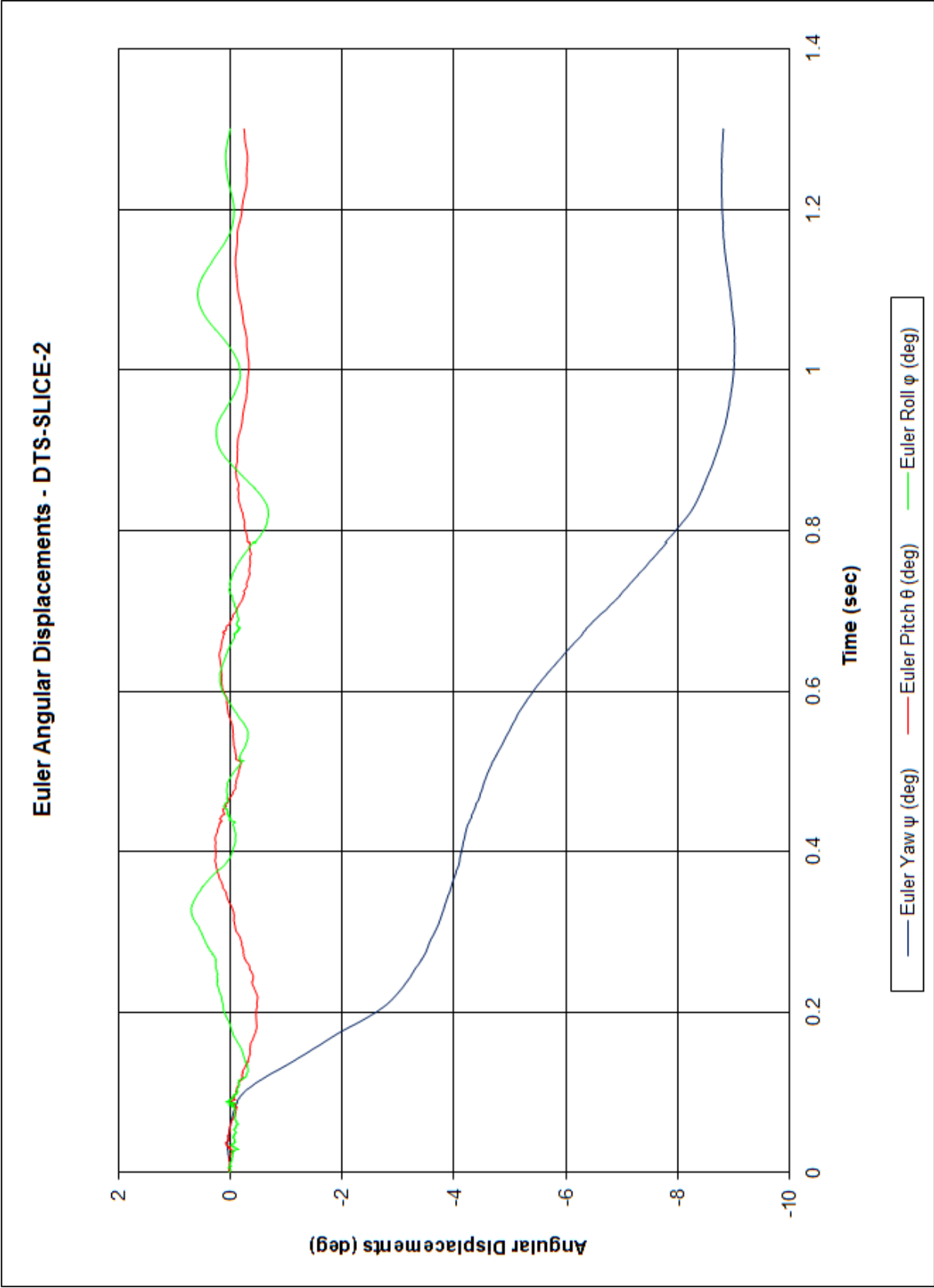


Figure D-15. Vehicle Angular Displacements (DTS-SLICE-2), Test No. IRA-3

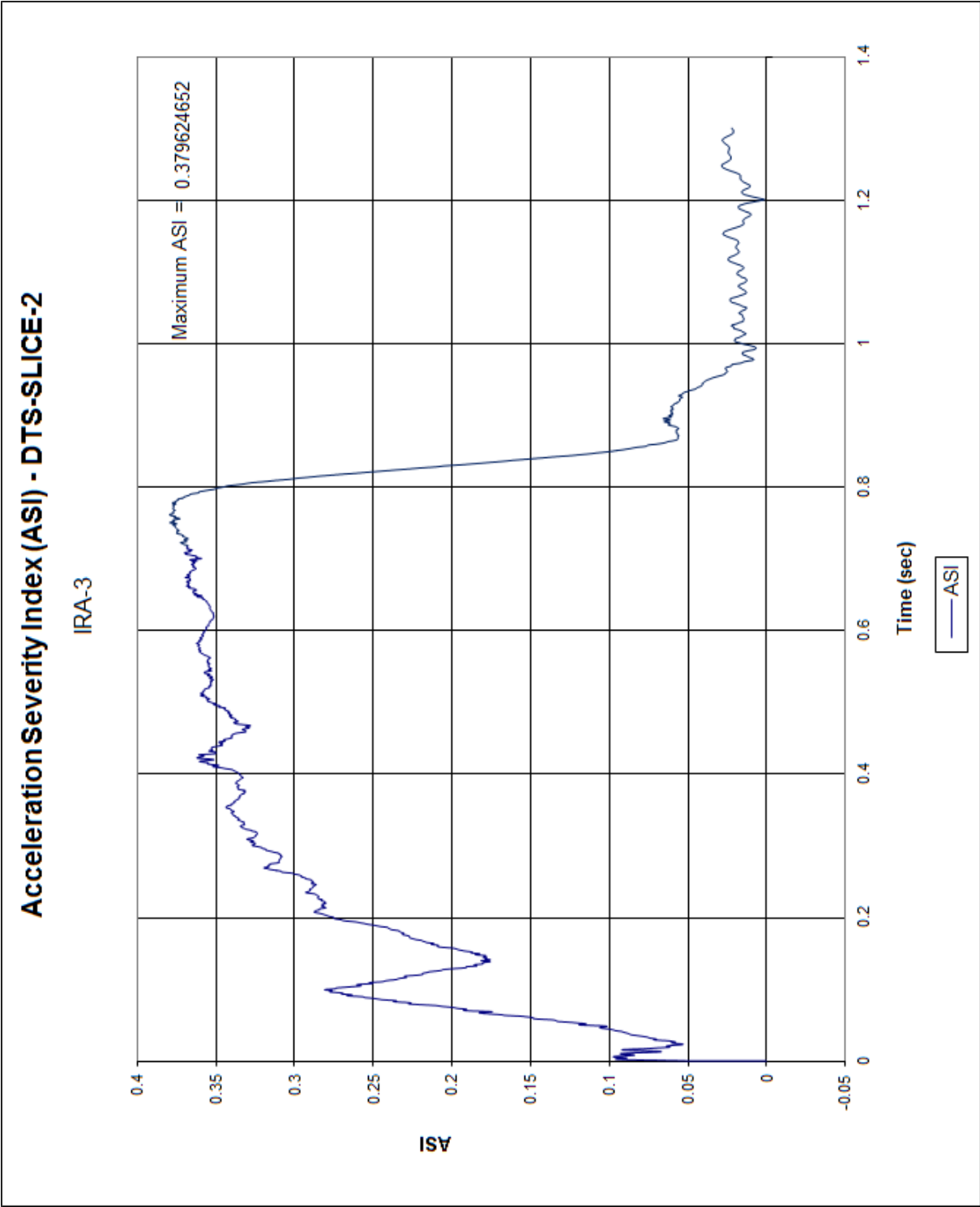


Figure D-16. Acceleration Severity Index (DTS-SLICE-2), Test No. IRA-3

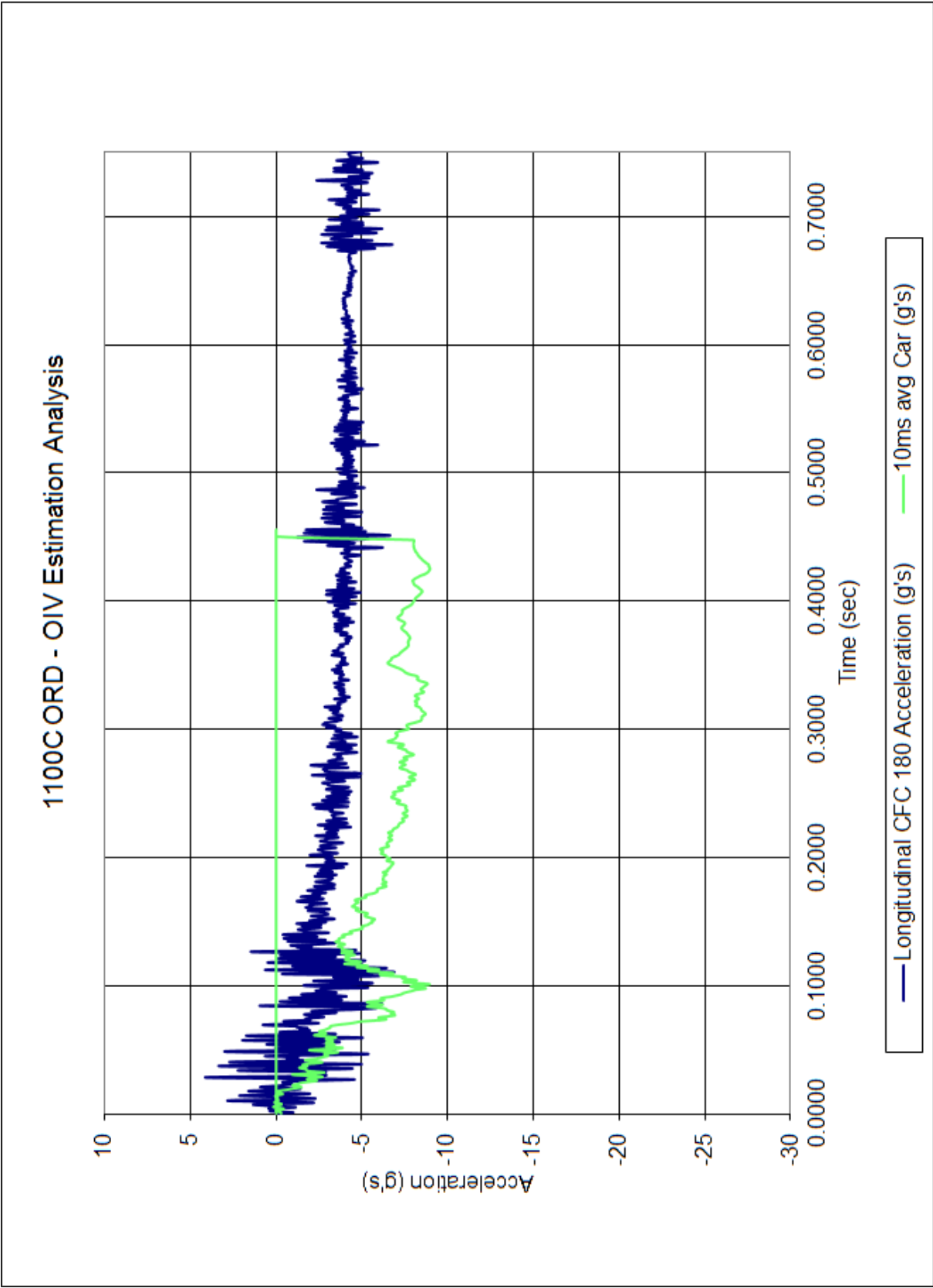


Figure D-17. 1100C ORD-OIV Estimation, Test No. IRA-3

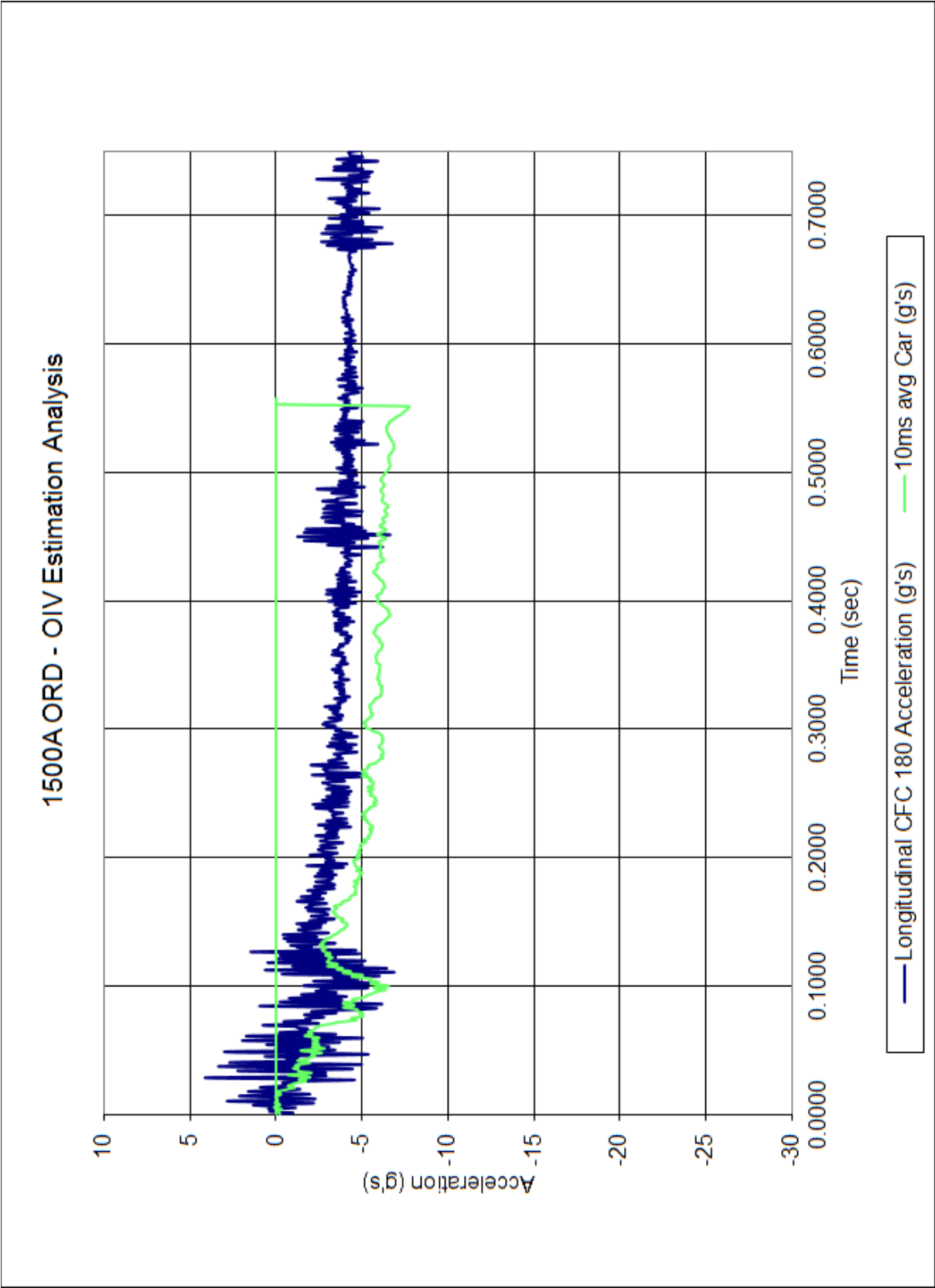


Figure D-18. 1500A ORD-OIV Estimation, Test No. IRA-3

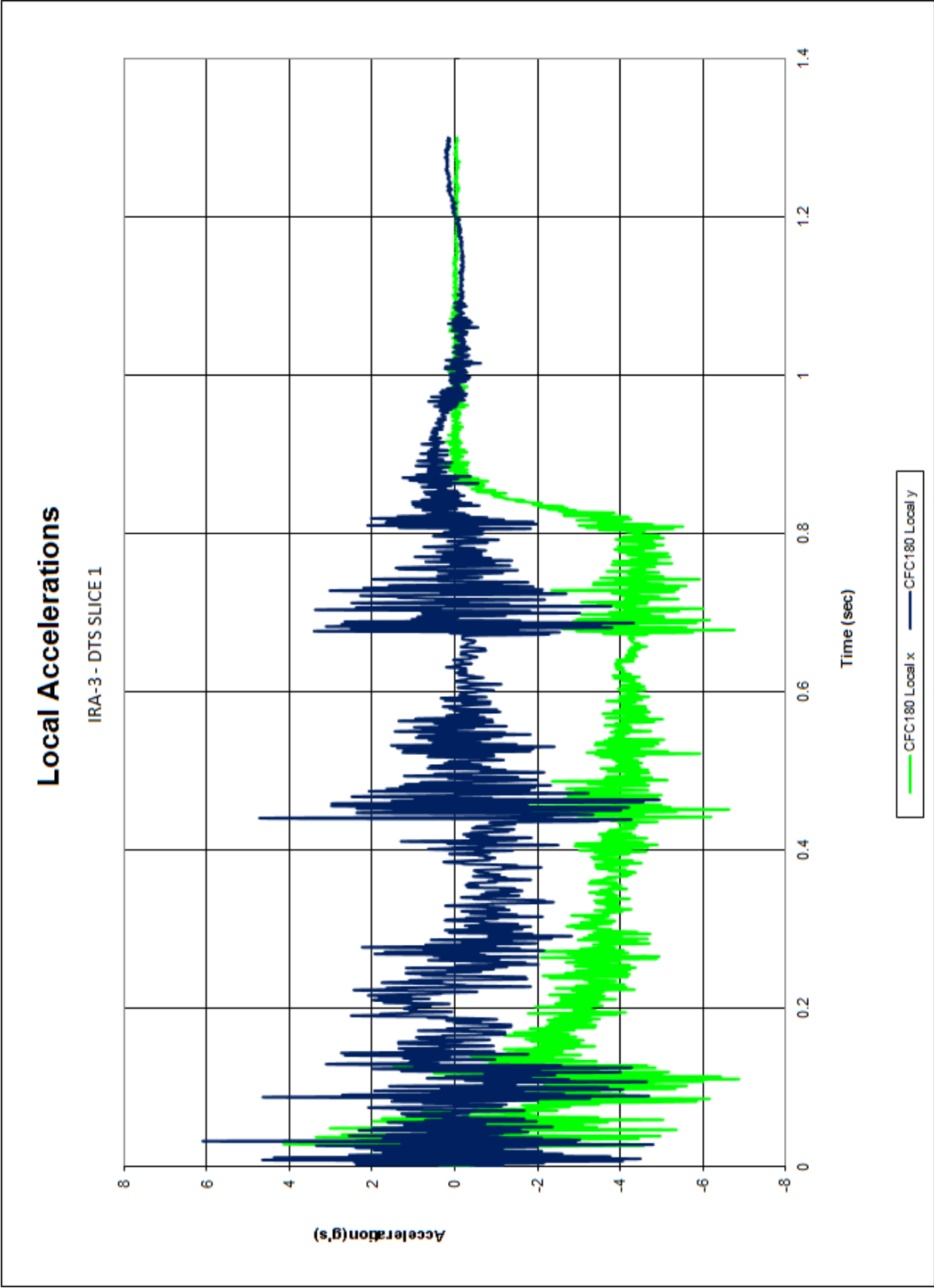


Figure D-19. Local Accelerations (DTS-SLICE-1), Test No. IRA-3

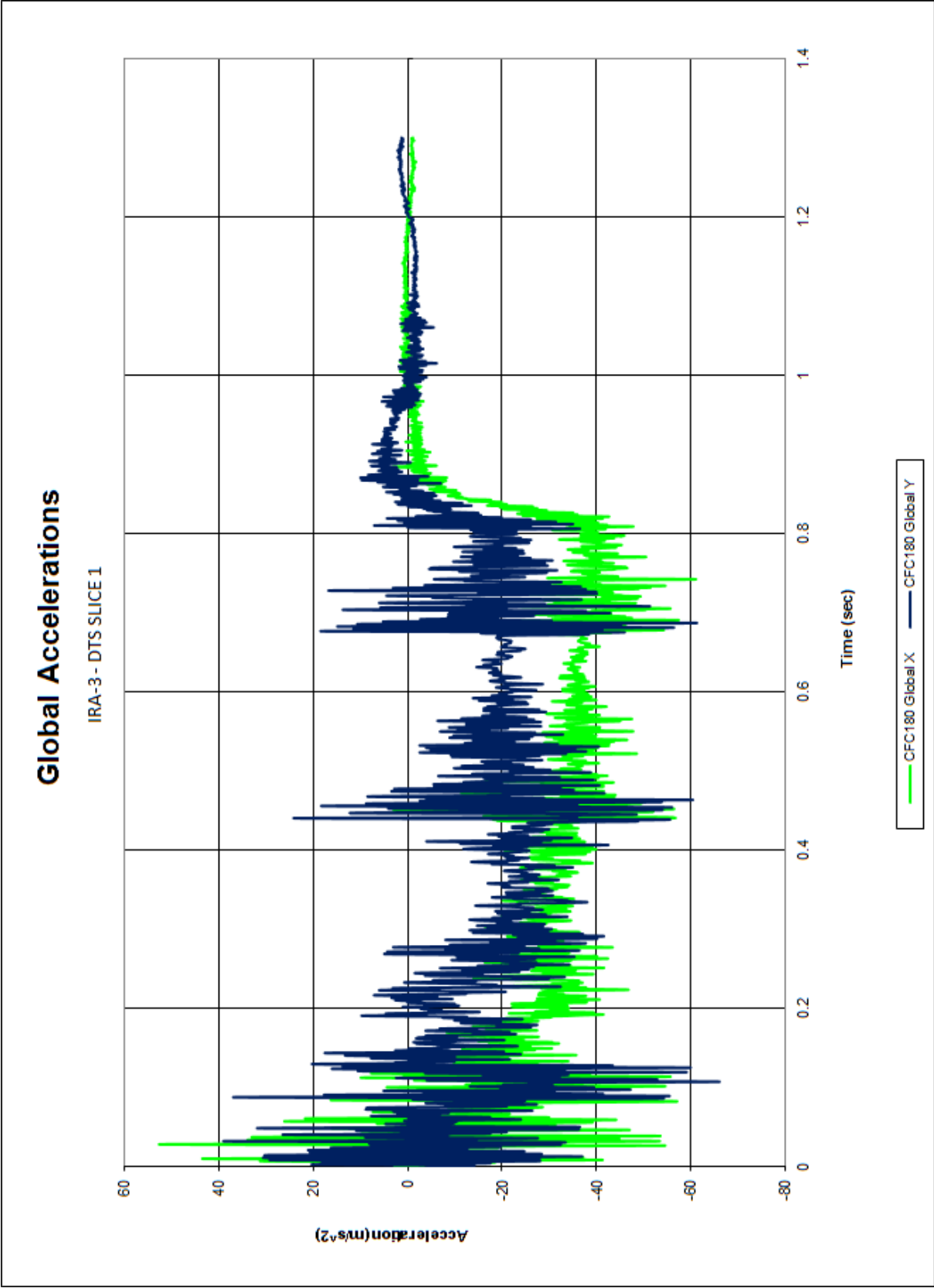


Figure D-20. Global Accelerations (DTS-SLICE-1), Test No. IRA-3

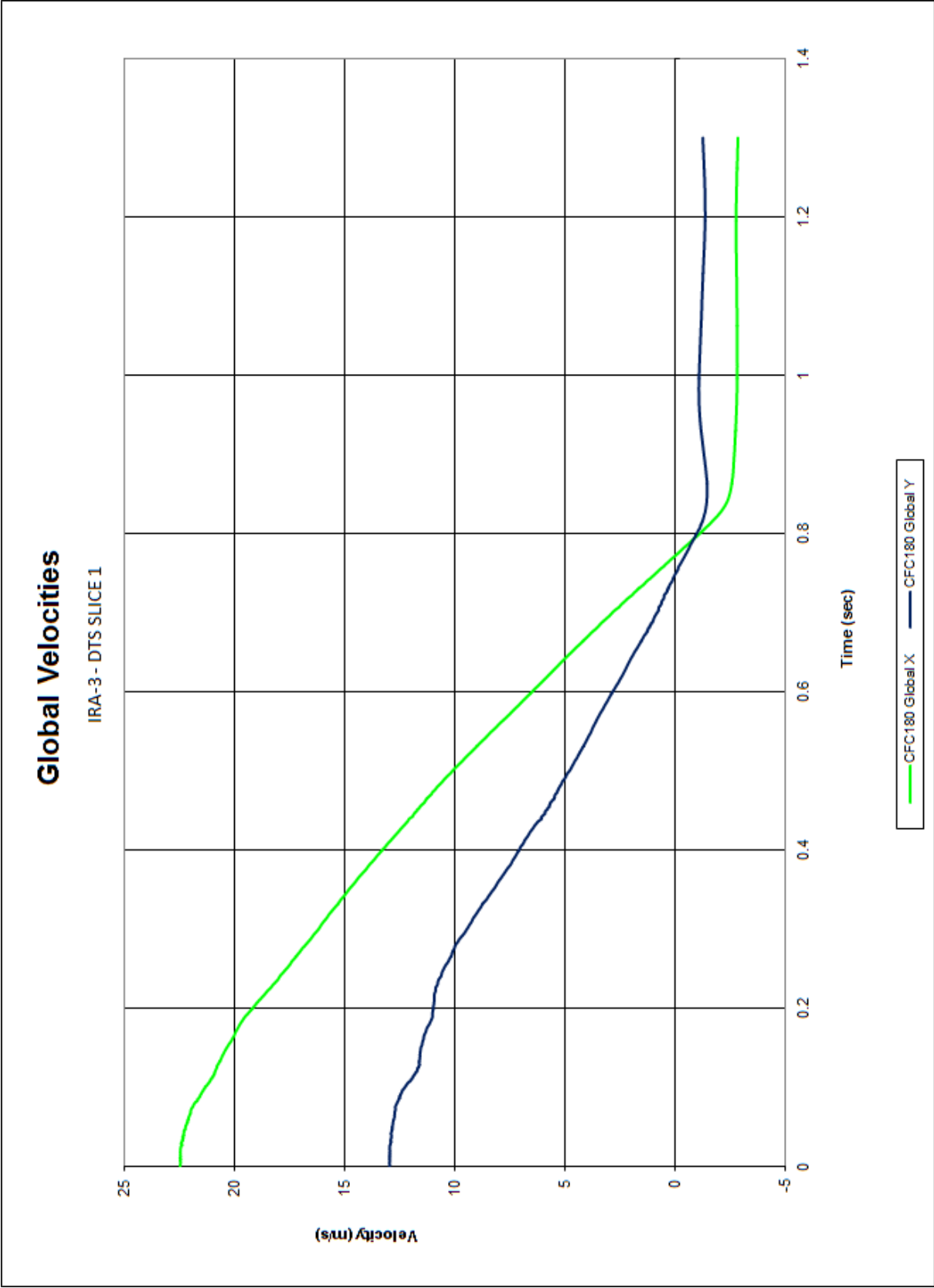


Figure D-21. Global Velocities (DTS-SLICE-1), Test No. IRA-3

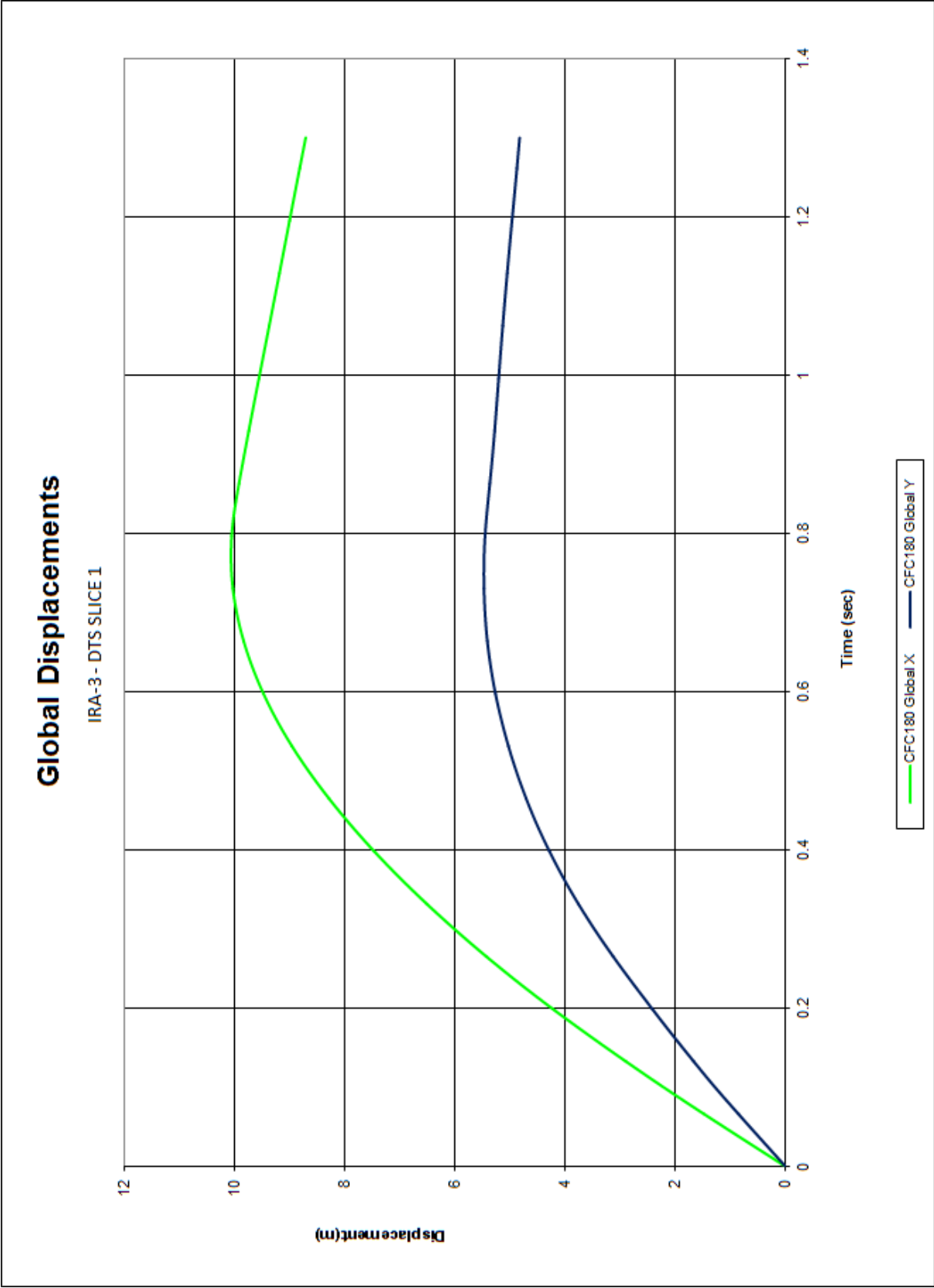


Figure D-22. Global Displacements (DTS-SLICE-1), Test No. IRA-3

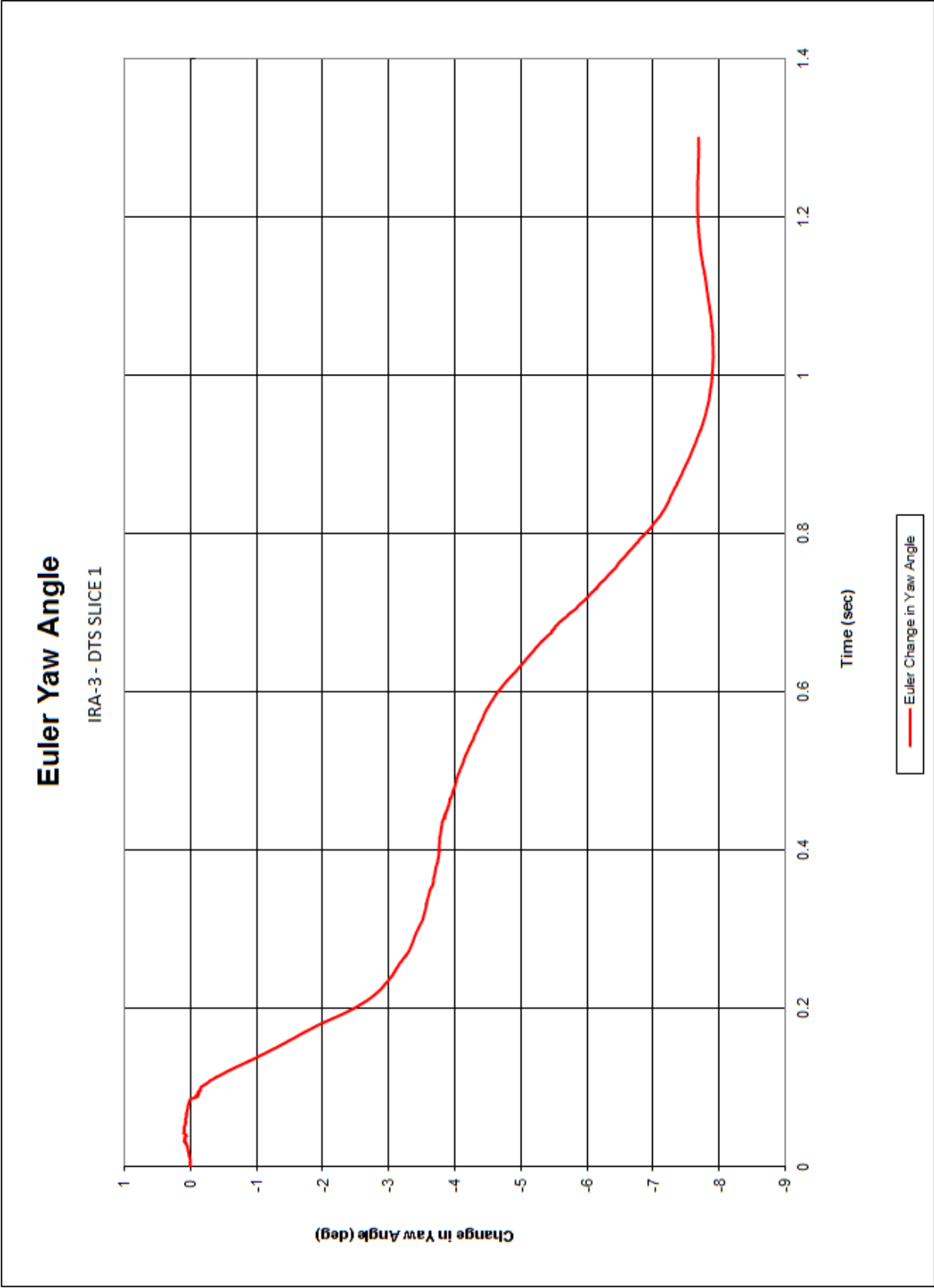


Figure D-23. Euler Yaw Angle (DTS-SLICE-1), Test No. IRA-3

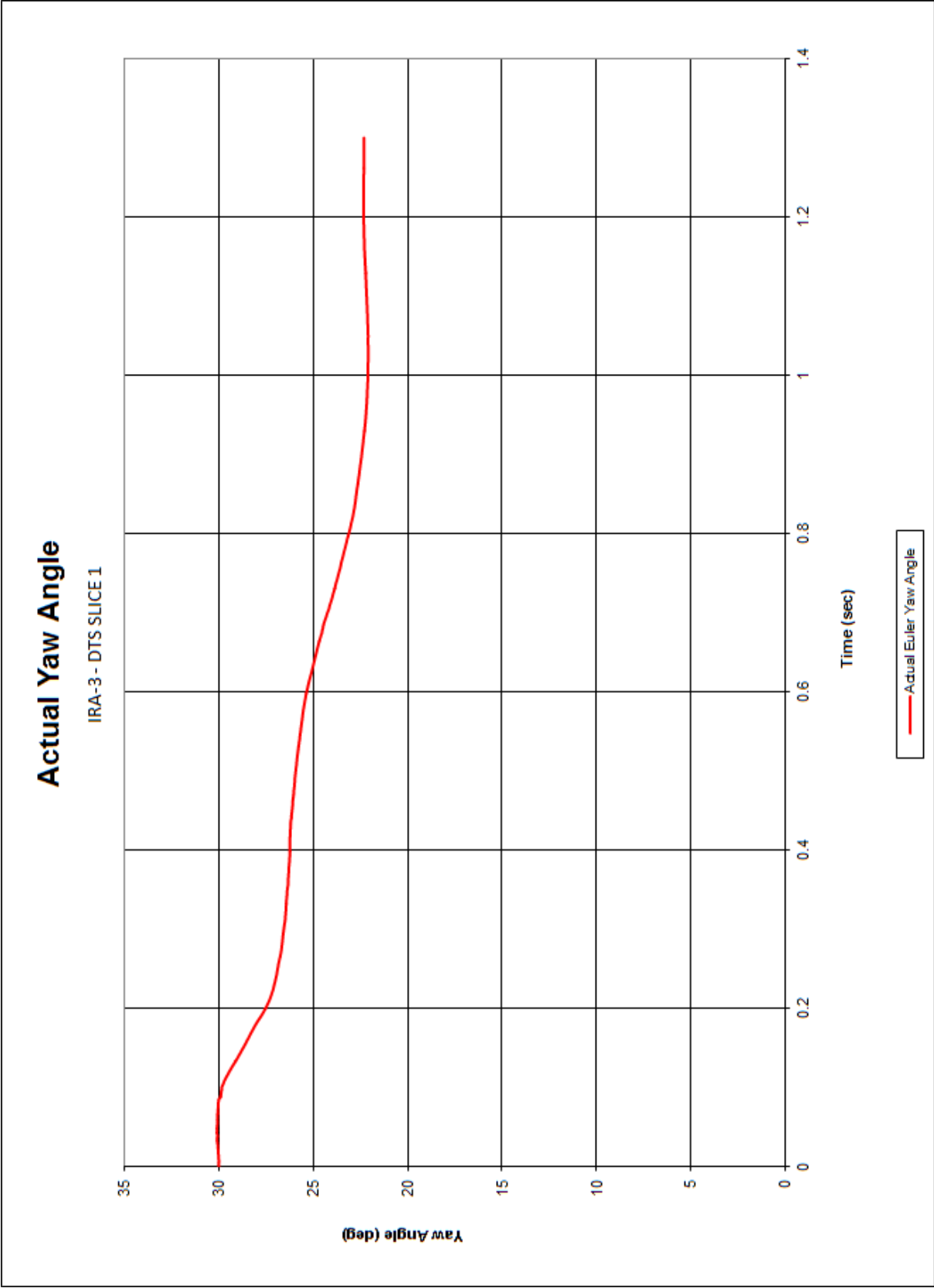


Figure D-24. Actual Yaw Angle (DTS-SLICE-1), Test No. IRA-3

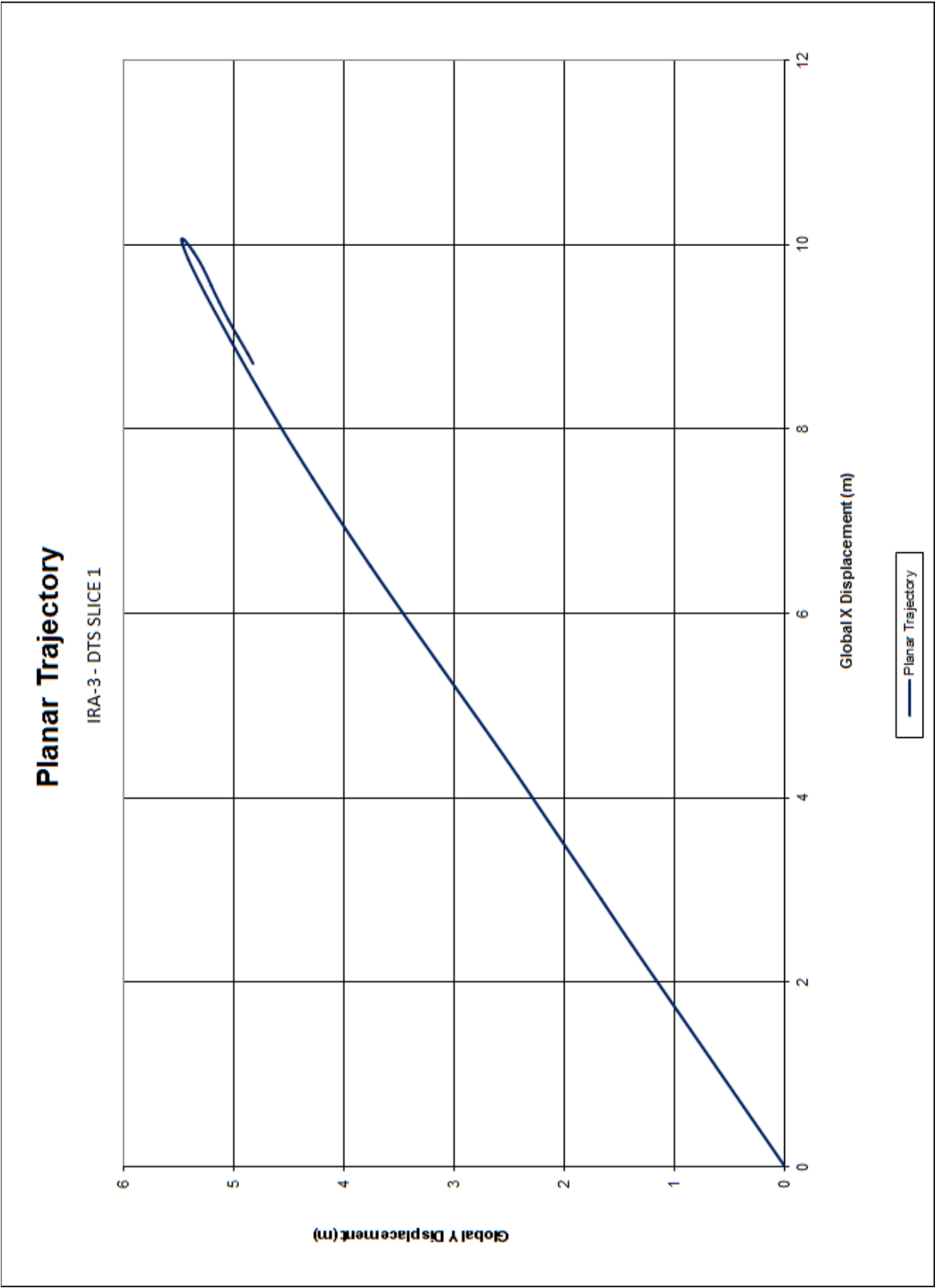


Figure D-25. Planar Trajectory (DTS-SLICE-1), Test No. IRA-3

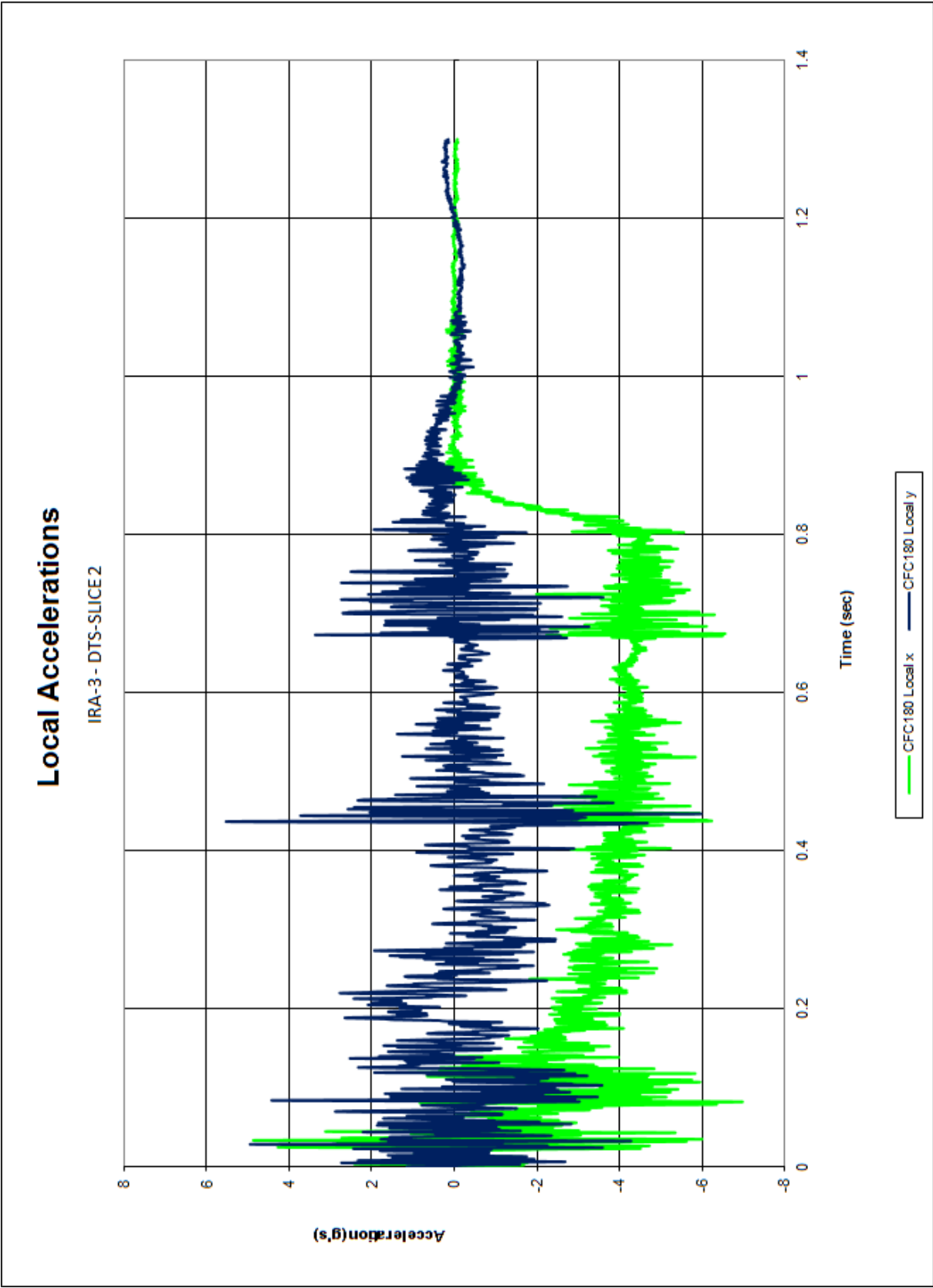


Figure D-26. Local Accelerations (DTS-SLICE-2), Test No. IRA-3

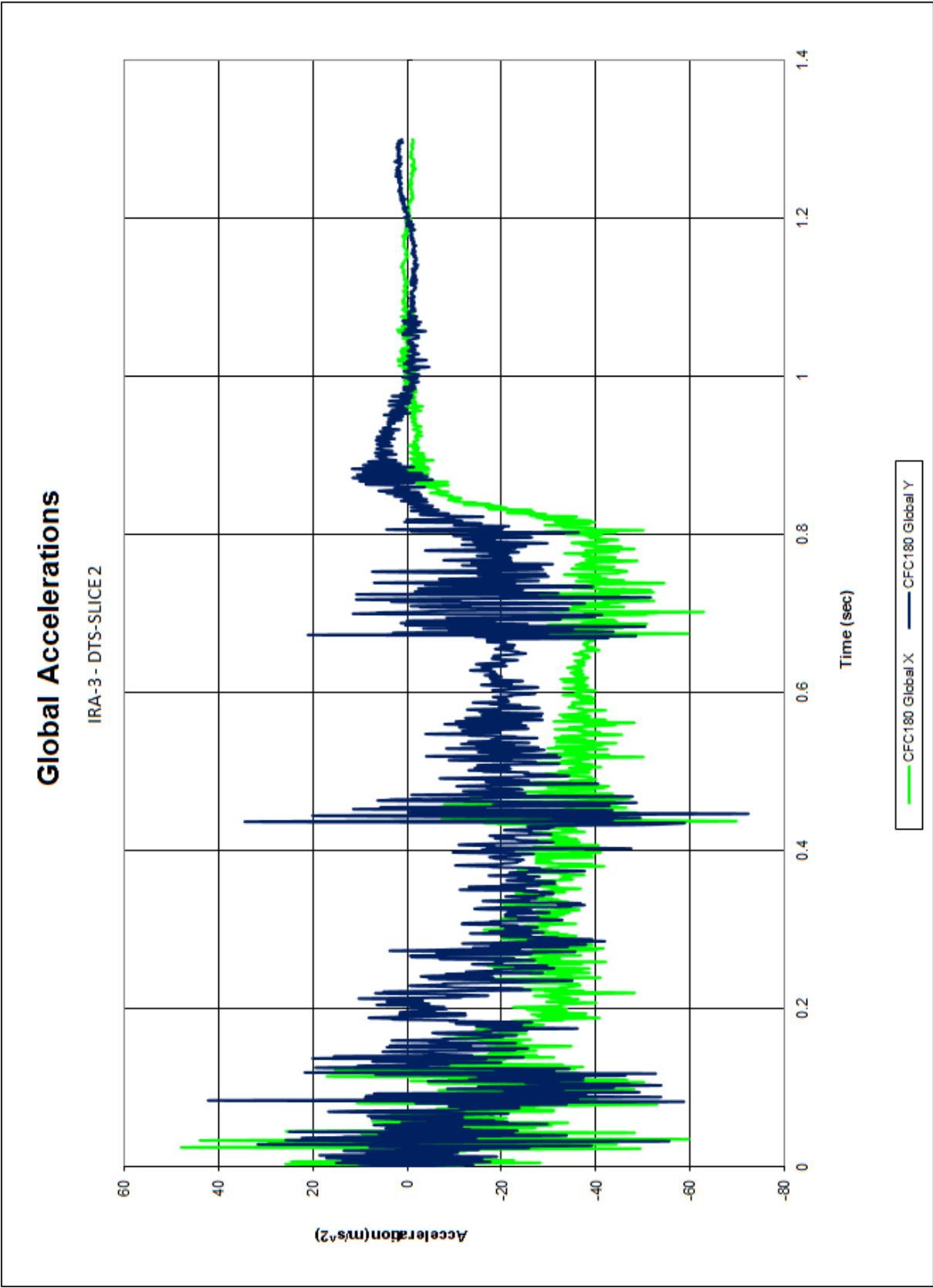


Figure D-27. Global Accelerations (DTS-SLICE-2), Test No. IRA-3

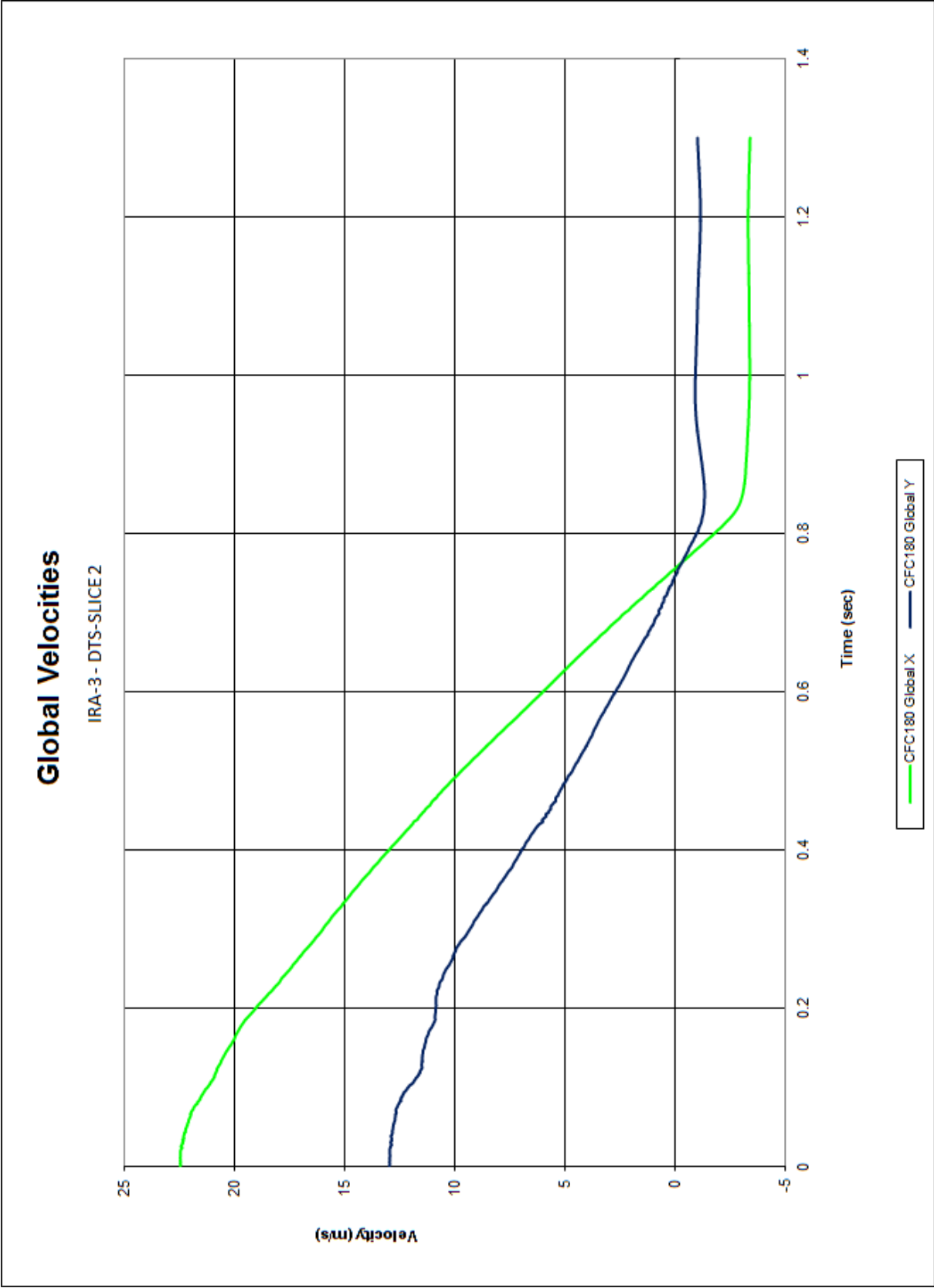


Figure D-28. Global Velocities (DTS-SLICE-2), Test No. IRA-3

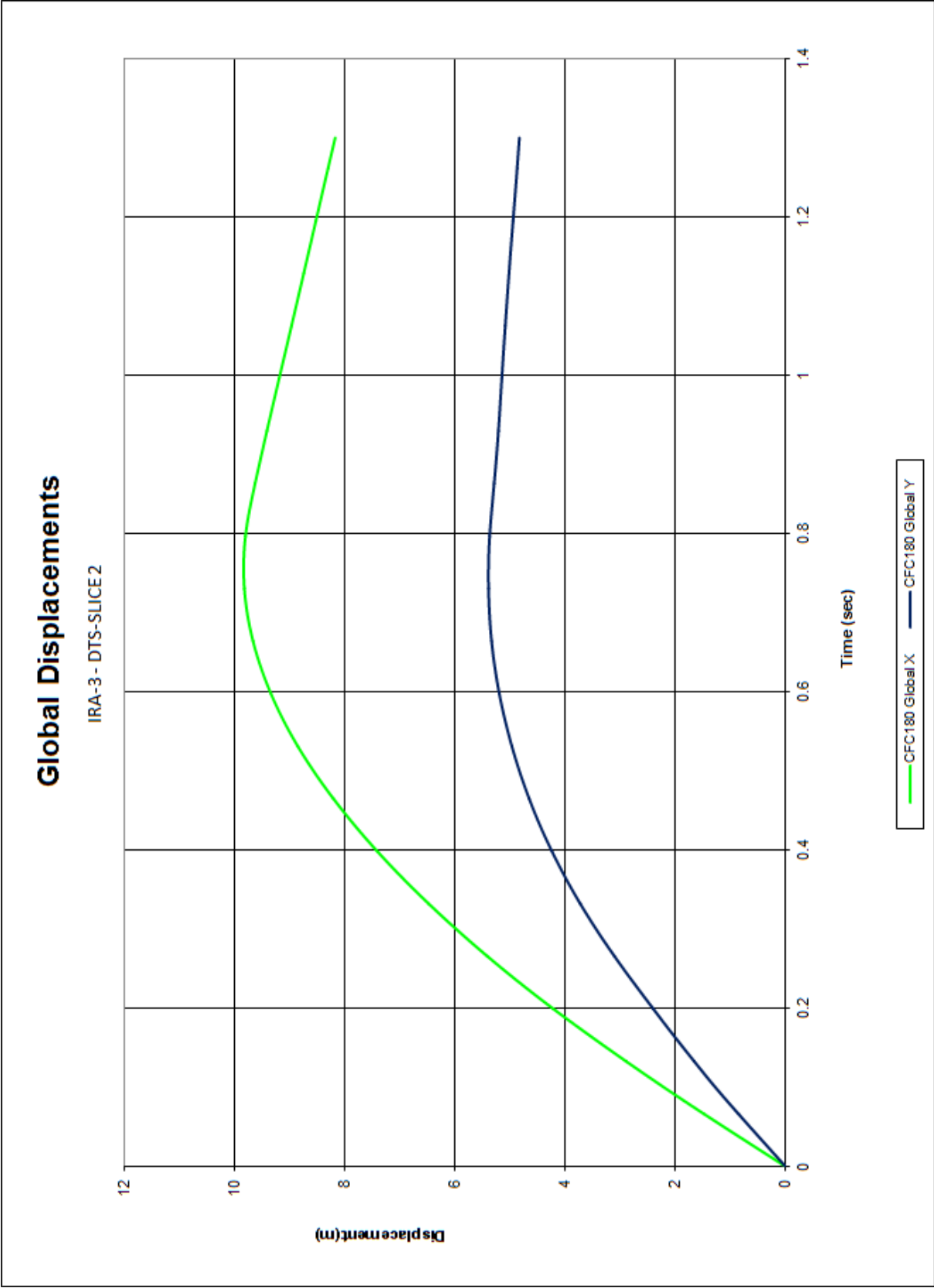


Figure D-29. Global Displacements (DTS-SLICE-2), Test No. IRA-3

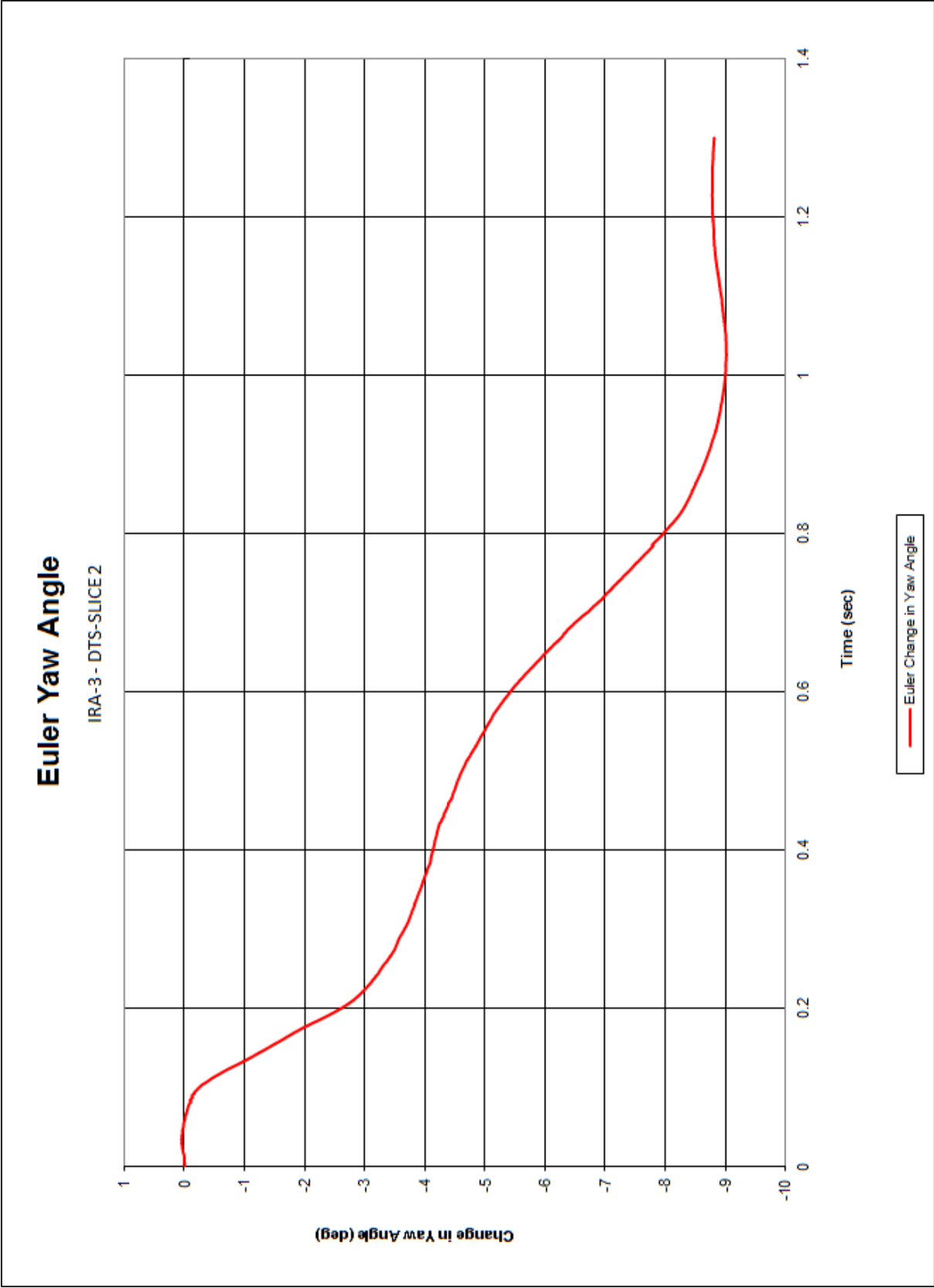


Figure D-30. Euler Yaw Angle (DTS-SLICE-2), Test No. IRA-3

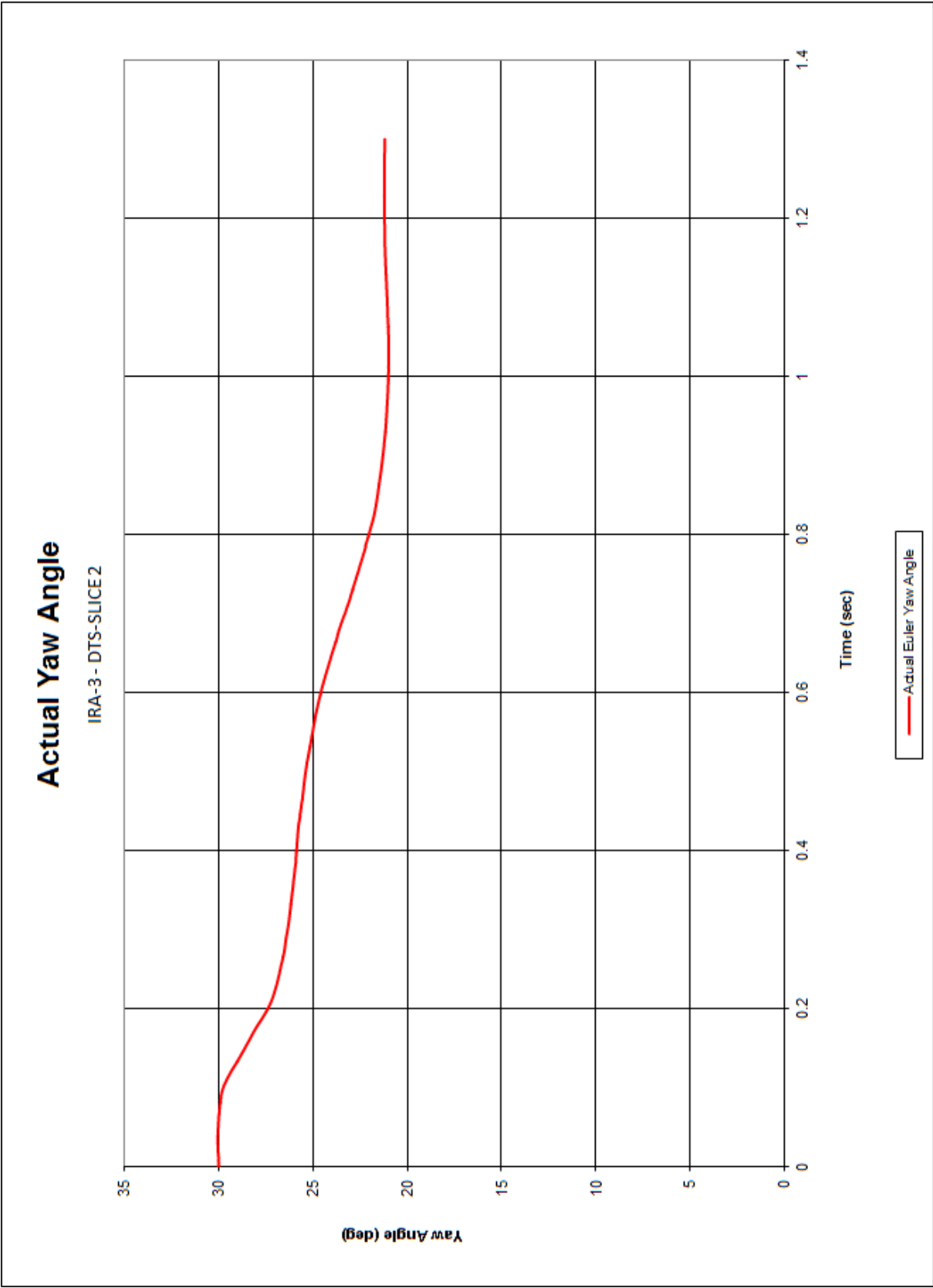


Figure D-31. Actual Yaw Angle (DTS-SLICE-2), Test No. IRA-3

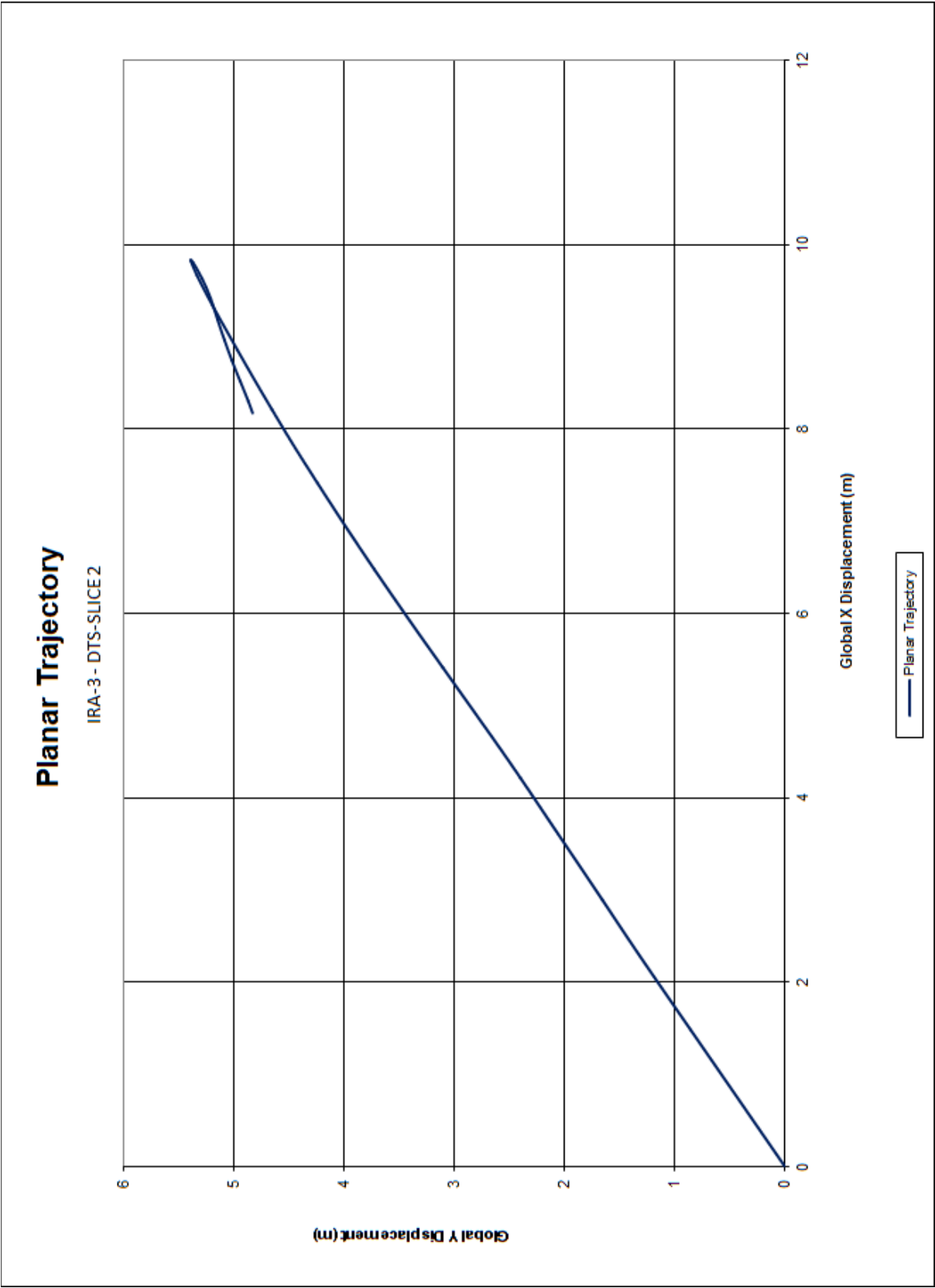


Figure D-32. Planar Trajectory (DTS-SLICE-2), Test No. IRA-3

Appendix E. Accelerometer and Rate Transducer Data Plots, Test No. IRA-4

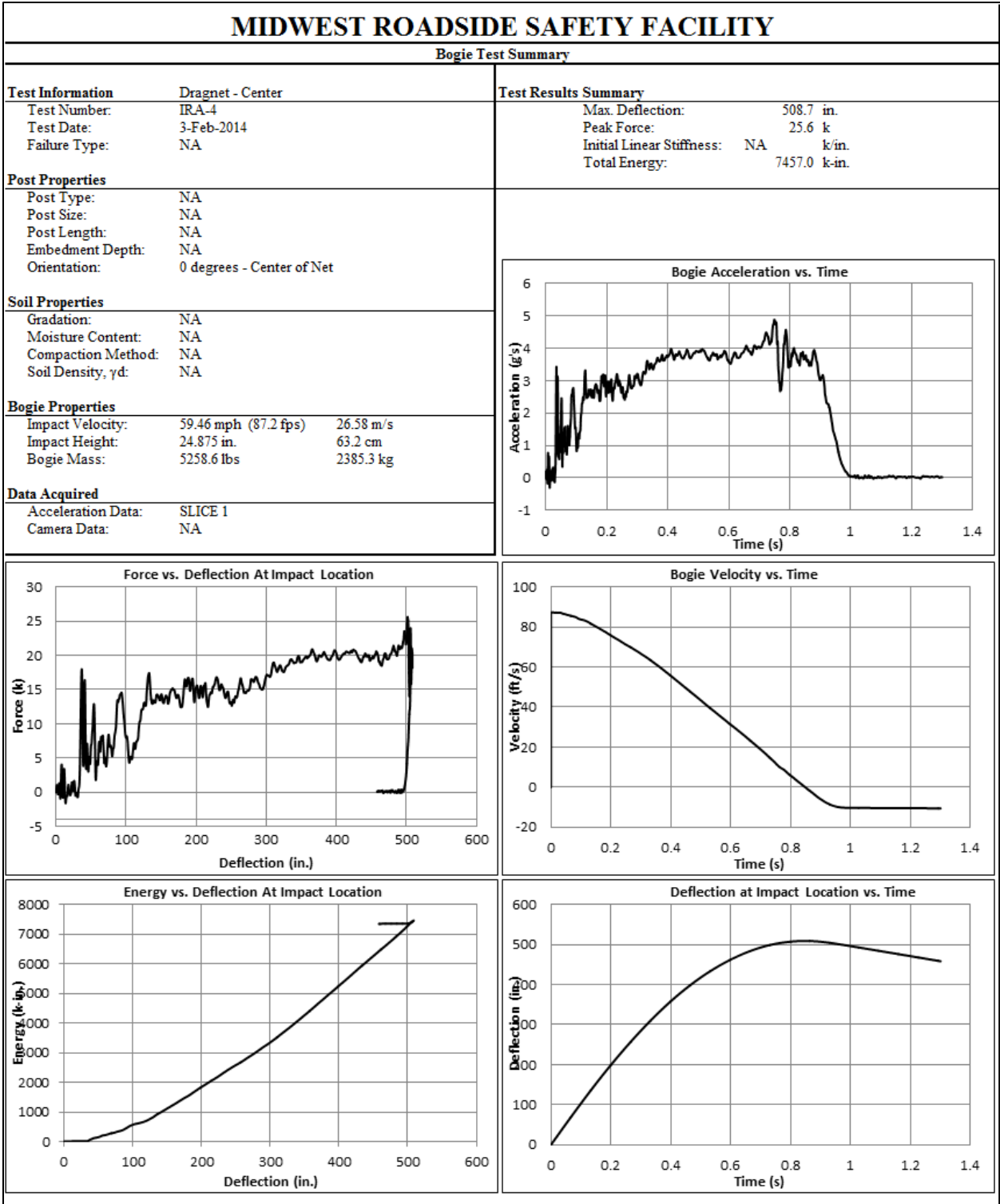


Figure E-1. Test No. IRA-4 Results (DTS-SLICE-1) [English Units]

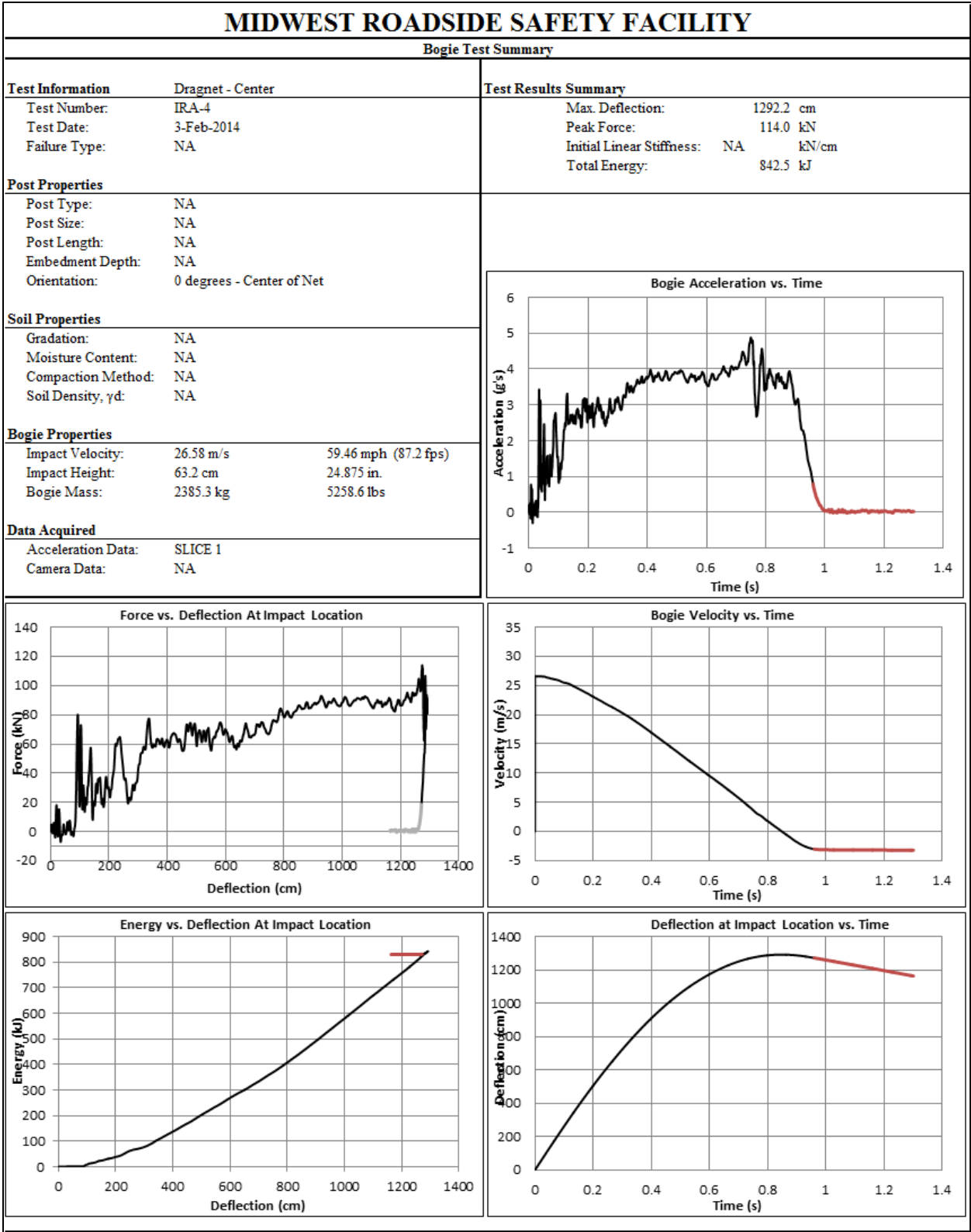


Figure E-2. Test No. IRA-4 Results (DTS-SLICE-1) [Metric Units]

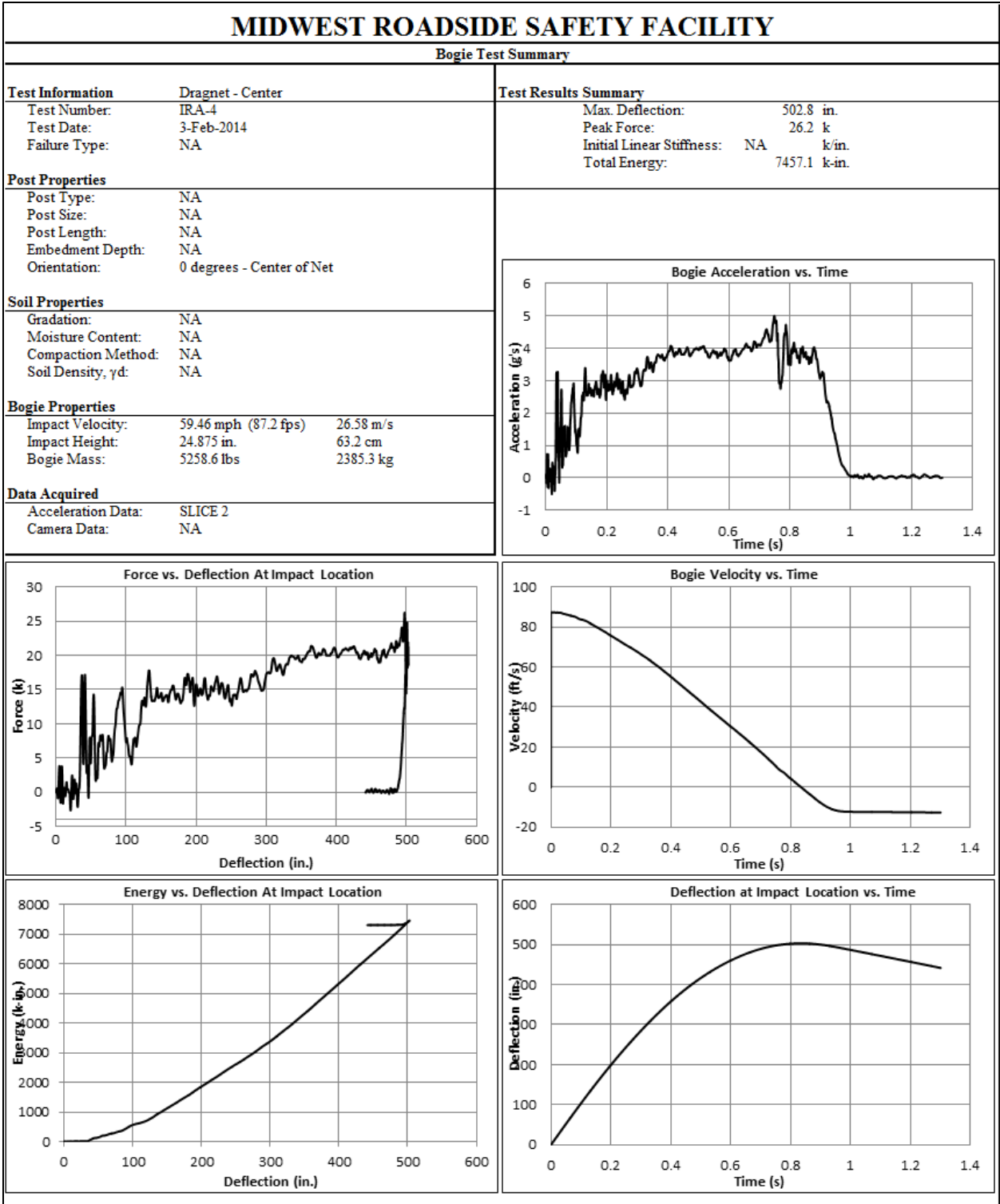


Figure E-3. Test No. IRA-4 Results (DTS-SLICE-2) [English Units]

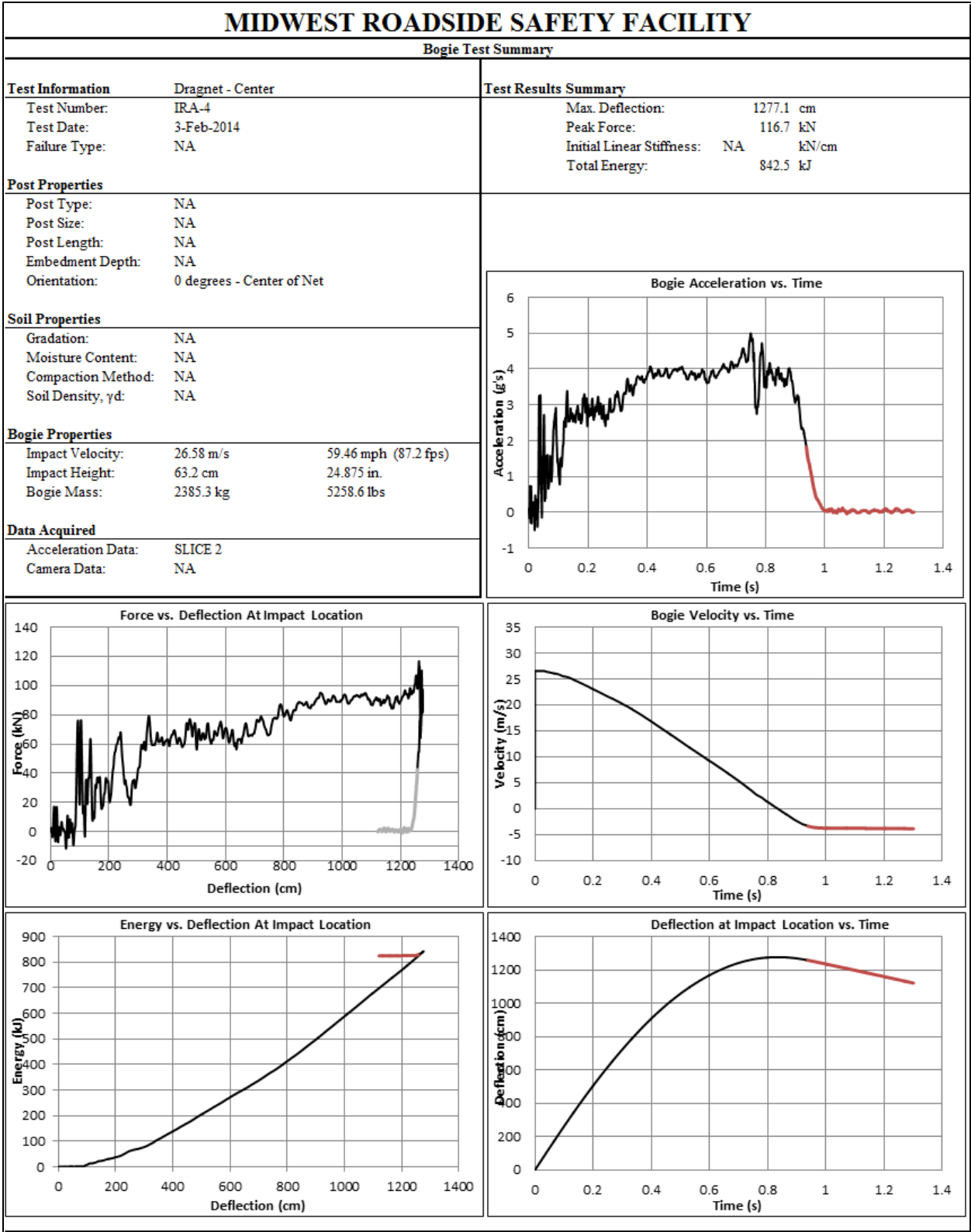


Figure E-4. Test No. IRA-4 Results (DTS-SLICE-2) [Metric Units]

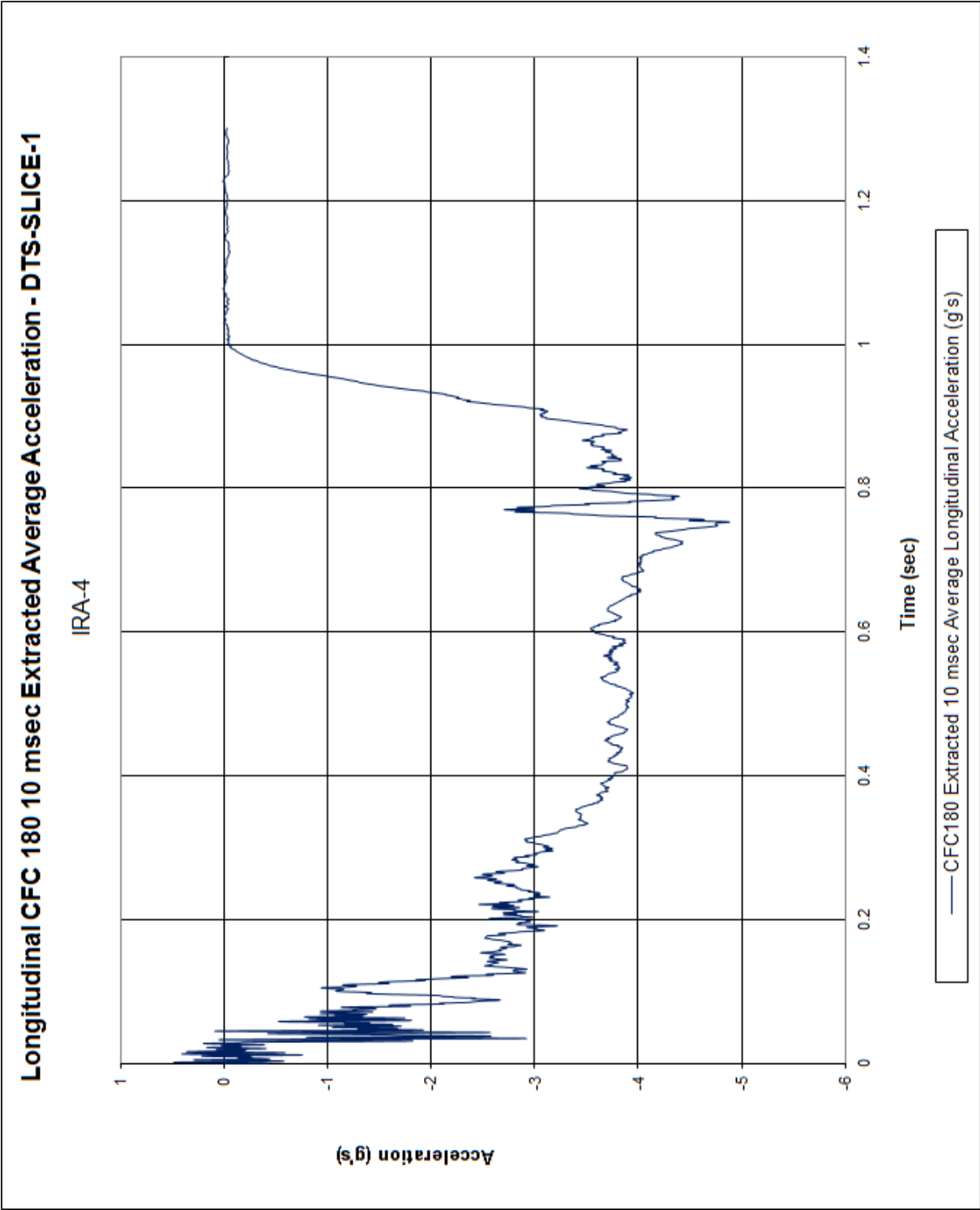


Figure E-5. 10-ms Average Longitudinal Deceleration (DTS-SLICE-1), Test No. IRA-4

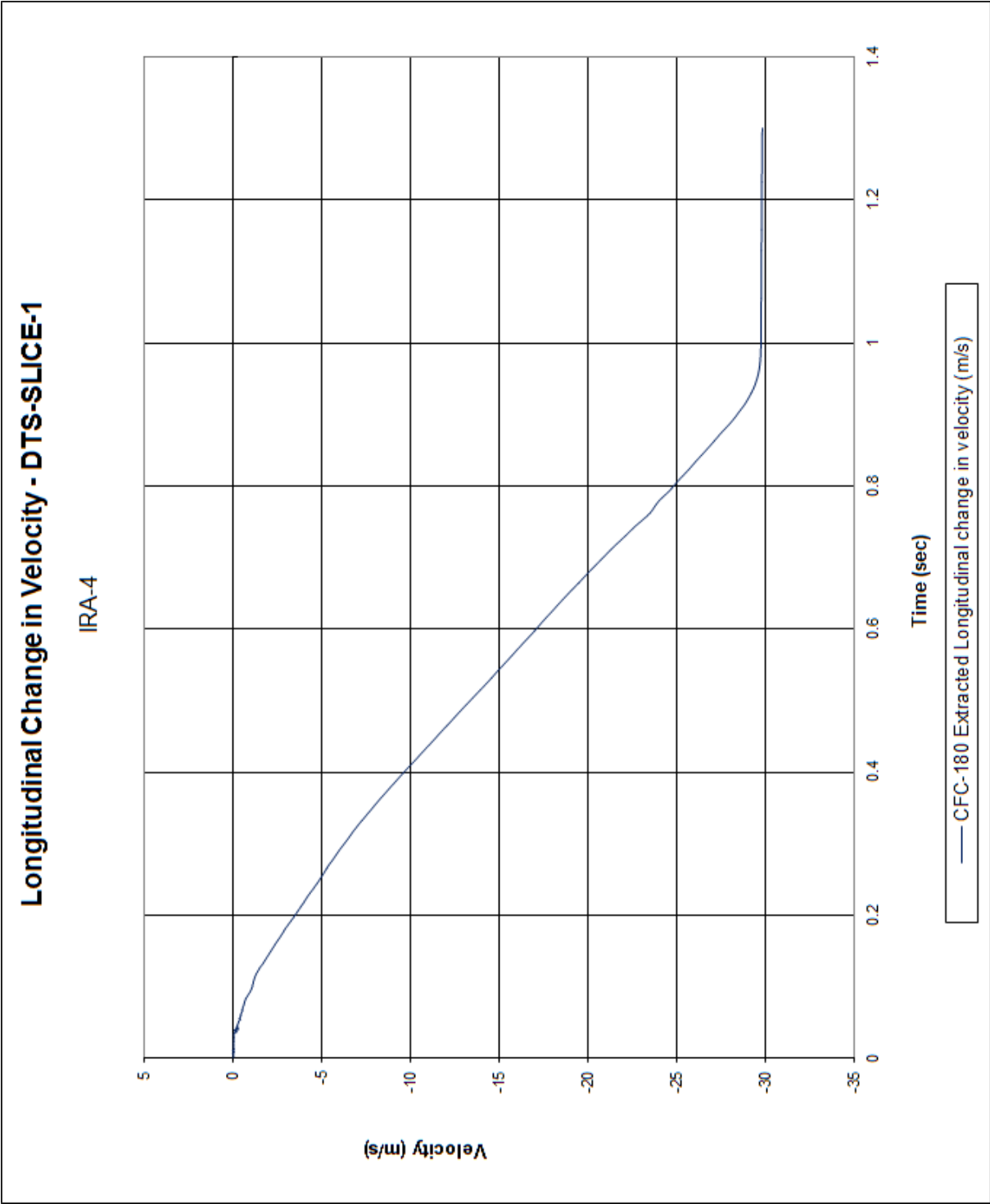


Figure E-6. Longitudinal Occupant Impact Velocity (DTS-SLICE-1), Test No. IRA-4

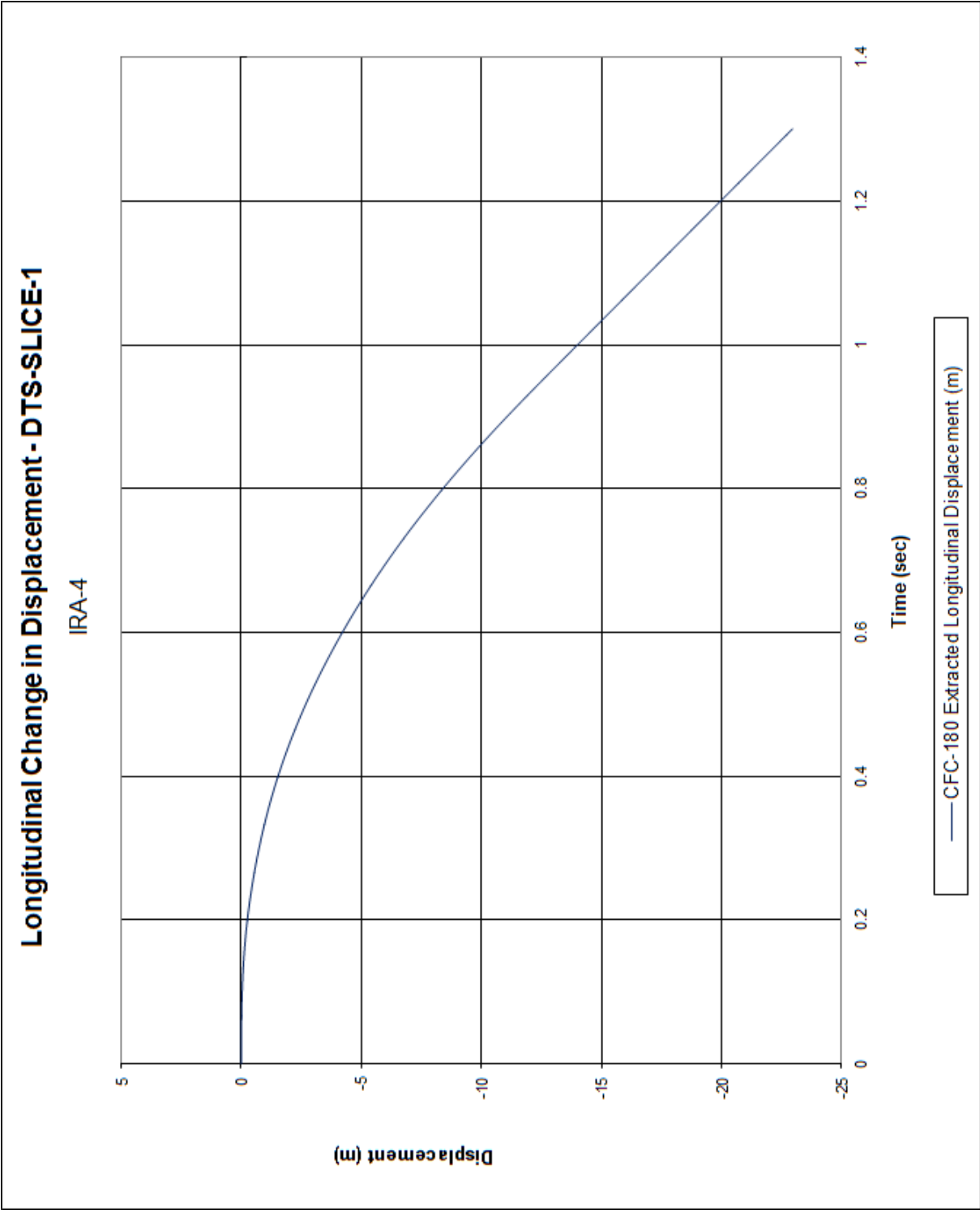


Figure E-7. Longitudinal Occupant Displacement (DTS-SLICE-1), Test No. IRA-4

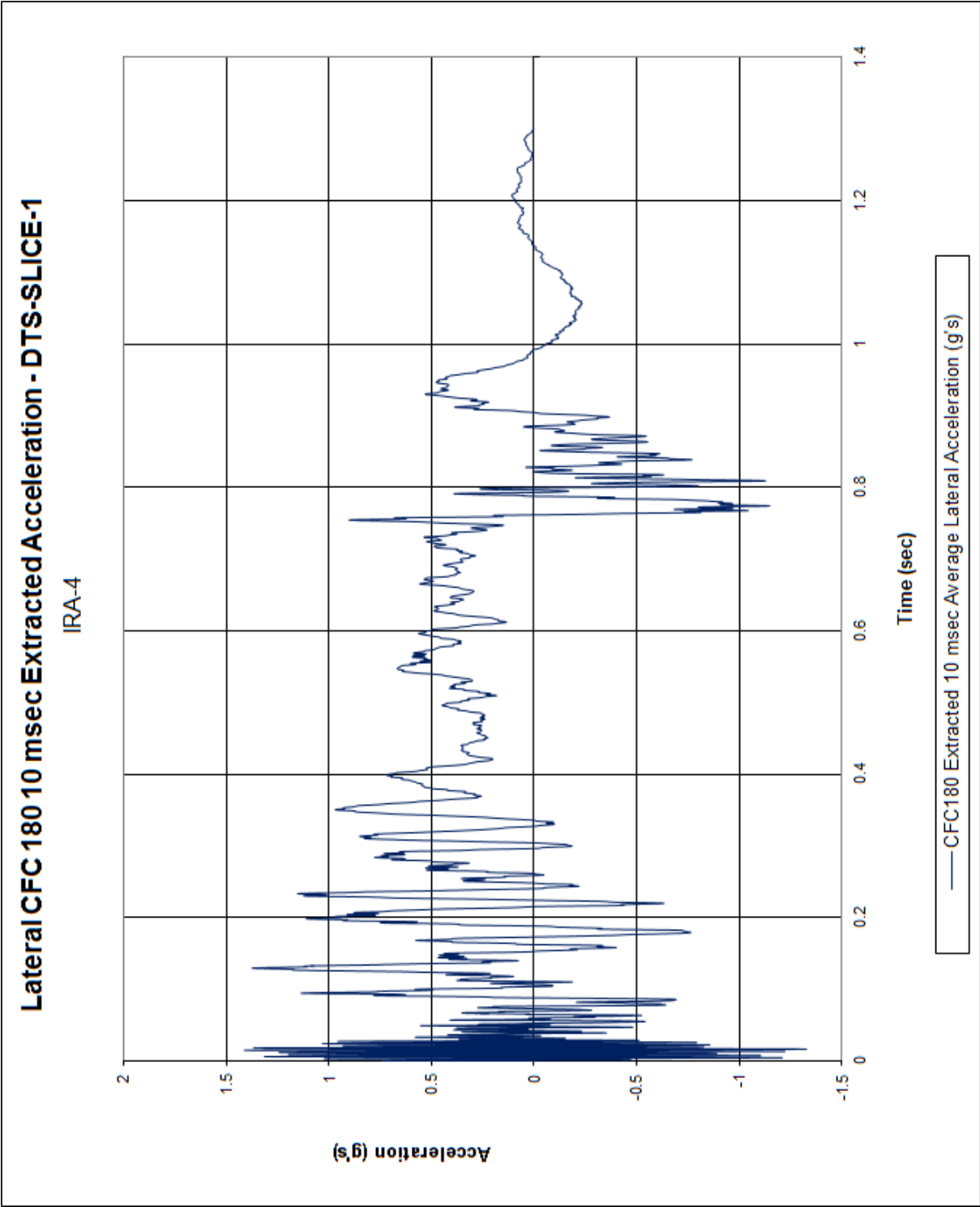


Figure E-8. 10-ms Average Lateral Deceleration (DTS-SLICE-1), Test No. IRA-4

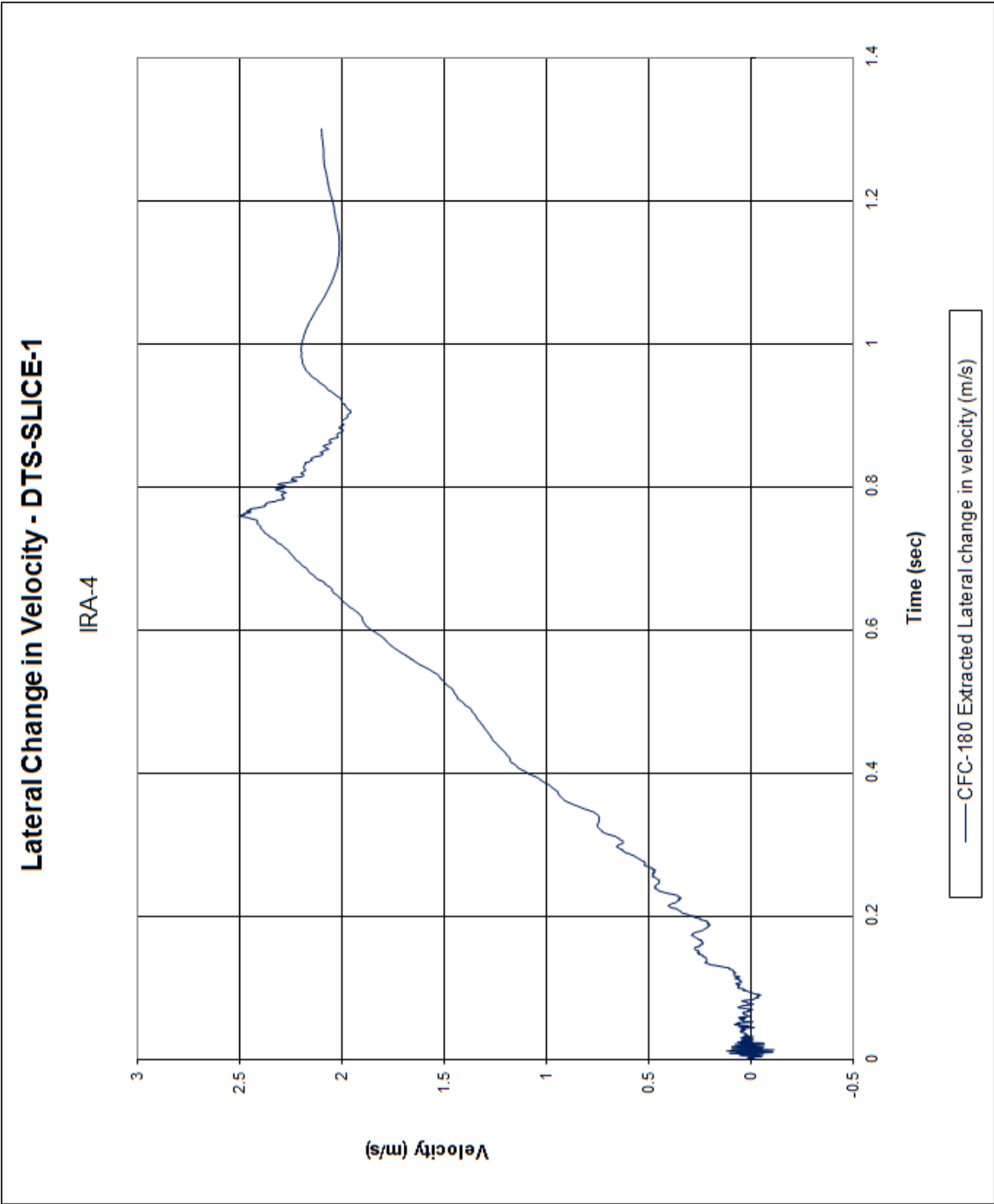


Figure E-9. Lateral Occupant Impact Velocity (DTS-SLICE-1), Test No. IRA-4

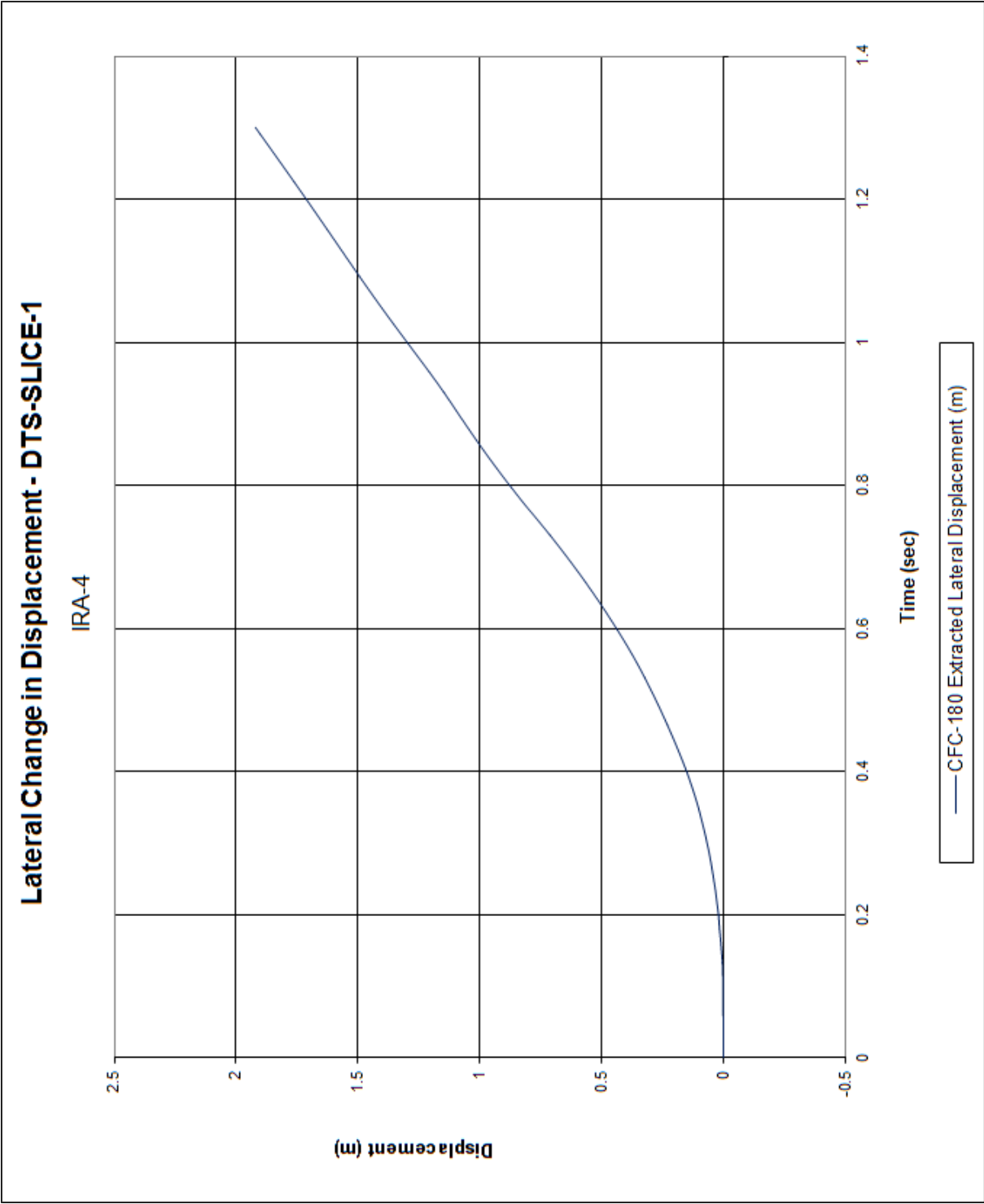


Figure E-10. Lateral Occupant Displacement (DTS-SLICE-1), Test No. IRA-4

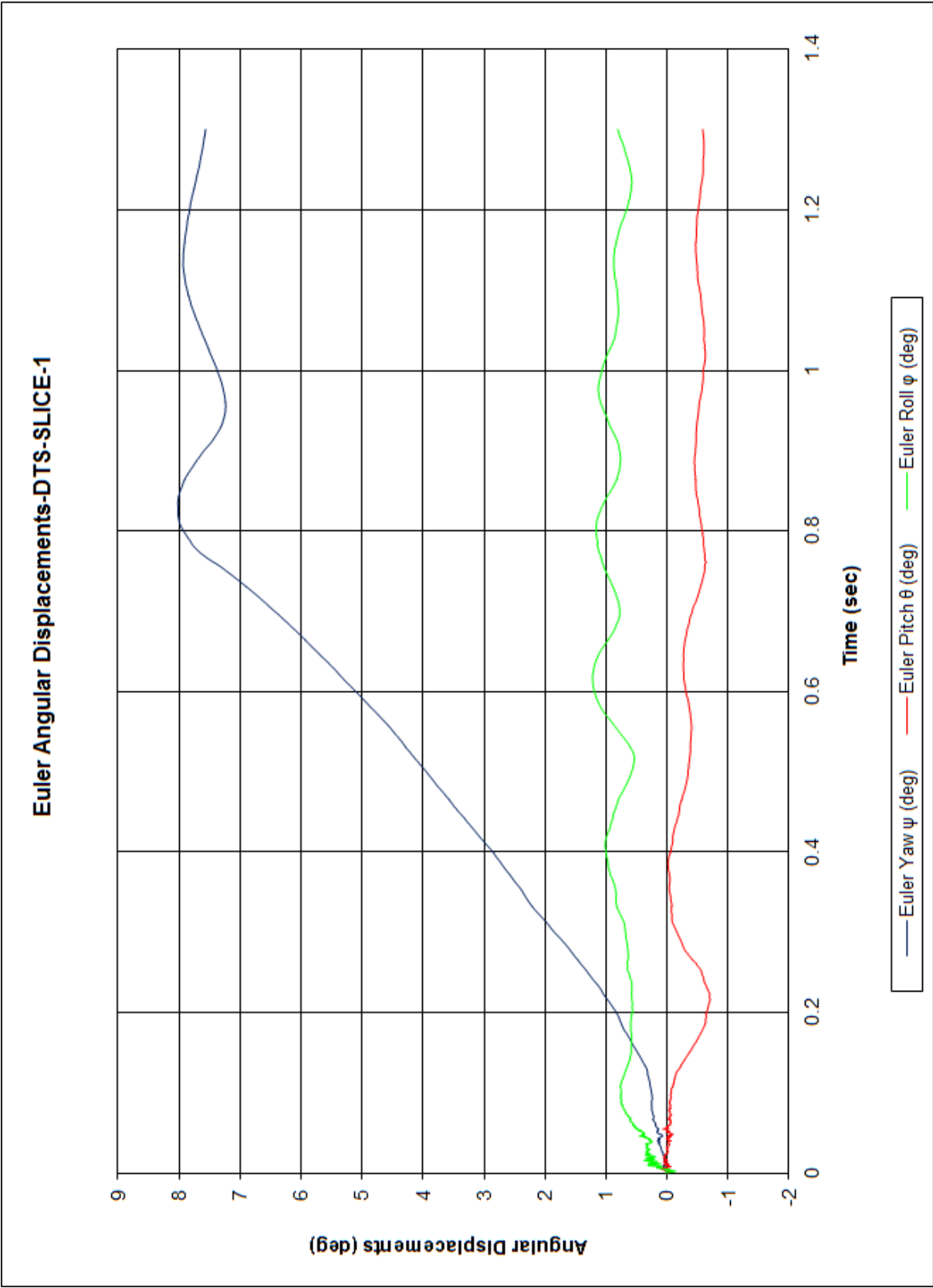


Figure E-11. Vehicle Angular Displacements (DTS-SLICE-1), Test No. IRA-4

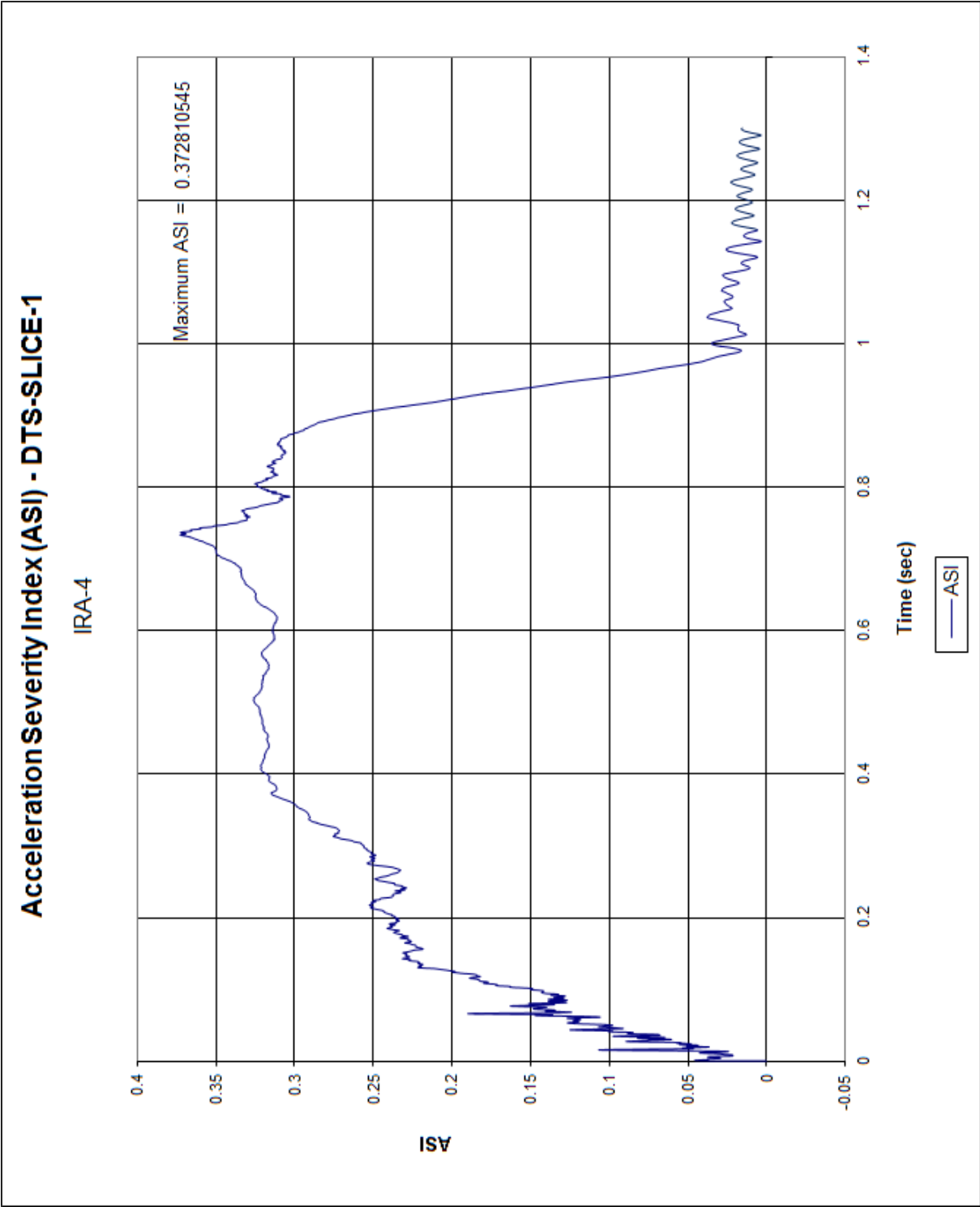


Figure E-12. Acceleration Severity Index (DTS-SLICE-1), Test No. IRA-4

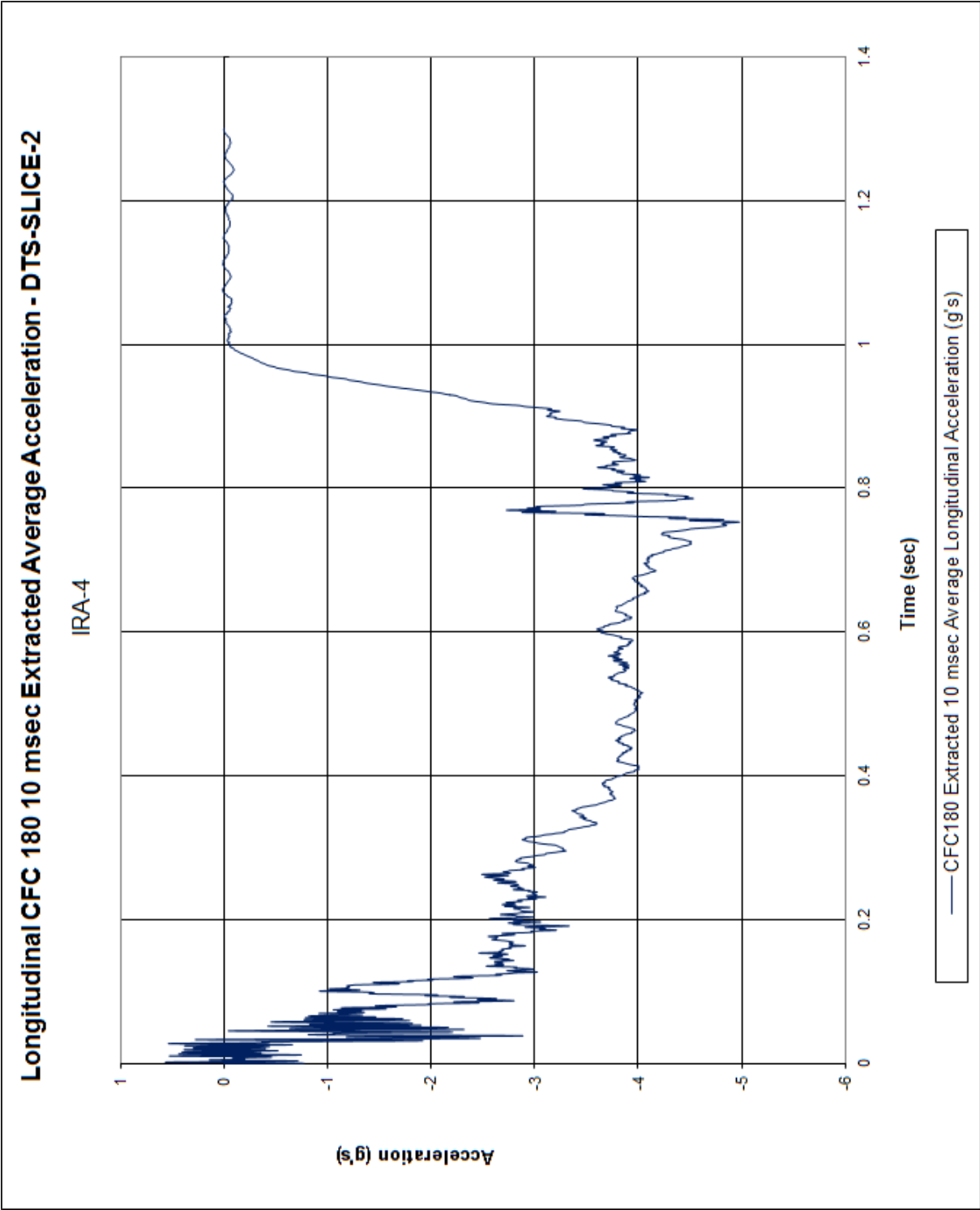


Figure E-13. 10-ms Average Longitudinal Deceleration (DTS-SLICE-2), Test No. IRA-4

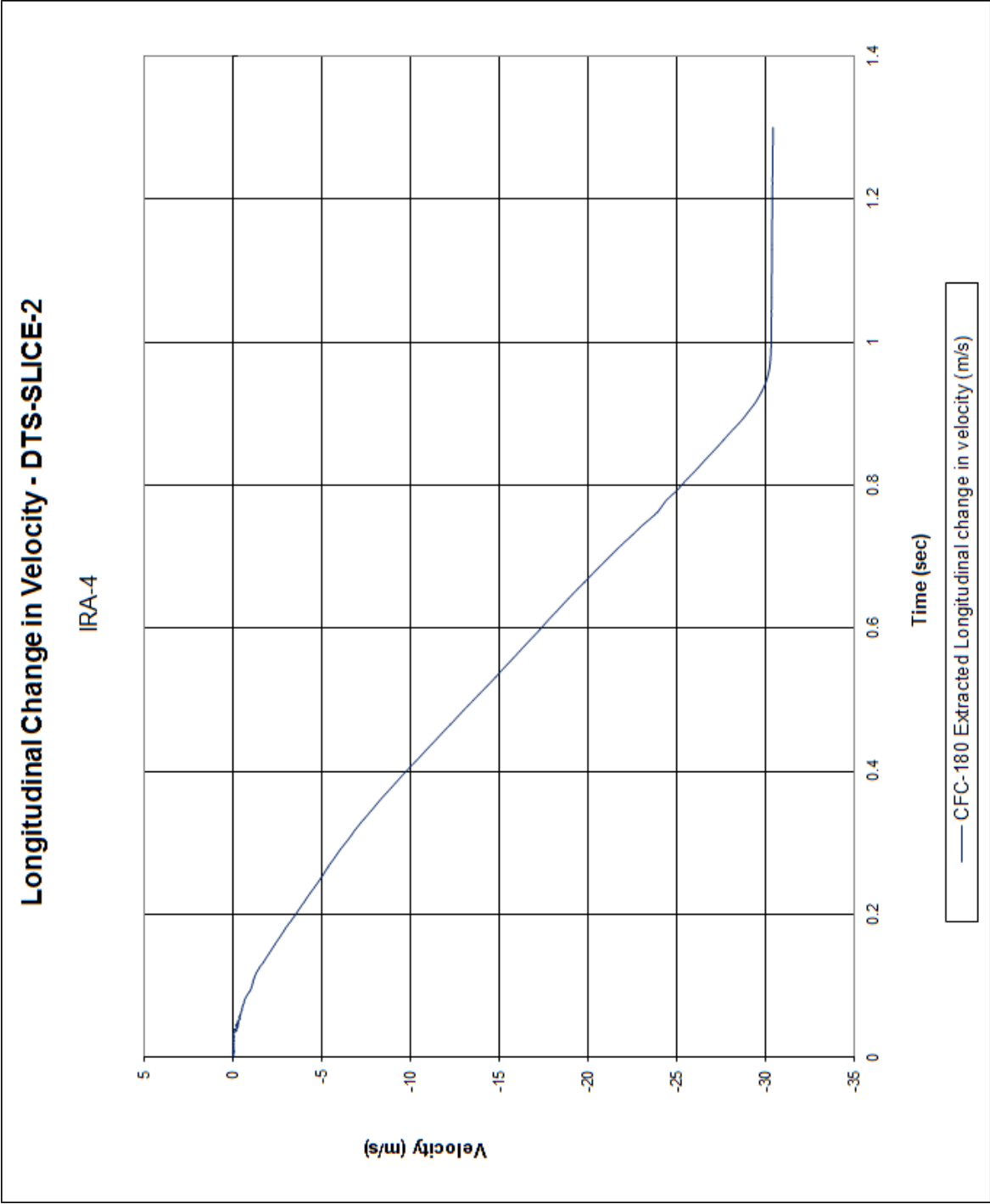


Figure E-14. Longitudinal Occupant Impact Velocity (DTS-SLICE-2), Test No. IRA-4

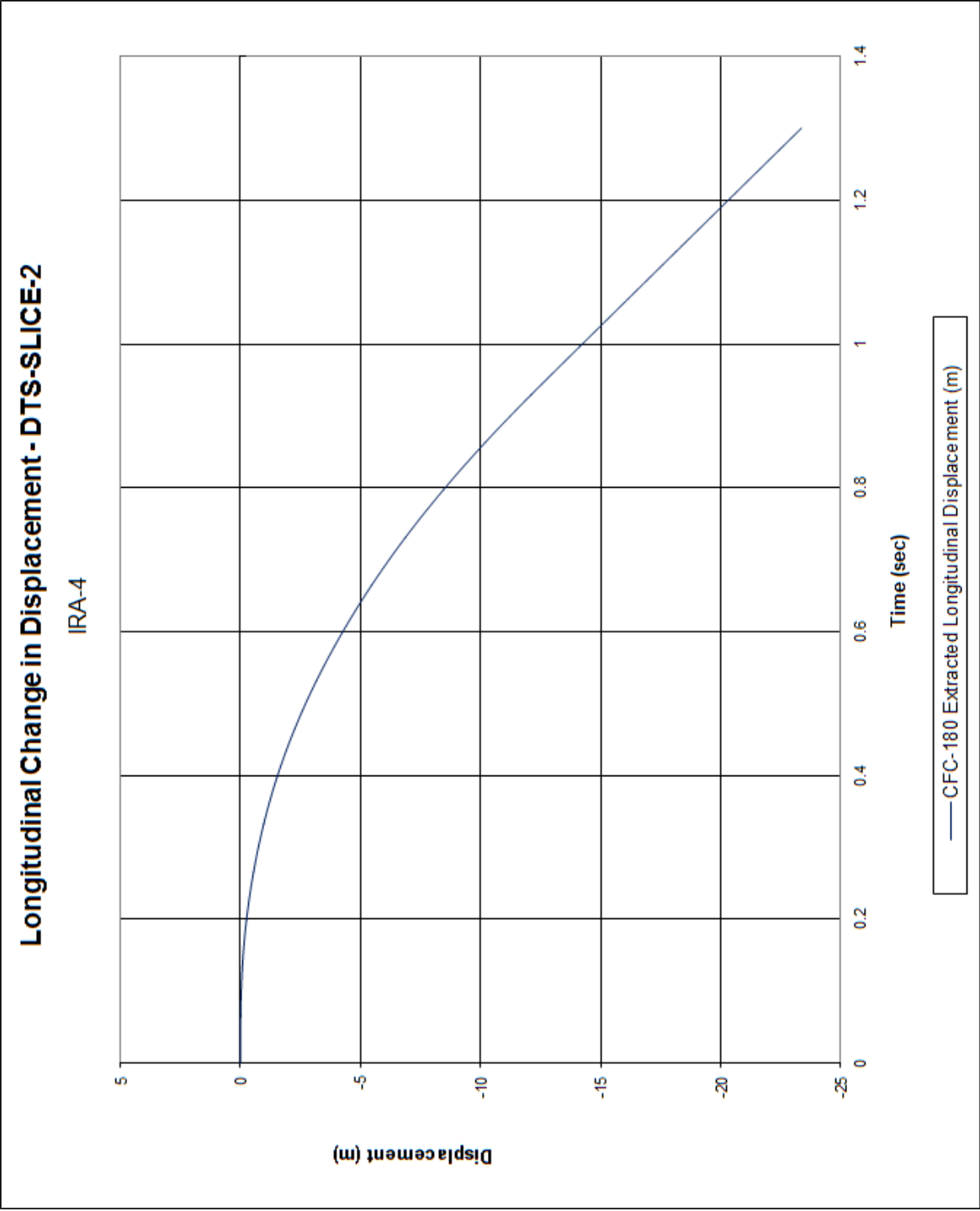


Figure E-15. Longitudinal Occupant Displacement (DTS-SLICE-2), Test No. IRA-4

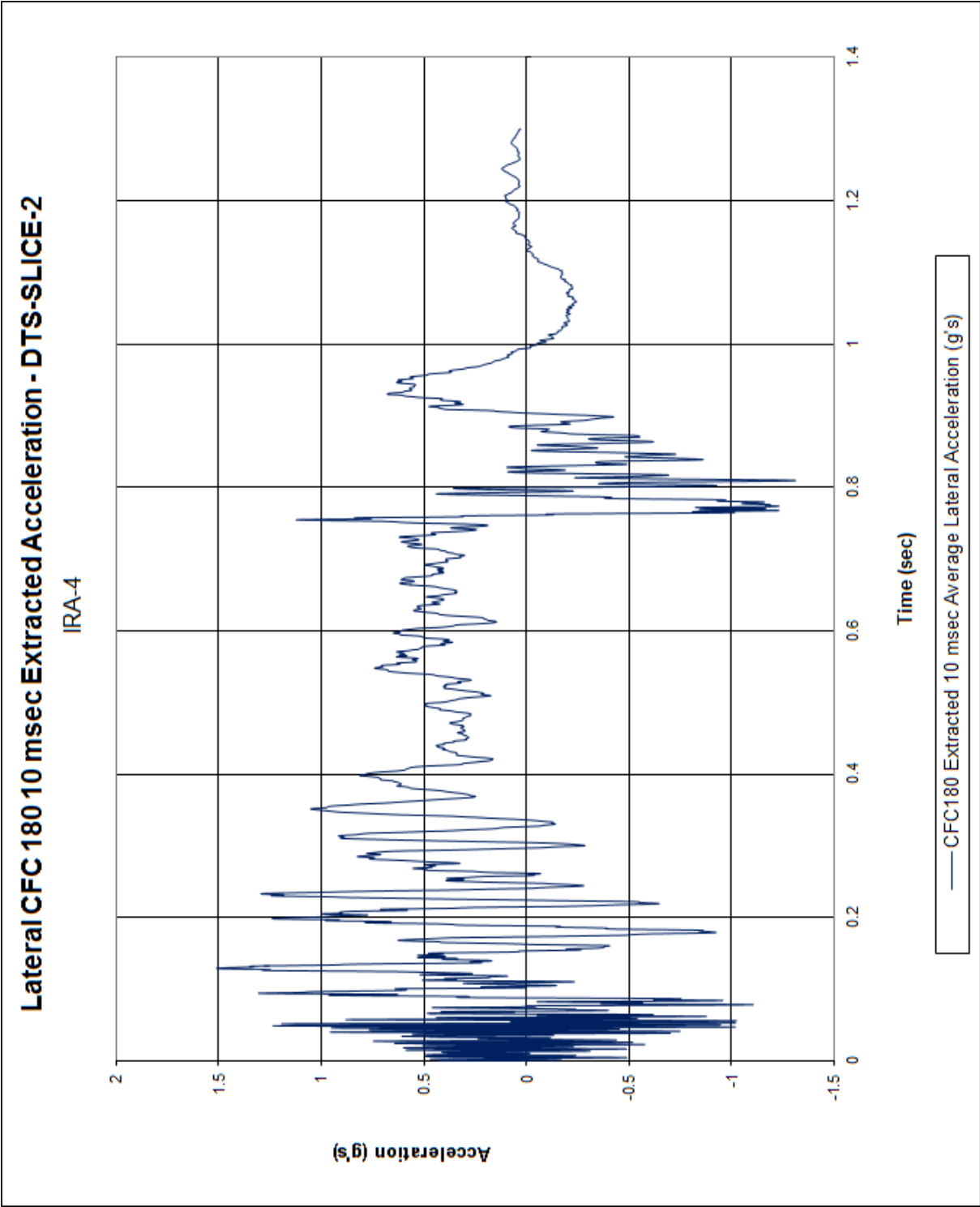


Figure E-16. 10-ms Average Lateral Deceleration (DTS-SLICE-2), Test No. IRA-4

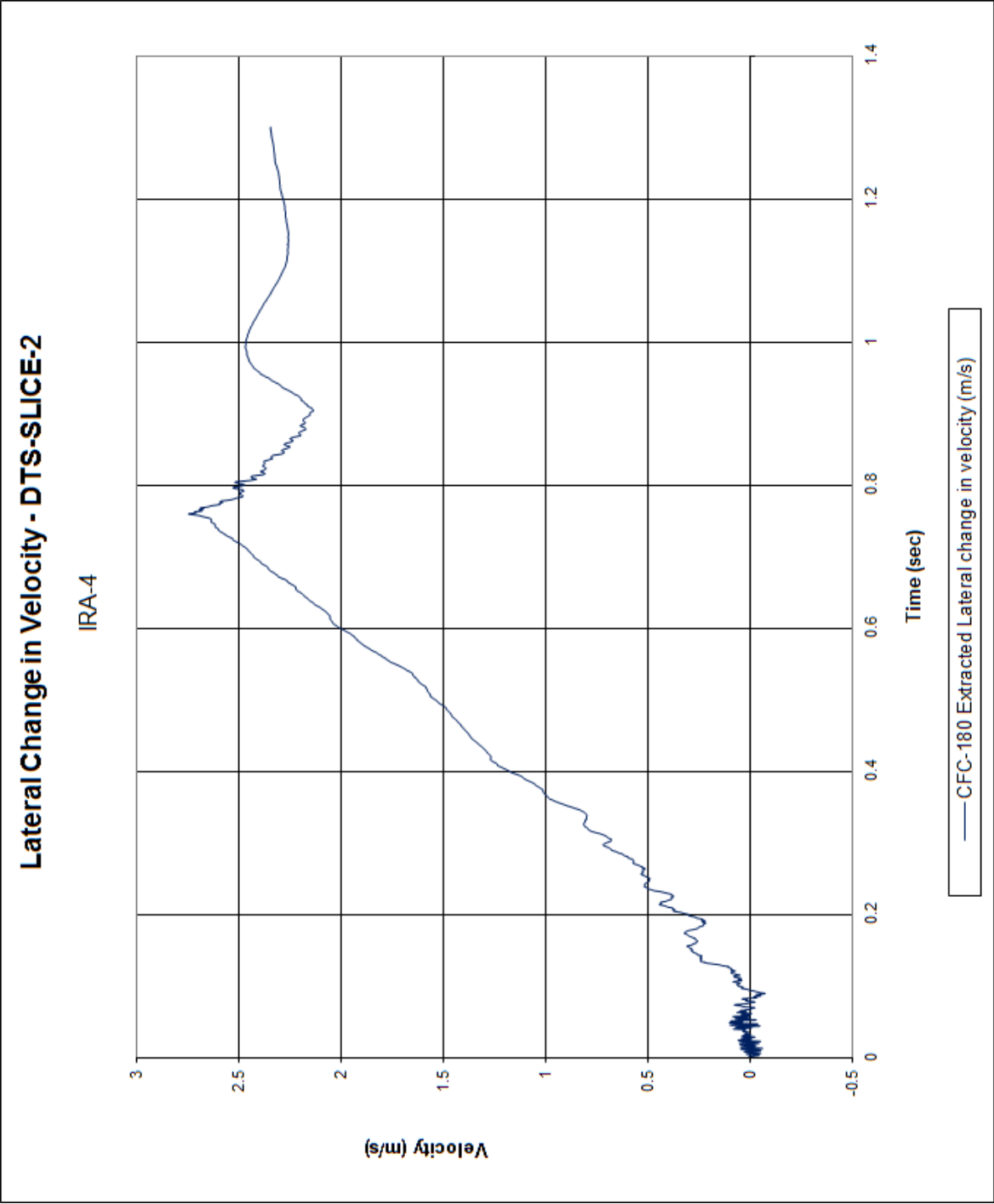


Figure E-17. Lateral Occupant Impact Velocity (DTS-SLICE-2), Test No. IRA-4

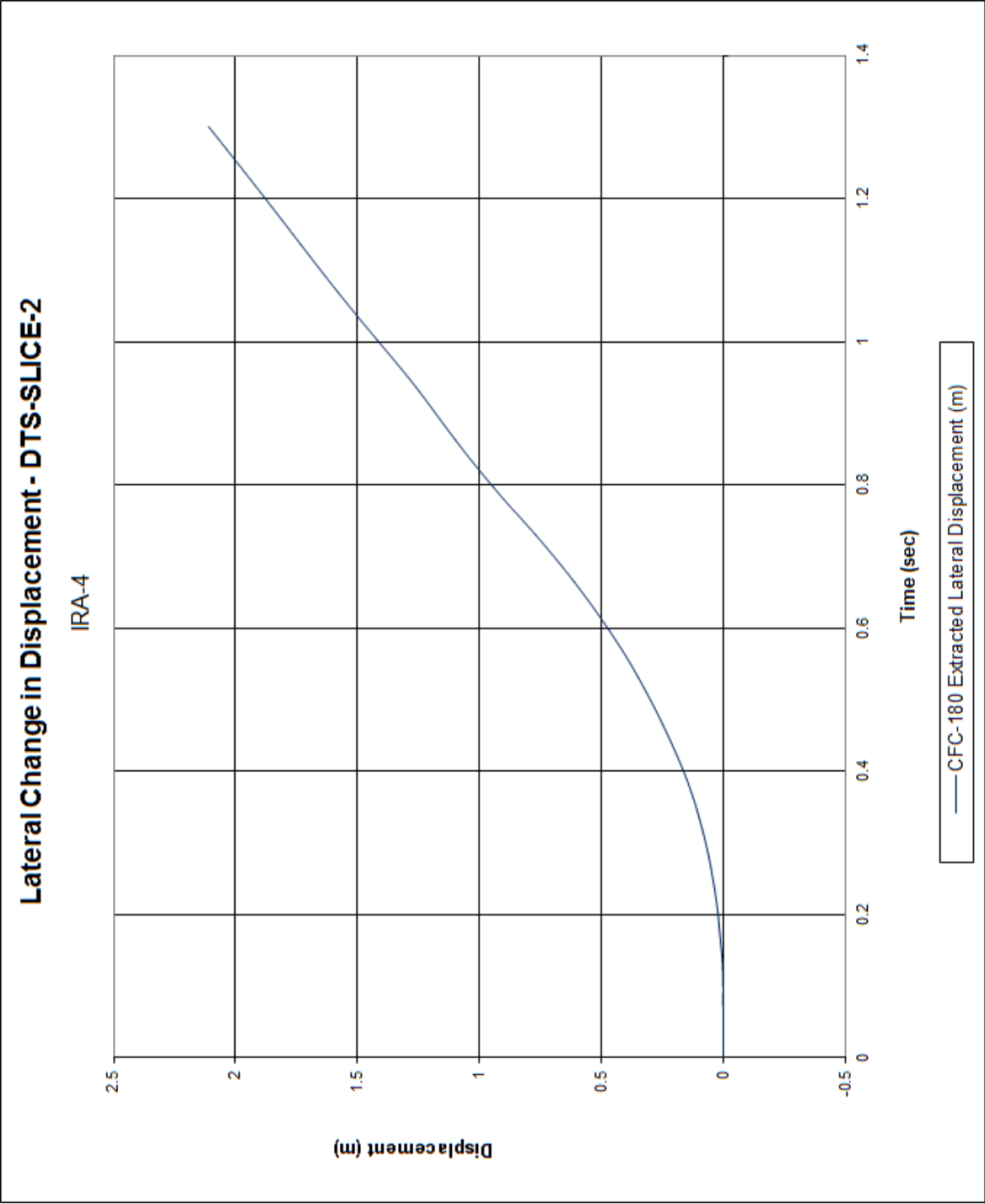


Figure E-18. Lateral Occupant Displacement (DTS-SLICE-2), Test No. IRA-4

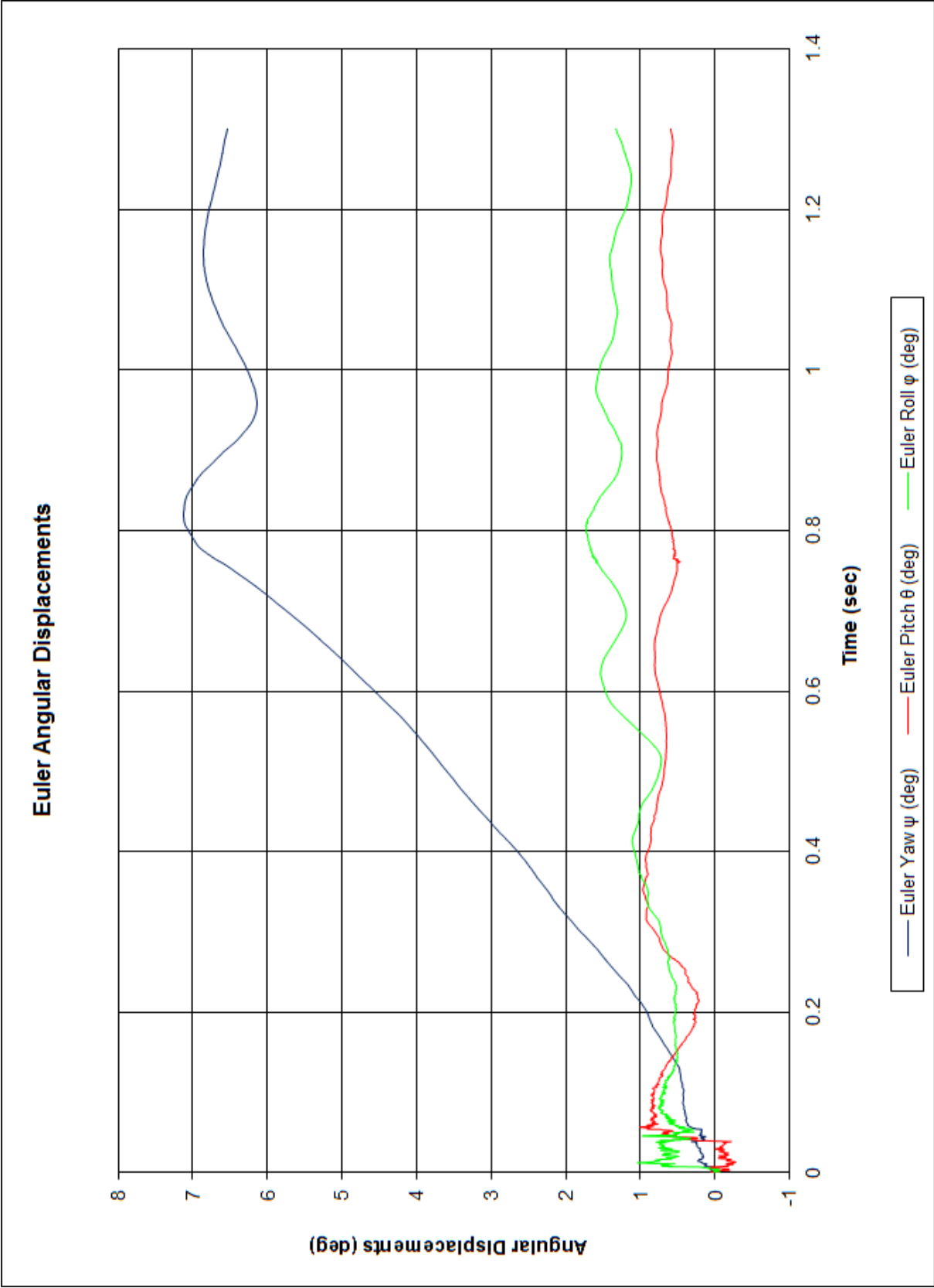


Figure E-19. Vehicle Angular Displacements (DTS-SLICE-2), Test No. IRA-4

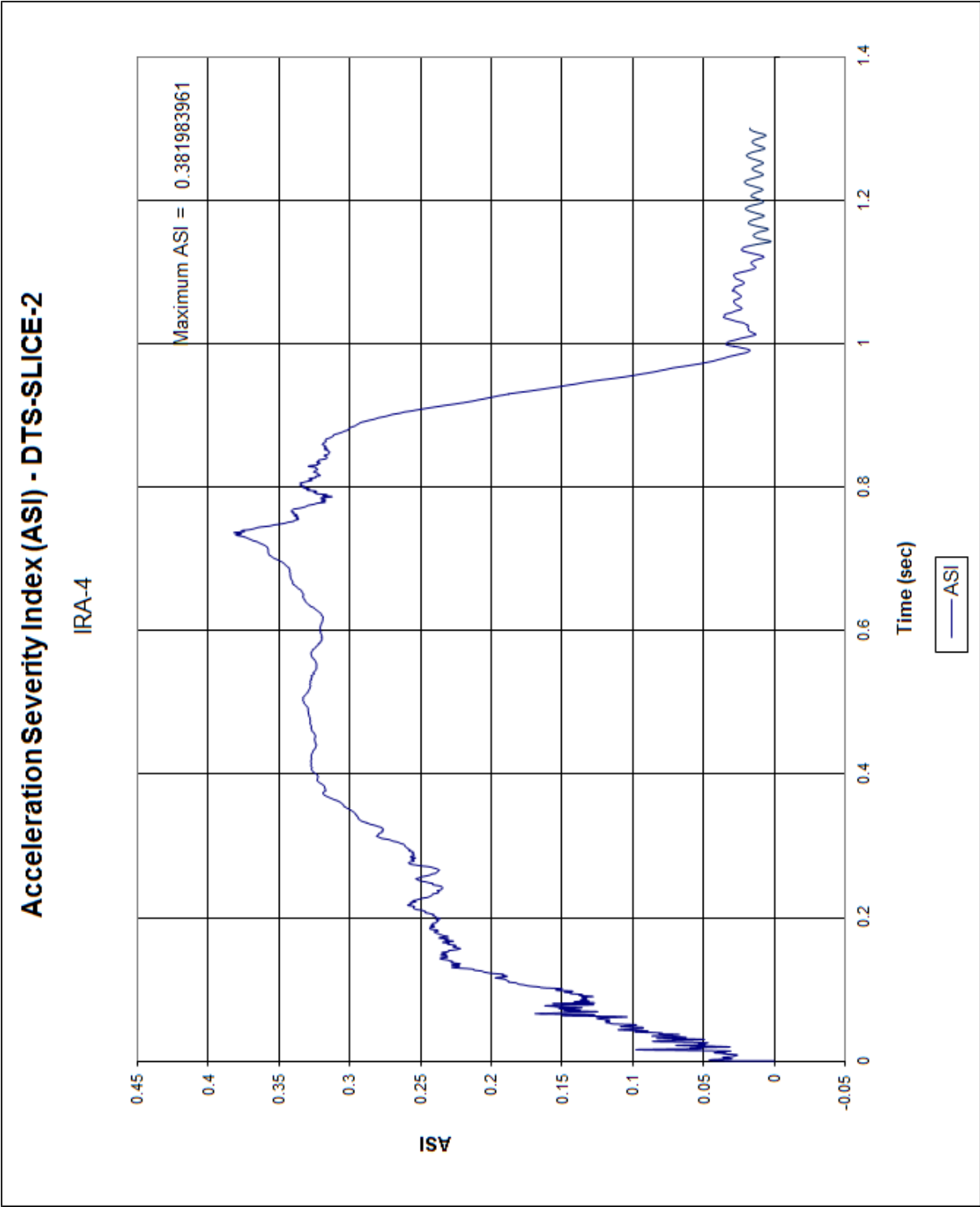


Figure E-20. Acceleration Severity Index (DTS-SLICE-2), Test No. IRA-4

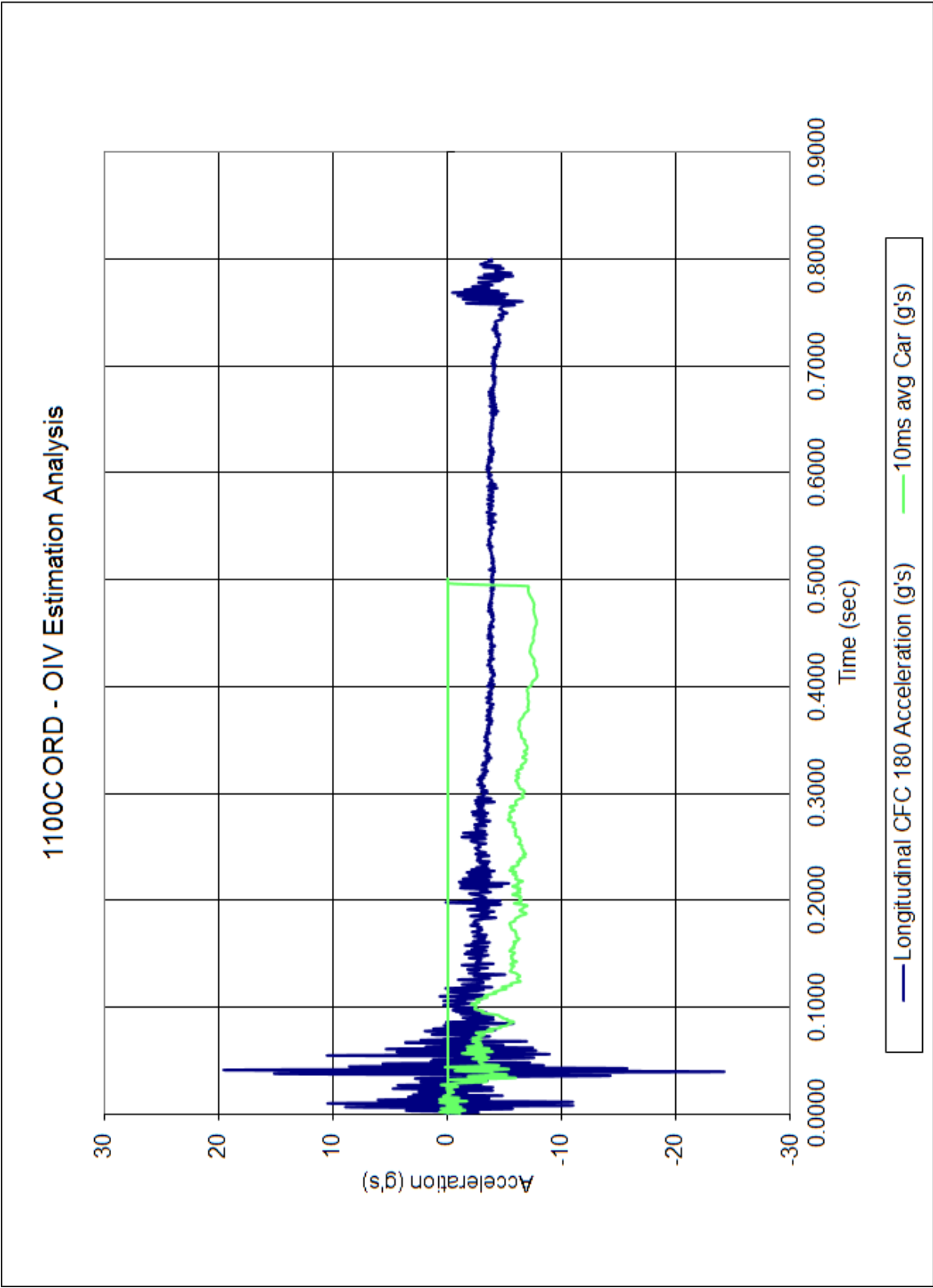


Figure E-21. 1100C ORD-OIV Estimation, Test No. IRA-4

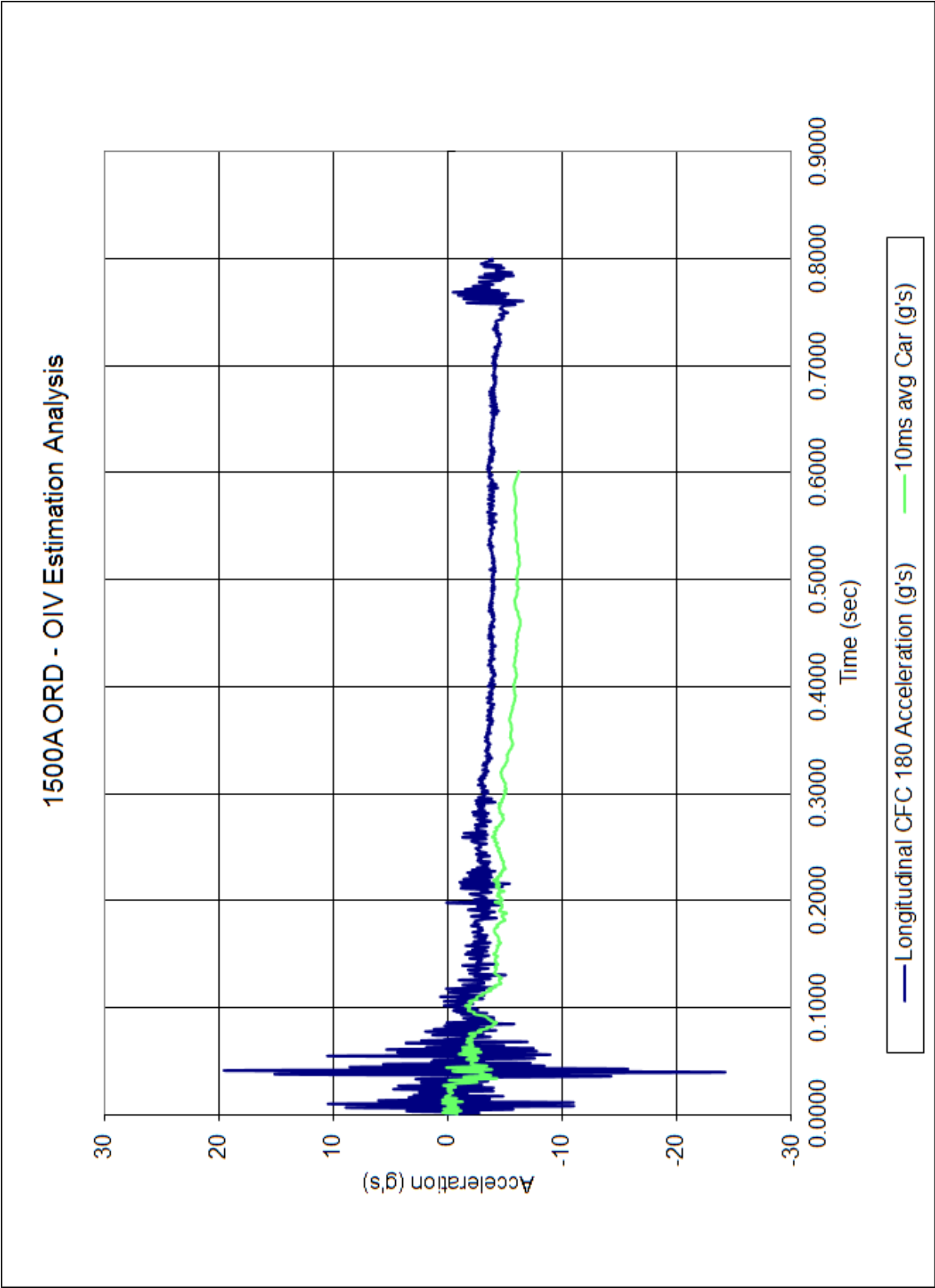


Figure E-22. 1500A ORD-OIV Estimation, Test No. IRA-4

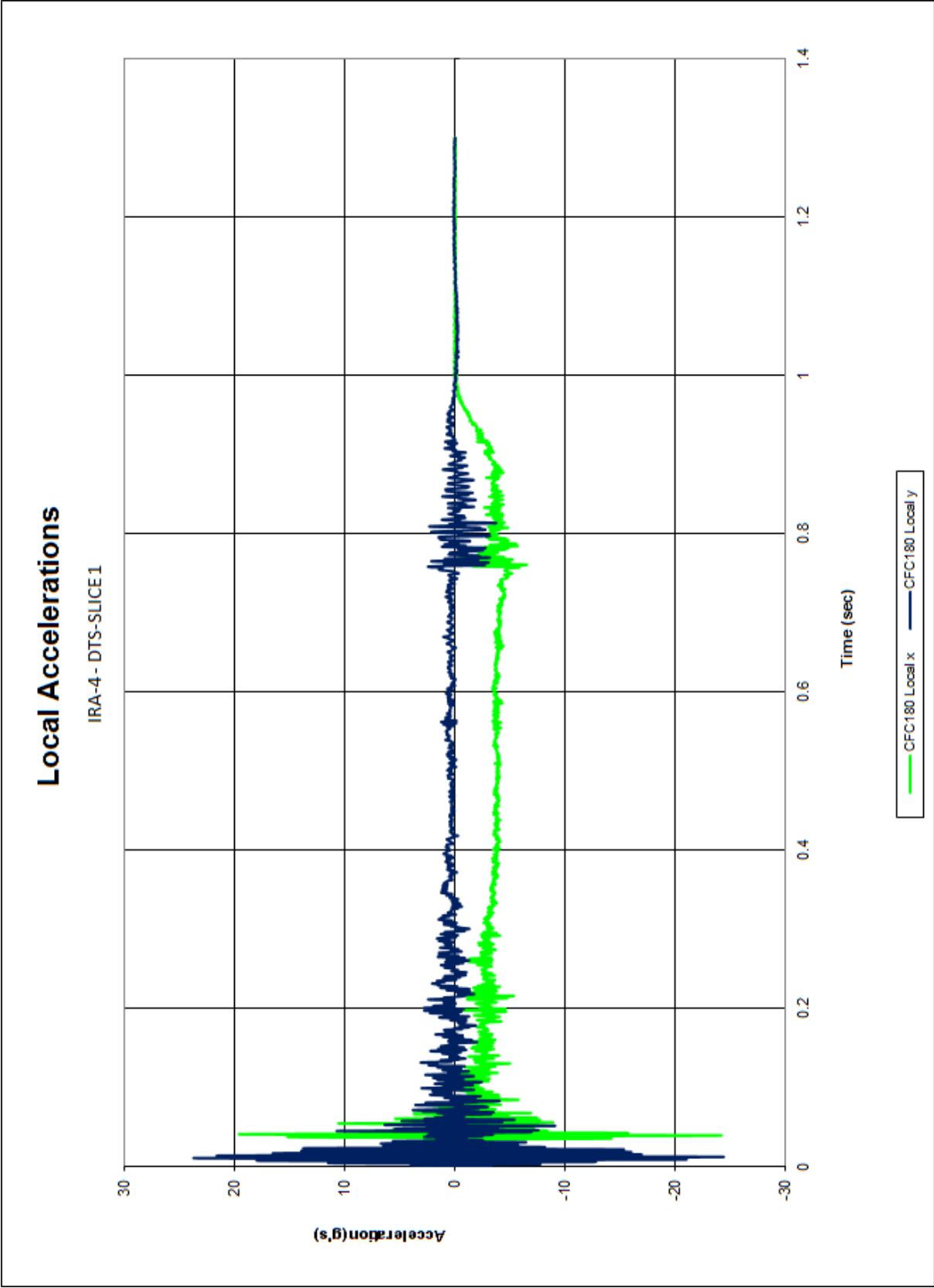


Figure E-23. Local Accelerations (DTS-SLICE-1), Test No. IRA-4

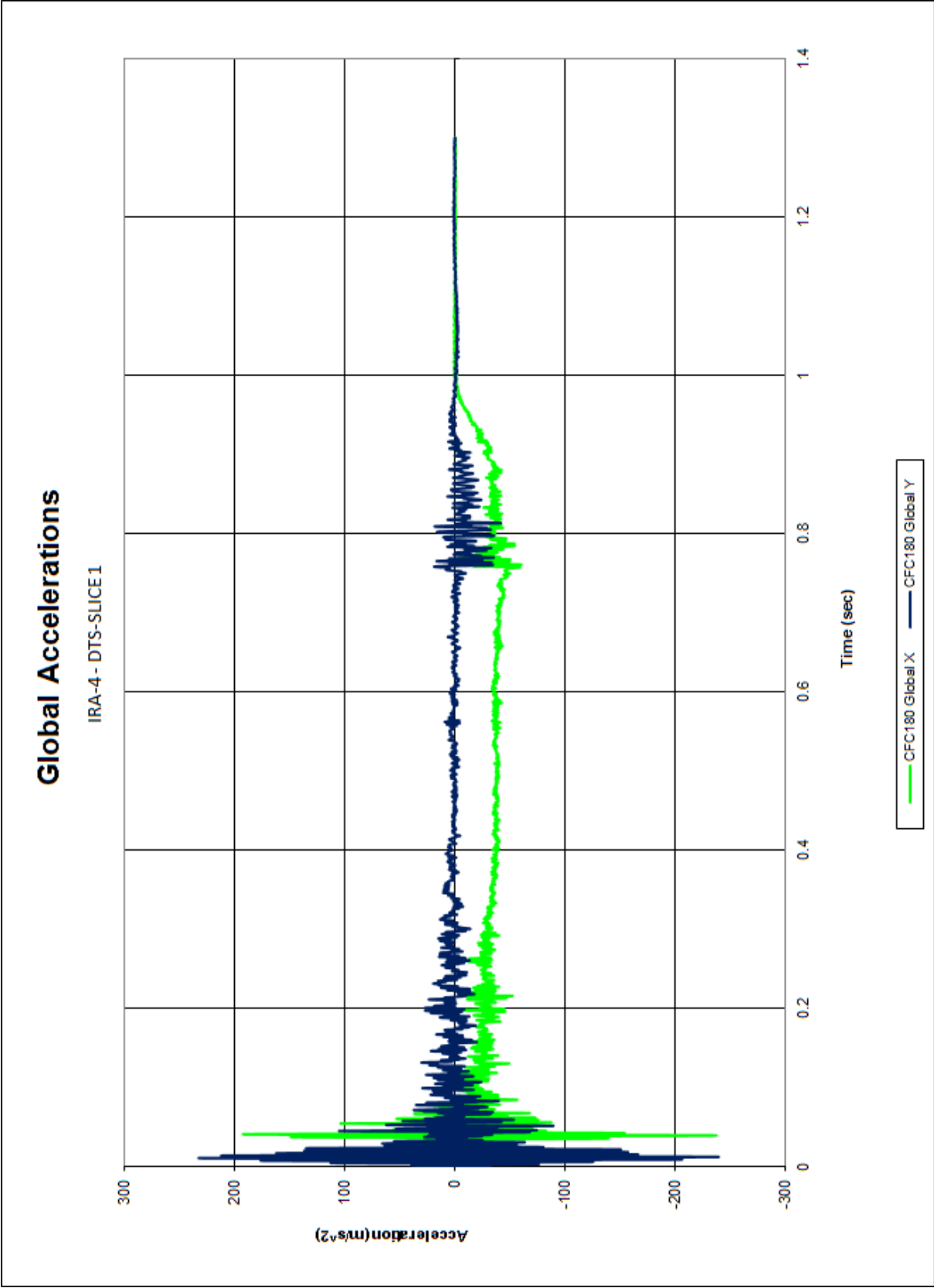


Figure E-24. Global Accelerations (DTS-SLICE-1), Test No. IRA-4

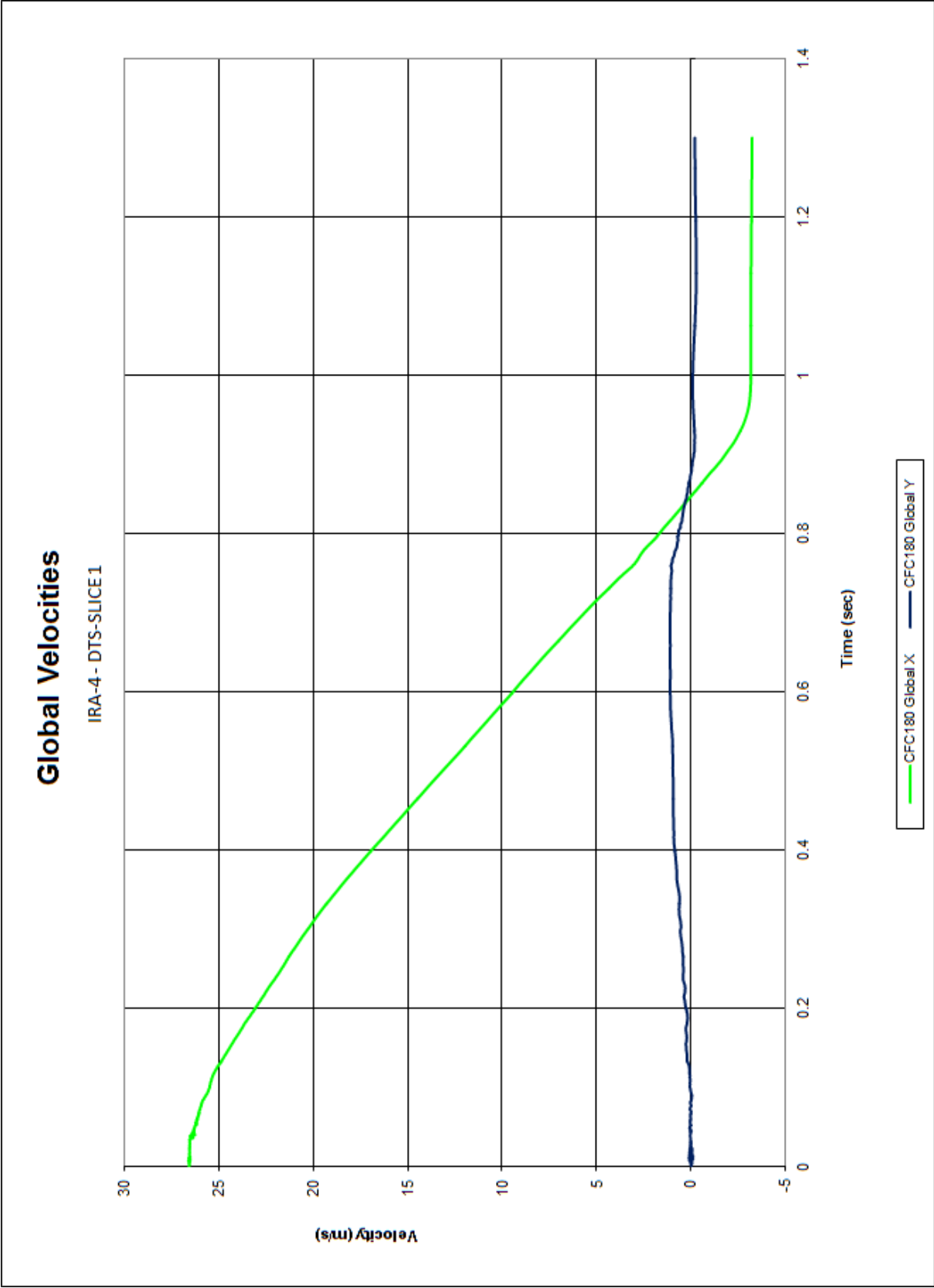


Figure E-25. Global Velocities (DTS-SLICE-1), Test No. IRA-4

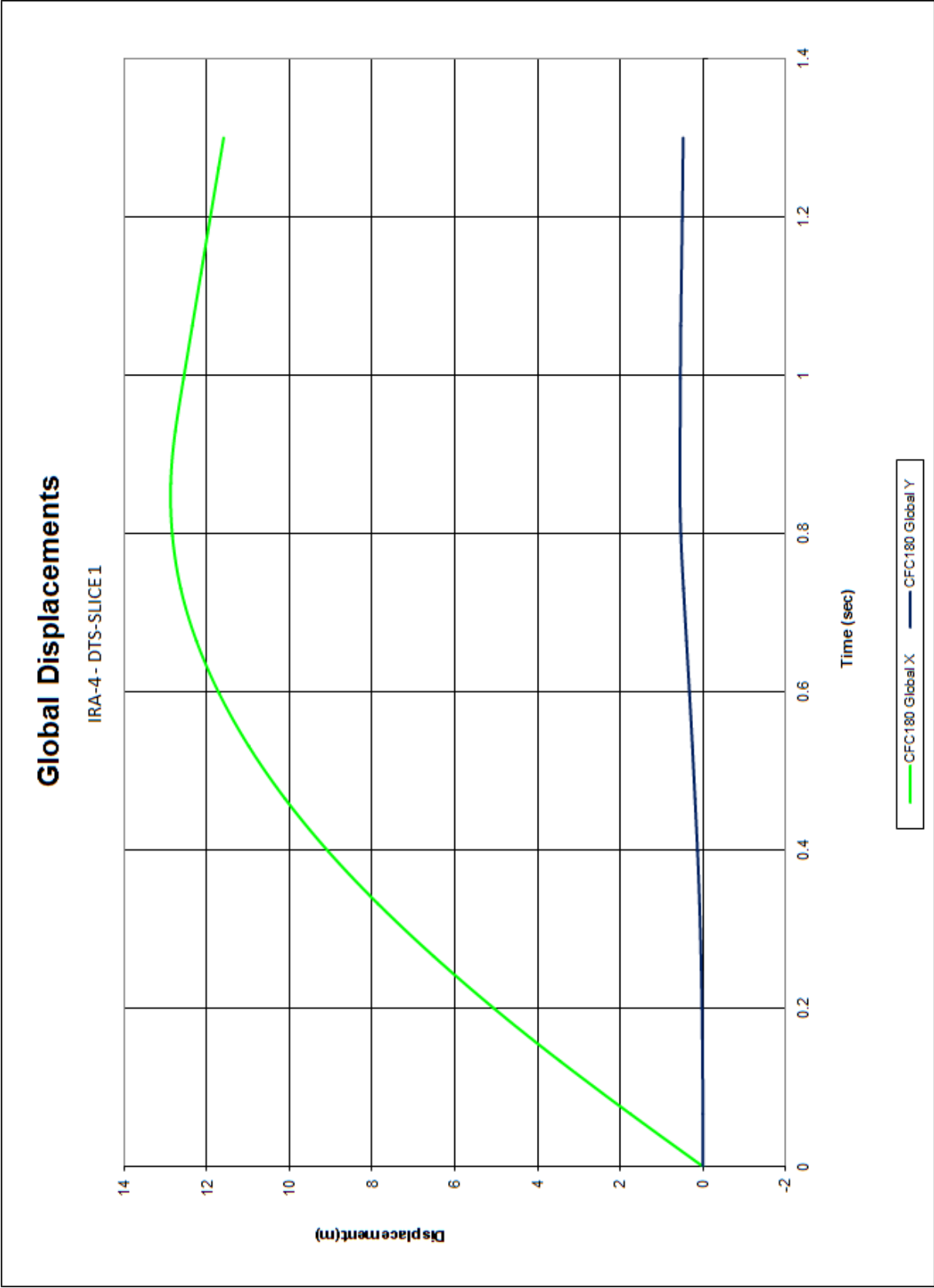


Figure E-26. Global Displacements (DTS-SLICE-1), Test No. IRA-4

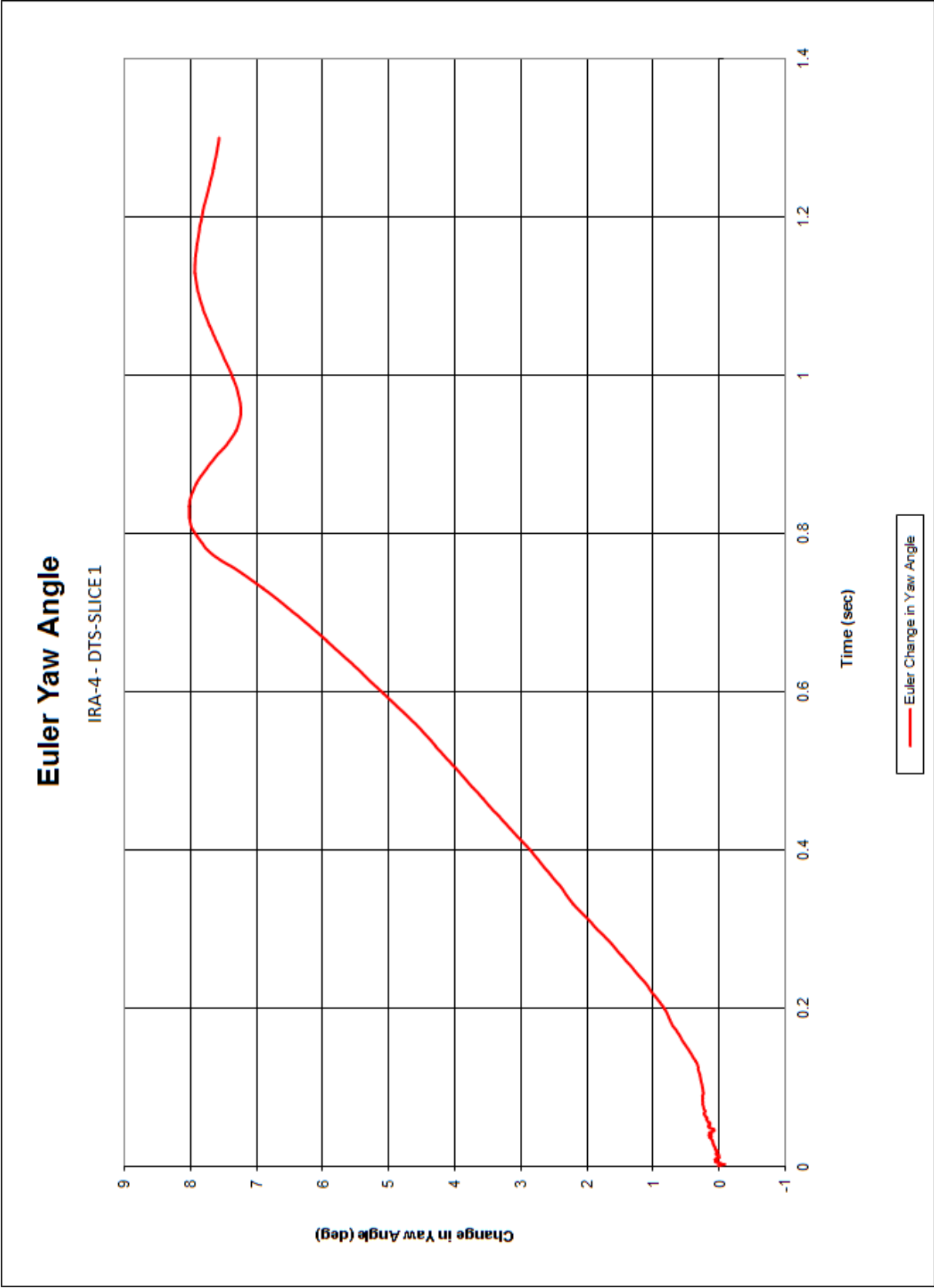


Figure E-27. Euler Yaw Angle (DTS-SLICE-1), Test No. IRA-4

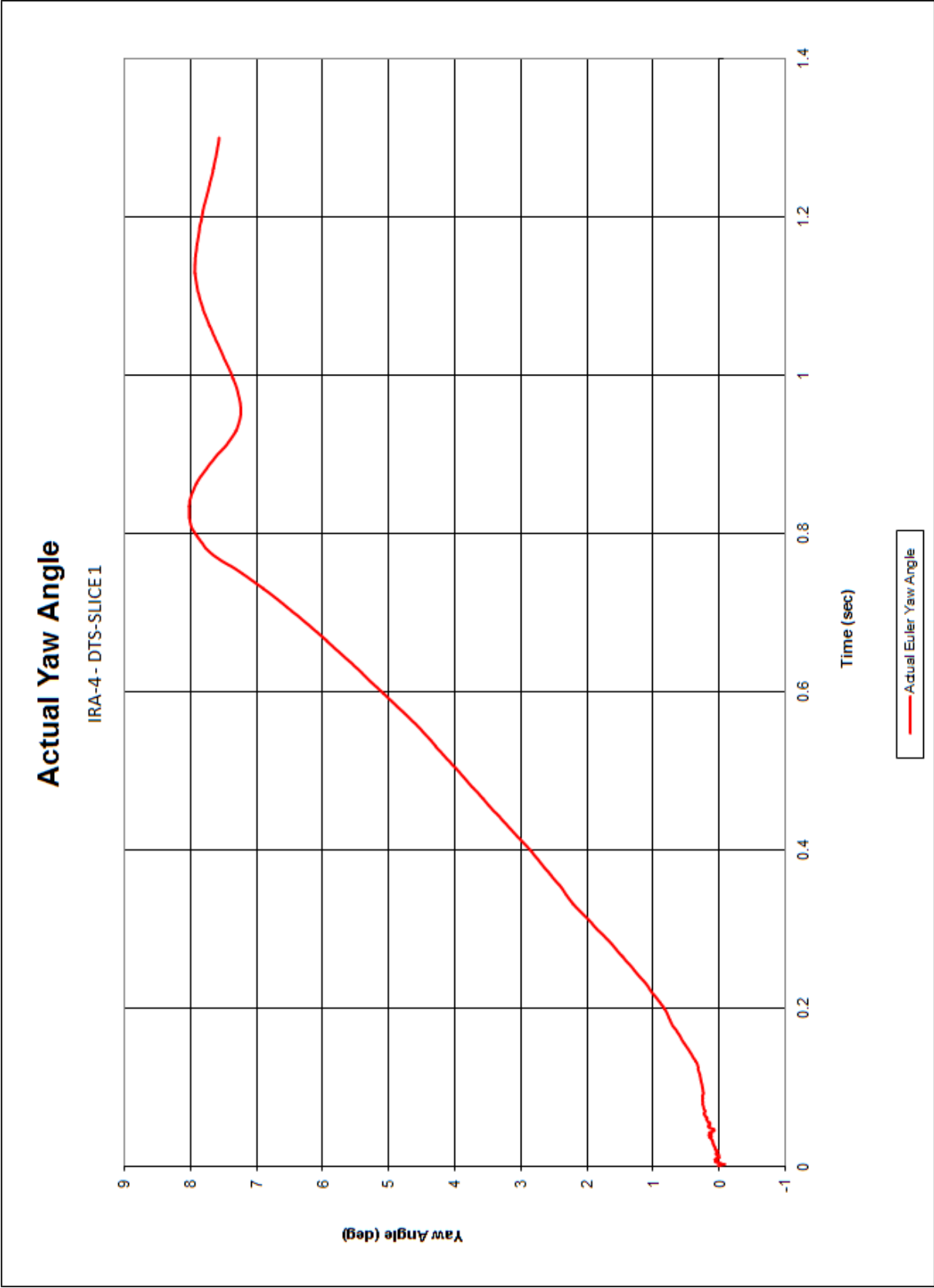


Figure E-28. Actual Yaw Angle (DTS-SLICE-1), Test No. IRA-4

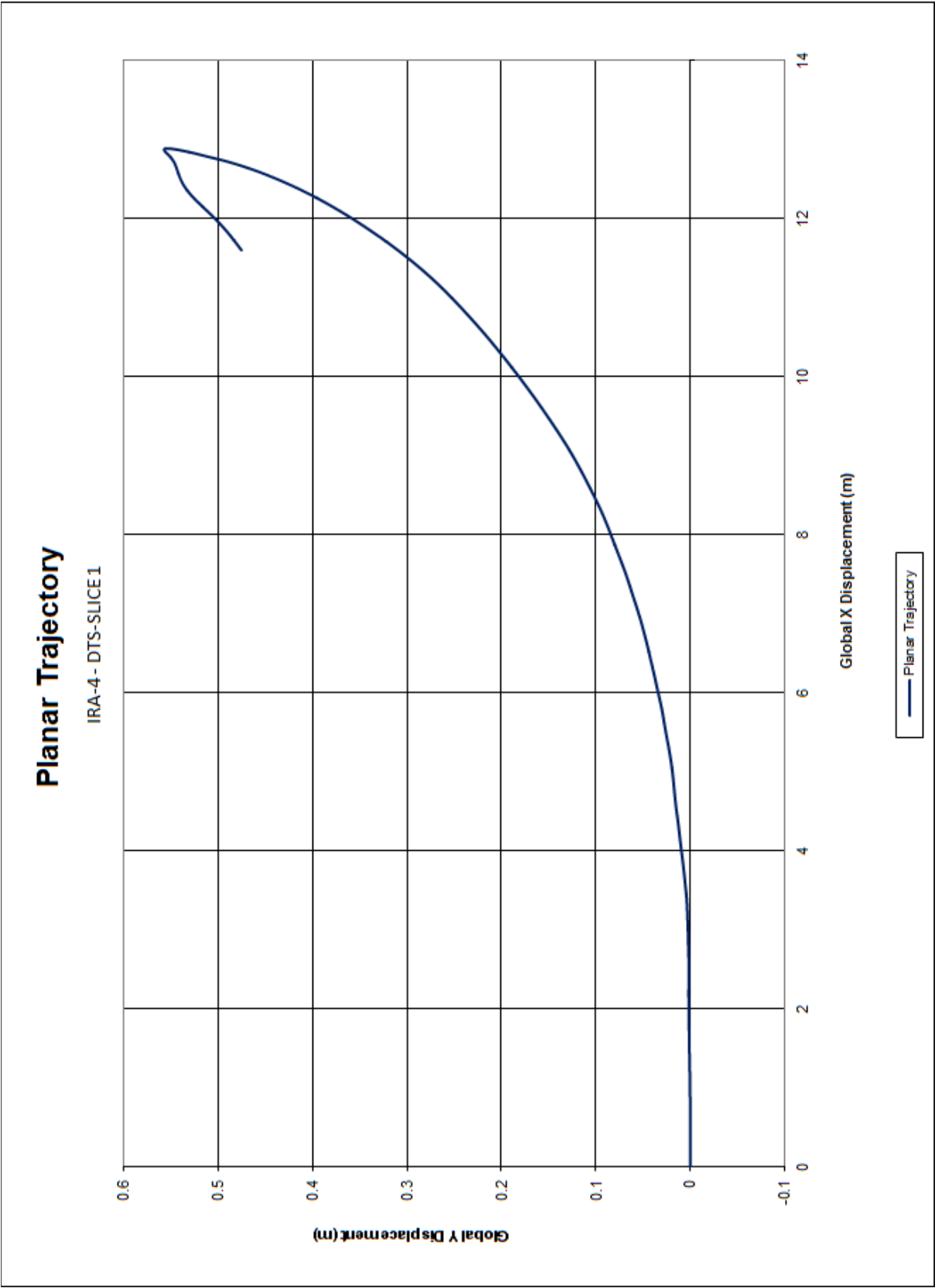


Figure E-29. Planar Trajectory (DTS-SLICE-1), Test No. IRA-4

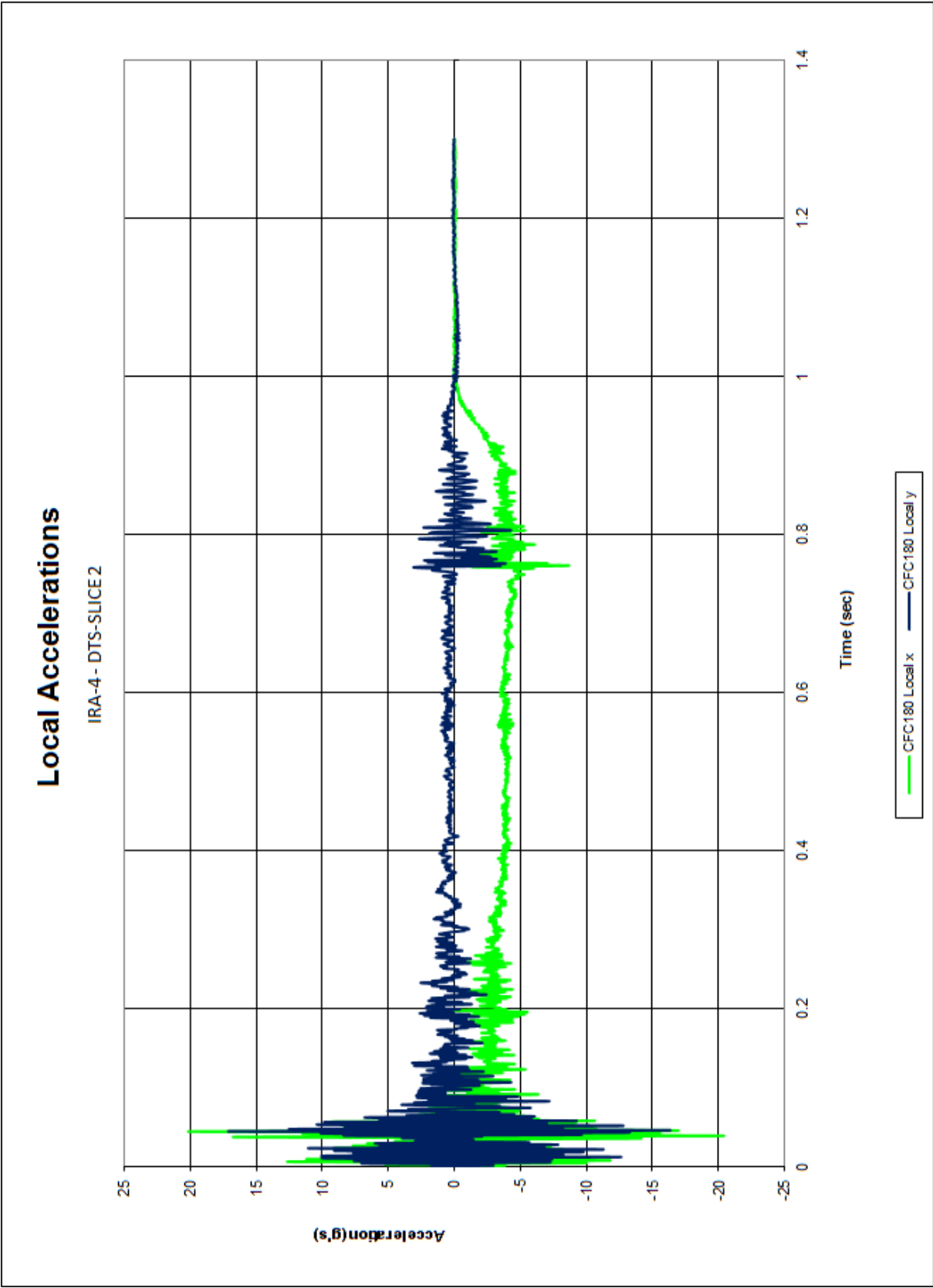


Figure E-30. Local Accelerations (DTS-SLICE-2), Test No. IRA-4

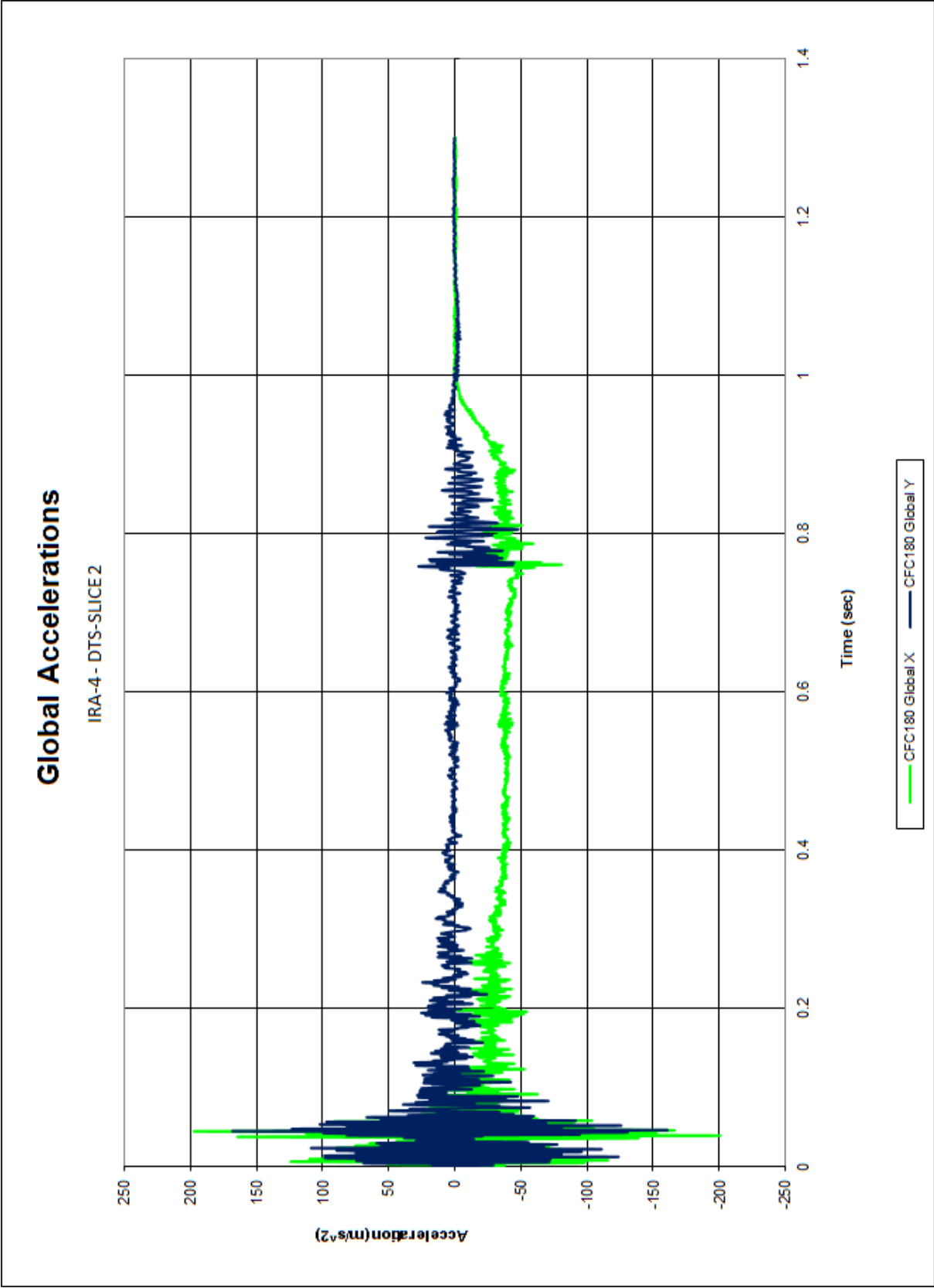


Figure E-31. Global Accelerations (DTS-SLICE-2), Test No. IRA-4

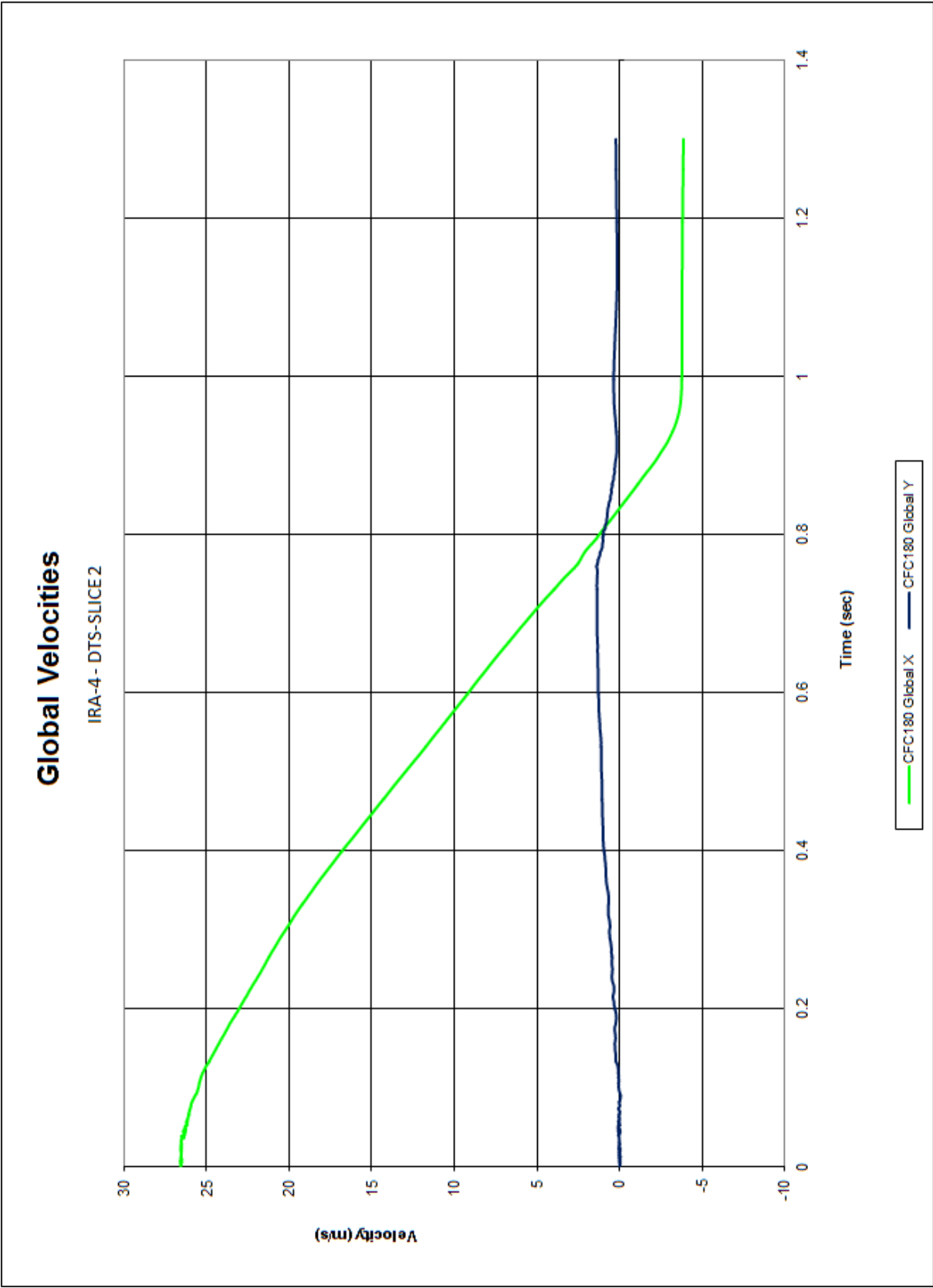


Figure E-32. Global Velocities (DTS-SLICE-2), Test No. IRA-4

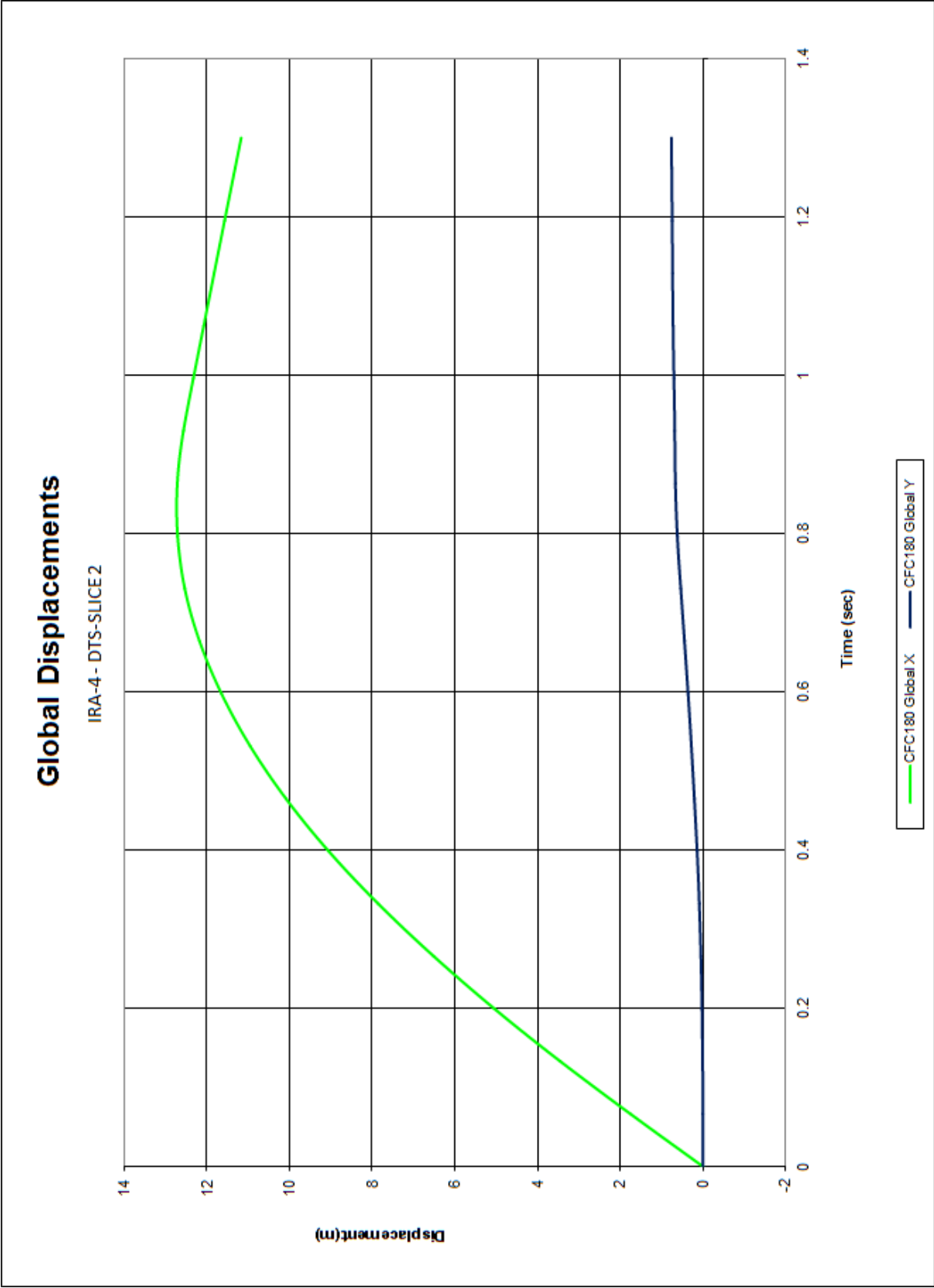


Figure E-33. Global Displacements (DTS-SLICE-2), Test No. IRA-4

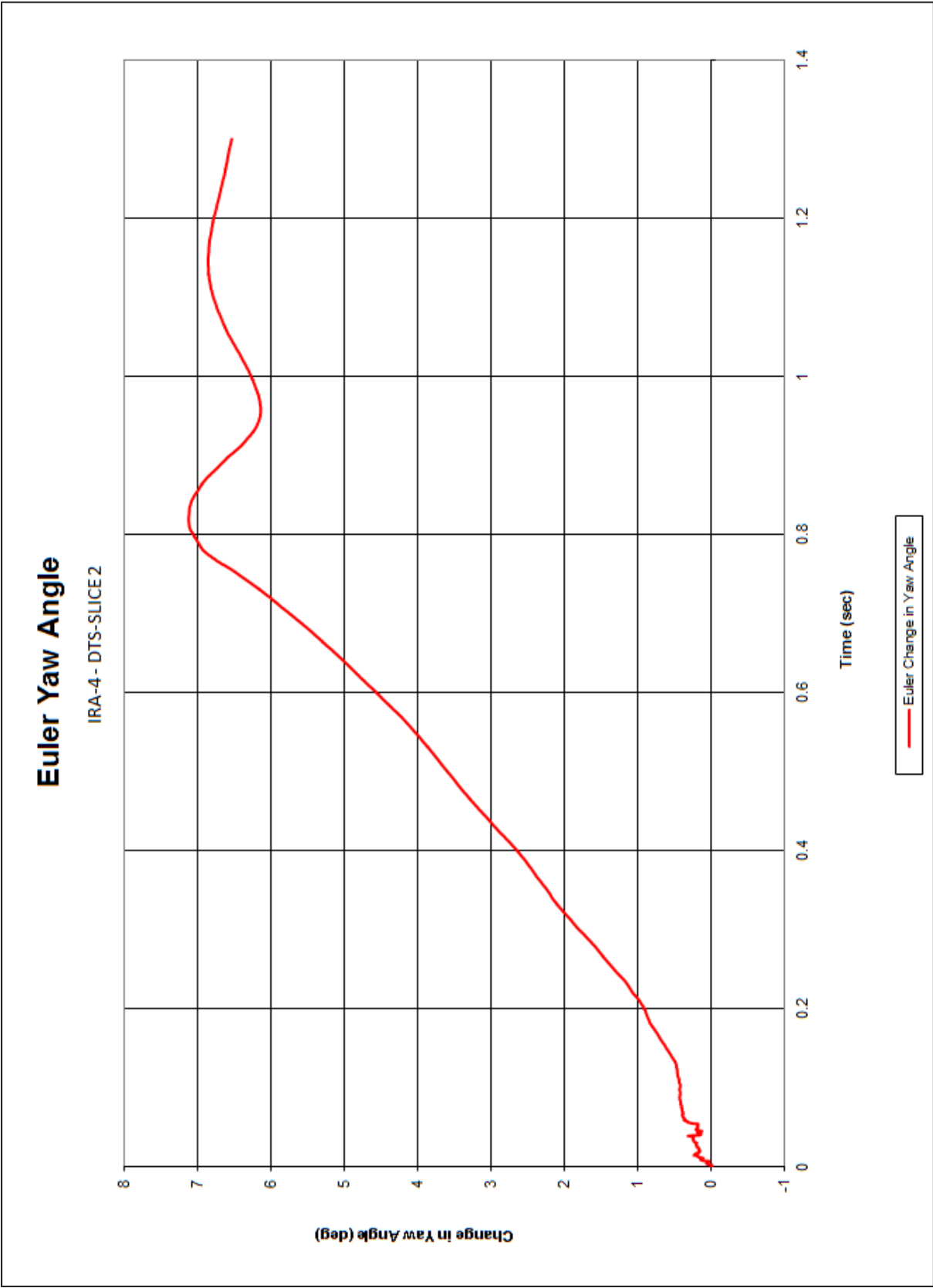


Figure E-34. Euler Yaw Angle (DTS-SLICE-2), Test No. IRA-4

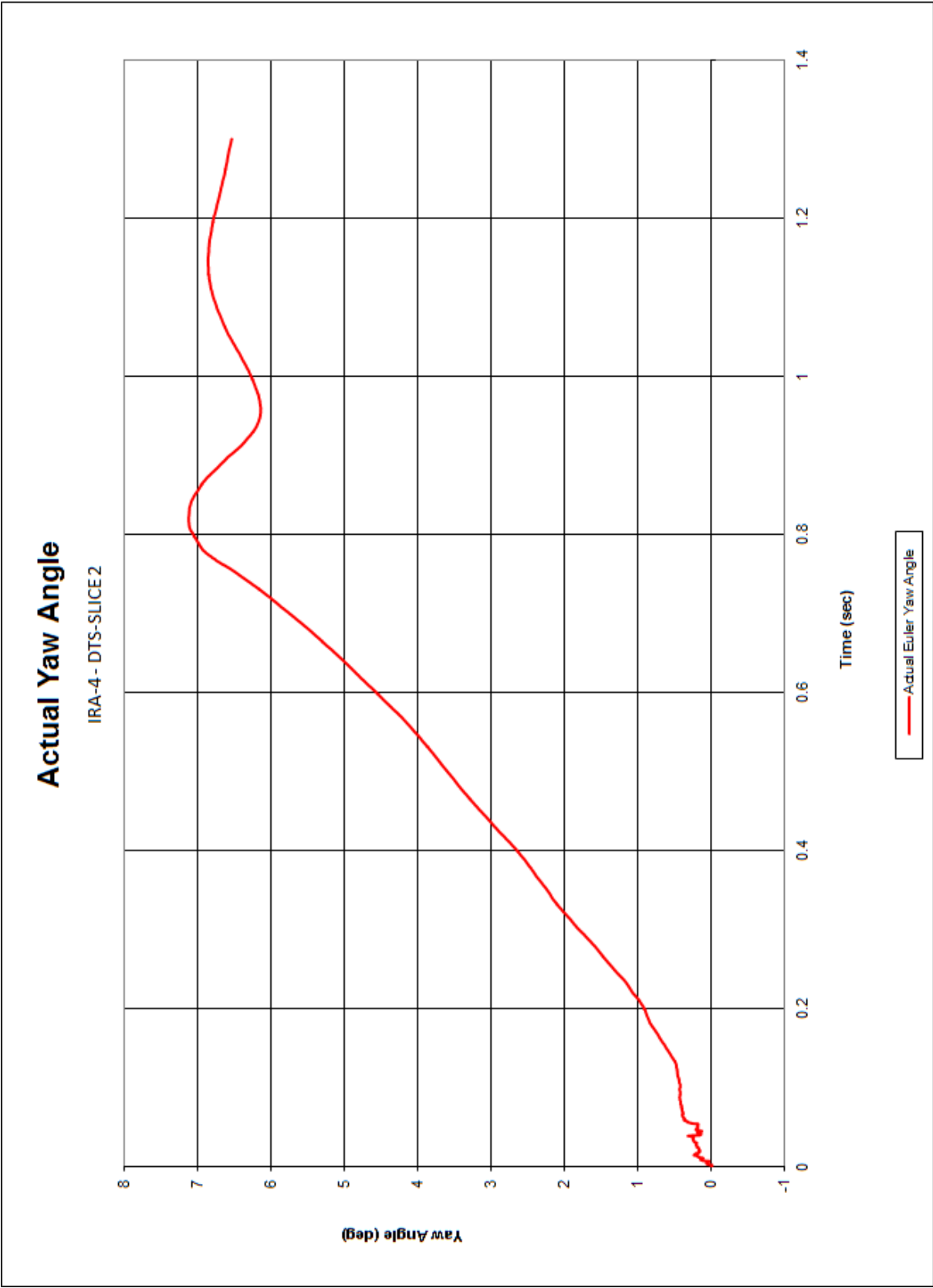


Figure E-35. Actual Yaw Angle (DTS-SLICE-2), Test No. IRA-4

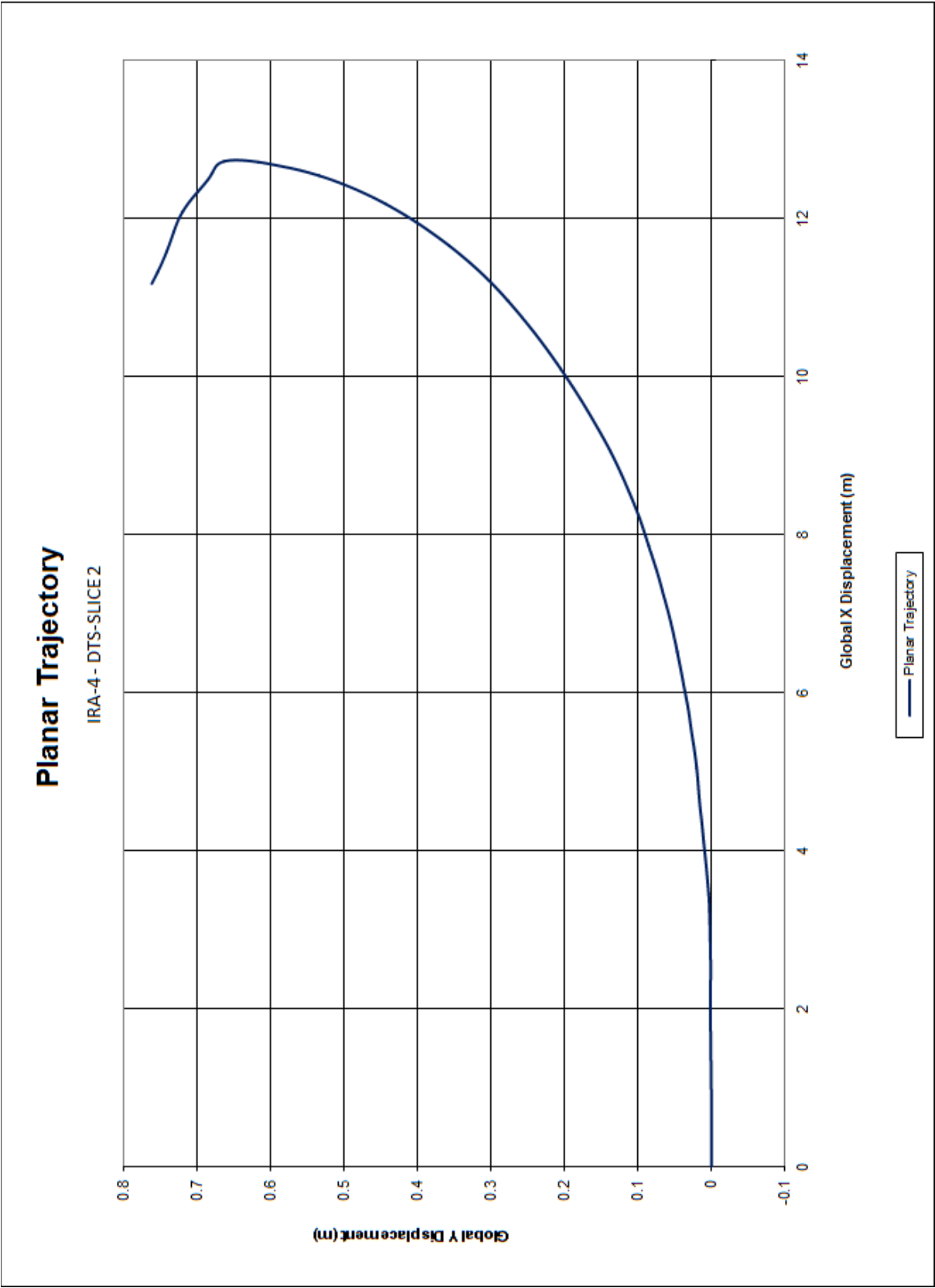


Figure E-36. Planar Trajectory (DTS-SLICE-2), Test No. IRA-4

Appendix F. Accelerometer Data Plots, Baseline Simulation

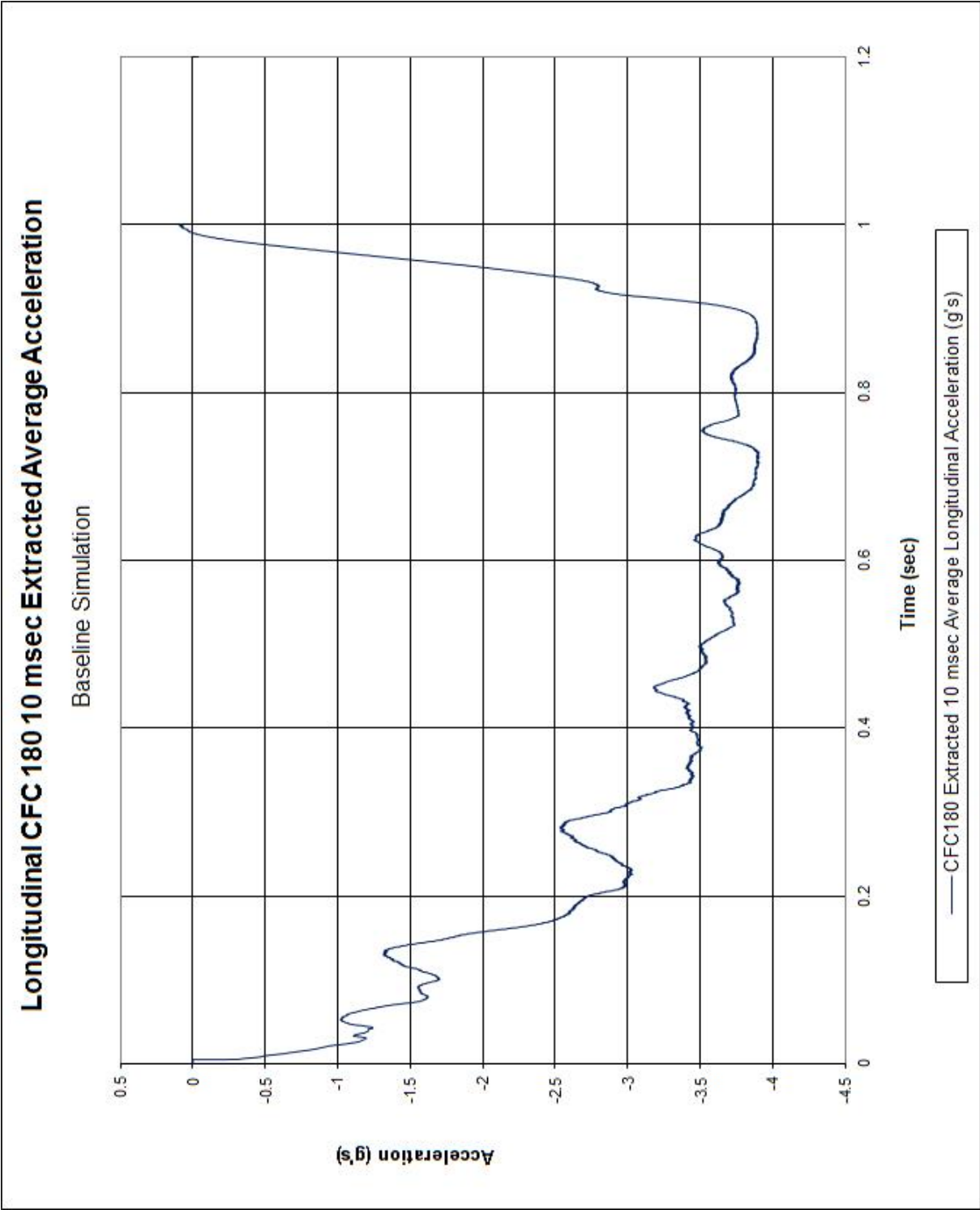


Figure F-1. 10-ms Average Longitudinal Deceleration, Baseline Simulation

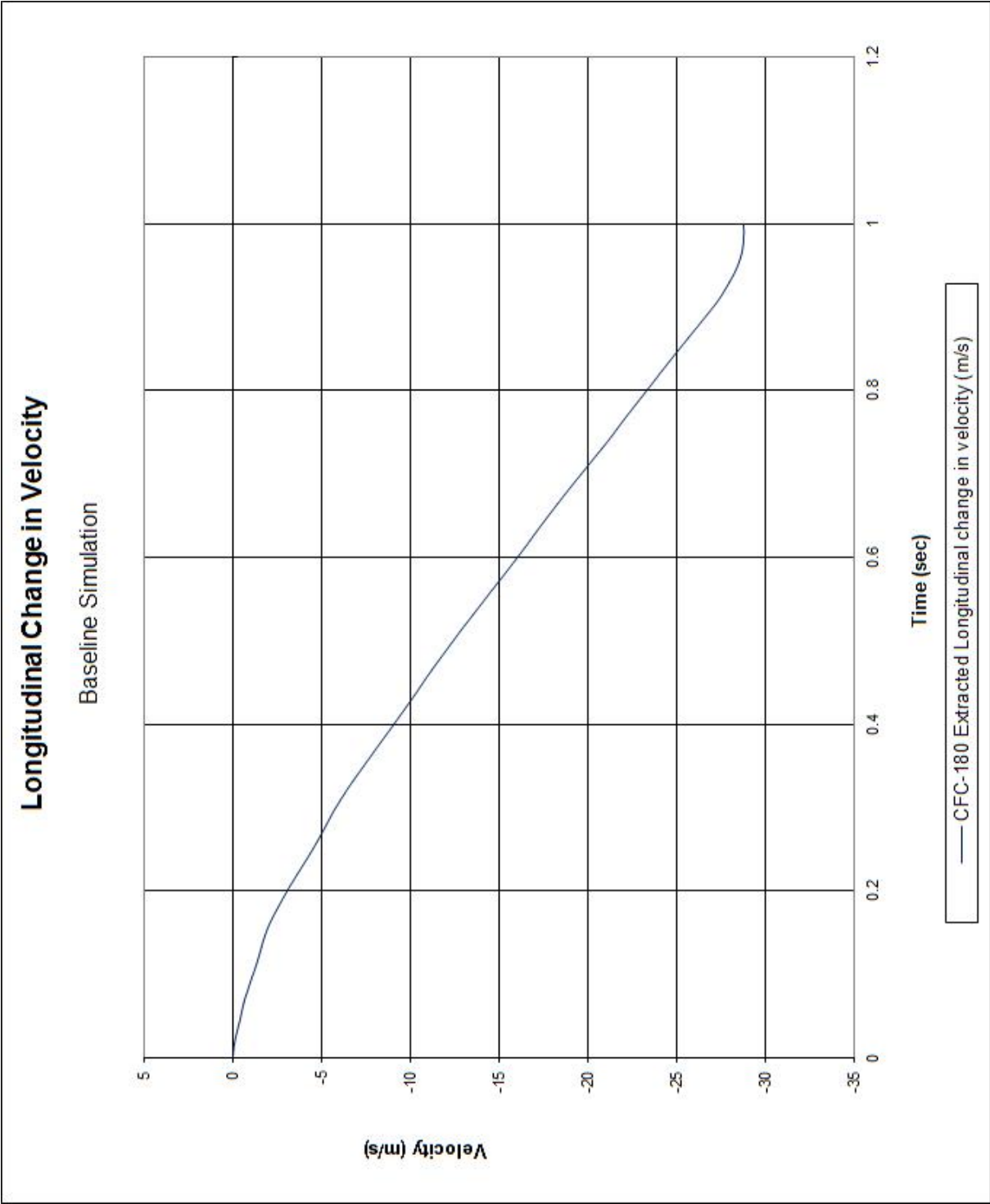


Figure F-2. Longitudinal Occupant Impact Velocity, Baseline Simulation

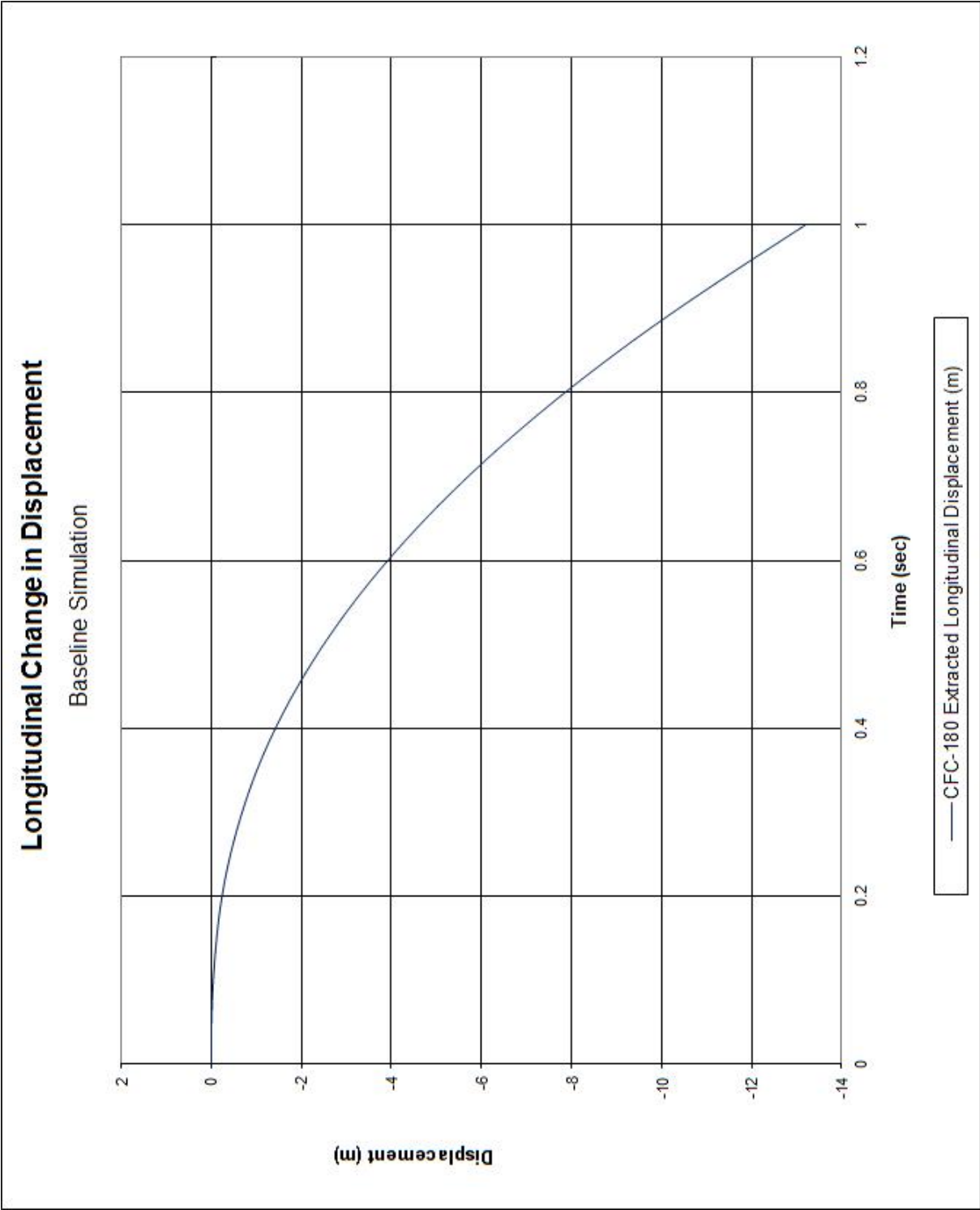


Figure F-3. Longitudinal Occupant Displacement, Baseline Simulation

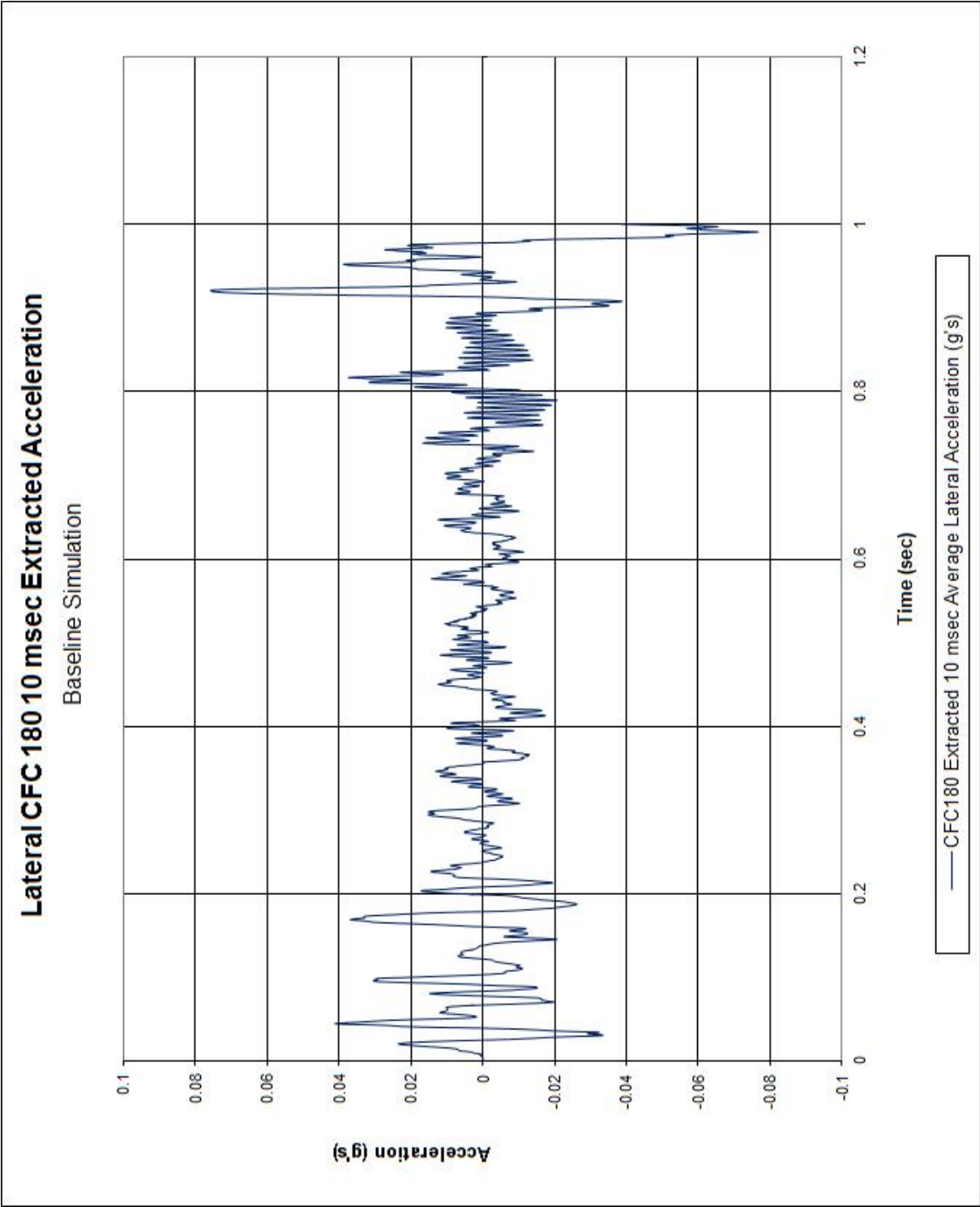


Figure F-4. 10-ms Average Lateral Deceleration, Baseline Simulation

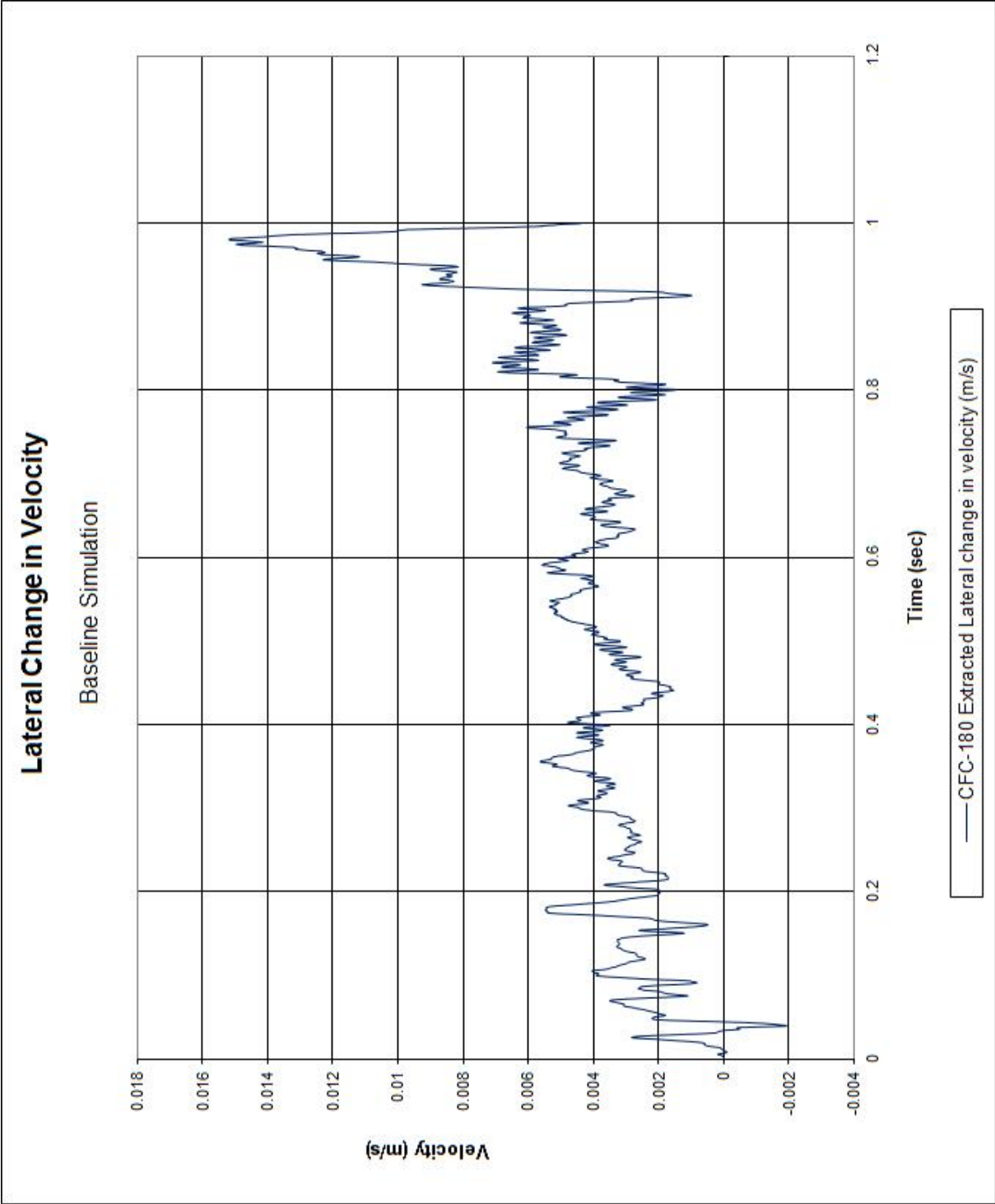


Figure F-5. Lateral Occupant Impact Velocity, Baseline Simulation

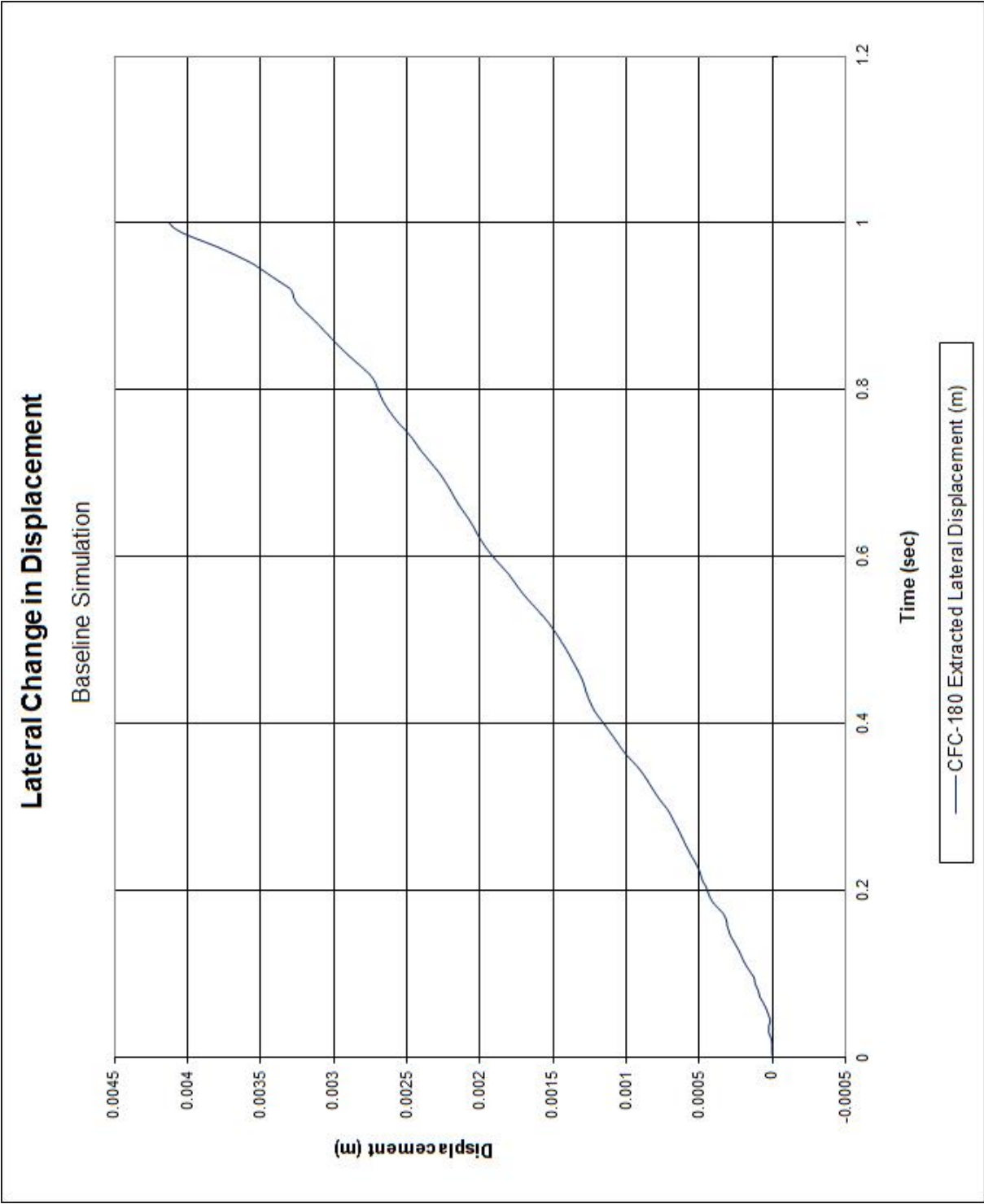


Figure F-6. Lateral Occupant Displacement, Baseline Simulation

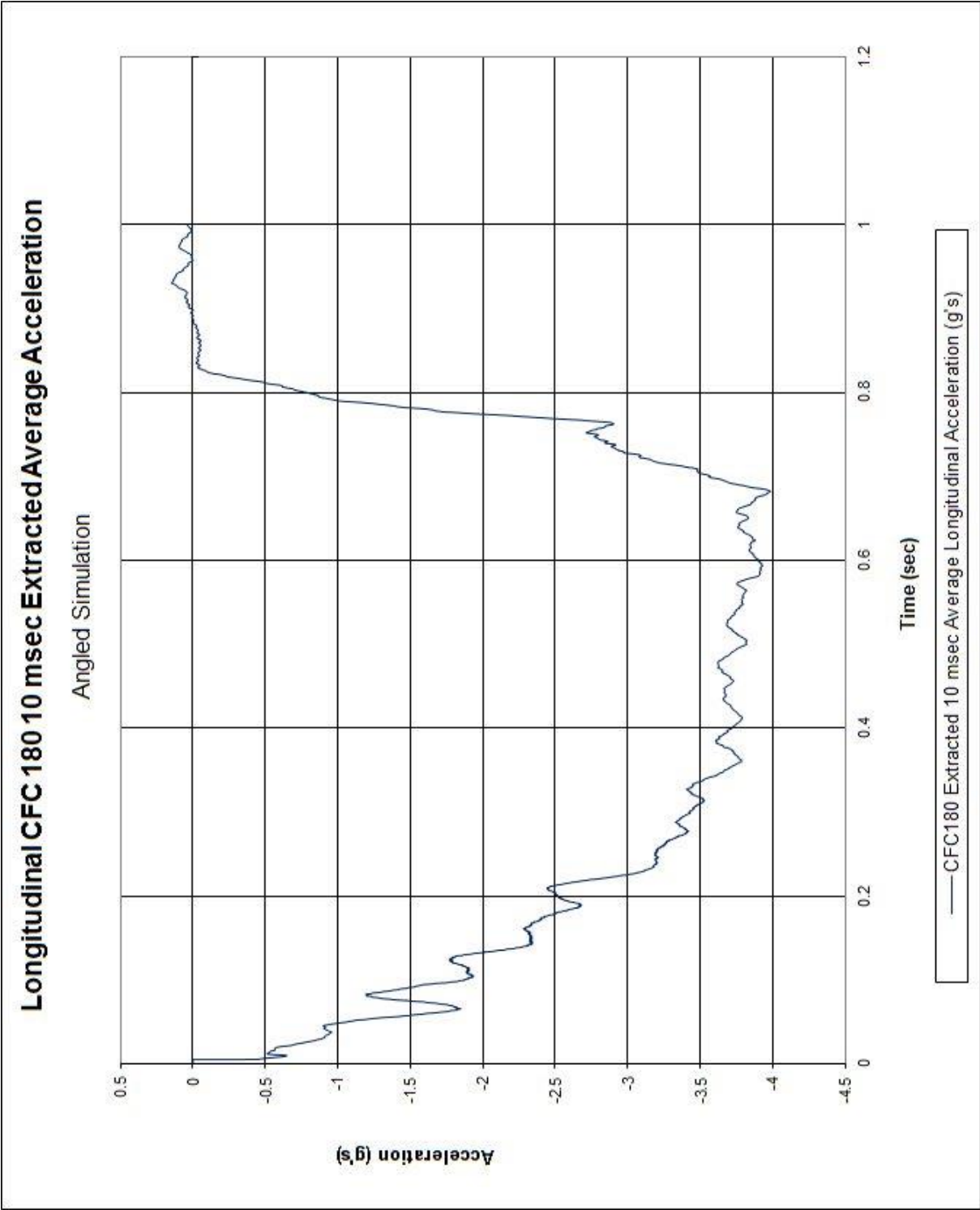


Figure F-7. 10-ms Average Longitudinal Deceleration, Angled Simulation

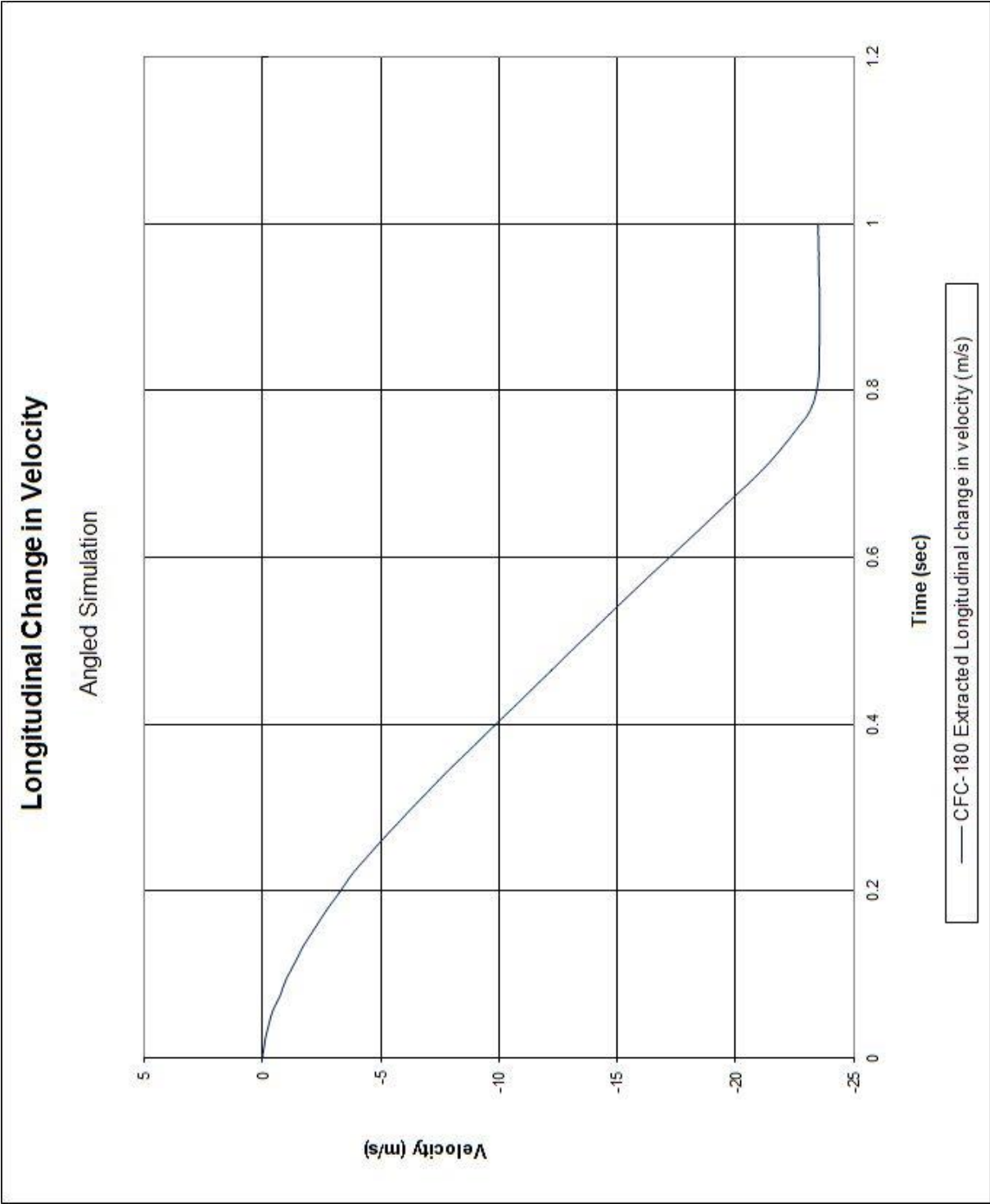


Figure F-8. Longitudinal Occupant Impact Velocity, Angled Simulation

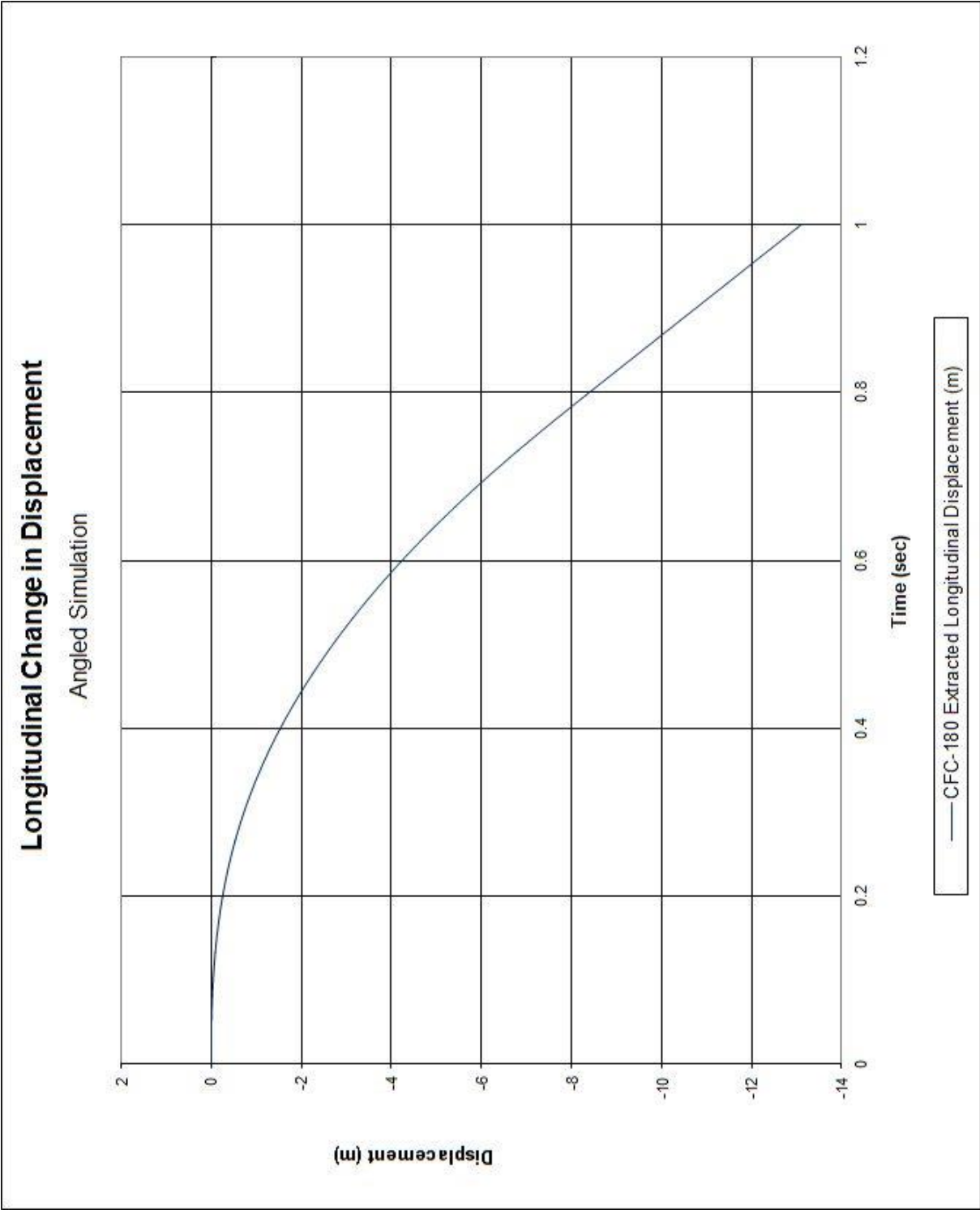


Figure F-9. Longitudinal Occupant Displacement, Angled Simulation

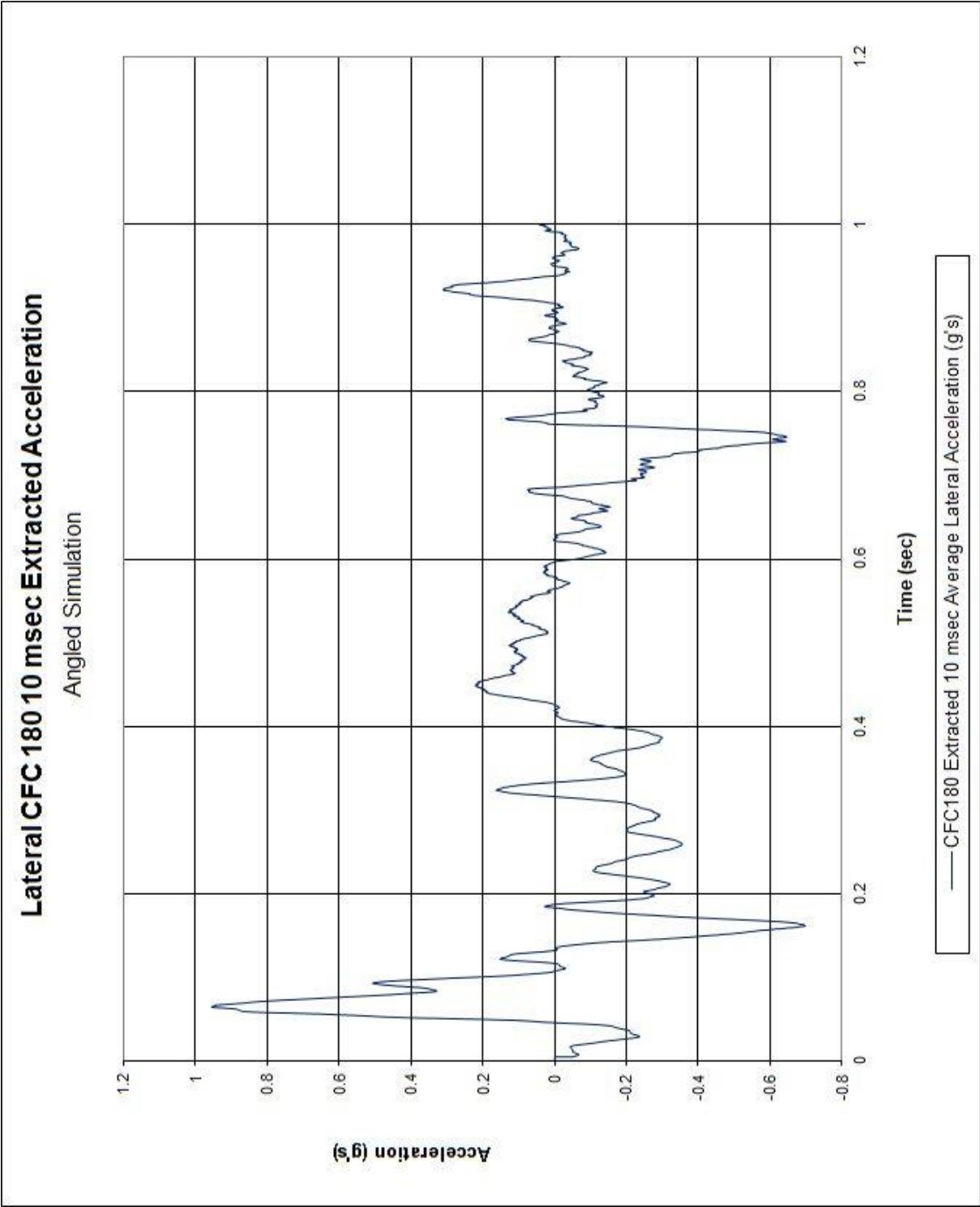


Figure F-10. 10-ms Average Lateral Deceleration, Angled Simulation

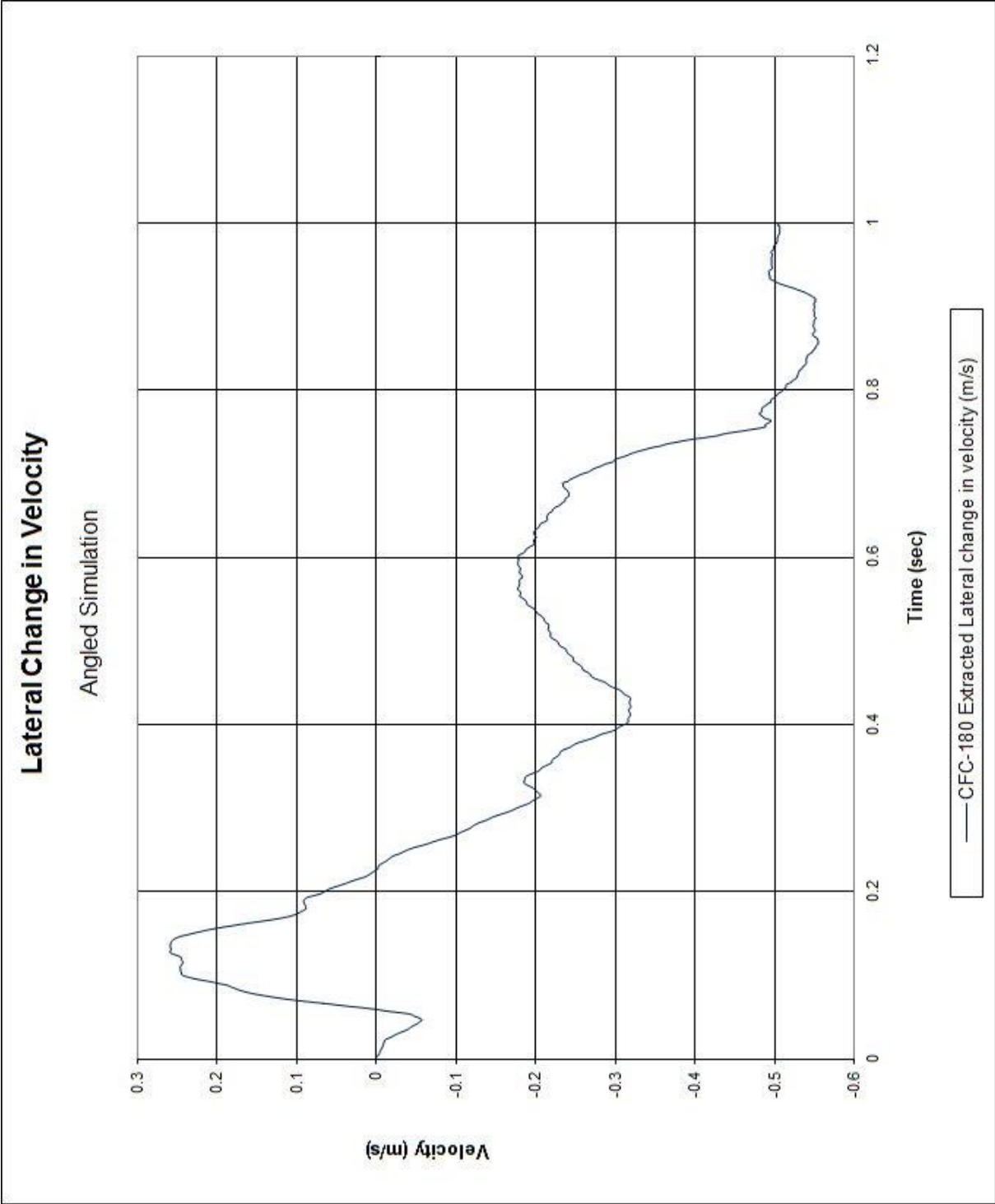


Figure F-11. Lateral Occupant Impact Velocity, Angled Simulation

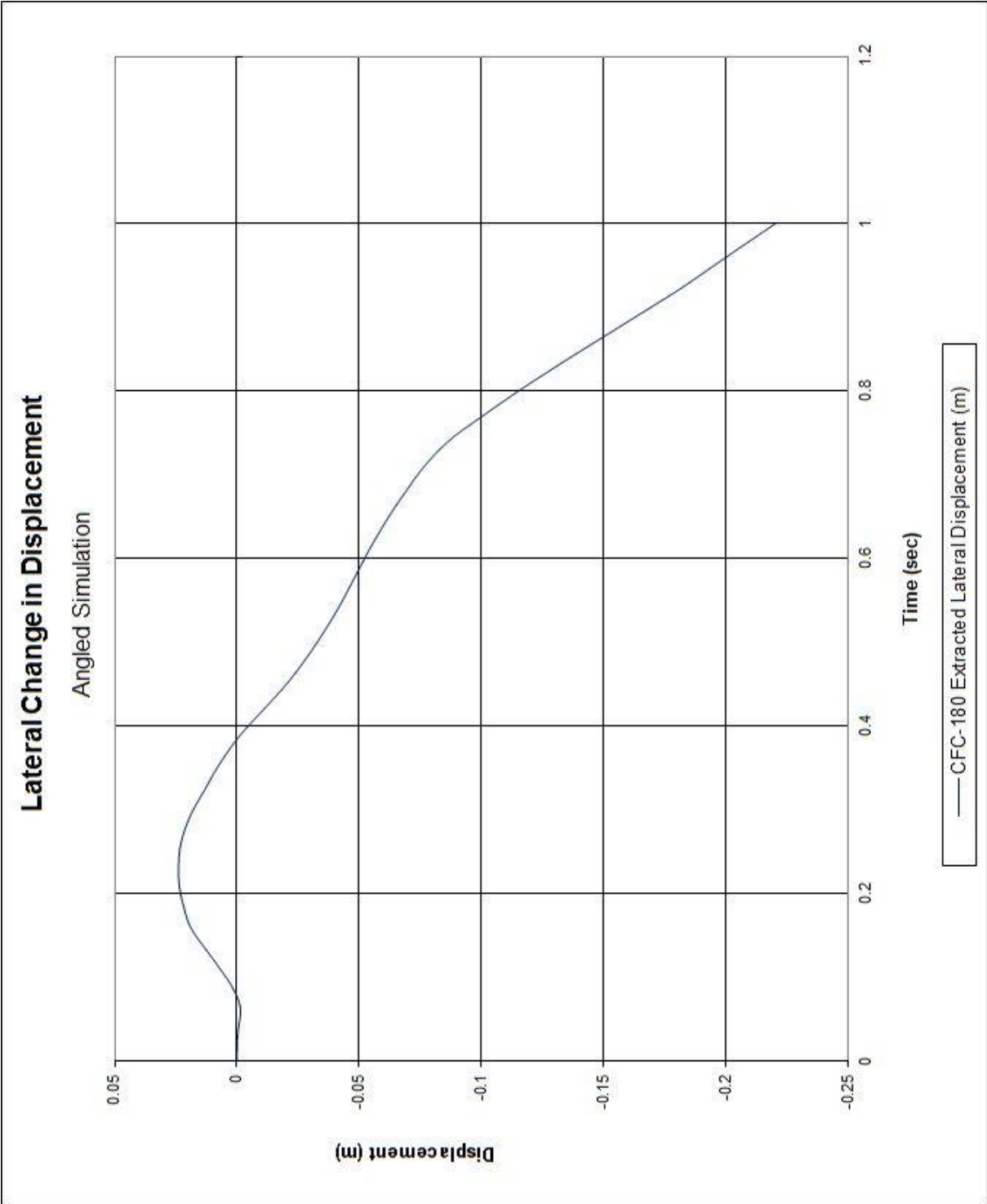


Figure F-12. Lateral Occupant Displacement, Angled Simulation

Appendix G. Potential Layout Analysis

V0	62.173	mph	Event (n)	Object	Mass (lb)	x (ft)
	91.187	ft/s	1	head	130	0
g	32.174	ft/s^2	2	Stage2	0	11
Mv	2425	lb	3	1	400	11.5
F_Stage1	20000	lb	4	2	700	14.5
F_Stage2	29000	lb	5	3	1400	17.5
a_Stage1	251.85	ft/s^2	6	4	1400	20.5
	7.83	g's	7	5	1400	23.5
a_Stage2	365.18	ft/s^2	8	6	1400	26.5
	11.35	g's	9	7	1400	29.5
X_max	13.1219	ft				

n	Me	x	x'	Vn	Vn'	t (n to n')	a_avg	a_et	a_net	a_tot
						91.19				
1	130.00	0.0	11.0	86.55	44.16	0.16832	4.27157	7.82754	0.00000	12.09910
2	0.00	11.0	11.5	44.16	39.81	0.01191	0.00000	11.34993	0.00000	11.34993
3	400.00	11.5	13.1	34.42	0.00	0.09425	2.07172	11.34993	0.00000	13.42165
4	700.00	14.5	13.1	0.00	0.00	0.00000	0.00000	0.00000	0.00000	0.00000
5	1400.00	17.5	13.1	0.00	0.00	0.00000	0.00000	0.00000	0.00000	0.00000
6	1400.00	20.5	13.1	0.00	0.00	0.00000	0.00000	0.00000	0.00000	0.00000
7	1400.00	23.5	13.1	0.00	0.00	0.00000	0.00000	0.00000	0.00000	0.00000
8	1400.00	26.5	13.1	0.00	0.00	0.00000	0.00000	0.00000	0.00000	0.00000
9	1400.00	29.5	13.1	0.00	0.00	0.00000	0.00000	0.00000	0.00000	0.00000

Figure G-1. Sand Barrel and End Terminal Impact, 1100C Small Car, Full Bullnose Crush Force

V0	62.173	mph	Event (n)	Object	Mass (lb)	x (ft)
	91.187	ft/s	1	head	130	0
g	32.174	ft/s^2	2	Stage2	0	11
Mv	5000	lb	3	1	400	11.5
F_Stage1	20000	lb	4	2	700	14.5
F_Stage2	29000	lb	5	3	1400	17.5
a_Stage1	125.43	ft/s^2	6	4	1400	20.5
	3.90	g's	7	5	1400	23.5
a_Stage2	181.88	ft/s^2	8	6	1400	26.5
	5.65	g's	9	7	1400	29.5
X_max	19.8194	ft				

n	Me	x	x'	Vn	Vn'	t (n to n')	a_avg	a_et	a_net	a_tot
						91.19				
1	130.00	0.0	11.0	88.88	71.69	0.13702	2.15533	3.89851	0.00000	6.05384
2	0.00	11.0	11.5	71.69	70.41	0.00704	0.00000	5.65284	0.00000	5.65284
3	400.00	11.5	14.5	65.32	56.35	0.04932	3.58067	5.65284	0.00000	9.23351
4	700.00	14.5	17.5	49.58	36.97	0.06932	3.71234	5.65284	0.00000	9.36518
5	1400.00	17.5	19.8	29.05	0.00	0.15970	2.71095	5.65284	0.00000	8.36379
6	1400.00	20.5	19.8	0.00	0.00	0.00000	0.00000	0.00000	0.00000	0.00000
7	1400.00	23.5	19.8	0.00	0.00	0.00000	0.00000	0.00000	0.00000	0.00000
8	1400.00	26.5	19.8	0.00	0.00	0.00000	0.00000	0.00000	0.00000	0.00000
9	1400.00	29.5	19.8	0.00	0.00	0.00000	0.00000	0.00000	0.00000	0.00000

Figure G-2. Sand Barrel and End Terminal Impact, 2270P Truck, Full Bullnose Crush Force

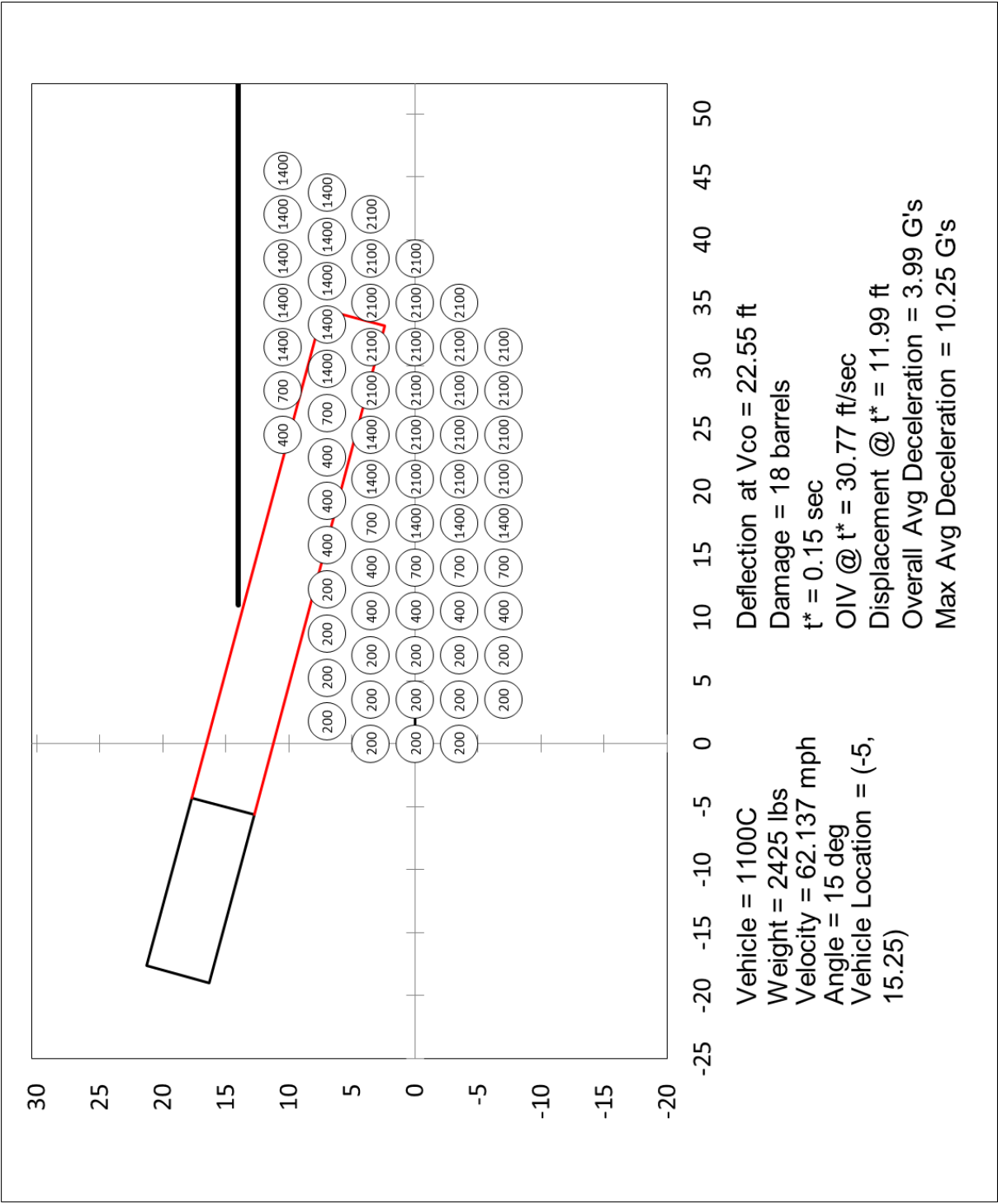


Figure G-3. Standard-Spacing Sand Barrel Array, 1100C, Case 1 Summary

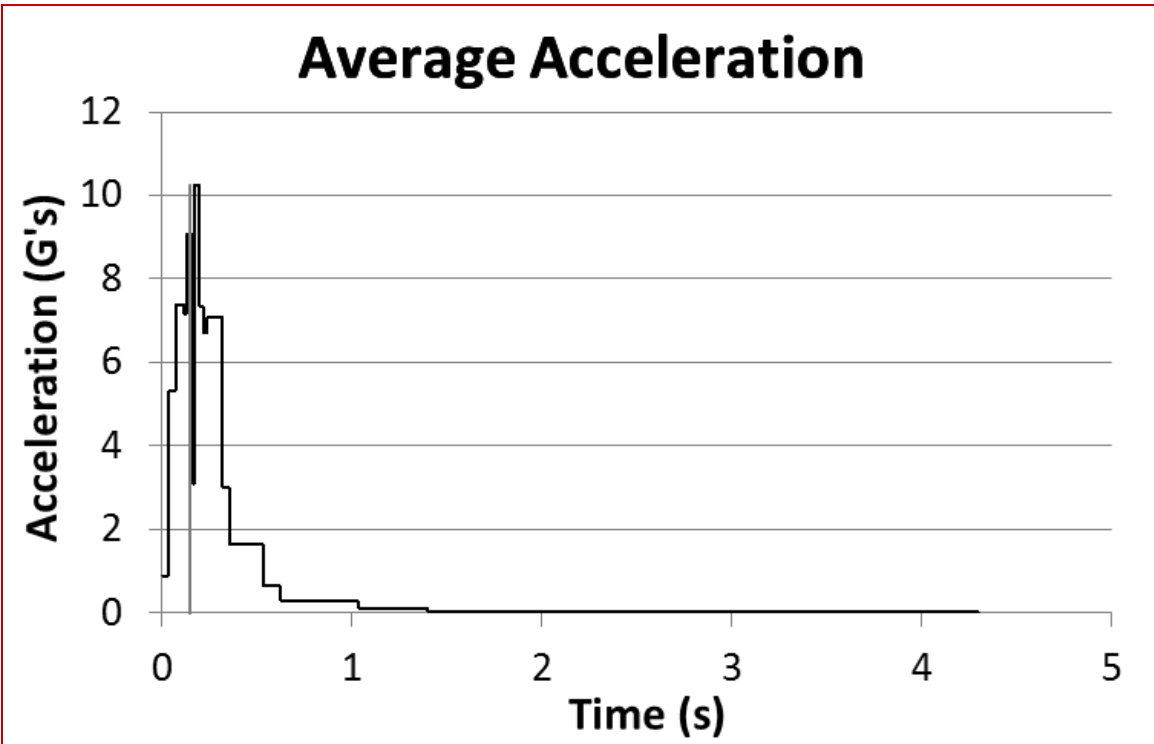
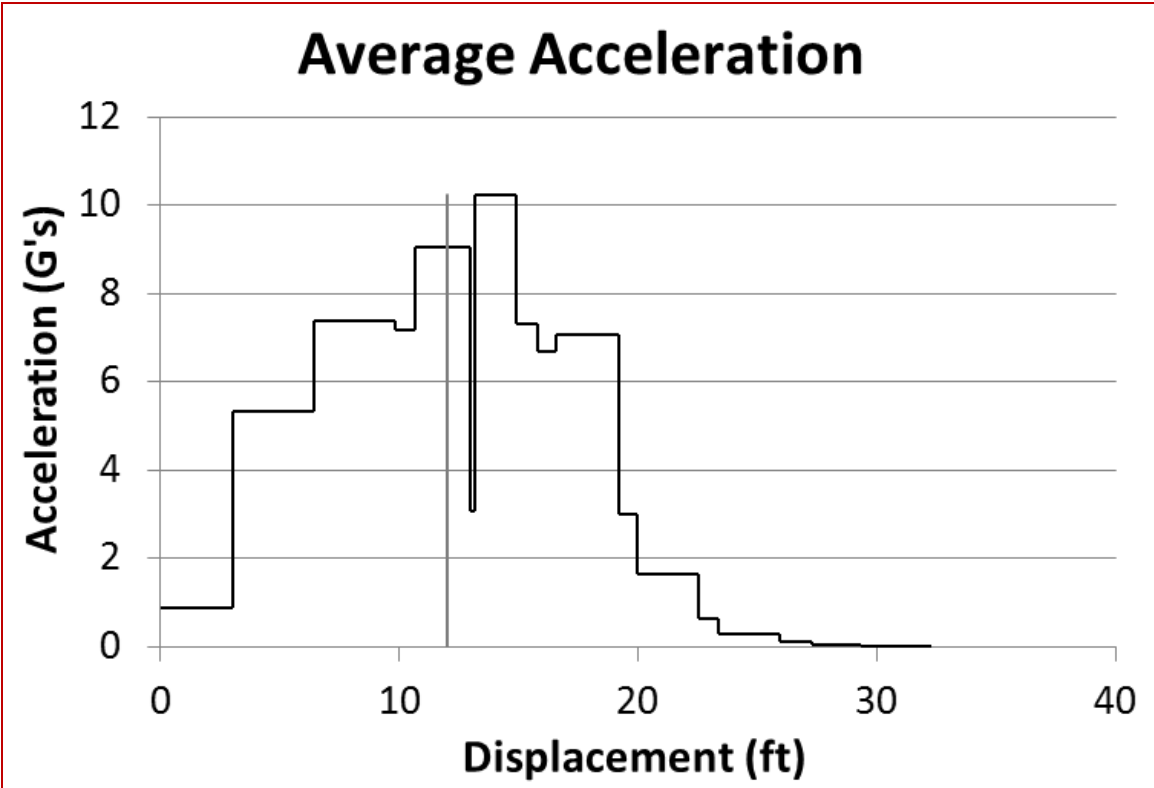


Figure G-4. Standard-Spacing Sand Barrel Array, 1100C, Case 1 Acceleration

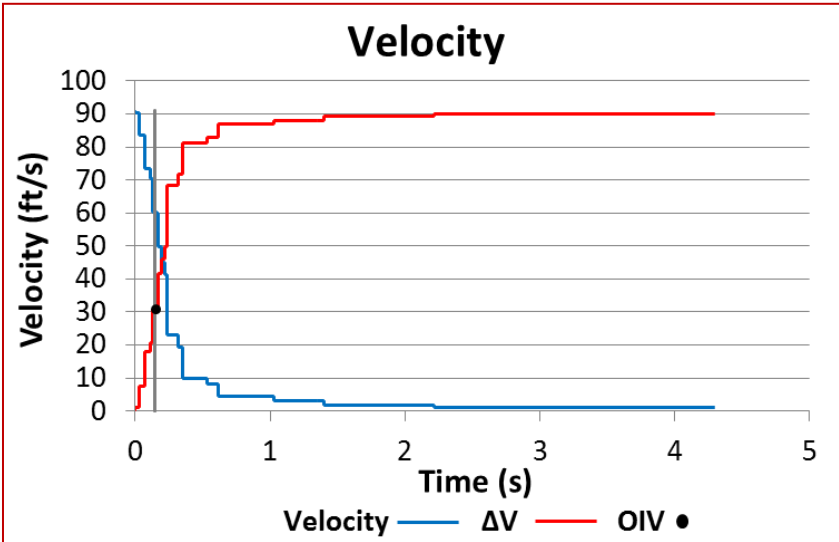
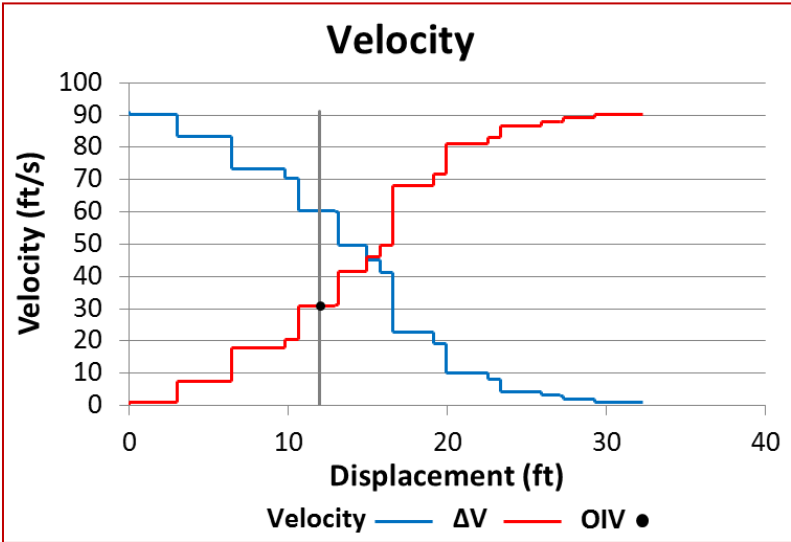
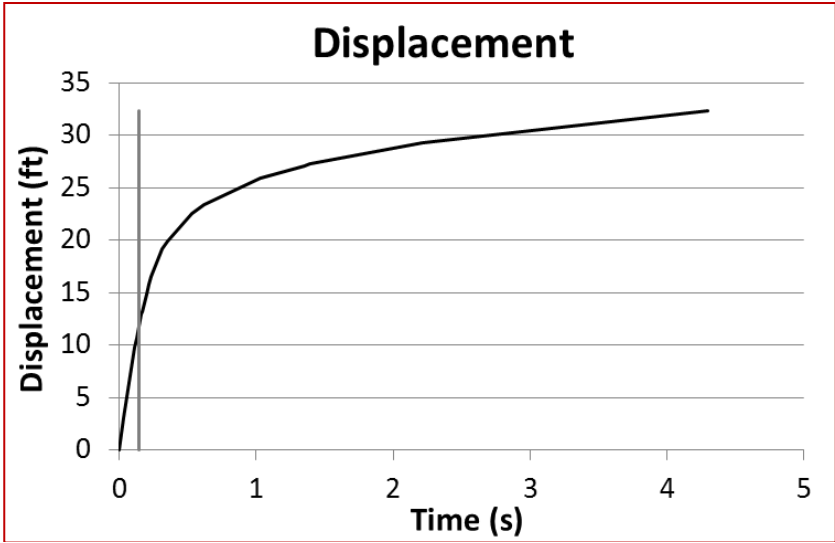


Figure G-5. Standard-Spacing Sand Barrel Array, 1100C, Case 1 Displacement and Velocity

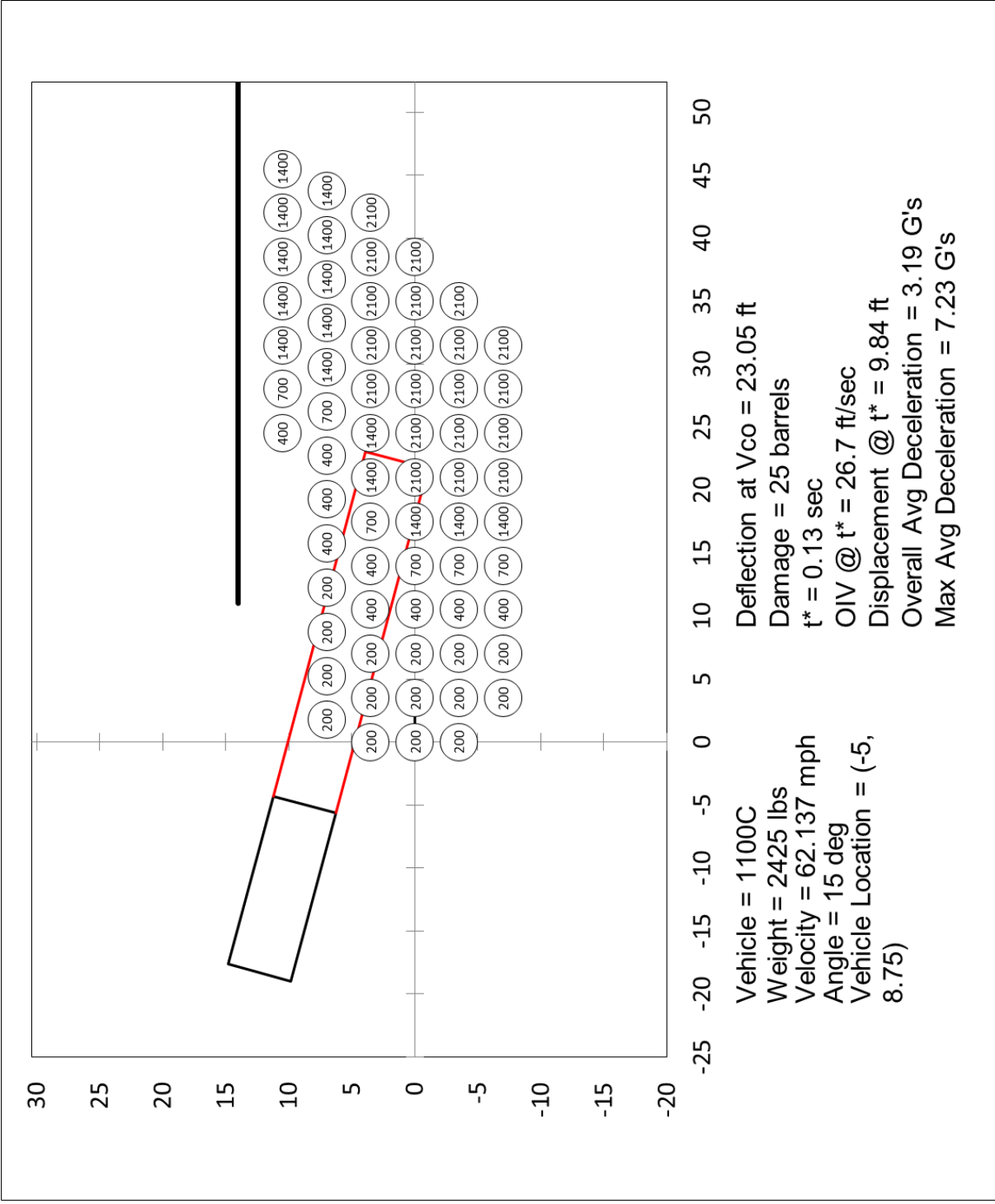


Figure G-6. Standard-Spacing Sand Barrel Array, 1100C, Case 2 Summary

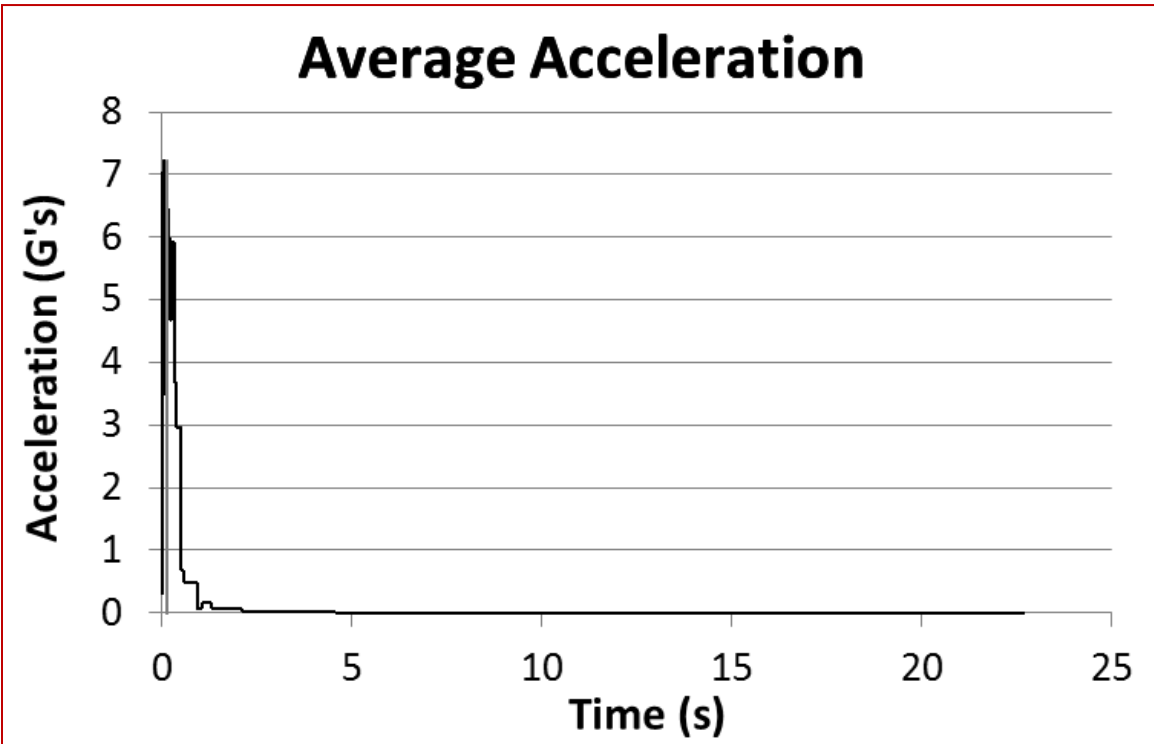
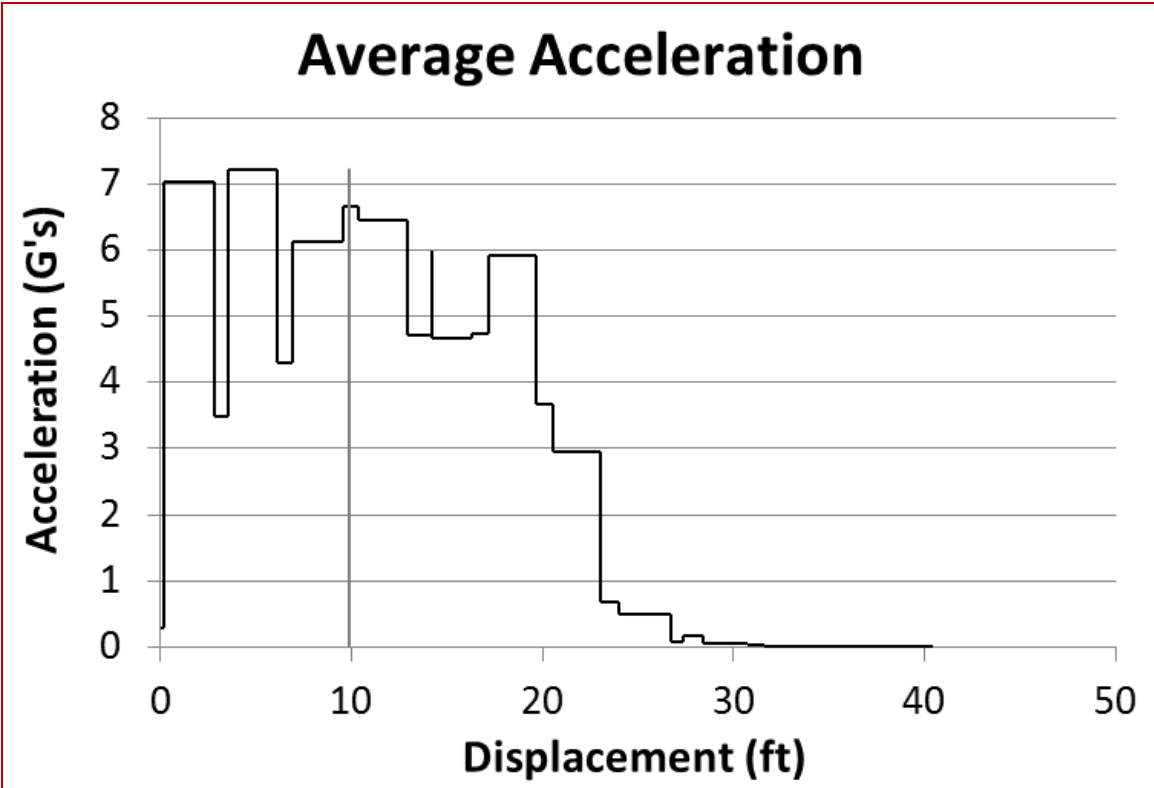


Figure G-7. Standard-Spacing Sand Barrel Array, 1100C, Case 2 Acceleration

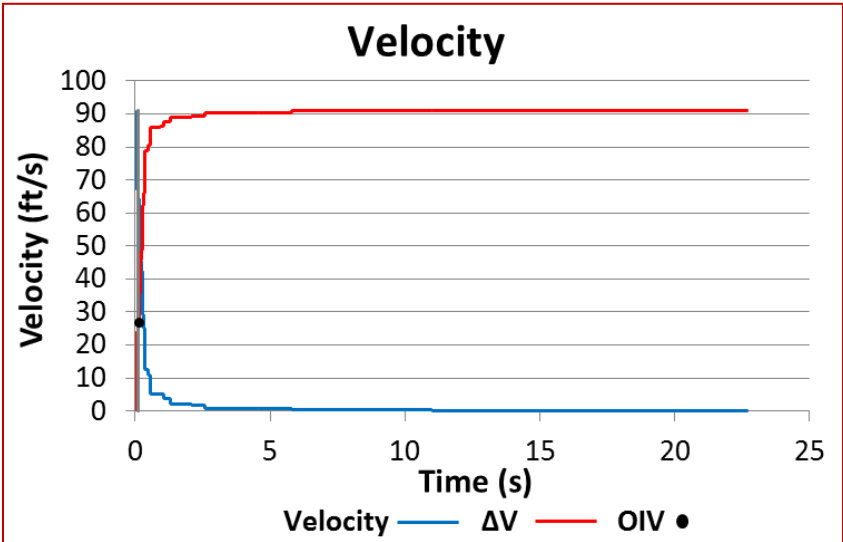
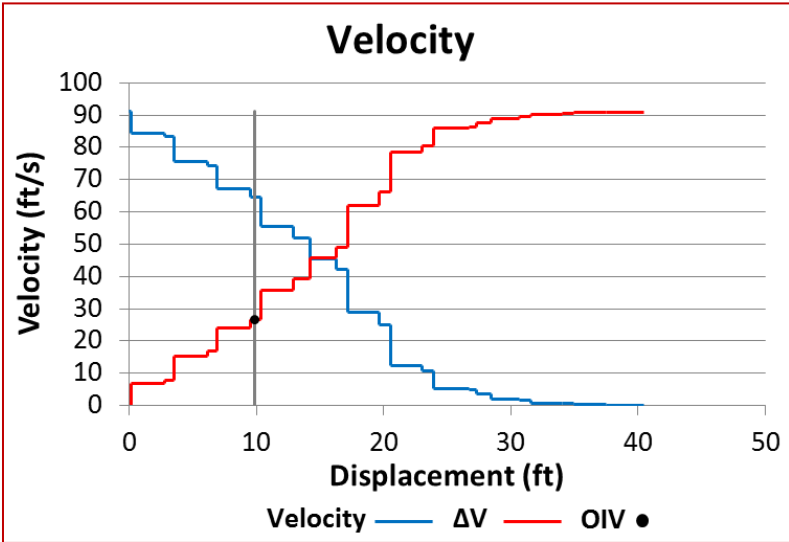
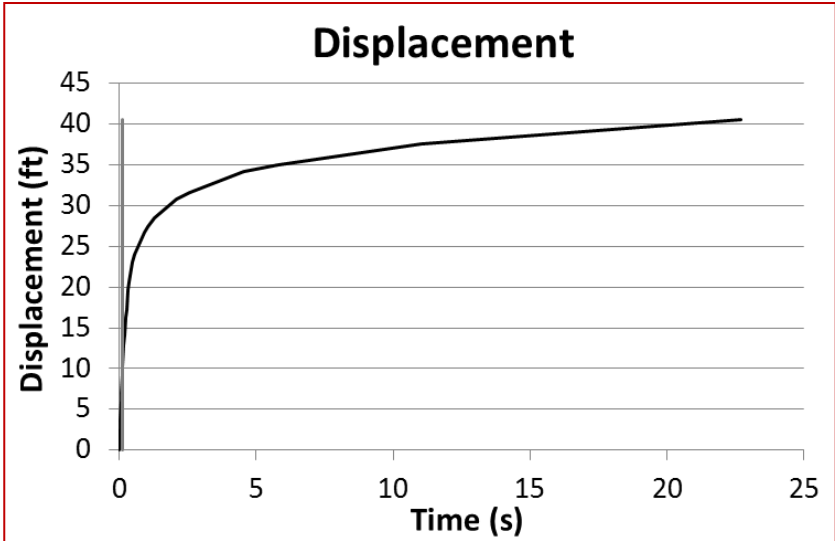


Figure G-8. Standard-Spacing Sand Barrel Array, 1100C, Case 2 Displacement and Velocity

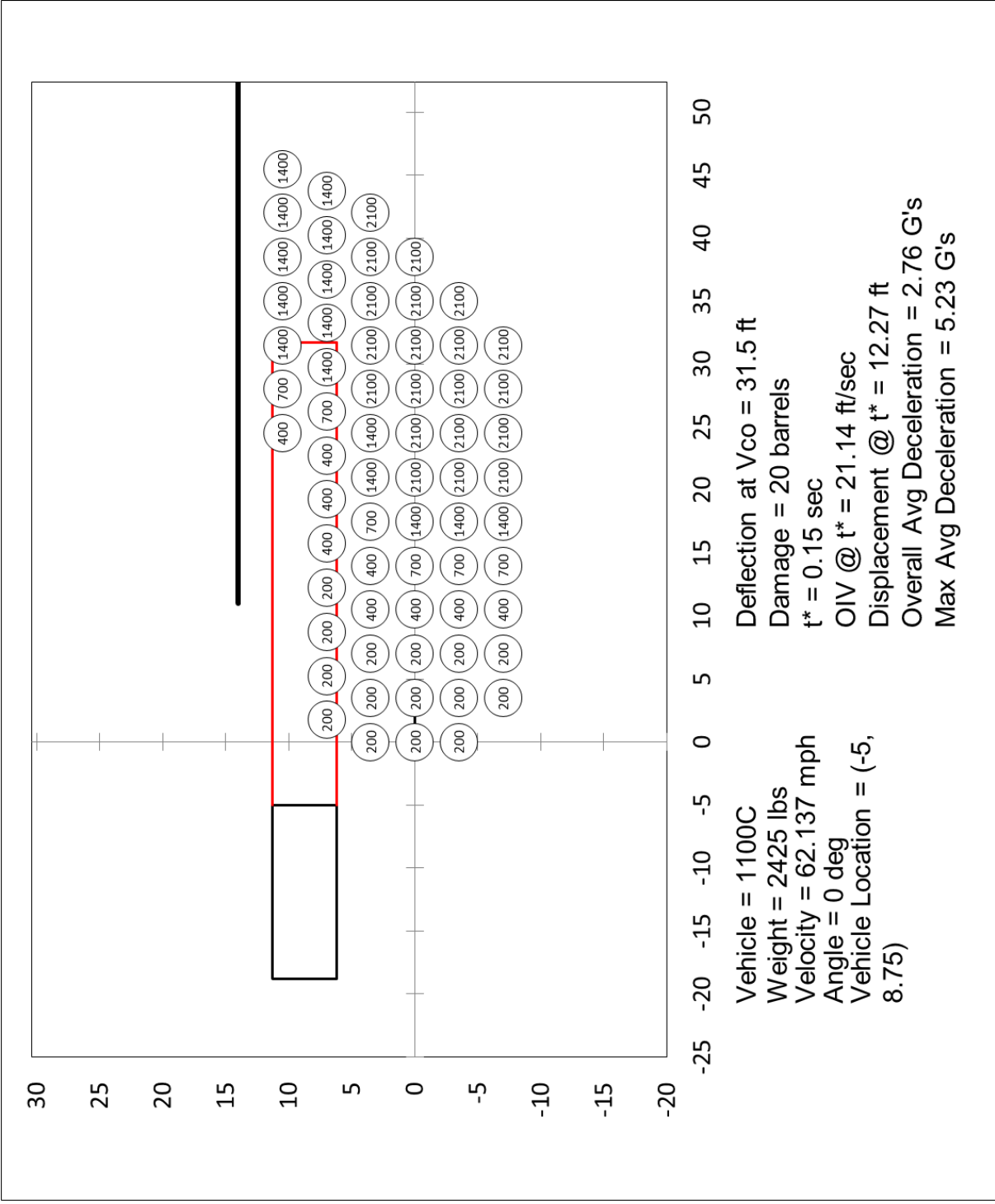


Figure G-9. Standard-Spacing Sand Barrel Array, 1100C, Case 3 Summary

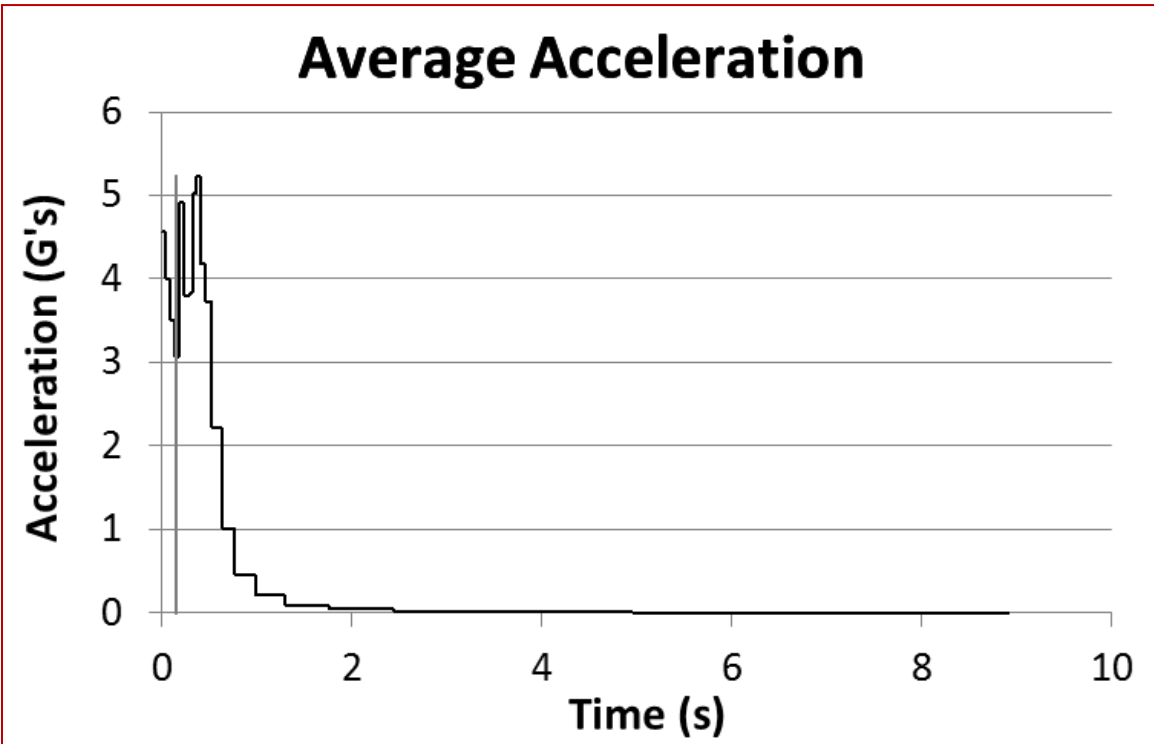
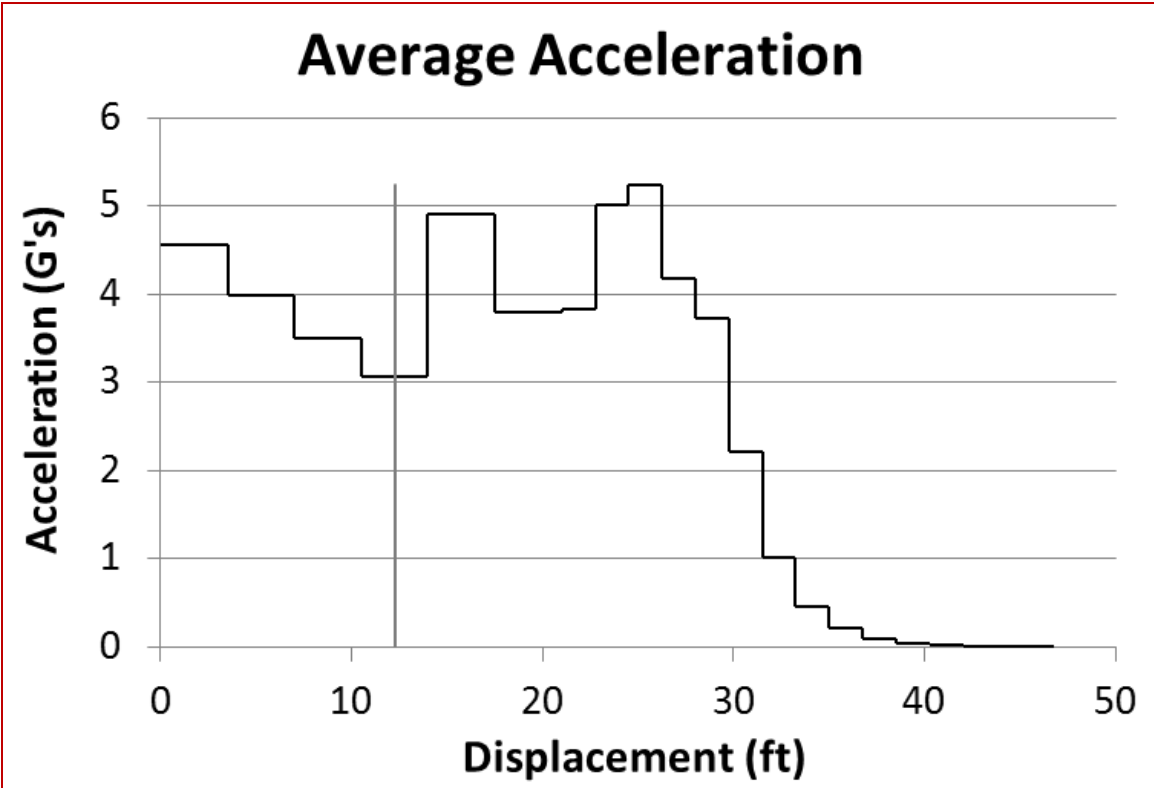


Figure G-10. Standard-Spacing Sand Barrel Array, 1100C, Case 3 Acceleration

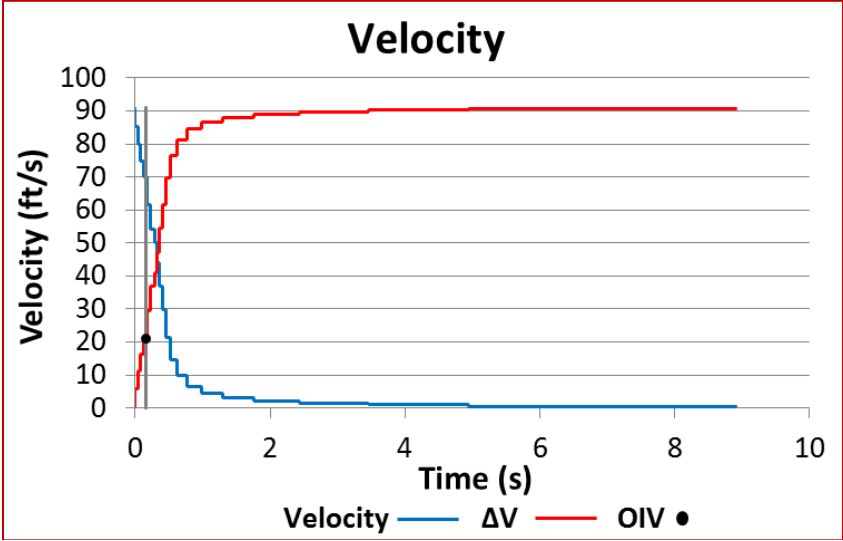
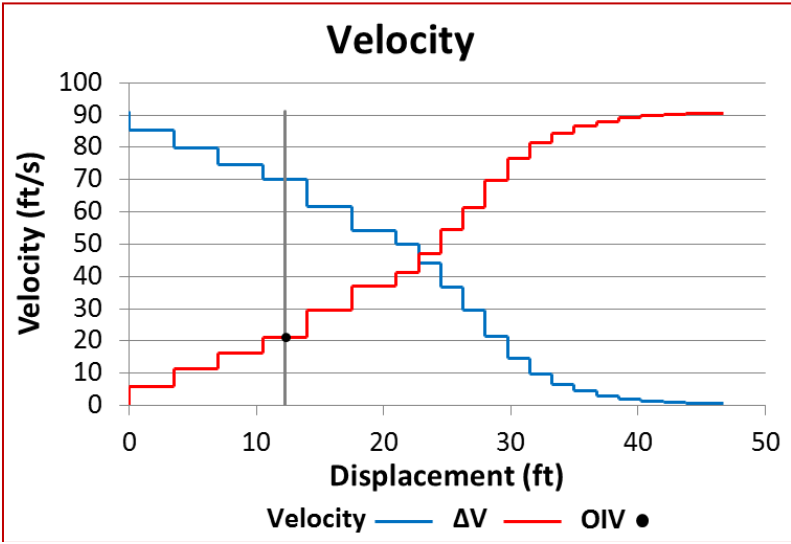
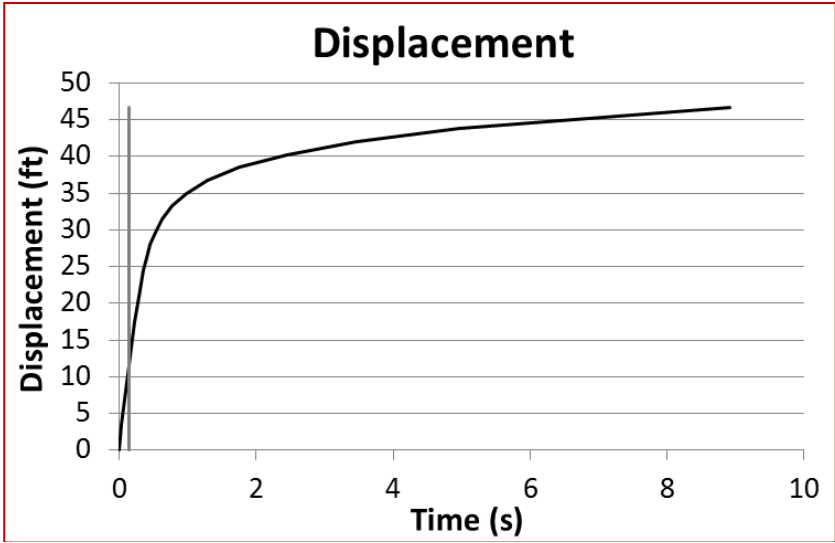


Figure G-11. Standard-Spacing Sand Barrel Array, 1100C, Case 3 Displacement and Velocity

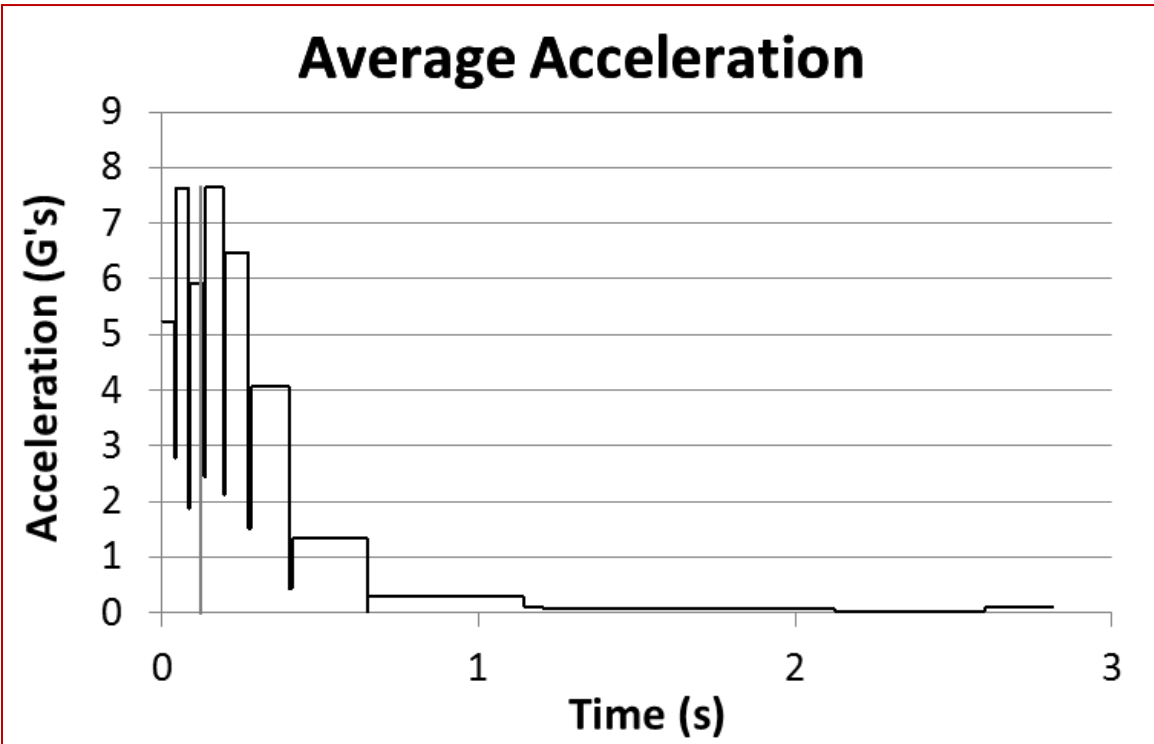
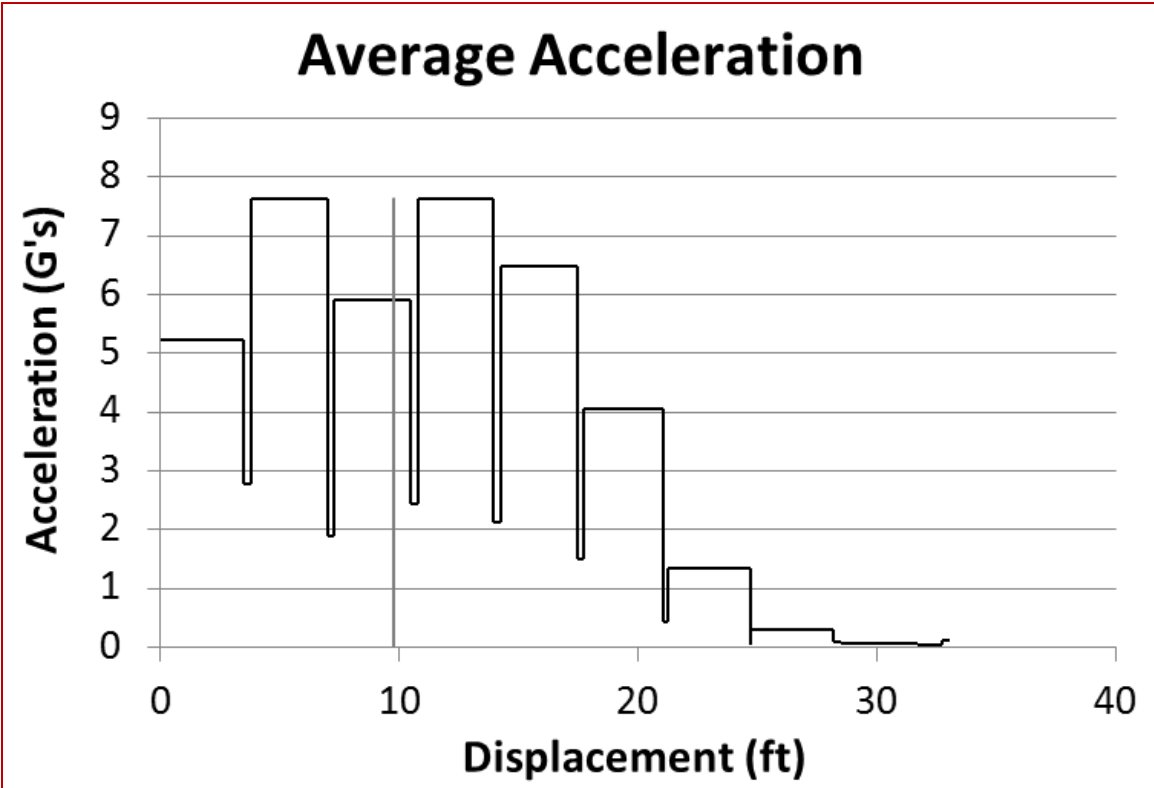


Figure G-13. Standard-Spacing Sand Barrel Array, 1100C, Case 4 Acceleration

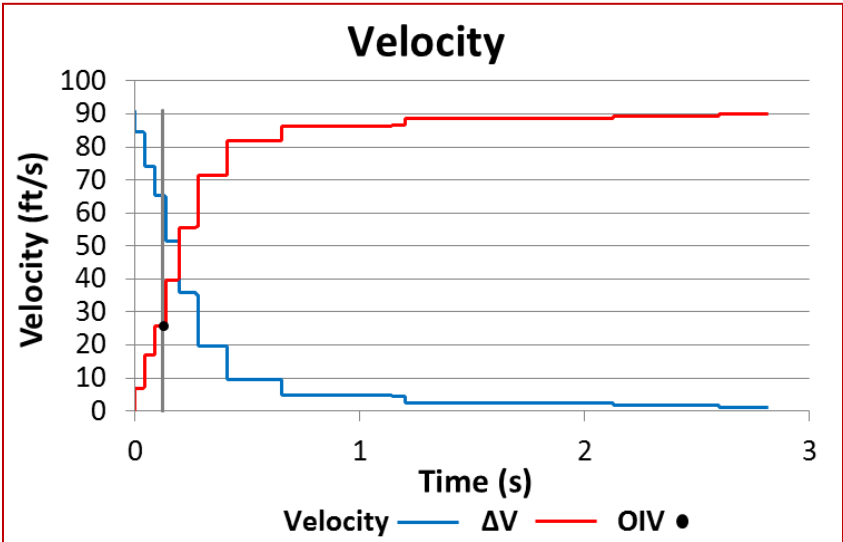
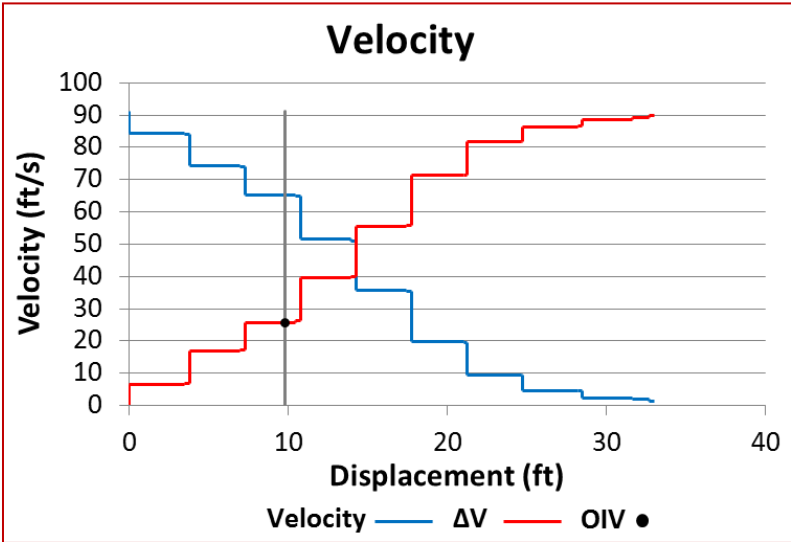
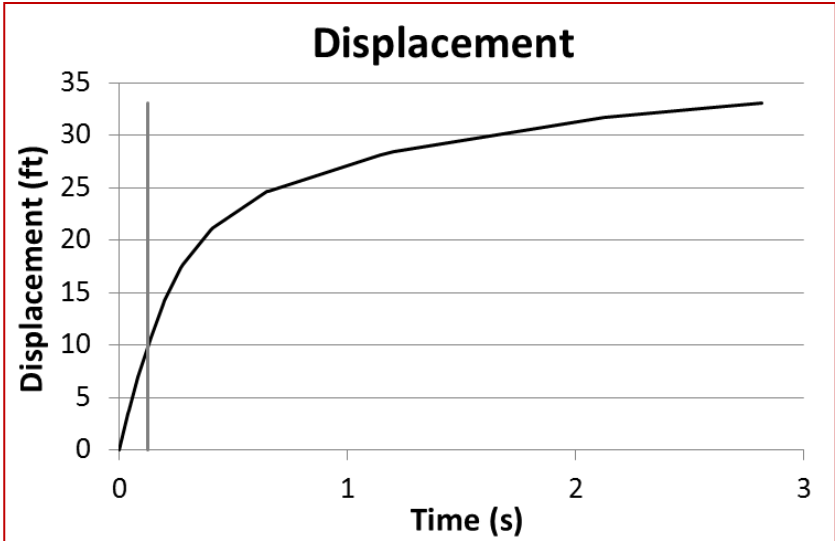


Figure G-14. Standard-Spacing Sand Barrel Array, 1100C, Case 4 Displacement and Velocity

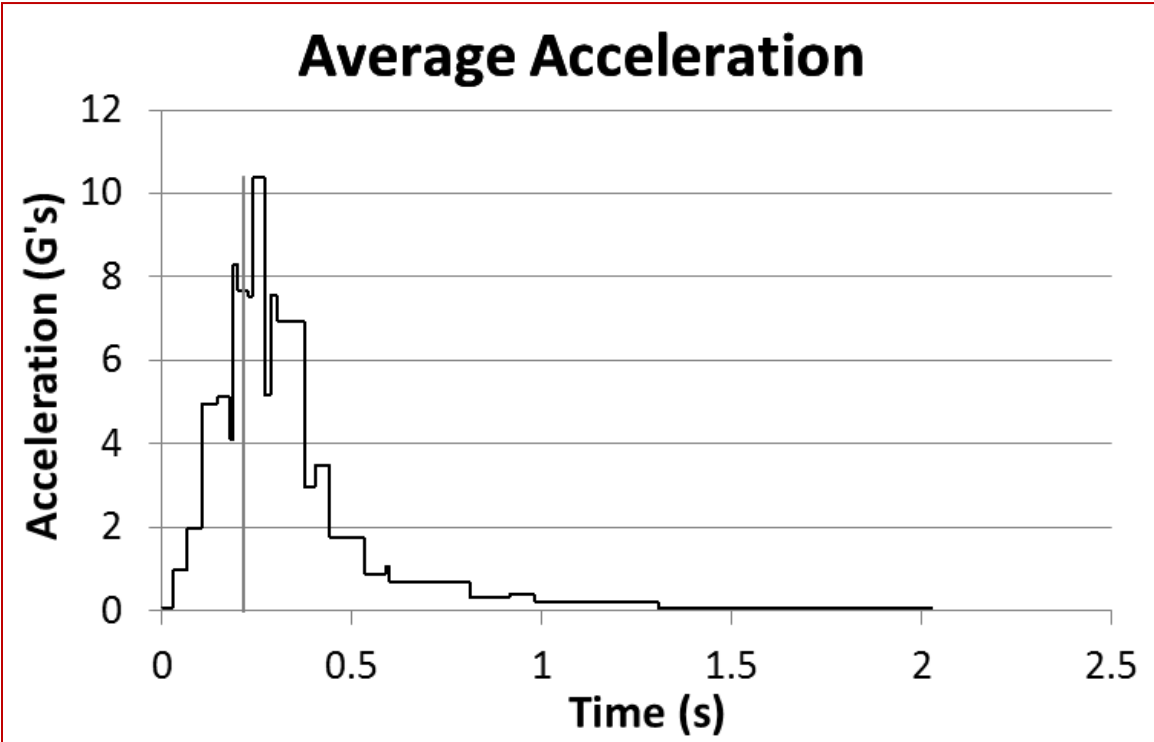
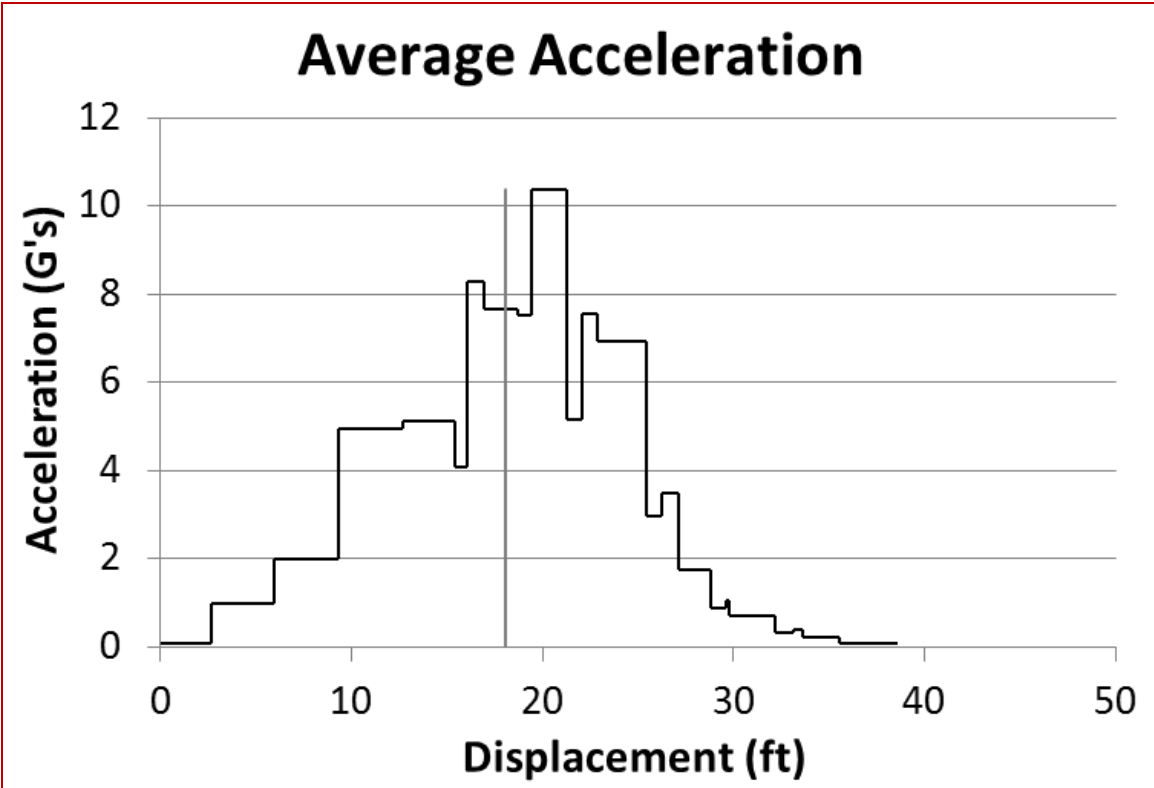


Figure G-16. Standard-Spacing Sand Barrel Array, 2270P, Case 1 Acceleration

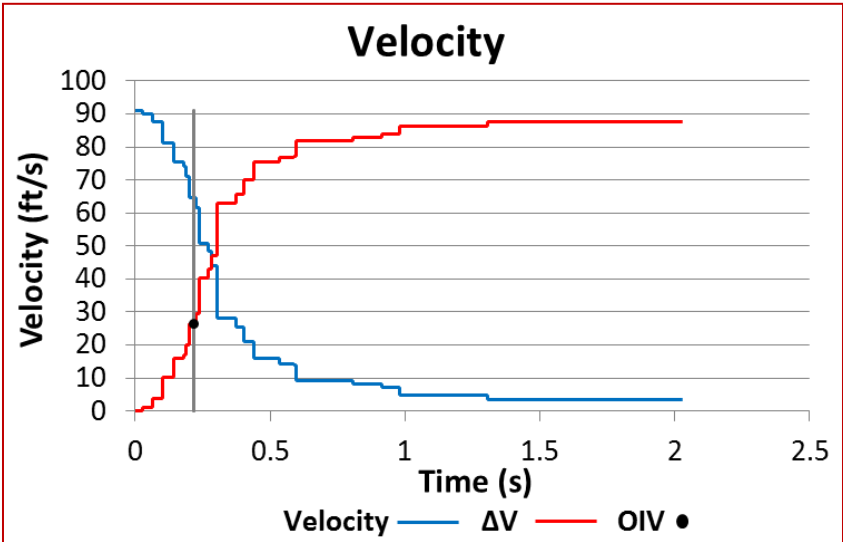
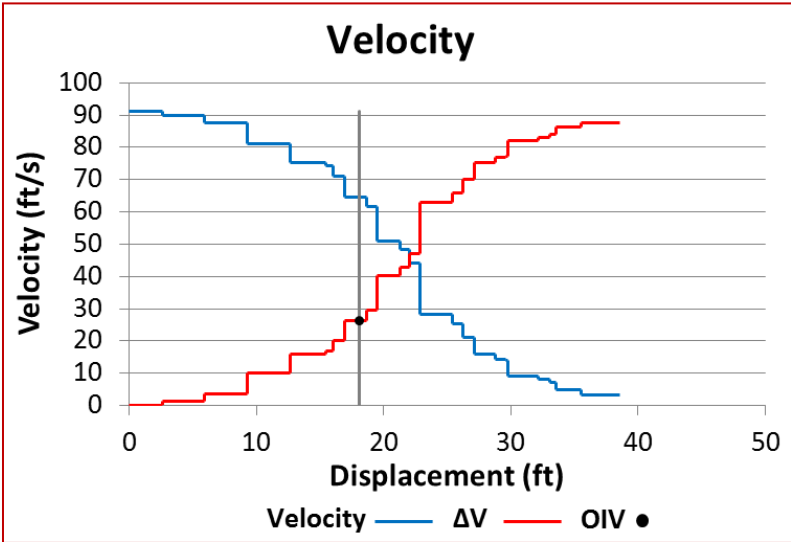
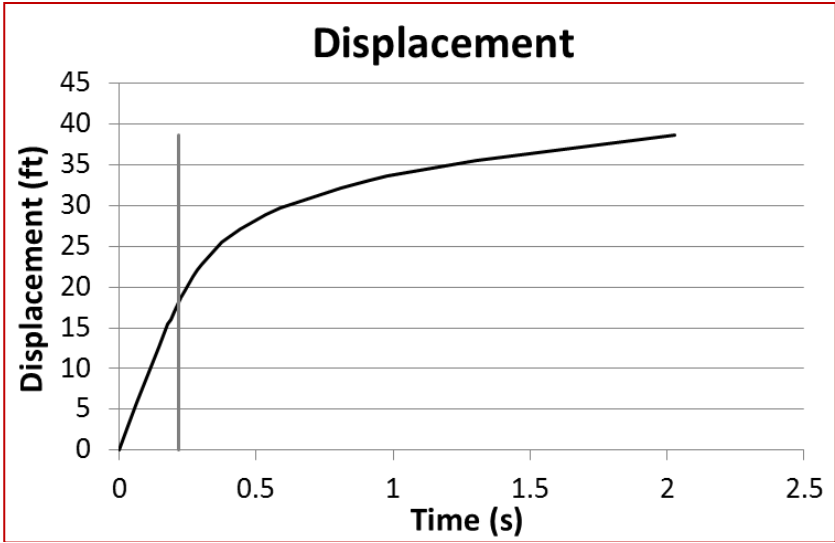


Figure G-17. Standard-Spacing Sand Barrel Array, 2270P, Case 1 Displacement and Velocity

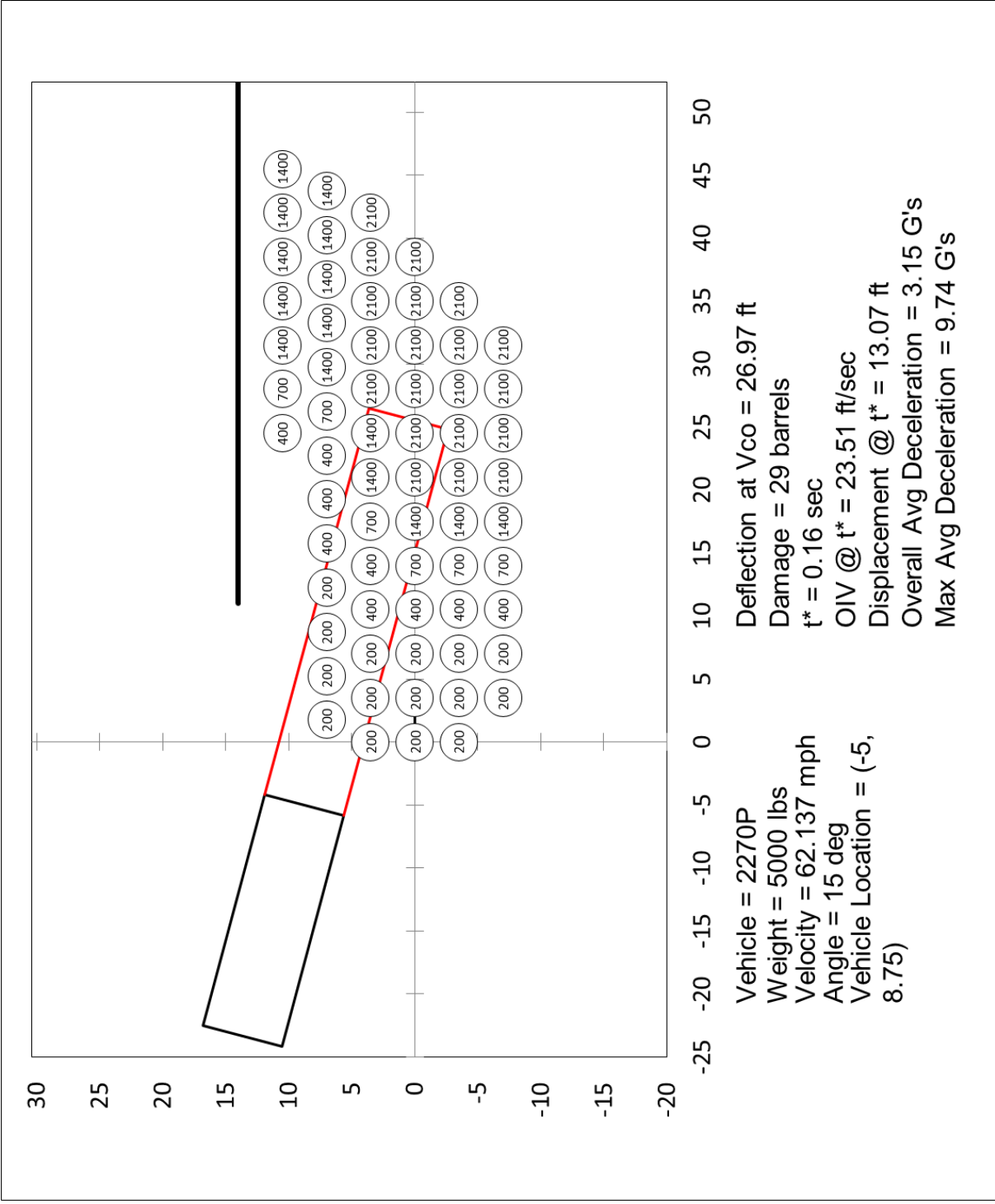


Figure G-18. Standard-Spacing Sand Barrel Array, 2270P, Case 2 Summary

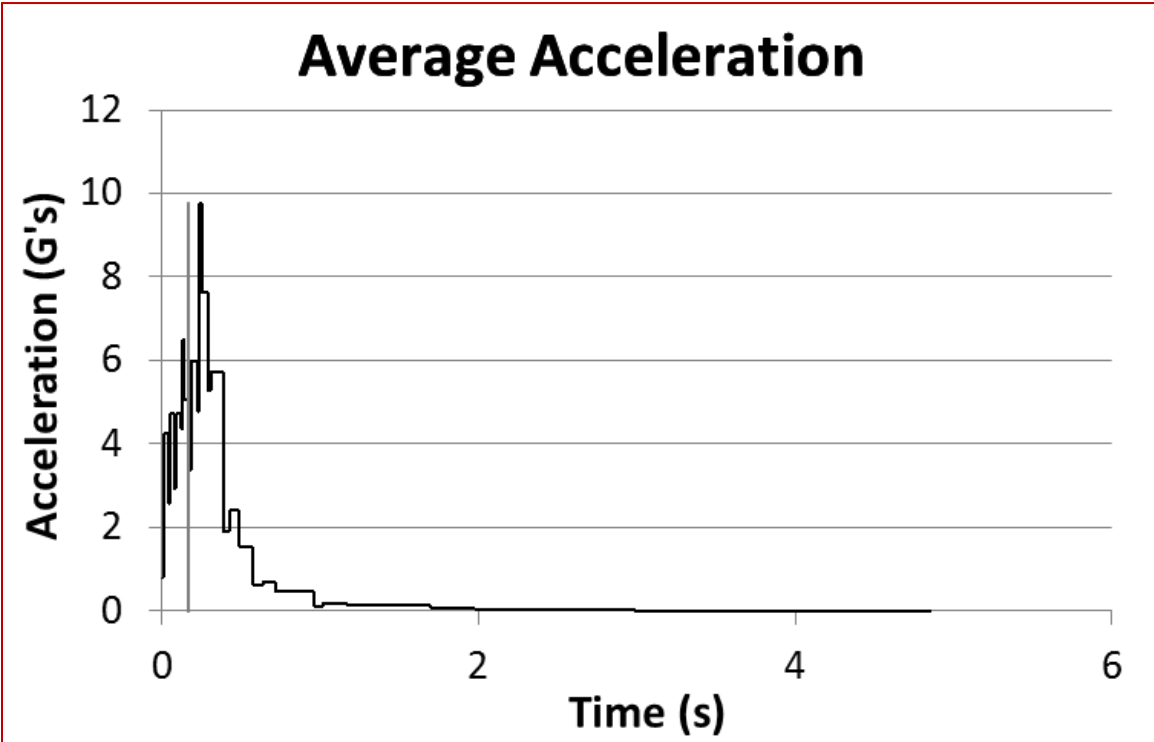
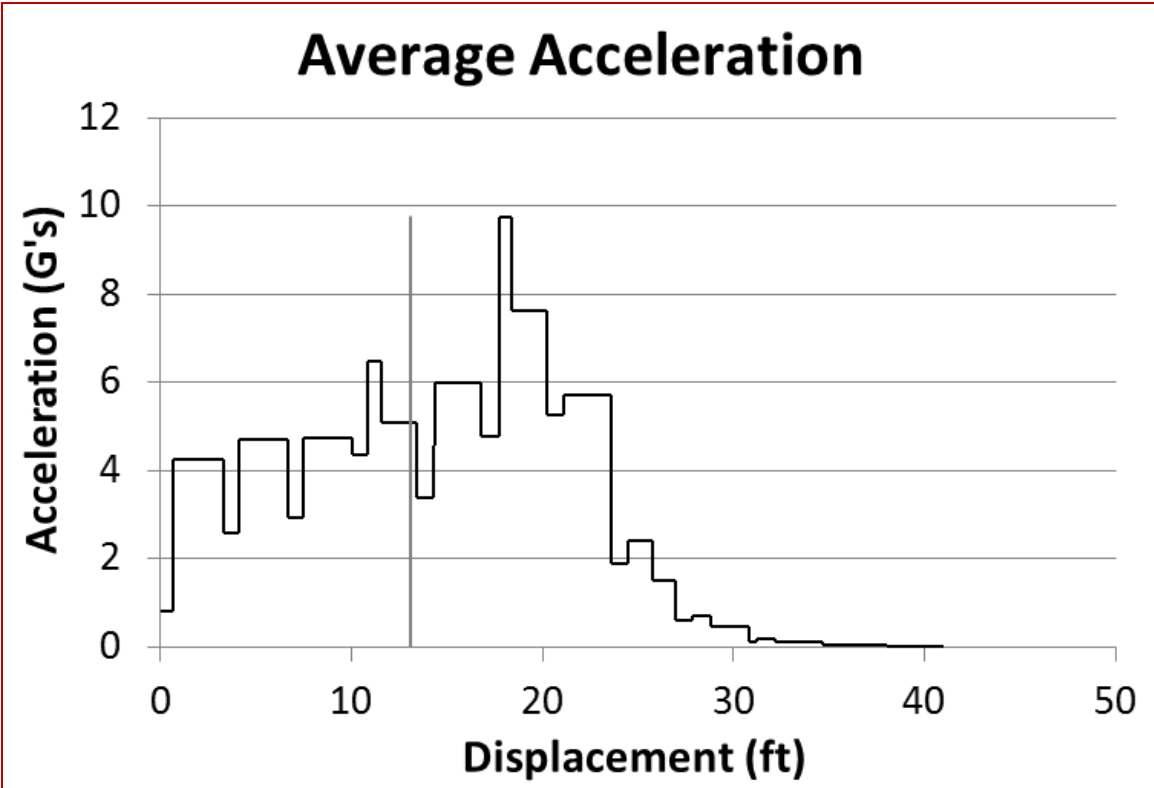


Figure G-19. Standard-Spacing Sand Barrel Array, 2270P, Case 2 Acceleration

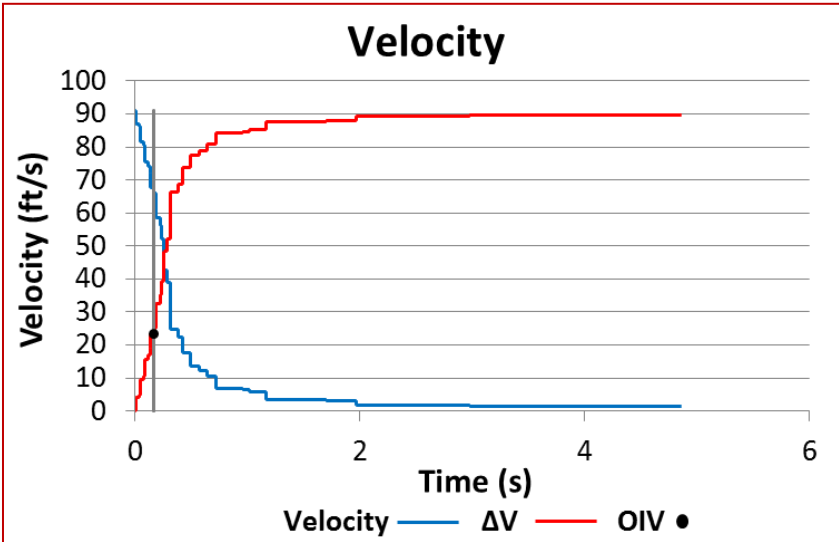
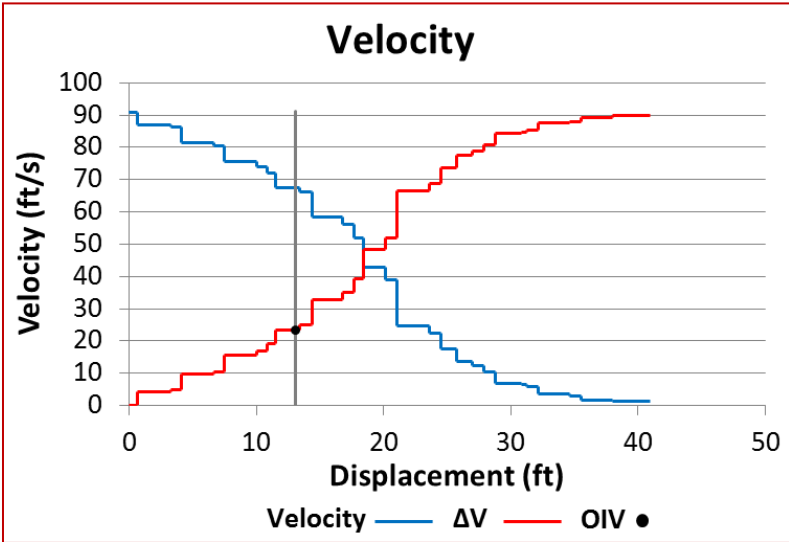
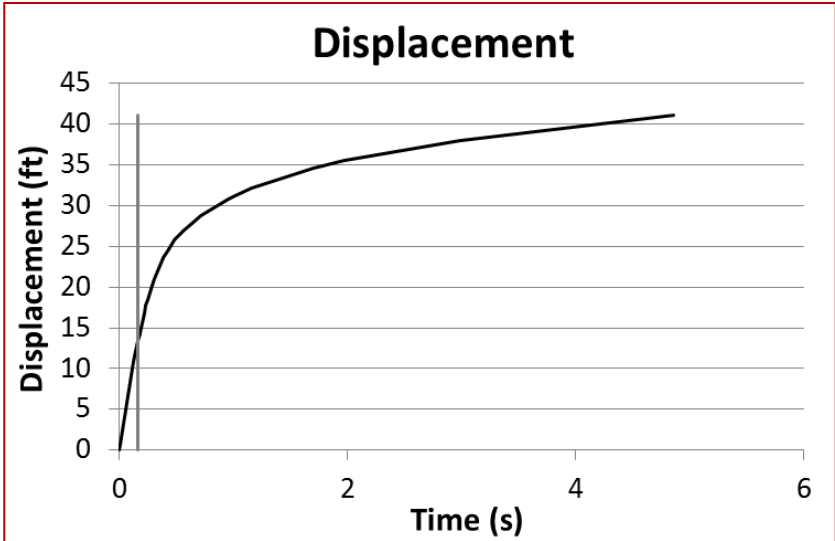


Figure G-20. Standard-Spacing Sand Barrel Array, 2270P, Case 2 Displacement and Velocity

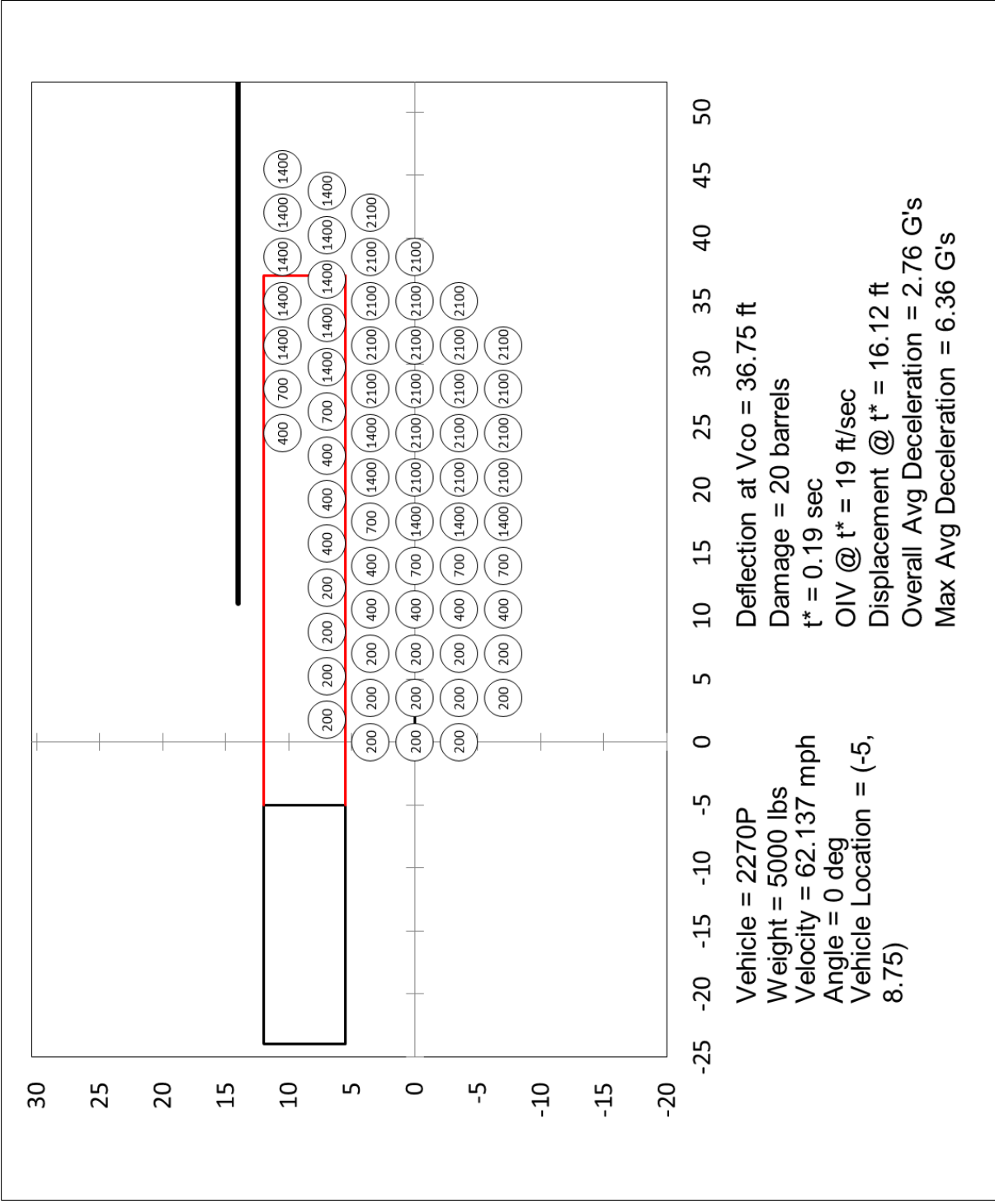


Figure G-21. Standard-Spacing Sand Barrel Array, 2270P, Case 3 Summary

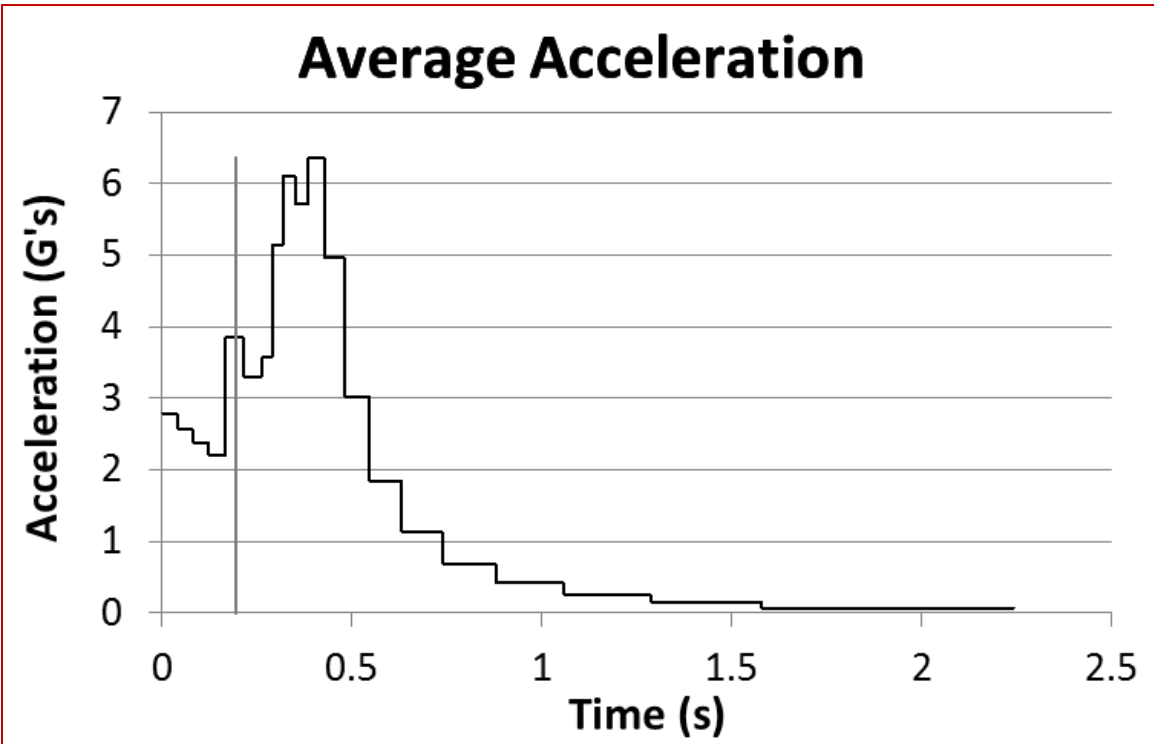
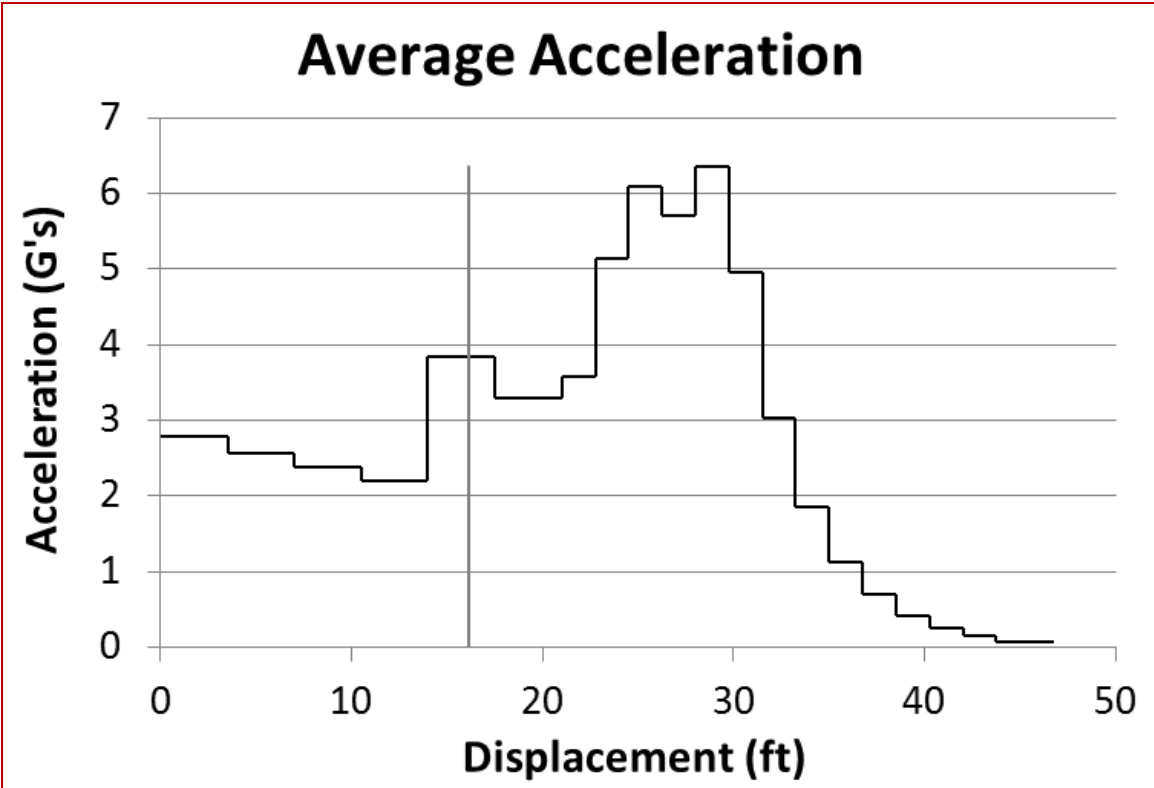


Figure G-22. Standard-Spacing Sand Barrel Array, 2270P, Case 3 Acceleration

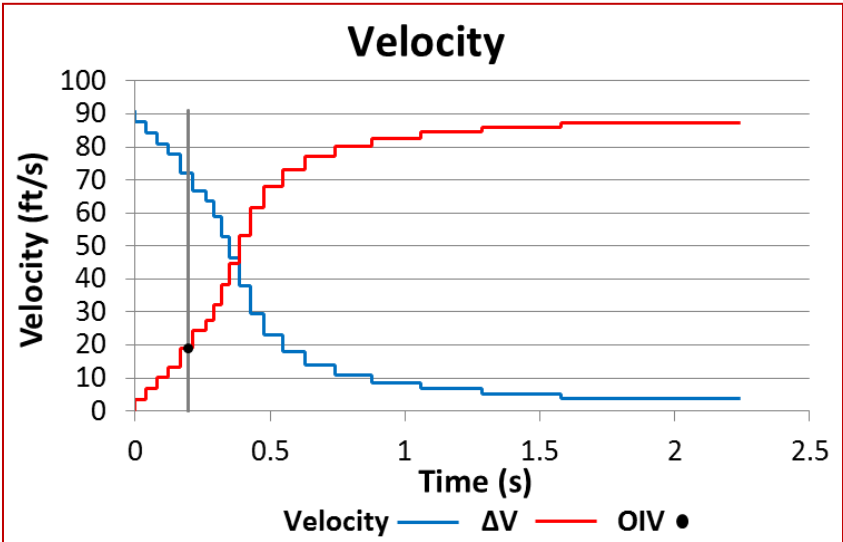
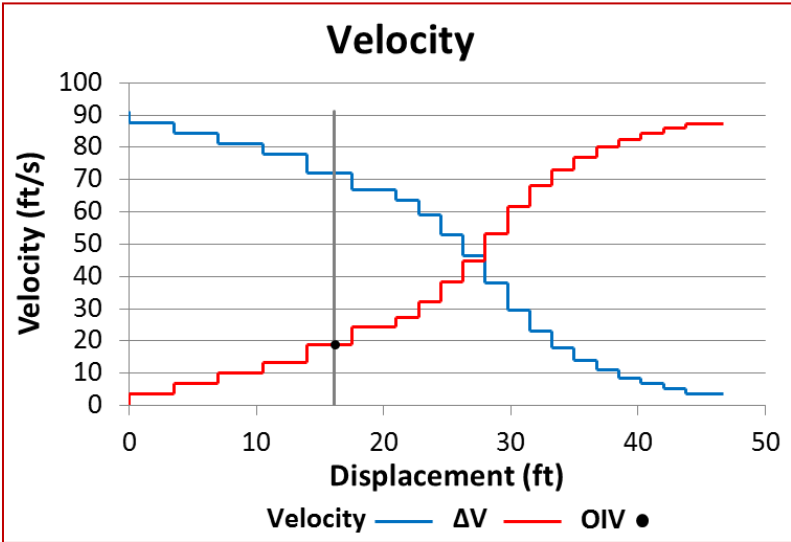
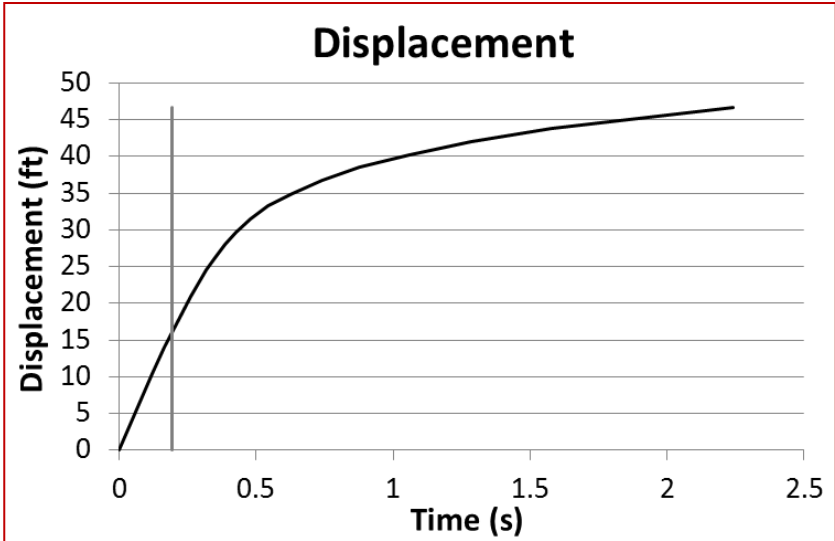


Figure G-23. Standard-Spacing Sand Barrel Array, 2270P, Case 3 Displacement and Velocity

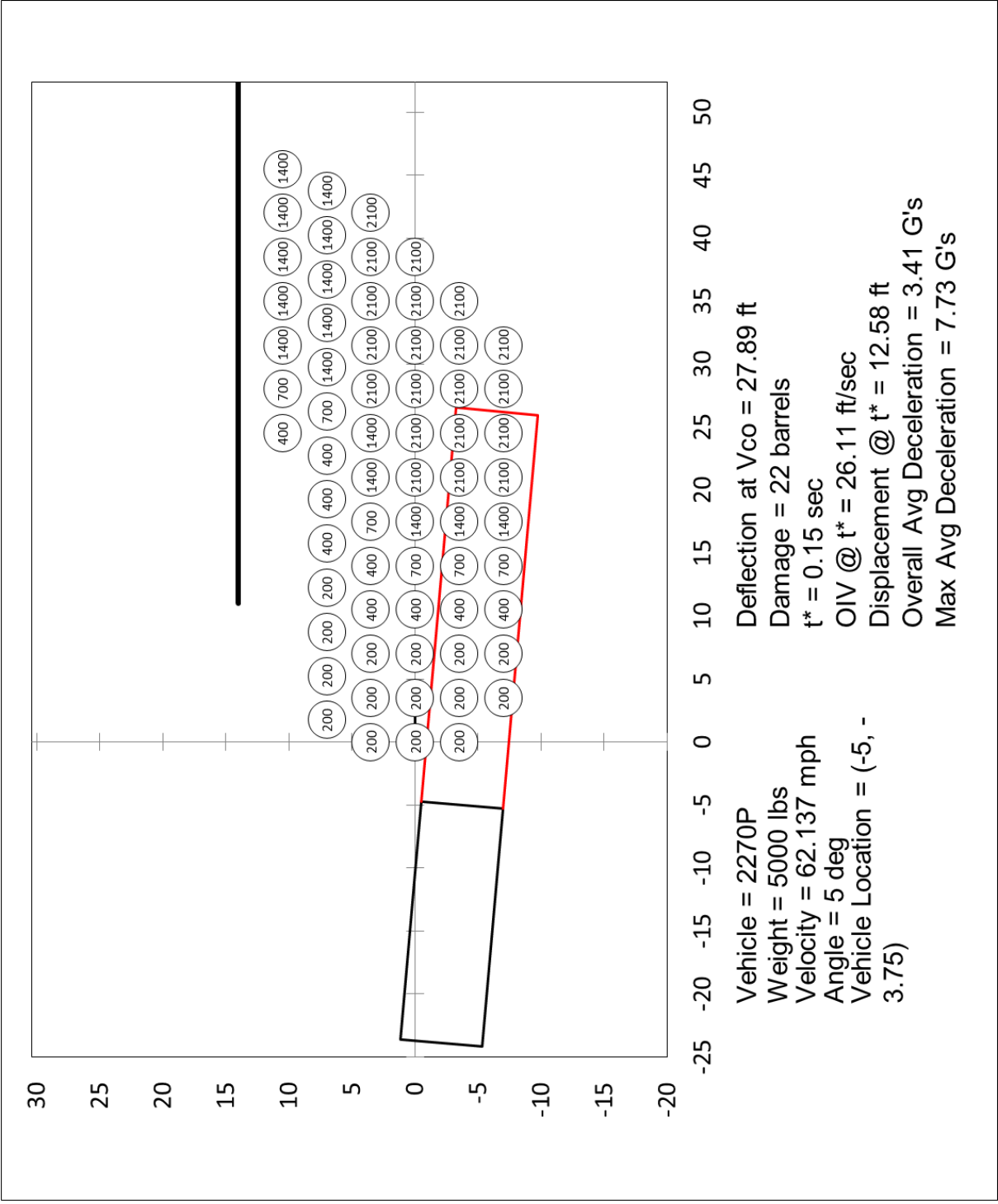


Figure G-24. Standard-Spacing Sand Barrel Array, 2270P, Case 4 Summary

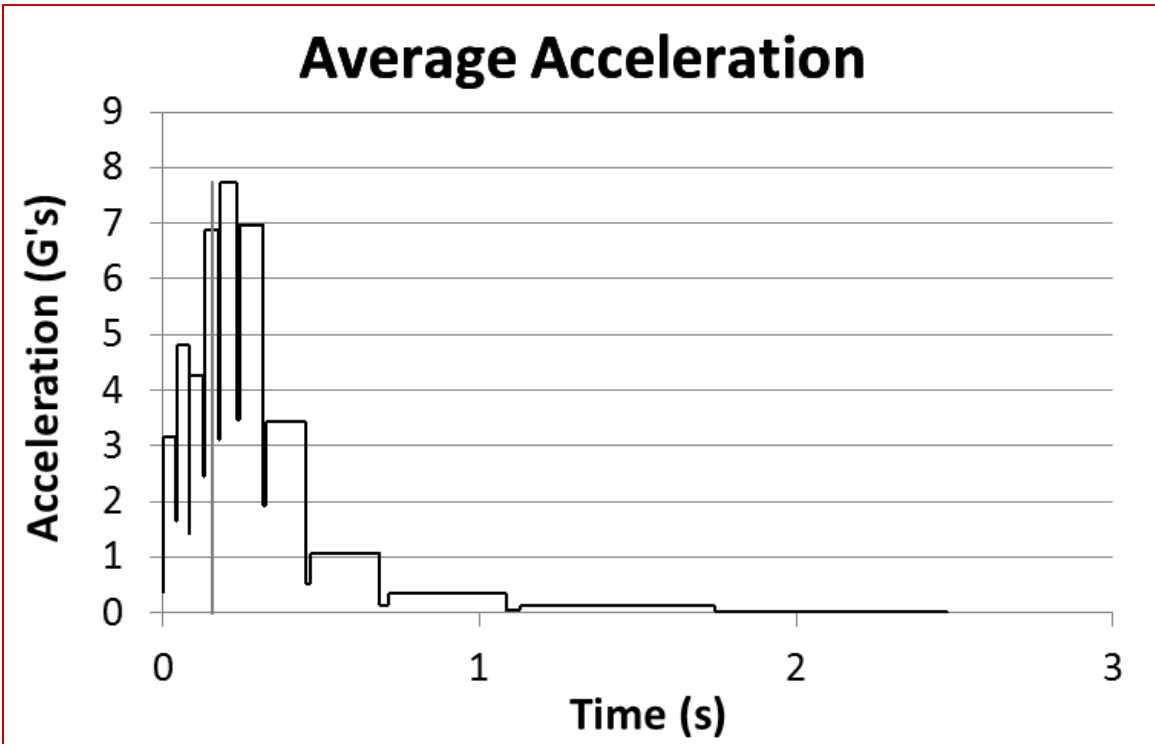
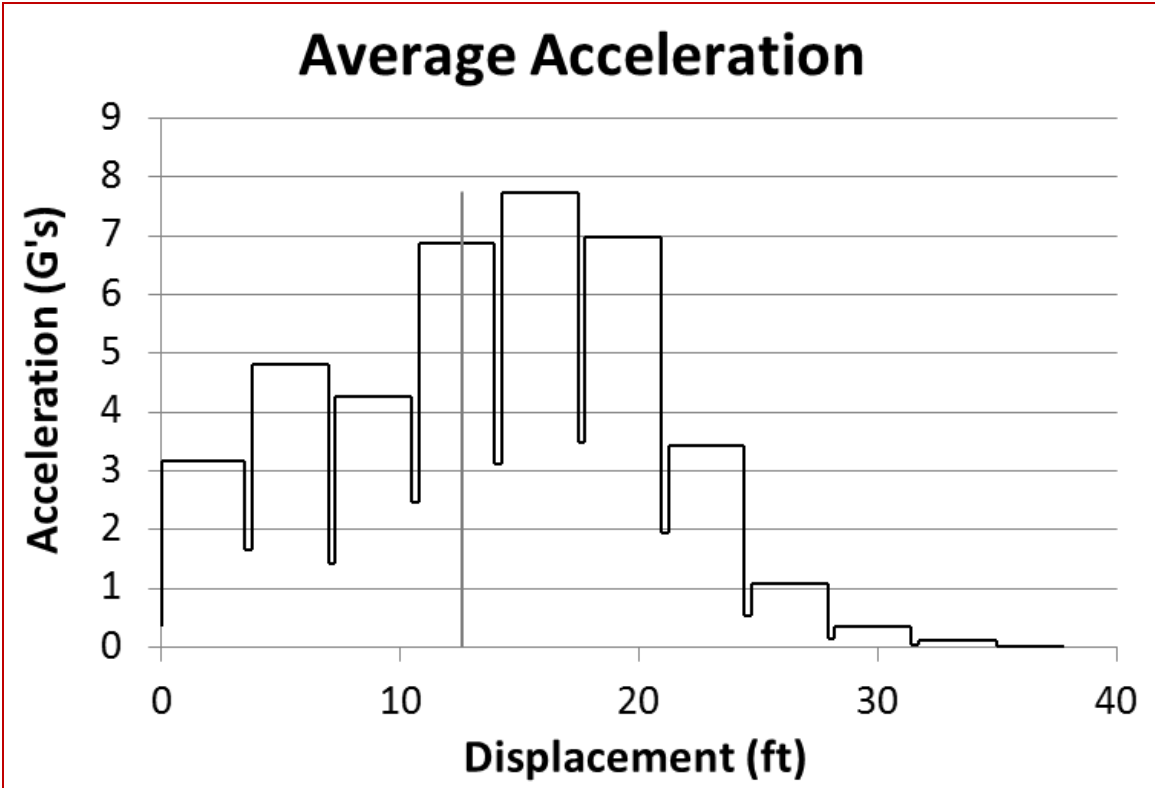


Figure G-25. Standard-Spacing Sand Barrel Array, 2270P, Case 4 Acceleration

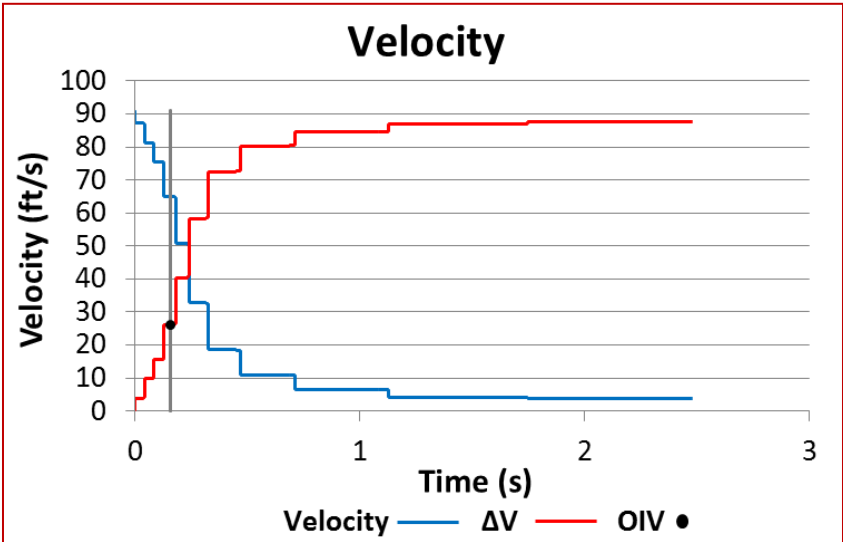
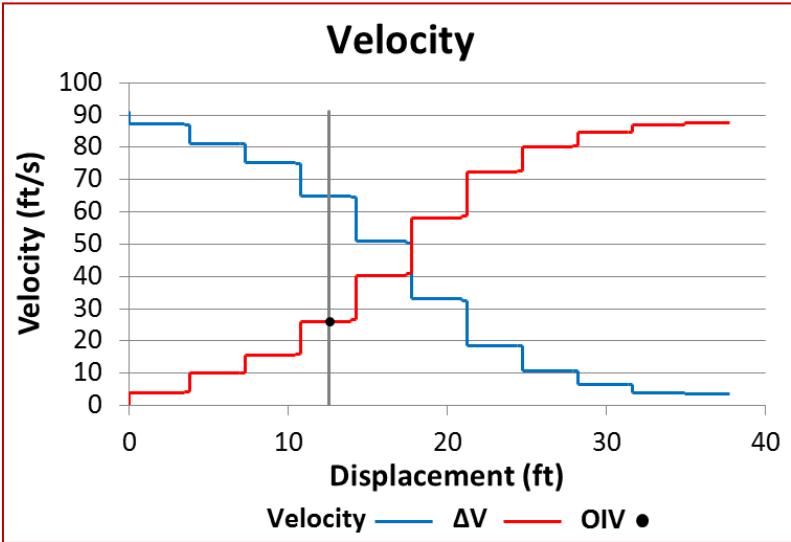
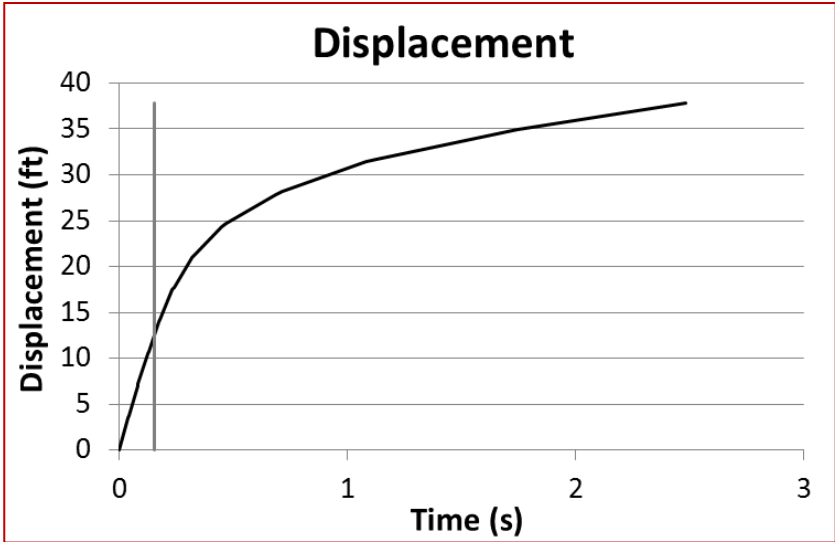


Figure G-26. Standard-Spacing Sand Barrel Array, 2270P, Case 4 Displacement and Velocity

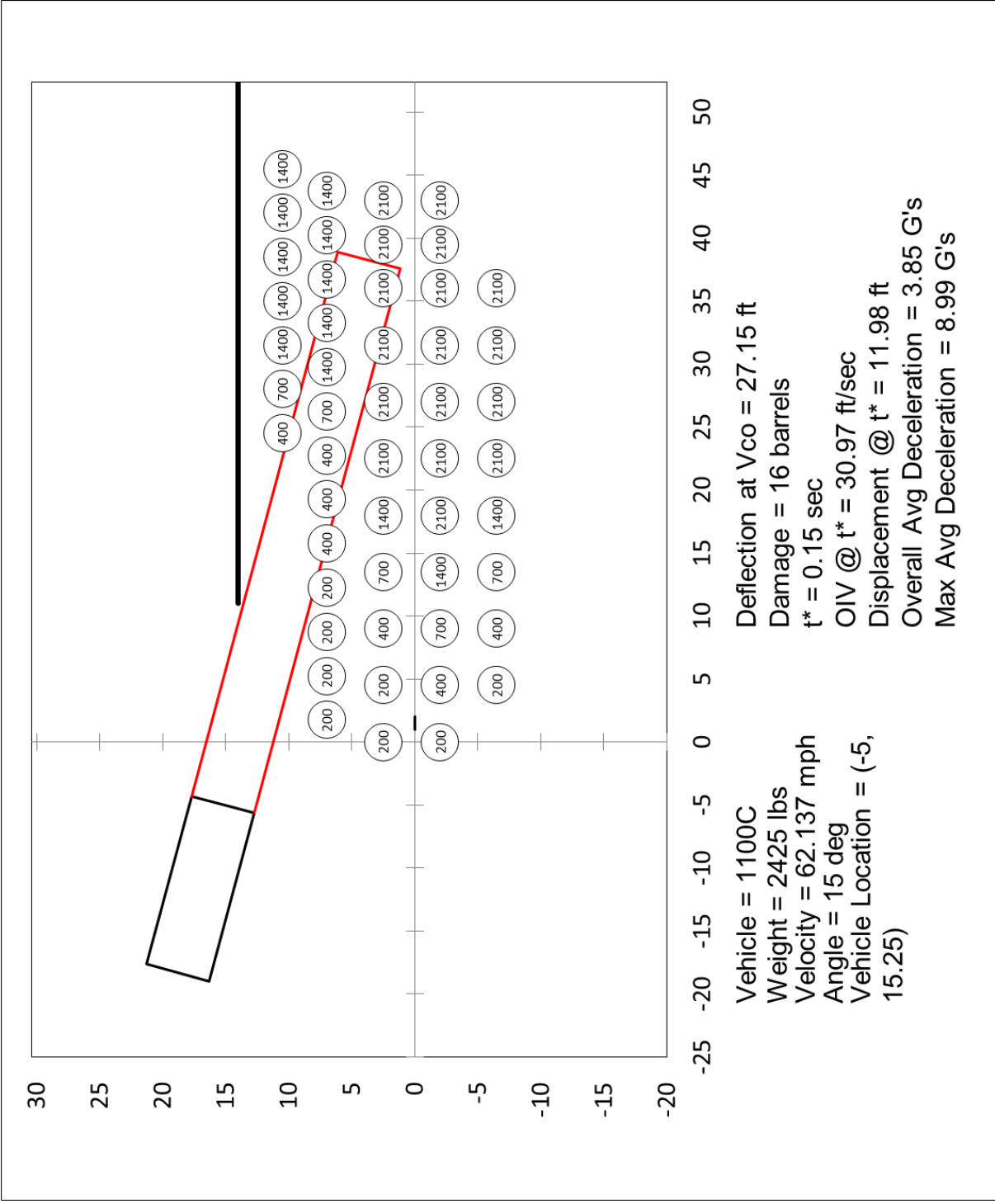


Figure G-27. Mixed-Spacing Sand Barrel Array, 1100C, Case 1 Summary

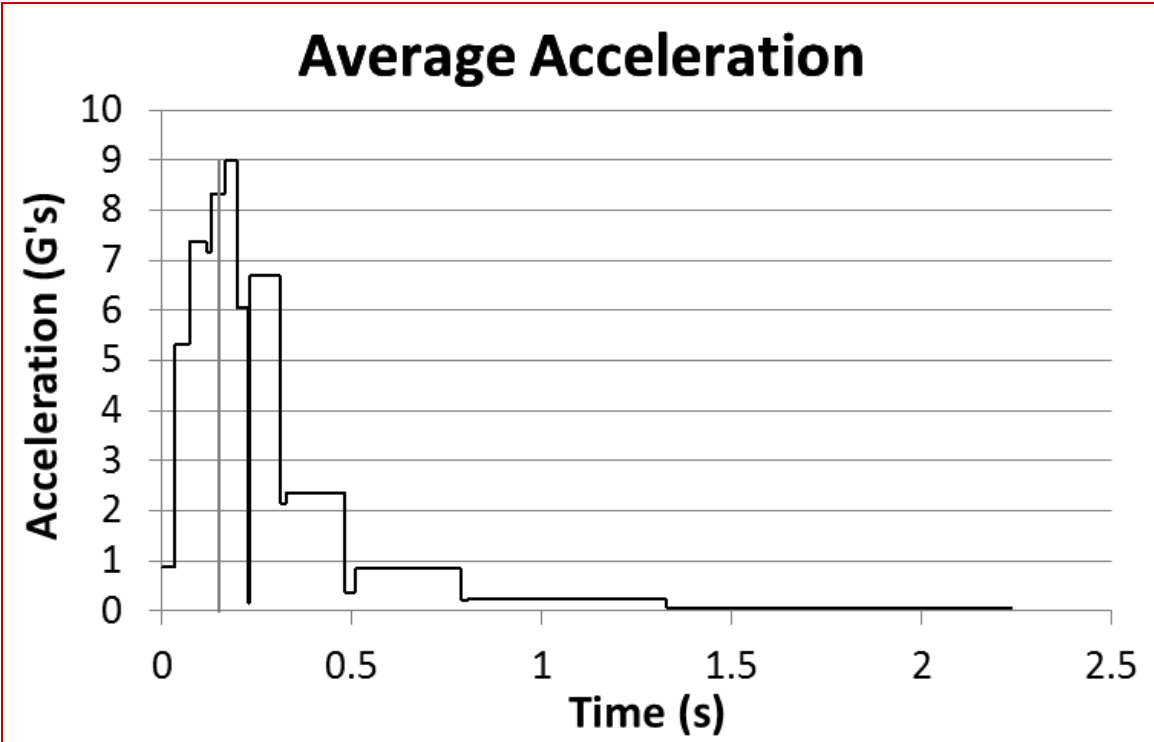
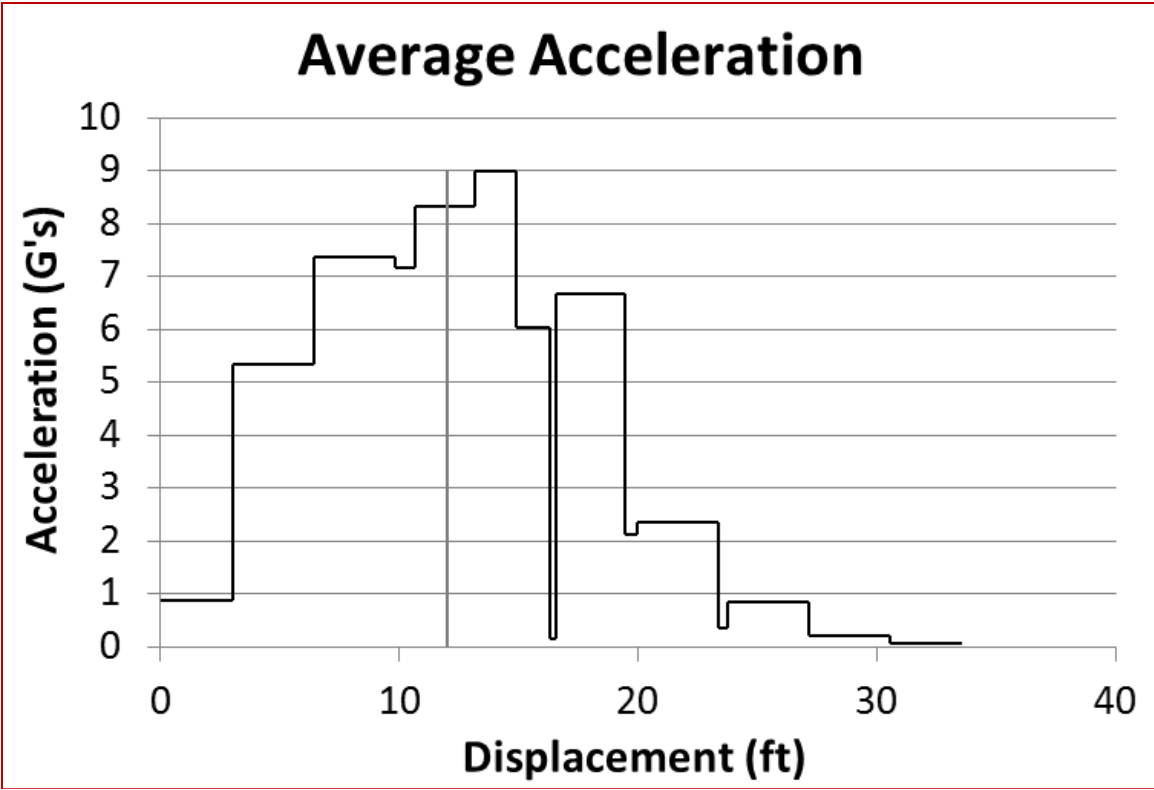


Figure G-28. Mixed-Spacing Sand Barrel Array, 1100C, Case 1 Acceleration

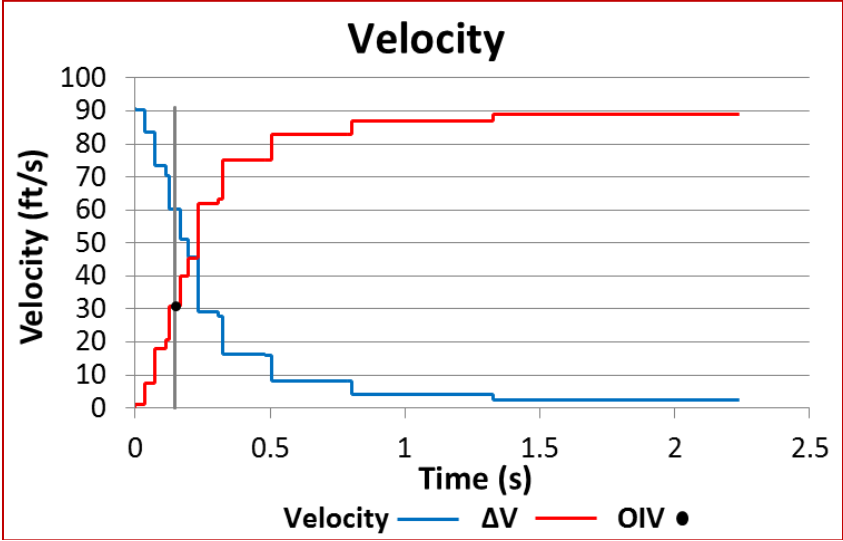
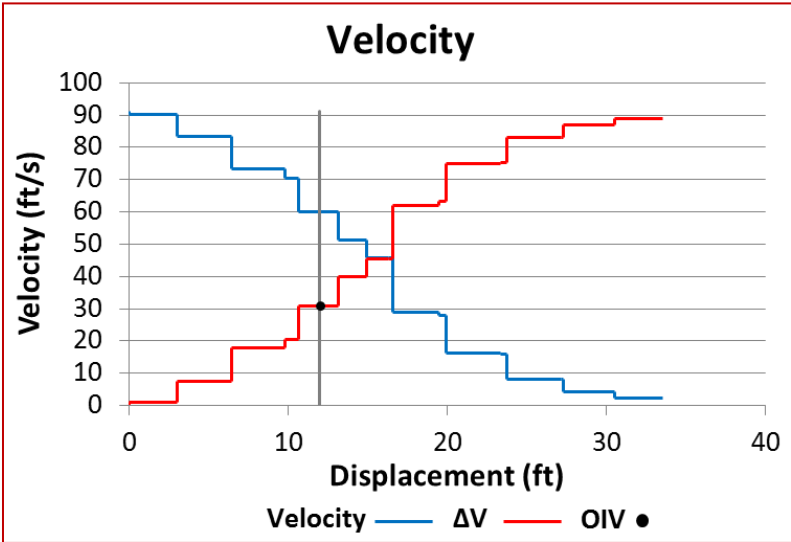
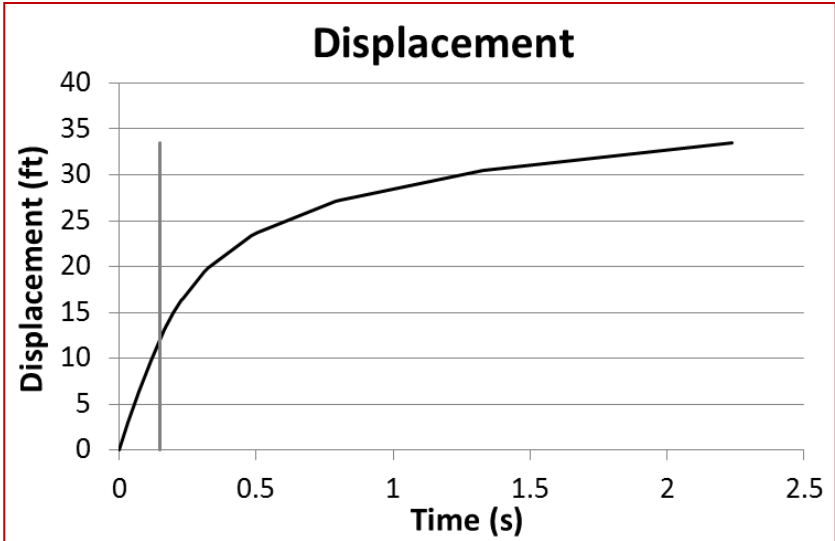


Figure G-29. Mixed-Spacing Sand Barrel Array, 1100C, Case 1 Displacement and Velocity

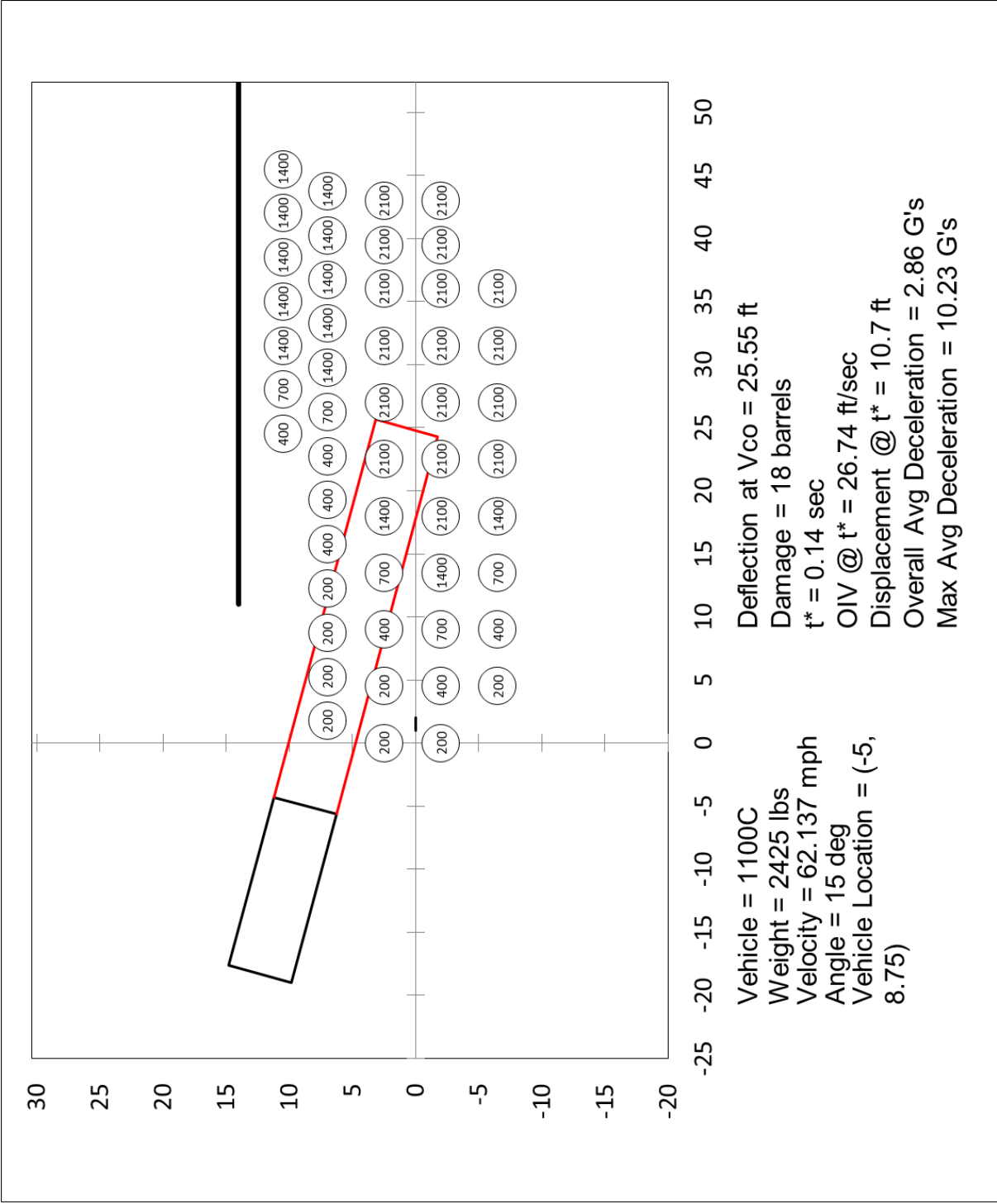


Figure G-30. Mixed-Spacing Sand Barrel Array, 1100C, Case 2 Summary

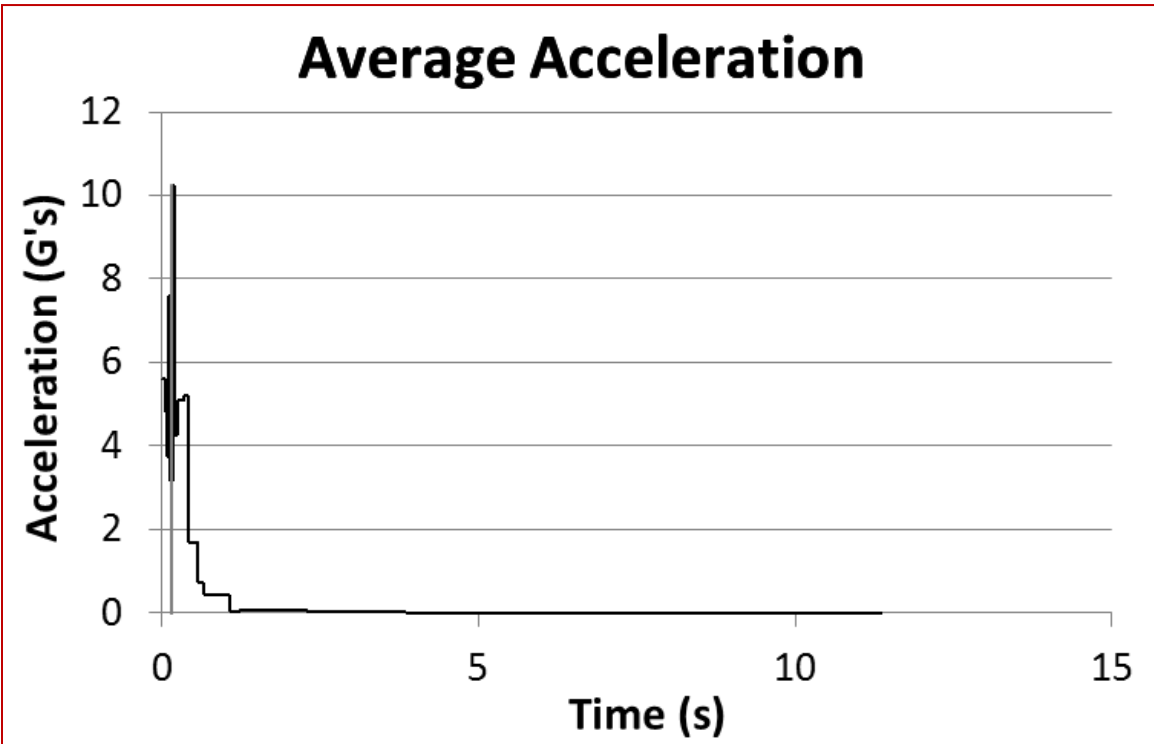
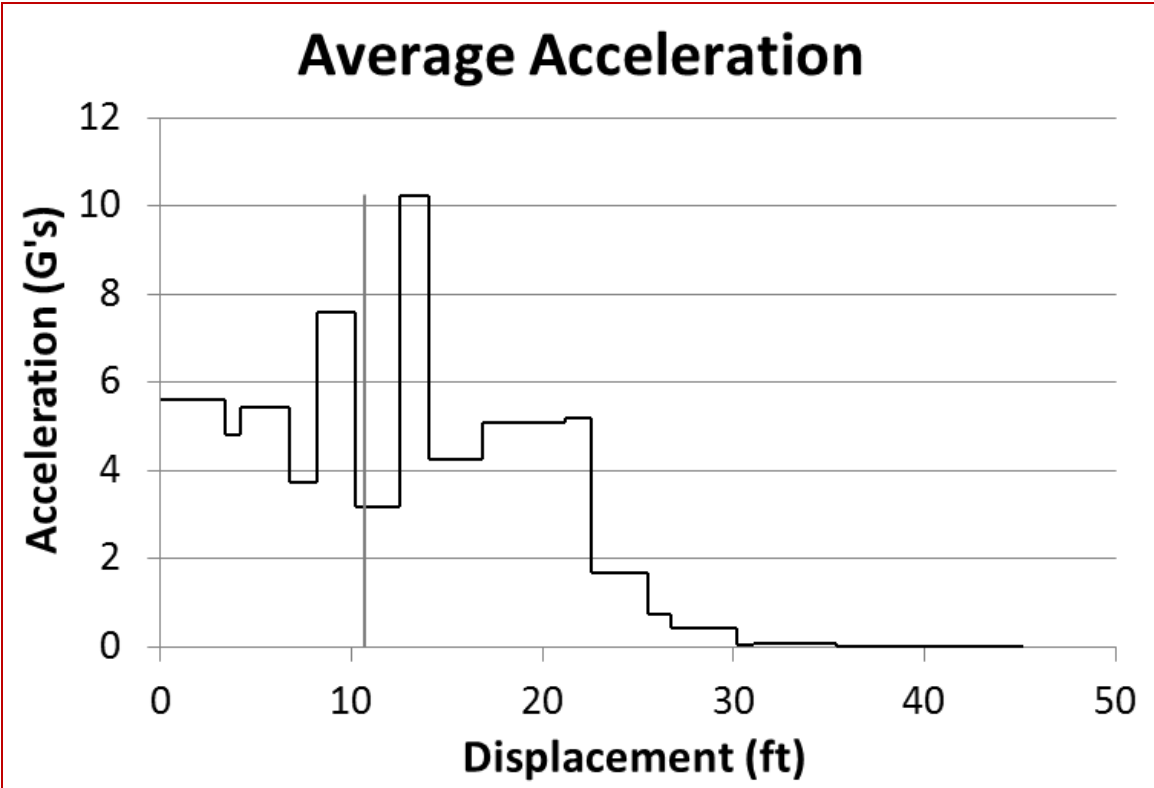


Figure G-31. Mixed-Spacing Sand Barrel Array, 1100C, Case 2 Acceleration

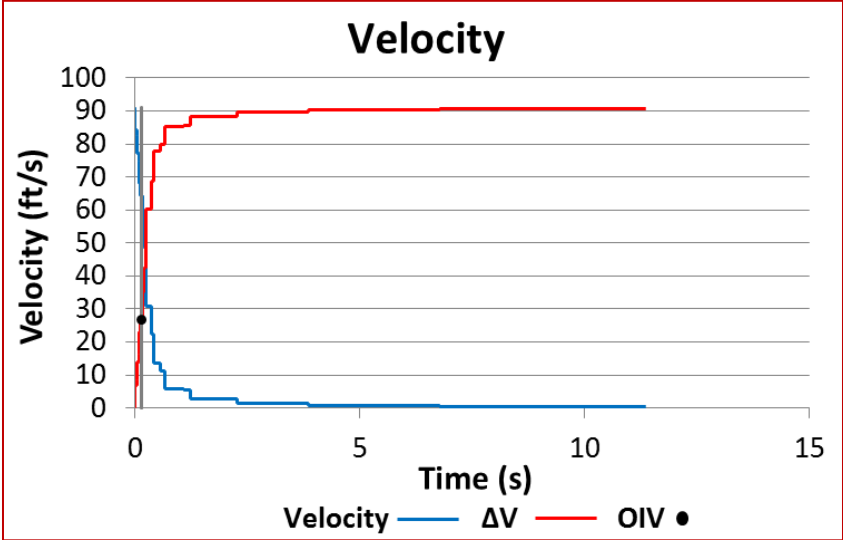
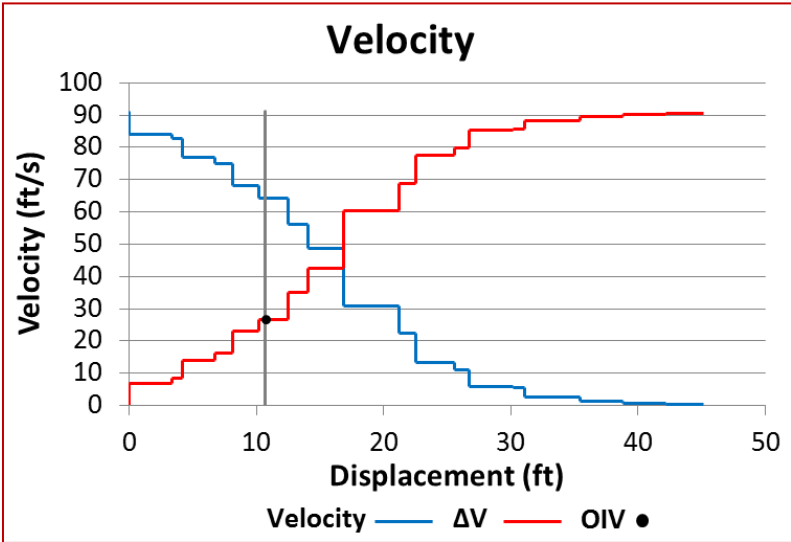
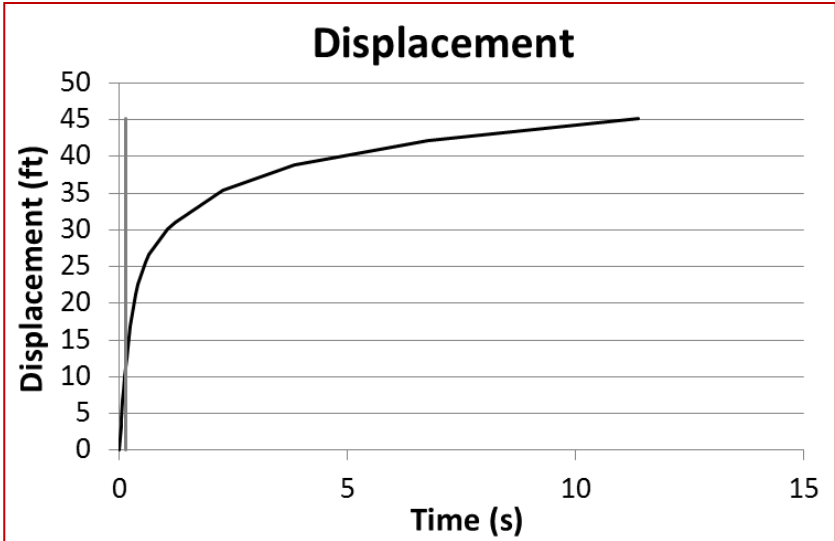


Figure G-32. Mixed-Spacing Sand Barrel Array, 1100C, Case 2 Displacement and Velocity

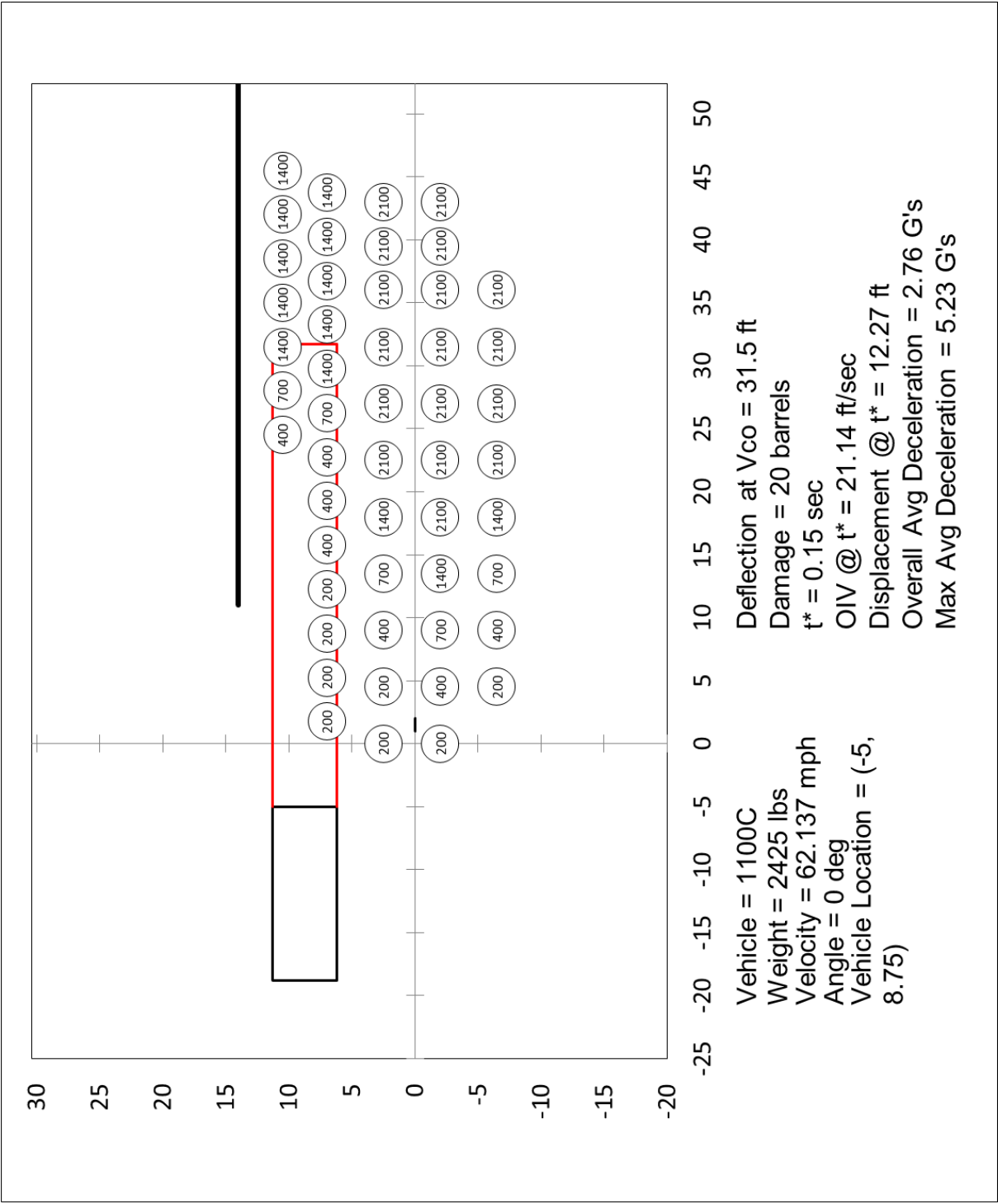


Figure G-33. Mixed-Spacing Sand Barrel Array, 1100C, Case 3 Summary

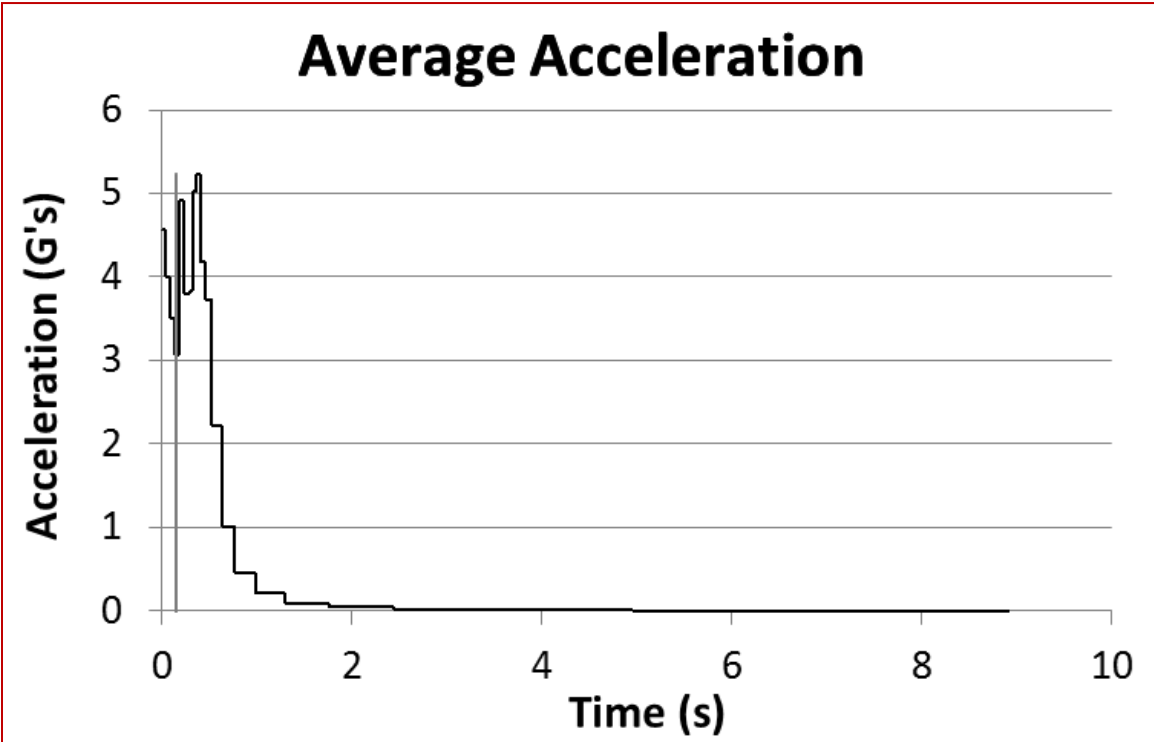
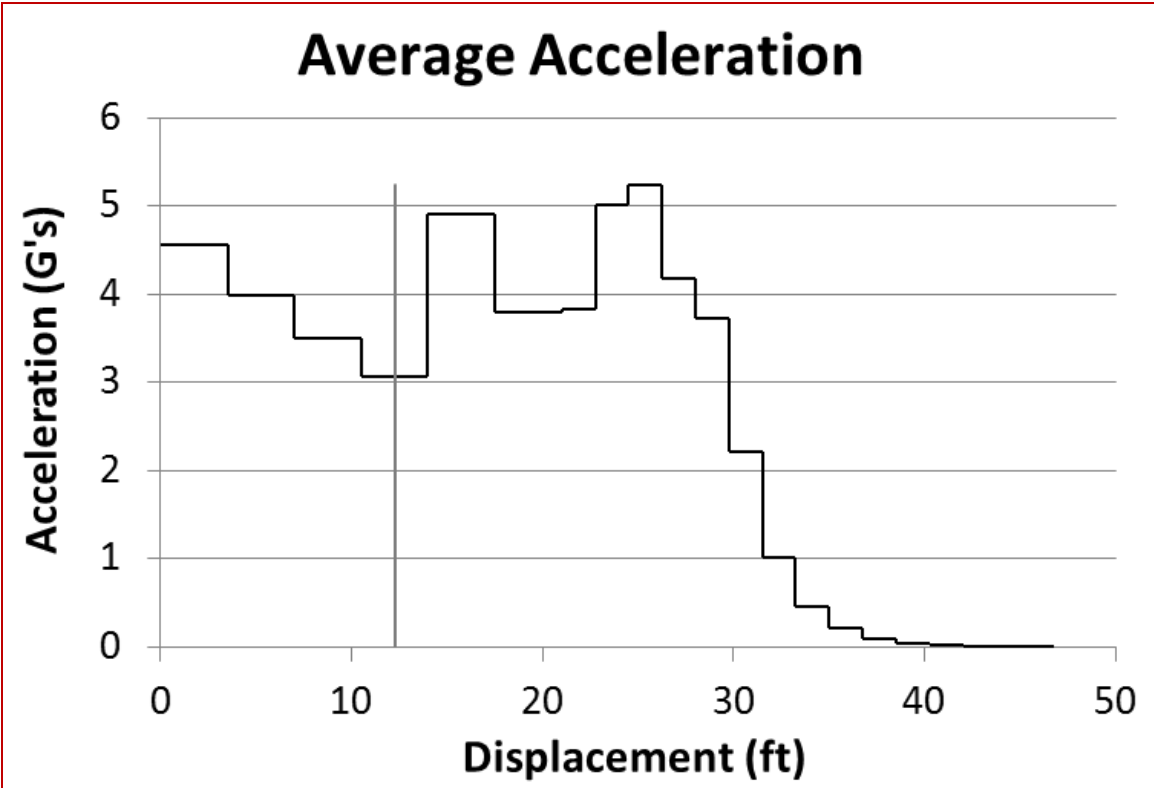


Figure G-34. Mixed-Spacing Sand Barrel Array, 1100C, Case 3 Acceleration

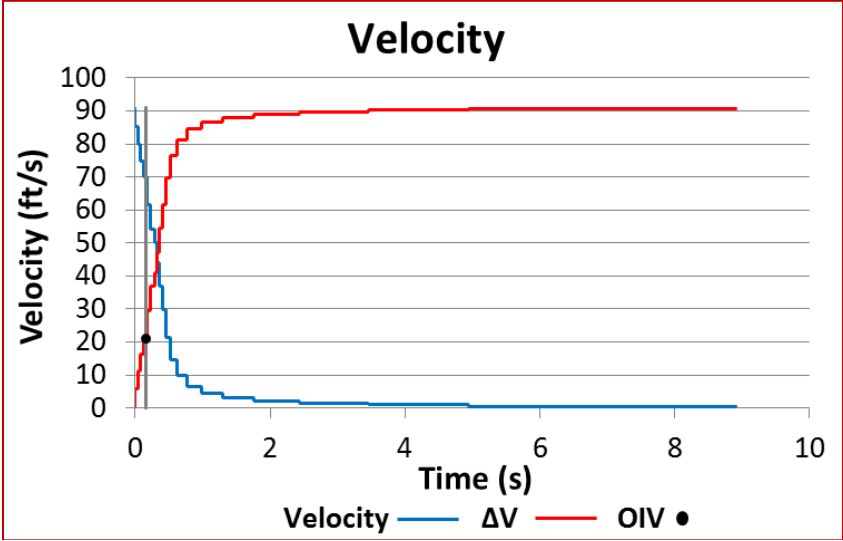
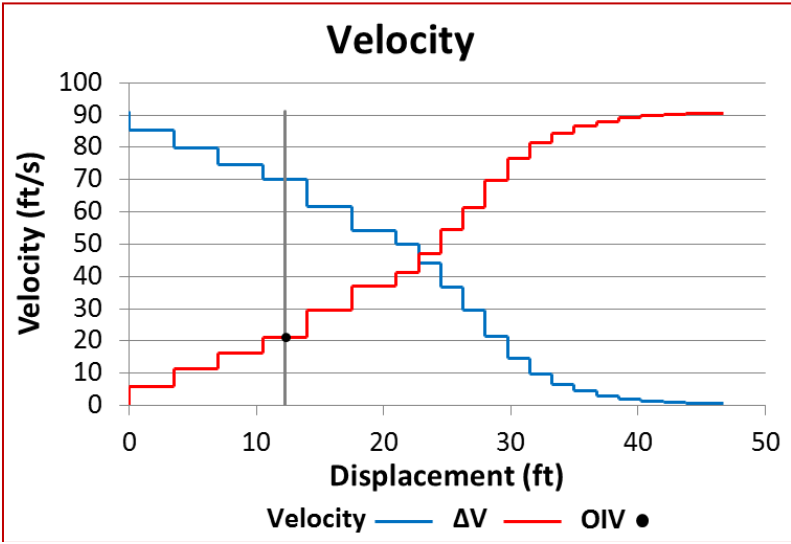
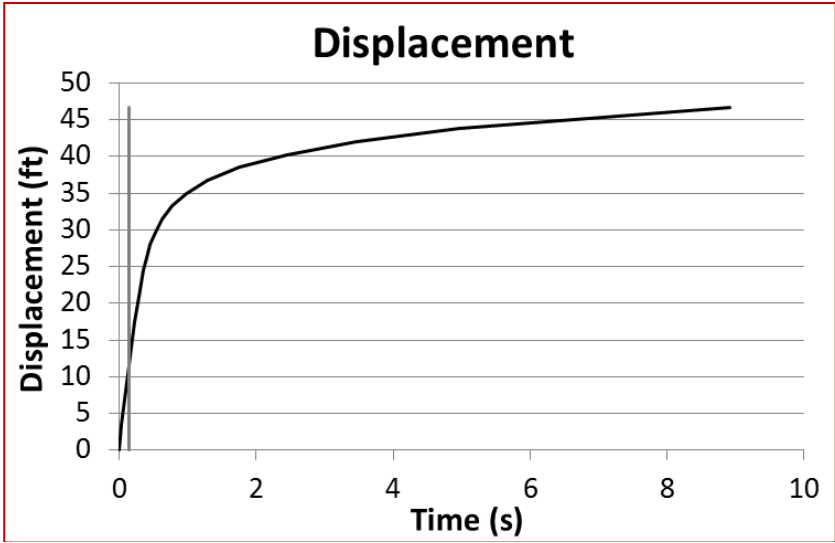


Figure G-35. Mixed-Spacing Sand Barrel Array, 1100C, Case 3 Displacement and Velocity

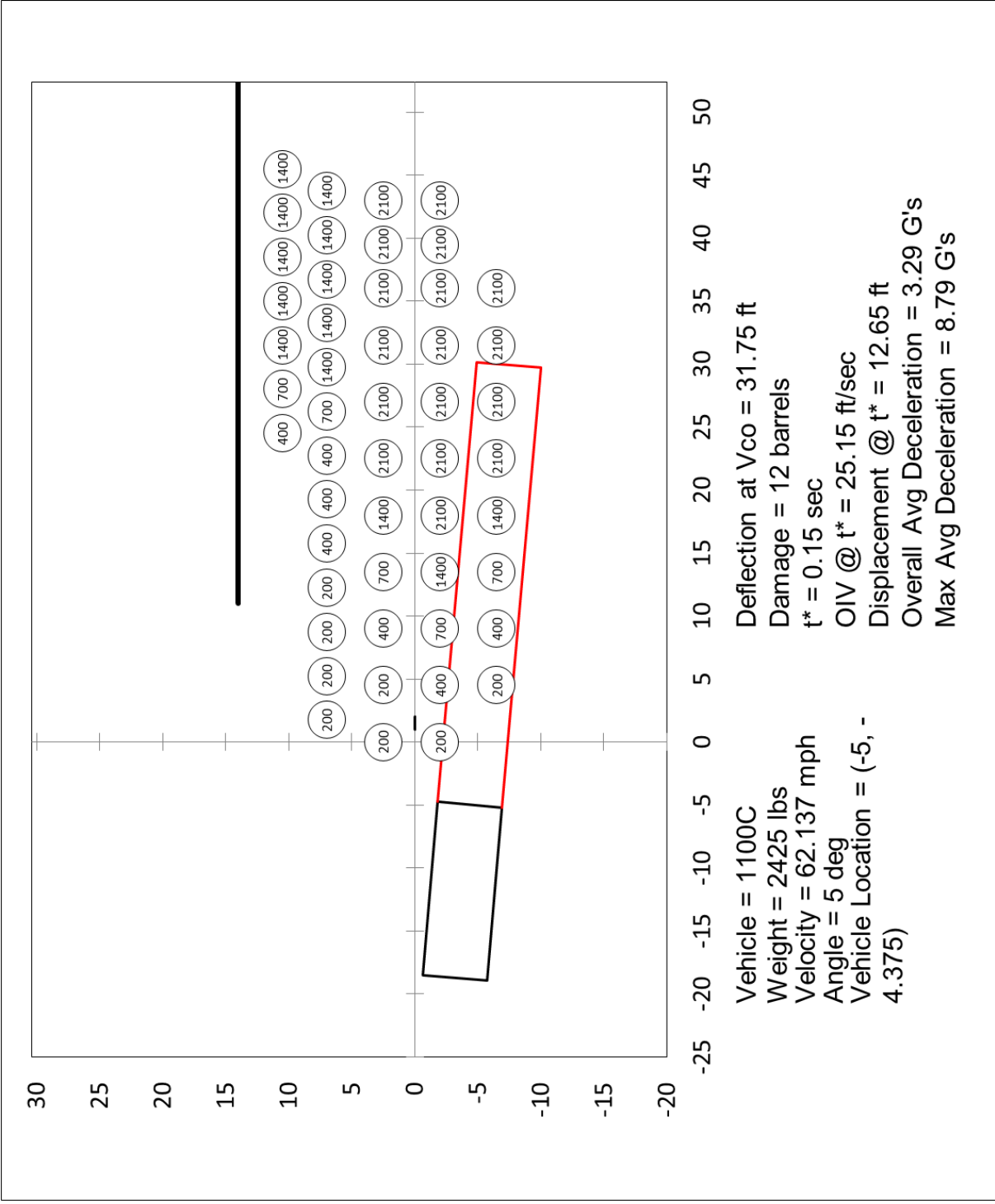


Figure G-36. Mixed-Spacing Sand Barrel Array, 1100C, Case 4 Summary

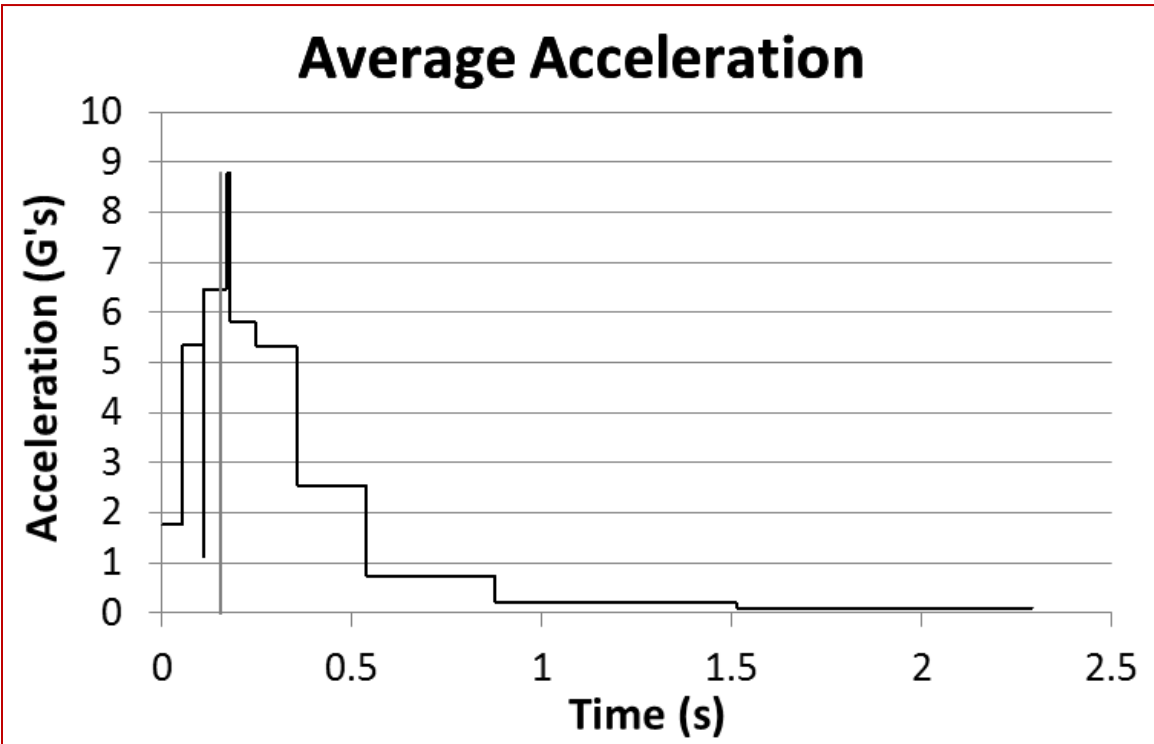
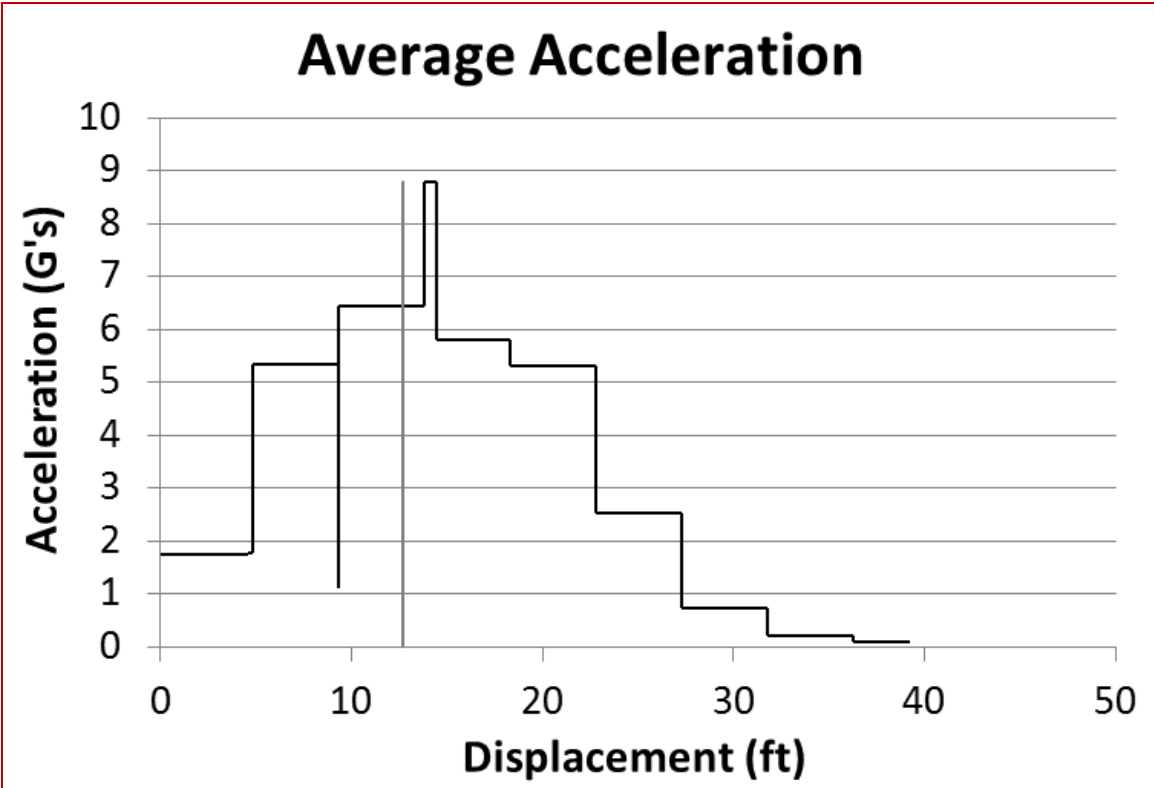


Figure G-37. Mixed-Spacing Sand Barrel Array, 1100C, Case 4 Acceleration

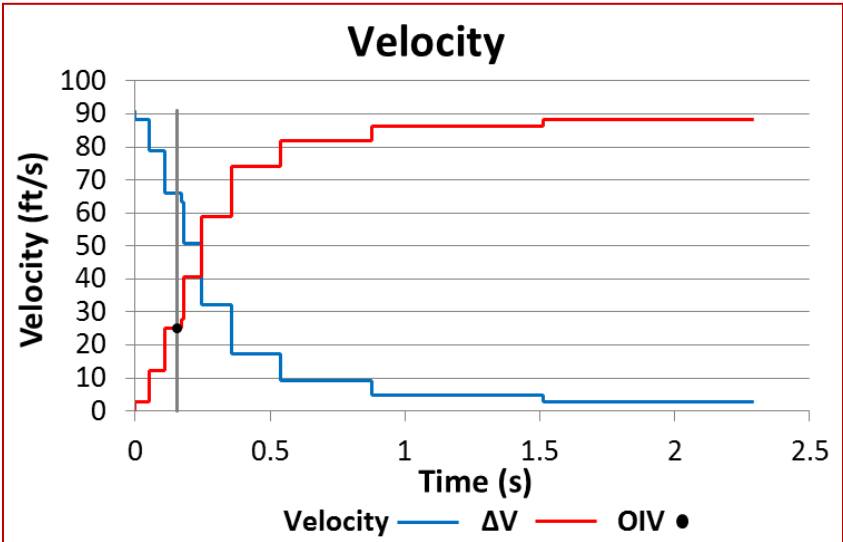
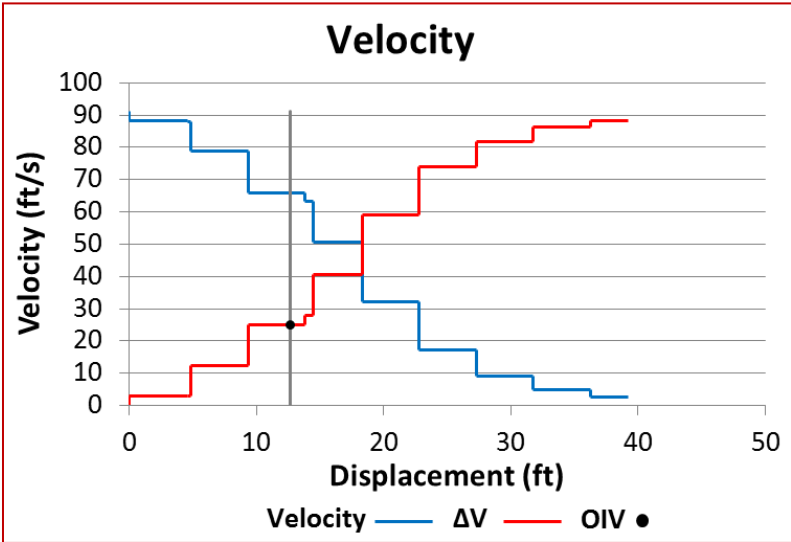
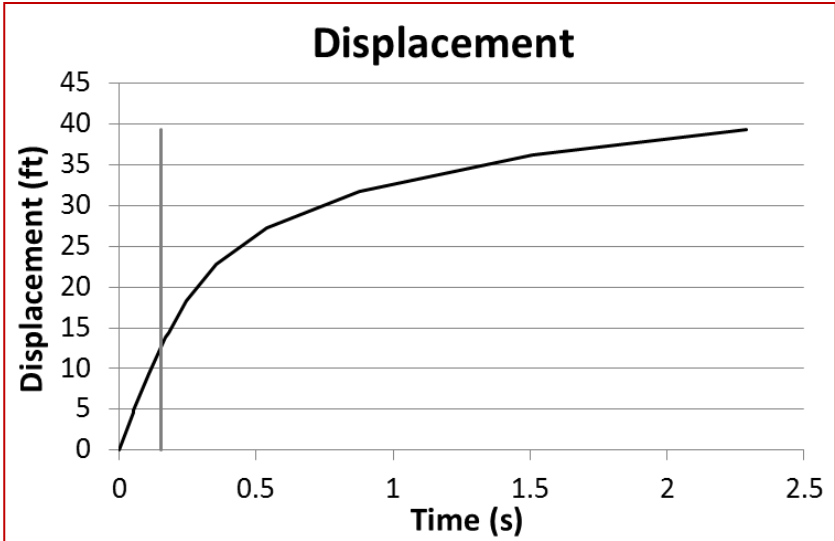


Figure G-38. Mixed-Spacing Sand Barrel Array, 1100C, Case 4 Displacement and Velocity

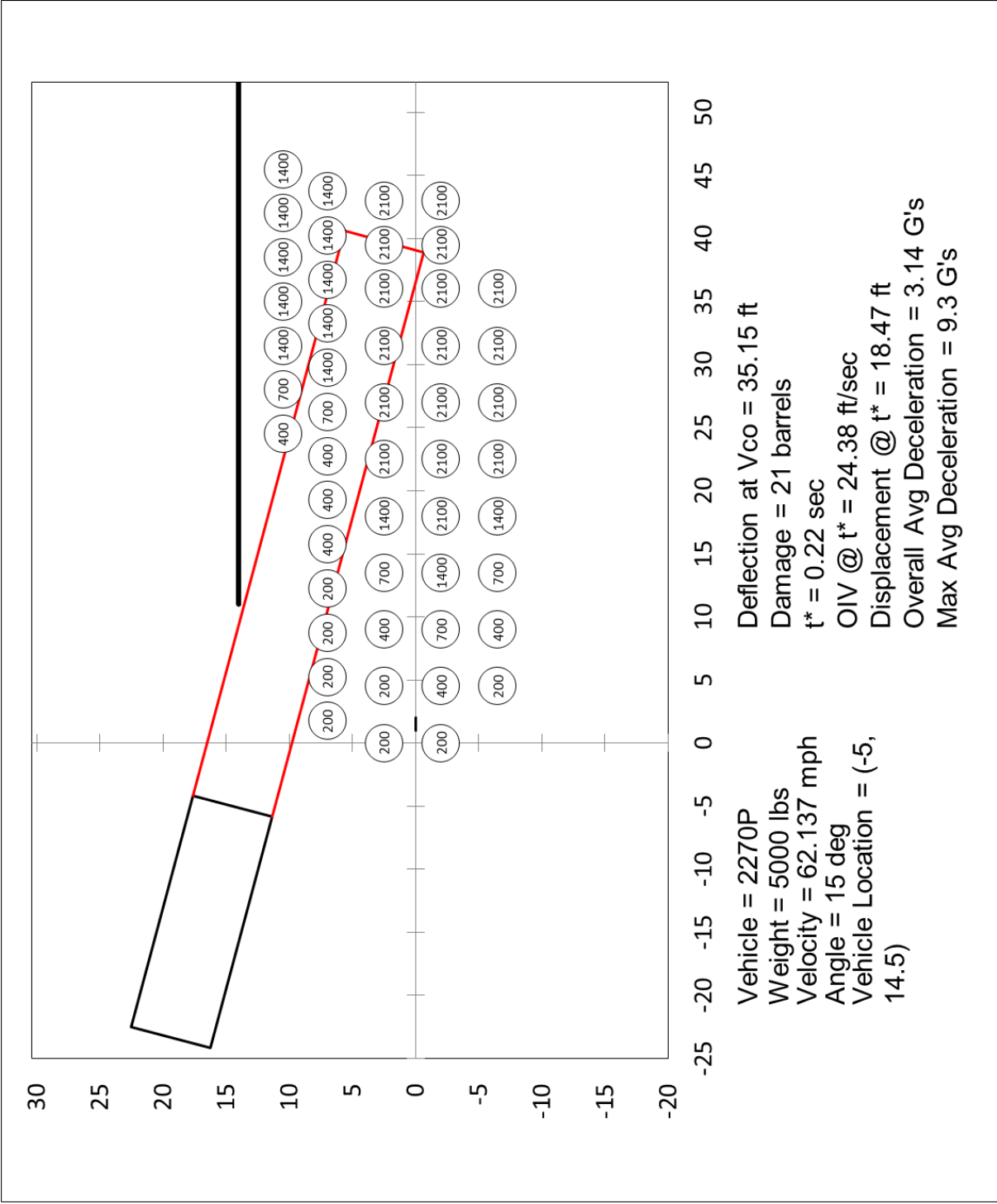


Figure G-39. Mixed-Spacing Sand Barrel Array, 2270P, Case 1 Summary

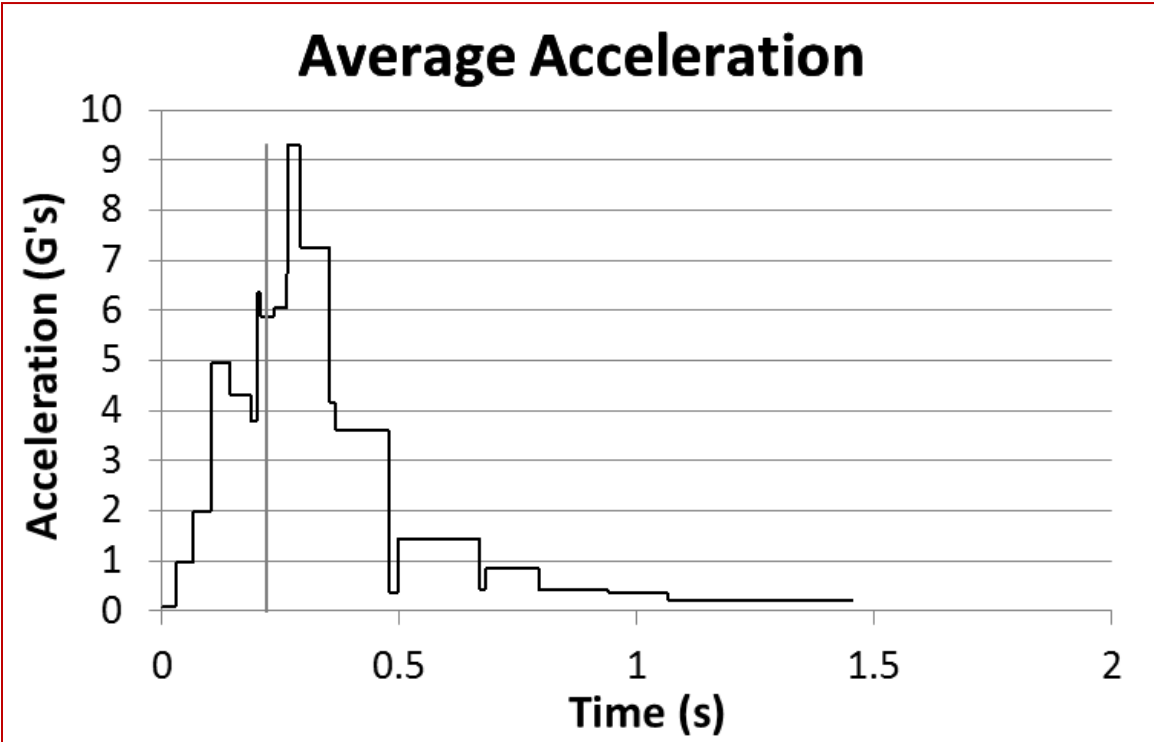
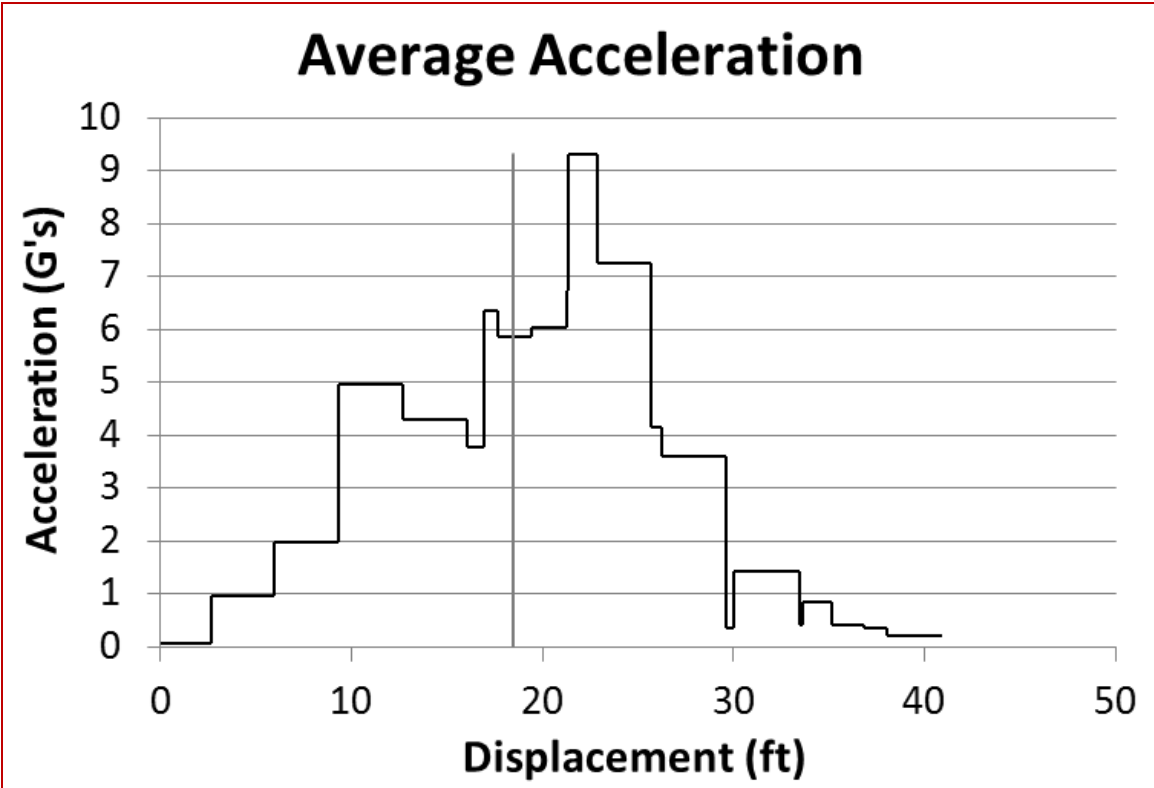


Figure G-40. Mixed-Spacing Sand Barrel Array, 2270P, Case 1 Acceleration

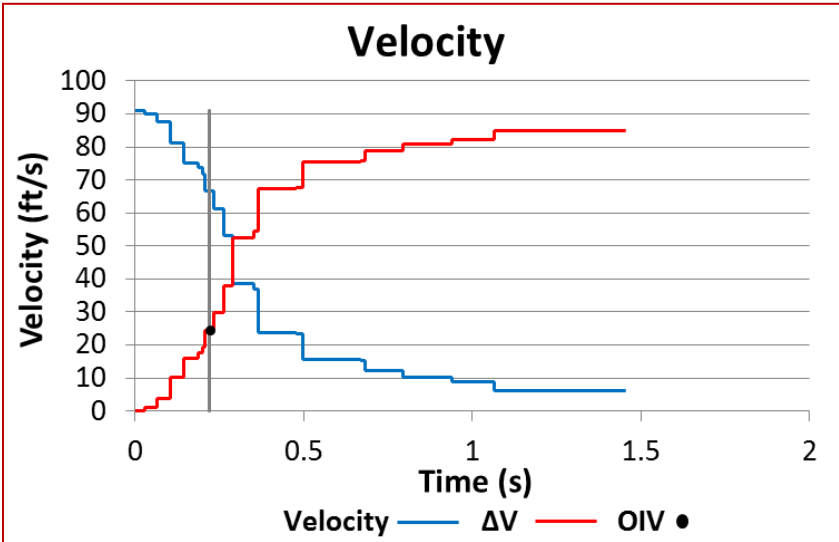
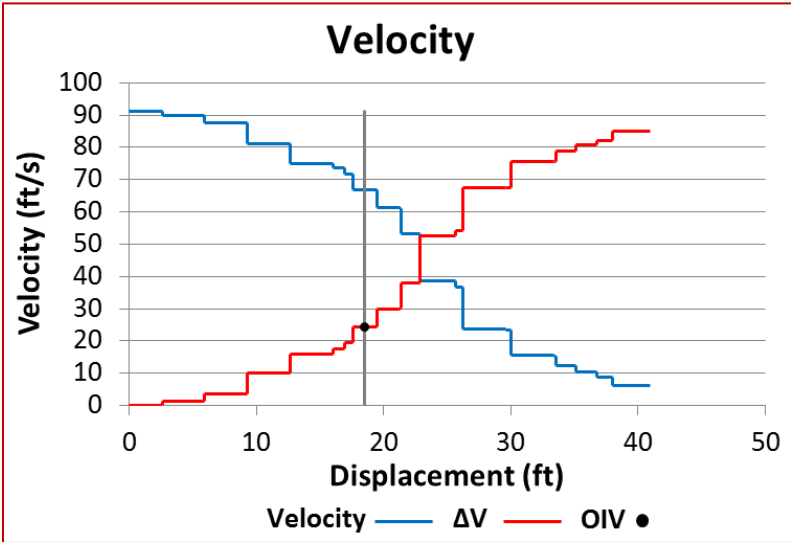
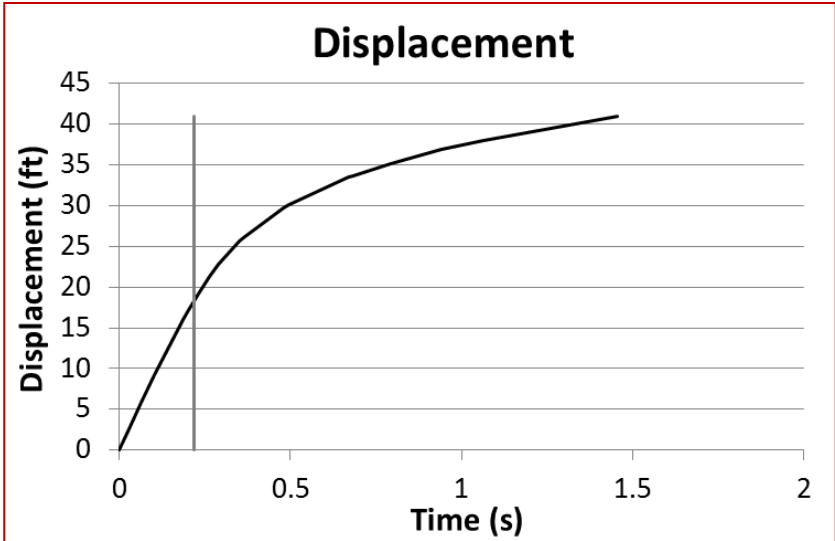


Figure G-41. Mixed-Spacing Sand Barrel Array, 2270P, Case 1 Displacement and Velocity

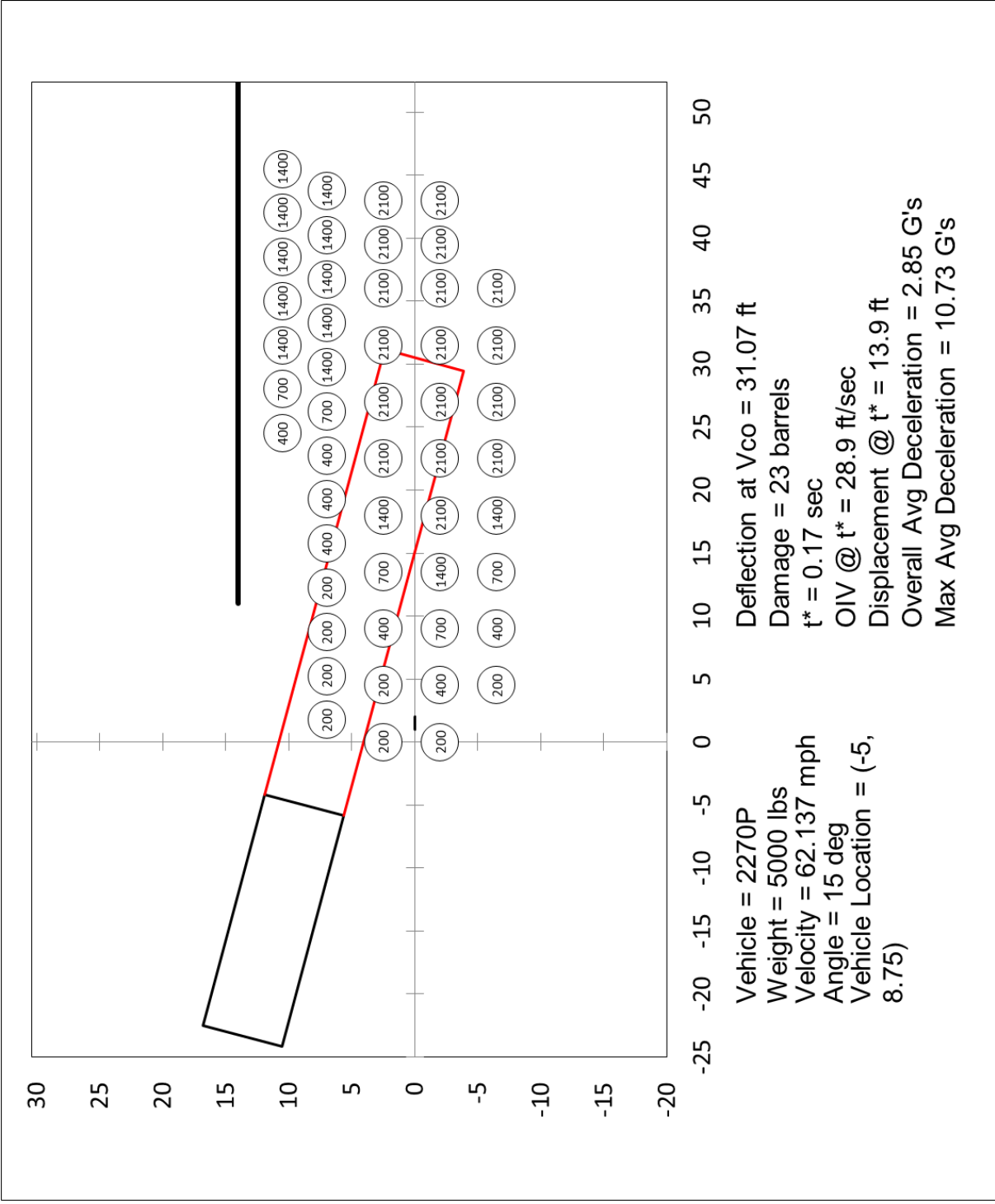


Figure G-42. Mixed-Spacing Sand Barrel Array, 2270P, Case 2 Summary

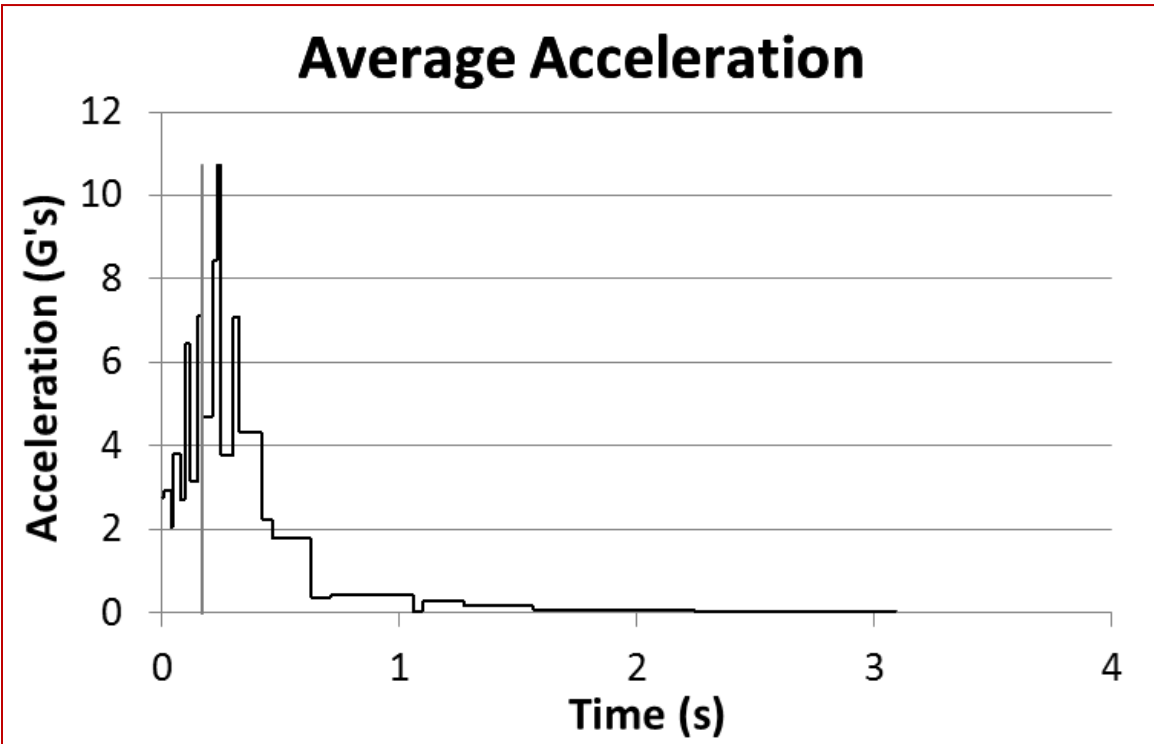
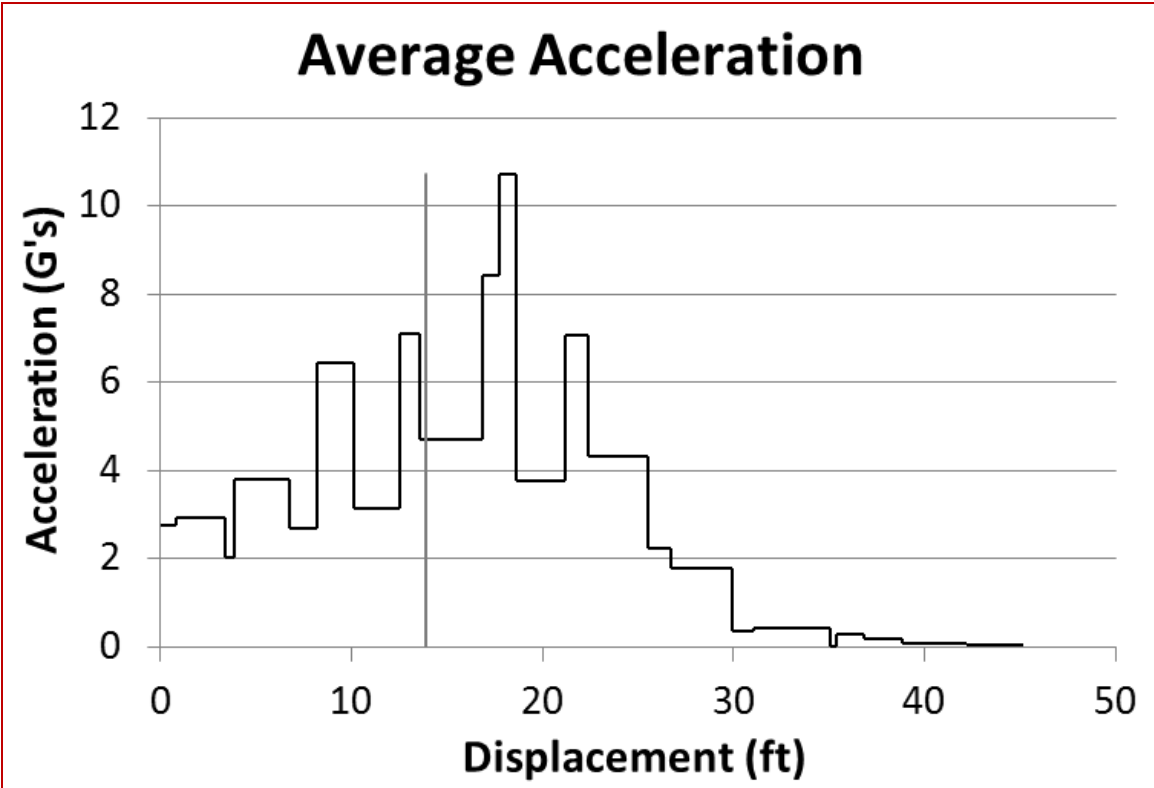


Figure G-43. Mixed-Spacing Sand Barrel Array, 2270P, Case 2 Acceleration

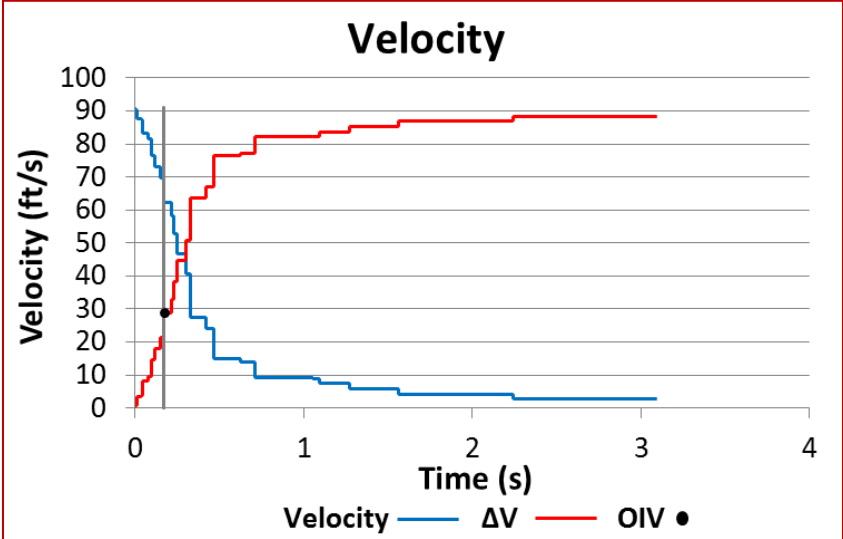
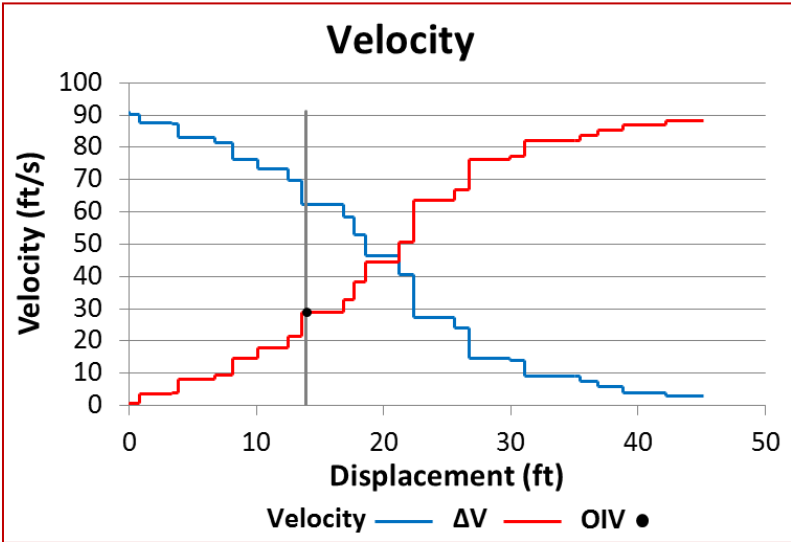
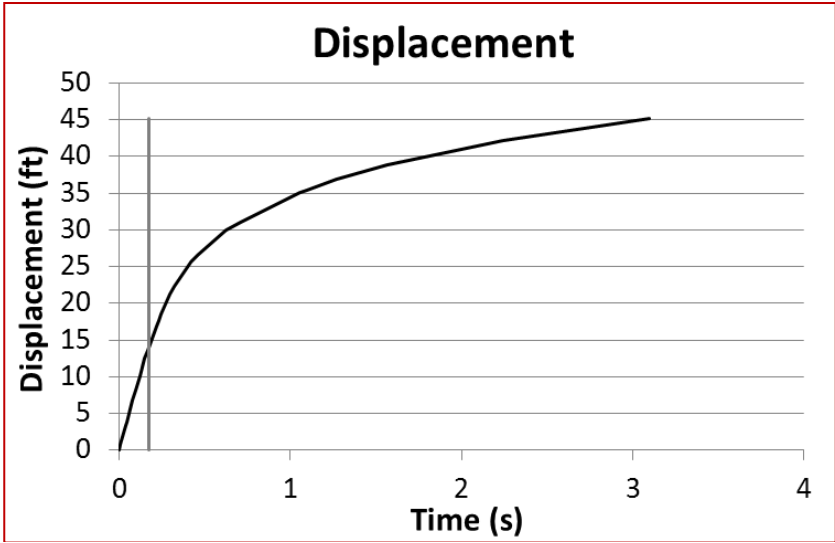


Figure G-44. Mixed-Spacing Sand Barrel Array, 2270P, Case 2 Displacement and Velocity

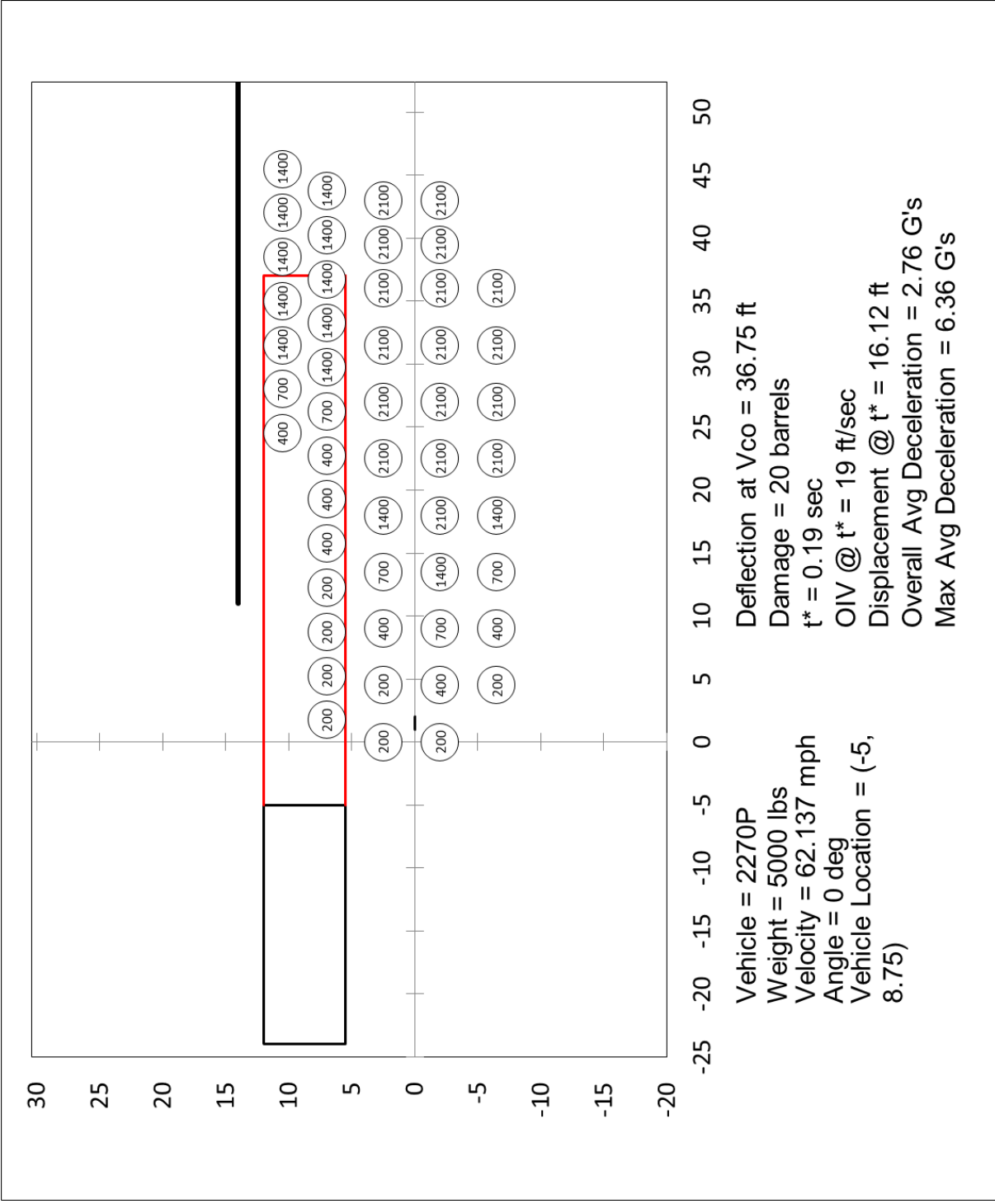


Figure G-45. Mixed-Spacing Sand Barrel Array, 2270P, Case 3 Summary

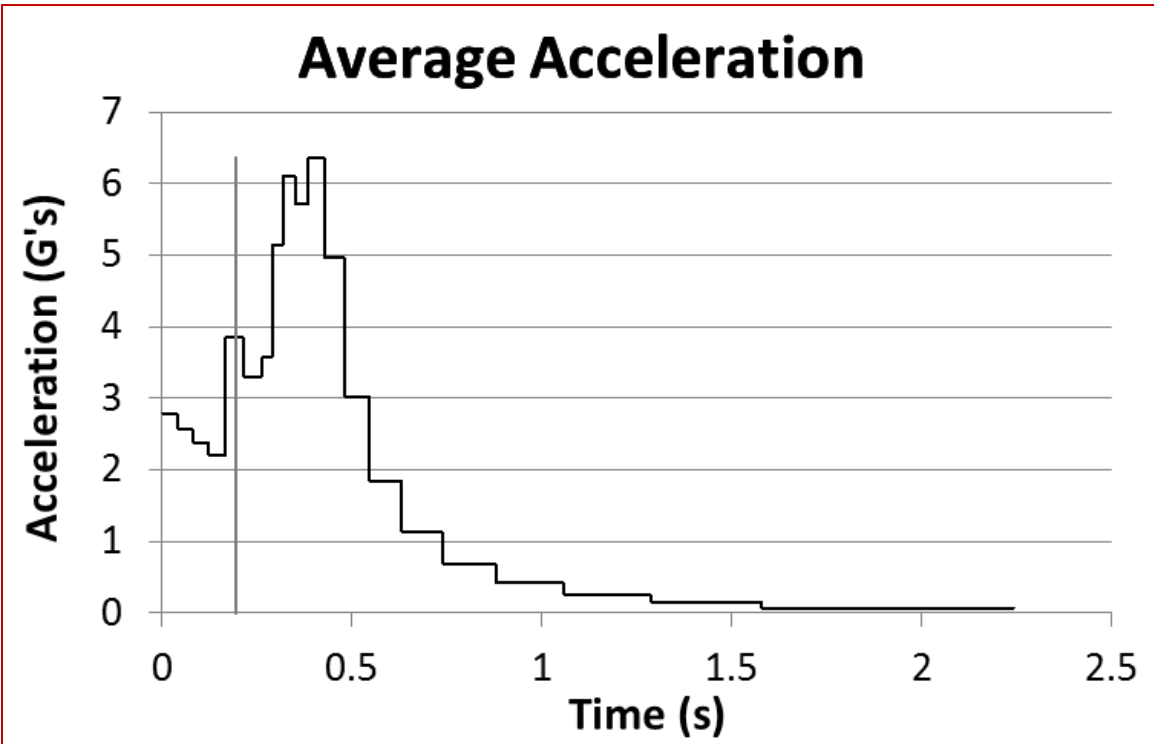
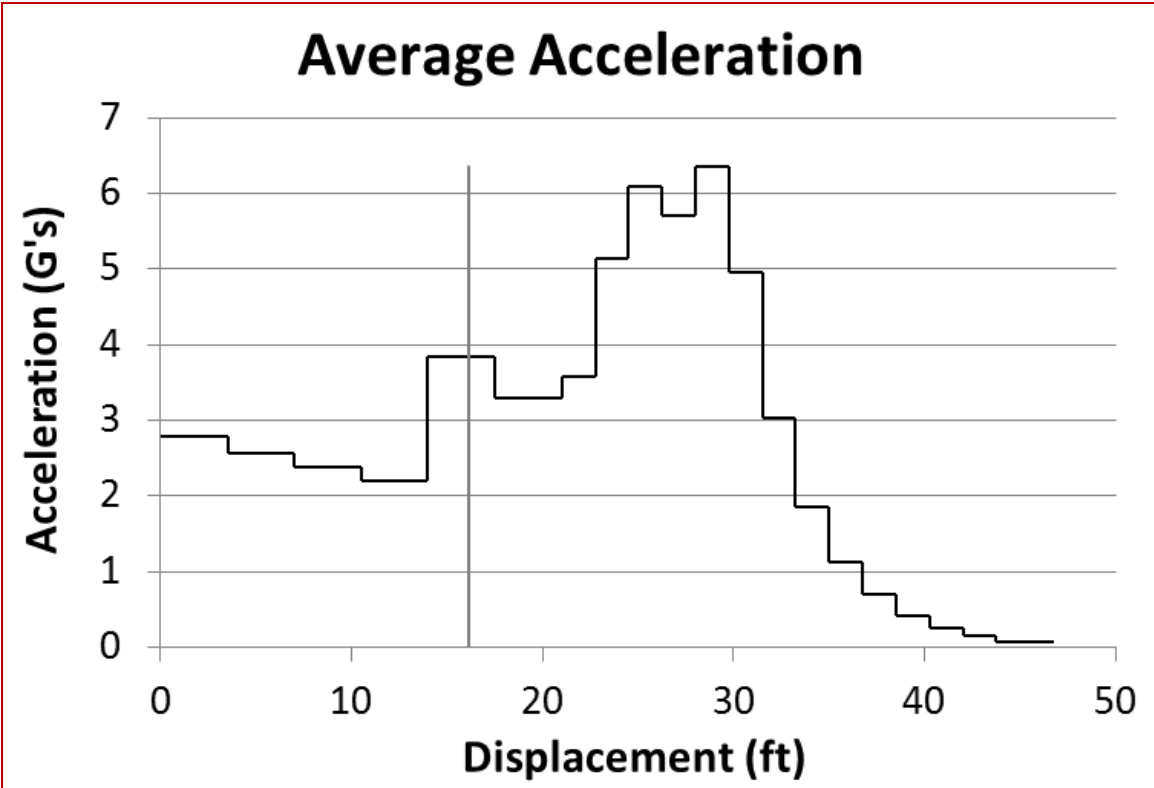


Figure G-46. Mixed-Spacing Sand Barrel Array, 2270P, Case 3 Acceleration

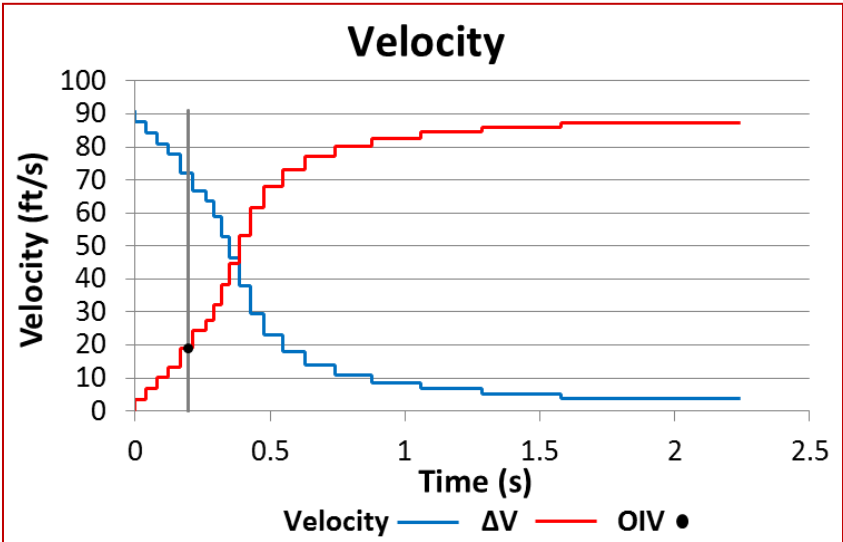
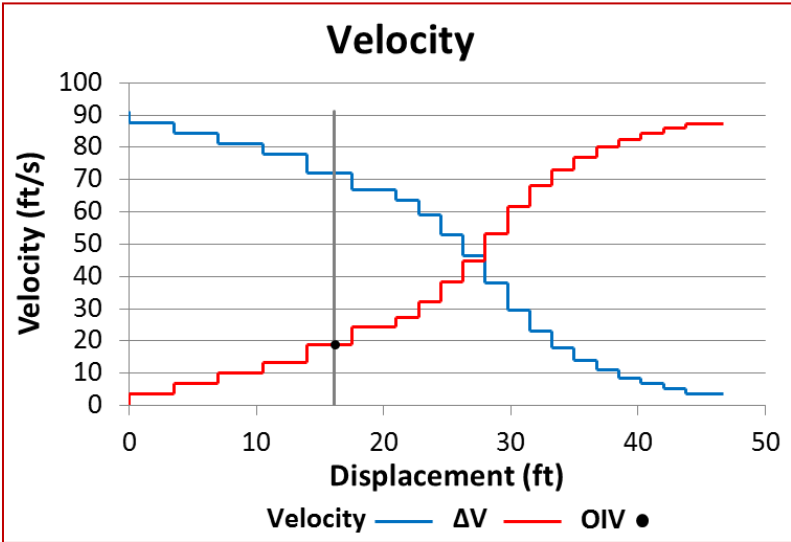
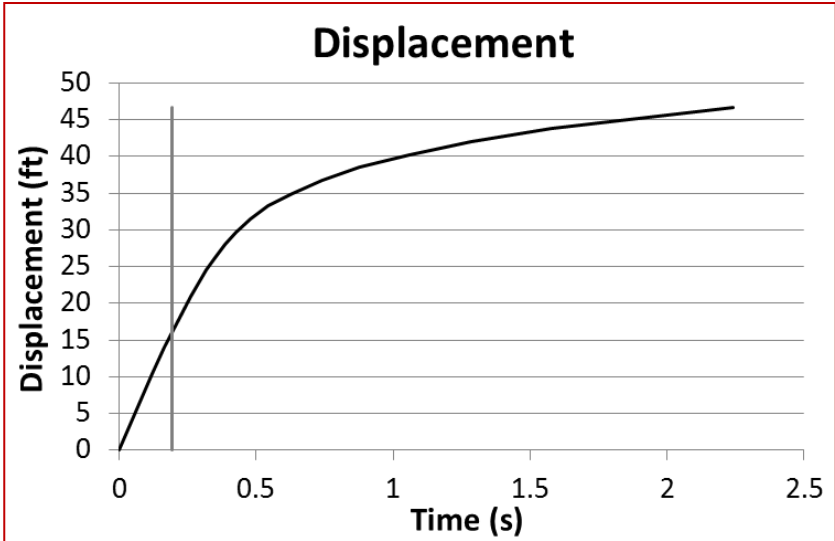


Figure G-47. Mixed-Spacing Sand Barrel Array, 2270P, Case 3 Displacement and Velocity

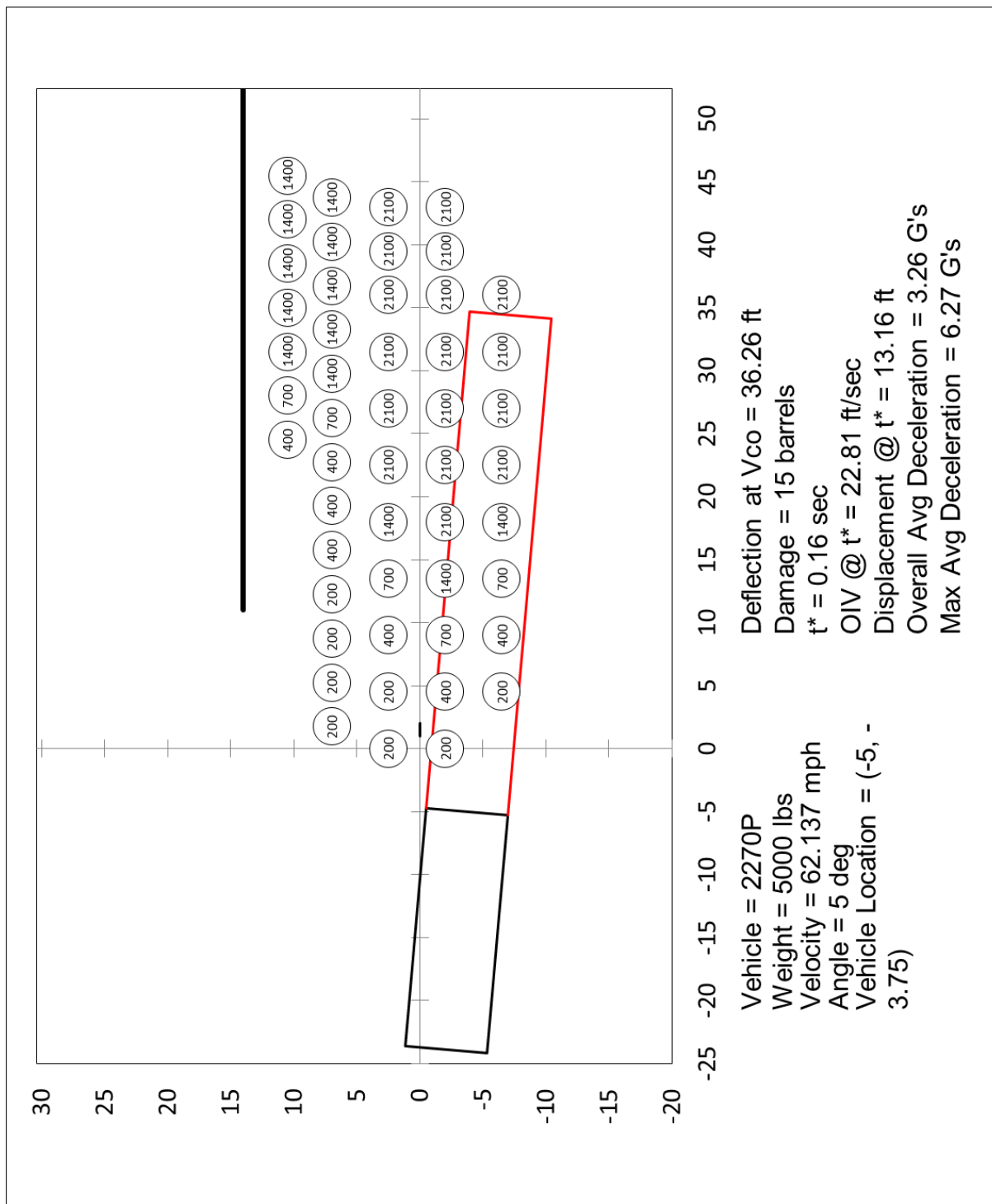


Figure G-48. Mixed-Spacing Sand Barrel Array, 2270P, Case 4 Summary

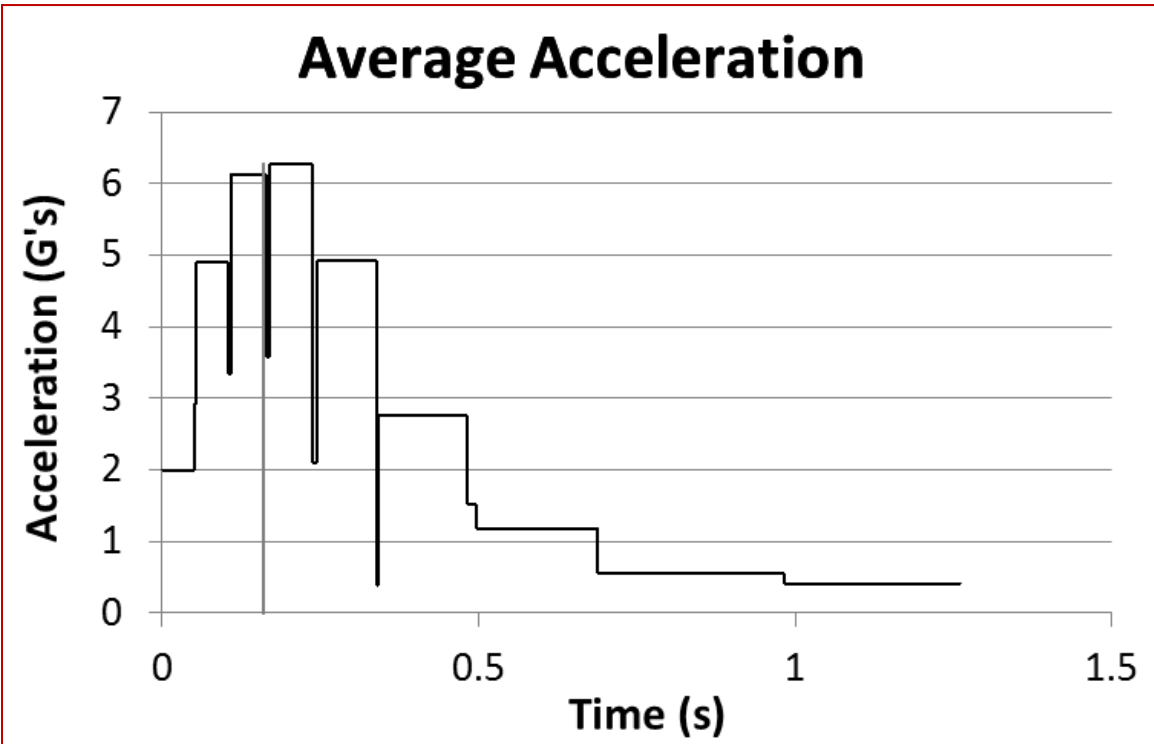
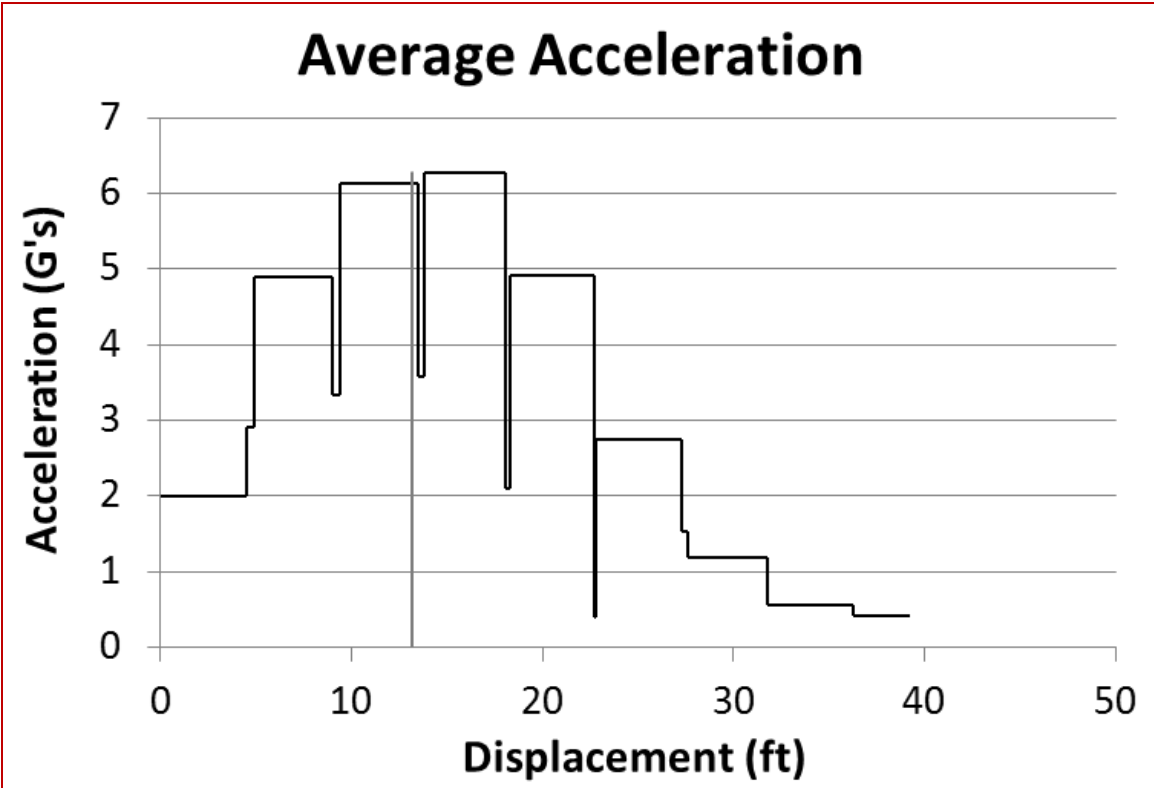


Figure G-49. Mixed-Spacing Sand Barrel Array, 2270P, Case 4 Acceleration

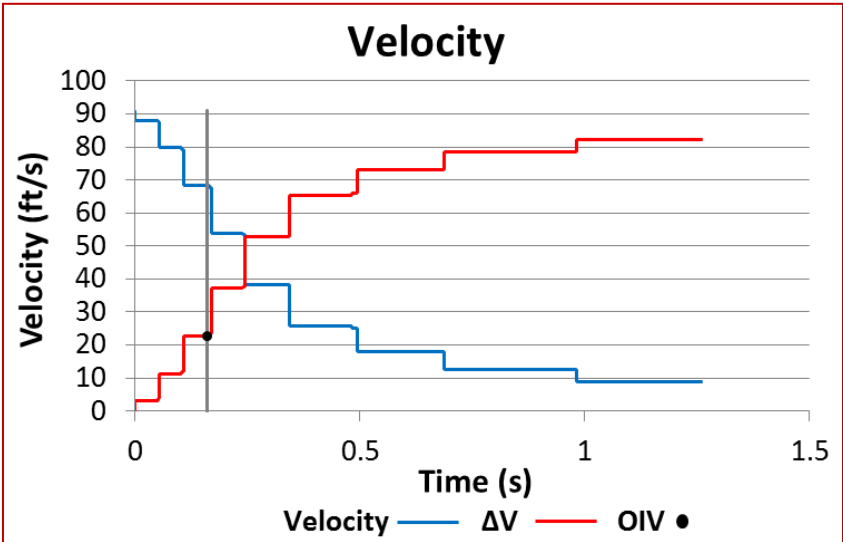
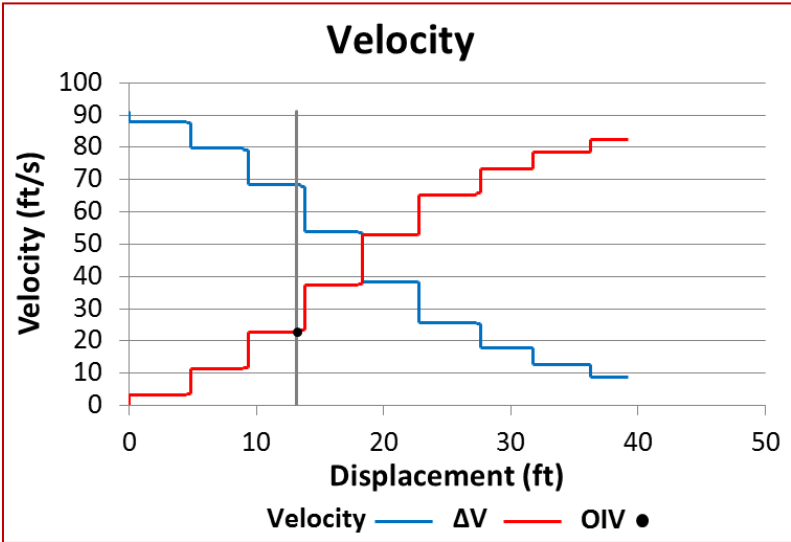
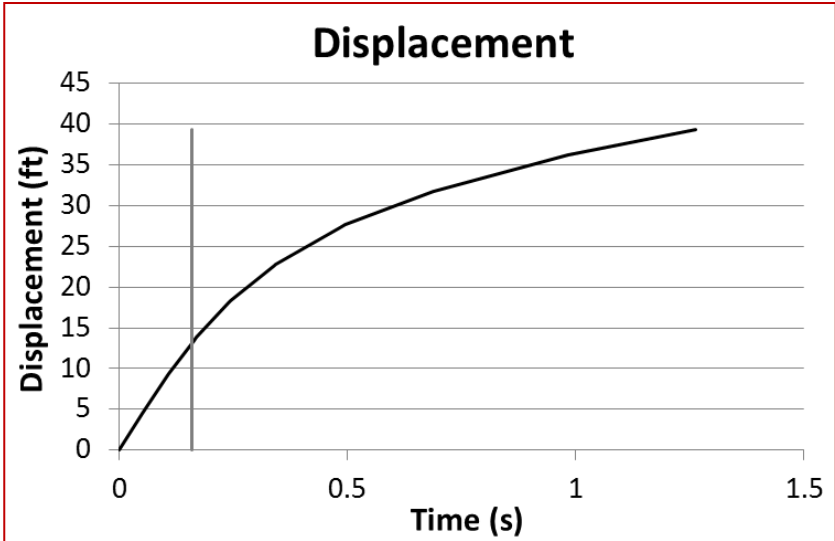


Figure G-50. Mixed-Spacing Sand Barrel Array, 2270P, Case 4 Displacement and Velocity

V0	62.173	mph
	91.187	ft/s
g	32.174	ft/s^2
Mv	5000	lb
F_Stage1	10960	lb
F_Stage2	10960	lb
a_Stage1	70.53	ft/s^2
	2.19	g's
a_Stage2	70.53	ft/s^2
	2.19	g's
T	13500	lbf
L	17	ft
X_max	40.1250	ft

n	Me	x	x'	Vn	Vn'	t (n to n')	a_et	a_net	a_tot
					91.19				
1	0.00	0.0	21.1	91.19	73.04	0.25726	2.19193	0.00000	2.19193
2	0.00	21.1	22.1	73.04	72.74	0.01378	2.19193	0.63094	2.82287
3	0.00	22.1	23.1	72.74	71.91	0.01384	2.19193	1.23681	3.42874
4	0.00	23.1	24.1	71.91	70.65	0.01400	2.19193	1.79723	3.98916
5	0.00	24.1	25.1	70.65	69.04	0.01426	2.19193	2.29930	4.49123
6	0.00	25.1	26.1	69.04	67.16	0.01459	2.19193	2.73791	4.92984
7	0.00	26.1	27.1	67.16	65.05	0.01501	2.19193	3.11409	5.30602
8	0.00	27.1	28.1	65.05	62.74	0.01550	2.19193	3.43282	5.62475
9	0.00	28.1	29.1	62.74	60.24	0.01609	2.19193	3.70097	5.89290
10	0.00	29.1	30.1	60.24	57.57	0.01676	2.19193	3.92587	6.11780
11	0.00	30.1	31.1	57.57	54.71	0.01756	2.19193	4.11447	6.30640
12	0.00	31.1	32.1	54.71	51.64	0.01850	2.19193	4.27294	6.46487
13	0.00	32.1	33.1	51.64	48.33	0.01963	2.19193	4.40653	6.59846
14	0.00	33.1	34.1	48.33	44.75	0.02101	2.19193	4.51964	6.71157
15	0.00	34.1	35.1	44.75	40.83	0.02275	2.19193	4.61585	6.80778
16	0.00	35.1	36.1	40.83	36.46	0.02503	2.19193	4.69812	6.89005
17	0.00	36.1	37.1	36.46	31.46	0.02820	2.19193	4.76882	6.96075
18	0.00	37.1	38.1	31.46	25.47	0.03301	2.19193	4.82991	7.02184
19	0.00	38.1	39.1	25.47	17.51	0.04167	2.19193	4.88294	7.07487
20	0.00	39.1	40.1	17.51	0.00	0.06583	2.19193	4.92922	7.12115
21	0.00	40.1	40.1	0.00	0.00	0.00000	0.00000	0.00000	0.00000
22	0.00	41.1	40.1	0.00	0.00	0.00000	0.00000	0.00000	0.00000

Figure G-51. Combined Net Arrestor and Bullnose Impact, 2270 Truck, Full Bullnose Crush

Force

V0	62.173	mph
	91.187	ft/s
g	32.174	ft/s ²
Mv	5000	lb
F_Stage1	8220	lb
F_Stage2	8220	lb
a_Stage1	52.89	ft/s ²
	1.64	g's
a_Stage2	52.89	ft/s ²
	1.64	g's
T	13500	lbf
L	17	ft
X_max	42.1250	ft

n	Me	x	x'	Vn	Vn'	t (n to n')	a_et	a_net	a_tot
					91.19				
1	0.00	0.0	21.1	91.19	77.98	0.24976	1.64395	0.00000	1.64395
2	0.00	21.1	22.1	77.98	77.70	0.01288	1.64395	0.63094	2.27489
3	0.00	22.1	23.1	77.70	76.93	0.01293	1.64395	1.23681	2.88076
4	0.00	23.1	24.1	76.93	75.76	0.01306	1.64395	1.79723	3.44118
5	0.00	24.1	25.1	75.76	74.27	0.01326	1.64395	2.29930	3.94325
6	0.00	25.1	26.1	74.27	72.53	0.01353	1.64395	2.73791	4.38186
7	0.00	26.1	27.1	72.53	70.59	0.01386	1.64395	3.11409	4.75804
8	0.00	27.1	28.1	70.59	68.47	0.01424	1.64395	3.43282	5.07677
9	0.00	28.1	29.1	68.47	66.20	0.01469	1.64395	3.70097	5.34492
10	0.00	29.1	30.1	66.20	63.79	0.01520	1.64395	3.92587	5.56982
11	0.00	30.1	31.1	63.79	61.23	0.01578	1.64395	4.11447	5.75842
12	0.00	31.1	32.1	61.23	58.51	0.01645	1.64395	4.27294	5.91689
13	0.00	32.1	33.1	58.51	55.62	0.01723	1.64395	4.40653	6.05048
14	0.00	33.1	34.1	55.62	52.55	0.01813	1.64395	4.51964	6.16358
15	0.00	34.1	35.1	52.55	49.27	0.01921	1.64395	4.61585	6.25980
16	0.00	35.1	36.1	49.27	45.72	0.02052	1.64395	4.69812	6.34207
17	0.00	36.1	37.1	45.72	41.86	0.02216	1.64395	4.76882	6.41277
18	0.00	37.1	38.1	41.86	37.58	0.02426	1.64395	4.82991	6.47385
19	0.00	38.1	39.1	37.58	32.73	0.02713	1.64395	4.88294	6.52689
20	0.00	39.1	40.1	32.73	27.01	0.03135	1.64395	4.92922	6.57317
21	0.00	40.1	41.1	27.01	19.66	0.03848	1.64395	4.96979	6.61373
22	0.00	41.1	42.1	19.66	0.00	0.05492	1.64395	5.00551	6.64946

Figure G-52. Combined Net Arrestor and Bullnose Impact, 2270 Truck, 75 Percent Bullnose

Crush Force

V0	62.173	mph
	91.187	ft/s
g	32.174	ft/s ²
Mv	2425	lb
F_Stage1	10960	lb
F_Stage2	10960	lb
a_Stage1	145.41	ft/s ²
	4.52	g's
a_Stage2	145.41	ft/s ²
	4.52	g's
T	13500	lbf
L	17	ft
X_max	27.1250	ft

n	Me	x	x'	Vn	Vn'	t (n to n')	a_et	a_net	a_tot
					91.19				
1	0.00	0.0	21.1	91.19	46.60	0.30664	4.51944	0.00000	4.51944
2	0.00	21.1	22.1	46.60	45.60	0.02223	4.51944	1.30091	5.82036
3	0.00	22.1	23.1	45.60	42.81	0.02276	4.51944	2.55013	7.06957
4	0.00	23.1	24.1	42.81	38.24	0.02437	4.51944	3.70563	8.22507
5	0.00	24.1	25.1	38.24	31.60	0.02760	4.51944	4.74083	9.26028
6	0.00	25.1	26.1	31.60	21.67	0.03436	4.51944	5.64517	10.16462
7	0.00	26.1	27.1	21.67	0.00	0.05708	4.51944	6.42080	10.94025
8	0.00	27.1	27.1	0.00	0.00	0.00000	0.00000	0.00000	0.00000
9	0.00	28.1	27.1	0.00	0.00	0.00000	0.00000	0.00000	0.00000
10	0.00	29.1	27.1	0.00	0.00	0.00000	0.00000	0.00000	0.00000
11	0.00	30.1	27.1	0.00	0.00	0.00000	0.00000	0.00000	0.00000
12	0.00	31.1	27.1	0.00	0.00	0.00000	0.00000	0.00000	0.00000

Figure G-53. Combined Net Arrestor and Bullnose Impact, 1100C Small Car, Full Bullnose

Crush Force

V0	62.173	mph
	91.187	ft/s
g	32.174	ft/s ²
Mv	2425	lb
F_Stage1	8220	lb
F_Stage2	8220	lb
a_Stage1	109.06	ft/s ²
	3.39	g's
a_Stage2	109.06	ft/s ²
	3.39	g's
T	13500	lbf
L	17	ft
X_max	29.1250	ft

n	Me	x	x'	Vn	Vn'	t (n to n')	a_et	a_net	a_tot
					91.19				
1	0.00	0.0	21.1	91.19	60.89	0.27782	3.38958	0.00000	3.38958
2	0.00	21.1	22.1	60.89	60.14	0.01667	3.38958	1.30091	4.69049
3	0.00	22.1	23.1	60.14	58.08	0.01689	3.38958	2.55013	5.93971
4	0.00	23.1	24.1	58.08	54.82	0.01750	3.38958	3.70563	7.09521
5	0.00	24.1	25.1	54.82	50.43	0.01859	3.38958	4.74083	8.13041
6	0.00	25.1	26.1	50.43	44.91	0.02027	3.38958	5.64517	9.03475
7	0.00	26.1	27.1	44.91	38.00	0.02290	3.38958	6.42080	9.81038
8	0.00	27.1	28.1	38.00	28.94	0.02740	3.38958	7.07798	10.46756
9	0.00	28.1	29.1	28.94	0.00	0.03715	3.38958	7.63086	11.02045
10	0.00	29.1	29.1	0.00	0.00	0.00000	0.00000	0.00000	0.00000
11	0.00	30.1	29.1	0.00	0.00	0.00000	0.00000	0.00000	0.00000
12	0.00	31.1	29.1	0.00	0.00	0.00000	0.00000	0.00000	0.00000

Figure G-54. Combined Net Arrestor and Bullnose Impact, 1100C Small Car, 75 Percent

Bullnose Crush Force

V0	62.173	mph
	91.187	ft/s
g	32.174	ft/s^2
Mv	5000	lb
F_Stage1	10960	lb
F_Stage2	10960	lb
a_Stage1	70.53	ft/s^2
	2.19	g's
a_Stage2	70.53	ft/s^2
	2.19	g's
X_max	32.5773	ft

Rank [n]	Object	Mass (lb)	x (ft)
1	head	0	0
1	Stage2	0	0
2	1	400	21.125
3	2	1400	24.625
4	3	2800	28.125
5	4	2800	31.625
6	5	2800	35.125
7	6	2800	38.625

n	Me	x	x'	Vn	Vn'	t (n to n')	a_avg	a_et	a_tot
									91.19
1	0.00	0.0	21.1	91.19	73.04	0.25726	0.00000	2.19193	2.19193
2	400.00	21.1	24.6	67.63	63.88	0.05323	3.94277	2.19193	6.13470
3	1400.00	24.6	28.1	49.91	44.69	0.07400	8.23610	2.19193	10.42803
4	2800.00	28.1	31.6	28.65	18.08	0.14981	6.09345	2.19193	8.28538
5	2800.00	31.6	32.6	11.59	0.00	0.16433	0.99744	2.19193	3.18937
6	2800.00	35.1	32.6	0.00	0.00	0.00000	0.00000	0.00000	0.00000
7	2800.00	38.6	32.6	0.00	0.00	0.00000	0.00000	0.00000	0.00000

Figure G-55. Combined Sand Barrel and Bullnose Impact, 2270 Truck, Full Bullnose Crush

Force

V0	62.173	mph
	91.187	ft/s
g	32.174	ft/s^2
Mv	5000	lb
F_Stage1	8220	lb
F_Stage2	8220	lb
a_Stage1	52.89	ft/s^2
	1.64	g's
a_Stage2	52.89	ft/s^2
	1.64	g's
X_max	34.3135	ft

Rank [n]	Object	Mass (lb)	x (ft)
1	head	0	0
1	Stage2	0	0
2	1	400	21.125
3	2	1400	24.625
4	3	2800	28.125
5	4	2800	31.625
6	5	2800	35.125
7	6	2800	38.625

n	Me	x	x'	Vn	Vn'	t (n to n')	a_avg	a_et	a_tot
									91.19
1	0.00	0.0	21.1	91.19	77.98	0.24976	0.00000	1.64395	1.64395
2	400.00	21.1	24.6	72.20	69.59	0.04937	4.49326	1.64395	6.13720
3	1400.00	24.6	28.1	54.37	50.85	0.06653	9.77425	1.64395	11.41820
4	2800.00	28.1	31.6	32.59	26.31	0.11884	7.88940	1.64395	9.53335
5	2800.00	31.6	34.3	16.86	0.00	0.31883	2.11203	1.64395	3.75598
6	2800.00	35.1	34.3	0.00	0.00	0.00000	0.00000	0.00000	0.00000
7	2800.00	38.6	34.3	0.00	0.00	0.00000	0.00000	0.00000	0.00000

Figure G-56. Combined Sand Barrel and Bullnose Impact, 2270 Truck, 75 Percent Bullnose

Crush Force

V0	62.173	mph	Rank [n]	Object	Mass (lb)	x (ft)
	91.187	ft/s				
g	32.174	ft/s^2	1	head	0	0
Mv	2425	lb	1	Stage2	0	0
F_Stage1	10960	lb	2	1	400	21.125
F_Stage2	10960	lb	3	2	1400	24.625
a_Stage1	145.41	ft/s^2	4	3	2800	28.125
	4.52	g's	5	4	2800	31.625
a_Stage2	145.41	ft/s^2	6	5	2800	35.125
	4.52	g's	7	6	2800	38.625
X_max	25.4295	ft				

n	Me	x	x'	Vn	Vn'	t (n to n')	a_avg	a_et	a_tot
						91.19			
1	0.00	0.0	21.1	91.19	46.60	0.30664	0.00000	4.51944	4.51944
2	400.00	21.1	24.6	40.00	24.13	0.10916	2.95969	4.51944	7.47913
3	1400.00	24.6	25.4	15.30	0.00	0.10519	1.80335	4.51944	6.32280
4	2800.00	28.1	25.4	0.00	0.00	0.00000	0.00000	0.00000	0.00000
5	2800.00	31.6	25.4	0.00	0.00	0.00000	0.00000	0.00000	0.00000
6	2800.00	35.1	25.4	0.00	0.00	0.00000	0.00000	0.00000	0.00000
7	2800.00	38.6	25.4	0.00	0.00	0.00000	0.00000	0.00000	0.00000

Figure G-57. Combined Sand Barrel and Bullnose Impact, 1100C Small Car, Full Bullnose

Crush Force

V0	62.173	mph	Rank [n]	Object	Mass (lb)	x (ft)
	91.187	ft/s				
g	32.174	ft/s^2	1	head	0	0
Mv	2425	lb	1	Stage2	0	0
F_Stage1	8220	lb	2	1	400	21.125
F_Stage2	8220	lb	3	2	1400	24.625
a_Stage1	109.06	ft/s^2	4	3	2800	28.125
	3.39	g's	5	4	2800	31.625
a_Stage2	109.06	ft/s^2	6	5	2800	35.125
	3.39	g's	7	6	2800	38.625
X_max	28.1524	ft				

n	Me	x	x'	Vn	Vn'	t (n to n')	a_avg	a_et	a_tot
						91.19			
1	0.00	0.0	21.1	91.19	60.89	0.27782	0.00000	3.38958	3.38958
2	400.00	21.1	24.6	52.27	44.37	0.07244	5.05324	3.38958	8.44282
3	1400.00	24.6	28.1	28.13	5.27	0.20962	6.09786	3.38958	9.48744
4	2800.00	28.1	28.2	2.44	0.00	0.02241	0.11274	3.38958	3.50232
5	2800.00	31.6	28.2	0.00	0.00	0.00000	0.00000	0.00000	0.00000
6	2800.00	35.1	28.2	0.00	0.00	0.00000	0.00000	0.00000	0.00000
7	2800.00	38.6	28.2	0.00	0.00	0.00000	0.00000	0.00000	0.00000

Figure G-58. Combined Sand Barrel and Bullnose Impact, 1100C Small Car, 75 Percent

Bullnose Crush Force

END OF DOCUMENT